JAERI-Conf
99-002

INDC(JPN)-182/U

JP9950303

PROCEEDINGS OF THE 1998 SYMPOSIUM ON NUCLEAR DATA NOVEMBER 19-20, 1998, JAERI, TOKAI, JAPAN

March 1999

(Eds.) Tadashi YOSHIDA* and Tokio FUKAHORI

日本原子力研究所
Japan Atomic Energy Research Institute

本レポートは，日本原子力研究所が不定期に公刊している研究報告書です。
入手の問合わせは，日本原子力研究所研究情報部研究情報課（〒319-1195　茨城県那珂郡東海村）あて，お申し越しください。なお，このほかに財団法人原子力弘済会資料センター（〒319-1195　茨城県那珂郡東海村日本原子力研究所内）で複写による実費頒布をおこなっております。

This report is issued irregularly.
Inquiries about availability of the reports should be addressed to Research Information Division, Department of Intellectual Resources, Japan Atomic Energy Research Institute, Tokai-mura, Naka-gun, Ibaraki-ken, 319-1195, Japan.

編集兼発行　　日本原子力研究所

JAERI-Conf 99-002 INDC(JPN)-182/U

Proceedings of the 1998 Symposium on Nuclear Data
November 19-20, 1998, JAERI, Tokai, Japan

(Eds.) Tadashi YOSHIDA* and Tokio FUKAHORI

Japanese Nuclear Data Committee
Tokai Research Establishment
Japan Atomic Energy Research Institute
Tokai-mura, Naka-gun, Ibaraki-ken

(Received January 28, 1999)

The 1998 Symposium on Nuclear Data was held at Tokai Research Establishment, Japan Atomic Energy Research Institute (JAERI), on 19th and 20th of November 1998. Japanese Nuclear Data Committee and Nuclear Data Center, JAERI organized this symposium. In the oral sessions, presented were 15 papers on accelerator facilities, astrophysics and nuclear data, international session, radiation damage study and nuclear data, and integral test of nuclear data. In the poster session, presented were 36 papers concerning experiments, evaluations, benchmark tests and on-line database on nuclear data. Those presented papers are compiled in this proceedings.

Keywords: Nuclear Data, Symposium, Proceedings, Nuclear Reaction, JENDL, Experiment, Evaluation, Benchmark Test, Cross Section

*Musashi Institute of Technology

1998年核データ研究会報文集
1998年11月19日～20日，東海研究所，東海村

日本原子力研究所東海研究所
シグマ研究委員会
（編）吉田　正*・深堀　智生

(1999年1月28日受理)

1998年核データ研究会が、1998年11月19日と20日の両日、日本原子力研究所東海研究所において開催された。この研究会は、日本原子力研究所のシグマ研究委員会と核データセンターが主催して開いたものである。口頭発表では、加速器施設、宇宙核物理と核データ、国際セッション、照射損傷研究と核データ、核データの積分テストについての15件の報告があった。ポスター発表では、36件の発表があり、それらは、核データの測定、評価や評価済核データのベンチマークテスト、オンラインデータベース等に関するものであった。本報文集は、それらの論文をまとめたものである。

東海研究所：〒319-1195 茨城県那珂郡東海村白方白根2-4
* 武蔵工業大学

Program Committee

Tadashi YOSHIDA(Chairman)	Musashi Institute of Technology
Takeo ARUGA	Japan Atomic Energy Research Institute
Tokio FUKAHORI	Japan Atomic Energy Research Institute
Hidero HARADA	Japan Nuclear Cycle Development Institute
Masayuki IGASHIRA	Tokyo Institute of Technology
Jun-ichi KATAKURA	Japan Atomic Energy Research Institute
Norio KISHIDA	Japan Atomic Energy Research Institute
Takaaki OHSAWA	Kinki University
Kazuhiro OYAMATSU	Nagoya University
Makoto SASAKI	Mitsubishi Heavy Industries, Ltd.
Teiko TAKADA	Japan Atomic Energy Research Institute
Atsushi ZUKERAN	Hitachi, Ltd.

プログラム委員会

吉田　　正（委員長）	武蔵工業大学
有賀　　武夫	日本原子力研究所
深堀　　智生	日本原子力研究所
原田　　秀郎	核燃料サイクル開発機構
井頭　　政之	東京工業大学
片倉　　純一	日本原子力研究所
岸田　　則生	日本原子力研究所
大澤　　孝明	近畿大学
親松　　和浩	名古屋大学
佐々木　　誠	三菱重工業（株）
高田　　禎子	日本原子力研究所
瑞慶覧　　篤	（株）日立製作所

This is a blank page.

Contents

目 次

This is a blank page.

1. Introduction

The 1998 symposium on nuclear data was held at Tokai Research Establishment, Japan Atomic Energy Research Institute (JAERI), on 19th and 20th of November 1998, with about 170 participants. Japanese Nuclear Data Committee and Nuclear Data Center, JAERI organized the symposium.

The program of the symposium is listed below. In the oral sessions, total 15 papers were presented on accelerator facilities, astrophysics and nuclear data, international collaboration, radiation damage study and nuclear data, and integral tests of nuclear data. In the poster session, presented were 36 papers concerning nuclear data experiments, evaluations, benchmark tests, on-line database on nuclear data, etc. Those papers are compiled in this proceedings.

Program

Oral Presentation [Talk + Discussion (min.)]

Nov. 19 (Thu.)

9:50-10:00

Session 1: Opening Address M. Nakagawa (JAERI)

10:00-12:00

Session 2: Accelerator Facilities Chairman: M. Igashira (TIT)

- Accelerator Applications and Nuclear Data -

2.1 Accelerator for Atomic Energy Research [25+5]
T. Shibata (KEK)

2.2 Progress of Neutron Science Project [25+5] Y. Oyama (JAERI)

2.3 The Present Status of Medical Application of Particle Accelerator
—Started Construction of a New Medically Dedicated Proton Accelerator Facility in Tsukuba — [25+5] T. Sakae (Tsukuba Univ.)

2.4 Accelerator Conceptual Design and Needs of Nuclear Data for Boron Neutron Capture Therapy [25+5] M. Sasaki (MHI)

12:00-14:00

Poster Session 1 (Odd Number) + Lunch

14:00-15:30

Session 3: Astrophysics and Nuclear Data Chairman: K. Oyamatsu (Nagoya Univ.)

3.1 Recent Development in Nuclear Astrophysics and the Nuclear Data [35+10]
S. Kubono (CNS)

3.2 Neutron Capture Cross Sections in keV-energy Region [35+10]
M. Igashira (TIT)

15:30-16:00 Coffee Break

16:00-17:50

Session 4: International Session Chairman: A. Hasegawa (JAERI)

4.1 Nuclear Data Needs in Thailand [25+5] S. Chongkum (OAEP)

4.2 Nuclear Power Development and Nuclear Data Activities in Malaysia [25+5]
G.A. Auu (MINT)

4.3 The Status Report on the Nuclear Data Project in Korea [25+5]
G.Kim (PAL)

18:00-20:00 RECEPTION at Akogi-ga-ura Club

Nov. 20 (Fri.)

9:30-10:50

Session 5: Radiation Damage Study and Nuclear Data
Chairman: M. Kawai(KEK)

5.1 Nuclear Data for Analyses of Radiation Damage Process [30+10]
T. Aruga (JAERI)

5.2 Nuclear Heating in Fusion Reactors [30+10] K. Maki (Hitachi)

10:50-11:10 Coffee Break

11:10-11:50

5.3 Problems in Damage Estimation Caused by High Energy Particles [30+10]
N. Watanabe (JAERI)

12:00-14:00

Poster Session 2 (Even Number) + Lunch

14:00-16:00

Session 6: Integral Test of Nuclear Data Chairman: A. Zukeran (Hitachi)

6.1 The MOX Core Critical Experiments for LWR's and the Analysis Based on JENDL-3.2 [30+10] T. Umano (Toshiba)

6.2 Measurement and Analysis of Decay Heat of Fast Reactor Spent Fuel [30+10] T. Aoyama (JNC)

6.3 Status and Future Program of Reactor Physics Experiments in JAERI Critical Facilities, FCA and TCA [30+10] S. Okajima (JAERI)

16:00-16:20

Session 7: Summary Talk N. Yamano (SAE)

Poster Session

Nov. 19 (Thu.) 12:00-14:00 (Odd Number), and Nov. 20 (Fri.) 12:00-14:00 (Even Number)

<Lobby of Auditorium>

P.1 Measurements of Double-Differential Neutron Emission Cross Sections of U-238, Th-232 for 2.6 and 3.5 MeV Neutrons T. Miura (Tohoku Univ.)

P.2 Measurement of Capture Cross Sections for Dy and Hf in the Energy Region from 0.003 to 10 eV Hyun-Je Cho (Kyoto Univ.)

P.3 Measurement of Fission Cross Section of Pa-231 using Lead Slowing-down Spectrometer K. Kobayashi (KUR)

P.4 Key Precursor Data in Aggregate Delayed-neutron Calculations T. Sanami (Nagoya Univ.)

P.5 Decay Heat Calculation for Minor Actinides in the Hybrid Method H. Takeuchi (Nagoya Univ.)

P.6 Application of Multimodal Fission Model to Nuclear Data Evaluation T. Ohsawa (Kinki Univ.)

P.7 Systematics of Average Radiative Width of Heavy Nuclide T. Murata (Aitel)

P.9 Comparison of BFS-73-1 Benchmark Test using JENDL-3.2, JEF-2.2 and ENDF/B-VI.3 Jung-Do Kim (KAERI)

P.12 Measurements of Secondary Particles Producted from Thick Targets Bombarded by Heavy Ions T. Kurosawa (Tohoku Univ.)

This is a blank page.

2. Papers Presented at Oral Sessions

This is a blank page.

JP9950304

2.1 Accelerators for Atomic Energy Research

Tokushi Shibata
Radiation Science Center
High Energy Accelerator Research Organization
1-1 Oho, Tsukuba, Ibaraki 305-0801
e-mail: tokushi.shibata@kek.jp

The research and educational activities accomplished using accelerators for atomic energy research were studied. The studied items are research subjects, facility operation, the number of master theses and doctor theses on atomic energy research using accelerators and the future role of accelerators in atomic energy research. The strategy for promotion of the accelerator facility for atomic energy research is discussed.

1. Introduction

Many research groups for atomic energy research in universities and institutes have used various accelerators. The research and educational activities accomplished using accelerators in the atomic energy research field were studied. The studied items are research subjects, facility operation, the number of master theses and doctor theses on atomic energy research using accelerators, and the future role of accelerators in atomic energy research.

The studies were carried out in cooperation with following facilities:
(1) Faculty of Engineering, Hokkaido University: 45 MeV electron LINAC,
(2) School of Engineering, Tohoku University: 4.5 MeV Dynamitron,
(3) JNC, O-arai Engineering Center: high power electron LINAC
(4) JAERI, Takasaki: 90 MeV Cyclotron
(5) Nuclear Engineering Research Laboratory, Univ. of Tokyo: 35 MeV LINAC,
(6) Research Lab. for Nuclear Reactors, Tokyo Institute of Technology: Pelletron,
(7) Research Reactor Institute, Kyoto University: 46 MeV electron LINAC and CW
(8) Faculty of Engineering, Osaka University: OCTAVIAN.

2. Subjects studied using accelerators

The main subjects at each facility are given in the following.

(1) Faculty of Engineering, Hokkaido University: 45 MeV electron LINAC:
Development of cold neutron sources, Pulse radiolysis, Generation and application of radiation, and Accelerator engineering.

(2) School of Engineering, Tohoku University, 4.5 MeV Dynamitron:
Nuclear data related to fast reactor, fusion reactor and new type reactor, Hydrogen behavior in material, Impact by ion beam, PIXE, Application of ion beam for medical, biological and environment research, and Educational activity for citizen and young students.

(3) JNC, O-arai Engineering Center, high power electron LINAC:
Feasibility study of a high-current electron LINAC for transmutation of nuclear waste.

(4) JAERI, Takasaki, 90 MeV Cyclotron:
Study of radiation resistance of material and apparatuses, Nuclear data for accelerator shielding, Production of radioisotope, Radiation effects, and Basic technology of accelerator and beam handling.

(5) Nuclear Engineering Research Laboratory, Univ. of Tokyo, 35 MeV LINAC:
Generation and measurements of ultra short electron beam pulse, Pulse radiolysis, Generation and application of positron beam, Free electron laser, and Acceleration using wake field generated by laser.

(6) Research Lab. for Nuclear Reactors, Tokyo Institute of Technology, Pelletron:
Data of neutron induced reactions, Nuclear reaction model and observable for evaluation of neutron data, and Study of collision between ion beam and atoms or molecules.

(7) Research Reactor Institute, Kyoto University, 46 MeV electron LINAC and C.W.:
Reactor physics through neutron production and transportation, Compilation of neutron cross section, Application of electron beam for irradiation, Production of positron, Generation of synchrotron radiation, Production of radioisotope, Parametric X-ray, Criticality of the sub-critical reactor, and Neutron transportation in a thorium system.

(8) Faculty of Engineering, Osaka University, OCTAVIAN:
Double differential cross section of neutron reactions, Integral experiment of neutron engineering for a D-T reactor, Radiation damage of material, Radiation transportation, Neutron effects in space, and Application of ion beam.

3. Operation of accelerator

The operation status, the number of subjects, and the number of collaborative subjects with outside groups at each facility are shown in table 1. The operation of accelerators is mostly more than 100 days per year.

Table 1 Operation status of accelerator

Facility	Operation	No. of subjects	No. of subjects in collaboration with outside group
Hokkaido Univ.	240 d	13	3
FNL Tohoku Univ.	150 d	11	7
Univ. of Tokyo	191 d	8	2
Tokyo Tech. Insti.	115 d	10	1~2
LINAC of KUR	1800 h	12	All
C.W. of KUR	30 d	1~2	All
OCTAVIAN	240 d	23	4

4. Research by graduate students

The number of graduate students who got Master thesis and Doctor thesis are shown in table 2.

Table 2 Number of Master and Doctor thesis

Facility	Master degree	Doctor degree
Hokkaido Univ.	143	7
FNL Tohoku Univ.	89	11
Univ. of Tokyo	33	13
Tokyo Tech. Insti.	80	6
LINAC of KUR	67	18
C.W. of KUR	3	0
OCTAVIAN	150	9

5. Future plan at each facility

The future plan for each facility is as follows:

(1) JAERI, Takasaki, 90 MeV Cyclotron:

High intensity positron beam facility, a few GeV super-conducting cyclotron, and a X-ray irradiation facility using electron accelerator are now discussed.

(2) Nuclear Engineering Research Laboratory, Univ. of Tokyo:
Femto second electron beam facility using radio-frequency acceleration and wake field acceleration generated by a high-power laser is planned.
(3) Research Reactor Institute, Kyoto University:
Replacement of a Cockcroft-Walton accelerator with a medium size accelerator for development of an accelerator driven sub-critical reactor is discussing.
(4) Faculty of Engineering, Osaka University, OCTAVIAN:
Ten times more intense neutron flux facility or multi-function quantum-beam center is now under discussion.

6. The expected role of the accelerator facility for atomic energy research

Various accelerators have been used by many scientists for atomic energy research. Accelerators are expected to play an important role in atomic energy research. Each facility is expecting that accelerators will be used in the following subjects.

(1) Faculty of Engineering, Hokkaido University:
Electron accelerators below 100 MeV will be useful for atomic energy research in universities for usage of neutron beam, application of variable energy X-ray field, and material research in extreme conditions.
(2) School of Engineering, Tohoku University:
Accelerators will be used as an analyzing device for research in environmental, material, medical, and biological fields. Fine beam control in space and time will be important in future use. The advanced measuring method of radiation and research facility for graduate students is also important.
(3) Nuclear Engineering Research Laboratory, Univ. of Tokyo:
Small or medium size accelerators are important for advanced research in atomic energy field at university while the large size accelerators will be used for atomic energy research at national laboratories for transmutation of long-lived nuclear waste and nuclear fuel.
(4) Research Lab. for Nuclear Reactors, Tokyo Institute of Technology:
Nuclear data will be crucial for development of transmutation of nuclear waste using accelerators. Neutron reaction cross sections for neutron rich nuclides are also interesting.
(5) Research Reactor Institute, Kyoto University:
Development of a new neutron source and energy production using accelerator driven sub-critical reactor will be critical issue for atomic energy research.
(6) Faculty of Engineering, Osaka University:

Accelerators will be important as a standard neutron source. Study of interaction of intense pulsed ion beam with various substances is interesting. Low-energy nuclear physics and nuclear data using neutron beam will be important.

7. Future accelerators for atomic energy research

Although large size accelerators will play an important role in national laboratories, various small seize accelerators are useful for atomic energy research in universities. Large size accelerators will be used for transmutation of nuclear waste, energy production by combining accelerators with sub-critical reactors, transmutation of thorium, and neutron sources. The development of high stability and high efficiency accelerators are crucial for these applications.

Various small size accelerators could be used as a specific device for nuclear research and application by various research groups of university. The machine in university should have unique feature such as high resolution of time and space, ultra-short pulse generation and so on.

The most accelerator facilities in universities were built when research groups for atomic energy were founded in universities. Since then these facilities have not had modification for improvement or replacement to an advanced facility. Thus systematic effort to improve the present situation is argent, The future plan of research activity using accelerators should be discussed at organizations related to atomic energy research, such as Liaison Committee for Atomic Engineering, Science Council of Japan, and Atomic Energy Society of Japan. The plan to promote research activity using accelerators for atomic energy obtained through deliberative discussions should be presented at the Atomic Energy Commission.

JP9950305

2.2 PROGRESS OF JAERI NEUTRON SCIENCE PROJECT

Yukio Oyama
Japan Atomic Energy Research Institute
Tokai-mura, Naka-gun, Ibaraki-ken Japan
oyama@fbshp.tokai.jaeri.go.jp

Neutron Science Project was started at Japan Atomic Energy Research Institute since 1996 for promoting futuristic basic science and nuclear technology utilizing neutrons. For this purpose, research and developments of intense proton accelerator and spallation neutron target were initiated. The present paper describes the current status of such research and developments.

I. INTRODUCTION

At the middle of 1970's, JAERI has initiated preliminary study for the partitioning and transmutation of long-lived radio-nuclides which are produced in nuclear power generation. In 1988, the Atomic Energy Commission set the long term partitioning and transmutation R&D program "OMEGA", i.e., Options Making Extra Gain from Actinide and fission products. In the course of discussion on proton accelerator development for the OMEGA project, it was recognized that neutron scattering community desires to have very high neutron source strength, two order of magnitude stronger than that of existing ones. This future source is also discussed in conjunction with continuation of JAERI role as a neutron supplier in future, because JAERI has been one of major neutron suppliers for basic science community in Japan with its research reactor JRR-3M.

Combining requirements of basic and nuclear sciences, JAERI had started the Neutron Science Project in 1996. The Neutron Science Project at JAERI is now preparing a conceptual design for a research complex utilizing spallation neutrons, including a high intensity pulsed and cw spallation neutron source. After completion of accelerator and facility constructions, the project will involve researches, utilizing neutrons, for basic science and technology development of accelerator transmutation of long-lived nuclides associated with nuclear power generation.

II. SCOPE OF NEUTRON SCIENCE PROJECT[1]

The Neutron Science Project aims at pushing researches, utilizing neutrons, for basic science and technology development of accelerator transmutation. The projects includes R&D and construction of an 8 MW (1.5 GeV, 5.3 mA) super-conducting proton linac, a 5 MW target station with compression storage rings to allow short neutron pulses for neutron scattering research, and research facilities for transmutation engineering, neutron physics, material irradiation, medical isotopes production, spallation RI beam production for exotic nuclei investigation.

Basic science in the Neutron Science Project covers neutron scattering researches such as structural biology for investigating the structure and dynamics of biological molecules, advanced material science (e.g., under extreme conditions), high-energy neutron science (e.g., spallation phenomena), nuclear cross-section measurements for transmutation study, heavy-ion science for creating unstable heavy nuclei through spallation, and synthesis of super heavy extremely-neutron-rich nuclei. Muon facility is also possible but has not been investigated yet in detail.

For nuclear energy research, a reduction of environmental impact of disposal in a deep geologic formation of high level long-lived radio-wastes from reprocessed fuels is the key question for nuclear transmutation technology. These long- lived activities are actinides such as Np-237, Am-241, Am-243 and Cm-244 and fission products such as Tc-99 and I-129. The nuclear transmutation is

carried out mainly by fast neutron fission for minor actinides. The system consists of sub-critical core with minor actinides fuels centered by spallation neutron target. For development of the system, research and developments will be made by this facility complex.

With rather high power beam for nuclear transmutation study, material irradiation facility is also considered which aims at material development for fusion reactor and nuclear transmutation system. Possibility of radio-isotope production facility utilizing lower energy proton beam from the low energy part of accelerator is also investigated.

III. ACCELERATOR AND RESEARCH FACILITY COMPLEX

Figure 1 shows preliminary layout of facilities planned in Neutron Science Project . A 5 MW of total beam power of 8 MW is led to neutron scattering facility and the rest is to the facilities for thermo-hydraulics and material developments. For neutron scattering facility, two proton compressor rings are considered for full beam power at the final stage. In addition, a small amount of beam is shared to neutron physics and spallation RI beam facilities. The schematic diagram of the accelerator complex is shown in Fig.2 and its specifications are summarized in Table 1.[2] The R&D items of the accelerator complex is accelerator components, RF power, cryogenic refrigerator and so on. The R&D of the low energy part up to RFQ has already been continued for several years and the 80 mA peak current with 10% duty has been achieved. The two compression rings are considered for 5MW beam current with specification in Table 2.

Neutron scattering facility is considered with higher priority in the project, because many attractive research areas are expected for basic science. The concept of facility layout is shown in Fig.3. As the facility is considered to be open for asia-oceanea region as well as domestic researchers, neutron beam lines is designed as many as possible. The present case can take 32 beam lines for three kinds of neutron energies which are equally shared. One of the beam lines is dedicated to hot (irradiated) samples for researching radiation effect. The building is designed as a large open space to handle shielding/moderator assembly. Because the target station is surrounded by 5.5-6 m-thick iron and 1m-thick concrete shield, the radiation control of the experimental hole is accessible for rad-worker.

A plan of research and development for accelerator-driven transmutation system is divided into four phases, i.e., basic research, engineering development, technology demonstration and commercial plant. In the current JAERI program, only basic and engineering phases are included. The basic phase is focusing to build up the data base for designing experimental and demonstration plants. The experimental plant is planned to be 30 MW thermal power in the second phase in which a small amount of minor actinide fuel is burned. For the first phase, thermo-hydraulic test with 1-2 MW beam power and reactor physics experiment with zero beam power around 1 W are considered. A concept of the thermo-hydraulic test facility is shown in Fig. 4. The proton beam is bent by 90 degree to the target core assembly which is simulating the target assembly for transmutation systems, e.g., typically tungsten rods cooled by Na. The facility includes thick shielding iron comparable to the neutron scattering facility and Na coolant loop. The reactor physics facility is similar to critical assembly which was used for fast reactor studies, because transmutation system is also considered to use a fast neutron spectrum. Only a difference from a fast reactor is sub-critical system. The time transient and response of sub-critical system will be studied by techniques of reactor physics experiment.

Neutron physics study including nuclear data for high energy region is also interested for transmutation physics. For this study, pulsed high energy neutron facility can be accompanied with a TOF facility. This study requires 10 mA beam with a few ns pulse width. With the thermo-hydraulic test facility, the proton and neutron irradiation facility can also be combined because both utilize 1-2MW beam. These integration will make the common utility effective, i.e., cooling system, shielding, waste management and so on.

Besides the facilities mentioned above, by utilizing the existing Tandem Van de Graff accelerator, spallation products can be accelerated up to a few ten MeV/u together with the super-

conducting cavity booster. A 10 mA of beam is used for production of trans-actinide isotopes from depleted Uranium Carbide target. This facility can be constructed only by adding target and on-line mass separator. A necessary modification of the existing facility was investigated for this facility.

By extracting a proton beam about 200 MeV at the low energy stage of the accelerator, many kinds of radio-isotopes (RI) can be produced for medical use. This energy range is suitable for creating a variety of RIs and eliminating undesirable RIs by spallation reaction. The facility should include chemical lab for separation of RI.

Muon utilization is one of the attractive application of high energy proton beam. The establishment of this facility is strongly requested from the muon science community in Japan, however, a practical design work has not been involved yet. This might be considered in the further design work.

IV. PROGRESS OF RESEARCH AND DEVELOPMENT

For the low energy part, the negative ion extraction from the volume type source is tested and 10 mA was obtained. The fabrication design of cw-RFQ test machine with 5.3 mA as well as 30 mA for pulse mode was started. For cw operation mode, the design parameters of DTL and SDTL were also investigated. To reduce RF power consumption and heat, low accelerator gradient is considered as 1.5 MeV/m. From the viewpoint of mechanics and beam dynamics, the end point energy was determined to 100 MeV.

The development of super-conducting cavity linac for 100 MeV to 1.5 GeV was started in 1996. The cavity fabrication is one of the key issues development, in which the mechanical strength and surface conditioning are concerned. The single test cavity was fabricated by cold rolling and press of pure Niobium metallic sheet with electron beam welding. In 1997, the vertical cavity test for b=0.5 (145 MeV) was successfully conducted with the maximum field strength of 24 MV/m at 4.2K and 44 MV/m at 2.1K. The multi-cavity with five cavities is being fabricated in this year for the next step.

The injection scheme is specially critical to compress the beam to shorter pulse less than 1 ms, because the conventional technology using charge stripping foil has a limit by heating up to accept the high current beam. In JAERI project, two ring scheme is considered for the reference design for 5 MW operation. However, the two ring increase the cost and makes another problem for fast beam switching and merging. To solve the problem of charge exchange foil, new charge exchange system, the LUCE method, the Laser Undurator Charge Exchange has been proposed.[3] In this scheme, an undulator is used for a foil as a stripping magnet but a charge exchange is made by two steps from H^- to H^0 and H^0 to H^+. The first step stripping is made by the undulator for Lorenz stripping and in the second step, a resonance excitation by laser is used together with Lorenz stripping by the second undulator.

A conceptual design study of target/moderator/reflector system has been extensively performed by neutronic calculations.[4] The study includes optimization of material, shape, size and relative positions for neutronic performance. The present configuration of target/moderator is shown in Fig5. The result showed clearly that mercury target is superior to Pb-Bi target. For the cryogenic moderators, reduction of nuclear heating is one of the key issues. For this purpose, a pre-moderator concept was extensively studied as well as neutron flux intensity and pulse width.

Thermo-hydraulic studies for solid and liquid targets have been performed.[5] The 1.5MW solid target of tungsten was studied for capability of heat removal so that operating temperature below 180 C was confirmed. For the mercury target, two concept of cross and return flows are investigated so that the maximum flow rate of 1.5 m/s and temperature rise of 171 C were obtained for 5MW beam.

For the cryogenic moderator, super-critical hydrogen (1.5 MPa and 20 K) was adopted so that temperature rise must be kept less than 3 degree even for peaking position in nuclear heating. These flow analysis and experimental confirmation study was started.

For material development, a test program of thermal shock, radiation damage and corrosion/erosion was being prepared.[6] The 1 J/pulse laser injection system is considered for studying stress wave phenomena. For radiation damage, triple ion beam irradiation is planned to simulate gas

production dominant condition. The mercury loop test is prepared for corrosion/erosion test in off beam condition. Experimental study of neutronics and thermodynamics of mercury target is performed at AGS facility in Brookhaven National Laboratory of USA under the ASTE collboration.[7] By this experiment, design codes are checked in comparison.

V. SAFETY AND NUCLEAR DATA ISSUES

Radiation safety is the important issue for operation of the accelerators and target systems. The detailed design of shielding structure has not been performed. At the present stage, a guide line concept is being developed, e.g., the accelerator components should be maintained without remote handling. The criteria of radiation protection should be based on the regulation law, but there exist new cases compared to the previous radiation facilities, especially on the transmutation facility. These new problems should be discussed in Japanese community including the government authority.

As for nuclear data required for the project, there are two kinds of areas, i.e., nuclear design of the target and radiation shielding design. The calculation tools are commonly high energy transport codes, such as, NMTC/JAERI and HETC. Those codes include elastic cross section for a collision probability as well as a simplized shielding code. Most frequently used data is a nuclide production cross section library which is required to estimate induced radio-activities and nuclear transmutations. For a shielding purpose, high energy proton induced reactions, e.g., (p,xn), is necessary to estimate neutron production from beam line components.

VI. CONCLUDING REMARKS

The JAERI Neutron Science Project is progressed more than expected, regardless of short period after starting the project. Especially the development of accelerators has been considerably progressed in the super-conducting cavity. The target development is under preparation for thermo-hydraulic and mechanical test devices, while a neutronics study has been progressed for optimizing target/moderator shape and configuration. As for international collaborations, the ASTE collaboration on the mercury target has started at BNL.

The total design of accelerator complex and the target system will be completed soon as the first round concept. On the other hand, a radiation safety assessment has just started at this April. The research and development phase will be continued for the next three years and then a check and review of the project is obligated by the government before moving to the construction phase.

ACKNOWLEDGMENTS

The authors would like to thank all the member of JAERI Neutron Science Project.

REFERENCES

1. T. Mukaiyama, Y. Oyama, M. Mizumoto, T. Takizuka and R. Hino, "Neutron Science Project at JAERI," *Proc. Topical Meeting on Nuclear Applications of Accelerator Technology (ACCAPP'97)*, Nov. 16-20, 1997, Albuquerque, USA (1997)

2. M. Mizumoto, J. Kusano, H. Hasegawa, N. Ouchi, H. Oguri, M. Kinsho, E. Chishiro, T. Tomisawa, Y. Touchi, Y. Honda, K. Mukugi, H. Ino, F. Noda, N. Akaoka, H. Kaneko and B. Fechner., "A Proton Accelerator for Neutron Science Project at JAERI," *Proc. 1st Asian Pacific Accelerator Conference*, March 23-27, 1998, KEK, Tukuba, Japan (1998)

3. Y. Suzuki, M. Kinsho, F. Noda, M. Mizumoto and I. Yamane, " A New Scheme of Charge Exchange Injection for High Intensity Proton Storage Ring with High Injection Energy," ibid. (1998)

4. N. Watanabe, M. Teshigawara, H. Takada, H. Nakashima, Y. Oyama, T. Nagao, T. Kai, Y. Ikeda and K. Kosako, "A Conceptual Design Study of Target-Moderator-Reflector System for JAERI 5MW Spallation Source," *Proc. 14th Meeting of Int. Collaboration on Advanced Neutron Source (ICANS-XVII)*, June 14-19, 1998, Illinois, USA (1998)

5. R. Hino, M. Kaminaga, T. Aso, H. Kogawa, S. Ishikura, A. Susuki, A. Terada, H. Kinoshita and K. Haga, "Spallation Target Development at JAERI," ibid. (1998)

6. K. Kikuchi, H. Kogawa, M. Futakawa, I. Ioka and R. Hino, "Material Development for Spallation Target at JAERI," ibid. (1998)

7. G. Bauer, J. Hastings and N. Watanabe, "A Spallation Target Test Experiment at the Brookhaven Alternating Gradient Synchrotron," ibid. (1998)

Table 1 Specification of Linac

Energy	1. 5GeV
Ion source	negative and positive hydrogen
Current 1st stage:	pulse: 1mA(Ave.), 16.7mA (peak)
2nd stage:	cw&pulse:5.3mA(Ave), 30mA(peak)
Accelerator type	
low energy	RFQ,DTL/SDTL (norm., 200MHz)
high energy	Super-conducting linac (600MHz)

Table 2 Compression Ring

Maximum Power	2.5 MW
Repetition	50Hz
Harmonic number	1
Chopping factor	0.6
Circumference	185.4 m
Number of proton	2.08×10^{14} protons

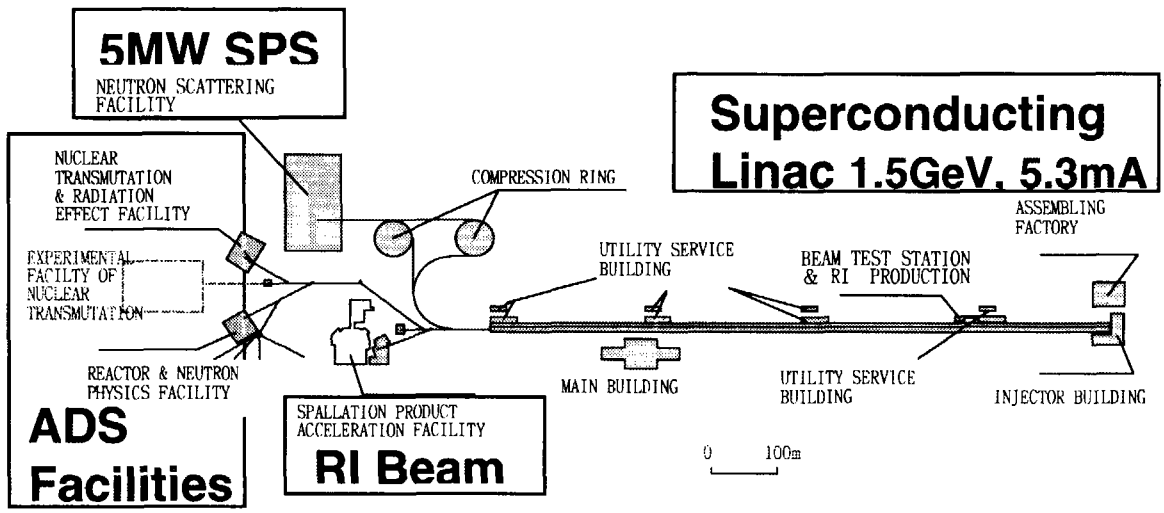

Figure 1 Preliminary Layout of Facility Complex

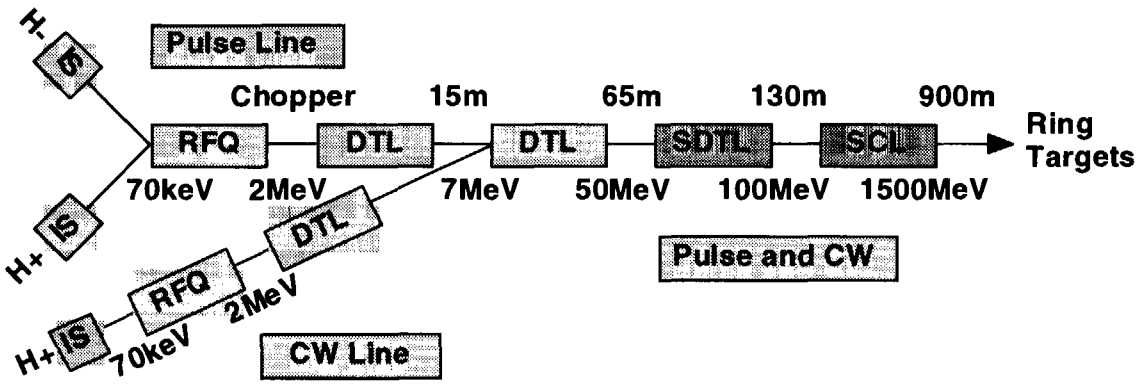

Figure 2 Schematic Diagram of Accelerator Configuration

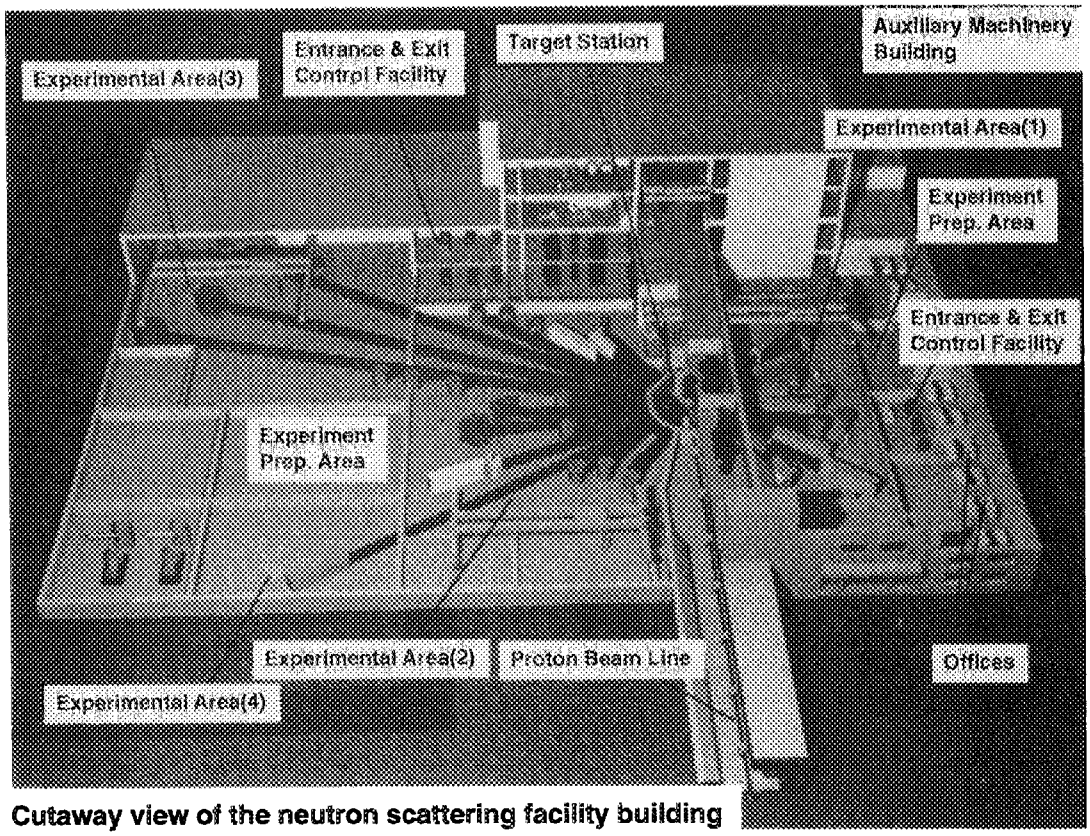

Figure 3 Concept of Neutron Scattering Facility

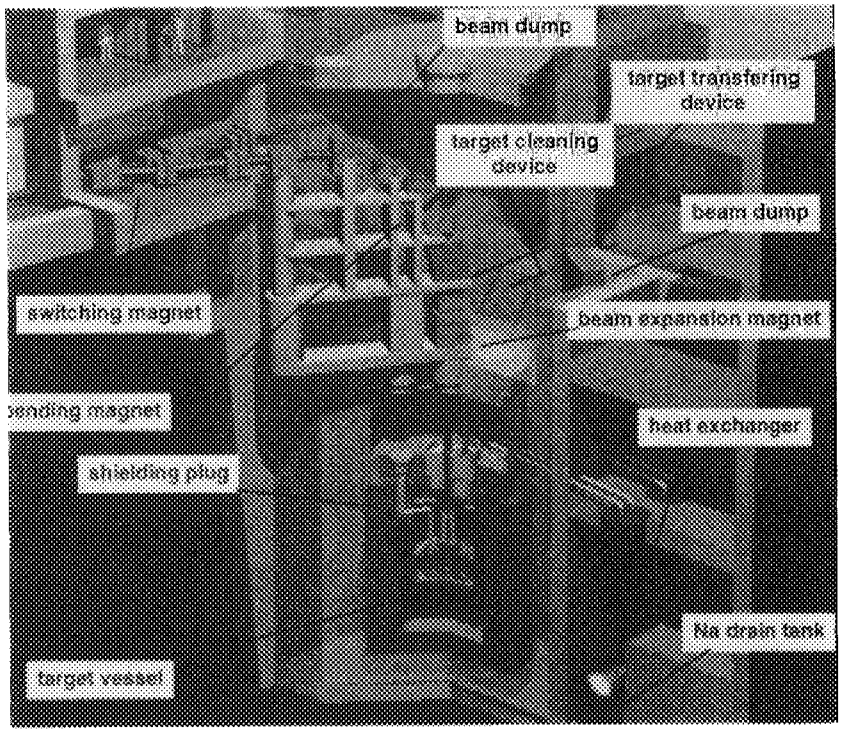

Figure 4 Concept of Transmutation Research Facility for Thermo-Hydraulics Test

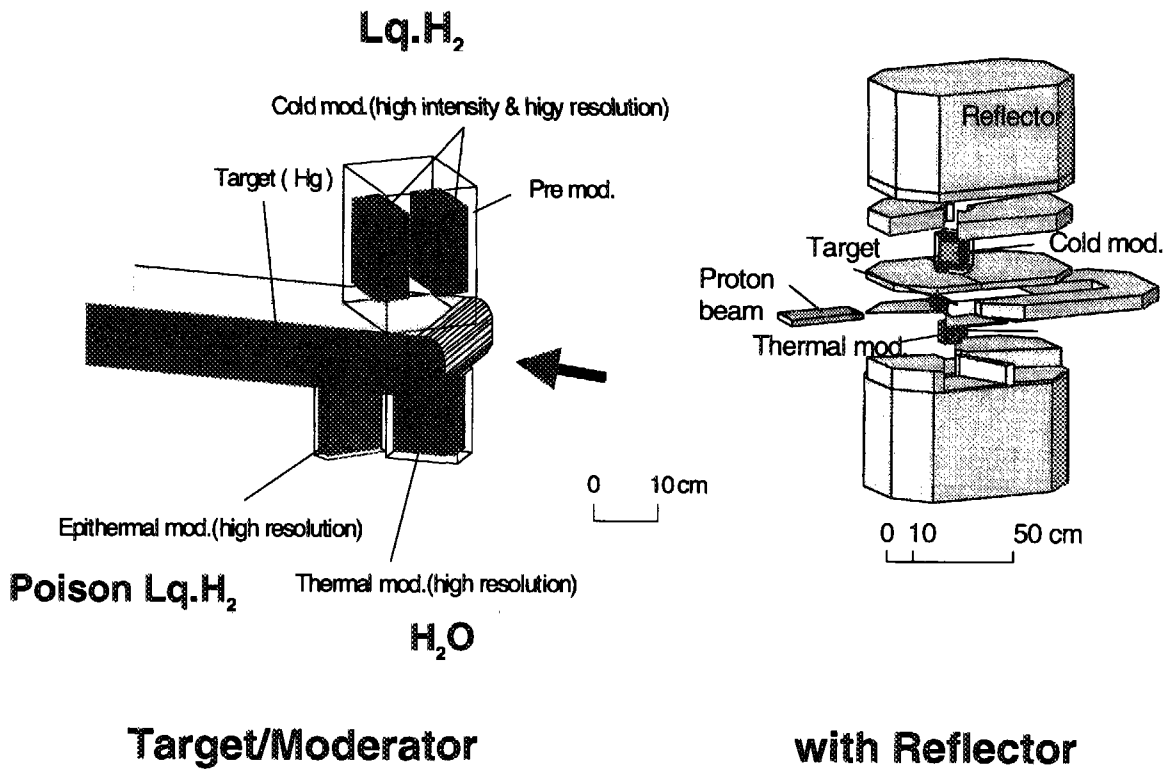

Figure 5 Target/Moderator Concept for Spallation Neutron Source of Neutron Scattering

JP9950306

JAERI-Conf 99-002

2.3 The present status of medical application of particle accelerator - Started construction of a new medically dedicated proton accelerator facility in Tsukuba -

Takeji SAKAE and Akira MARUHASHI

Proton Medical Research Center (PMRC), University of Tsukuba

Ten-nodai 1-1-1, Tsukuba 305-8575, Japan

e-mail: sakae@medaxp.kek.jp

A new facility of PMRC starts the construction in the neighborhood of Tsukuba university hospital, in order to establish technical skill for practical use in the cancer treatment and to grope for new skill. The facility has a linac injection system, a compact synchrotron, two rotating gantry rooms and two fixed horizontal beam lines. The outline of the design arranged for the facility is reviewed. As one of the important technique for the treatment, investigation into target adjusting accuracy in respiration-gated proton irradiation is presented.

1. Introduction

Medical application of particle accelerators is in progress recently owing to the rapid advance of accelerator technology and computer performance. Cancer treatment by heavy charged particles (proton, heavy ion) has advantage in its sharply controllable dose distribution without surrounding irradiation. As the next step following the proton radiotherapy (about 600 patients) at PMRC which has begun at 1983 in KEK , a new facility for proton therapy starts the construction in the neighborhood of Tsukuba university hospital. The purpose of the facility is to establish technical skill for practical use in the treatment and to grope for new skill such as scanning beam irradiation. In this report, the outline of the design for the facility is reviewed. The respiration-gated irradiation system was developed for the treatment of moving organ [1,2,3,4] with relation to the respiration. The technique is one of the importance for the cancer treatment in the new facility.

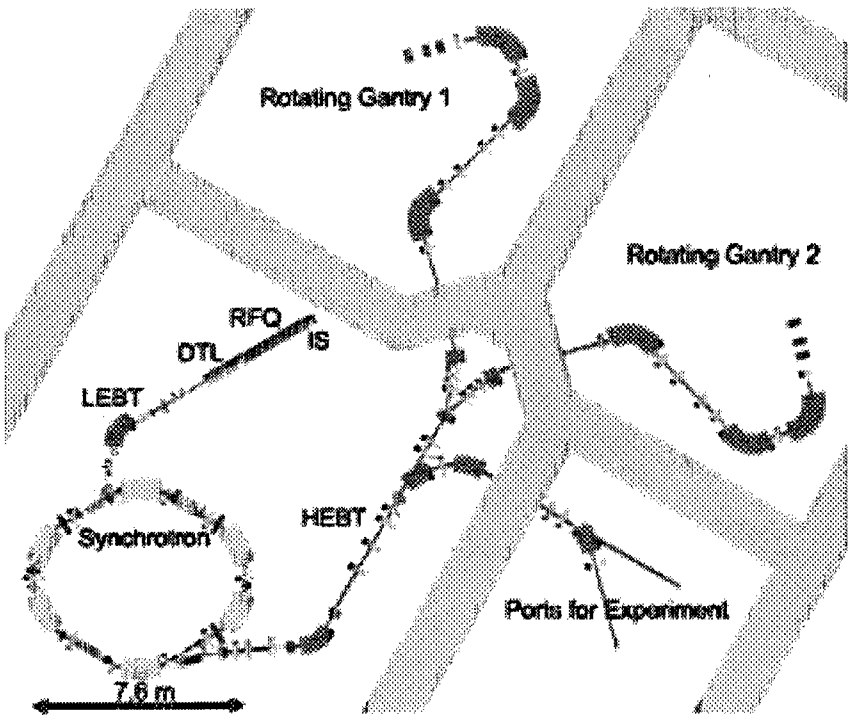

Fig. 1 Layout of the new facility in PMRC, Tsukuba.

Accuracy of the target adjustment in the irradiation synchronized with the respiration is investigated.

Table 1 Principal parameters of the accelerator proposed for the new facility.

Injector (Duo-plasmatron+RFQ+ Alvarez -DTL)		
	Beam energy	7 MeV
	Peak current	15 mA
	Pulse	5 - 100 micro sec
	Momentum spread	+-0.3%
	Emittance(90%)	<1 pi mmmrad
	RF	425MHz
Synchrotron (Multiturn injection, Separated functional lattice)		
	Extraction energy	70-270 MeV
	Size	7.6 x 6.7 m
	Circumference	23 m
	Extracted Particle Number	1.8×10^{11} ppp
	Typical operation cycle	2 sec
RF Cavity (8 FINEMET cores)		
	Operation frequency	1.6 – 8.2 MHz
	Gap voltage	1.3kV
	Accelerating gap	40 mm

2. Outline of the facility.

The facility has a linac injection system (7MeV), a compact synchrotron (70-270 MeV) with separated functional lattice, two rotating gantry rooms and two fixed horizontal beam lines. The layout of the facility is shown in figure 1. Table 1 is the list of principal parameters of the accelerator proposed for the facility. In the accelerator, a broad band RF cavity using FINEMET is adopted because of its compactness and simple operation. The accelerated beam is extracted through the diffusion resonant extraction scheme developed by Hiramoto et al [5,6]. The diffusion is achieved by RF perturbation with nominal cycle time of 2 sec. This extraction scheme can make the current stable in the spill of beam emission and useful flexibility for the respiration-gated irradiation. Radiation dose rate of 2 Gy/min on the average can be obtained by the system even though intermittent irradiation for the respiration synchronized treatment. By using the rotating gantry, optimized irradiation angles are selectable in order to avoid damaging critical organs. In the nozzle of the gantry, scattering method is adopted to make beam spreading. To get sufficient beam spreading by the distance (3.2m) from the scatterer to the target position, new methods are developed for the facility. Dual-ring double scattering method [7] and hybrid filtering method are shown schematically in figure 2 with filtering apparatus in comparison with single scattering method.

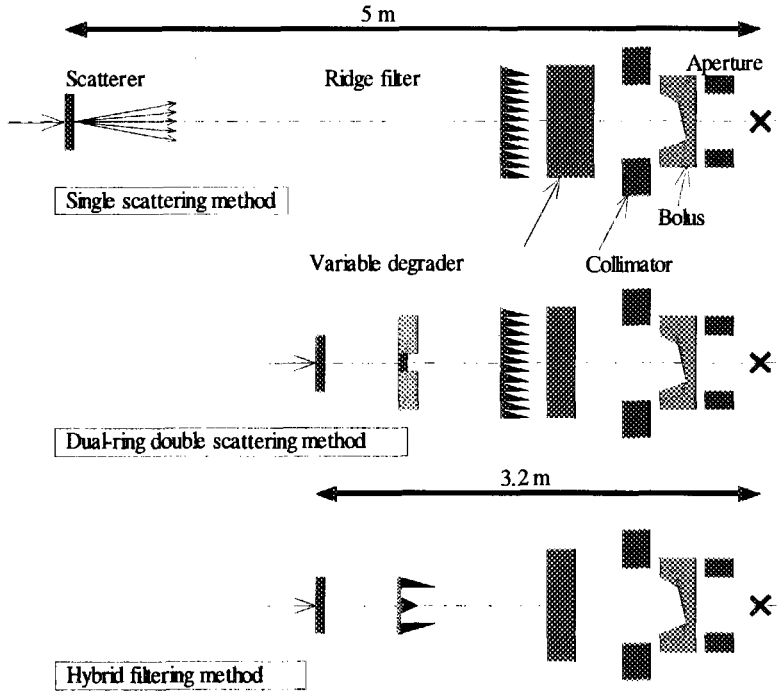

Fig. 2 Scattering methods for beam spreading.

3. Accuracy of target adjustment in the proton irradiation.

Precise measurement of target position on proton radiotherapy are performed in present facility of

PMRC to estimate the accuracy of the target adjustment in the irradiation synchronized with respiration. In order to estimate the target position in X-ray projected images, pattern matching of the moving region of interest is calculated for a frame of pictures one by one. The organ motion calculated by the pattern matching is shown in figure 3(b). The respiration signal given by measuring tension of body surface and the gate for irradiation are shown in figure 3(a). The correspondence between the respiration signal given by the tension measurement and the motion of the target organ is investigated [8]. By using the data, position deviation of the target during the irradiation period can be estimated as a function of discrimination level making the irradiation gate. On condition of usual treatment in which fraction of the irradiation gate is 0.2-0.3, the position deviation is clarified to be about 1mm in mean value and about 3-4mm in maximum value [8].

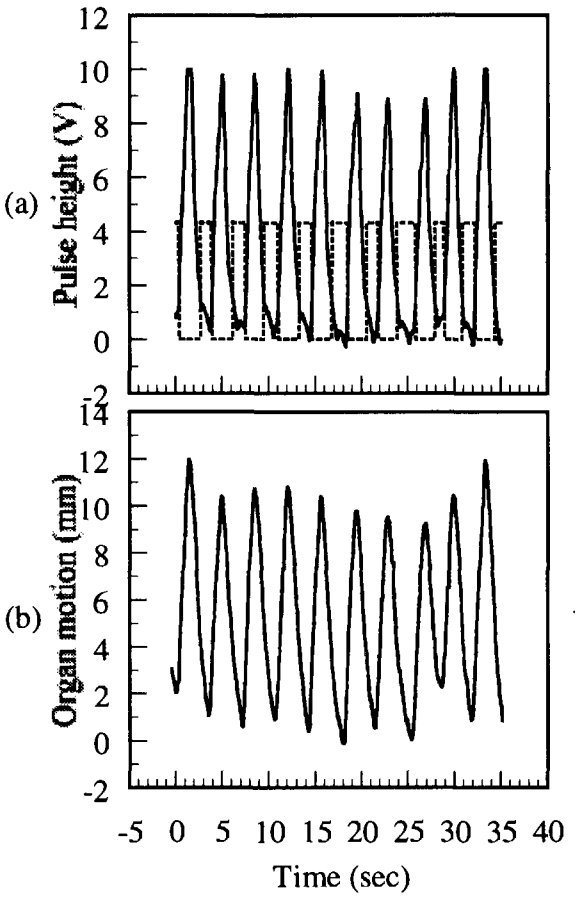

Fig. 3 Respiration signal with gate for irradiation(a), and organ motion (b).

4. Summary

Outline of the design proposed for the medically dedicated proton accelerator facility in Tsukuba is presented. By the new facility, not only reliable technique for practical cancer treatment but also challenging technique such as beam scanning can be investigated.

References

[1] K. Ohara, S. Kubota, M. Akisada, T. Inada, T. Kitagawa, T. Okumura and F. Kure, Nippon Acta Radiol. 47, 488-496, 1987.

[2] K. Ohara, T. Okumura, M. Akisada, T. Inada, T. Mori, H. Yokota and Caraguas, Int. J. Radiat. Oncol. Biol. Phys. 17, 853-857, 1989.

[3] T. Okumura, H. Tsuji and H. Tsujii, Compensation of target motion, Ion Beams in Tumor Therapy, CHARMAN&HALL, 308-315, 1993.

[4] T. Okumura, H. Tsuji, Y. Hayakawa, A. Maruhashi, T. Inada and H. Tsujii, Proceedings of the Xith Int. Cof. On the use of Computers in Radiation Therapy, 20-24, 1994.

[5] K.Hiramoto et al., Nucl. Instr. Methods, A322,154, 1992.

[6] K.Hiramoto, J. Hirota, M. Umezawa, H. Sakurabata, M. Katane, K. Matsuda and M. Tadokoro, Proceedings of 9th Workshop for Medical Proton Accelerator, 29-33, 1998.

[7] Y. Takada, Jpn. J. Appl. Phys. 33, 353-359, 1994.

[8] T. Sakae, to be published.

JP9950307

2.4 Accelerator Conceptual Design and Needs of Nuclear Data for Boron Neutron Capture Therapy

Makoto SASAKI and Toshiyuki YAMANAKA
Mitsubishi Heavy Industries, Ltd. (MHI), 3-1, Minatomirai 3-chome, Nishi-ku, Yokohama 220-0012,
e-mail:mksasaki@atom.hq.mhi.co.jp

Hitoshi YOKOBORI
Advanced Reactor Technology Co., Ltd. (ARTECH), 15-1 Tomihisa-cho, Shinjuku-ku, Tokyo 162-0067

An optimization study has been made on an accelerator-based facility for the boron neutron capture therapy. The energy of the incident proton and the arrangement of the moderator assemblies are optimized. The beam current and the accelerating voltage are determined so that the accelerator power becomes minimum. The proposed facility is equipped with a 2.5 MeV proton accelerator of 10-25 mA, a lithium target, and a heavy water moderator contained in an aluminum tank. Each of these equipments is feasible, if proper R&D works have been done. Our new design requires the beam power of less than a hundred kW for the accelerator, although that of our previous design was 1 MW. The reduction of the beam power makes the cooling system for the target much simpler. The essential issues for realization of this concept are long-life lithium targets under high heat flux and high current proton accelerators with average currents of more than 10 mA

It is necessary for the reasonable design of a small-sized and low cost facility to get good accuracy nuclear reaction data. Especially, the latest Li/Be(p,n) neutron yield data in a range of threshold energy - few MeV are required for exact evaluation of neutron energy spectrum used therapy. And damage data by low energy proton beam are also important to evaluate integrity of target material

1. Introduction

We have been studying nuclear reactor concepts suitable for the boron neutron capture therapy at a hospital since July, 1988. One concept was proposed at the 3rd Asian Symposium on Research Reactors in 1991 [1] and an advanced concept was proposed at the 5th Symposium on Advanced Nuclear Energy Research in 1993 [2]. Since construction of a nuclear reactor at a hospital is considered to have difficulty in obtaining public acceptance, we have proposed a deuteron accelerator of 1 MW beam power as an alternative neutron source. The accelerator is based on the concept of ESNIT [3] design which uses the Li (d, n) reaction by a 20mA-50MeV accelerator. A numerical study of optimizing the moderator assemblies was presented in the 1st International Workshop on Accelerator-Based Neutron Sources for Boron Neutron Capture Therapy, Jackson, in 1994 [4]. But an accelerator with 1 MW beam power is too massive and also too expensive for a hospital use. We have challenged to reduce the accelerator beam power thoroughly using the Li (p, n) reaction instead of the Li (d, n) reaction. We have been working to reduce the beam power of the accelerator required for medical treatment. In this paper the measures to reduce the beam power are described with several numerical results.

2. Optimization of Facility

2.1 Design objectives

We have studied to reduce the beam power of the accelerator based on the following design objectives: The time interval for clinical treatment will be less than 1-2 hours. The therapeutic neutron fluence (time integrated flux) at the irradiation field should be more than 6 x 10^{12} n/cm^2 for the epi-thermal neutron(1eV-1keV). The contaminant at the irradiation field should be less than 2Gy for the fast neutron (> 1keV) dose and less than 1Gy for the gamma-ray dose.

2.2 Procedure

It is necessary to slow the neutrons produced by the nuclear reaction of the charged particle with the target down to the epi-thermal neutron energy, which is the most suitable for the treatment. It is also required to decrease the number of high-energy neutrons, which are harmful for the treatment, and to increase the number of epi-thermal neutrons sufficiently for the treatment. At the irradiation field of a patient, the ratio of the fast neutron dose to the epi-thermal neutron fluence must be less than 2Gy/ (6 x 10^{12}n/cm^2) = 3.3 x 10^{-13}Gy $\cdot$ cm^2, in order to make the amount of the fast neutron dose less than 2Gy, and to make the amount of the epi-thermal neutron fluence more than 6 x 10^{12} n/cm^2.

A neutron source of unit strength is fixed on the target, then the neutron flux distribution in the moderator has been calculated by the neutron transport analysis method with the acceleration energy and the composition of the moderator material as parameters. The distribution of the ratio of the fast neutron dose to the epi-thermal neutron fluence has been derived from these analyses, and the minimum thickness of the moderator, which satisfies the above condition, is determined. The required neutron source strength at the target has been estimated so as to make the epi-thermal neutron fluence in the irradiation field exceed 6 x 10^{12} n/cm^2.

For each incident energy the beam current, which produces a sufficient neutron source strength, has been evaluated from the neutron yield data, and the one, which makes the accelerator beam power minimum has been selected.

2.3 Planning an accelerator concept for BNCT facility

The acceleration energy is limited up to 20MeV to make the accelerator compact. Because of the easiness of making the ion source and the high efficiency of the neutron production in low energy proton has been selected as an acceleration particle and lithium as a target material. From our neutron irradiation system design experience of the nuclear reactor for BNCT aluminum is chosen as moderator material for the removal of the fast neutron. To increase the epi-thermal neutron flux heavy water is used. The ratio of the mixture of aluminum and heavy water is changed as a parameter of the analysis.

Analytical models are as follows: a 2-dimensional cylindrical model described in Fig.1 is used by the 2-dimensional discrete ordinates neutron and gamma ray coupled transport code, DORT [5]. The number of energy groups for neutron is 21 and the number of gamma-ray energy groups is 9. The nuclear group constants have been processed from the JENDL-3 (SSTDL-100/40) nuclear cross section library [6].

We have studied sixteen cases of combination of the moderator composition and the incident proton energy. The moderator is composed of homogeneous mixture of heavy water and aluminum. The contents of heavy water are 100,70,40 and10 percent. The incident proton energies are 2.5, 5, 10 and 20 MeV.

3. Specifications of Accelerator Facility

The fast neutron dose and the epi-thermal neutron fluence distributions in the assemblies are described in Fig.2 and Fig.3 where the incident proton energies are 2.5MeV and 10MeV,respectively. From these analytical results, the minimum moderator thickness have been derived and are shown in Table 1. The required beam current (mA) and the beam power (kW) vs. the incident proton energy are shown in Fig.4.

Through the analyses the following results have been derived: the lower the

acceleration energy, the less beam power is required but more beam current is required. The beam power required for the treatment in an hour is 63 kW. (^{7}Li (p, n) ^{7}Be: 25 mA in 2.5MeV)

For the high current proton accelerator of the BNCT facility the specifications of the accelerator equipments are determined and described in Table 2. Because more than several milliampere currents and a few to several million electron volt acceleration voltages are challenges, our basic design of the accelerator is based on the JAERI's R&D work. [7]. Each of these equipments is feasible, if proper R&D works have been done.

4. Target and Moderator Assenbly

A light water coolant should remove the heat of the proton beam power dissipated in the thin lithium target. To improve the heat removal capability, corrugated panels are attached onto the opposite surface of the aluminum base metal on which lithium is deposited by evaporation. The numerical result in Fig. 5 shows that the peak heat flux of the incident proton beam should be reduced to less than 160 W/cm^2 since the melting of the target should be avoided. A cylindrical tank filled with heavy water, which has a 30cm diameter and a 25cm height is used as a moderator of the neutron energy. The concept of the cooling structure in the target assembly is shown in Fig. 6.

5. Requirements on Nuclear Data

First, we require the latest energy and angular distribution data of neutron and γ production by the reaction in a range of threshold energy to a few MeV Another engineers and we make a design of an accelerator facility for BNCT use the same nuclear data as shown in Fig. 7 and Fig. 8 [8]. For example, existence and height of Li(p,n)resonant reaction at about 2.3MeV is needed to evaluate efficiency of neutron production. The precise cross section curve of Li/Be(p,n) reaction near the threshold energy is so sensitive to decide incident proton energy in order to obtain lower energy neutron. γ Production data is needed to shielding calculations of a target and an accelerator. Because this data was published in 1975, we think more precise data can be measured with new methodology and new instruments. It is necessary for the reasonable design of a small-sized and low cost facility to get good accuracy nuclear reaction data.

Next, we have no damage data by low energy and high intensity proton beam. He atoms are accumulated inside of a target surface by irradiation of proton beam. It is also important to evaluate integrity of target materials.

6. Conclusion

Based on these concepts, a typical arrangement of the facility is proposed in Fig. 9. A high current proton accelerator of 10 mA, Li (p, n) type target with a high heat flux condition, and an aluminum tank moderator assembly containing heavy water (D_2O). Development of a high current accelerator, which has more than the several mA capacity is the essential issue for the facility. It is also necessary to continue the effort to reduce the beam power requirement.

References

[1] Sasaki, M., Hirota, J.,Tamao,S., Kanda, K., and Mishima, Y., "Design Study of a Medical Reactor for Boron Neutron Capture Therapy," *Proceedings of the 3rd Asian Symposium on Research Reactor*, Hitachi, Japan (1991).

[2] Sasaki, M., Hirota, J., Tamao, S., Kanda, K., and Mishima, Y., "Progress in Study of a Medical Reactor for Boron Neutron Capture Therapy," *Proceedings of the 5th International Symposium on Advanced Nuclear Energy Research*, Mito, Japan (1993).

[3] Oyama, Y., Yamaguchi, S., Kosako, K., and Maekawa, H., *Calculation of Neutron Field Generated at Thick Li Target Bombarded with 10-40 MeV Deuterons for Energy Selective Neutron Irradiation Test Facility*, JAERI-M 92-191 (1992).

[4] Hirota, J., Ikeda, K., Sasaki, M., and Yokobori, H., "Design Study of a Deuteron Linac Facility for Boron Neutron Capture Therapy," *Proceedings of the 1st International Symposium on Accelerator-based Neutron Source for NCT*, Jackson, Wyoming (1994).
[5] Rhoades, W.A., and Childs, R.L., *Nuclear Science & Engineering* 99, pp88-89 (1988).
[6] Hasegawa, A., "Development of a Common Nuclear Group Constants Library System: JSSTDL-295n-104g Based on JENDL-3 Nuclear Data Library," *Proceedings of the International Conference of Nuclear Data for Science and Technology*, Julich, FRG (1991).
[7] Hasegawa K., Mizumoto, M., Kusano, J., Ito, N., Oguri, H., Touchi, Y., Ino, H., and Mukugi, K., "The R&D Status on the Front End of the High Intensity Proton Accelerator in Japan," *Proceedings of the 1996 Linac Conference*, Geneva, Switzerland (1996).
[8] Liskien, H., and Pauksen, A., "Neutron Production Cross Sections and Energies for the Reactions ^{7}Li(p,n)^{7}Be and ^{7}Li8p,n)^{7}Be*", Atomic Data and Nuclear Data Tables, 15, pp57-84 (1975).

TABLE 1. Minimum Thickness of the Moderator

Composition (contents of D_2O)	(in unit: cm) Acceleration Energy (MeV)			
	2.5	5.0	10	20
100%	21	28	44	**
70%	24	33	49	**
40%	31	42	59	143
10%	49	66	83	110

** not analyzed

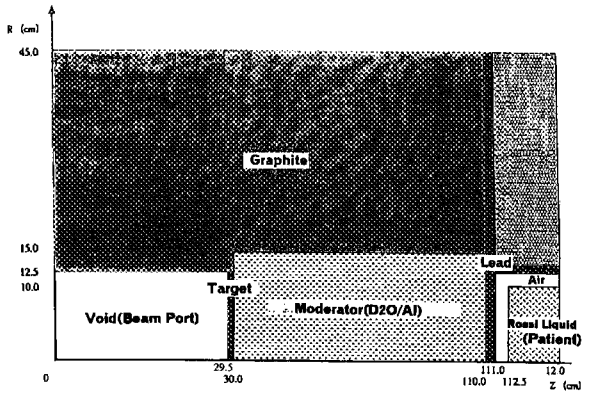

FIGURE 1. Analytical Model of Neutron Moderator Assembly

TABLE 2. Specifications of Accelerator for BNCT

Ion Source	
Particle	proton
Extraction Energy	several tens - 100 keV
Beam Current	120 mA (peak)
Duty	10-100%
R F Q	
Extraction Energy	a few MeV
Beam Current	20 mA (average)
Duty	10 100%
Transmission Rate	around 90%
R F Power Source	
Peak Power	around 850kW
Duty	10 100%

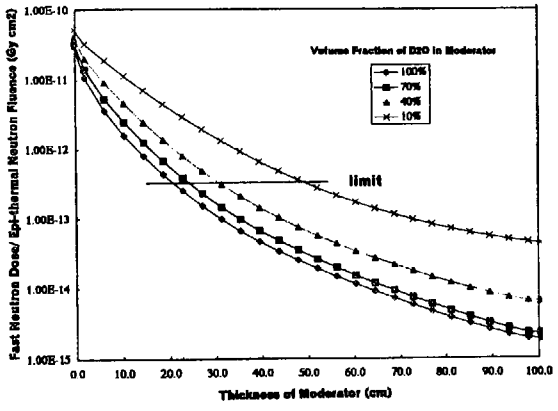

FIGURE 2. Fast Neutron Dose/Epi-thermal Neutron Fluence (Ep = 2.5 MeV)

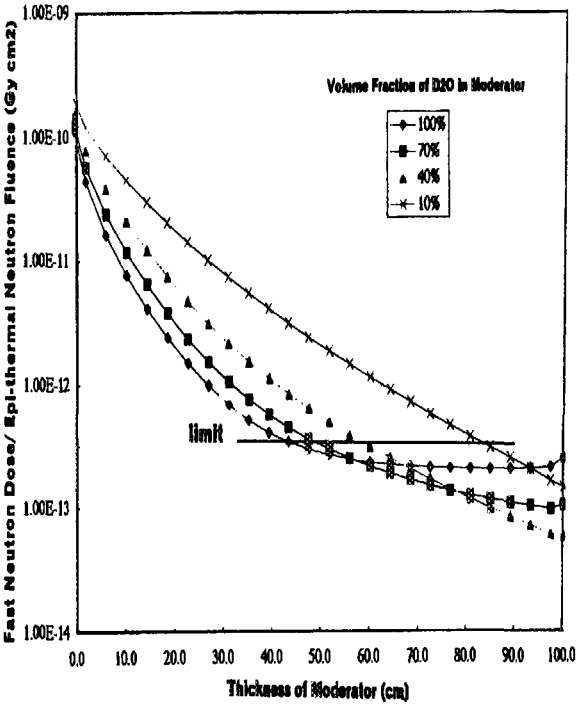

FIGURE 3. Fast Neutron Dose/Epi-thermal Neutron Fluence (Ep = 10 MeV)

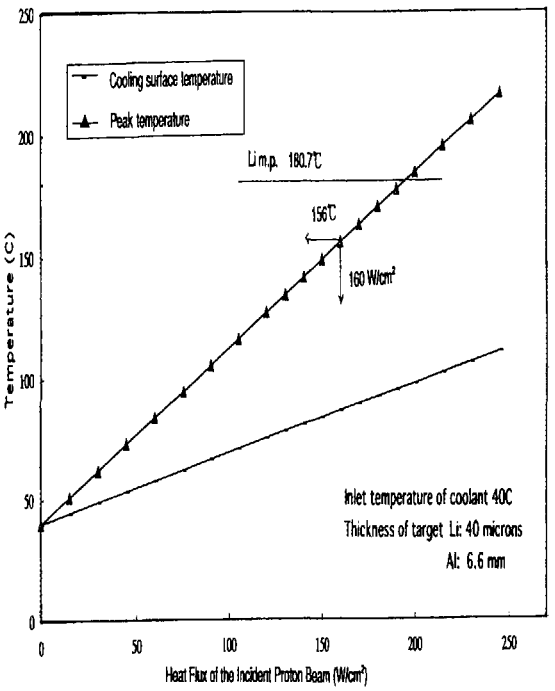

FIGURE 5. Relation between Temperature of Target and Incident Heat Flux Density

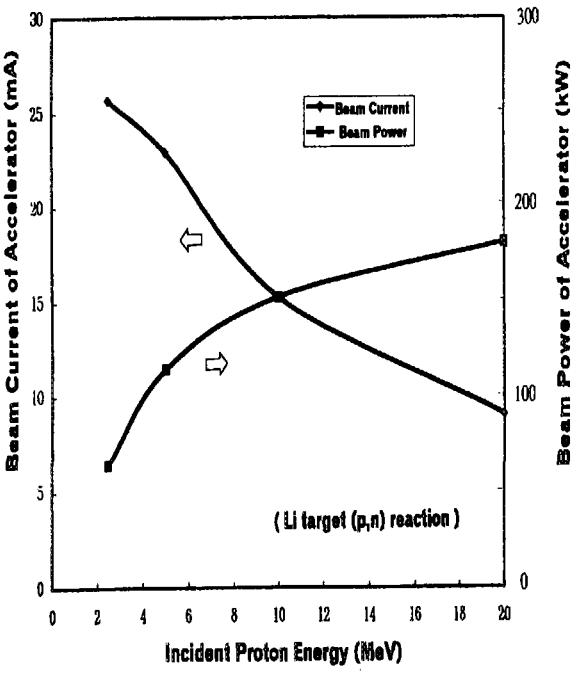

FIGURE 4. Incident Proton Energy vs. Beam Strength of Accelerator (Irradiation Time 1 Hour)

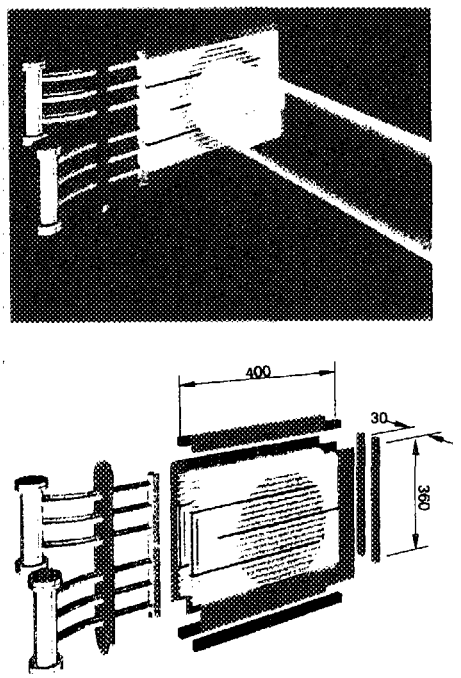

FIGURE 6. Concept of the Cooling Structure in Target Assembly

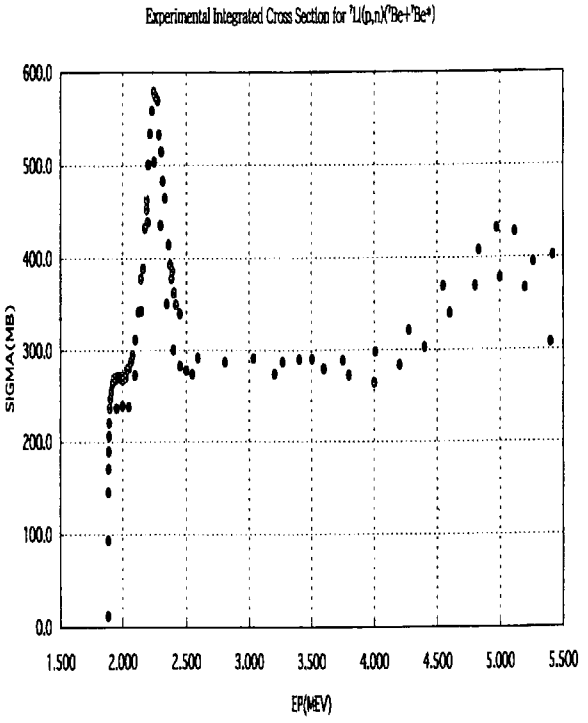

FIGURE 7. ^{7}Li(p,n) Reaction Cross Section

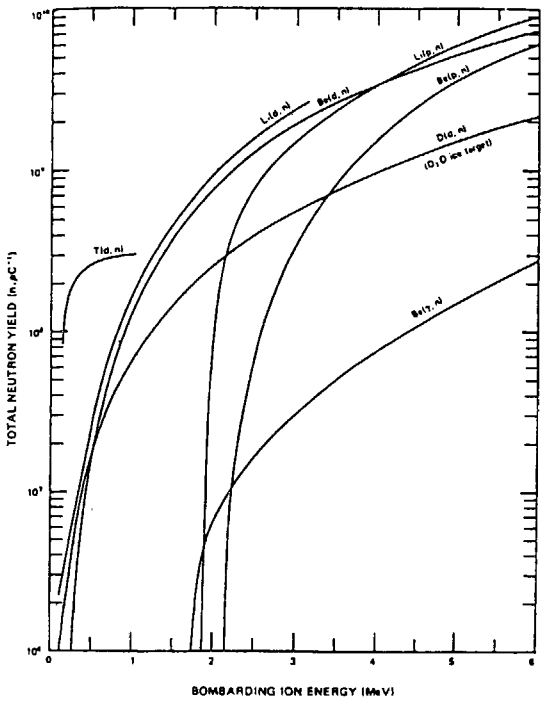

FIGURE 8. Total Neutron Yield Curve of Li/Be(p,n) and Li/Be(d,n) Reactions

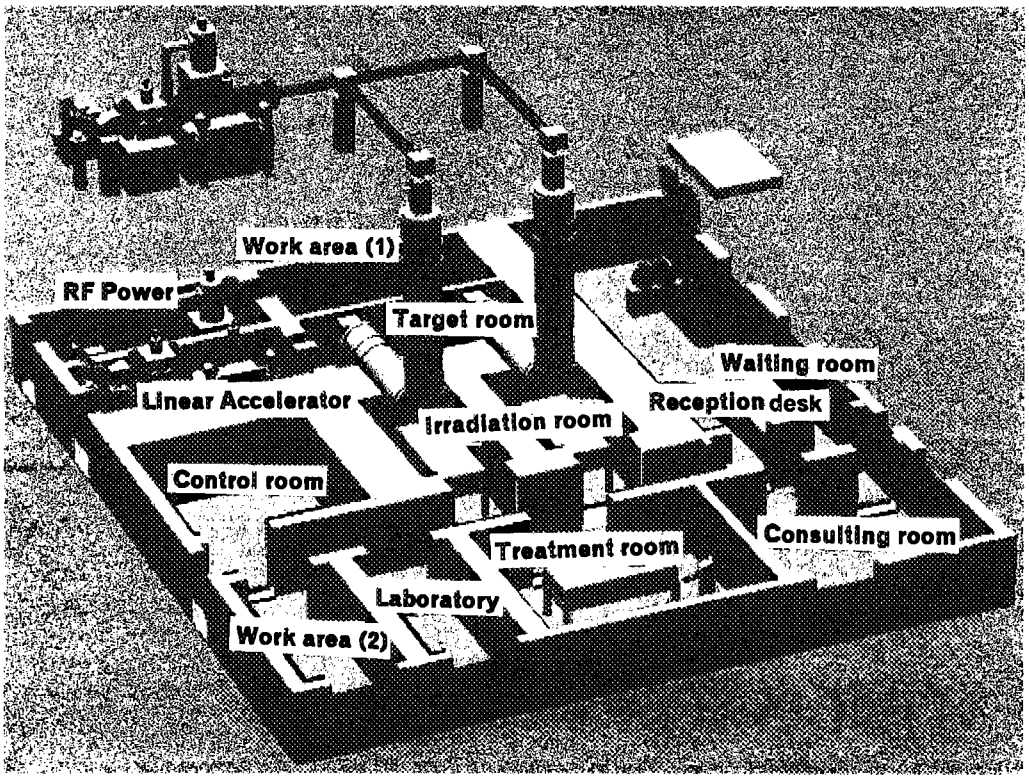

FIGURE 9. View of an Accelerator Based BNCT Facility

2.5 Development in Nuclear Astrophysics

S. Kubono

Center for Nuclear Study (CNS), University of Tokyo,
3-2-1 Midori-cho, Tanashi, Tokyo, 188-0002 Japan

Abstract: A brief review is given on recent developments in nuclear astrophysics, specifically investigations of explosive phenomena in the universe, including recent works on the rapid-proton capture process and the rapid-process. The scope of nuclear astrophysics and the nuclear data compilation for nuclear astrophysics are also discussed.

I. Explosive Phenomena and Radioactive Nuclei

Nuclear reactions are one of the key elements for the evolution of the universe. There are many nuclear effects observable in the universe. These nuclear effects give us rich information about the nuclear processes that have taken place, and thus they are very critical clues for understanding the stellar events. We may discuss in this paper how we can approach the astrophysical problems from a nuclear physics point of view. Astrophysical models together with the nuclear physics information should explain the stellar event of interest. These critical tests will eventually give the real picture for the stellar phenomena. Nucleosynthesis involving stable nuclei has been studied for many years, but there are still many important nuclear reactions that have not been well examined yet mostly at low temperatures.

On the other hand, nuclear reactions that involve radioactive nuclei were much less investigated in the past [1]. Explosive phenomena such as supernovae and the very early universe just after the big bang inevitably involve radioactive nuclei of very short half-lives due to fast successive nuclear reactions before cooling through nuclear decays. A typical example of evidence of radioactive nuclei among the stellar events would be seen in supernova. For instance, the light curve of the supernova SN1987A is well explained by the nuclear decay of ^{56}Co, and the gamma rays of ^{56}Fe following the beta decay of ^{56}Co were also observed [2].

Since explosive phenomena, which take place in high-temperature and high-density sites, include successive nuclear reactions, the nucleosynthesis-flow goes away from the line of stability on the nuclear chart [1]. Figure 1 shows schematically various nucleosynthesis scenarios on the nuclear chart. The pp-chain and some cycles are effective more or less around the line of stability, as they take place in relatively low-density regions at low temperatures. By contrast, rapid processes such as the rapid-proton capture (rp) process [3] that is an explosive hydrogen burning process, go through the proton-rich or neutron-rich unstable nuclear region. The development of physics and technology of radioactive nuclei in nuclear physics stimulated these investigations in the last decade. This provides not only an opportunity for investigations of nuclear astrophysical problems but also new facets for

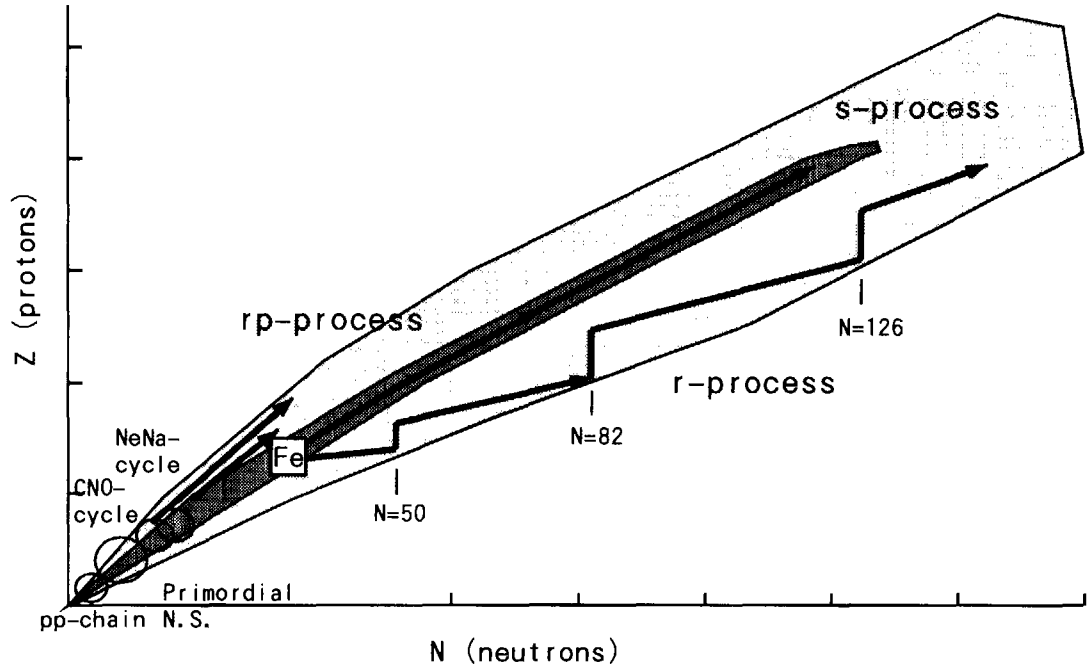

Fig. 1 A schematic view of pathways of explosive nucleosynthesis in the universe, depicted on the nuclear chart.

understanding scenarios of nucleosynthesis in the universe. For instance, neutron halo structures will dramatically alter the reaction rates of (n,γ) cross-sections, which are related to the s-process nucleosynthesis. The magic numbers of shell closure known near the line of stability would not hold necessarily for the nuclei far from the line of stability, which may change the r-process route.

In this short report, we will review briefly recent development specifically on the experimental works on the rp-process and the r-process.

II. Rapid-Proton Capture Process

Hydrogen burning is one of the basic scenarios of stellar nuclear burning. Specifically, the hydrogen burning under a condition of high temperature and high density, which is called the rp-process, has attracted many investigators in the last decade since they could be related to the explosive phenomena, such as novae and X-ray burst. Here, one can discuss the observations with the stellar models quantitatively in terms of the energy, the elemental abundances and the evolution.

The rp-process was proposed in 1981 by Wallace and Woosley [3]. Because of lack of nuclear physics information for the nuclei relevant, the pathway of breakout from the Hot-CNO cycle, which leads to the onset of the rp-process, was not identified clearly in the original paper. The suggested pathway of the onset and early stage of the rp-process is,

$^{15}O(\alpha,\gamma)^{19}Ne(p,\gamma)^{20}Na(p,\gamma)^{21}Mg(\beta)^{21}Na(p,\gamma)^{22}Mg(\beta)^{22}Na(p,\gamma)^{23}Mg(p,\gamma)^{24}Al(p,\gamma)^{25}Si$ . . . .

Along this pathway suggested for the rp-process, a series of experiments were

performed to clarify the onset mechanism at the cyclotron of the Center for Nuclear Study (CNS), University of Tokyo [1]. Many new resonances were discovered above the proton thresholds in the nuclei relevant. The summary of the works is presented in Fig. 2, which shows ignition temperature of each process along the pathway mentioned above. Here, the estimated temperature of the first process, $^{15}O(\alpha,\gamma)^{19}Ne$, is taken from refs. [4,5]. As to the reaction of $^{22}Na(p,\gamma)^{23}Mg$, the S-factor was taken from ref. [6]. A new resonance was first identified at 7.643 MeV in the present experiment of $^{24}Mg(p,d)^{23}Mg$ just around $T_7 = 5$ for the Gamow window [7], where there was no estimate made before for the reaction rate.

Figure 2 suggests that the $^{15}O(\alpha,\gamma)^{19}Ne$ reaction is limiting the onset of the rp-process. However, note that none of the values in the figure is definitive because the decay properties of the critical levels for the nucleosynthesis are not known yet. These are one of the hottest subjects being or to be investigated with radioactive nuclear beams. So far, the ignition temperature of the $^{15}O(\alpha,\gamma)^{19}Ne$ reaction seems too high to give a condition that leads to a major flow-out of CNO material to heavier mass elements under ordinary nova conditions [8]. Therefore, this reaction should be of great importance to study nucleosynthesis in novae. Of course, the nova models also need to be developed to conclude the speculation above. For instance, a measurement of the α decay widths of the crucial resonant states in ^{19}Ne is underway at CNS using the reaction of $^{19}F(^3He,t)\,^{19}Ne(4.033)(\alpha)\,^{15}O$.

The second possible reaction sequence for the breakout off the HCNO cycle, which leads to an onset of the rp-process [3], more likely at stellar sites under higher temperatures and higher densities, is $^{14}O(\alpha,p)^{17}F(p,\gamma)^{18}Ne(\alpha,p)^{21}Na\ldots$. Here, a new type reaction (α,p) sets in at the explosive burning. The reaction rate of $^{14}O(\alpha,p)^{17}F$ was investigated theoretically before [9,10]. However, there still is a large uncertainty in the rate, although many experimental efforts were also made [11,12]. The second

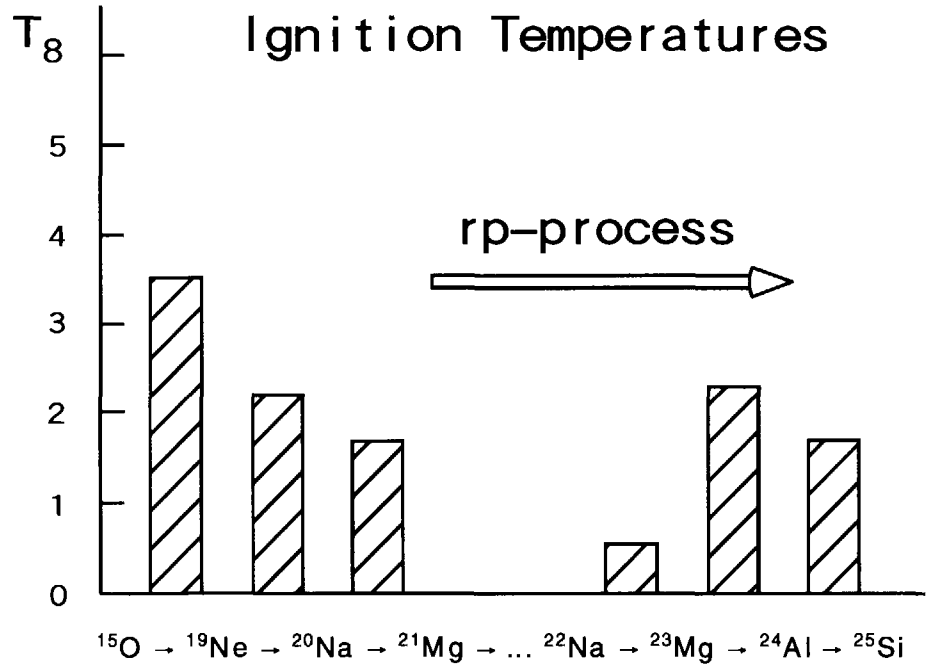

Fig. 2 The estimated ignition temperatures of the nuclear reactions along the possible rp-process under nova conditions.

and the third reactions of the sequence also are not known yet.

Recently, proton and alpha resonances in ^{18}Ne were investigated at CNS, revealing properties of some crucial resonances for the problem [13]. There is a long-standing question about the presence of a 3^+ state around the proton threshold in ^{18}Ne. However, there was no evidence observed here even with a high precision measurement, but some assignments of spin parity and excitation energies as well as the natural widths were made successfully for some critical resonant states. These values give better estimates for the reaction rates of $^{14}O(\alpha,p)^{17}F$ and $^{17}F(p,\gamma)^{18}Ne$. For the present problem, the resonance strength of the $^{14}O(\alpha,p)$ reaction is needed to be determined eventually by the direct simulation method.

The second process, $^{17}F(p,\gamma)^{18}Ne$, is now being investigated with a radioactive nuclear beam of ^{17}F at Oak Ridge National Laboratory. The third process is also under investigation at Louvain-la-Neuve with a ^{18}Ne beam. Specifically, the (α,p) process should be investigated systematically to clarify the role of the process under high temperature conditions. So far, most estimates were made with statistical model calculations.

There are some other critical problems to be investigated for the rp-process. They include waiting points, bottlenecks, and the termination of the rp-process. The waiting points determine the time duration of the explosion, and the bottlenecks restrict the pathway of the rp-process. The termination defines the total energy release of the process as well as the elemental production.

III. Rapid-Process

Although nucleosynthesis of heavy elements is not so important for the evolution of the universe and energy generation, they are very useful for understanding the mechanism of stellar events and also for cosmochronology. Figure 1 suggests two different mechanisms for heavy element synthesis, the slow (s)- and rapid (r)- processes.

The r-process should take place in a very high neutron-density region ($n_n \sim 10^{21}$ cm^{-3}) at high temperature ($T_9 \sim 2 - 3$) with a very short time scale, suggesting a nucleosynthesis flow-path far away from the line of stability. The path may be around the nuclear region that have a neutron separation-energy of 2 - 3 MeV, where the half-lives of the beta decays and the neutron capture rates balance. The peaks in the r-process nuclei suggest magic numbers of neutron shell in the very neutron rich region. The most plausible site for the r-process is considered to be in the hot bubble region in Type II supernovae [14], although it is not confirmed yet.

The nucleosynthesis of the r-process is least known experimentally among the nucleosynthesis scenarios since the nuclei on its possible path are quite difficult to produce in the laboratories. Only some nuclei around the possible waiting points at N = 50 and 126 were observed so far. The nucleus $^{130}Cd_{82}$ was produced and first investigated [15] at CERN-ISOLDE by a high-energy spallation reaction; the half life was determined to be 203 ms, whereas the nucleus $^{80}Zn_{50}$ was produced as a fission product of ^{238}U, and studied at the high-flux reactor at Brookhaven National Laboratory, giving $T_{1/2}$ = 550 ms [16]. Therefore, the r-process time scale should be not less than 550 ms, since ^{80}Zn is considered to be one of the waiting points of the r-process.

Further experiments on very neutron rich nuclei are really needed for the study of the r-process.

Recently, a new production method of very neutron-rich nuclei was developed, which uses Coulomb fission of an accelerated U beam at very high energy at GSI. The long-standing desire of nuclear physicists was realized by this method, i.e., a very neutron-rich "doubly closed shell" nucleus, $^{78}_{28}Ni_{50}$ was produced [17]. Further experimental information such as the half-lives, beta-decay Q values, and masses are needed for the neighboring nuclei around ^{78}Ni.

New developments in experimental technology open a new research field that was not accessible before. Such new achievement was attained for bound-state beta decay measurements. Some nuclei become unstable against weak decay when all the electrons are removed if the Q-value is very small. Such condition of fully ionization and storage of the ions was realized using the high-energy heavy ion accelerator and the storage/cooler ring ESR at GSI. The bound state beta decay of $^{187}Re^{78+}$ was beautifully measured [18], resulting in a half-life of about 12 years that is many orders of magnitude shorter than those under normal condition of ^{187}Re, $T_{1/2}$ = 4.23 x 10^{10} yr. This will influence on the s-process scenario. This method is very powerful for investigating such beta-decay relevant to the p-process and cosmochronology. The ring is also being used to determine the masses of short-lived radioactive nuclei as well as their half-lives. These are also very important inputs for the study of the r-process.

IV. Prospects

There are many other interesting developments for the problems of nucleosynthesis, which were not discussed here, although experimental study in general is still in a quite early stage in many subjects in nuclear astrophysics.

For the solar model problem, the ^{7}Be(p,γ)^{8}B reaction is still a crucial reaction to be investigated. Especially, an experiment with a ^{7}Be beam should be of great interest. There are also some other reactions relevant to the pp-chain such as the ^{3}He(^{4}He,γ)^{7}Be reaction. As for stellar models, the reaction rate of ^{12}C(α,γ)^{16}O still remains a critical subject to be further studied. The ^{12}C and ^{16}O burning processes are also of great importance.

There are several important reactions for the HCNO cycle and the early stage of the rp-process that require radioactive beams. They include ^{15}O(α,γ)^{19}Ne(p,γ)^{20}Na(p,γ)^{21}Mg, ^{14}O(α,p)^{17}F(p, γ)^{18}Ne(α,p)^{21}Ne, etc. The real pathway from the HCNO to the rp-process is important for learning the transmutation of CNO material to the heavier elements, and also the energy generation in novae and x-ray bursts. The reactions around Si are also needed for investigating the mechanism of recent novae that showed a presence of considerable amounts of Si and S. The reactions around ^{40}Ca and ^{56}Ni could be a bottleneck for the rp-process, and need to be investigated. The mapping of the proton-drip line, and the study of the reaction and the structure of the related nuclei near the proton drip line at A > 60 are crucial for learning the termination of the rp-process and possible production of the p-process nuclei.

The most challenging subject is the investigation of the r-process. Coulomb fission processes at high energy, as demonstrated at GSI, could be a possibility for the

production of very neutron-rich nuclei along the postulated r-process pathway. The technical development of a highly efficient production method at the ISOL-based facilities is really awaited here.

Although we did not discuss on the nucleosynthesis of long-lived nuclei such as ^{22}Na, ^{26}Al and ^{44}Ti, they are of great interest as their amounts will be quantitatively determined from line-gamma observations [1]. The nuclear reactions associated to these nuclei should be carefully investigated.

These nuclear reactions will be investigated experimentally at the RIKEN facility and the radioactive beam facility of KEK. Further opportunity will be provided in the RIB project at RIKEN in a few years. Although I emphasized in this report the importance of reaction studies with radioactive nuclear beams, it should be mentioned that the indirect method is also indispensably important for nuclear astrophysics. Since the cross sections become extremely small at low temperature, the indirect method is often the only possible way that gives information relevant to astrophysical problems.

Nuclear data work is also quite important, but the current situation is very serious. There is no organization that takes care of it systematically after the Fowler's effort. This requires worldwide effort by the nuclear physicists and astrophysicists working for the astrophysical problems. This should be one of the urgent subjects to be solved.

References

[1] S. Kubono, Prog. Theor. Phys. 96 (1996) 275
[2] S. Kumagai, T. Shigeyama, and K. Nomoto, Astron. Astrophys. 243 (1991) L13
[3] R. K. Wallace, S. E. Woosley, Astrophys. J. Suppl. 45 (1981) 389
[4] P. V. Magnus, et al., , Nucl. Phys. A506 (1990) 332
[5] Z. Q. Mao, H. T. Fortune, A. G. Lacaze, Phys. Rev. Lett. 74 (1995) 3760
[6] S. Schmidt, et al., Nucl. Phys. A591 (1995) 227
[7] S. Kubono, et al., Z. Phys. A348 (1994) 59
[8] S. Wanajo, et al., 1999, Astrophys. J., submitted
[9] M. Wiescher M., Gorres J., F. -K. Thielemann, Astrophys. J. 326 (1988) 384
[10] C. Funk and K. Langanke, Nucl. Phys. A480 (1988) 188
[11] A. Garcia, et al., Phys. Rev. C43 (1991) 2012
[12] K. I. Hahn, et al., Phys. Rev. C54 (1996) 1999
[13] S. H. Park, et al., Phys. Rev. C (1999), in press
[14] K. Takahashi, and H. –Th. Janka. Proc. Int. Symp. Origin of Matter and Evolution of Galaxies (Atami, Japan, 1996), ed. T. Kajino, S. Kubono and Y. Yoshii, World Scientific Pub. Co., 1997, 213
[15] K. -L. Kratz, H. Gabelmann, W. Hillebrandt, B. Pfeiffer, K. Schlšsser, and F. -K. Thielemann, Z. Phys. A 325 (1986) 489
[16] R. L. Gill, et al., Phys. Rev. Lett. 56 (1986) 1874
[17] M. Bernas, Proc. Fourth Int. Conf. Radioactive Nuclear Beams (Omiya, Japan, 1996), ed. S. Kubono, T. Kobayashi, and I. Tanihata, Nucl. Phys. A616 (1997) 352c
[18] F. Bosch, et al., Phys. Rev. Lett. 77 (1996) 5190

JP9950308

2.6 Neutron Capture Cross Sections in the keV Region

Masayuki IGASHIRA and Toshiro OHSAKI

Research Laboratory for Nuclear Reactors, Tokyo Institute of Technology

2-12-1 O-okayama, Meguro-ku, Tokyo 152-8550, Japan

e-mail: iga@nr.titech.ac.jp

Neutron capture cross sections in the keV region are reviewed on the basis of our measurements for about 40 nuclides from ^{1}H to ^{237}Np. It is shown that the p-wave neutron plays a very important role in the non-resonant capture reaction by some light nuclides at stellar energy and that careful measurements for medium and heavy nuclides agree with each other at least within uncertainties of about 10 %.

1. Introduction

Neutron capture reaction plays an important role in the nucleosynthesis in the primordial univers 10 to 1,000 s after the big bang and in stars. A thermonuclear reaction rate is given by a Maxwellian average as a function of temperature T as follows:

$$N_A < \sigma v >= N_A \frac{2}{\sqrt{\pi}} \sqrt{\frac{2kT}{\mu}} \frac{\int_0^\infty \sigma(E) E e^{-E/kT} dE}{\int_0^\infty E e^{-E/kT} dE}, \qquad (1)$$

where v and E are the velocity and energy of neutron in the center of mass system, respectively, N_A is the Avogadro's number, σ the capture cross section, k the Boltzmann's constant, and μ the reduced mass. In case of non-resonant neutron capture, the reaction rate is usually expanded as follows:

$$N_A < \sigma v >= A + BT_9^{1/2} + CT_9 + \cdots, \quad (T_9 = T / 10^9 {}^\circ K), \qquad (2)$$

where the first and third terms in the right-hand side mean the s- and p-wave neutron capture contributions, respectively. In case of general capture, more complicated expansions are used. Then, the expansion coefficients are evaluated from nuclear databases such as JENDL-3.2 for studies on nucleosynthesis. Since the value of kT is around 30 keV, accurate capture cross sections in the keV region are necessary for the determination of coefficients.

This paper reviews the present status of keV-neutron capture cross sections on the basis of our measurements for about 40 nuclides from ^{1}H to ^{237}Np.

2. General view of 30-keV Maxwellian averaged cross sections

Maxwellian (kT=30 keV) averaged capture cross sections are shown in Fig. 1 which are calculated from the data of JENDL-3.2[1]. The cross sections range from 10^{-3} to 10^{4} mb except for the extremely small value of ^{15}N. The general characteristics are the increase with mass number(A) and the saturation around A = 100. Moreover, the dips around A = 90, 140, and 210 are clearly observed which correspond to the neutron magic numbers of 50, 82, and 126. The cross section of ^{15}N should be two or three orders as large as the extremely small value by reason of p-wave neutron capture contribution described below.

3. Cross sections of light nuclides

As seen from Fig. 1, the capture cross sections of light nuclides(A<18) are very small(< 1 mb), so the measurement has been difficult without an activation method. For example, the cross section of ^{12}C, to which an activation method is inapplicable, was measured as 0.2 ± 0.4 mb[2] at 30 keV, but the cross sections of ^{7}Li were measured with errors of about 20 % in the keV region with an activation method[3].

On the other hand, thermal neutron capture cross sections have been measured for almost all stable nuclides, and the 1/v law is well-known for the s-wave neutron capture cross section. Therefore, the cross sections in the keV region of light nuclides such as ^{12}C and ^{16}O have been ordinarily evaluated using the 1/v law and the thermal neutron capture cross sections. The evaluated values of ^{12}C and ^{16}O are 3.2 and 0.17 μ b at 30 keV, respectively.

Our group has measured the capture cross sections of ^{7}Li, ^{12}C, and ^{16}O in the keV region[4-9], and the measured values at 30 keV are 39.3 ± 6.0, 15.4 ± 1.0, and 34 ± 4 μ b, respectively. The value of ^{7}Li is in good agreement with the previous measurement[3] and the evaluation, 41 μ b, from the 1/v law and the thermal neutron capture cross section. However, our results of ^{12}C and ^{16}O are 5 and 200 times as large as the evaluations, respectively.

We have adopted a prompt γ-ray detection method with an anti-Compton NaI(Tl) spectrometer, and observed the branching ratios of neutron capture states. The observed ratios for the ^{12}C and ^{16}O target nuclei are shown in Figs. 2 and 3, respectively, together with the ratios of the thermal neutron capture states. The striking feature of 30- or 40-keV neutron capture is the strong transitions to the s- and d-states, which implies the predominance of p-wave neutron capture because the electric dipole(E1) transition is predominant in the non-resonant neutron capture. In case of thermal neutron capture, the strong E1 transitions to the p-states are observed. As for ^{7}Li, the ratios of 30-keV neutron capture states are the same as those of thermal neutron capture states[4,10].

We have also obtained the partial capture cross sections of ^{12}C[5-7] corresponding to the branching ratios, and those to the ground and first excited states of ^{13}C are shown in Fig. 4. The solid line shows the 1/v law normalized to the partial capture cross section at thermal energy. Our results for the ground state below 100 keV are well explained by the 1/v law, but our results at 200 and 550 keV exceed the 1/v law. This excess should be ascribed to the d-wave neutron capture contribution. The dotted line shows a fitting of the v law, which is expected for the p-wave neutron capture, to our results for the first excited state. Our results strongly support the

v law, i.e., the p-wave neutron capture.

Figure 5 shows the bound states of relevant compound nuclei. The states are categorized into three groups by the spin and parity selection rule: Those with a solid line could be populated by the E1 transition from the states formed by the p-wave neutron capture, those with a dashed line could be populated by the E1 transition from the states formed by the s-wave neutron capture, and the others are indicated by dotted lines. The p-wave neutron capture would become important in the keV region for the target nuclei whose compound nuclei have solid line states, while the s-wave neutron capture would be still predominant for the target nuclei whose compound nuclei have no solid-line states. As for ^{15}N, its compound nucleus has only solid line states, so a large contribution of p-wave neutron capture would be expected for the keV-neutron capture. In fact, its capture cross section calculated on the basis of a direct neutron capture model is about 10 μ b at 30 keV[11], which is about 500 times as large as that evaluated from the 1/v law and the thermal neutron capture cross section.

4. Cross sections of medium and heavy nuclides

The capture cross sections of medium and heavy nuclides are considerably large compared with those of light nuclides, as shown in Fig. 1, except for some nuclides near the neutron magic numbers. Therefore, if an enough amount of chemically and isotopically purified sample is prepared, the capture cross sections of those nuclides could be measured with a prompt γ -ray detection method which is applicable to all target nuclides.

The capture cross sections of ^{147}Sm, ^{163}Dy, and ^{237}Np are shown in Figs. 6 - 8. The large values of Kononov et al.[12] and Mizumoto[13] in Fig. 6 could be ascribed to the influence of the water in their oxide powder samples[14]. Our results of ^{147}Sm are in good agreement with the measurements by Macklin[15] and Wisshak et al.[16] and the evaluations of ENDF/B-VI[17]. As for ^{163}Dy, all the measurements[18-20] well agree with each other. The evaluation of ^{163}Dy for ENDF/B was done many years ago[21], and does not reproduce the measurements. There has existed a large discrepancy between the measurements for ^{237}Np by Hoffman et al.[22] and Weston and Todd[23], as shown in Fig. 8. Our results completely support those of Weston and Todd. Individual laboratories have adopted their own experimental technique. Therefore, the good agreement seen in Figs. 6- 8 implies the reliability of their data, although there still exists detailed discussion about accuracy within 5 - 10 %.

5. Conclusion

The 30-keV Maxwellian averaged capture cross sections range from 10^{-3} to 10^{4} mb. The cross sections increase with mass number(A), and are saturated around A = 100. There exist the dips around A = 90, 140, and 210 which correspond to the neutron magic numbers of 50, 82, and 126.

The p-wave neutron plays a very important role in the non-resonant capture reaction by some light nuclides at stellar energy. Careful measurements for medium and heavy nuclides agree with each other at least within uncertainties of about 10 %.

References

[1] Nakagawa T. et al.: J. Nucl. Sci. Technol., **32**, 1259 (1995).
[2] Macklin R. L. et al.: Phys. Rev., **129**, 2695 (1963).
[3] Imhof E. L. et al.: Phys. Rev., **114**, 1037 (1959).
[4] Nagai Y. et al.: ApJ., **381**, 444 (1991).
[5] Nagai Y. et al.: ApJ., **372**, 683 (1991).
[6] Ohsaki et al.: ApJ., **422**, 912 (1994).
[7] Kikuchi T. et al.: Phys. Rev. C, **57**, 2724 (1998).
[8] Igashira M. et al.: Nucl. Phys., **A536**, 285 (1992).
[9] Igashira M. et al.: ApJ., **441**, L89 (1995).
[10] Nagai Y. et al.: unpublished.
[11] Rauscher T. et al.: ApJ., **429**, 499 (1994).
[12] Kononov V. N. et al.: Sov. J. Nucl. Phys., **26**, 500 (1977).
[13] Mizumoto M.: Nucl. Phys., **A357**, 90 (1981).
[14] Mizumoto M. and Sugimoto M.: Nucl. Instr. and Meth., **A282**, 324 (1989).
[15] Macklin R. L.: Reports EXFOR 12966.003 (1986).
[16] Wisshak K. et al.: Phys. Rev. C, **48**, 1401 (1993).
[17] ENDF/B-VI data file for ^{147}Sm (MAT=6234), evaluated by R.Q.Wright, R.E.Schenter, F.M.Mann and A.Prince (1989).
[18] Beer H. et al.: Reports EXFOR 12881.002 (1984).
[19] Bokhovko M. V. et al.: Yadernie Const., **4**, 8 (1988).
[20] Voss F. et al.: Report FZKA-6104, Forschungszentrum Karlsruhe (1998).
[21] ENDF/B-VI data file for ^{163}Dy (MAT=6646), evaluated by R. F. Schenter and F. Schmittroth (1974).
[22] Hoffman M. et al.: Bull. Am. Phys. Soc., **21**, 655(JE3) (1976).
[23] Weston L. W. and Todd J. T.: Nucl. Sci. Eng., **79**, 184 (1981).

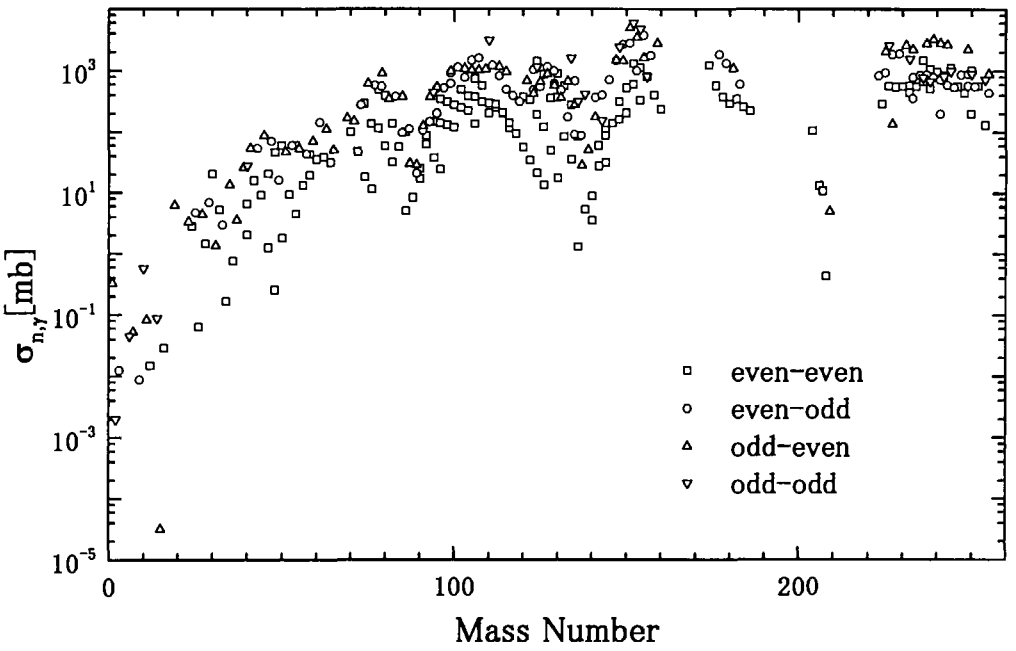

Fig.1. Maxwellian (kT=30keV) averaged neutron capture cross sections calculated from the data of JENDL-3.2.

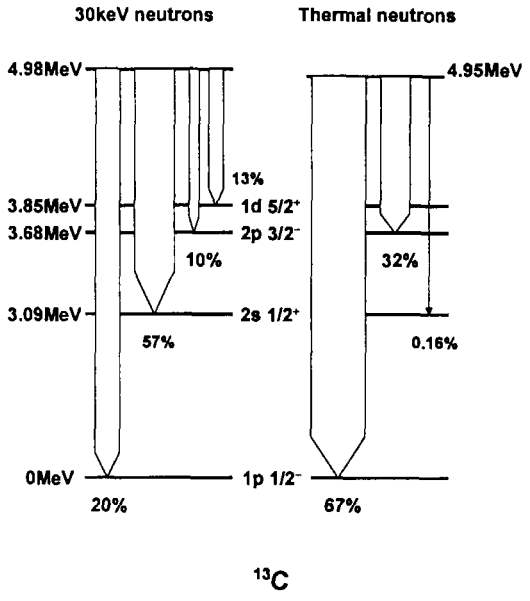

Fig.2. Branching ratios of neutron capture states of ^{13}C

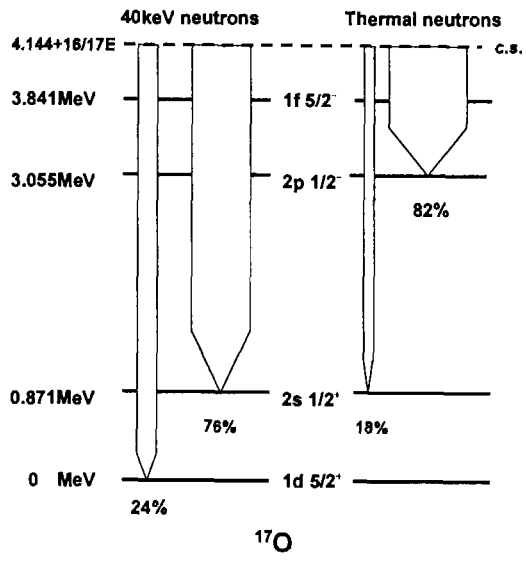

Fig.3. Branching ratios of neutorn capture states of ^{17}O

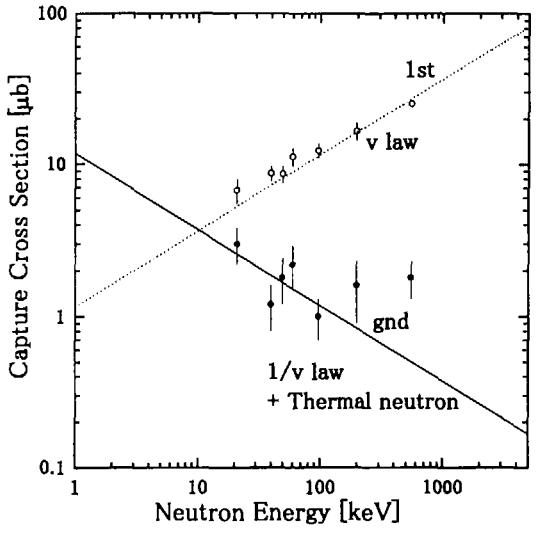

Fig.4. Partial neutron capture cross sections to the ground and first excited states of ^{13}C

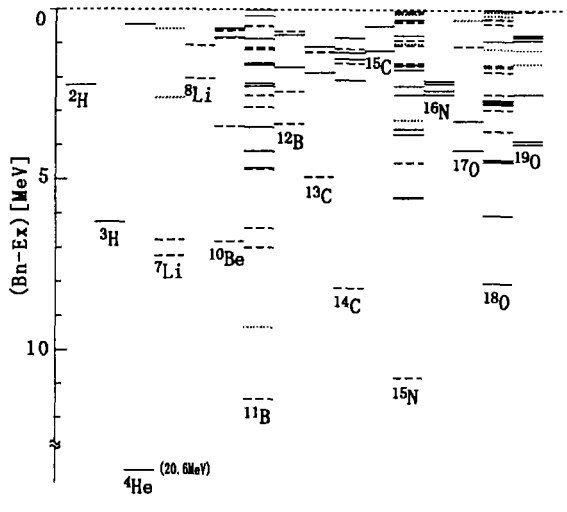

Fig.5. Bound states of relevant compound nuclei

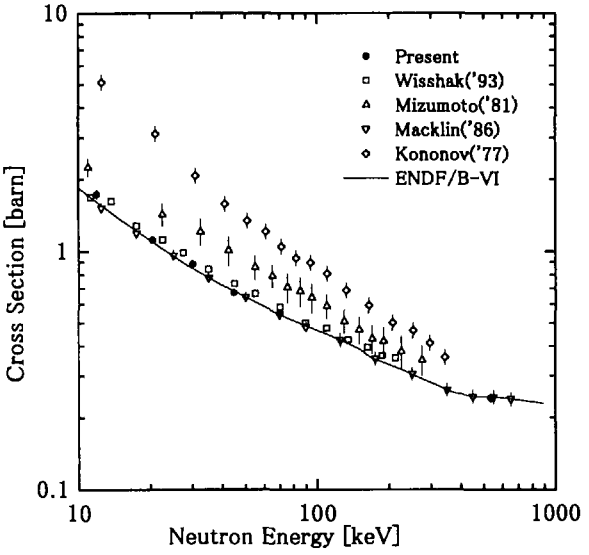

Fig.6. Neutron capture cross sections of ^{147}Sm

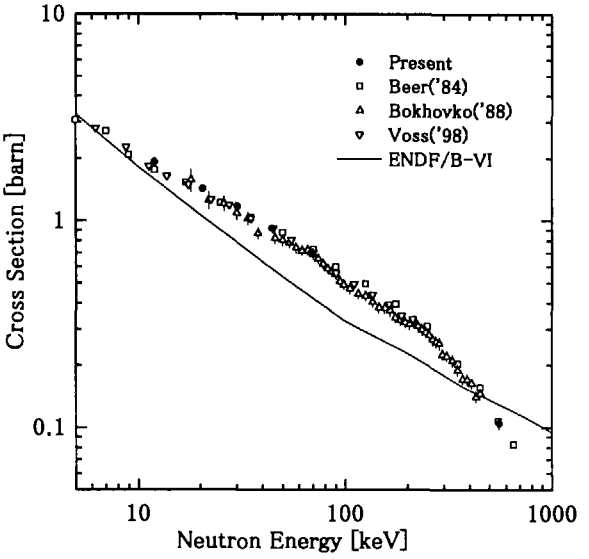

Fig.7. Neutron capture cross sections of ^{163}Dy

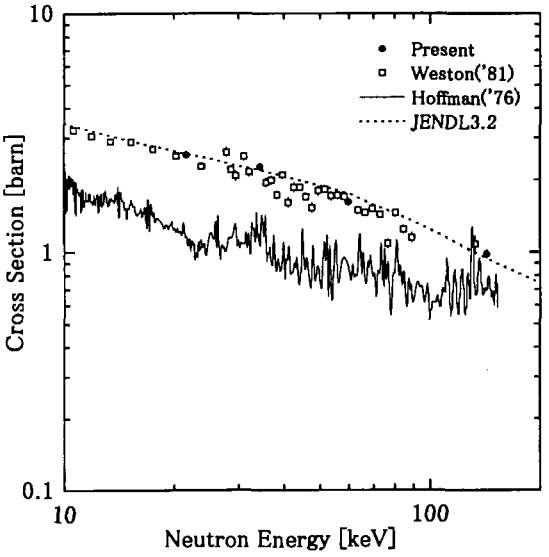

Fig.8. Neutron capture cross sections of ^{237}Np

JP9950309

2.7 Nuclear Data Needs in Thailand

Somporn Chongkum
Physics Division, Office of Atomic Energy for Peace
Vibhavadee-Rangsit Road, Chatuchak,
Bangkok 10900, THAILAND
e-mail : somporn@oaep.go.th

The major nuclear facilities in Thailand are composed of nuclear research reactor , neutron generators, electron linear accelerators and 1 GeV Synchrotron facility, which is under construction. The other small facilities are radioisotope sources and X ray tubes for X ray diffraction and fluorescence studies. Nuclear data activities in each institutions are mainly for application purposes, e.g., utilization of 2 nanosecond pulsed neutron time-of-flight facility at Chiangmai University, research reactor utilization at Office of Atomic Energy for Peace, and nuclear data for industrial applications.

Office of Atomic Energy for Peace (OAEP) is the function arm for nuclear institutions in Thailand. Its major roles are nuclear regulatory, coordinating for nuclear affairs and foreign relations, R&D for nuclear science and technology and giving nuclear services. Nuclear data activities concerning Thai Research Reactor (TRR-1/M1) are for examples : neutronics and thermalhydraulics for reactor operation, neutron energy spectrum and neutron flux measurement for neutron activation analysis and isotope production, neutron and gamma doses, shielding and material testing for radiation safety, and neutron beam experiments.

OAEP is taking part in the areas of regional cooperation on utilization of nuclear research reactors, education and training, sharing of research reactor experimental facilities, establishment of nuclear data program and information exchange. The nuclear data reports have been shared among institutions in Thailand through OAEP, which is served as a central nuclear data depository including e.g., the data bank of International Nuclear Information Services (INIS) IAEA, IAEA-NDS, Joint Research Centre Commission of the European Communities and Japanese Nuclear Data Committee (JNDC).

This report shows the nuclear facilities in Thailand, the roles of the Office of Atomic Energy for Peace on nuclear data depository and nuclear power development program. The main activities at the Thai Research Reactor TRR-1/M1 concerning nuclear data needs for specific uses in both theoretical and experimental aspects are also described.

1. Introduction

In order to support the research and utilization in nuclear technology, many institutions have exploited nuclear facilities and man power to perform this task. The major facilities in Thailand are composed of these followings :

1) Thai Research Reactor (TRR-1/M1) - 2 MW TRIGA Mark III type at the Office of Atomic Energy for Peace (OAEP) which has been utilized for the production of radioisotopes mainly for medical use, neutron activation analysis, reactor physics research, and radiation technology application [1].
2) Neutron generators at Chulalongkorn and Chiangmai Universities, e.g., utilization of 2 nanosecond pulsed neutron time-of-flight facility [2].
3) Electron beam accelerators, using for medical therapy, sterilization of medical supplied products and for gems coloration.
4) 1 GeV Synchrotron facility of Ministry of Science Technology and Environment (MOSTE), which is under construction [3].
5) The other small facilities which using radioisotopes, in more than 100 industries, 30 medical institutes, 30 R&D institutes and 10 agriculture institutes.

Nuclear Data activities in each institutions are manly aiming for basic nuclear studies and application purpose. The Office of Atomic Energy for Peace (OAEP) is taking part in the areas of regional cooperation on utilization of nuclear research reactors, education and training, sharing of research reactor experimental facilities, establishment of nuclear data program and information exchange. The nuclear data reports have been shared among institutions in Thailand through OAEP, which is served as a central nuclear data depository including e.g., the data bank of International Nuclear Information Services (INIS) IAEA, IAEA-NDS, Joint Research Centre Commission of the European Communities and Japanese Nuclear Data Committee (JNDC).

2. Organization of OAEP

The execution of the country atomic energy program has been centered by the Office of Atomic Energy for Peace (OAEP), which was established since 1961. Its duties were given in compliance with the resolution of the Thai Atomic Energy Commission (Thai A.E.C.), the policy making organ of the government of Thailand. In accordance with its statutory function, OAEP responsibilities comprise three main aspects of activities, mamely :

1) regulatory role persuant to the Atomic Energy for Peace Act.
2) co-ordinating role for nuclear affairs and foreign relations.
3) research and development in nuclear technology.

At present, OAEP consists of 11 divisions, as shown in the chart.

Organization Chart

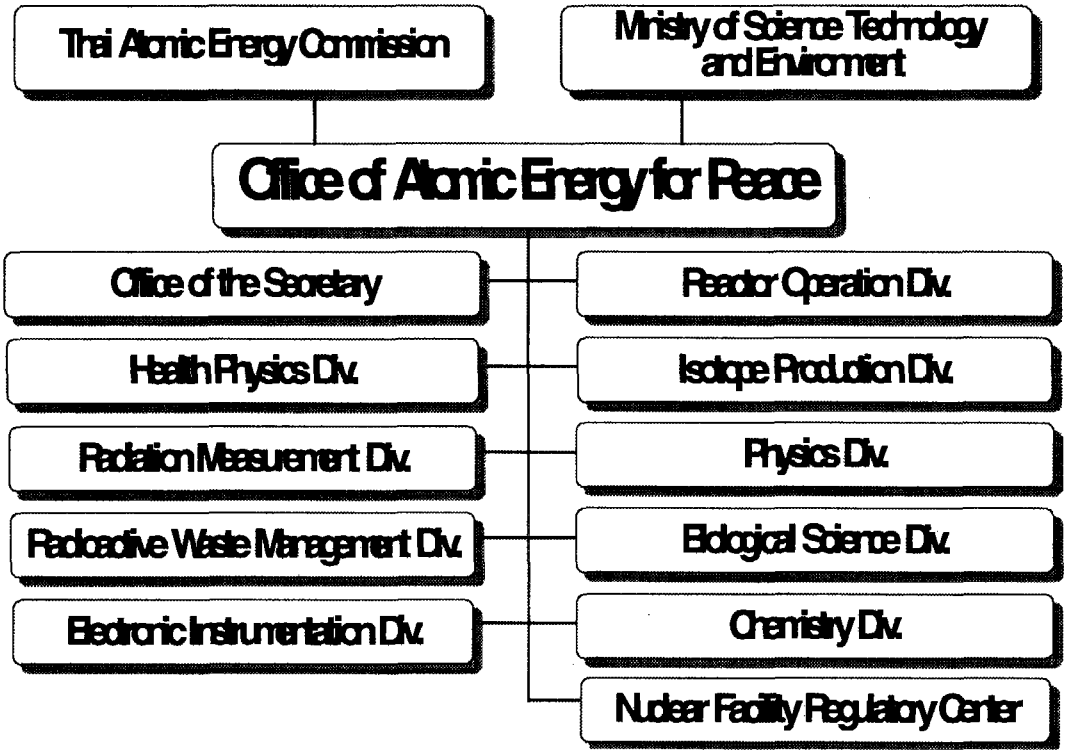

Thai Atomic Energy Commission

Sub Committees

1. Reactor Safety
2. Medical Application
3. Agricultural Application
4. Industrial Application
5. Irradiated Food Testing
6. Nuclear Material Safeguard
7. Nuclear Law
8. Licensing of Radioisotopes
9. Nuclear Power Plant Program
10. Cooperation in Nuclear Science with Science Technology Agency, Japan

3. Nuclear Power Development Program

The electricity demand in Thailand is rapidly increasing roughly 1,000 MW every years since last two decades. Thailand was first introduced the nuclear power as an electricity generation option in 1967, but the nuclear industry in the country was slowly developed due to various problems, e.g., public opposition, economic repercussion and the uncovering of the indigenous petroleum resources. Nonetheless, the Electricity Generating Authority of Thailand (EGAT), the main power producer, still continued to follow-up the nuclear power program, implementation and nuclear technology studies [4].

In 1984, the International Atomic Energy Agency (IAEA) assisted Thailand in undertaking of an energy and nuclear power planning study. The result showed that the proper time of introducing nuclear power around the year 2004 with units capacity of 900 MW and this provided the basis for the long range power planning.

Faced with dwindling indigenous fossil resources and restrictions on the use of further hydro as an energy source, EGAT has essentially reconsidered introducing nuclear power plants to provide a significant fraction of the long-term future electricity demand. The first nuclear power station of 2,000 MW was originally planned for commissioning by 2006. Study on the viability of such plan was conducted in 1992 on the preliminary basis of comparing the nuclear option with the equivalent thermal generating alternatives. In conjunction with this, the justification to conduct the studies on feasibility, siting and environmental impacts was perused. The study revealed that the nuclear option is economically viable and that the respective studies are justified.

Led by a team of expert from IAEA, a workshop seminar on launching a nuclear power program in Thailand was organized for the decision makers in August 1993. Conclusion was drawn that top priority must be given to the implementation of the following three activities :

1) Legislation of nuclear power laws and establishment of independent and competent nuclear regulatory body
2) Extensive public acceptance campaign
3) Proceeding of manpower development, siting and feasibility study.

In July 1996, the National Committee comprising various concerned government and private agencies has been set up and chaired by the Ministry of Science, Technology and Environment. Under the steering of this committee would be four sub-committees namely : Sub-committee on economic viability & infrastructure; sub-committee on technology & safety; sub-committee on environmental impact and sub-committee on public information. The committee is responsible for all the work and activities related to the development of nuclear power including all studies and recommendations for government decision.

4. Nuclear Data Needs in Thailand

The main nuclear facilities in Thailand which are under construction are the nuclear research reactor and the synchrotron facility. The nuclear data needs for both facilities will be described accordingly.

4.1 Research Reactor

Office of Atomic Energy for Peace is in the process of establishing a new Nuclear Research Center, the major project will be the construction of a 10 MW Research Reactor, on Isotope Production Facility and a Centralized Waste Processing and Storage Facility. The objectives of the reactor are as follows :

- Beam experiment : Neutron Scattering (NS), Neutron Radiography (NR), and Prompt Gamma Neutron Activation Analysis (PGNAA)
- Medical therapy of patients through the Boron Neutron Capture Therapy (BNCT) technique.
- Radioisotope production for medical, industrial and agricultural
- Applied research and technology development in the nuclear field
- Training in reactor physics (neutron physics, thermal hydraulics, reactor experiments, etc.).

The existing 2 MW TRIGA Mark III research reactor is still in operation and will be decommissioned soon after the completion of the new reactor commissioning approximately in the year 2001. The nuclear data needs will be mainly on the specific purposes, e.g., reactor operation, spent fuel transportation and radioactive waste management.

a. Reactor Operation

Besides the nuclear data needs for the design and development of reactor core, reactor dosimetry is the topic much relating to nuclear data. Reactor dosimetry studies are critical examination of evaluated neutron fluence and neutron spectrum.

Non-destructive measurement and calcuation of fuel burnup are interesred for the point of view of control and management of reactor fuels by using correlation between activity ratio of fission products from post irradiation examination.

b. Spent Fuel Transportation

The cast to contain the spent fuels should have enough shielding ability against the intense radiation of the fission product contained. Fission yield data the product nuclides and nuclear decay data of those are used to calculate the fission product inventory in the spent fuel.

For the purposes of shielding analysis, the intensity of radiation source in the spent fuel, that is of neutron and gamma rays, has to be evaluated with confidence.

c. **Waste Management**

In order to establish adequate management system of the radioactive waste, it is necessary to evaluate various factors of the waste, e.g., generation and inventory, heat generation, shield calculation, criticality both in the treatment process and in the disposal, and long term safety analysis. The nuclear data requirements involve basic decay data of the actinide nuclides as will as the daughter nuclides in the radioactive decay chains and those of the fission products.

4.2 Synchrotron Facility

The Siam Photon Project promoted by the National Synchrotron Research Center of Thailand which composes of a) 40 MeV electron Linac b) 1 GeV Booster Synchrotron and c) 1 GeV electron storage ring will be built. The major facilities are transferred from the shut down SORTEC Laboratory in Tsukuba, Japan. The building construction and facility commissioning will be finished around begin of the year 2001. The project aims at promoting the scientific researches based on spectroscopic methods in the vacuum ultraviolet and soft X-ray regions.

Radiation safety is the main task of the Project as followings : Radiation Shielding Analysis, Radiation Safety Control, Radiation Measurement, Analysis and Control, Research on Radiation Production, Transport and Shielding. The verification of shielding calculation for Linac tunnel shielding, Booster Synchrotron and Storage Ring will be done for design analysis. Thus the specific nuclear data is needed for high energy electron and Bremsstrahlung shielding design.

5. Conclusion

This report shows the nuclear facilities in Thailand, the roles of the Office of Atomic Energy for Peace on nuclear data depository and nuclear power development program. The main activities at the Thai Research Reactor TRR-1/M1 and 1 GeV Synchrotron facility concerning nuclear data needs for specific uses in both theoretical and experimental aspects are also described.

In addition to elaborate the base data file for the calculation codes, it might be much helpful to provide such a code system involving necessary data library and indicating confidence limit to the results obtained by the code in connection with its applicability range.

References

[1] Outline of Office of Atomic Energy for Peace (1995).
[2] Vilaithong. T. et.al "A 2 Nanosecond Pulsed Neutron Beam Facility for Research in Science and Technology, International Report 1991.
[3] Pairsuwan W. and Ishii T. : "The Saim Photon Laboratory" J.Synchrotron Rad. (1998).
[4] Electricity Generating Authority of Thailand, "Electric Energy Situation" EGAT Annual Report (1997).

JP9950310

2.8 NUCLEAR POWER DEVELOPMENT AND NUCLEAR DATA ACTIVITIES IN MALAYSIA

Gui, Ah Auu
Malaysian Institute for Nuclear technology Research
Ministry of Science, Technology and the Environment
43000 Kajang, Selangor Darul Ehsan, Malaysia
e-mail: gui@mint.gov.my

Abstract

In this paper, research activities on nuclear power requirement carried out jointly by MINT and other organizations are described. Also discussed are activities on neutronics such as TRIGA reactor fuel management, storage pool criticality, and reactor fuel transfer cask calculations. In addition, recent work on radiation transport activities in MINT such as skyshine and photon phantom dose calculations using the MCNP and MRIPP computer codes are presented. Finally, nuclear data measurement works by researchers in Malaysian universities are described.

1. Introduction

A new nuclear era began in Malaysia with the establishment of the Tun Dr. Ismail Atomic Research Center (PUSPATI) in 1972. It was renamed the Nuclear Energy Unit (UTN) in June 1983 and then, the Malaysian Institute for Nuclear Technology Research (MINT) in August 1994. Initially, research activities in MINT centered around our 1 MW(t) TRIGA Mark II reactor. The scope of research has widened considerably with the addition of more facilities such as the Gamma Irradiation Facility (SINAGAMA), Electron-Beam Machine (EBM) Facility, Radiation Vulcanization of Natural Rubber Latex (RVNRL) Facility, and Thermal Oxidation Plant (TOP).

In anticipation of increasing manpower requirement in the nuclear technology and nuclear power sectors, the Department of Nuclear Science was set up at the National University of Malaysia (UKM) in 1979. Nuclear related researches also intensified in other local universities.

This paper presents activities on nuclear power, neutronics, shielding, and radiation transport that are carried out in MINT. Nuclear data related works done at local universities are also discussed.

2. Nuclear Power Development

Concerned about over dependence on oil as the energy source for Malaysia, a feasibility study of generating electricity using nuclear power plant was carried out by NEB, the National Electricity Board (predecessor of Tenaga Nasional Berhad, TNB). The results indicated that commissioning

of a medium-sized nuclear power plant was economically feasible around 1986/87[1]. However, with the discovery of more oil and natural gas, the nuclear power option was reassessed in late 1979[2]. The study that was carried out by NEB under an IAEA technical assistant project, recommended that the nuclear option should be kept as the last option and priority was to be given to the development of natural gas, coal, and hydro as the energy source.

In 1984-1985, another review on the nuclear power option, covering the period from 1985-2010 was conducted jointly by NEB and MINT (known as the Nuclear Energy Unit then) under an IAEA technical assistance project. The most optimistic scenario of the study expected that Malaysia would use electricity from nuclear power plant in the year 2005.[3]

Subsequently, several studies[4,5] related to nuclear power planning were carried from 1985 until 1989. These include the studies on the demand of energy and electricity, financial implication, manpower assessment, industrial capability assessment, uranium resources assessment, and nuclear power plant site selection survey. However, due to the low priority accorded to the nuclear power option, the se studies were discontinued since 1989.

3. Neutronics

The objectives of reactor fuel management program at MINT is to ensure save and economic utilization of TRIGA reactor fuel. To this end, computer codes are used to simulate various core configurations before choosing the "best" fuel pattern for the core. The criteria for the fuel configuration are:- (1) the effective multiplication factor (k_{eff}) should be $1.03 \leq k_{eff} \leq 1.05$ and (2) the maximum power fraction of fuel element ≤ 1.6.

Initially, the SRAM[6] code developed at the Pennsylvania State University was modified for fuel management calculations. However, from 1990 onwards, TRIGAM[7], a modification of the TRIGAC code developed at Institute Josef Stefan, Ijubjana, was used for TRIGA reactor fuel management. The fuel data was obtained from the results of WIMS[8] calculations. At present, MINT TRIGA reactor is operating with core number 10 that will be replaced by core number 11 next year.

In the unlikely event that all of the fuel elements in the reactor core have to be transferred out of the core, a temporary fuel storage pool (1.5 m I.D. cylinder filled with water) is to be constructed to safely store all these fuel. The MCNP Monte Carlo code[9] is used to perform criticality calculations in the design of the fuel storage pool. Based on the limited space available in the reactor hall and the requirement that $k_{eff} \leq 0.8$, it is decided that the fuel should be stored in a square array with a lattice spacing of 7 cm. The 13 by 13 array can accommodate a total 127 fuel elements while satisfying the above constrains. The fuel storage pool is one of the facilities to be constructed in the project to upgrade our reactor supporting facilities.

4. Radiation Transport

In order to use the fuel storage pool, a fuel element transfer cask is needed to transfer the fuel elements from the reactor tank to the fuel storage pool. The transfer cask design is done using computer codes such as ANISN[10], and ORIGEN[11]. The preliminary design is an annular cylinder with 4"-thick lead shield.

Skyshine radiation refers to radiation emanating from a source close to the ground into the atmosphere that get scattered by the air and arrive at a detector near the ground. Since the skyshine dose is normally very low, computational intensive calculations are needed in the analysis of skyshine problems. Hence, simplified methods such as the line-beam and conical-beam methods[12] have been developed for routine skyshine analysis and preliminary design of nuclear facilities.

Critical to the use of the line-beam and the conical-beam methods is the availability of the corresponding response functions. Line-beam and conical-beam response functions (LBRFs and CBRFs) for neutron and associated secondary photons have been evaluated by the author[13] using the MCNP code. These modern response functions are expressed in dose equivalent units based on ICRP recommendations[14,15] for three irradiation geometries:- effective dose equivalent for an anthropomorphic phantom [AP irradiation geometry], dose equivalent on the principal axis at a depth of 10 mm for radiation incident in the plane parallel beam [PAR] and isotropic irradiation geometries on the ICRU sphere [ISO]. These response functions are fitted with empirical formulas to facilitate their use in the line-beam and conical-beam methods. Correction for the effect of ground on the skyshine dose is effected through ground correction factors. These correction factors defined as the ratio of skyshine dose with air-ground interface to that of infinite-air medium, are evaluated from MCNP results. Empirical equations for these factors are tabulated[13].

Details of the evaluation of these response functions are described elsewhere[13]. The skyshine response functions are available from Radiation Shielding Information Center (RSIC), Oak Ridge National Laboratory (DLC-188/SKYDATA).

Figure 1 illustrates the result of applying the beam response functions to an open silo skyshine problem. In this problem, a point, isotropic, and mono-energetic source emitting neutrons of energy E (14 or 3.25 MeV) is placed 1 m below the top and on the axis of a cylindrical silo of 2 m inner radius.

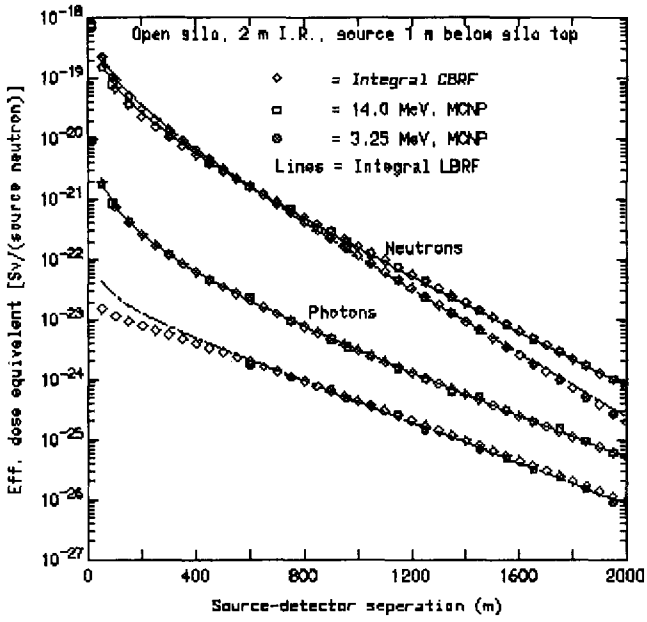

Figure 1: Integral line-beam and conical-beam method results for the open silo skyshine problem. Also shown are results calculated directly using the MCNP code.

The above response functions are for neutron source and detector both located at the same elevation. As an extension of the above work, the response functions for the source and detector located at different heights will be evaluated at MINT. Besides, the improvement of the response functions for low energy neutron source is also considered at MINT.

MINT is participating in a regional project coordinated by the International Atomic Energy Agency (IAEA)[16]. In this project the MRIPP computer code that is based on the MCNP code and the 3-D MRI geometry, is used to calculate the photon dose due to radioactive sources in the lung of the Asian Reference Man. The calculated results together with the measured results for the phantom that was on loan from the IAEA, will give the necessary calibration factors for internal dose assessments.

In another local institution of higher learning, a simple Monte Carlo code has been used to calculate the self-absorption correction for gamma ray counting of samples under different sample-detector geometries[17].

5. Nuclear Data Measurement

Nuclear and atomic data measurements are mainly performed in the universities. For example, the $^{10}B(n,t)2\alpha$ and $^{6}Li(n,t)\alpha$ reaction cross sections for neutron spectra in various TRIGA reactor irradiation facilities have been measured by researchers at UKM. The targets were irradiated in

the Thermal Column, Rotary Rack, PAUS Delayed Neutron Analysis System, and the Central Thimble facilities of MINT TRIGA reactor.
Other activities carried out at UKM, in collaboration with Julich Research Center (KFA), include measurements of tritium atom production rates via ternary fission of UO_2 and ThO_2 and determination of the excited functions of $^{9}Be(n,xt)$, $^{10}B(n,t)2\alpha$, and $^{14}N(n,t)^{12}C$ reactions. The $^{10}B(n,t)2\alpha$ cross section for neutrons with energy range from 0.025 eV to 10.6 MeV and the $^{14}N(n,t)^{12}C$ cross section for neutron energy range of 5.0 to 10.6 MeV were also determined[18].

Experiments to measure the ^{241}Am-gamma photon scattered by low- to high-Z elements have been performed by the physics group at the University of Science Malaysia (USM). However, recent activities concentrate on measuring the gamma photon spectra back scattered by medium-Z elements such as Zn (Z=30), Mo (Z=42), and W (Z=74). Both the coherent and incoherent scattering of gamma photon are being investigated. Details of the measurements are given by Chong et al.[19]

6. Conclusions

Activities on nuclear power, neutronics, radiation transport, and nuclear data measurements carried out in Malaysia are presented. Unfortunately, the momentum to continue these activities have decreased greatly due to the low priority given to the nuclear power option and the difficulty of obtaining support for these works.

References

[1] Ahmad Tajuddin, A. and Gui, A. A., "An Outlook on Energy and Energy Research in Malaysia," paper presented at the Workshop on The Strengthening of Energy Research Capacity in Developing Countries, Stockholm, Sweden, (1982).

[2] National Electricity Board (NEB) Malaysia, "The Possible Role of Nuclear Power in Malaysia: 1985-2000", National Electricity Board, (1979).

[3] "Nuclear Option Review for Malaysia," A Joint Report of the National Electricity Board of the States of Malaya and the Nuclear Energy Unit of the Prime Minister's Department, (1985).

[4] National Electricity Board (NEB) Malaysia, "Assessment of the FINPLAN Model to Analyze the Financial Viability of WASP Expansion Plans," NEB, (1989).

[5] "Preliminary Assessment of the Malaysian Industrial Capability in the Power Sector, Part I: Main Report," A Joint Report by the Nuclear Energy Unit of the Prime Minister's Department and the National Electricity Board Malaysia, (1989).

[6] Levin, S. H., Private communications.

[7] Mele, I. and Ravnik, M.., "TRIGAC - A New Version of TRIGAP Code," Institute Josef Stefan, Ijubjana, Yugoslavia, (1992).

[8] Askew, J. R., Fayers, F. J., Kemshell, and F. B.WIMS, "A general Description of the Lattice Code WIMS," Journ. Of the Brit. Nucl. Energy Soc., 5, 4, 564 (1966).

[9] "MCNP: A General Monte Carlo Code for Neutron and Photon Transport, Version 3A," LA-7396-M, Rev. 2, Briesmeister, J. F., Ed., Los Alamos National Laboratory, (1991).

[10] Engle Jr., W. W., "A User's Manual for ANISN, a One Dimension Discrete Ordinates Transport Code with Anisotropic Scattering," K-1693, Oak Ridge Gaseous Diffusion Plant, Oak Ridge National Laboratory, (1967).

[11] Croff, A. G., "ORIGEN2: A Versatile Computer Code for Calculating the Nuclide Compositions and Characteristics of Nuclear Materials," Nucl. Tech., 62, 335 (1983).

[12] Shultis, J. K., Faw, R. E., and Bassett, M. S., "The Integral Line-Beam Method for Gamma Skyshine Analysis," Nucl. Sci. Eng., 107, 228 (1991).

[13] A. A. GUI, J. K. SHULTIS, and R. E. FAW, "Response Functions for Neutron Skyshine Analyses," *Nucl. Sci. and Eng.*, 125, 111, (1997).

[14] ICRP, "Data for Use in Protection Against External Radiation," Annuals of the ICRP, Vol. 17, No. 2/3, Publication 51, International Commission on radiological Protection, Pergamon Press, Oxford, UK (1987).

[15] ICRP, *Statement form the 1985 Paris Meeting of the International Commission on Radiological Protection*, Publication 45, International Commission on radiological Protection, Pergamon Press, Oxford, UK (1985).

[16] Lau, H. M., IAEA Intercomparison of In-Vivo Counting System using an Asian Phantom.

[17] Ahmad Saat, Appleby, P. G., and Nolan, P. J., "Self-absorption Corrections of Various Sample-Detector Geometries in Gamma-ray Spectrometry Using Simple Monte Carlo Simulations," Proc. INC '97, International Nuclear Conference, Oct. 27-28, Kuala Lumpur, Malaysia (1997).

[18] Suhaimi A. and Gui, A. A., "Nuclear And Atomic Data Activities in Malaysia", Proc. 1995 Symposium on Nuclear Data, Nov. 16-17, 1995, JAERI, Tokai, Japan, p. 62 (1996).

[19] Chong, C. S., Elyaseery, I. S., Shukri, A., and Tajuddin A. A., " Gamma Ray Spectrum of Am-241 in a Back Scattering Geometry Using a High Purity Germanium Detector," Proc. INC '97, International Nuclear Conference, Oct. 27-28, Kuala Lumpur, Malaysia (1997).

2.9 The Status Report on the Nuclear Data Project in Korea

G. N. Kim, W. Y. Baek, H. S. Kang, J. Y. Choi, M. H. Cho, I. S. Ko, W. Namkung
Pohang Accelerator Laboratory, POSTECH
San 31 Hyojadong, Namgu, Pohang, 790-784, Korea
Phone: +82(562)279-1105 e-mail: gnkim@postech.ac.kr

J. H. Chang
Korea Atomic Energy Research Institute,
P.O. Box 105, Yusung, Taejon, 305-600, Korea
Phone: +82(42) 868-2884 e-mail : jhchang@kaeri.re.kr

The nuclear data project as one of the nation-wide nuclear R&D programs was launched by the Korea Atomic Energy Research Institute (KAERI) in 1996. Its main goals are to establish a nuclear data system, to construct the infrastructure for the nuclear data productions and evaluations, and to develop a highly reliable nuclear data system. In order to build the infrastructure for the nuclear data production, KAERI wants to build an intense pulsed neutron source by utilizing accelerator facilities, technologies, and manpower at the Pohang Accelerator Laboratory (PAL). The PAL proposed the Pohang Neutron Facility (PNF), which consists of a 100-MeV electron linac, a water-cooled Ta target, and at least three different time-of-flight (TOF) paths. The 100-MeV electron linac was designed and constructed based on experiences obtained from construction and operation of the 2-GeV linac at PAL. We report a status report on the nuclear data production and evaluation in Korea.

1. Introduction

As the nuclear power program in Korea expanded since 1980, lots of projects on the nuclear power development and the nuclear R&D applications have been growing rapidly. Accordingly the intensive neutron source is needed to support nuclear R&D activities, medical and industrial applications of radioisotopes, and nuclear data productions. The Korea Atomic Energy Research Institute (KAERI) constructed a 30-MW Korea Multi-purpose Research Reactor (KMRR) called HANARO (Hi-Flux Advanced Neutron Application Reactor) and operated it since 1995[1].

The nuclear data project as one of the nation-wide nuclear R&D programs was launched by the KAERI in 1996[2]. Its main goals are to establish a nuclear data system, to construct the infrastructure for the nuclear data productions and evaluations, and to develop a highly reliable nuclear data system. In order to build the infrastructure for the nuclear data production, KAERI wants to build an intense pulsed neutron source by

utilizing accelerator facilities, technologies, and manpower at the Pohang Accelerator Laboratory (PAL). The PAL proposed the Pohang Neutron Facility (PNF), which consists of a 100-MeV electron linac, a water-cooled Ta target, and at least three different time-of-flight (TOF) paths[3]. The 100-MeV electron linac was designed and constructed based on experiences obtained from construction and operation of the 2-GeV linac at PAL.

We present the status of the PNF and activities on the nuclear data production and evaluations in Korea.

2. The Status of Pohang Neutron Facility

2.1. Design of 100-MeV Electron Linac

We assumed that the klystron is operated at 85% of its maximum capacity and 10% of the power is dissipated in the wave-guide system. The design of the 100-MeV electron linac is based on experiences obtained from the construction and the operation of the 2-GeV linac at PAL [4]. The energy gains attainable with one SLAC-5045 klystron for various beam modes are given in Table 1.

Table 1. Electron beam modes and parameters.

Mode	Pulse Width [ns]	Beam Current [A]	Beam Energy [MeV]	Beam Power, kW (RF pulse rep. Rate)	
				(180pps)	(300pps)
Short Pulse	2	5	97	0.17	0.3
	10	5	88	0.8	1.3
	100	1	79	1.4	2.4
Long Pulse	1000	0.3	77	4.1	6.9

* The klystron is operated with the pulse repetition rate of 300 pps and with the RF pulse width of 2-μs.

Assuming a negligible beam loading, we can obtain 100-MeV with one SLAC-5045 klystron in the 2-ns operation mode. Table 1 shows that we can obtain a maximum beam power of 6.9-kW by operating the klystron in the pulse repetition rate of 300 pps. In the case of the high-power operation the energy gain is reduced by a large amount due to the multi-bunch beam loading.

The 100-MeV electron linac consists of an e-gun, an S-band prebuncher and buncher, two accelerating sections, and various components, as shown in Figure 1. The electron beam is generated either by an RF-gun or by a triode thermionic gun for which a Cockcroft-Walton-type DC voltage generator supplies the accelerating voltage of 120 kV. Electron beams from the e-gun then enter to the bunching system, which consists of a prebuncher and a buncher. The prebuncher is a re-entrant type standing-wave cavity made of stainless steel with a resonant frequency of 2,856 MHz. The buncher is a traveling-wave structure with 14 cavities including the input and the output coupler cavities. The bunched beams are then accelerated to 100 MeV by passing them through two SLAC-type accelerating sections fed by one SLAC 5045 klystron.

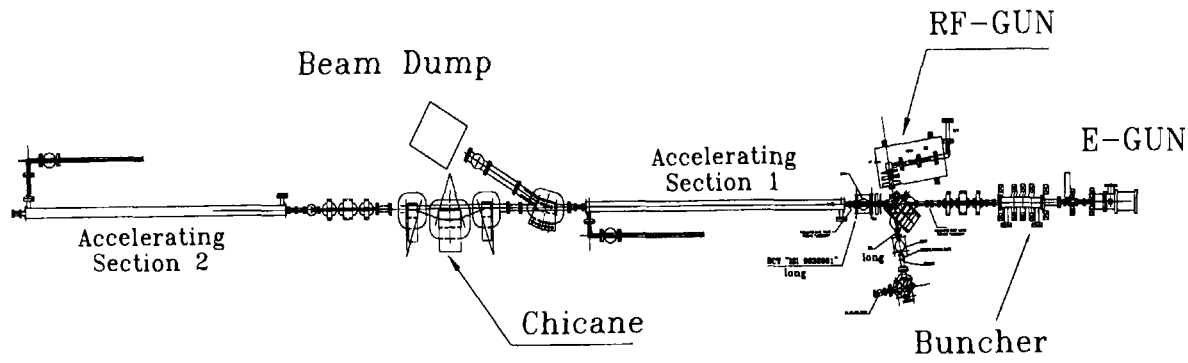

Fig. 1. Schematic diagram of the 100-MeV electron linac

To compensate for the multi-bunch beam loading in the accelerating section, we installed a chicane system consisting of three magnets between the two accelerating sections. In the first accelerating section, the posterior bunches in a beam pulse gradually decrease energies compare to the prior bunches due to the multi-bunch beam loading. While the beam traverses the chicane, bunches with lower energies make a longer detour than those with higher energies do. After traversing the chicane, the space between bunches changed and then the bunch with higher energy accelerated with a less accelerating phase in the second accelerating section. Therefore, the beam energies are averaged out to the value of the steady state beam loading. This can lower the multi-bunch beam loading to ± 1.3 %. However, when we compensate by using a chicane system we pay a price in return because an additional energy spread is generated within one bunch due to the acceleration on the off-crest phases in the second accelerating section. To minimize the latter effect, it is important to produce short bunch lengths in the bunching system. With these two effects considered together, the total energy spread at the end of the linac is about ± 2% for a beam with a bunch length of 4 ps and about ± 4 % for 8 ps. We expect a total beam-energy spread of lower than ± 5 % when using this energy-compensation system.

2.2. Construction of Test-Linac

We have constructed a test-linac for the various R&D activities of the neutron facility by utilizing the existing components and infrastructures at PAL. The test-linac consists of a thermionic RF-gun, an alpha magnet, four quadrupole magnets, two SLAC-type accelerating sections, a quadrupole triplet, and a beam-analyzing magnet. We have used a thermionic RF-gun instead of a triode gun, which is different from the 100-MeV linac for the neutron facility. The RF-gun is a one-cell cavity with a 6-mm-diameter tungsten dispenser cathode. The RF-gun produces electron beams with average current of 300 mA, a pulse length of 6-μs, and about 1-MeV energy [5]. The alpha magnet is used to match the longitudinal acceptance from the gun to the first accelerating section. An electron moves along an 'α'-shaped trajectory in the alpha magnet, and the bend angle is 278.6°. A high-energy electron has a longer path length than a low-energy electron; thus, the length of the electron beam is neither lengthened nor shortened in the beam transport line from the gun to the first accelerating section. Four quadrupole magnets are used to focus the electron beams in the beam transport line from the gun to the first

accelerating section. The quadrupole triplet installed in between the first and the second accelerating sections is used to focus the electron beams during the transport to the experimental beam line at the end of the linac. Three beam-current transformers (BCT) and three beam-profile monitors are installed to monitor the beam quality during the beam operation. The beam-analyzing magnet at the end of the linac has a bending angle of 30 degree and a zero pole-face rotation.

The test-linac is located inside a tunnel beside the PLS 2-GeV linac. The building has three levels: the tunnel in 6 m below ground level, the klystron gallery is on the ground floor, and utilities, including the air-condition and the air handling units, are on the second floor. There is 3-m-thick concrete shield between the tunnel ceiling and the klystron gallery.

After the RF-conditioning of the accelerating structures and the wave-guide network, we performed the beam acceleration test. The maximum RF power from a SLAC 5045 klystron was reached to 45 MW. The RF power fed to the RF-gun was 3 MW. The beam acceleration experiment was performed after any breakdown had disappeared through the RF structures. The bunched electron beam at the alpha magnet was accelerated in the accelerating sections and transported to the end of the test-linac. The maximum energy is 75 MeV up to now which is still lower than the target value. The measured beam currents at the entrance of the first accelerating structure and at the end of linac are 100 mA and 40 mA, respectively. The length of electron beam pulse is 1.8 μs and the pulse repetition rate is 12 Hz. The measured energy spread is ± 1% at minimum. The energy spread was reduced when optimizing the RF phase of the RF-gun and the magnetic field strength of the alpha magnet.

2.3. TOF Facility

The design of the target system is done using the MC simulation codes, EGS4 and MCNP4. The target system, 4.0-cm in diameter and 5.1-cm in length, is composed of ten sheets of Ta plate, and there is 0.1-cm water gap between them, in order to cool the target effectively [6]. The estimated flow rate of the cooling water is about 5 liters per minute in order to maintain below 45 °C. The housing of the target is made of titanium. The conversion ratio obtained from MCNP4 code from a 100-MeV electron to neutrons is 0.032. The neutron yield per kW beam power at the target is 2.0×10^{12} n/sec, which is about 2.5% lower than the calculated value based on the Swanson's formula [7].

The pulsed neutron facility based on the electron linac is a useful tool for high-resolution measurements of microscopic neutron cross sections with the TOF method. In the TOF method, the energy resolution of neutrons depends on the TOF path length. Since we have to utilize the space and the infrastructures in the laboratory, TOF paths and experimental halls are placed in the same level as the electron linac. Two or three different TOF paths range between 10-m and 100-m are arranged for experiments with various energy ranges.

In order to get experiences for the TOF method, we constructed a 15-m long TOF path perpendicular to the test-linac. With this, the test of the Ta-target system and a data acquisition system will be performed. There is another TOF facility at the end of the PLS 2-GeV linac. The 2-GeV electron beams are bent to 10 degrees relative to the linac and injected to the target inside the beam dump area. Bremsstrahlung induced by high-energy

electrons has been used to study the systematics of photospallation reactions, since mono-energetic photons that have enough intensity to produce isotopes are not available.

3. Activities on Nuclear Data Production and Evaluation

For activities on the nuclear data production, we have joined two facilities: one is the TOF facility using a 46-MeV electron linac of the Research Reactor Institute in Kyoto University (KURRI)[8] and the other is the IBR-30 pulsed neutron booster of the Joint Institute for Nuclear Research (JINR)[9] in Dubna. We have measured capture cross sections for Hf and Dy samples at KURRI[10], and capture cross sections for ^{232}Th at JINR[11] in this year. We have planned to measure transmission cross sections for Hf and Dy natural samples and capture cross sections for ^{162}Dy and ^{164}Dy isotope samples at KURRI.

For activities on the nuclear data evaluation, KAERI has been served a nuclear data web server since 1994 [12]. The web server has a "Table of Nuclides" with graphic interface which contains the mass of nuclides, the decay and half life, the decay scheme, the neutron capture cross section, the fission yield and the neutron cross section. An interactive cross section plotter is provided to compare the cross sections between each evaluated files. The average users of the web server are about 1700 per month and continually increase every year. The calculator to calculate the attenuation factor for an electron and X-ray is also provided for medical users. The KAERI maintained various libraries for Monte-Carlo simulations and soft-wares for data evaluations in order to provide those to domestic users. There is an activity for data evaluation of photo-nuclear reactions in cooperation with a group in JAERI.

There was a workshop for nuclear data production and evaluation at PAL on August 7 and 8, 1998. The aim of the workshop was to review recent progress, exchange ideas and search future directions in the nuclear data production and evaluation. There are three subjects covered in this workshop: (1) Neutron Facility, (2) Neutron Cross Section Measurements and Detectors, and (3) Data Evaluation and MC. The attendees in this workshop are 52 peoples included 6 persons from Japan. There were 18 papers presented in this workshop. During this workshop, we have discussed various subject related to the nuclear data production and evaluation from the basic subject to the applications. Therefore, we have understood the importance of nuclear data and the necessity of the pulsed neutron facility, the PNF and the nuclear data center in Korea. We also discussed with attendees from JAPAN about the possibility for collaboration between both countries in the future.

4. Summary and Discussion

The nuclear data project was launched by KAERI from 1996 in order to support nuclear R&D activities, medical and industrial applications. We have constructed and tested a test-linac for the pulsed neutron facility by utilizing the existing components and infrastructures at PAL. The characteristics of accelerated electron beams are about 75 MeV of energy, 12 Hz of repetition rate, 1.8 μs of pulse width and about 40 mA of peak current. We made a 15-m TOF path perpendicular to the test-linac in order to test a Ta-target system and a data acquisition

system.

We have joined two facilities to get experiences for cross section measurements at KURRI in Japan and at JINR in Russia. In these facilities, we have measured capture and transmission cross sections for various samples. There are also several activities for data evaluations at KAERI with international collaborators.

The workshop for nuclear data production and evaluation was held on August 7 and 8, 1998 at PAL. The aim of the workshop was to review recent progress, exchange ideas and search future directions in the nuclear data production and evaluation. During this workshop, we have discussed various subjects on the nuclear data production and evaluation.

Acknowledgements

This work is supported in part by POSCO, MOST, and by Korea Atomic Energy Research Institute.

References

[1] http://hanaro.kaeri.re.kr/.

[2] Ministry of Science and Technology of Korea (1997), "1997 Request for Project on Long-Term Nuclear R&D Program".

[3] G. N. Kim, *et. al.*, "Proposed Neutron Facility using 100-MeV electron linac at Pohang Accelerator Laboratory," Proceedings of International Conference on Nuclear Data for Science and Technology, p. 556, May 19-24, 1997, Trieste, Italy.

[4] J. Y. Choi, *et. al.*, "Design of 100-MeV Electron Linac for Neutron Beam Facility at PAL," Proceedings of 1997 KAPRA Workshop, p. 88, June 26-27, 1997, Seoul, Korea.

[5] H. S. Kang, G. N. Kim, M. H. Cho, W. Namkung, and K. H. Chung, IEEE Trans. Nucl. Sci. **44**, 1639 (1997).

[6] W. Y. Baek, *et. al.*,, "Design of the Photoneutron Target for Pulsed Neutron Sources at PAL," Proceedings of Workshop on Nuclear Data Production and Evaluation, August 7-8, 1998, Pohang, Korea.

[7] W. P. Swanson, "Radiological Safety Aspects of the Operation of Electron Linear Accelerators," IAEA Technical Reports No. 188 (1979).

[8] K. Kobayashi, *et. al.*, Annu. Rep. Res. Reactor Inst. Kyoto Univ. **22**, 142 (1989).

[9] http://www.jinr.dubna.su/.

[10] H. J. Cho, *et. al.*, "Measurement of Neutron Capture Cross Sections for Dy and Hf between 0.001 and 10 eV using Total Absorption Detector," Proceedings of Workshop on Nuclear Data Production and Evaluation, August 7-8, 1998, Pohang, Korea.

[11] W. Y. Baek, et. al., "Investigation of γ-multiplicity Spectra and Neutron Capture Cross Sections of 232Th in the energy region 21.5 eV-215 eV," Proceedings of Workshop on Nuclear Data Production and Evaluation, August 7-8, 1998, Pohang, Korea.

[12] http://hpngp01.kaeri.re.kr/.

JP9950312

2.10 Nuclear Data for Analysis of Radiation Damage Processes

T. Aruga
Department of Materials Science Research,
Japan Atomic Energy Research Institute,
Tokai, Ibaraki 319-1195, Japan
aruga@maico.tokai.jaeri.go.jp

Parameters needed to analyze radiation damages for neutron irradiations are presented, taking iron samples irradiated with JMTR neutrons for an example. Special interests have been put on a comparison between results obtained by irradiations for one case with a full neutron spectrum and the other with a Cd-shielded neutron spectrum. A possibility is described that although atomic displacement rates for the two case differ only less than 2 %, production rates of freely migrating defects can differ appreciably, due to recoiled atoms by (n, γ) reactions. More over, it is also suggested that although the median energy of PKA, defined as a PKA energy above (or below) which one half of the total atomic displacements are to be produced, may differ only slightly between the two cases, final radiation effects can be significantly different.

The effects of charged particles emitted with high energies due to nucleon irradiations are stressed in relation to the significance of defects produced by PKAs with lower energies than several keV, especially for the case of irradiations with highly energetic nucleons as anticipated in GeV proton irradiations.

1. Introduction

Nuclear data has been playing important roles in predicting radiation damages of materials to be used in nuclear energy facilities, through giving the atomic density of atoms displaced from normal lattice sites or displacements per atom (dpa) and concentrations of foreign atoms produced by nuclear reactions, mainly gas atoms like helium and hydrogen atoms. The method for calculating the dpa due to collisions in cascades originating from a single knock-on atom produced by reactions with irradiation neutrons have been established and have been written in ASTM standard[1]. That is, once energy spectra of PKA are given, the dpa is calculated based on LSS theory[2] on the partition of PKA energies between electronic excitation energies and kinetic energies of nuclear motion of atoms. In the calculations, an energy partition function called a damage efficiency expressed by Robinson[3] in a fitted equation of reduced PKA energy has been used widely in common. So, the method for calculating dpa is called the NRT model[4].

Present study has been motivated by the possibility that under a certain condition neutron irradiations could bring about quite different consequences upon irradiation effects, even if displacement rates did differ less than a few per cent. The possibility is originating from the fact informed[5] concerning in-reactor irradiation creep experiments performed in Japan Material Testing Reactor (JMTR), in which the irradiation creep rate for the specimen irradiated with the full neutron spectrum has been considerably enhanced by over one order, as compared with that observed for the specimen irradiated with the spectrum, the thermal region of which was cut by appropriate cadmium shieldings with the displacement rates, dpa/s, for the both cases being almost comparable and other conditions pertinent to this kind of experiments being the same, such as the irradiation temperatures and the levels of the applied stress. Although details of the experimental procedures and the results are to be soon published, the significances of the PKA spectra which have recently been recognized and demonstrated experimentally in the context of production rates of freely migrating point defects surviving displacement cascades, therefore closely related with nuclear data, should be examined beforehand, in the present study.

2. Damage parameters and PKA energy spectra

Neutron spectra used to obtain damage parameters for the both cases are given in Ref.[6] and the respective damage parameters are given in Table 1. Although the sample material used actually in the in-reactor irradiation creep experiment is Type 304 stainless steel with the standard composition of chromium(18.5 in mass %), nickel(9.1) and iron(the rest balanced approximately) as major elements, an elemental iron (Fe) is used as an irradiated sample for the present calculations. This simplification will not introduce significant errors on the final consequences, so long as the irradiation time is as short as a few hundreds of hours like the present case.

Note that an apparent large difference in displacement(dpa) cross sections between the two spectra is entirely due to the difference in the total neutron fluxes used in averaging the cross sections, the values of dpa/s differ merely 2 %, where dpa/s for the full spectrum case is larger by the contribution of (n,γ) reactions with the thermal neutrons below 1 eV.

Also given in Table 1 are indexes for PKA spectra, $T_{1/2}$(dpa) and average T in keV. The former is called a median PKA energy, defined as a PKA energy above (or below) which one half of the total atomic displacements are to be produced, while the latter is an energy averaged over the distribution of PKA populations. The median PKA energies $T_{1/2}$(dpa) differing by 10 % between the cases are depicted in Fig. 1 (a) and (b) for the full spectrum case and the thermal neutron shielded case, respectively, in each curve representing cumulative fractions of displacement below a PKA energy of T keV. In the figures, the values of median of PKA distributions are also shown to be 480 and 580 eV for the respective cases, which are far smaller than both values of $T_{1/2}$(dpa) and average T. These cumulative fractions are obtained using PKA energy dependencies of PKA populations and displacements per atom, which are given in Fig. 2(a) and (b) for the respective cases. A remarkable difference in the PKA energy dependencies of dpa between the two cases is the contribution of displacements due to PKAs below 1 keV for the full spectrum case, which are all resulting from (n,γ) reactions with the thermal neutrons below 1 eV. This is demonstrated in Fig. 3(a) and (b) which show contributions of each reaction to the PKA energy spectra as a function of PKA energy, for the respective cases. The results given above have been obtained using an evaluated nuclear data file of JENDL-3.2[7] and the displacement threshold energy Ed of 40 eV according to calculational procedures already described in the previous proceeding[8].

3. What is meant by damage parameters and PKA energy spectra

It has been recognized that defects survival rates are enhanced with an decrease in the median PKA energy. This understanding has been obtained by experimental observations mainly through electrical resistivity measurements for samples irradiated at liquid helium temperatures near 4K, where the nascent defects are maintained as surviving the displacement cascades, and also through large scaled computer simulations of displacement cascades by molecular dynamics calculations starting with a given PKA energy. The result shown in Fig. 4[9] from the literature will best describe the significances of PKA spectra which have on the displacement damage processes: in the figure, fractions of defects that survive cascade quench are given as a function of the median recoil(PKA) energy, as normalized to the dpa calculated by the NRT model. This result indicates that with an increase in PKA energy, although cascade volumes and a number of atoms displaced will increase, fewer defects can be transported beyond a highly agitated cascade core to survive the cascade region, after the kinetic energy is imparted to the lattice atoms and the lattice is cooled (or quench in 10^{-11} s after the initiation of the cascade), and most of the defects, i.e. interstitials and vacancies annihilate by recombinations during this thermal spike. Note that it is the point defects, which survive the cascades and become mobile under temperatures high enough, that bring about radiation effects such as microstructural developments and mechanical properties degradations of the irradiated materials.

The importance of the lower energy PKAs in radiation damages is further demonstrated in Fig. 5[10], in which relative efficiencies of various ions for producing long-range, freely migrating defects are plotted as a function of the median PKA energy. The result has been

obtained by measuring quantitatively radiation induced segregation in two concentrated alloys under irradiations with various ions of various energies to alter the median PKA energy but at approximately the same dpa/s, at temperatures ranging 600-900 K. The radiation induced segregation of particular atoms is possible only under the existence of long-range, freely migrating defects. The relative efficiencies here are normalized to that of 1MeV protons. It is noted that the general shape of the curve in Fig. 6 is qualitatively very similar, indicating the lower the PKA energies, the higher the efficiencies of production of freely migrating defects.

It is not so simple for the creep rate enhancement by over one order mentioned above to be understood merely on the analogy of the significance of the lower median PKA energy. In fact, the difference of 10 % between the two $T_{1/2}$ values i.e. 55 keV and 60 keV (Table 1) is insignificant, referring to the $T_{1/2}$ dependencies of the defect survival rates and production efficiencies of freely migrating defects, in Fig. 4 and Fig. 5. However, the occurrence of a large number of population of PKAs peaked below 1 keV, as shown in Fig. 2 for the full spectrum neutron irradiation due to (n,γ) reactions, is considered to play a substantial role in enhancing the creep rate through by itself a relatively high rate of providing freely migrating defects to lattices under the stress.

Furthermore, another result obtained by the sophisticated experiment of measuring the radiation induced segregation in Cu-Au alloy, given in Fig. 6[11], indicates that the effect of lower energy PKAs on enhancing radiation damages is strongly affected by a coexistence of displacement cascades by high energy PKAs. Therefore, the observed creep rate enhancement could be possible under a detailed balance among factors like the existence of peaked PKA distribution below 1keV, a favorable extent of both spatial and temporal distributions of displacement cascades due to high energy PKAs mainly due to (n, n), (n, n') and (n,α) reactions; note that those distributions due to high energy PKAs being common to the both neutron spectra and only difference being the peaked PKA distribution below 1 keV due to (n,γ) reactions in which are emitted high energy photons peaked around 7.5 MeV from Fe. Any way, the accumulation of experimental data is further required to establish the profound understanding concerning these phenomena.

It is known that light ion irradiations produce lower energy PKAs because of long-range Coulomb interactions, which results in higher survival rates of freely migrating defects, as shown in Fig. 5, for the case of H and He irradiation. Taking niobium for example, cumulative fractions of damage energy below T keV of PKA are given as a function of PKA energy T, in Fig. 7[12], for irradiations with light ions of proton, deuteron and alpha, comparing with fission neutron irradiation, where damage energy multiplied with 0.8/(2Ed) gives number of displacements in the NRT model. Note that these light ion irradiation results in the median PKA energies lower than a few keV.

In view of the importance of the light ion irradiation, light mass charged particles, such as proton, alpha as emitted from nuclear reactions are also considered to produce PKA spectra distributed largely in a lower energy region than a few keV and are considered to contribute more to a formation of freely migrating defects than PKAs produced in fission neutron irradiations. Therefore, importance of nuclear data about charged particles production reaction cross sections and energy spectra of emitted charged particles should be stressed, especially for the case where copious reaction channels become open or nuclear spallations take place and so called internal light ion irradiation can not be neglected.

According to the theoretical prediction, energy distributions of emitted light particles at nuclear spallations are shown to be distributed to be peaked around a few MeV and to be distributed up to several hundreds of MeV[13]. Such a broad energy distribution of light particles is considered to produce both lower energy PKAs and higher energy ones. Moreover, if the cross sections of these light particle emission reactions increase with increasing incident energies of nucleon like neutrons, as is shown in Fig. 8[14], the effect of the internal bombarding by these light particles can be considered to be more important to the radiation damages than currently assumed. So far a number of studies have been done to estimate radiation damages for materials to be used as components of spallation neutron facilities,

however, damage parameters like dpa cross sections and gas atom production rates have only been described. However, it seems impractical to evaluate data of both energy spectra and cross sections for a dreadfully large number of reaction channels: instead, realistic and effective representations for these quantities based on sound systematics seem highly desirable for radiation damage analysis.

In summary, the damage parameters for analyzing radiation damage processes were mentioned, referring to significance of lower energy PKAs. Following points are stressed:
1. Taking iron irradiated with JMTR neutrons as an example, a possibility is described that displacement damages produced by PKAs with energies lower than a keV order due to recoiled atoms from (n, gamma) reactions can contribute significantly to radiation damages.
2. From the point of view that highly energetic charged light particles also produce PKAs distributed dominantly in energy regions lower than a keV order, evaluations of nuclear data such as cross sections, and energy spectra of charged particles emitted from the nuclear reactions will be urgently required, for damage analyses of materials to be irradiated with GeV order nucleons.

Acknowledgments
The author would like to thank Dr. Yuji Kurata for kindly informing him of the results on the in-reactor creep experiment.

References
[1] Annual Book of ASTM standards, Volume 12.02, E521-96, p.156 and E693-94, p. 254 (1996).
[2] Lindhard J.,. Scharff M. and Schiott H. E., Kgl. Dan. Vidensk. Scjsk. ,Mat.-fys. Medd. 33(14) (1963).
[3] Robinson M. T., Proc. B. N. E. S. Nucl. Fusion Reactor Conf., p.364 (1969).
[4] Norgett M. J., Robinson M. T. andTorrens I. M., J. Nucl. Eng. and Des. 33, 50. (1975).
[5] Y. Kurata, private communication.
[6] Shimakawa S., Komori Y., Nagao Y. and Sakurai F., JAERI-Tech 95-023 (1995).
[7] Nakagawa T. et al., J. Nucl. Sci. Technol., 32 , 1259 (1995).
[8] Aruga T. and Shiraishi K., JAERI-M 89-026, p. 342 (1989).
[9] Jinkle S. J. and Singh B. N., J. Nucl. Mater., 199, 173 (1993).
[10] Hashimoto T., Rehn L. E. and Okamoto P. R., Phys. Rev., B38, 12868 (1988).
[11] Iwase A., Rehn L. E., Baldo P. M. and Funk L., J. Nucl. Mater., 238,224 (1996).
[12] Kirk M. A. and Greenwood L. R., J. Nucl. Mater., 80, 159 (1979).
[13] Daemen L. L. et al., LA-UR 95-1792, p. 487 (1994).
[14] Wechsler M. S., et al., ASTM STP 870, p. 1189 (1985).

Table 1. Comparison of Damage Parameters

	Full Neutron Spectrum	Thermal Neutron Shielded Spectrum
Total Flux (/cm^2/s)	3.5×10^{14}	2.2×10^{14}
Displacement Cross section σ_d(b)	150	230
rate (dpa/s)	5.2×10^{-8}	5.1×10^{-8}
$T_{1/2}$(dpa) (keV)	55	60
Average T (keV)	8.5	11.7

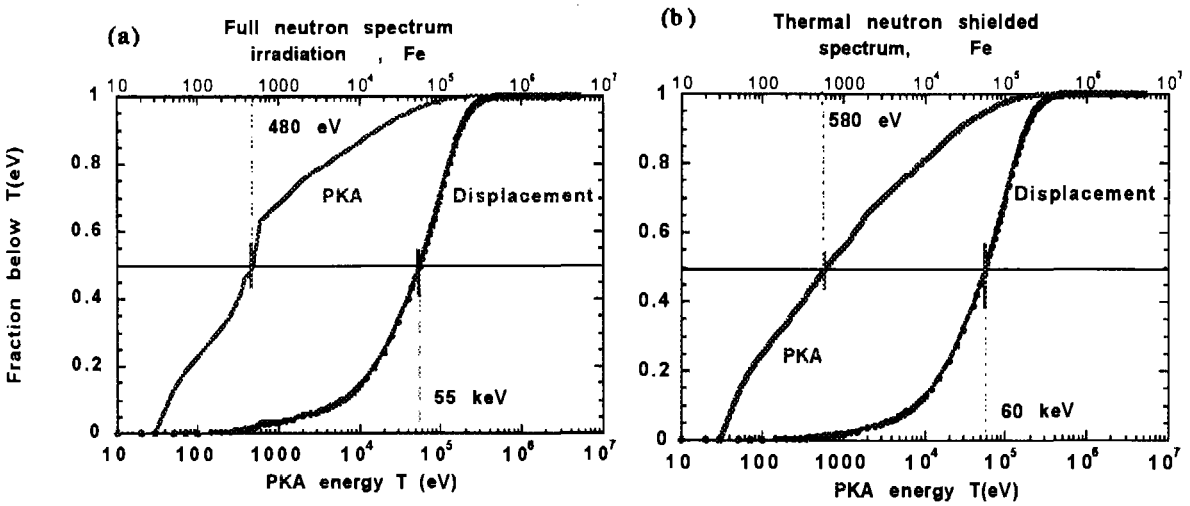

Fig. 1. Cumulative fractions of PKAs and displacements below PKA energy T (eV).

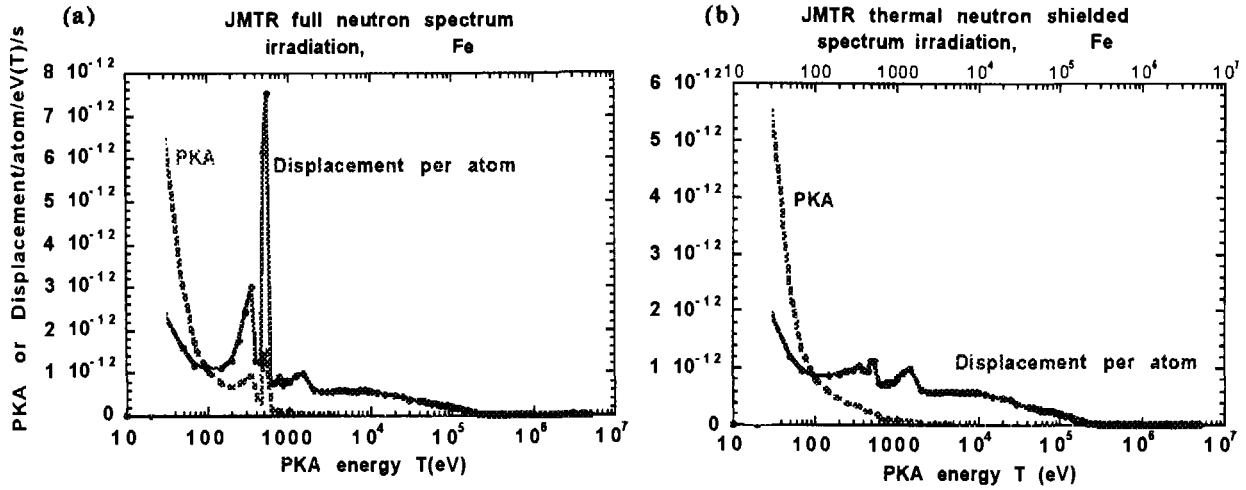

Fig. 2 . PKA energy dependencies of PKAs and displacements per atom.

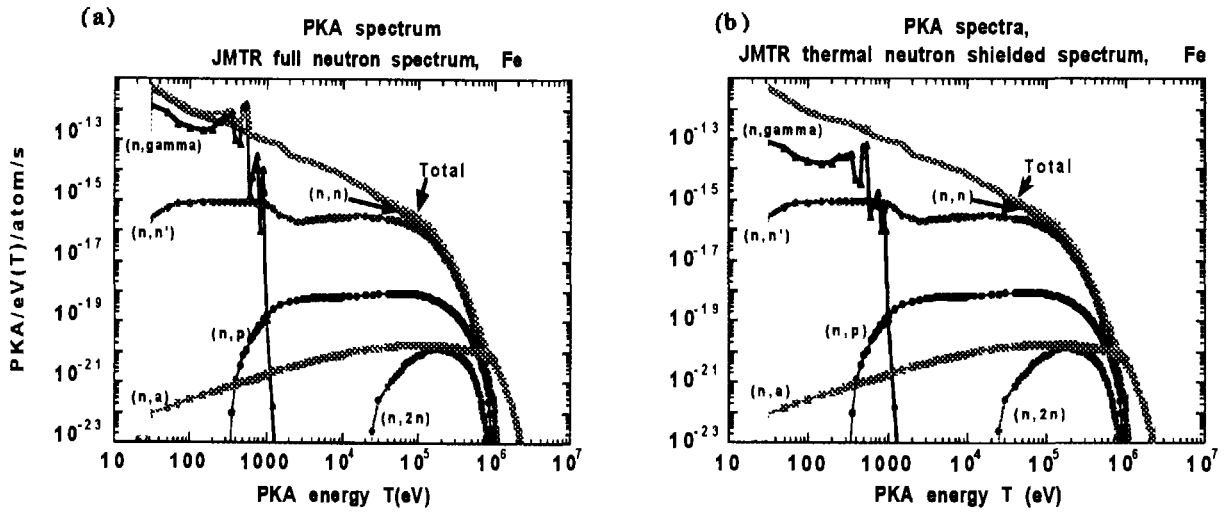

Fig. 3 . Reaction wise PKA energy spectra.

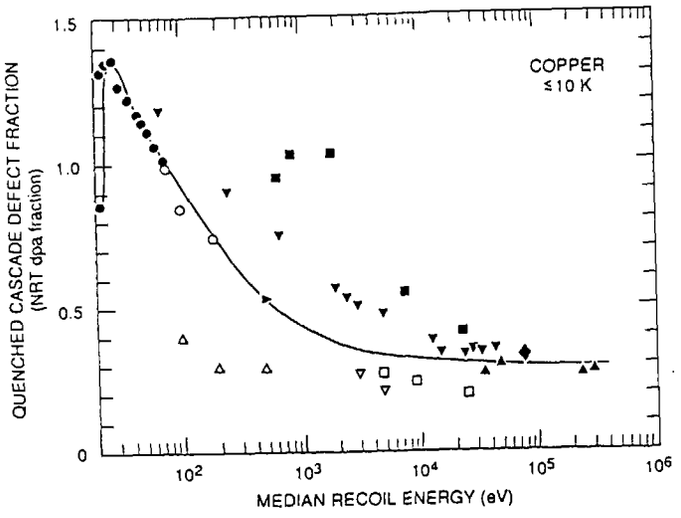

Fig. 4 . Dependence of the survived (quenched) cascade defect fraction on median PKA energy in copper. The open symbols refer to molecular dynamics calculations[9].

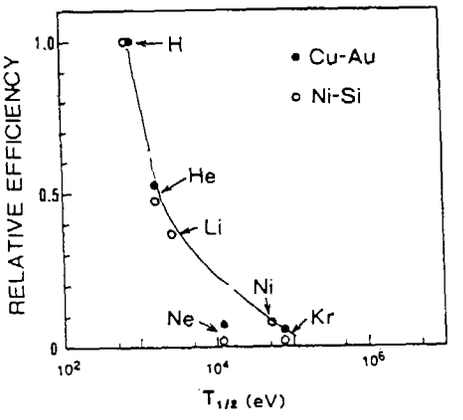

Fig. 5. Relative efficiencies for producing freely migratingdefects as a function of median PKA energy[10].

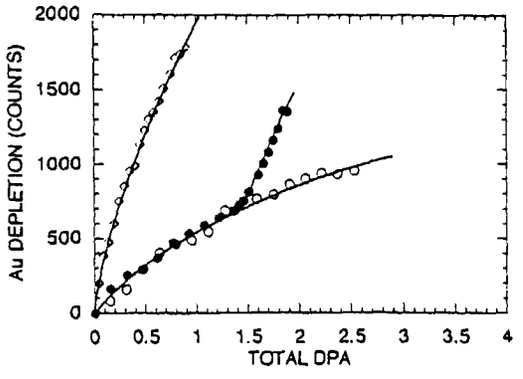

Fig. 6. Amount of near-surface Au depletion (inverse segregation) as a function of total dpa for 2h dual(1.5MeV He + 800keV Cu) beam irradiation and subsequent He only irradiation(solid circles). open diamonds: He only, open circles: 4h dual beams[11].

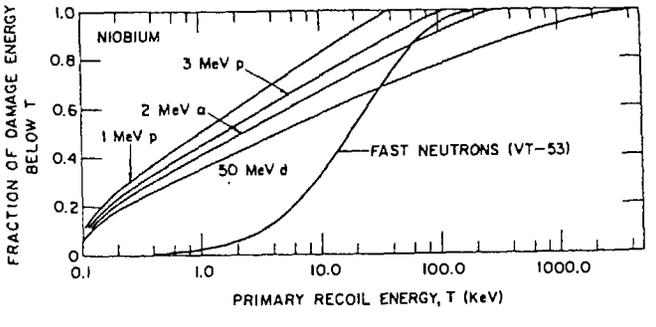

Fig. 7. Cumulative fractions of damage energy distributions below PKA energy T for different types of irradiating particles[12].

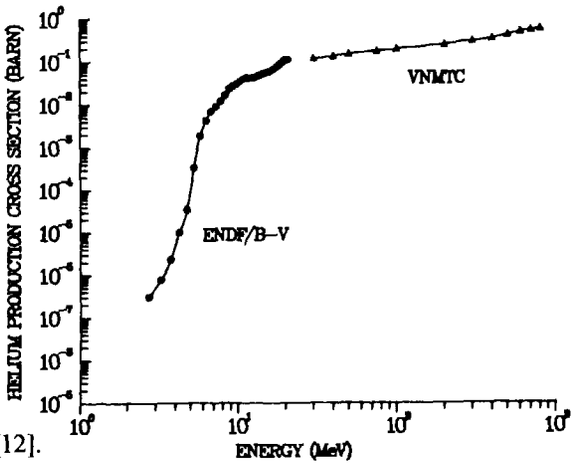

Fig. 8. Helium production cross section versus neutron energy[13].

2.11 Nuclear Heating in Fusion Reactors

Koichi Maki
Power & Industrial Systems R & D Division, Hitachi Ltd.
7-2-1 Omika-cho, Hitachi-shi, Ibaraki-ken,319-12 Japan
e-mail: *kmaki@erl.hitachi.co.jp*

Abstract

Nuclear heating rates are estimated with multiplying neutron and gamma-ray fluxes by nuclear heating constants of KERMA factors. The gamma-ray KERMA factors can be given exactly by the value of gamma-ray energy deposition of (incident gamma-ray energy) – (outgoing gamma-ray energy). On the other hand there are two methods to calculating the neutron KERMA factors. One is a direct method and the other an energy balance method. In the direct method the neutron KERMA factors are given by kinematics. The uncertainties in KERMA factors by this method are considered the same as those in nuclear data of 20-30%. The KERMA factors by the energy balance method have several ten per cent uncertainties, because of deduction between large values each other. In fact since all nuclear data are not always consistent with each other and have uncertainties, we had better apply the direct method. In considering decay heat of short half life nuclides into KERMA factors, there are some problems such as application to shorter pulse operation than the half life of the nuclides. It is emphasized that nuclear heat and decay heat should be separately treated.

1. Introduction

In fusion reactors neutrons produced by DT or DD reaction interact and make various types of reactions such as (n, γ), (n, n), etc. with materials constructing the first wall, blankets and divertors, etc. In these reactions secondary neutrons, gamma-rays and/or charged particles are created and target nuclides are knocked on. The charged particles and the knocked nuclides move in the materials in short range and lose their kinetic energy by exchanging into thermal energy. The neutrons and gamma-rays travel in the materials in farther longer range than the charged particles and also exchange their energy into thermal energy. The thermal energies exchanged from kinetic energies are so called nuclear heat. Nuclear heating rates are estimated with multiplying nuclear heating constants in neutron and gamma-ray, respectively, so called neutron KERMA (kinetic energy released in materials) and gamma KERMA factors by neutron and gamma-ray fluxes calculated by the codes of ANISN, DOT, DORT, TORT, etc.

In the present paper, firstly, subjects of nuclear heat in fusion reactors are described, that is, positions where maximum nuclear heating rates and their uncertainties should be considered in nuclear and structural design are described. Secondly, calculation method for nuclear heat is illustrated and the KERMA factors are defined. Further more the KERMA factors by an energy balance method and a direct method. Thirdly, it is described that nuclear heating rates calculated by using the direct method and the energy balance method KERMA factors are compared with experimental nuclear heating rates. Lastly, an example is presented that decay heat was treated of being included in nuclear heat and problems in this treatment are discussed.

2. Subjects of nuclear heat in fusion reactors

In tokamak type fusion reactors the nuclear heating rates at the first wall, blanket, divertor and superconductive magnets, etc. are restricted in a certain range since their temperatures must be controlled. An example of maximum nuclear heating rates are presented about the ITER [1]. The principal values of the ITER are presented in Table 1. The bird eye view of the ITER is illustrated in Fig.1. The first wall, one of the severest positions in nuclear and thermal design mentioned above, is located in nearest position from the plasma and is combined blanket vessels. Maximum temperature is restricted by material application allowable temperature and temperature gradient is restricted by allowable thermal stress. The

Table 1 Principal values of the ITER

items	design values
Total fusion power	1.5 GW
Burn time	1000 s
Plasma current	21 MA
Maximum toroidal magnetic field	5.7 T
Neutron first wall loading	1MW/m^2
Neutron first wall fluence	1MWa/m^2

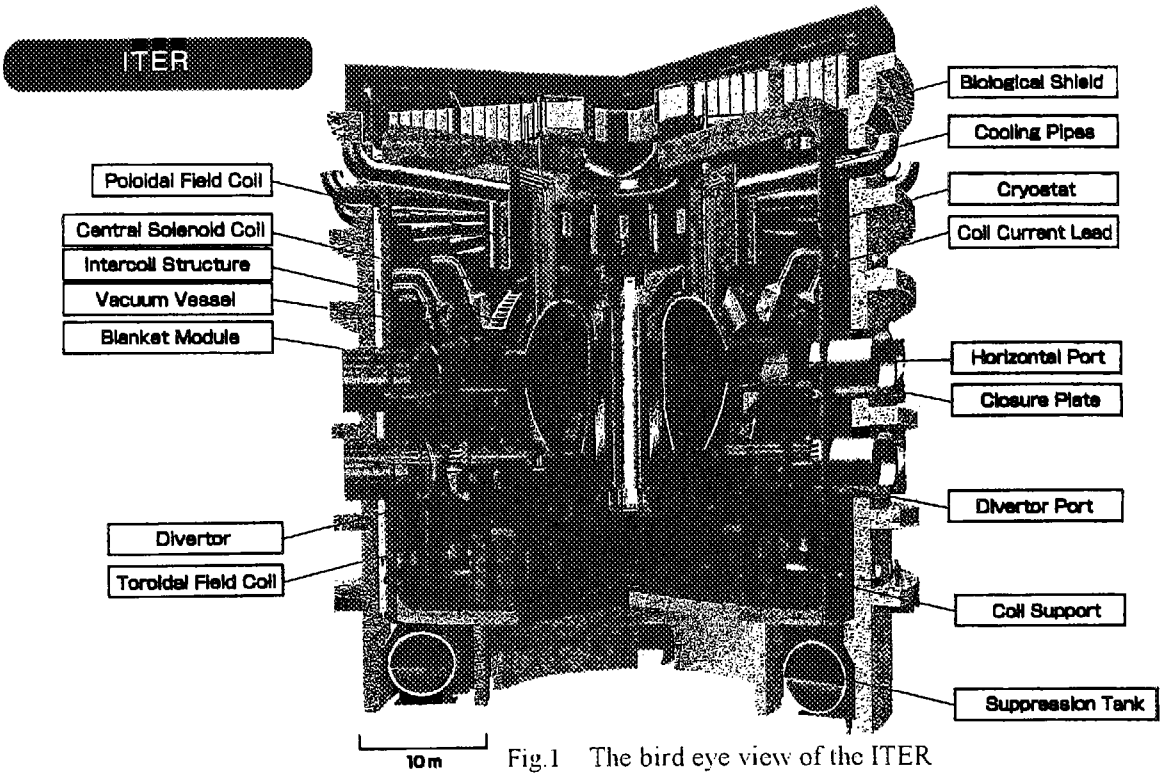

Fig.1 The bird eye view of the ITER

divertors are located at the bottom of the plasma chamber. The reason for severeness with nuclear heating rates is the same as that for the first wall.

The blankets surround the first wall. Temperature in the blanket should be controlled into the design windows. Lower limit is restricted due to release tritium produced by reaction of neutron with lithium and upper limit is restricted by material application allowable temperature. In superconductive magnets nuclear heating rate is also restricted in order to prevent the magnets from quenching. Since estimated nuclear heating rates have uncertainties, we must allow for design margin in thermal and nuclear design. The design margin should be restricted as small as possible from the view point of reactor cost. Nuclear data used in calculating nuclear heating rates are required for high accuracy as wall as that in neutron and gamma-ray flux calculation codes. Maximum nuclear heating rates and their required accuracy at various position for neutron wall loading of 1MW/m^2 in the typical experimental fusion reactor of ITER are shown in Table 2.

Table 2 Nuclear heating rates and their required accuracy at various position for neutron wall loading of 1MW/m^2 in typical experimental fusion reactor.

positions	maximum nuclear heating rate	required accuracy
the first wall	~15 W/cm^3	~20 %
inside blanket	~10 W/cm^3	10~20 %
surface of divertor	~5 W/cm^3	~20 %
vacuum vessel	~0.1 W/cm^3	~50 %
toroidal coil	~0.001 W/cm^3	~30 %

3. Calculation method for nuclear heat

3.1 Nuclear heat

Nuclear heating rates are estimated with multiplying nuclear heating constants in neutron and gamma-ray, respectively, so called "neutron KERMA and gamma KERMA factors," by neutron and gamma-ray fluxes calculated by the codes of ANISN, DOT, DORT, TORT, etc. The nuclear heating rates are estimated as following equation,

$$H(r) = \int_E \phi(r,E) \sum_i \sum_x N_i(r)\, \sigma_{ix}(E)\, \varepsilon_{ix}(E) dE \qquad (i: nuclide,\ x: reaction), \qquad (1)$$

where, $\phi(r,E)$ is flux of energy E at spatial point r and $N_i(r)$ is number density of nuclide i, and $\sigma_{ix}(E)$ and $\varepsilon_{ix}(E)$ are respectively microscopic cross sections of reaction x and energy deposited per reaction x for nuclide i at energy E. In the equation (1), $\Sigma\, \sigma_{ix}(E)\, \varepsilon_{ix}(E)$ is defined as the KERMA

factor, that is,

$$K_i = \sum_x \sigma_{ix}(E)\, \varepsilon_{ix}(E), \tag{2}$$

Using the KERMA factors, we presented the nuclear heating rates as,

$$H(r) = \sum_i N_i(r) \left(\int K_{in}(E_n)\ \phi(r,E_n)\, dE_n + \int K_{i\gamma}(E\gamma)\ \phi(r,E\gamma)\, dE\gamma \right), \tag{3}$$

where $K_{in}(E_n)$ and $K_{i\gamma}(E\gamma)$ are respectively neutron and gamma reaction KERMA factors.

3.2 Calculation of KERMA factor

There are two methods to calculating the neutron KERMA factors. One is an energy balance method and the other a direct method. In the energy balance method the neutron KERMA factors are calculated by following equation.

$$K(En) = \sum_{\text{reaction}}^{x} (En + Q_{n,x}) \cdot \sigma_x(En) - (\varepsilon_n \cdot \sigma_{n\text{-prod}}(En) + \varepsilon_\gamma \cdot \sigma_{\gamma\text{-prod}}(En)). \tag{4}$$

Where $Q_{n,x}$ is Q-value of reaction x, $\sigma_{n\text{-prod}}$ and $\sigma_{\gamma\text{-prod}}$ are secondary neutron production cross section and gamma-ray production cross section, respectively, and ε_n and ε_γ are outgoing neutron and gamma-ray energies in the center of mass system. In MCNP code, nuclear heat is given by the value of (incident neutron energy + Q-values in all reactions) - (outgoing neutron and gamma-ray energies). In MCNP code nuclear heating rates can be estimated easily without the KERMA factor set.

In the direct method the neutron KERMA factors are given by following equation.

$$K(En) = \sum_{\text{reaction}}^{x} (Ec + Ep) \cdot \sigma_x(E_R) \tag{5}$$

where En, Ec and Ep are incident neutron energy, charged particle energy and knocked on energy in the laboratory system, respectively, σ_x is a cross section of reaction x and E_R is relative kinetic energy. The values of Ec and Ep are estimated by kinematics and energy conservation in collision. These values can be estimated in accordance with the method described in reference [2].

The gamma-ray KERMA factors can be given exactly by the value of gamma-ray energy deposition of (incident gamma-ray energy) – (outgoing gamma-ray energy) as following equation,

$$K_i(E\gamma) = \sigma^i_{pe} E\gamma + \sigma^i_{pp}(E\gamma - 1.02) + \sigma^i_{cd} E\gamma, \tag{6}$$

where σ^i_{pe}, σ^i_{pp}, and σ^i_{cd} are photo-electric, Compton absorption and pair creation microscopic cross sections for nuclide i, respectively. And 1.02MeV means energy of two electron masses.

4. Comparison with experimental data.

In the energy balance method and method in MCNP code, if nuclear data of the secondary neutron and the outgoing gamma-ray energies, and the Q-values in all reactions are consistent with each other, the nuclear heating rates can be given as exact values. But if not so, KERMA factor by energy balance method or nuclear heating rates in MCNP cannot be estimated as exact values, because of deduction of large values each

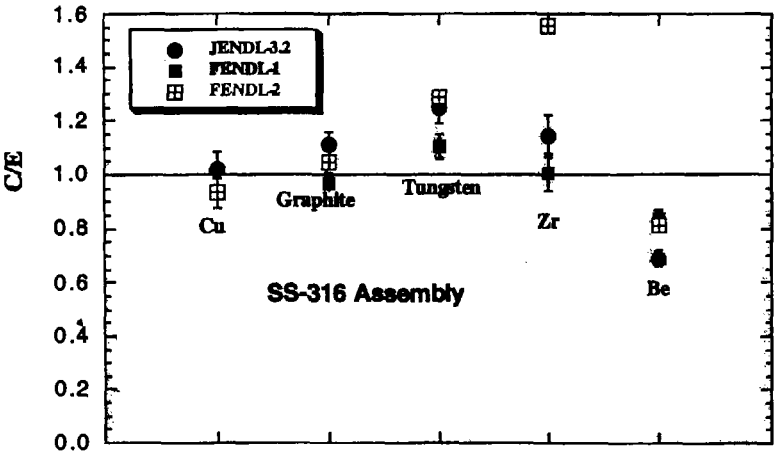

Fig.2 C/E of external probe materials at the first position in the SS316 assembly [3].

other.

The nuclear heating rates by the energy balance method and the direct method are compared with the experimental data observed by the FNS facility [3]. The values of E/C for nuclear heating rates of copper, graphite, tungsten, zirconium and beryllium in SS316 assembly are illustrated in Fig.2. In this figure the KERMA factors symbolized as FENDL-2 are estimated by the energy balance method, and JENDL-3.2 by the direct method. These two data are compared each other in the present paper. The discrepancies of C/E for nuclear heating rates in zirconium and tungsten by the energy balance method are approximately 50% and 30%, respectively. On the other hand the discrepancies of C/E for nuclear heating rates by the direct method are 25% at the maximum. In Fig.3 values of C/E for nuclear heating rates of copper, graphite, SS316, tungsten, zirconium, beryllium and chromium in copper assembly are shown. In also copper assembly the discrepancies of C/E for nuclear heating rates in zirconium and tungsten by the energy balance method are approximately 60% and 40%, respectively. In Fig.4 values of C/E for nuclear heating rates of graphite, chromium, copper, iron, nickel, SS316, aluminum, molybdenum, niobium, vanadium, tungsten, zirconium, beryllium, silicon and titanium in graphite assembly are presented. From this figure, the maximum discrepancy of C/E for nuclear heating rates by the energy balance method is approximately 35% and the maximum discrepancy of C/E for nuclear heating rates by the direct method symbolized as JENDL-3.2 is at most 20%.

From these observed data, it is summarized that the uncertainties in KERMA factors calculated by the direct method are considered the same as those in nuclear data of 20-30% and uncertainties in KERMA factors by the energy balance method or in nuclear heating rates in MCNP are at most 60%. If we restrict the uncertainties in KERMA factors estimated by the energy balance method or in nuclear heating rates to the same as those by the direct method, nuclear data must be required to highly accurate of several % in addition to consistency in nuclear data of the secondary neutron and the outgoing gamma-ray energies, and the Q-values in all reactions. In fact since all nuclear data are not always consistent with each other and have uncertainties, it is emphasized that we had better apply a direct method avoiding deduction of large values each other.

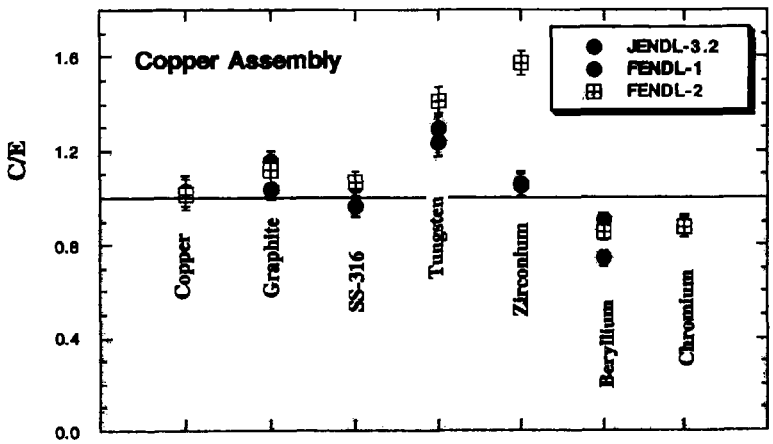

Fig.3 C/E of external probe materials at the first position in the copper assembly [3].

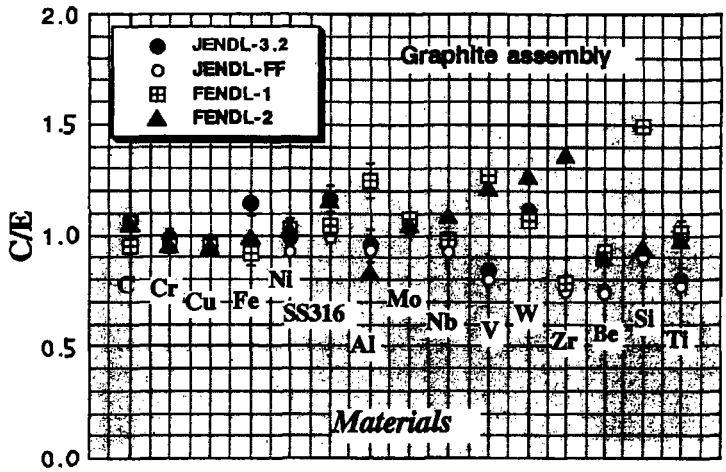

Fig.4 C/E of external probe materials at the first position in the graphite assembly [3].

5. Treatment of decay heat

The KERMA factors in KAOS/LIB-V [4] based on ENDF/B-V include decay heat of short half life (<1 day) nuclides. The nuclear heating rate is given as,

$$H(r) = \sum_i N_i(r) [\int \{K_{in}(E_n) + K_{id}^{ch}(E_n) + K_{id}^{\gamma}(E_n)\} \phi(r,E_n) dE_n] + \int K_{i\gamma}(E\gamma)\, \phi(r,E\gamma) dE\gamma \ ], \qquad (7)$$

where, charged particle decay KERMA is given as $K_{id}^{ch} = \Sigma \sigma_{ix}(E)\, E_{ixd}^{ch}(E)$ and gamma decay KERMA as $K_{i\delta}^{\gamma} = \Sigma \sigma_{ix}(E)\, E_{ixd}^{\gamma}(E)$. Typical example of the case including decay KERMA into nuclear heat KERMA in copper is illustrated in Fig.5. In considering decay heat into KERMA factors, there are some problems such as application to shorter pulse operation than 1day, etc. The nuclear heating rate and decay heat should be separately treated.

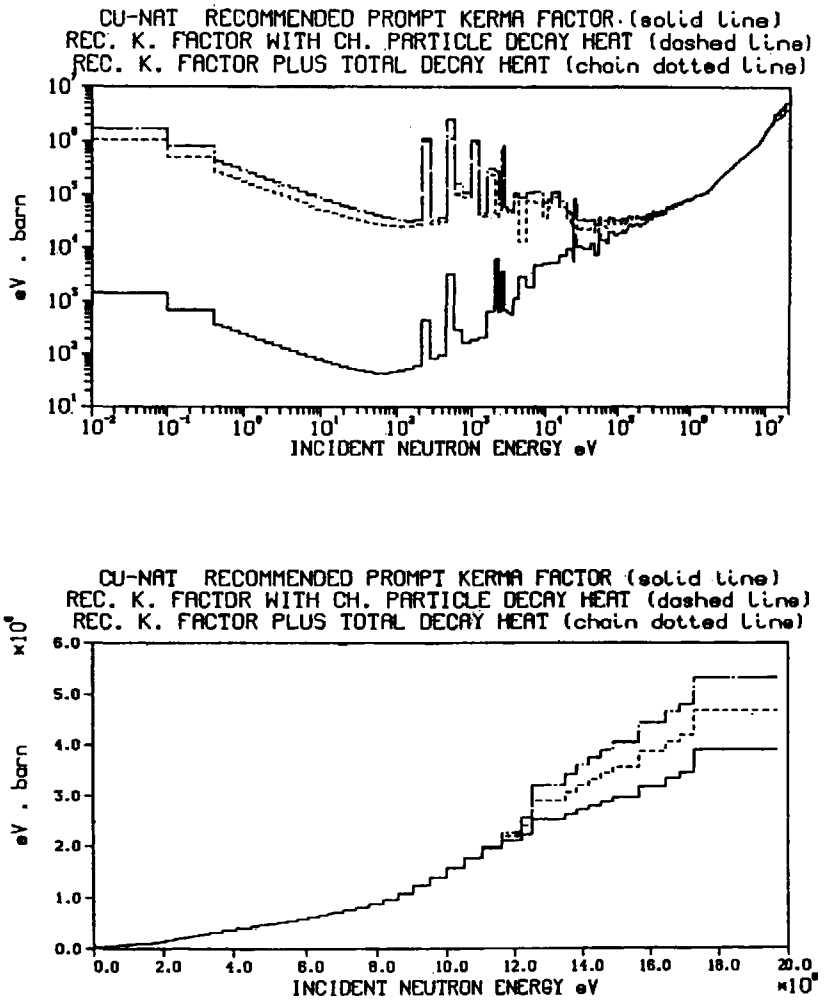

Fig.5 KERMA factors of prompt and decay heat in copper [4]

6. Conclusion.

From these discussions, following remarks are obtained.

(1) The KERMA factors by energy balance method including MCNP method have several ten per cent uncertainties, because of deduction between large values each other.

(2) The uncertainties in KERMA factors calculated by the direct method are considered the same as those in nuclear data of 20-30%.

(3) In fact since all nuclear data are not always consistent with each other and have uncertainties. we had better apply a direct method avoiding deduction between large values each other.

(4) If the uncertainties in KERMA factors by the energy balance method including MCNP method are improved the same as those by the direct method, nuclear data must be required to highly accurate of several % in addition to consistency among nuclear data.

(5) In considering decay heat into KERMA factors, there are some problems such as application to shorter pulse operation than 1day, etc. The nuclear heating rate and decay heat should be separately treated.

References

[1] ITER Joint Team, : "ITER Design Report," J. Plasma and Fusion Research, Vol.73, Supplement (1997).

[2] K. Maki, et al., :"Nuclear Heating Constant KERMA Library – Nuclear Heating Constant Library for Fusion Nuclear Group Constant Set FUSION-J3 - ," JAERI-M 91-073 (1991).

[3] Y. Ikeda, et al., :" Experimental Validation of Nuclear Heating for ITER Structural Materials," 20th Symp. on Fusion Technology (SOFT98 held at Marseille, France on Sep. 7-11, 1998) .

[4] Y. Farawila, et al., :"KAOS/LIB: A Library of Nuclear Response Functions Generated by KAOS-V Code from ENDF/B-V and Other Data Files," ANL/FPP/TM-241 (1989).

JP9950314

2.12 Material Issues for Spallation Target by GeV Proton Irradiation

Noboru Watanabe
Center for Neutron Science, Japan Atomic Energy Research Institute
Tokai-mura, Naka-gun, Ibaraki-ken, 319-1195 Japan

The importance of material issues in intence pulsed spalltion sources is described in connection with R&D of the JAERI 5 MW source.

1. Introduction

Materials used for a neutron target and its surroundings in intense spallation neutron sources suffer from serious radiation damage due to GeV proton and associated neutron irradiation. Material issues are most important which determine not only the life of important components such as a neutron target but also take an important role in radiation safety. The proton beam power in the JAERI pulsed spallation source is about 5 MW (1.5 GeV, 3.33 mA) and the peak beam current density at the incident proton beam window of the target is estimated to be in a range of 50-80 $\mu A/cm^2$, assuming a parabolic or Moffet beam distributions in the horizontal and the vertical directions with an elliptic beam footprint of approximately 70 cm^2. Since a heavy liquid metal target is the only realistic one which can accept such a high beam power, we chose mercury as the first candidate of the target material. The target container will have lateral dimensions lager than the beam footprint, at least, by about 4 cm in the horizontal direction and 3 cm in the vertical direction and an active length of about 70 cm with a dome window (see the illustration in Fig. 1). The proton beam power per pulse (repetition rate: 50 Hz, pulse length: about 1 μs) reaches at 100 kJ which brings about an energy deposition of about 60 kJ per pulse in mercury . In such conditions a beam window is considered to receive a static stress of approximately 100 MPa and a dynamic stress larger than 200 MPa, due to the pressure wave caused by such an energy input in a very short time duration (about 1 μs), and a radiation damage of several tens dpa per year. An important feature of the radiation damage due to the proton irradiation is much higher hydrogen and helium production rates per dpa than the case of 14 MeV neutron irradiation. The available data for such radiation damage are very scarce and the accumulation of the data base is highly desired.

In the present paper the importance of material problems in R&D of an intense pulsed spallation neutron source is given with recent R&D activities of the JAERI spallation source and some of recent activities on material irradiation and testing in the world community are shortly reviewed.

2. Operational experience of spallation targets

Many uranium (U, depleted or enriched) targets have so far been used in various spallation neutron facilities of small and medium proton beam powers (KENS: 3-5 kW; INNS: 6-8 kW; ISIS: 160 kW), due to their higher neutron yield per proton compared to other non-actinide heavy metal targets such as tantalum (Ta), tungsten (W), etc.; about 1.7 times higher yield than a latter in case of a depleted U-target, about 4 times or more in case of a highly enriched one. However, the service life of those U-targets were much shorter than expected. For example, in the worst case at ISIS the shortest life was approximately only one month. Table 1 summarizes important operational records of various U-targets so far been used (total number of thermal cycles due to frequent proton-beam trips from the accelerator, total number of protons incident upon the target etc. by the end of their lives) together with some data on Ta- targets used at ISIS, based on the reported data [1-3]. In case of U-targets, it used to be considered as the end of the service life, when an appreciable, sometimes a detectable, amount of fission products appeared in the primary cooling water or in its cover gas. In case of a Ta target, it is still not clear when we shall stop the operation.

All the U-targets in the table were water (H_2O or D_2O) cooled solid targets, consisting of numbers of target discs of appropriate thicknesses to ensure the necessary heat removal. Each target disc was clad by Zircaloy-2 (diffusion bonding by HIP). In spite of various efforts so far been devoted to improve the service life, for example, adopting a much lower operating temperature than 400 °C, above which the swelling becomes serious, a proper alloying, making fine grains in metal U, etc., it was not successful to overcome the

situation up to now.

Table 1 Some important records of neutron targets so far been used at various spallation neutron facilities

Target	Proton Energy, MeV	Thermal Cycles	Total Protons, mA hrs	Peak Temperature, °C	Time-average beam current, μA	Relative Total Number of Fissions to U #5
ISIS U #1	780	—	92.4	—	30	0.31
ISIS U #2	800	40000	53.1	120	40	0.18
ISIS U #3	800	10389	174.9	130	65	0.59
ISIS U #4	800	4147	138.8	150	75	0.47
ISIS U #5	800	5074	295.6	165	90	1.00
ISIS U #6	800	2628	126.1	180	110	0.43
ISIS U #7	800	1805	107.2	215	125	0.36
ISIS U #8		Not Used			—	—
ISIS U #9	800	815	113.2		150	0.381
IPNS Depleted #1	450	89600	240.0	225	10 - 14	0.39
IPNS Enriched #1	450	28000	128.8	175	14 - 16	1.07
KENS U #1	500	~ 40000	~ 50	~ 120	~ 5	~ 0.1
ISIS Ta #1	800	73378	1751.6		170	3.80**
ISIS Ta #2*	800	21138	618.1		170	1.34**

* Still in use

** Relative value of total number of neutrons to ISIS U #5

Therefore, It is being commonly recognized that the use of an U-target beyond the proton beam power at present ISIS, 160 kW, would be very difficult and impractical. Thus, the use of a non-actinide target becomes unique solution at a higher power level. The ISIS Ta#1 target had been used up to about 1750 mA-hr in the integrated proton current, almost 6 times as high as the highest value of the U-target (ISIS U#5). This target retired, not due to a failure but just for destructive inspections. Although we have to wait the results of the tests on the Ta#1 discs (non-clad) for detailed information on radiation damage, it has been reported that the discs seemed to have an enough ductility yet, suggesting that such a solid target could be used up to a proton-beam power level of about 1 MW. However at 5 MW the above time-integrated current can be reached only by 3 weeks and when we consider other factors than radiation damage, the use of a liquid metal target would be more practical than a solid target.

3. Liquid metal target

Among the candidates of liquid metal targets (Mercury (Hg), lead bismuth eutectic (Pb-Bi), molten lead (Pb)), Hg has various advantage over other candidate due to various reasons; (1) no radiation damage in target material itself, (2) liquid state even at room temperature (no need of preheating), (3) higher atomic number density than other two candidates, resulting in a higher neutron luminosity from target, etc.

Figure1 shows the calculated axial distributions of leakage fast neutrons from Hg targets towards moderator, determined at 2 cm from the target surface, for a cylindrical and a flat (rectangular cross section) targets, compared with those of Pb-Bi ones. It will be clear from this figure that an Hg target is always superior to Pb-Bi one and a flat target, accordingly with a flat proton-beam footprint, is much better than a cylindrical one.

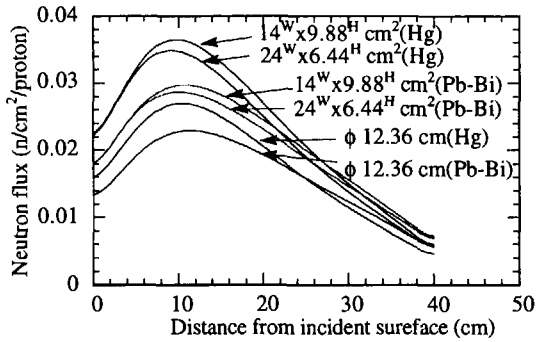

Fig. 1 Spatial (axial) distribution of leakage neutron intensities form various targets

4. JAERI 5 MW pulsed spallation neutron source

The JAERI 5 MW pulsed spallation source aims at realizing the highest slow neutron intensity worldwide, mainly for neutron scattering experiments for condensed matter research [4,5]. For this purpose R&D of a high-efficiency target-moderator-reflector system becomes indispensable. We have proposed an advanced concept for this as shown in Fig. 2 [6,7]. Important advantages of the present configuration are (1) the use of optimized flat target with flat proton beam, (2) a new target-moderator configuration which enables

all the moderator to sit at the highest fast- neutron luminosity region on the target, (3) the use of coupled liquid (supercritical) hydrogen moderator with premoderator [8-11] for high-intensity and high-resolution cold neutron experiments, (4) a proposed new concept of target-moderator coupling "extended premoderator" for above mentioned moderators [12], etc. With extensive optimization studies based on the above concept of target-moderator-reflector system, following neutronic performances can be predicted;

(i) time averaged cold neutron intensity per MW of proton beam is approximately comparable to the one forth value of that from the second cold neutron source in the high-flux reactor at ILL, Grenoble, as shown in Fig. 3. This means that at 5 MW the projected source could provide 1.25 times higher time-averaged cold neutron intensity than the ILL. From the predicted pulse characteristics it turns out that the peak cold neutron intensity at 50 Hz is approximately 100 times higher than the ILL, with which many breakthroughs in various fields of research can be expected;.

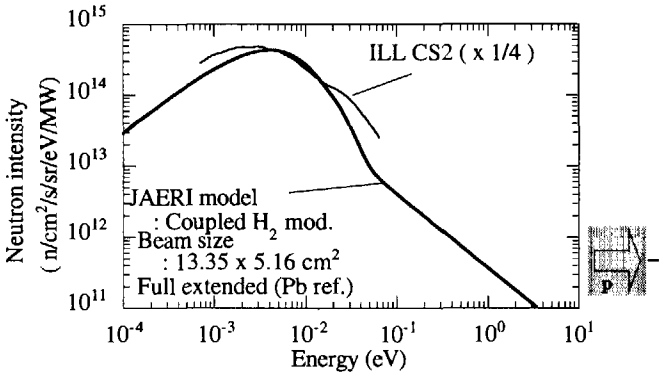

Fig. 3 Neutron spectral intensities from the moderator

(ii) It was confirmed that all moderators could be positioned approximately at the highesr luminosity region witout any cross talk between adjacenet moderators, resulting in the highest slow neutron intensities.

5. Engineering issues

In order to realize the above performance we have to solve various engineering problems. Figure 4 shows the energy deposition in an Hg target along the beam center line for 1.5 GeV proton incidence [13,14]. Here, the maximum proton beam current density was assumed to be 48 μA/cm^2, whatever the beam profile is. Note that the maximum power density in the target reaches at 1.75 kW/cm^3 (1.75 GW/m^3), which is much higher than a corresponding value in a power reactor and that this is the time-average

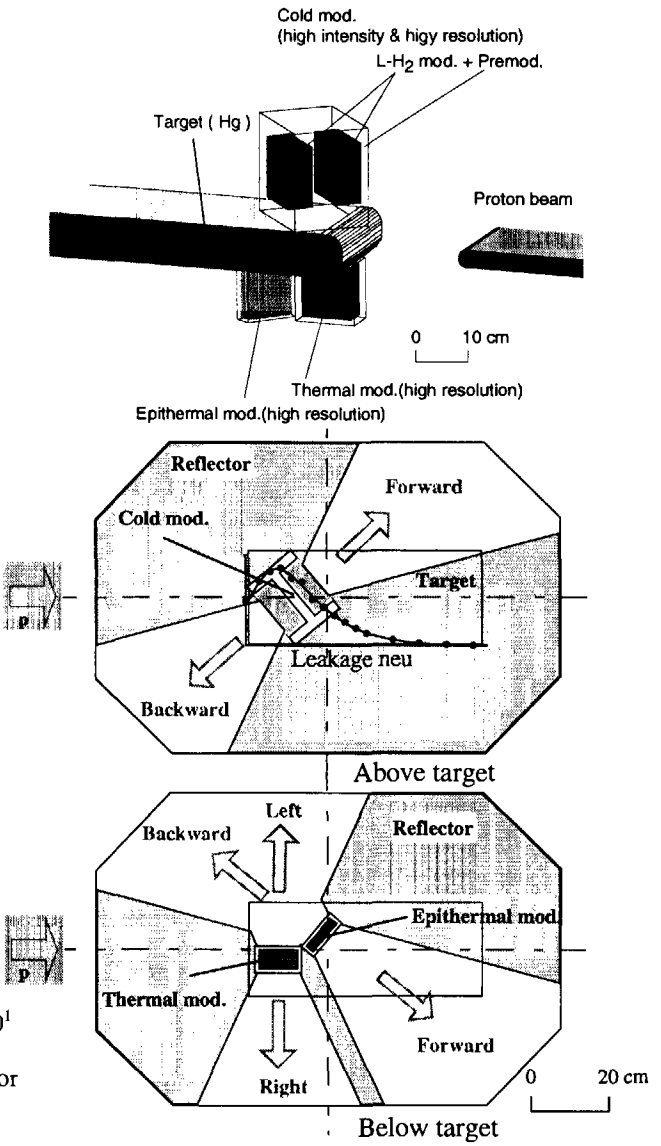

Fig. 2 Layout of target-moderator-reflector system

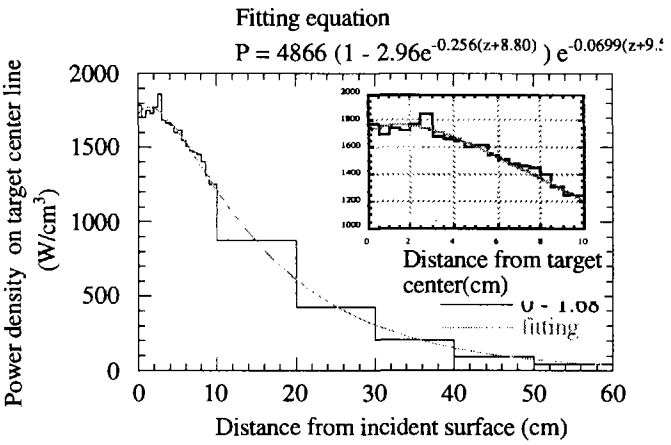

Fig. 4 Energy deposition in target as a function of distance from incident surface (cylindrical Hg target of 12.86 cm ϕ)

power densities, not at the pulse peak. The proton beam power of 5 MW corresponds to 100 kJ/pulse at 50 Hz which is given in a very short time of about 1 μs. Various important parameters and typical values for an Hg target, operated at a proton beam power of 5 MW with a repetition rate of 50 Hz. are summarized in Table 2.

Table 2 Main parameters of JAERI 5 MW Hg target

Parameter	JAERI SNS (expected values)	AGS Tests
Proton beam energy (GeV)	1.5	23
Protons per pulse	4.2×10^{14}	3×10^{12}
Pulse duration (μsec)	~ 1	~ 0.3
Beam energy per pulse (kJ)	100	12
Energy deposited in Hg per pulse (kJ)	~ 60	6
Expected peak energy density in Hg (MJ/m^3)	47	3
Peak local temperature rise in Hg (K)	26	1.6
Peak pressure increase in Hg (MPa)	105	7.1

Such a sudden power deposition in the incident window of the target container and the target material produces pressure waves which attack the target container, especially the incident window. As a simple case, if we assume a cylindrical Hg target of 20 cm in diameter with a semi-spherical dome window as shown in Fig. 5, calculated values of maximum stress levels at the center of the incident window and at a typical point on the cylindrical surface reach at the values listed in Table 3 [15] and the time behaviors at the window center become as shown in Fig. 6 [15]. A rectangular (uniform) beam density distribution gives the highest stress level than other distributions.

In order to validate the calculations, measurements of pressure waves in an Hg target and resulting stress in an target container are being in progress under an international collaboration using the AGS proton synchrotron at Brookhaven National Laboratory. Figure 7 shows measured deformation velocity at a point of the cylindrical surface of the container [16], due to the stress caused by pressure wave. The data is still very preliminary, but the JAERI team was successful to detect such data using a Doppler Laser instrument developed at JAERI and it was confirmed that the calculated result was very close to the measurement, although there exist small discrepancies between them Since in the container used in the experiment, there were many small flanges, etc. around the cylindrical surface, the measured condition was somewhat different from the ideal calculational model. Nevertheless, it can be said that the stress level and timing of the first peak is well reproduced by the calculation. Thus, the use of the present calculation codes, model, assumptions, etc. seems to be acceptable, at least in the first order estimation.

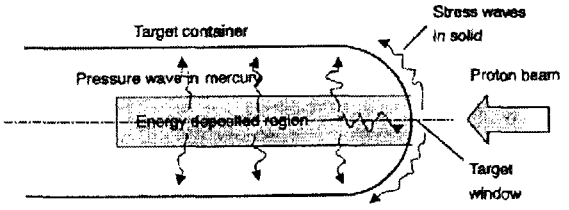

Fig. 5 Concept of pressure wave propagation in target container

Table 3 Approximate level of stress in target container window and vessel for different beam-density distributions

Beam profile	Max stress on window (MPa)	Max stress on cylinder (z=12 cm)*
Uniform	170 (110)	136
Gaussian	100 (80)	110
Parabolic	100 (90)	120
Moffett	0 (90)	120 - 140

*12 cm from incident surface

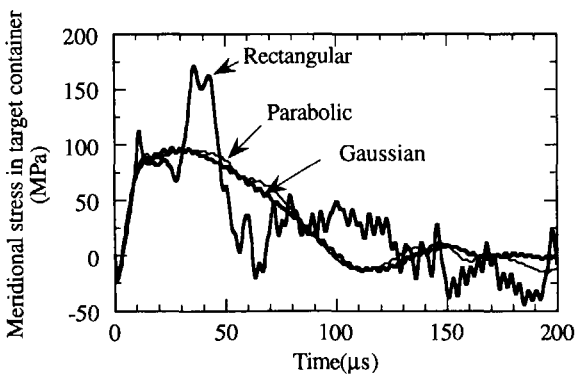

Fig. 6 Meridional stress changes at the center of window under various beam profile; rectangular, paraboric and Gaussian

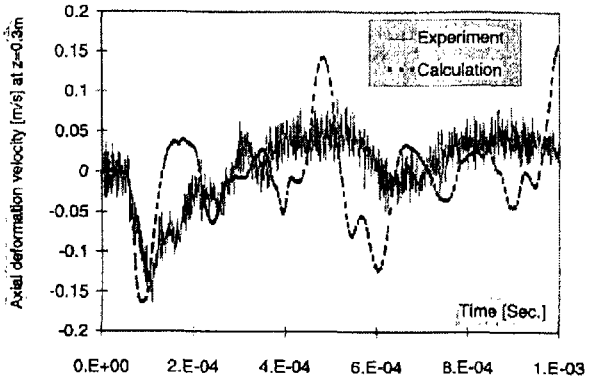

Fig. 7 Measured and calculated deformation velocity

The calculated values of the stress levels in the target container are to be compared to those of the allowable design stress of a typical candidate material for the target container: For instance, for SUS316, 137-110 MPa (at 423-673 K) for membrane + bending and 200-160 MPa (at 423-673 K) for membrane. In case of an uniform beam distribution the maximum stress level exceeds the allowable design stress, while in case of round distributions as Parabolic one, the level is below the allowable design stress. However, in more realistic case, a flat target, higher stress levels will be brought about. It reaches even at about 480 MPa, which is much higher than the allowable design stress, at a flat surface, if we assume a cavitation effect of the pressure wave. Therefore, an effective way to mitigate such pressure wave must be established. Skala, et al. have proposed to inject small helium gas babbles into Hg [17]. In addition to the dynamic stress mentioned above, there is a static stress, due to a static temperature difference in the window, which is 90-100 MPa under the beam current density of 48 $\mu A/cm^2$.

The effect of radiation damage on the mechanical properties of candidate materials must be considered under such stress and coolant (target material) flow conditions at the service temperature. The frequency of the dynamic stress is at least 50 Hz, the repetition rate of the pulsed proton beam, but if we take into account successive reflected waves as shown in Fig. 7, it becomes to an order of 20 kHz, Characteristics of materials for such *very high frequency fatigue* have not been well known.

6. Radiation damage

In an intense pulsed spallation source a proton beam window is subject to the most serious radiation damage, in which we must consider the effects not only of fast neutrons below 20 MeV, but also of those above 20 MeV and incident protons. For the projected JAERI source (1.5 GeV protons, 3.33 mA (5 MW), 48 $\mu A/cm^2$ in current density), dpa (displacement per atom) values for a typical candidate material (stainless steal) have been calculated [18], which are summarized in Table 4 compared with corresponding values estimated for SNS [19] and [20] ESS. Values estimated for the first wall of a fusion reactor (CTR with 1 MW/m^2) are also shown for reference.

Table 4 Comparison of important radiatopm damage parameters in the incident proton beam window in intense spallation sources

	dpa/y				Helium appm He/y	Hydrogen appm H/y
	Neutrons (E < 20 MeV)	Neutrons (E > 20 MeV)	Protons	total		
JAERI (5 MW)	39.45	6.89	21.16	67.5	2,270	
SNS (1 MW)	~ 12.5	~ 1.4	~ 8.9	22.8	1,014	10,840
ESS (5 MW)				~ 60	4,500	70,000
CRT (1 MW/m^2)				18	250	800

Although there are some differences in the dpa values per MW (dpa/MW) between the three spallation sources, due to different proton energies, accordingly different proton currents, different calculation codes and different assumed maximum current densities, those values are more than three times as large as a corresponding value in the first wall of a fusion reactor. As far as radiation damage in terms of dpa is concerned, the contribution from protons is only about one third of the total in the spallation sources. However, the material property change is very much different from those in a fusion reactor and a fast reactor, even for the same dpa. For example, the production rates of helium (He) and hydrogen (H) per dpa in the beam window of a spallation source are one order of magnitude and about 30 times larger than those in the first wall of a CTR, respectively. Note that the corresponding values for a fast fission reactor are negligibly small compared to the above mentioned values. Such large He and H production rates cause serious material hardening and He/H embrittlement. It is still not clear whether all hydrogenous produced can be retained in the material. Some experiments by triple beam bombardment indicated that a large amount of H diffused out from the surface at elevated temperatures. It must be confirmed by experiments whether such a H diffusion can be expected, even in a much deeper H distribution in an actual beam window, . In the ESS project a higher operating temperature of a Hg target is tentatively assumed expecting such effects.

In order to accumulate data base for radiation damage of some important materials by proton beam

irradiation, extensive irradiation experiments are under progress by using 800 MeV protons from LAMPF proton linac and 560 MeV protons at PSI (installed in the Zircaloy target of SINQ) and some preliminary data are being available. Some irradiated samples are available from used (spent) components; for example, Inconel 718 from a beam window used at LAMPF [21], Ta from ISIS target, etc. Most of those samples were irradiated at natural temperature, and so on. Experiments under more realistic environments (in a service temperature, under stress, in flowing Hg, etc.) are most important and such experiments using 72 MeV protons from the Injector-I cyclotron at PSI and 600 MeV protons from the proton linac at Moscow Meson Factory are under planning. JAERI is partly participating in the present irradiation program at PSI but more active participation is highly required in very near future.

References

[1] L. M. Carpenter and A. G. Hins: Experience with IPNS target, Proc. ICANS-XII (Abingdon. UK, 24-28 May 1993) T-1.
[2] T. A. Broome: Prospects for target and methane moderators at ISIS, Proc. ICANS-XIII (PSI, Villigen, Switzerland, Oct. 11.-14, 1995) p. 632.
[3] N. Watanabe: not published
[4] Y. Yamada, et al.: Physica B Vol. 241-243 (1998) 42.
[5] Y. Oyama, et al.: AccApp'98, 2nd Int. Topical Meeting on Nuclear Applications of Accelerator Technology (Gatlinburg, TN, USA, Sept. 20-23, 1998): p.337.
[6] N. Watanabe, et al.: AccApp'98, 2nd Int. Topical Meeting on Nuclear Applications of Accelerator Technology (Gatlinburg, TN, USA, Sept.. 20-23, 1998): p.3.
[7] N. Watanabe, et al.: A conceptual design study of target-moderator-reflector system for JAERI 5 MW spallation source, Porc. ICANS-XIV (Starved Rock Lodge, Utica, Illinois, June 14-19, 1998), in press.
[8] N. Watanabe, et al.: Preliminary optimization experiments of coupled liquid hydrogen moderator for KENS-II, Advanced Neutron Sources 1998, Institute of Physics Conf. Series No. 97, Institute of physics, Bristle and NY., p.787.
[9][10] Y. Kiyanagi, N. Watanabe, H. Iwasa: Nucl. Instr. Meth. A312 (1992) 561 & A342 (1994) 558.
[11] Y. Kiyanagi, S. Sato, H. Iwasa, F. Hiraga and N. Watanabe: Physica B 213, (1995).857.
[12] N. Watanabe, et al.: Towards a high-efficiency pulsed cold neutron source, Porc. ICANS-XIV (Starved Rock Lodge, Utica, Illinois, June 14-19, 1998), in press.
[13] M. Teshigawara, et al.: in preparation
[14] S. Ishikura, et al.: Analyses on pressure wave propagation and dynamic stress in mercury target, Proc. ICANS-XIV (Starved Rock Lodge, Utica, Illinois, June 14-19, 1998), in press.
[15] S. Ishikura, et al.: in preparation.
[16] M. Futakawa, K. Kikuchi, H. Conrad and AGS Collaboration: Measurement of pressure wave in mercury target, Proc. ICANS-XIV (Starved Rock Lodge, Utica, Illinois, June 14-19, 1998), in press.
[17] K. Skala and G. S. Bauer: On the pressure wave problem in liquid metal targets for pulsed spallation neutron sources, Proc. ICANS-XIII (PSI, Villigen, Switzerland, Oct. 11.-14, 1995) p. 559.
[18] H. Takada and K. Iga: private communication and in preparation.
[19] M. S. Wechsler, et al.: Calculation of Radiation Effects on 316 Stainless Steel Container Materials for the NSNS, Proc. Symp. on Materials for Spallation Neutron Sources (Ireland, Florida, Feb. 10-12, 1997).
[20] G. S. Bauer: Spallation Neutron Source Material Research at SINQ, Research proposal, PSI.
[21] F. Carsughi, et al.; Investigations on Inconel 718 irradiated with 800 MeV protons, to appear in J. Nucl. Mater (Nov. '98).

JP9950315

2.13 The MOX core critical experiments for LWRs and the analysis based on JENDL-3.2

Takuya UMANO
Nuclear Engineering laboratory, Toshiba corporation
4-1 Ukishima-cho, Kawasakiku, Kawasaki-shi, 210-0862 Japan
E-mail: raum@rcg.nel.rdc.toshiba.co.jp

Hiromi MARUYAMA (Hitachi), Makoto SASAKI (MHI), Masahiro TATSUMI (NFI), Toru YAMAMOTO, Hirofumi MATSU-URA*(NUPEC)
* Current address: Hitachi engineering corporation

NUPEC and CEA have launched an extensive experimental program called MISTRAL to study highly moderated MOX cores for the advanced LWRs. The analyses with using SRAC system and MVP with JENDL-3.2 library are progressing on the experiments of the MISTRAL and the former EPICURE programs. Various comparisons have been made between calculation results and measurement values.

1. Introduction

Nuclear Power Engineering Corporation (NUPEC), French Atomic Commission (CEA) and CEA's industrial partners have launched an extensive experimental program called MISTRAL (MOX: Investigation of Systems Technically Relevant of Advanced Light water reactors) [1,2,3] in order to obtain the core physics parameters of high moderation MOX cores that will be used to improve the core analysis methods. NUPEC is conducting this study on behalf of the Japanese Ministry of International Trade and Industry (MITI). This experimental program is progressing in the EOLE facility at CEA Cadarache center. This program started in 1996 and scheduled to be finished by 2000. Among four cores of the program, the experiments of Core 1 and Core 2 have already been finished by the end of April in 1998. Within a part of collaboration of NUPEC and CEA, NUPEC also obtained the experimental data of the EPICURE program that CEA has conducted for 30% MOX loading in PWRs. Figure 1 shows UH1.2 core configuration that was devoted to study on a UO_2 reference core in the

EPICURE program. Figure 2 shows MH1.2 core configuration that was devoted to study on basic characteristics of a MOX core in the EPICURE program.

2. EOLE critical facility

Experiments have been performed in the EOLE facility that is a tank type critical assembly. A cylindrical Aluminum vessel (diameter = 2.3 m, height = 3m) is installed with stainless steel over structures. Fuel pins of the facility are standard PWR types and the active length of the pin is about 80 cm. Four types of enrichment are prepared for MOX pins and one type for UO_2 pin. Grid plates are fixed in an inner tank and they provide flexibility of the core configurations. The reactivity of a core is controlled mainly with boron (boric acid) concentration in water and core size. At the critical states and the various measurements, the water level of the tank is always kept at the height that is about 20 cm higher from the top of active length of fuel pins. Small reactivity is compensated with the use of a pilot rod. Core excess reactivity without the pilot rod is determined through the inhour equation with measuring the doubling time after withdrawal of the pilot rod. Four pairs of cluster-type safety rods are utilized for the shutdown.

3. Core configurations and measurements in the MISTRAL program

Figure 3 shows the core configuration of MISTRAL Core 1. It consisted of about 750 regular enriched UO_2 (3.7% in ^{235}U) fuel pins in a lattice pitch of 1.32 cm and was designed as a reference for the high moderation MOX cores. Figure 4 shows the core configuration of Core 2. This is a high moderation full-MOX core consisting of about 1600 MOX (7% enrichment) fuel pins in the same lattice pitch of Core 1. Core 3 is devoted to the physical study of a 100% MOX lattice with higher moderation than Core 2. This configuration consists of about 1350 MOX 7% fuel pins in the lattice pitch of 1.39 cm. Core 4 is a PWR mock-up configuration. The measurement items are selected for each core configuration from following items:

(1) Critical mass and boron concentration

(2)Buckling measurement with using reaction rate distribution measurements

(3) Boron worth

(4) Spectrum indices measurement

(5) Modified conversion factor, 238U capture/total fission

(6) Isothermal temperature coefficients

(7)Reactivity worth and associated reaction rate distribution of a single absorber (Natural B_4C, enriched B_4C, Ag-In-Cd alloy, and UO_2-Gd_2O_3) at the center of

the core

(8) Reactivity worth and associated reaction rate distribution of the substitution of 9 central fuel pins by water holes

(9) Reactivity worth and associated reaction rate distribution of a cluster absorber

(10) Void coefficient

(11) β eff

4. Experimental methods

Various kinds of experimental methods are applied to obtain physical parameters of the cores in the MISTRAL program. The number of fuel pins, core, temperature, the boron concentration and doubling time are measured to determine the core critical mass. A neutron source multiplication method (a sub-critical method) is utilized for the reactivity measurement. An integral gamma scanning method is applied to determine the fission densities of the fuel pins. Miniature fission chambers of several kinds of isotopes are adopted for the determination of energy dependent neutron flux and also for spectral index measurements. The effective delayed neutron fraction of a core (β eff) is measured with use of the core noise method which has been utilized in the international benchmark of β eff's at the MASURCA and the FCA fast critical facilities.

5. Calculation methods

The analysis has been performed using SRAC system and MVP with JENDL-3.2 which were developed at JAERI. SRAC system is a deterministic type code. In SRAC, the processed 107-energy group's nuclear data library is prepared and the combination of a cell calculation and a core calculation is performed. The MVP is a continuous energy Monte Carlo code that is utilized to obtain reference calculation results for the SRAC system such as core eigen-values. In the SRAC system, the conventional collision probability method is applied for generating the 16-group collapsed and homogenized unit cell cross sections. The neutron energy spectrum affected by the neutron leakage is calculated with the B1 approximation taking the measured geometrical buckling into account. The resonance absorption reaction of Pu isotopes should be precisely evaluated at epi-thermal and thermal ranges for MOX fuels. Therefore, an ultra fine group resonance reaction calculation module, PEACO, is fully utilized for the analysis. The thermal cut-off energy was carefully studied and determined to be 1.855eV. After generating 16-group cell cross sections (fast range - 8 groups and thermal range - 8 groups) , core calculations in 1/4 symmetry configuration are performed with the use of CITATION and TWOTRAN module of the SRAC system. In two-dimensional

calculations, the axial leakage is calculated with using the measured axial buckling of a core. For a single absorber calculation, a 3×3 cell model is adopted in the collision probability calculation of the absorber cell at the core center. Also detailed cell models in the collision probability calculation is adopted for the spectral indices analysis.

6. Calculation results

Varieties of comparisons between calculations and measurements are progressing for UH1.2, MH1.2, MISTRAL Core1 and 2. Table 1 shows the differences of Keffs for 4 configurations. The calculated Keffs agree well with the experimental values. Table 2 shows the root-mean-square (R.M.S) differences of radial power distribution. The differences are as much as the uncertainty of measurement. Table 3 shows the C/E values of spectral indexes and conversion factor. Two typical spectral indices and modified conversion factors show the agreement within two times of the uncertainty of measurement error.

Acknowledgment

The authors thank Prof. Oka of the University of Tokyo and other members of the implementation committee of "Study of Advanced LWR Cores for Effective Use of Plutonium," in NUPEC for their technical advice and suggestions.

References

[1] S. Cathalau and J.C. Cabrillat et al: "MISTRAL: an experimental program in the EOLE facility devoted to 100% MOX core physics", International Conference on Physics of Reactors: Physor 96, Vol. 3 (H- 84-92) September 16-20,1996 Mito. Japan

[2] S. Cathalau and P. Fougeras et al: "First validation of neutronic lattice parameters of over moderated 100% MOX fueled PWR cores on the basis of the MISTRAL experiment" ANS topical meeting Long Island, p.393 (1998).

[3] K. Kanda and T. Yamamoto et al: "MOX fuel core physics experiments and analysis - aiming for Plutonium effective use ", (in Japanese) Journal of the Atomic Energy Society of Japan, No.11, Vol. 40. 1998.

Table.1 The differences of Keff between calculation and measurement for each experimental core

PROGRAM	EPICURE	MISTRAL	EPICURE	MISTRAL
CORE NAME	UH1.2	CORE1	MH1.2	CORE2
FEATURE	Uranium CORE	Uranium CORE	Partial MOX	Full MOX
FUEL PIN	3.7% UO2	3.7% UO2	3.7%UO2 + 7% MOX	7% MOX (Mainly)
H/HM	3.7	5.1	3.7	5.1
CORE DIAMETER	~ 50 cm	~ 40 cm	~ 70 cm	~ 60 cm
MVP	+ 0.51 %Δk ±0.02 % (1σ)	+ 0.39 %Δk ±0.03 % (1σ)	+ 0.43 %Δk ±0.02 % (1σ)	+ 0.65 %Δk ±0.02 % (1σ)
SRAC (Pij + TWOTRAN)	+ 0.07 %Δk	− 0.19 %Δk	+ 0.29 %Δk	+ 0.37 %Δk

Table. 2 The R.M.S differences of radial power distribution between calculation and measurement for each experimental core

PROGRAM	EPICURE	MISTRAL	EPICURE	MISTRAL
CORE NAME	UH1.2	CORE1	MH1.2	CORE2
FEATURE	Uranium CORE	Uranium CORE	Partial MOX	Full MOX
MVP	1.0 %	1.7 %	1.2 %	1.6 %
SRAC (Pij + CITATION)	0.8 %	2.0 %	0.9 %	1.3 %

Measurement uncertainty UO2 rod ~1.0 % : MOX rod ~ 1.5 % (1σ)

Table. 3 The C/E values of spectral Indexes and modifies conversion factor for each experimental core

PROGRAM		EPICURE		MISTRAL	MISTRAL
CORE NAME		MH1.2		CORE1	CORE2
FEATURE		Partial MOX		Uranium CORE	Full MOX
FUEL PIN		3.7%UO2 + 7% MOX		3.7% UO2	7% MOX (Mainly)
H/HM		3.7		5.1	5.1
POSITION		UO2 REGION	MOX REGION	CENTER	CENTER
SPECTRAL INDICES	239Pu/235U	1.02 (2.0)	1.05 (2.1)	1.01 (2.4)	1.04 (1.5)
	241Pu/235U	0.96 (2.9)	0.97 (2.9)	1.00 (3.6)	1.02 (2.3)
CONVERSION FACTOR		−	−	1.02 (3.0)	1.01 (2.7)

Modified conversion factor = (238U capture)/(Total Fission) , ( ) Measurement uncertainty % (1σ)

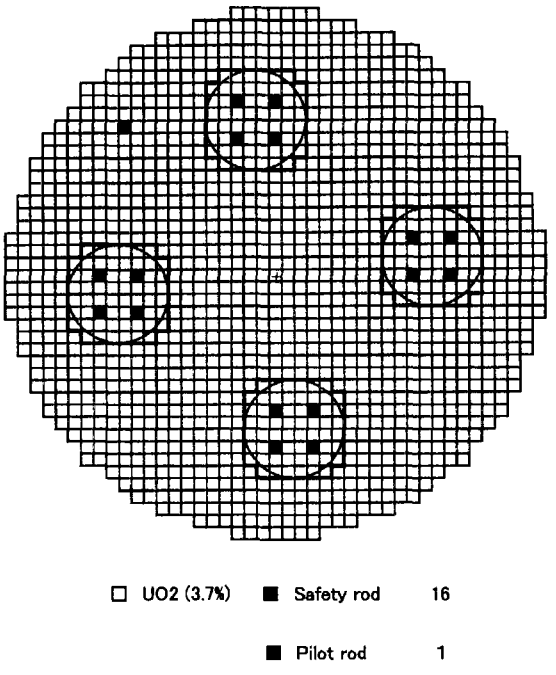

Fig. 1 The core configuration of UH1.2

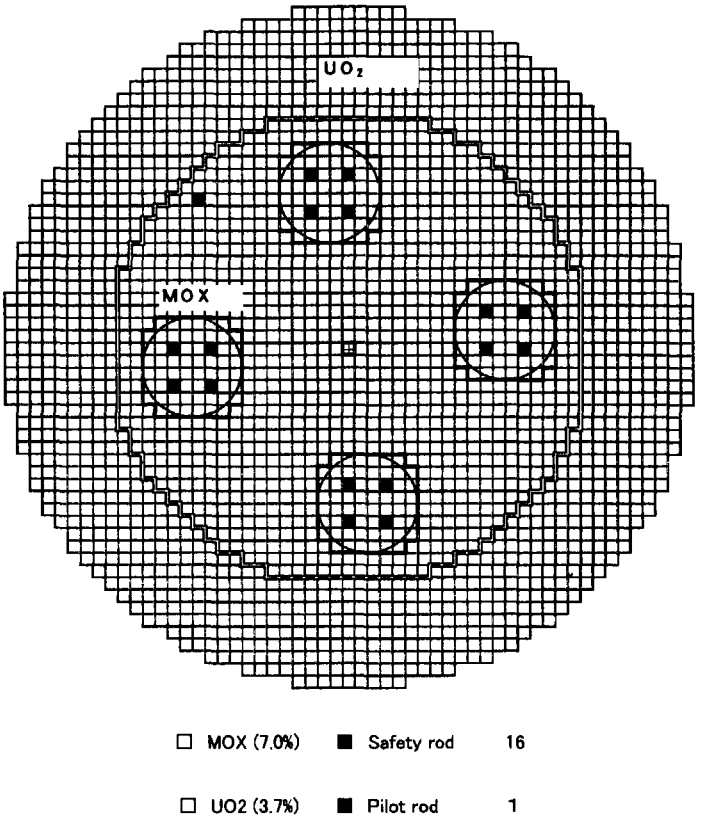

Fig. 2 The core configuration of MH1.2

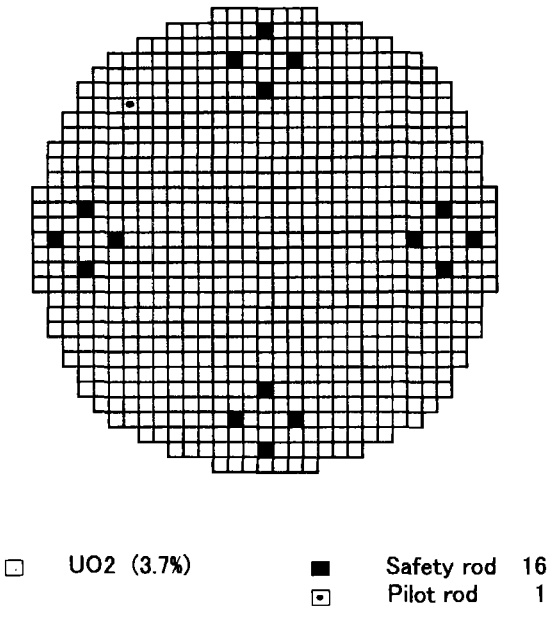

Fig. 3 The core configuration of MISTRAL-1

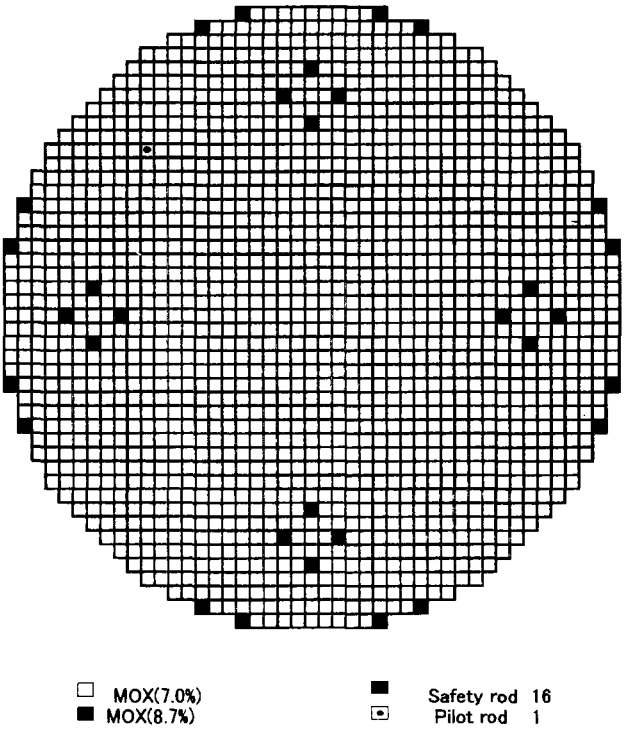

Fig.4 The core configuration of MISTRAL-2

JP9950316

2.14 Measurement and Analysis of Decay Heat of Fast Reactor Spent Fuel

Takafumi AOYAMA, Shoichi NOSE and Soju SUZUKI
Experimental Reactor Division, Irradiation Center, Oarai Engineering Center
Japan Nuclear Cycle Development Institute
4002 Narita-cho, Oarai-machi, Ibaraki-ken 311-1393 JAPAN
E-mail : aoyama@oec.pnc.go.jp

Decay heat of the JOYO Mk-II spent fuel subassemblies was measured using the calorimetric method as a non-destructive examination. The measurement of the subassembly was taken in the spent fuel storage pond at JOYO. Its burn-up was approximately 60 GWd/t and the cooling time was between 24 and 258 days. The measured decay heat was compared with the calculated values by "ORIGEN2" code using the cross section library of JENDL-3.2, and the decay data and the fission yield data library of JNDC-V2. Calculated to Experimental (C/E) values for the measured subassembly were 0.96 - 0.90. The decay heat generated by ^{238}Pu and ^{241}Am, which amount to 1 % of initial composition of the fresh fuel, reached 6 % - 17 % of decay heat during 24 - 258 days of cooling time. These results indicate that the initial composition and the burn-up calculation of actinides are important to accurately evaluate the decay heat of spent fuel.

1. Introduction

Decay heat of the spent fuel is important not only from the standpoint of reactor safety concerning decay heat removal at reactor shut down, but also for the thermal design of the spent fuel storage and handling facility. The accuracy of the decay heat calculation depends on the individual heat generation rate from the decay nuclides of fission products and actinides, and the burn-up calculation for its production and transmutation. Due to the lack of data, obtaining an evaluation of decay heat accuracy has not been achieved yet.

In order to obtain the experimental data and to improve the calculation accuracy, the decay heat of spent fuel subassemblies of the JOYO Mk-II core was measured using the calorimetric method as a non-destructive examination. The measured decay heat was compared with the calculated values by the "ORIGEN2" code using the cross section library of JENDL-3.2, and the decay data and the fission yield data library of JNDC-V2.

2. Measurement

2.1 Decay Heat Measurement System [1]

The decay heat measurement was taken in the spent fuel storage pond at JOYO. The system diagram is described in Fig. 1. The spent fuel subassembly contained in a stainless steel can was set inside the container which has an adiabatic double tube. The coolant water flowed at a constant rate between the canned spent fuel subassembly and the inner tube of the container. The generated heat from the spent fuel subassembly was obtained by means of the calorimetric method as shown in Eq.1 by measuring the coolant temperature difference between inlet and outlet of the container, and the coolant flow rate.

$$Q_D = F \times Cp \times \Delta T \times V \times As \times A\gamma \quad (1)$$

where

Q_D : Decay heat (W)

F : Energy conversion factor (4.187×10^3 W · s/kcal)

Cp : Specific heat of water (kcal/kg/℃)

ΔT : Coolant temperature difference between Inlet and Outlet (℃)

V : Coolant flow rate (kg/s)

As : Heat loss correction factor

$A\gamma$: Gamma heat loss correction factor

The accuracy of measuring the decay heat using this system was determined by the measurement error of coolant temperature and flow rate namely the sensor error, and heat loss which influences the heat balance in the system. Two types of heat losses were considered with the correction factors of As and $A\gamma$, which are explained in the next section.

2.2 Calibration for Measured Heat and Accuracy

In order to verify the heat loss from the decay heat measurement system, a dummy fuel subassembly in which an electric heater was inserted was used to calibrate the system. The calibration tests were performed under similar conditions to those of real spent fuel subassemblies. The heat generated was between 0.40 kW and 1.25 kW and at a coolant flow rate of 0.5 - 1.0 ℓ /min. The calibration curve for the case of 0.5 ℓ /min as shown in Fig. 2 indicates good linearity over the range of this experiment.

The other calibration relates to radiation heating. The decay heat was generated by alpha, beta and gamma-rays which were released from the radioactive nuclides as fission products, activated products and actinide nuclides. Neutrons moderated in the water may induce fission reactions with the fissile material in the spent fuel, however, the ORIGEN2 [2] [3] calculation showed that the heat induced by fission was approximately 5×10^{-5} W per subassembly, and can be negligible for this measurement system. As alpha and beta-rays have short track lengths, most of the radiation energy was deposited within the inner tube of the container, which is eventually used to heat the coolant water. On the other hand, part of the gamma-rays penetrated outside the container, where gamma-ray energy was used only to heat the water in the pond.

Therefore, the gamma-ray energy penetration was evaluated and measured heat was corrected to account for the gamma heat loss. The gamma-ray penetration was calculated by the point kernel shielding code "QAD-CG" [4]. The correction factor $A\gamma$ was then obtained by subtracting the gamma heat that is dissipated at the outer surface of the inner tube of the iron container, from the total heat of radiation produced in the spent fuel. The $A\gamma$ shown in Fig. 3 decreases with cooling time because the short lived nuclides, which have higher energy gamma-rays that can penetrate more than lower energy gamma-rays, decay down during a longer cooling period.

As a result of the calibration test mentioned above, the error in measuring the decay heat of spent fuel subassembly by this system which is shown in Fig. 4, was evaluated with regards to the coolant temperature difference between inlet and outlet of the container, and the coolant flow rate. Considering the experimental conditions (shown in Fig. 4) that were determined with the predicted decay heat, the margin of error in this experiment was estimated between 2 % and 7 %.

2.3 Measured Spent Fuel Subassembly

The fuel specification and irradiation condition of the measured spent fuel subassemblies are shown in Table 1. Two subassemblies of the JOYO Mk-II spent fuel (PFD549 and PFD244) were used for this experiment. These subassemblies were irradiated for 456 EFPDs (Effective Full Power Days) and for 525 EFPDs in the core. They reached the subassembly averaged burn-up of 58,200 and 57,900 MWd/t, respectively. The decay heat was measured during a certain interval of time between 24 and 258 days.

3. Calculation

The measured decay heat was compared with the calculated values by the "ORIGEN2" code using the cross section library of JENDL-3.2 [5], and the decay data and fission yield data library of JNDC-V2 [6] [7] [8] [9]. The neutron flux used as an input to the "ORIGEN2" was calculated by the JOYO Mk-II core management code system "MAGI" [10].

The details of the calculation method of "MAGI" and "ORIGEN2" are shown in Table 2. The neutron flux distribution was calculated by "MAGI" on the basis of a three dimensional diffusion theory with seven neutron energy groups. The neutron cross sections were collapsed from the 70 group JFS-3-J3.2 cross section set which was processed from the JENDL-3.2 library, assuming the neutron spectrum of the relevant core region. The reactor power history and the core configuration in each operational cycle of the JOYO Mk-II core were simulated exactly to the "MAGI" calculation. The irradiation history including reactor shutdown period due to refueling and annual inspection were also considered in the "ORIGEN2" calculation.

The error rate of the neutron flux calculation was evaluated to be less than 5 % in the fuel region according to the comparison between "MAGI" and reactor dosimetry test results based on the foil activation method. The axial distribution of neutron flux based on the calculation from "MAGI" was confirmed by comparing the relative distribution of measured (^{144}Pr) and calculated burn-up.

4 Results and Discussion

4.1 Measured Decay Heat and Comparison with Calculation

Comparison of measured and calculated decay heat is shown in Fig. 5. The measured decay heat for PFD549 subassembly at 24, 66, 103, 140, 200 and 258 days of cooling after irradiation were 1.23 ± 0.03, 0.686 ± 0.024, 0.518 ± 0.022, 0.422 ± 0.021, 0.305 ± 0.020 and 0.261 ± 0.019 kW, respectively. The ratios of calculated to measured values (C/E) ranged from 0.96 to 0.90, which indicates a slight decrease over a longer cooling period. The C/E values for PFD244 subassembly were, however about 0.1 smaller than those of PFD549 subassembly.

4.2 Effect of Initial Composition of Actinides

Table 3 shows the weight (grams) of fissile materials contained in both subassemblies, where the weight of ^{238}Pu and ^{241}Am are not included in the PFD244 subassembly. ^{238}Pu was added to ^{240}Pu, and ^{241}Am was not included in the fabrication record (mill sheet) due to the relatively lower importance of fissile materials. However, this was not the case for PFD549.

In order to investigate the effect of the initial composition of actinides on the decay heat calculation, sensitivity analysis was conducted based on the fuel composition of the PFD549 subassembly. Calculation cases are described in Table 4, where fabricated data was used as a reference. In other cases, either the weight of ^{241}Am was excluded, or the weight of ^{238}Pu was added into ^{240}Pu in the same manner as it was treated for the PFD244 subassembly.

The calculated decay heat from each actinide was compared and shown in Fig. 6. The largest difference was observed for the decay heat from ^{242}Cm, followed by ^{238}Pu. As seen from the burn-up chain in Fig. 6, ^{242}Cm was mainly produced from ^{241}Am (n, γ) reaction, which gives a difference of decay heat to as much as 41W at 24 cooling days.

Considering the absence of actinides as a initial composition, Fig. 7(a) indicates a change of C/E values. The ratio between the decay heat reference and calculated case without ^{238}Pu and ^{241}Am was shown in Fig. 7(b). This resulted in the decay heat generated by ^{238}Pu and ^{241}Am reached 6 % - 17 % of the total heat during 24 - 258 days of cooling after irradiation.

4.3 Effect of Burn-up Calculation

Because of their longer life times, the decay heat from minor actinides becomes dominant after a certain cooling time period after irradiation. In order to investigate the effect of the decay heat from minor actinides, the production and transmutation of minor actinides were calculated by the "MAGI", which uses the same burn-up chain as "ORIGEN2". The decay heat was then calculated by multiplying the number of actinide nuclides with "MAGI" by the decay heat generation rate from individual nuclide, which are incorporated in the "ORIGEN2".

In this case, the fission products were treated as a lumped nuclide in "MAGI", the number of individual nuclide was obtained based on the calculation results from "ORIGEN2" so as to conserve the total weight of fission products calculated by "MAGI".

Comparison between "MAGI" and "ORIGEN2" calculations are shown in Table 5. Some discrepancies exist in the number of individual minor actinide, namely radioactivity due to the difference of neutron spectrum which affects the cross section used for the burn-up calculation. However, only 4 % change to the total decay heat was observed. The decay heat generated by fission products were within 2 % between "MAGI" and "ORIGEN2" calculations.

5. Conclusion

Decay heat of the JOYO Mk-II spent fuel subassemblies with burnup of 58,200 MWd/t and 57,900 MWd/t was measured and compared with the calculation. The measured decay heat of the subassembly at 24 days of cooling after irradiation was approximately 1.23 ± 0.03 kW. The C/E values were approximately between 0.96 and 0.90, which showed slight dependency on cooling time. The decay heat generated by ^{238}Pu and ^{241}Am, which amount to 1 % of initial composition of fresh fuel, reached 6 % - 17 % of decay heat during 24 - 258 days of cooling after irradiation. Some discrepancies exist in the number of individual minor actinide that were calculated by the JOYO core management code system "MAGI" and "ORIGEN2", which demonstrates a little change of the total decay heat. These indicate that the burn-up calculation and initial composition of actinides are important to accurately evaluate the decay heat.

As a result of this study, experimental data were obtained from the decay heat of fast reactor spent fuel subassemblies which have a shorter cooling time of less than 100 days. This data will be used to validate the analytical method and nuclear data.

Acknowledgements

The authors would like to note the contribution of Mr. H. Nagasaki and Mr. A. Tamai of Nuclear Engineering System Inc. for the decay heat measurement and the calculation by "ORIGEN2" and that of Mr. M. Nagatani and Y. Kato of Information Technologies Japan Inc. for the neutron flux and burn-up calculation by "MAGI". We also greatly appreciate the valuable recommendations and encouragement by Prof. T. Yoshida of Atomic Energy Research Laboratory of Musashi Institute of Technology.

References

1. Torimaru, T., et al.: PNC TN9410 98-034 (1998) (in Japanese).
2. Croff, A. G.: ORNL-5621, (1980).
3. Croff, A. G.: Nuclear Technology, Vol. 62, 335 (1983).
4. Cain, V. R.: ORNL CCC-307, (1977).
5. Nakagawa, T., et al.,: J. Nucl. Sci. Technol., Vol. 32, No. 12, 1259 (1995).
6. Tasaka, K., et al.: JAERI 1320, (1990).
7. Suyama, K., et al.: Proceedings of the 1997 Symposium on Nuclear Data, JAERI, Tokai, JAPAN, 9 (1998).
8. Yoshida, T., et al.: Proc. of International Conference on Nuclear Data for Science Technology, Mito, Japan, p.889 (1988).
9. Katakura, J.: J. At. Energy Soc. Japan, Vol. 38, No. 7, 609 (1996) (in Japanese).
10. Arii, Y., et al.: J. At. Energy Soc. Japan, Vol. 39, No. 4, 315 (1997) (in Japanese).

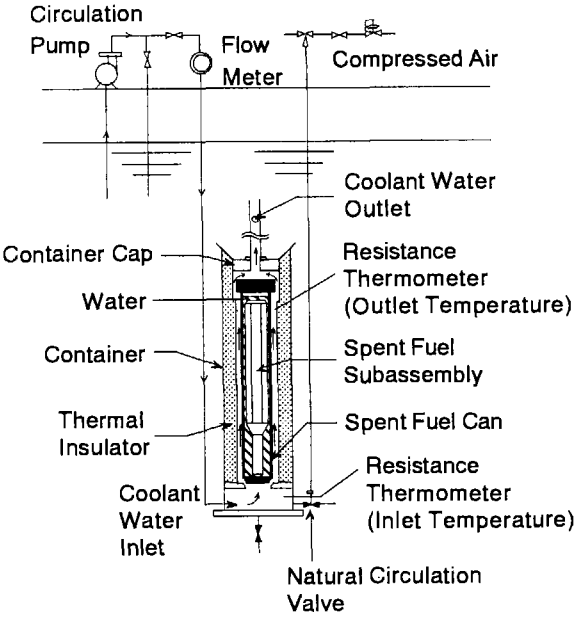

Fig. 1 Decay Heat Measurement System Diagram

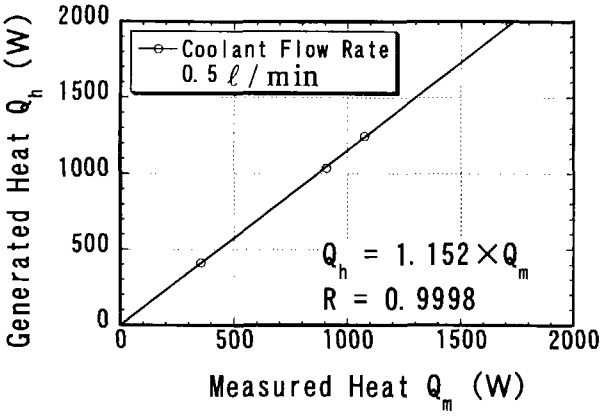

Fig. 2 Heat Calibration Curve for Decay Heat Measurement System

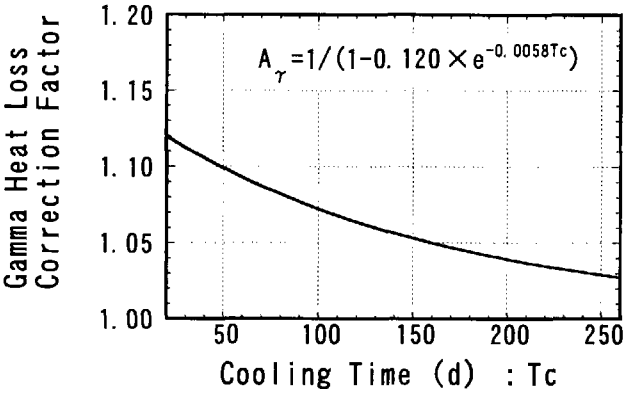

Fig. 3 Gamma Heat Loss Correction Factor

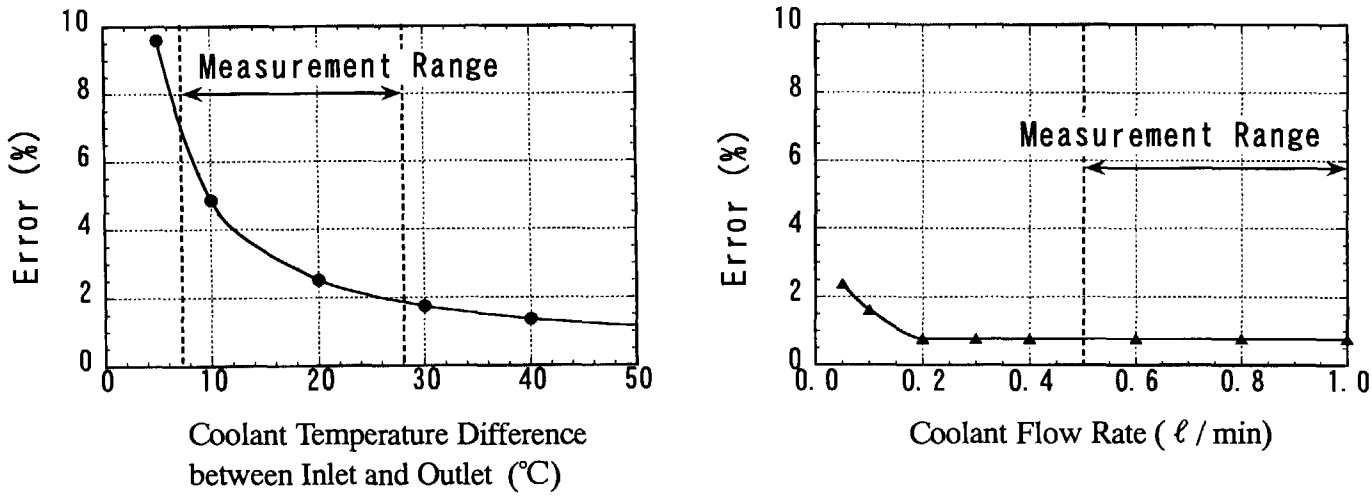

Fig. 4 Error Rate of the Decay Heat Measurement System

Table 1 Outline of Irradiation Condition for JOYO Mk-II Spent Fuel Subassemblies

(PFD549 Subassembly)

MOX Fuel Content	^{235}U Enrichment : 18.6% Pu Content : 28.5%
Irradiation Condition	Core Resident Period : 1990.12.14～1997.9.24 ϕ total : 3.3×10^{15} n/cm^2/s Irradiation Days : 171days (at 2B1) ϕ total : 2.1×10^{15} n/cm^2/s Irradiation Days : 285days (at 4D1)
Φ total	9.9×10^{22} n/cm^2 (Subassembly Averaged)
Burnup	58,200 MWd/t (Subassembly Averaged)
Cooling Time	24～258 days

(PFD244 Subassembly)

MOX Fuel Content	^{235}U Enrichment : 13.6% Pu Content : 28.9%
Irradiation Condition	Core Resident Period : 1990.2.14～1997.9.24 ϕ total : 2.7×10^{15} n/cm^2/s Irradiation Days : 240days (at 3A1) ϕ total : 2.0×10^{15} n/cm^2/s Irradiation Days : 285days (at 5E3)
Φ total	1.05×10^{23} n/cm^2 (Subassembly Averaged)
Burnup	57,900 MWd/t (Subassembly Averaged)
Cooling Time	31～224 days

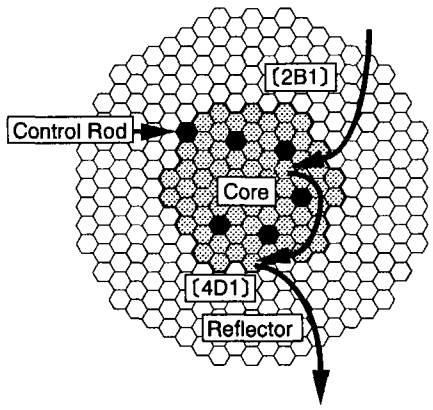

[Location in the Core for PFD549]

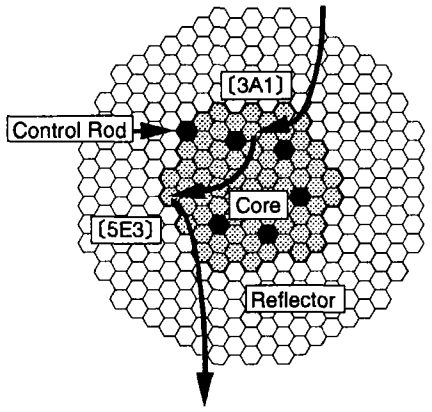

[Location in the Core for PFD244]

Table 2 Decay Heat Calculation Method

Item	MAGI	ORIGEN2
Cross Section	JFS-3-J3.2*1	
Geometry	3D Hex-Z	One Point Approx.
Energy Group	7	1*2
Flux Calculation	Diffusion	--------
Burn-up Calculation	Matrix Exponential	
Fission Yield, Decay Data	Lumped FP*1	JNDC-V2

Note *1 : JAERI Fast Set Version 3 (based on JENDL-3.2)

*2 : Collapsed using 600MWe size FBR core center spectrum

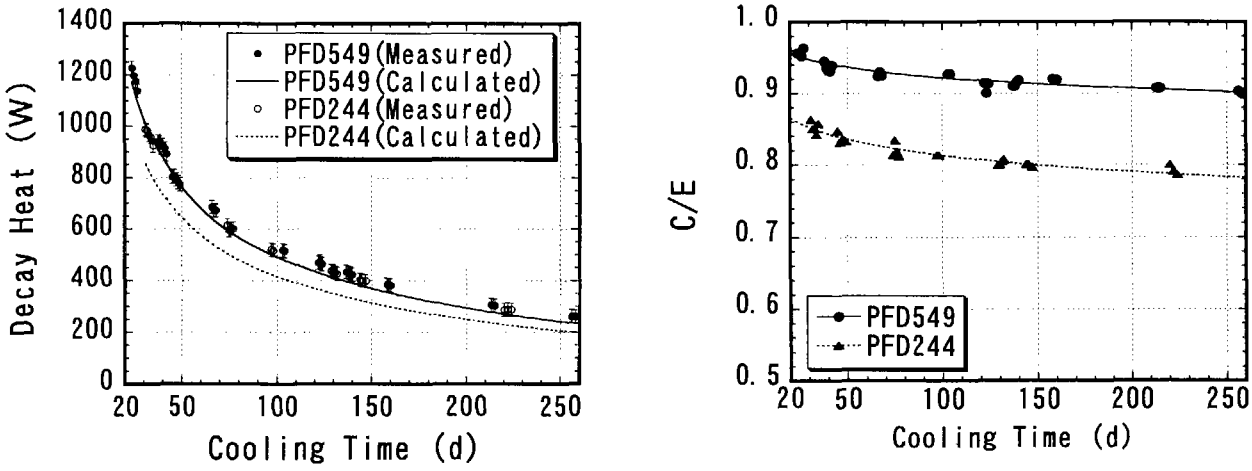

Fig. 5 Measured and Calculated Decay Heat of the JOYO Mk-II Spent Fuel Subassemblies

Table 3 Initial Composition of Actinides for the JOYO Mk-II Spent Fuel Subassemblies

(Unit : g)

Nuclide	PFD549	PFD244
^{235}U	1418	1019
^{238}U	6307	6582
^{238}Pu	35	-----
^{239}Pu	1975	2130
^{240}Pu	727	671
^{241}Pu	249	213
^{242}Pu	113	99
^{241}Am	25	-----

Table 4 Calculation Case Parameters for PFD549 Subassembly

(Unit : g)

Nuclide	Calculation Case for PFD549			
	Reference	without ^{238}Pu	without ^{241}Am	without ^{238}Pu and ^{241}Am
^{238}Pu	35	0	35	0
^{240}Pu	727	762	727	762
^{241}Pu	249	249	249	249
^{241}Am	25	25	0	0

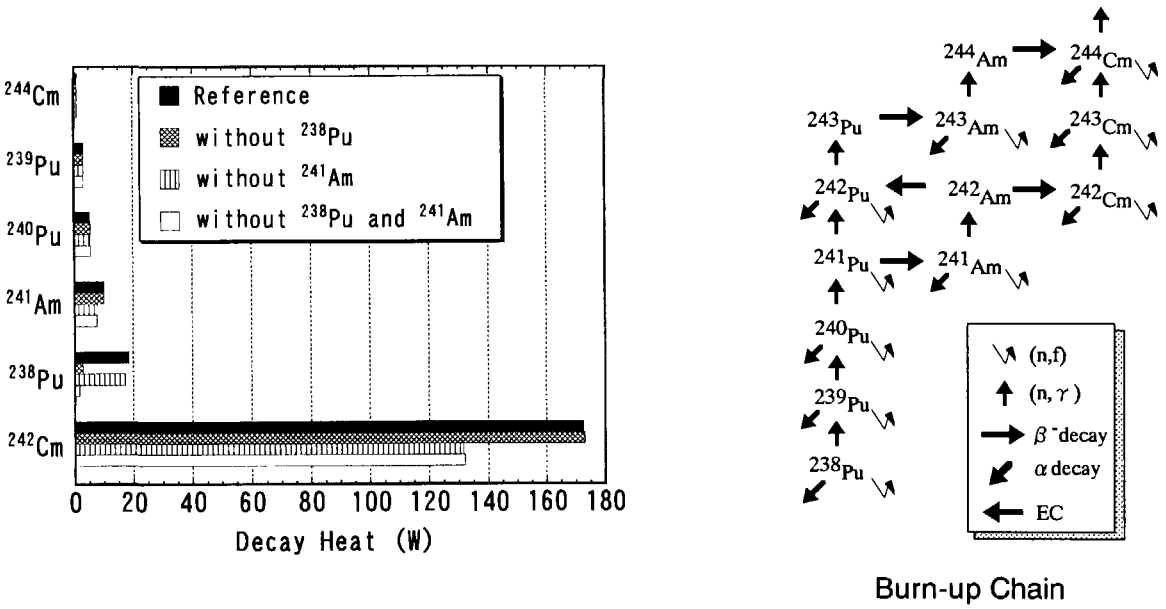

Fig. 6 Comparison of Decay Heat Produced from Actinide Nuclides (at 24 Cooling Days)

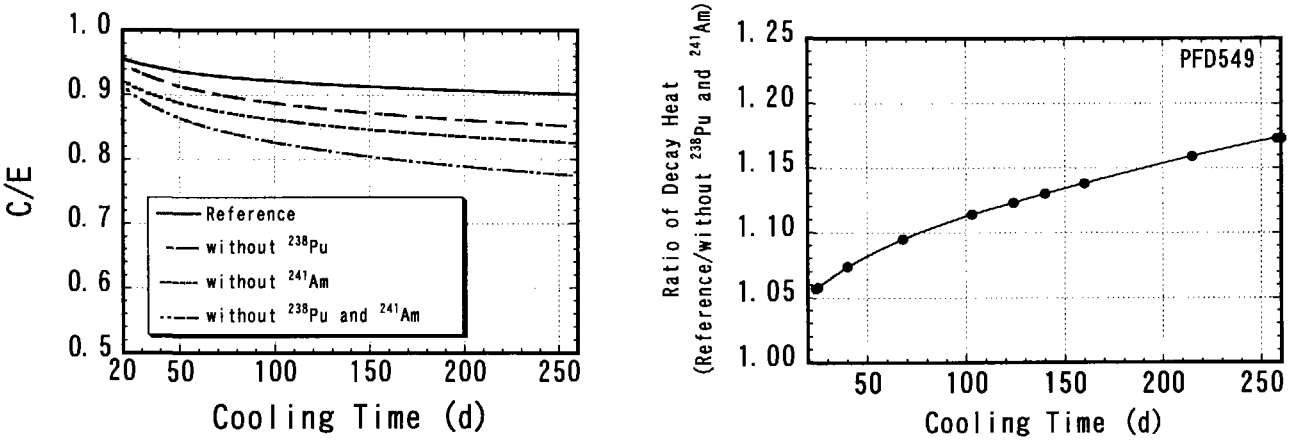

(a) Change of C/E (b) Decay Heat Calculation Result

Fig. 7 Decay Heat Calculation Result

Table 5 Comparison of Radioactivity and Decay Heat Calculation between MAGI and ORIGEN2 (at 24 Cooling Days)

Nuclide	Radioactivity (Bq)		Decay Heat (W)		
	MAGI	ORIGEN2	MAGI	ORIGEN2	MAGI / ORIGEN2
^{242}Cm	1.42×10^{14}	1.73×10^{14}	142	174	0.82
^{238}Pu	2.00×10^{13}	2.07×10^{13}	17.9	18.5	0.97
^{241}Am	1.12×10^{13}	1.12×10^{13}	10.1	10.1	1.00
^{240}Pu	6.11×10^{12}	6.35×10^{12}	5.14	5.35	0.96
^{239}Pu	3.99×10^{12}	3.97×10^{12}	3.32	3.30	1.01
^{244}Cm	6.17×10^{11}	1.15×10^{12}	0.58	1.09	0.53
^{241}Pu	5.86×10^{14}	5.96×10^{14}	0.49	0.50	0.98
Actinide	7.79×10^{14}	8.41×10^{14}	180	213	0.85
FP	8.71×10^{15}	8.85×10^{15}	932	950	0.98
Total	9.49×10^{15}	9.76×10^{15}	1122	1172	0.96

JP9950317

2.15 Status and Future Program of Reactor Physics Experiments in JAERI Critical Facilities, FCA and TCA

Shigeaki OKAJIMA*, Toshitaka OSUGI*, Ken NAKAJIMA†, Takenori SUZAKI†, and Yoshinori MIYOSHI†

* *Reactor Physics Laboratory, Department of Nuclear Energy System*

† *Criticality Safety Laboratory, Department of Fuel Cycle Safety Research*

Japan Atomic Energy Research Institute

Tokai-mura, Naka-gun, Ibaraki-ken 319-1195

e-mail: okajima@fca001.tokai.jaeri.go.jp

The critical facilities in JAERI, FCA (Fast Critical Assembly) and TCA (Tank-type Critical Assembly), have been used to provide integral data for evaluation of nuclear data as well as for development of various types of reactor since they went critical in 1960's.

In this paper a review is presented on the experimental programs in both facilities. And the experimental programs in next 5 years are also shown.

1. Introduction

There are three critical facilities in JAERI-Tokai: FCA (Fast Critical Assembly)[1], TCA (Tank-type Critical Assembly)[2] and VHTRC (Very High Temperature Reactor Critical Assembly). The FCA went critical in 1967, the TCA in 1962 and the VHTRC in 1985. At present the former two facilities are operated, while the VHTRC are kept the stand-by state. These facilities have been used to provide integral data for evaluation of nuclear data as well as for development of various types of reactor.

In this paper a review, focused on the nuclear data validation, is presented on the recent experimental programs in the facilities in operation, FCA and TCA.

2. Review of Reactor Physics Experiments in FCA

In early 1980's, IX series of assemblies, which consisted of seven different version of cores IX-1 to IX-7, were built to cover wide range of neutron spectra. These assemblies IX-1 to IX-6 were composed with 93% enriched uranium and diluent material of graphite or stainless steel for adjusting neutron spectrum in lower energy region or in higher energy region respectively. The assembly IX-7 was composed with 20% enriched metal uranium. At each assembly, criticality (keff), fission rates and sample reactivity worths of conventional materials were measured to check the reliability of neutron fields calculation prior to the measurement of integral data for minor actinides.[3, 4] The measured keff values were analyzed by the MVP code with the JENDL-3.2 library. The comparison between calculation and experiment is shown in Fig. 1. The calculation overestimates the measurements in IX-1, -2 and -3 cores. This overestimation is caused by the smaller capture cross section of ^{235}U in the JENDL-3.2 library.

The Doppler effect measurements have been carried out since 1968 in various mock-up cores. The accumulated data of the Doppler effect measurements for ^{238}U cover a wide range of the neutron energy spectra of cores from a small experimental fast reactor to a large commercial fast reactor. To evaluate the calculation accuracy of the ^{238}U Doppler effect, the measured data in the FCA were analyzed.[5] Figure 2 shows the comparison between calculated and measured values. In MOX fuel mock-up cores, the JENDL-3.2 calculation agrees well with the experimental values within 5 %. In Pu/^{235}U cores, the calculation overestimates the measurement. When the calculated results were

compared between JENDL-3.1 and JENDL-3.2 libraries, the JENDL-3.2 calculation gives 3 - 5 % larger Doppler reactivity worths in MOX fuel mock-up cores than the JENDL-3.1 calculation because of the extension of the unresolved resonance region of ^{238}U. In Pu/^{235}U cores, the JENDL-3.2 calculation gives 3 - 15 % larger values than the JENDL-3.1 calculation. The calculation in the Pu/^{235}U cores shows larger increase than that in MOX fuel mock-up cores. This larger increase is caused by the softer neutron spectrum below 10 keV in addition to the extension of the unresolved resonance region of ^{238}U. The former effect is given by the smaller capture cross section of ^{235}U in the JENDL-3.2 library.

To improve the prediction accuracy of the βeff, which allows the conversion between calculated and measured reactivity values, the international benchmark experiments were carried out.[6, 7] Three different core configurations were selected from view points of systematic change of the nuclide contribution from ^{235}U, ^{238}U and ^{239}Pu to the βeff as shown in Fig. 3 : XIX-1 (U-core), XIX-2 (Pu/NU core) and XIX-3 (Pu core). The six organizations from five countries participated in these experiments. The βeff measurement was carried out by each participant with their own measurement technique, and the measured results were compared with each other. From this comparison, the βeff value in each core was finalized within 3% of uncertainty. The analysis is under going to evaluate the delayed neutron data in JENDL-3.2. These experiments have been conducted under the NEA/NSC Working Party on International Evaluation Cooperation (WPEC), Subgroup 6 on Delayed Neutron Data Validation.

3. Review of Reactor Physics Experiments in TCA

In 1980's, a mock-up experiment for High-Conversion LWRs was carried out. Low enriched uranium fuel rods were used to simulate the high-conversion LWR cores (tight lattice cores), in which the ratio of moderator to fuel was ranged in 0.5 to 1.5. This ratio was smaller than in the conventional LWR core. In this experiment the following parameters were measured[8, 9] : criticality (keff), power distribution, reactivity worth for absorber materials and reaction rate ratios. Figure 4 shows the comparison between calculated and measured keff values for the cores including standard lattices of TCA. The calculation with JENDL-3.2 overestimates the experimental results. When the calculation is compared between JENDL-3.2 and JENDL-3.1, the calculation with JENDL-3.2 gives about 1% larger than those with JENDL-3.1. This increment of calculated keff values from JENDL-3.1 to JENDL-3.2 is due to the smaller capture cross section of ^{235}U in JENDL-3.2.

In the benchmark experiment concerning to the criticality safety, the following experiments were mainly performed: the measurements of reactivity effects for various materials, which would be used in fuel reprocessing plants, and the development of subcriticality monitoring technology. Furthermore, from view points of nuclear data validation of delayed neutron, the effective delayed neutron fraction (βeff) was measured by a couple of measurement techniques. The first technique is the substitution method. In this technique the value of βeff was determined from the reactivity worth for Sb-Cd-Pb rod which had the same dimension to the fuel rod and adjusted the contents to simulate the same absorption cross-section as the fuel rod.[10] Another technique was based on the measurement of the buckling coefficient of reactivity.[11] The measured βeff values are compared in Table 1. The good agreement is found in these values. These data can be used to evaluate the delayed neutron data in JENDL-3.2.

An integral experiment for FP nuclides was carried out to validate the FP cross-section data since the accurate estimation of FP nuclides reactivity effects are needed in burn-up credit calculation.[12] In the experiment, the reactivity worth of solution containing FP nuclides was measured. The calculation was carried out using the SRAC code for the cell calculation and the TWOTRAN code for the flux calculation.[13] In this calculation, the JENDL-3.2 library was used except for Er. The ENDF/B-V library was used for Er. Figure 5 shows the comparison of the reactivity worth between calculation and measurement. The calculated reactivity worths for FP nuclides with JENDL-3.2 agree well with experiments except for Er. In the Er sample, the calculation overestimates the measured values.

4. Future Experimental Program in FCA and TCA

The experimental programs in next 5 years in both facilities are planed. In FCA,

- Mock-up experiments of GEM (Gas Expansion Module) for the prototype fast reactor
- Basic experimental study for ADS (Accelerator Driven Subcritical System)
- Mock-up experiment for the nitride fueled fast reactor
- Integral experiment for the minor actinides (2nd phase)
- Doppler effect measurements of Th, W and Er.

And in TCA,

- Kinetics experiment focused on the spatial dependency
- Critical experiment for the advanced LWR
- Critical experiment for the MOX fueled high-conversion LWR
- Experiment on criticality safety for storage and transportation of nuclear fuels
- Integral experiment for FP nuclides.

The main reactor physics parameters, such as criticality, reaction rate ratio, etc., are measured to know the core characteristics. A set of these data and their analysis will be useful to validate the nuclear data.

5. Conclusion

Both critical facilities in JAERI, FCA and TCA, have been operated for more than 30 years to provide integral data for evaluation of nuclear data as well as for development of various types of reactor. A variety of integral data has been measured in these facilities and contributed to the evaluation of nuclear data through their analyses. From the recent analysis, it was pointed out that the capture cross section of ^{235}U in resonance energy range is small in the JENDL-3.2 library. These data are to be used for the reevaluation work of JENDL-3.3 library.

Future experimental programs in both facilities were also shown. In these programs the main reactor physics parameters, such as criticality, reaction rate ratio, etc., will be measured. These measured data can fill up the data base of the integral data for the evaluation of nuclear data.

References

(1) Hirota J.: *JAERI 1289* (1984).
(2) Tsuruta H. : *JAERI 1254* (1977).
(3) Mukaiyama T., Obu M., Nakano M., *et al.*: *Proc. Int. Conf. Nuclear Data for Basic and Applied Science*, vol. 1, p.483-488, (Santa Fe, 1985).
(4) Okajima S., Mukaiyama M., *et al.*: *Proc. Int. Conf. Nuclear Data for Science and Technology*, p.983-986, (Mito, 1988).
(5) Okajima S.: *Proc. of Int. Conf. on the Physics of Reactors PHYSOR 96*, E-247 - E-254, (Mito, 1996).
(6) Okajima S., Sakurai T., Mukaiyama T.: *Proceedings of the 1996 Symposium on Nuclear Data, JAERI-Conf 97-005*, p.71-76, (1997).
(7) Sakurai T., Okajima S., *et al.*: *Proc. of Int. Conf. on the Physics of Nuclear Science and Technology*, 182-189, (Long Island,1998).
(8) Nakajima K., Akai M., *et al.*: *J. Nucl. Sci. and Technol.*, **31**, 1160, (1994)
(9) Nakajima K.: *Proceedings of the 1994 Symposium on Nuclear Data, JAERI-Conf 95-008*, p.137, (1995).
(10) Nakajima K.: Private communication (1998).
(11) Suzaki T.: *Proc. of 1996 Fall Meeting of AESJ*, A29, (1996).
(12) Komuro Y., Suzaki T., *et al.*: JAERI-Research 97-088 (1997).
(13) Sakurai K., Yamamoto T.: *J. Nucl. Sci. and Technol.*, **34**, 202, (1997).

Table 1 Comparison of βeff values measured in TCA standard core, 1.83U

	βeff values
Method A*	: 0.00767 ± 0.00017 (C/E=1.02)
Method B	: 0.00754 ± 0.00012 (C/E=1.03)
Calculation**	: 0.00780

Method A : Substitution method
Method B : Method based on buckling coefficient of reactivity

* Preliminary results
** SRAC (CITATION, 17Gr, X-Y) + JENDL-3.2

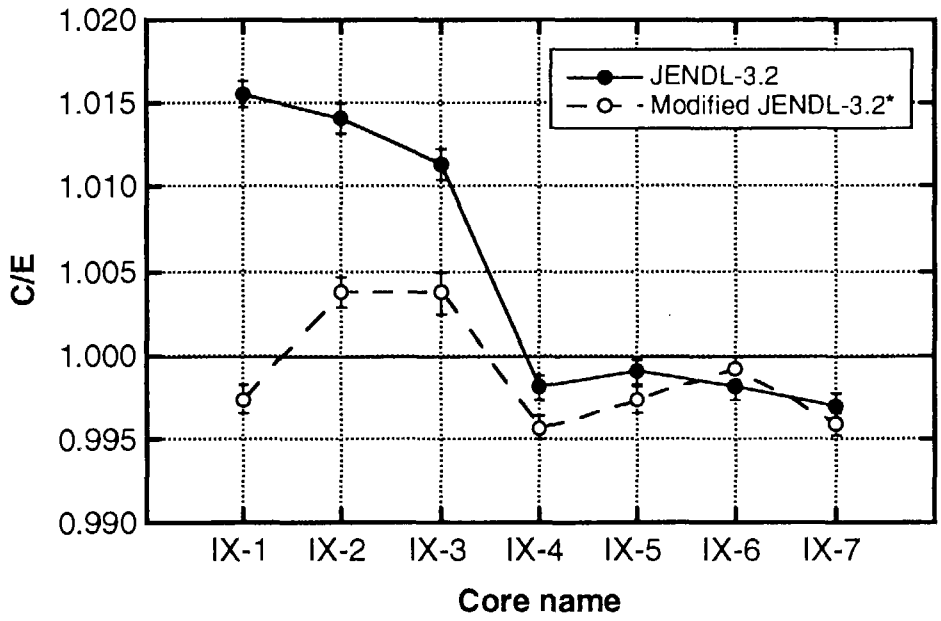

Fig. 1 C/E values of criticality (keff value) in FCA IX cores
(Calculation was carried out by MVP code)
* Cross section data of U-235 was replaced from JENDL-3.2 to JENDL-3.1

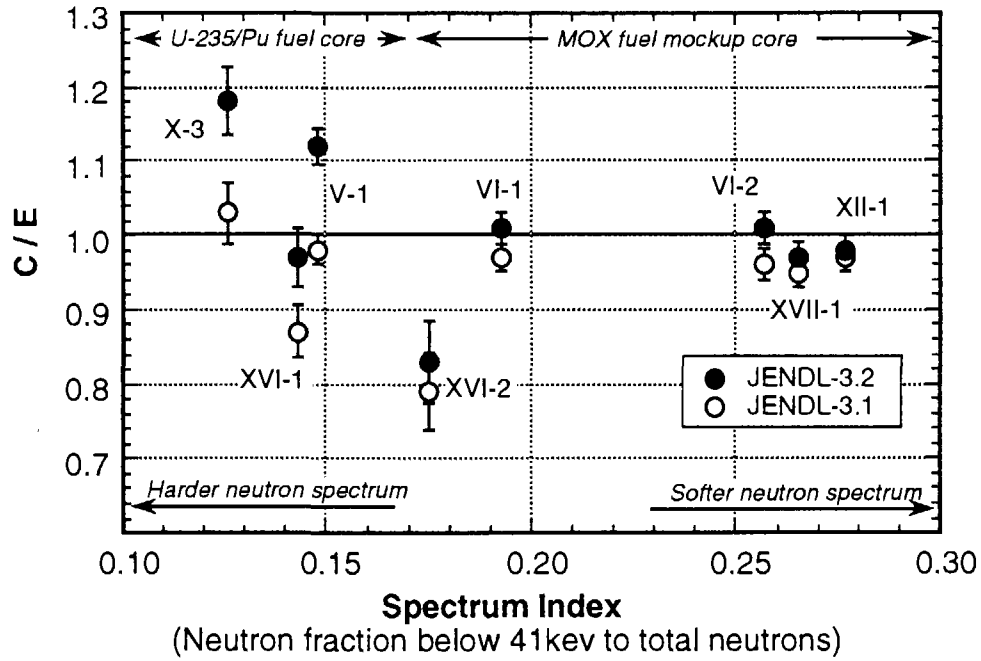

Fig. 2 C/E values of U-238 Doppler reactivity worths measured in FCA cores

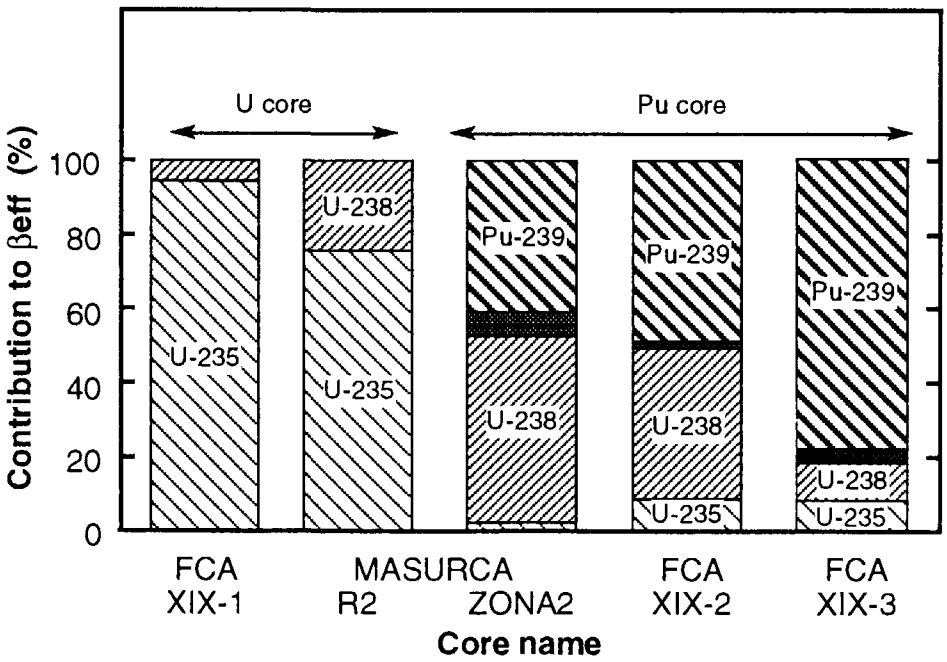

Fig. 3 Nuclide contribution to βeff values in βeff benchmark cores

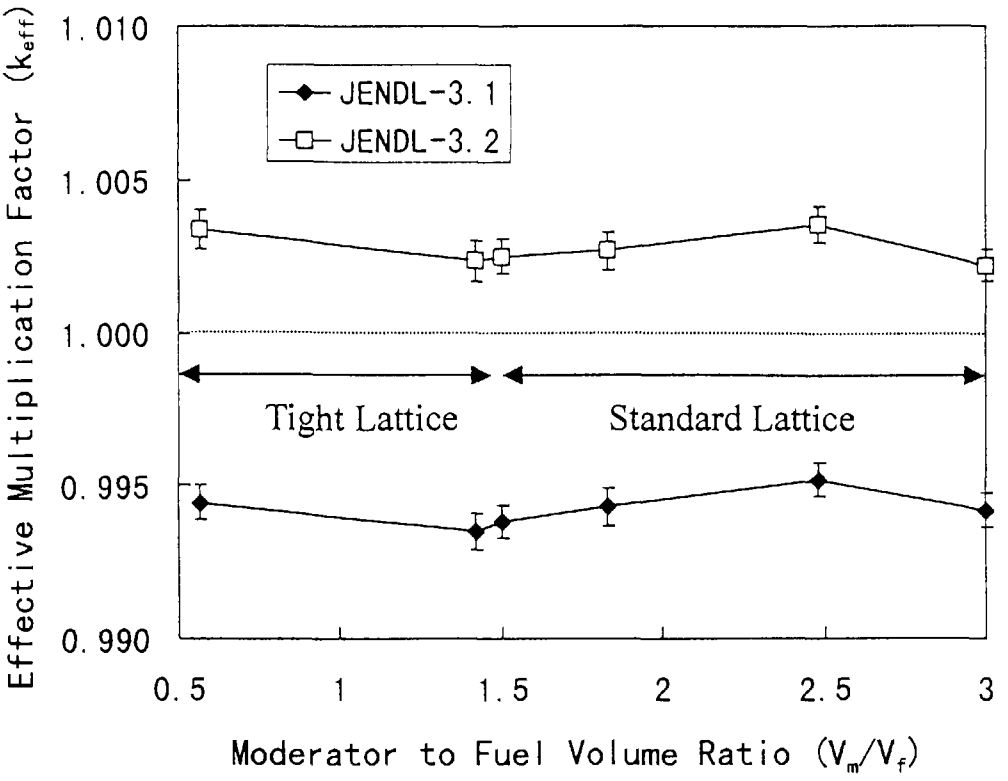

Fig. 4 Comparison of keff values in TCA cores between JENDL-3.2 and JENDL-3.1
(Measured keff value is 1.00, Calculation was carried out by MVP code.)

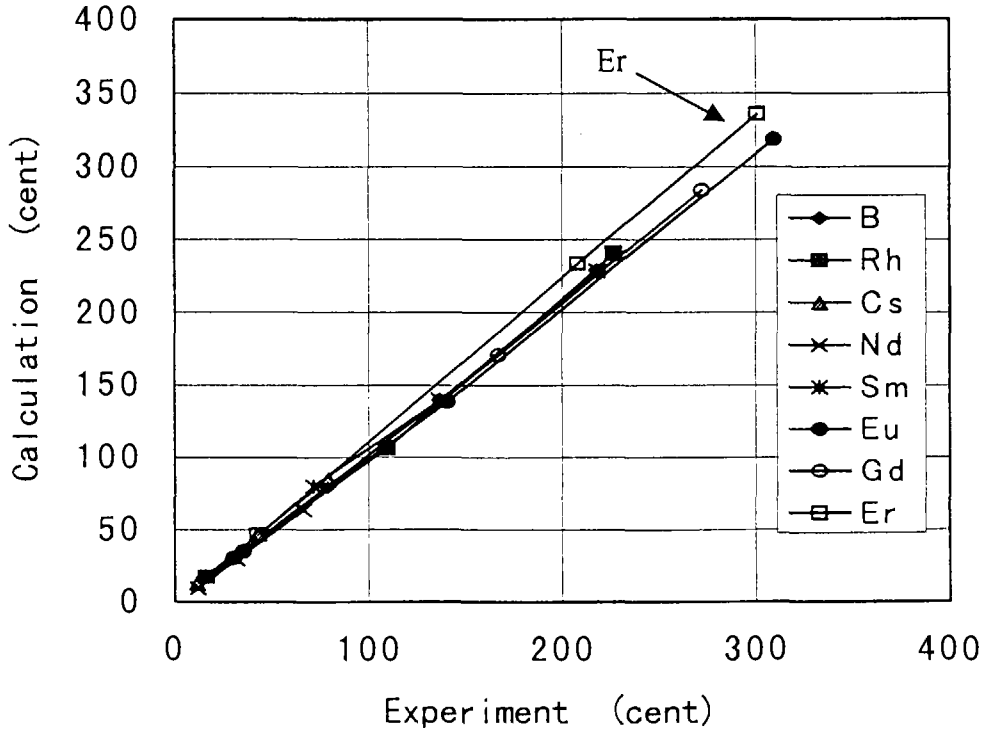

Fig. 5 Comparison between calculated and measured reactivity worths for FP nuclides

This is a blank page.

3. Papers Presented at Poster Sessions

This is a blank page.

JP9950318

3.1 Measurements of Double-Differential Neutron Emission Cross Sections of ^{238}U and ^{232}Th for 2.6 and 3.6 MeV Neutrons

Takako MIURA, Mamoru BABA, Masanobu IBARAKI, Toshiya SANAMI,
Than Win, Yoshitaka HIRASAWA, and Naohiro HIRAKAWA
Department of Quantum Science and Energy Engineering, Tohoku University
Aramaki-Aza-Aoba 01 , Aoba-ku, Sendai, 980-8579, Japan

Double-differential neutron emission cross sections (DDXs) of ^{238}U and ^{232}Th were measured using the time-of-flight (TOF) method for 2.6 and 3.6 MeV neutrons. The data for ~3 MeV incident neutrons are required because of a large change of the spectra from discrete to continuum between 2 MeV and 4 MeV. The present data show that discrete structures consisting of Ex~0.7 and ~1.0 MeV groups of excited states are dominant in 2.6 MeV, while a continuum is major in 3.6 MeV.

1. Introduction

^{238}U and ^{232}Th are one of the main constituent elements in breeder reactors. The energy spectra of scattered neutrons from ^{238}U and ^{232}Th, therefore, are of great importance to evaluate the slowing down of neutrons in the reactors and to neutronics-design of the reactors. However, experimental data of secondary neutron spectra of ^{238}U and ^{232}Th are very scarcely. Hence large differences exist among the evaluated data.

In our previous works, the double differential neutron emission cross sections (DDXs) of ^{238}U and ^{232}Th were measured for 1.2, 2, 4, 6, 14 and 18 MeV neutrons /1//2/. In the present work, the DDXs were measured for 2.6 and 3.6 MeV neutrons using the time-of-flight (TOF) method following our previous works. The data around 3 MeV incident energies are required because a large change of the spectra was found between 2 and 4 MeV.

2. Experiment

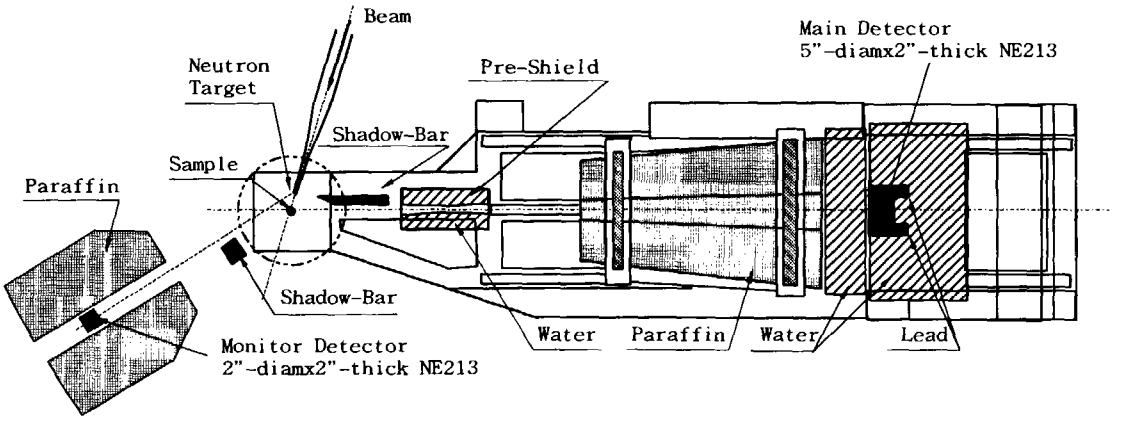

Fig.1 Experimental geometry

DDXs of ^{238}U and ^{232}Th for 2.6 and 3.6 MeV neutrons were measured using the TOF method at Tohoku University 4.5 MV Dynamitron facility. The experimental arrangement is shown in fig.1. Primary neutrons of 2.6 and 3.6 MeV were produced by the T(p,n) and D(d,n) reaction using a Ti-T and D_2 gas cell (1cm-diam×1.5cm-long, 1atm) target, respectively. In the 2.6 MeV source neutron spectrum, contaminant neutrons lower than 1.2MeV were found with an intensity of ~17 % fraction to the primary neutrons. The effect of the contaminant neutrons was corrected for based on a Monte-Carlo calculation /3/. Scattering samples were metallic cylinders of elemental uranium and thorium, 2-cm-diam ×5-cm-long, and encased in 0.5-mm-thick aluminum cans. An empty aluminum-can was used for the background measurement. The neutron detector was a massively shielded NE213 scintillator, 12.7-cm-diam×5.1-cm-thick, and the flight path was ~4 m. Neutron spectra were measured at 6 angles between 30° and 145°. A monitor detector of a NE213 scintillator, 5.08-cm-diam×5.08-cm-thick, measured the spectrum and intensity of source neutrons at ~40° relative to the incident beam. This detector was shadowed from the samples to avoid radiations from the uranium and thorium samples. Three-parameter data for TOF, pulse-shape (n-γ) and pulse-height were collected in a list mode. Absolute cross sections were determined relative to the H(n,n) cross section by measuring a polyethylene sample. A curve of relative efficiency was determined by measurement of the fission neutron spectrum from ^{252}Cf and calculation of SCINFUL-code /4/.

3. Data Reduction

The TOF spectra for 2.6 and 3.6 MeV incident neutrons are shown in fig.2 and fig.3, respectively. Foreground spectra and a background spectrum were normalized using counts of the monitor detector. The TOF spectra were converted into energy spectra considering the relative efficiency. The energy spectra were corrected further for the effects of sample-dependent backgrounds and finite-sample-size by a Monte-Carlo calculation /3/.

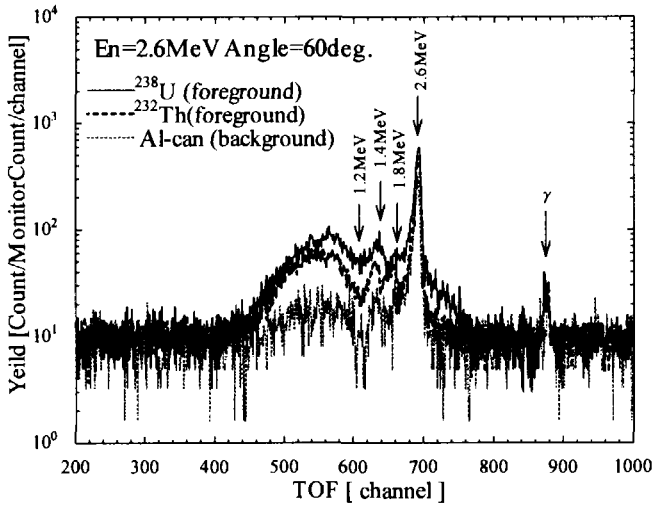

Fig.2 TOF spectra for En=2.6 MeV at 60°

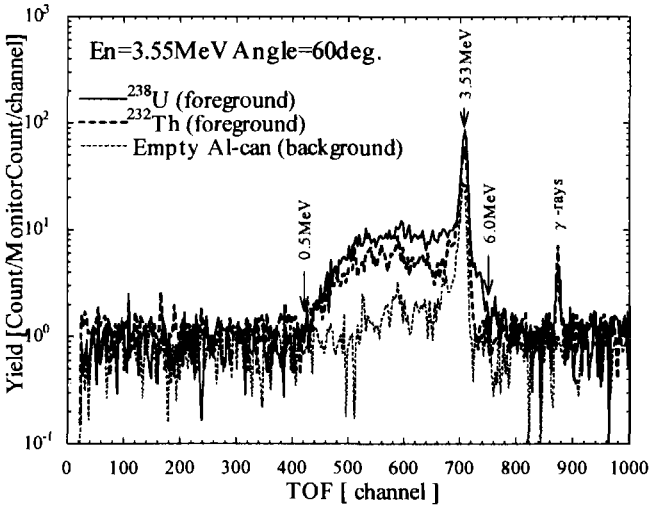

Fig.3 TOF spectra for En=3.6 MeV at 60°

3. Result

Figure 4 and Fig.5 show the present DDX results for 2.6 and 3.6 MeV incident neutrons in comparison with the evaluated nuclear data, respectively. ^{238}U and ^{232}Th are even-even nuclei with close atomic numbers. For this reason, they show similar structures of excited states around Ex~0.7 and ~1 MeV due to vibration levels. In the spectra for 2.6 MeV, the discrete structures of Ex~0.7 and ~1 MeV groups are distinct, while in the case of 3.6 MeV, the spectra change to continuous. For ^{238}U, the data of JENDL-3.2 are fairly close to the present data, but for ^{232}Th, the data of both JENDL-3.2 and ENDF/B-VI overestimate the excitation of Ex~0.8 and ~1.2 MeV groups in both incident energies.

Figure 6 and fig.7 show angular distributions of the elastic group (0^+, 2^+, 4^+, 6^+) for 2.6 and 3.6 MeV incident neutrons, respectively. For ^{238}U, both the evaluated data are in agreement with the present data. For ^{232}Th, the data of JENDL-3.2 is slightly different from the present data in the distribution.

[1] M. Baba *et al.*, J. Nucl. Sci.and Technol., **27** (1990) 601-616.
[2] S. Matsuyama *et al.*, JAERI-M 91-032.
[3] M. Baba *et al.*, Nucl. Instrum. and Methods **A372** (1995) 354-365.
[4] V. V. Verbinski *et al.*, Nucl. Instrum. and Methods **A65** (1968) 8.

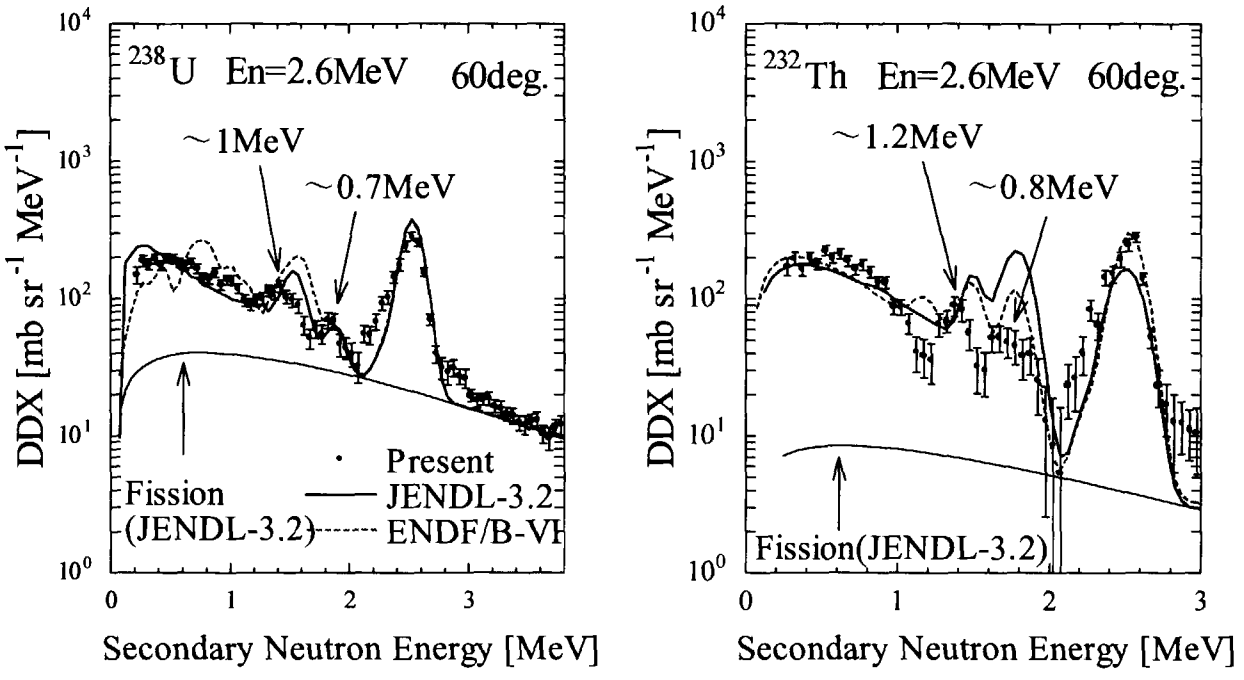

Fig.4 DDXs of ^{238}U and ^{232}Th for En=2.6 MeV at 60°

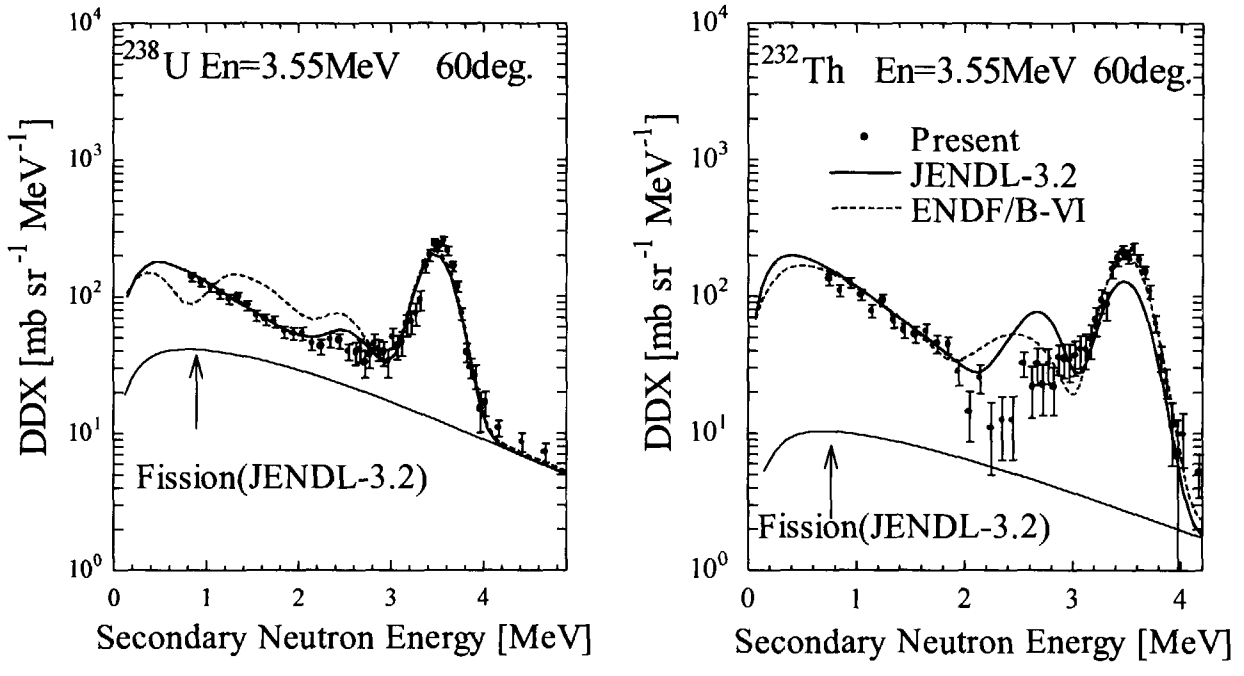

Fig.5 DDXs of ^{238}U and ^{232}Th for En=3.6 MeV at 60°

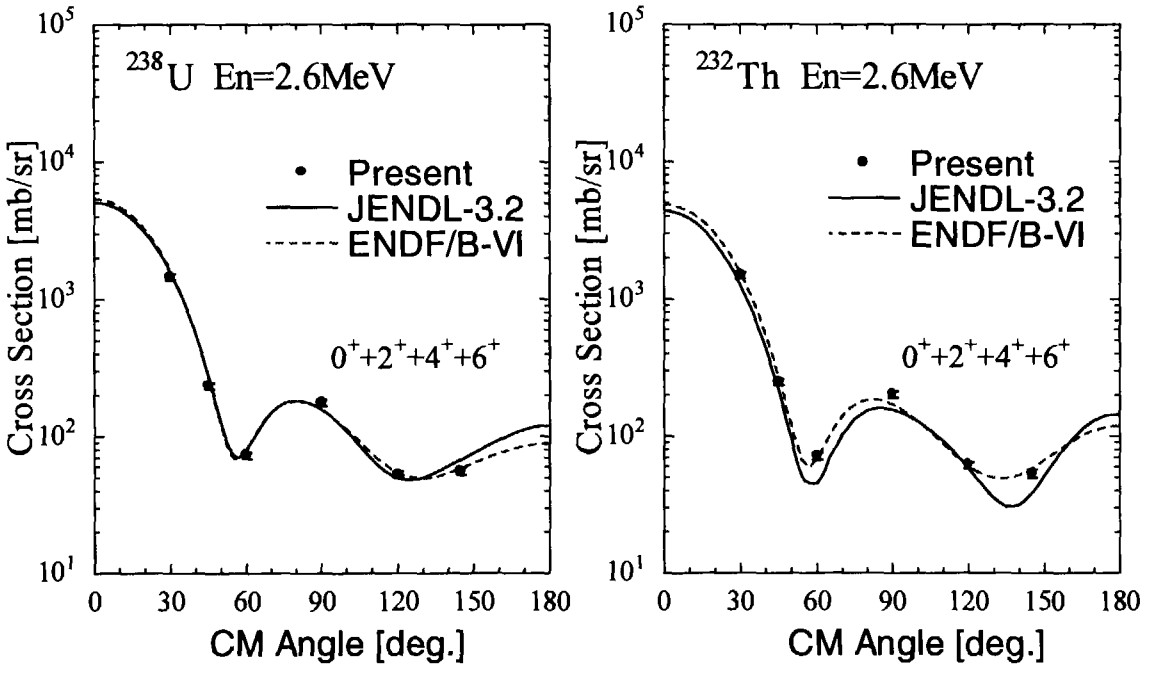

Fig.6 ADXs of ^{238}U and ^{232}Th for En=2.6 MeV

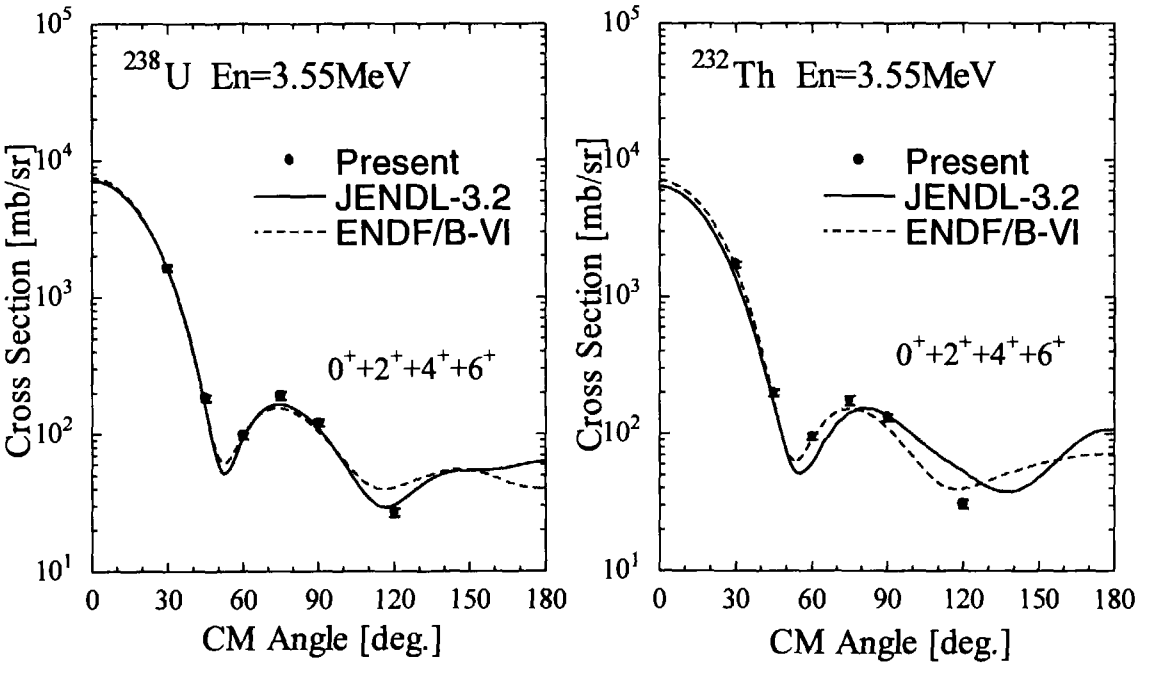

Fig.7 ADXs of ^{238}U and ^{232}Th for En=3.6 MeV

JP9950319

3.2 Measurement of Capture Cross Section of *Dy* and *Hf* in the Energy Region from 0.003 *eV* to 10 *eV*

°Hyun-Je Cho[1], Katsuhei Kobayashi[1], Shuji Yamamoto[1], Yoshiaki Fujita[1], Guinyun Kim[2], Jonghwa Chang[3], Seung Kook Ko[4]

1. Research Reactor Institute, Kyoto University
   Kumatori-cho, Sennan-gun, Osaka, 590-0494, Japan
2. Pohang Accelerator Laboratory, POSTECH
   San 31, Hyojadong Namgu, Pohang, 790-784, Korea
3. Korea Atomic Energy Research Institute, KAERI
   P.O.Box 105, Taejeon, 305-600, Korea
4. Department of Physics, University of Ulsan
   San 1, Moogedong, Namgu, Ulsan, 680-749, Korea

Applying a detector assembly of $Bi_4Ge_3O_{12}$ (BGO) scintillators (each size: 5×5 cm^2, 7.5 *cm* thick) to prompt capture gamma-rays measurement as a total energy absorption detector, the absolute measurement of capture cross sections of nat-*Hf* and nat-*Dy* has been made in the energy region from 0.003 *eV* to 10 *eV* by the linac time-of-flight (TOF) method using a 12.7 *m* station. Incident thermal neutron flux was absolutely determined by using the BGO detection system with a *Sm* sample. To extend the neutron flux measurement from the thermal neutron region to higher neutron energies, the $^{10}B(n,\alpha\gamma)$ reaction was applied. Absolute capture yield for the sample was obtained by the saturated capture yield at a large resonance of the sample. The inside of the through-hole in the BGO detection system is covered with ^{6}LiF tiles of 3 *mm* in thickness, which are useful to shield neutrons scattered by the sample below 100 *eV*. The effects by the scattered neutrons at higher energies have been investigated using a graphite sample.

The measured capture cross section of *Dy* shows good agreement with the existing experimental data and the evaluated data in ENDF/ B-VI. The present values of *Hf* are also in good agreement with those of the previous data and the JENDL-3.2 and ENDF/B-VI data.

Ⅰ. Introduction

Dysprosium (*Dy*) and hafnium (*Hf*) are promising absorbing materials for control rods of thermal reactors[1-3] and are often used as activation foils for neutron dosimetry[4]. The neutron capture cross sections of these samples are of great importance for design and development of nuclear reactors. In the past, many capture cross sections have been investigated experimentally and theoretically[5~11]. Below thermal neutron energy region, Knorr and Schmatz[5] derived the capture cross section of *Dy* using the neutron transmission data. Widder[6] measured the data between 0.1 *eV* and 2 *eV* by using a Moxon-Rae detector. For *Hf*, Blair obtained the capture cross section between 0.01 and 0.8 *eV*[10]. These evaluated data are given in JENDL- 3.2[12] and ENDF/B-VI[13].

Much effort has been spent to overcome the various difficulties in the measurement, especially in the resonance energy region. According to the Nuclear Data Request List[14], accuracy of 5 % is requested for both reactions in the thermal and resonance energy regions. Therefore, it is still necessary for us to measure and improve these capture cross sections using the recent experimental techniques.

This paper describes the absolute measurement of neutron capture cross sections of *Dy* and *Hf* using the BGO detection system as a total energy absorption detector as we did before[15]. In order to determine the neutron flux impinging on the sample, the neutron detection efficiency was calibrated by a *Sm* sample and/or a ^{10}B sample at thermal neutron energy. The ^{10}B sample was employed to measure the energy dependent neutron flux. The detection efficiency of the capture events for the BGO detectors was obtained by the saturated yield method[15]. Finally, the measured results are compared with the existing experimental data and the evaluated cross section values in JENDL-3.2[12] and ENDF/B-VI[13].

Ⅱ. Experimental Method

1. Samples

The *Dy* and the *Hf* samples were a metallic plate 1.8×1.8 cm^2 (purity was 99.9 %) and the thickness was 0.025 *mm*, respectively. The sample was set at the center of the through-hole of the BGO detection system. To measure the absolute thermal neutron flux, we used a metallic plate of *Sm* (99.8 %), 1.8×1.8

cm^2 and 0.5 *mm* thick. Boron-10 sample (powder in a thin *Al* case of 1.8×1.8 cm^2 and 0.5 *mm* in thickness) was also employed to measure the energy dependent neutron flux as we used before[15].

2. Experimental Arrangement

The experimental arrangement is almost same as before[15]. The flight path used in the experiment was in the direction of 135° to the linac electron beam. Photoneutrons from the water-cooled *Ta* target hit a capture sample placed at the distance of 12.7 *m* from the target. The neutron collimation system was mainly composed of B_4C, CH_4, Li_2CO_3 and *Pb* materials, and tapered from about 12 *cm* in diameter at the entrance of the flight tube to 1.5 *cm* at the detector. The neutron intensity during the time-of-flight (TOF) experiment was monitored by a BF_3 counter placed in the neutron beam.

3. Pulsed Neutron Source

Fast neutrons, which were produced by the 46 *MeV* linac at the Research Reactor Institute, Kyoto University (KURRI), were moderated by an octagonal water tank, 30 *cm* in diameter and 10 *cm* thick. The operating conditions of the linac were as follows; the repetition rate of 40 *Hz*, the pulse width of 3 μs, the electron energy of 30 *MeV* and peak current of 0.4 *A*.

4. Data Acquisition

Output signals from the BGO detectors were led to the coincidence circuit, by which the signal-to-noise ratio could be improved. In case of the ^{10}B sample, the conventional TOF measurement (anti-coincidence method) was made, because the $^{10}B(n, \alpha\gamma)$ reaction had no cascade gamma and emitted a single gamma-ray of 478 *keV*. The detailed description of the TOF measurement and the data taking is seen in the previous paper[15].

In case of the background measurement, a thick ^{10}B plug (1.11 g/cm^2) was placed before the BGO detection system to black out the neutron beam.

Ⅲ. Results and Discussion

Absolute measurement of the capture cross section was performed through the flux determination with thermal neutrons, calibration of the BGO detection efficiency for capture gamma-rays, derivation of the capture yield, and the

correction for capture yield. The measured neutron capture cross sections of *Dy* and *Hf* are shown in Figs. 1 and 2. The experimental uncertainties are in the range of 2.5 to 6.2 %, which are mainly due to the statistical ones and the systematic errors in the background subtraction, the standard cross section of the $^{10}B(n, \alpha\gamma)$ reaction, the correction for multiple scattering, neutron self-shielding, gamma-ray self-absorption, variation of the incident neutron energy spectra and deviation of the detector efficiency from linearity.

Figure 1 shows the measured result of *Dy*. The capture cross sections measured by Widder[6] is in good agreement with the present values. Theoretical results by Knorr and Schmatz[5] at lower energy region seem to be a little higher than the measurement. The ENDF/B-VI data are close to the present value not only at the off-resonance but also at the resonance energy region.

The data obtaibed by Blair[10] is in good agreement with the present measurement, as shown Fig. 2. The evaluated data in JENDL-3.2 and ENDF/B-VI show good agreement with the measurement.

In the resonance energy region, the resonance parameters have to be investigated by analyzing the measured data with a computer code, in future.

Ⅳ. Conclusion

The capture cross sections of *Dy* measured by Widder is in good agreement within the uncertainties with the present measurement. However, Knorr and Schmatz gave a little higher values below 0.005 *eV*. The ENDF/B-VI data show general agreement with the present result. In case of *Hf*, the data by Blair is in good agreement with the present measurement. The evaluated data in JENDL-3.2 and ENDF/B-VI are in general agreement with the present.

The data measured in the resonance energy region should be analyzed to get the resonance parameters in future.

Reference

[1] V.D.Risovany, E.P.Klochkov and V.B.Ponomarenko, Hafnium in Nuclear Engineering, *NIIAR*, 143 (1993).

[2] E.P.Klochkov, V.D.Risovany and Z.I.Chechetkina, Hafnium Application in

Nuclear Reactor Control Members. Review. M., *TSNIIatominform* (1985).
[3] E.P.Klochkov and V.D.Risovany, Hafnium in Nuclear Engineering-Atomnaya Energuiya Za Rubezhom, No. 10, 12 (1987).
[4] Technical Reports Series No. 273, *"Handbook on Nuclear Activation Data"*, IAEA, Vienna (1987).
[5] K.Knorr and W.Schmatz, *AKE* 16(9), 49 (1970).
[6] F.Widder, Eidg. Inst. Reaktorforsch., Wuerenlingen, reports, *EIR-217* (1975).
[7] R.C.Block, G.G.Slaughter, L.W.Weston and F.C.Vonderlage, CEN Saclay, Essonne, *61SACLAY, 203* (1961).
[8] J.H.Gibbons, R.L.Macklin, P.D.Miller and J.H.Neiler, *Phys. Rev.* 129, 2695 (1963).
[9] M.V.Bokhovko, L.E.Kazakov, V.N.Kononov, E.D.Poletaev and V.M.Timokhov, Jadernye Konstanty, *Obninsk reports*, YK 4, 8 (1988).
[10] (Eds.) I.M.Blair and T.W.Conlon, Nuclear Physics Division, AERE Harwell; M.C. Moxon, J.E. Jolly and D.A.J. Endacott, *AERE-PR/NP21*, p 41 (1974).
[11] Wang Chunhao, Xia Yijun, Yang Jinfu, Yang Zhihua and Wang Shiming, *Chinese J. of Nuclear Physics* 12(1), 89 (1990).
[12] (Eds.) K. Shibata and T. Narita, *JAERI-Data/Code 98-006* (1998).
[13] (Ed.) R.F.Rose, *"ENDF-201, ENDF/B-VI Summary Documentation"*, *BNL-NCS-17541*, 4th Ed. (ENDF/B-VI) Brookhaven National Laboratory (1991), and *"ENDF/B-VI MOD 2 Evaluation"*, by P.G.Young (1996).
[14] The NEA High Priority Nuclear Data Request List, 4.C. Absorber Materials, *NEA Nuclear Science Committee*, Status in October 1997.
[15] S.Yamamoto, Y.Fujita, T.Shibata and S.Selvi, *Nucl. Instrum. Methods.*, A 249, 484 (1986).

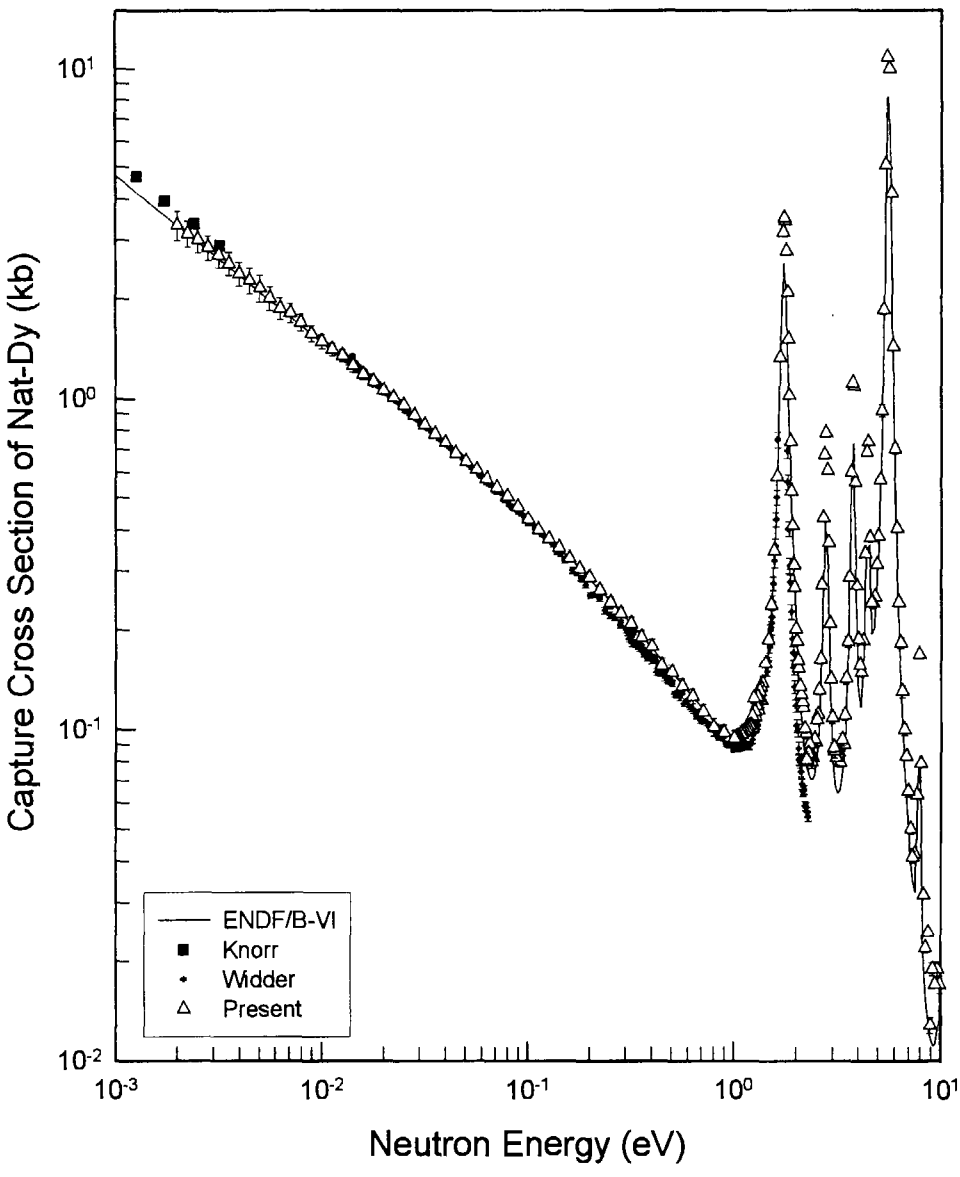

Fig. 1. The capture cross section of *Dy* between 0.003 and 10 *eV*.

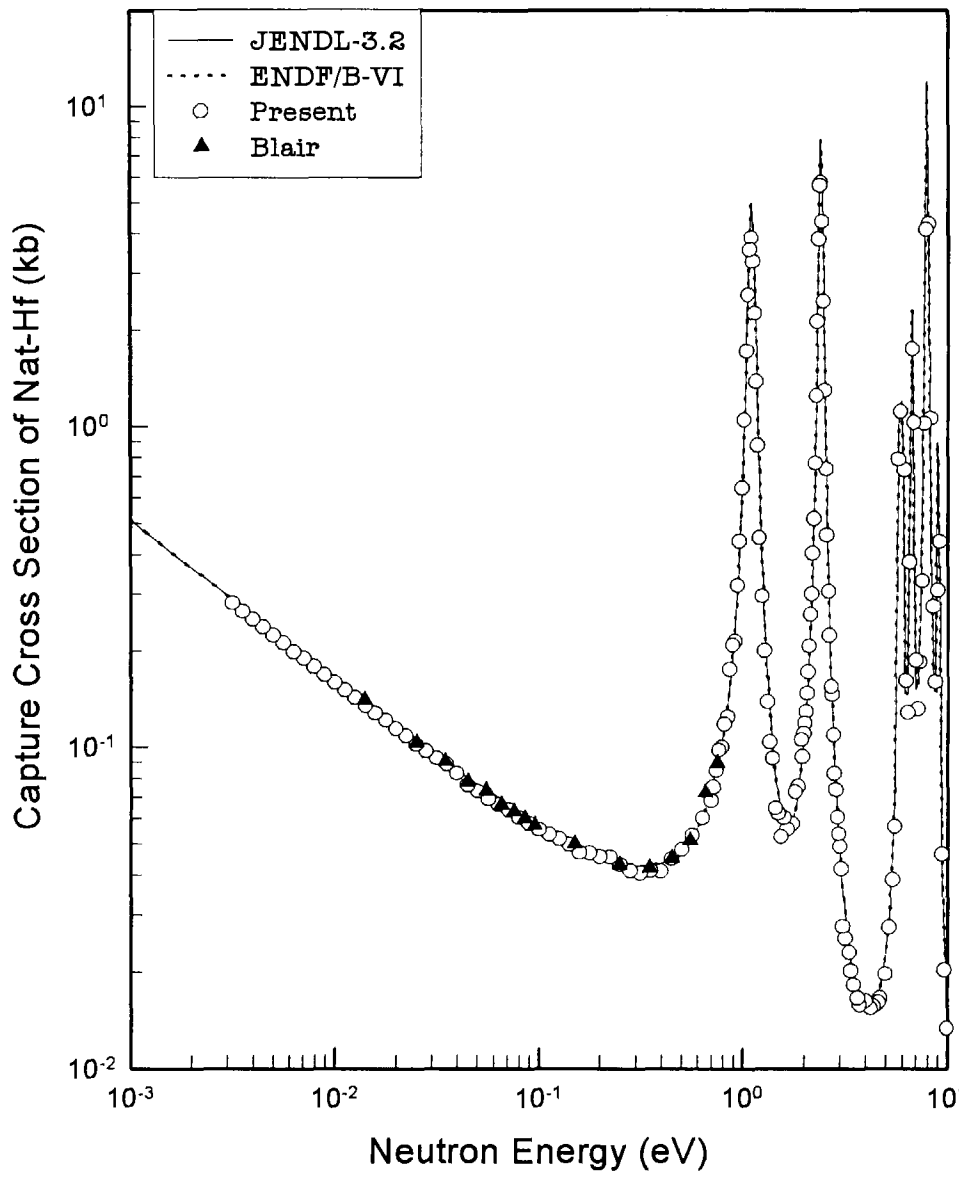

Fig. 2. The capture cross section of *Hf* between 0.003 and 10 *eV*.

3.3 Measurement of Fission Cross Section of Pa-231 using Lead Slowing-down Spectrometer

Katsuhei Kobayashi[1], Shuji Yamamoto[1], Tetsuya Kai[1*], Hyun-Je Cho[1**], Hajimu Yamana[1], Yoshiaki Fujita[1], Toshiaki Mitsugashira[2], and Itsuro Kimura[3]

1 Research Reactor Institute, Kyoto University
Kumatori-cho, Sennan-gun, Osaka 590-0494, Japan
* Present address: Japan Atomic Energy Research Institute
Tokai-mura, Naka-gun, Ibaraki 319-1195, Japan
** Visiting Scientist from University of Ulsan, Korea
2 The Oarai-branch, Institute for Material Researche, Tohoku University,
Oarai-machi, Higashiibaraki-gun, Ibaraki 311-1313, Japan
3 Department of Nuclear Engineering, Kyoto University
Yoshida-honmachi, Sakyo-ku, Kyoto 606-8501, Japan

Making use of a back-to-back type double fission chamber and Kyoto University Lead slowing-down Spectrometer (KULS) driven by a 46 MeV electron linear accelerator (linac) at the Research Reactor Institute, Kyoto University (KURRI), the neutron- induced fission cross section of Pa-231 has been measured from 0.1 eV up to 10 keV with energy resolution (FWHM) of about 40 %. The cross section of the ^{235}U(n,f) reaction in ENDF/B-VI was used as a reference one for the measurement of the fission cross section. The measured result has been compared with the evaluated data in ENDF/B-VI, JENDL-3.2 and JEF-2.2, whose data were broadened by the energy resolution of the KULS.

1. Introduction

Protactinium(Pa)-231 is one of the most interesting nuclei which are related to the production of U-232 in the ^{232}Th-^{233}U fuel cycle[1-3]. The fission phenomena, fission energy and mass distributions for the neutron-induced fission of Pa-231 have been investigated[4,5]. Although several measurements of the ^{231}Pa(n, f) cross section have been reported at higher energies, the fission cross section has rarely been measured in the lower/resonance energy region[6]. One of the reasons may be due to sub-barrier fission which results in a low fission cross section. In addition, Pa-231 is a radioactive actinide element. Then, the pure sample and an intense neutron source are required to overcome the severe experimental conditions for the fission cross section measurement.

Wagemans et al. measured the thermal neutron-induced fission cross section of Pa-231[5,7]. Leonard et al. made the cross section measurement at 20 energy points between 0.37 eV and 0.52 eV[8]. No experimental data has been obtained in the

energy range of thermal neutron to 100 keV except for those measured by Leonard et al. The evaluated fission cross section data are stored in ENDF/B-VI[9], JENDL-3.2[10] and JEF-2.2[11]. The ENDF/B-VI and the JEF-2.2 data are markedly discrepant from the JENDL-3.2, especially above about 10 eV.

In the present study, we measure the neutron-induced fission cross section of Pa-231 in the range of 0.1 eV to 10 keV relative to that of the ^{235}U(n, f) reaction by making use of a back-to-back (BTB) type double fission chamber[12] and a lead slowing-down spectrometer[13] coupled to the 46 MeV electron linear accelerator (linac) of the Research Reactor Institute, Kyoto University (KURRI). Below 1 keV, the relative measurement to the ^{10}B(n, α) reaction has been done with a BF_3 counter, as before[14,15]. The result obtained is compared with the data evaluated in ENDF/B-VI, JENDL-3.2 and JEF-2.2.

2. Samples and Fission Chamber

2.1. Chemical Purification of Pa-231

We have purified the Pa-231 sample by an anion-exchange method from the daughter nuclides, before we proceed to make the electrodeposited layer. The stock solution of Pa-231 in 9M HCl was loaded to a column packed with anion-exchange resin (DOWEX-1 X 8 of 400 mesh), and the column was rinsed with about 10 columns of volume of 9M hydrochloric acid to wash out the daughter nuclides. Then, Pa-231 was quantitatively eluted with 9M hydrochloric acid containing 0.1 M hydrofluoric acid. We have repeated twice the procedures dissolving the Pa-231 sample with nitric acid and making it dry by evaporation. The dried-up sample was dissolved in a few mℓ of 2-methyl-propanol. By using this solution for non-aqueous electrolysis, Pa-231 was electrodeposited onto an aluminum plate of cathode under 400 V bias for 20 minutes.

2.2. Number of Pa-231 and U-235 Atoms

The amount of Pa-231 deposited was determined by analyzing the α spectrum having energies in the range of 4.74 to 5.03 MeV. Considering the detection efficiency, the α intensities and the half-life, the number of the Pa-231 atoms was found to be $(3.32 \pm 0.09) \times 10^{16}$. The uncertainties were estimated by taking account of (a) counting statistics of the α measurement, (b) geometrical detection efficiency, and (c) uncertainty in the decay data used.

For highly enriched uranium sample (U-235: 99.91%), we also employed the electrodeposited layer which we used in the previous measurement[15]. The number of the U-235 atoms was determined to be $(2.81 \pm 0.03) \times 10^{16}$ by analyzing the α spectrum at energies of 4.152 to 4.597 MeV.

2.3. Double Fission Chamber

An ionization chamber with two parallel plate electrodes has been employed for the current measurement. Since the back-sides of the Pa-231 and the U-235 deposits face each other, it is called a back-to-back (BTB) type double fission

chamber[12]. The chamber is made of aluminum and is 40 mm in diameter, 39 mm in length, and the wall thickness of the chamber is ~2 mm[14,15]. The fission chamber is filled with a mixed gas of 97 % Ar and 3 % N_2 at a pressure of 1 atm. The fission chamber collects most of the energy of the fission fragments but not those of the α particles, in order to get good discrimination between pulses of α particle and fission fragment.

3. Lead Slowing-down Spectrometer

A lead slowing-down spectrometer has been installed in coupling to the 46 MeV linac at KURRI. This Kyoto University Lead Slowing-down Spectrometer (KULS)[13] is composed of 1600 lead blocks (each size : 10 x 10 x 20 cm^3, purity : 99.9 %) and the blocks are piled up to make a cube of 1.5 x 1.5 x 1.5 m^3 (about 40 tons in weight) without any structural materials. The KULS is covered with Cd sheets of 0.5 mm in thickness to shield it against low energy neutrons scattered from the surroundings. At the center of the KULS, an air-cooled photoneutron target of Ta is set to generate pulsed fast neutrons. One of the experimental holes in the KULS is covered by Bi layers of 10 to 15 cm in thickness to shield from high energy capture γ-rays (6 to 7 MeV) produced by the Pb(n, γ) reaction in the spectrometer.

Characteristics of behavior of neutrons in the KULS have been studied by experiments using the resonance filter method[13]. The slowing-down constant K in the relation of $E=K/t^2$ was determined to be 190 ± 2 (keV$\cdot\mu s^2$) for the bismuth hole in the KULS[13] by the least squares method using the measured relation between the neutron slowing-down time t in μs and the average neutron energy E in keV. The energy resolution for the experimental holes was also deduced from the measured data to be about 40 % at energies between a few electron-volts and about 500 eV and was worse than that below a few electron-volts and above about 500 eV[13]. The relation between the neutron slowing-down time and the energy, and its energy resolution were also verified by Monte Carlo calculations[13].

4. Measurement and Analysis

4.1. Fission Ratio Measurement

The energy-dependant cross section of the ^{231}Pa(n, f) reaction is given by the following relation :

$$\sigma_{Pa}(E) = \frac{C_{Pa}(E)}{C_U(E)} \frac{N_U}{N_{Pa}} \sigma_U(E) \quad , \tag{1}$$

where, $C_{Pa}(E)$; fission counts of Pa-231 at energy E,
$C_U(E)$; fission counts of U-235 at energy E,
N_U ; number of U-235 atoms in the U-235 deposit,
N_{Pa} ; number of Pa-231 atoms in the Pa-231 deposit,
$\sigma_U(E)$; energy-dependent reference cross section of the ^{235}U(n,f) reaction.

The fission cross section of U-235 is a well-known reference cross section and has been used to determine the neutron flux in the current measurement. The cross section values of $\sigma_U(E)$, whose data were broadened by the resolution function of the KULS, were taken from ENDF/B-VI[9]. The typical operating conditions that the KULS was driven were as follows ; the pulse repetition rate was 240 Hz, the pulse width 22 ns, the electron peak current $\sim$1 A, and the electron energy $\sim$31 MeV. After the measurement for more than $\sim$30 hours, the deposited layers of Pa-231 and U-235 in the BTB chamber were interchanged, and another measurement was made for $\sim$45 hours. A background run was carried out without the sample deposits. It was found that the effect of the background-counts was $\sim$0.2 % at most in the cross section values as those in the previous experiments[14,15].

4.2. BF_3 Counter

Below 200 eV, there exist strong neutron resonance peaks in the fission cross sections of Pa-231 and U-235. Therefore, we have employed the $^{10}B(n, \alpha)$ cross section that shows a smooth and a good 1/v energy dependence in the relevant energy region. The $^{10}B(n, \alpha)$ reaction is a well-known standard cross section and is often applied to cross section measurements as a reference[16]. In order to measure the energy-dependent neutron flux in the resonance energy region, a BF_3 counter was placed in the bismuth hole of the KULS instead of the BTB chamber, as we did before[14,15].

4.3. Electronics and Data Taking

Two identical electronic circuits were employed for the fission-count measurements by the Pa-231 and the U-235 layers in the BTB chamber, as we did before[14,15]. Through the amplifiers and the discriminators, signals from the chamber were fed into a time digitizer, which was initiated by the linac electron burst. Two sets of 4096 channels with a channel width of 0.5 μs were allotted to the slowing-down time measurements for the BTB chamber. Pulse height distributions of the fission events were measured together with the slowing-down time measurements.

For the relative measurement to the $^{10}B(n, \alpha)$ cross section, output signals from the BF_3 counter were also fed to the time digitizer through the amplifiers and the discriminators, and were stored in almost the same way as for the measurement with the BTB chamber.

5. Results and Discussion

Making use of the BTB chamber and the KULS, the cross section of the $^{231}Pa(n, f)$ reaction was measured relative to that of the $^{235}U(n, f)$ reaction at energies from 0.1 eV to 10 keV. In the resonance energy region below 1 keV, the fission cross section was also measured relative to the $^{10}B(n, \alpha)$ cross section to avoid the resonance interference between Pa-231 and U-235, and the result was normalized to the absolute

value of the Pa-231 fission cross section determined relative to the ^{235}U(n, f) cross section between 200 eV and 1 keV. The cross section data were obtained by summing up the slowing-down time data in intervals of ~0.12 lethargy width.

Since the Pa-231 sample was chemically purified and was almost free from impurities, no correction was made for the impurity effect. The experimental uncertainties are in the range from 4 % to 40 %, and the major uncertainties are due to the statistical error(2~40%), the error in the reference cross section(~2%) and the number of the Pa-231 and U-235 atoms(2.9%).

The cross sections measured by Leonard et al. are in the range from 30 to 200 mb at 20 energy points between 0.37 eV and 0.52 eV, while the current data show 52 to 64 mb with the uncertainties from 4.7 to 5.4 %. Figure 1 shows the current measurement and the evaluated data in ENDF/B-VI, JENDL-3.2 and JEF-2.2, whose data are broadened by the resolution function of the KULS. The ENDF/B-VI and the JEF-2.2 data almost overlap above 0.1 eV and the later is slightly lower than the former below 0.1 eV. Although the ENDF/B-VI values are in good agreement with the measurement below 4 eV, they are higher near the bump of 5 eV and above about 20 eV obviously. To the contrary, the JENDL-3.2 data are lower than the measured result above about 100 eV as the neutron energy increases.

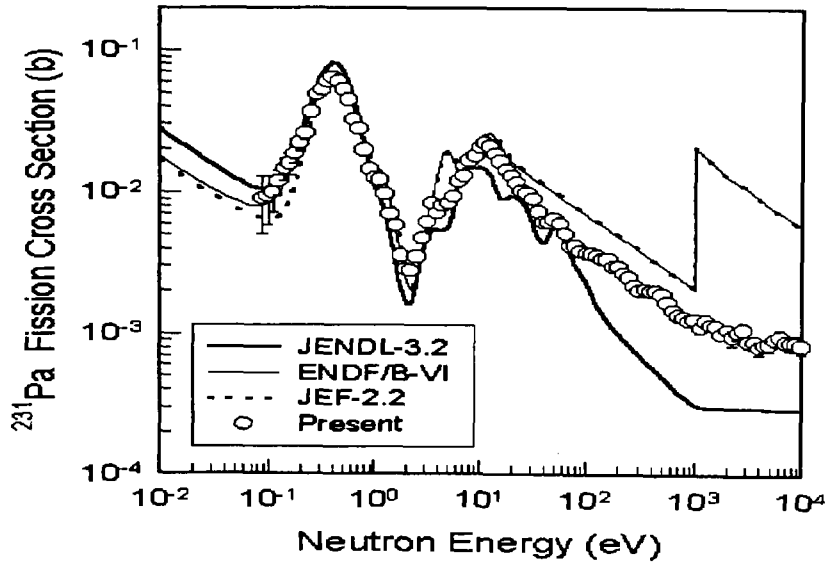

Fig. 1 Comparison of the measured result and the evaluated data in ENDF/B-VI, JENDL-3.2 and JEF-2.2, whose values are broadened by the resolution function of the KULS.

6. Conclusion

The cross section of the ^{231}Pa(n, f) reaction has been measured from 0.1 eV to 10 keV relative to that of the ^{235}U(n, f) reaction, making use of the BTB-type double fission chamber and the lead slowing-down spectrometer KULS at KURRI. No

experimental data has been measured before in the energy region from thermal neutron energy to 100 keV except for those by Leonard et al. at energies between 0.37 eV and 0.52 eV. The evaluated data in ENDF/B-VI and JEF-2.2 are in general agreement with the current measurement below 4 eV and are much higher above 20 eV. The JENDL-3.2 data are much lower than the measurement above 100 eV.

References

(1) IAEA Technical Reports Series No.52, "Utilization of Thorium in Power Reactors", IAEA (1966).
(2) Srinivasan, M. and Kimura, I., J. Nucl. Sci. Technol., 28, 375 (1991), and Proc. Indo-Japan Seminar on Thorium Utilization, Dec.10-13, 1990, Bombay (1991).
(3) Kuz'minov, B. D. and Manokhin, V. N., "Status of Nuclear Data for the Thorium Fuel Cycle", INDC(CCP)-416, 98-10986(76) Translated from Russian, IAEA, p.1 (1998).
(4) Wagemans, C. et al., Nucl. Phys., A285, 32 (1977).
(5) Asghar, M. et al., Nucl. Phys., A311, 413 (1978).
(6) McLane, V. et al., "Neutron Cross Sections", Vol.2, Neutron Cross Section Curves, Academic Press, Inc., Boston (1988).
(7) Wagemans, C. et al., Annals of Nuclear Energy, 5, 267 (1978).
(8) Leonard, B. R. et al., Bull. Am. Phys. Soc., 6, 8(A8) (1961).
(9) Rose, R. F. (Ed.), "ENDF-201, ENDF/B-VI Summary Documentation", BNL-NCS-17541, 4th Ed. (ENDF/B-VI) Brookhaven National Laboratory (1991), and "ENDF/B-VI MOD 2 Evaluation", by P. G. Young (1996).
(10) Shibata, K. and Narita, T. (Eds.), JAERI-Data/Code 98-006 (part II) (1998).
(11) Nordborg, C. and Salvatores, M., Proc. Int'l Conf. Nucl. Data Science and Technology, Gatlinberg, Tennessee, May 9-13, 1994, Vol.2, p.680, ANS (1994).
(12) Obu, M., JAERI-M 9757, JAERI (1981).
(13) Kobayashi, K. et al., Nucl. Instr. and Meth. in Phys. Research A, 385, 145 (1997).
(14) Yamamoto, S. et al., Nucl. Sci. Eng., 126, 201 (1997).
(15) Kobayashi, K. et al., J. Nucl. Sci. Technol., To be published.
(16) "Nuclear Data Standards for Nuclear Measurements", Technical Reports Series, No. 227, IAEA (1983).

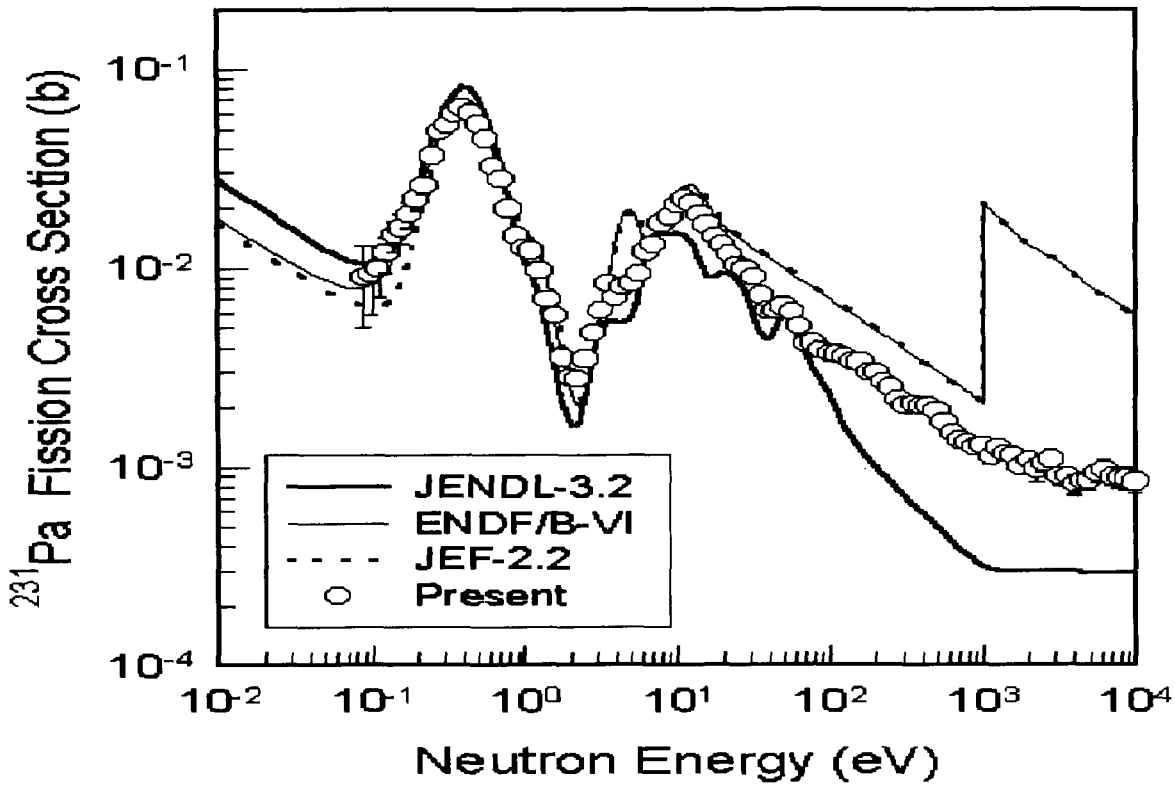
^{231}Pa Fission Cross Section (b)
10^{-1}
10^{-2}
10^{-3}
10^{-4}
10^{-2}
10^{-1}
10^{0}
10^{1}
10^{2}
10^{3}
10^{4}
Neutron Energy (eV)
JENDL-3.2
ENDF/B-VI
JEF-2.2
Present

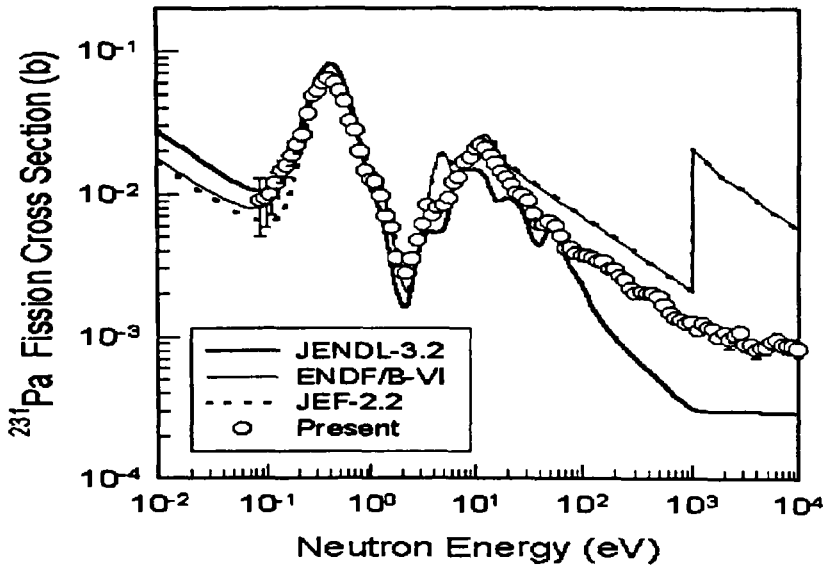
^{231}Pa Fission Cross Section (b)
10^{-1}
10^{-2}
10^{-3}
10^{-4}
10^{-2}
10^{-1}
10^{0}
10^{1}
10^{2}
10^{3}
10^{4}
Neutron Energy (eV)
JENDL-3.2
ENDF/B-VI
JEF-2.2
Present

JP9950321

3.4

Key precursor data in aggregate delayed-neutron calculations

T.Sanami, K.Oyamatsu, Y.Kukita
Department of Energy Engineering and Science, Nagoya University

The reactivity calculations with the delayed neutron (DN) six-group parameter sets in ENDF/B-VI were reported to give significant underestimates for long period (tens of seconds). The parameter sets were obtained form the summation calculations with ENDF/B-VI fission yields and decay data files. In this paper, we try to identify the precursor data that cause the significant underestimates. Because of the relatively long time scale, we examine the DN activity after infinite irradiation, and find that the summation calculation gives significantly smaller DN activity at about 30 s than the currently used six-group parameter set by Tuttle, although this feature does not looks important for the DN activity after a fission burst. From the time dependence of the DN activity, we find that the fission yields of ^{88}Br, ^{136}Te, and ^{137}I are the most probable sources for the underestimate. Furthermore, in order to achieve the required precision (5 %) for the DN activity, it is also necessary to perform precise measurements of their Pn values.

1. Introduction

The delayed-neutron six-group parameter sets in ENDF/B-VI were derived from delayed-neutron (DN) summation calculations for the first time. However, reactivity calculations with these parameter sets were found to give appreciable underestimates for long period (tens of seconds) compared with the sets obtained from macroscopic measurements [1]. In this paper, we examine the summation calculations and identify precursor data responsible for the underestimate.

First, we examine the DN activity after infinite irradiation, $N_d(t)$, because the irradiation time in a operating reactor is essentially infinite compared with half lives of DN precursors. Second, we examine the difference between the summation calculation and Tuttle's evaluation obtained from macroscopic measurements. From this analysis, we identify precursor data (fission yields and decay data) relevant to the underestimates.

2. Analyses

The summation calculation with ENDF/B-VI fission yield and decay data is compared with Tuttle's evaluation [2][3] obtained from macroscopic measurements. As shown in Fig.1 , the difference between the two evaluations are evident for $N_d(t)$ at about 30 s, although the deviation is not so clear in the activity after a fission burst (Fig.2). Here, the definitions of the irradiation conditions are shown in Fig.3. This behavior of $N_d(t)$ must be responsible for the underestimate for long periods (tens of seconds) in reactivity calculations. We define $\Delta N_d(t)$ as the difference of the DN activity between the summation calculation and Tuttle's evaluation, and examine it in detail.

The difference $\Delta N_d(t)$ stems most probably from DN precursors whose half lives are about 30 s with large DN yields. The DN yield of precursor i after infinite irradiation, N_{di} is given by

$$N_{di} = P_{ni} Y_{si} .$$

where P_{ni} is the delayed-neutron emission probability of nuclide i. The quantity Y_{si} can be regarded as the "cumulative fission yield" of precursor i for infinite irradiation. It is defined, with the usual cumulative fission yield Y_{ci} and the decay constant λ_i, as

$$Y_{si} = Y_{ci}/\lambda_i + \sum_{j \neq i} b_{j \to i} Y_{cj}/\lambda_j$$

Here, $b_{j \to i}$ is the branching ratio decaying from nuclide j to i. Figure 4 shows the DN yields from individual precursors after infinite irradiation. From this figure, we see that ^{137}I,^{87}Br,^{88}Br,^{138}I and ^{136}Te are possible sources of the difference $\Delta N_d(t)$.

We assume that the sources of $\Delta N_d(t)$ are erroneous independent fission yields and/or Pn values since the decay constants of the five precursors are precisely known as shown in Fig. 5. As for $\Delta N_d(t)$, we neglect buildup of the precursors decaying from parent nuclides because the fission yields of the parents are sufficiently small. To identify the erroneous data, we fit $\Delta N_d(t)$ to the following function

$$\overline{\Delta N_d}(t) = \sum_i a_i e^{-\lambda_i t} .$$

Here, λ_i's are the decay constants of the five precursors, and a_i's are fitting parameters. As shown in Fig. 6 , this fitting works well especially for ^{238}U, for which $\Delta N_d(t)$ takes large values. Then, the deficit of the total DN yield in the summation calculation can be written as

$$\int_0^\infty \overline{\Delta N_d}(t) dt = \sum_i \frac{a_i}{\lambda_i} .$$

Hence, the deficit of the DN yield from precursor i is given by a_i / λ_i.

Figure 7 shows the DN yields (A) and the obtained deficits (B) of the five precursors. For ^{88}Br and ^{136}Te , the sum of their DN yields are also shown because their half lives are too close to obtain a_i values separately in the fitting. From this figure, we see that the DN yields from ^{88}Br, ^{136}Te, and ^{137}I are substantially different between the summation calculation and Tuttle's evaluation. Unfortunately, the $\Delta N_d(t)$ value is found too large to be explained by uncertainties of precursor data given in ENDF/B-VI [4]. However, the most probable sources of the underestimate must be their fission yields because of their large uncertainties (23 % for ^{88}Br and ^{136}Te, 8 % for ^{137}I) as shown in Fig. 8. We also note that the uncertainties of their Pn values are also relatively large (6-9 %, see Fig.9) compared with the required precision (5 %) for $N_d(t)$. Actually, the latest evaluation in Table of Isotopes (8th ed.) gives slightly different Pn values with larger uncertainties than ENDF/B-VI.

3. Conclusion

The underestimate in the reactivity calculation with ENDF/B-VI must be attributed to behavior of $N_d(t)$ at about 30 s. The fission yields of ^{88}Br, ^{136}Te, and ^{137}I are the most probable sources for the underestimate so that much higher precision is required for these values. Furthermore, in order to achieve the required precision (5 %) for $N_d(t)$, it is also necessary to perform precise measurements of their Pn values. Therefore it is highly desirable to improve the fission yields and Pn values of ^{88}Br, ^{136}Te, and ^{137}I.

References

[1] G.D.Spriggs, Nucl. Sci. Eng. 114, (1993) 342-351.
[2] R.J. Tuttle, Nucl. Sci. and Eng. 56, (1975) 37-71.
[3] R.J. Tuttle, INDC(NDS)-107/G+Special (1979)
[4] T.Miyazono et al, Proc. 1996 Sympo. on Nucl. Data, JAERI-Conf 97-005, (1997) 83-88.

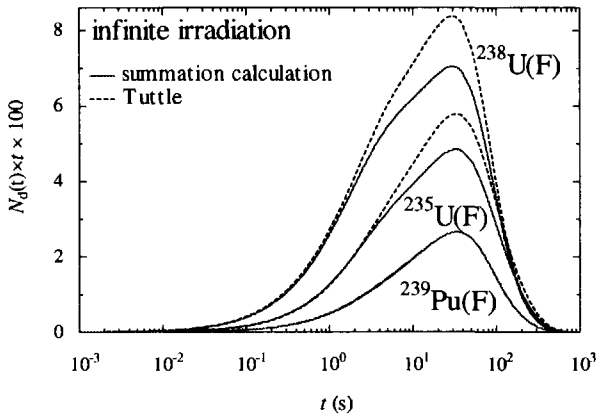

Fig.1 Delayed-neutron activities obtained from summation calculations and Tuttle's six-group parameter sets after infinite irradiation.

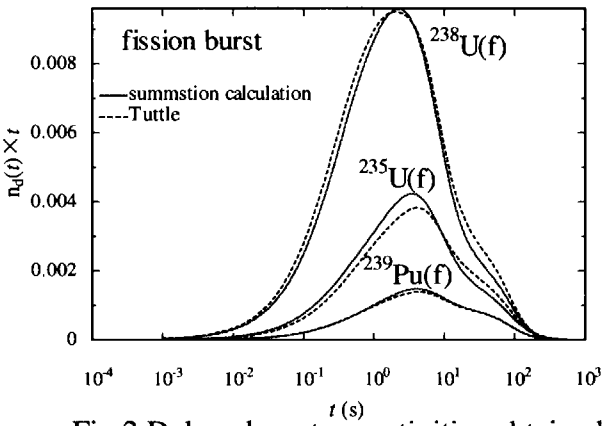

Fig.2 Delayed-neutron activities obtained from summation calculations and Tuttle's six-group parameter sets after fission bursts.

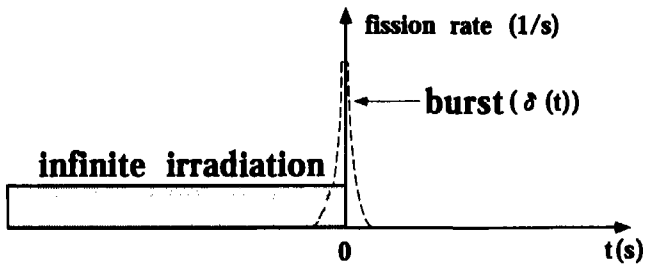

Fig.3 The definitions of infinite irradiation

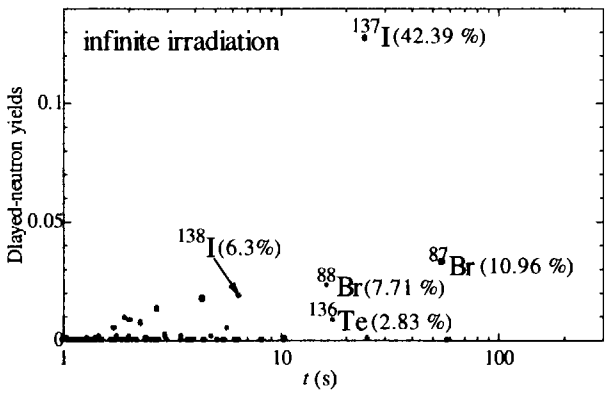

Fig.4 The delayed-neutron yields for ^{238}U(f). The values in the parentheses show ratios of individual DN yields to the total DN yields.

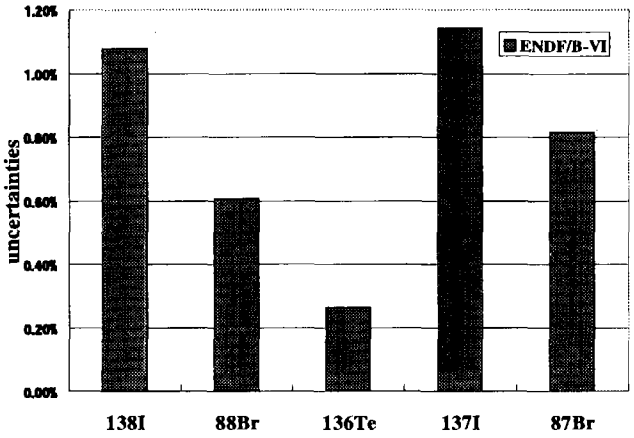

Fig.5 The uncertainties of the decay constants of ^{138}I, ^{88}Br, ^{136}Te, ^{137}I, and ^{87}Br.

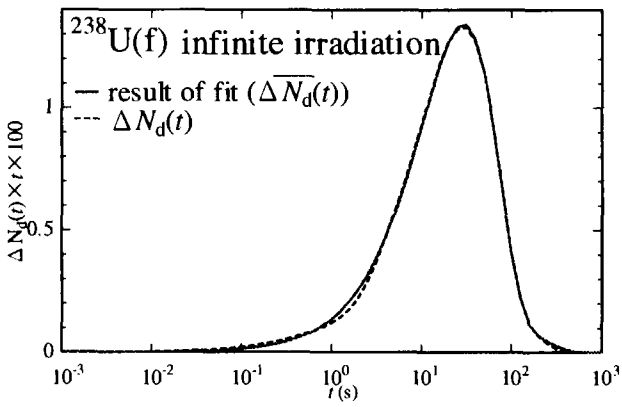

Fig.6 Result of the fitting.

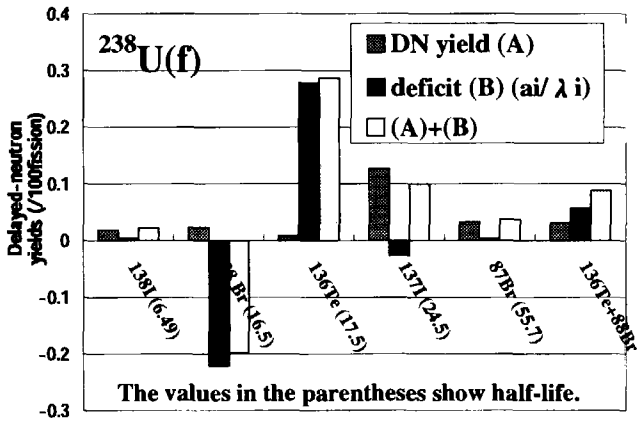

Fig.7 DN yields from individual precursors after infinite irradiation. Shown are the DN yields (A) and their deficits (B) in the summation calculation.

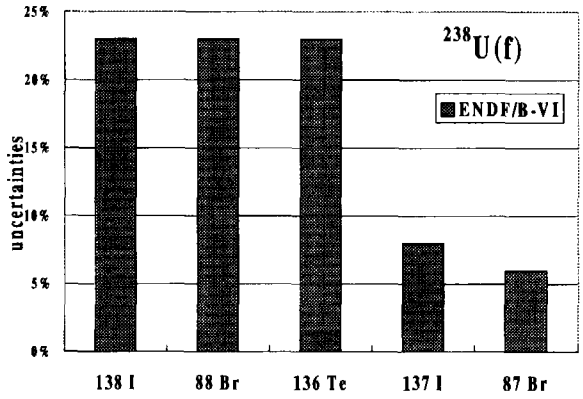

Fig.8 The uncertainties in the cumulative fission yields of ^{138}I, ^{88}Br, ^{136}Te, ^{137}I, and ^{87}Br for ^{238}U(f).

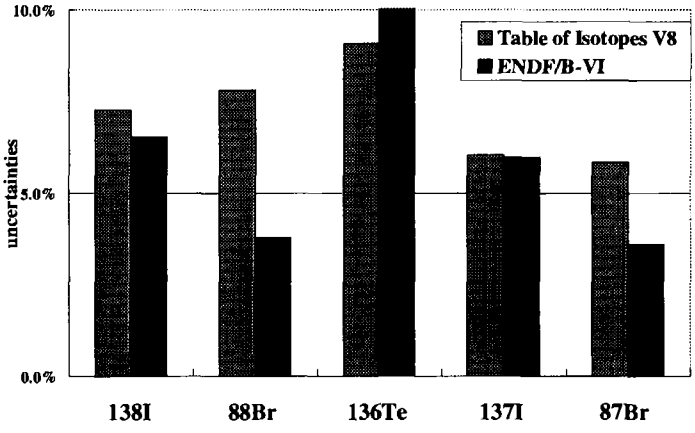

Fig.9 The uncertainties of Pn for ^{138}I, ^{88}Br, ^{136}Te, ^{137}I, and ^{87}Br.

JP9950322

3.5 Decay Heat Calculation for Minor Actinides in the Hybrid Method

H. Takeuchi, K. Oyamatsu, Y. Kukita
Department of Energy Engineering and Science, Nagoya University

For evaluation of decay heat from the fission of minor actinides (MAs) we are currently forced to rely only on summation calculations since there has been no direct measurement for these nuclides. In this paper, we use an alternative approach (named "hybrid" method) to evaluate the MA decay heat power using the measured decay heat powers for major actinides at YAYOI. Results for the fast fissions of ^{237}Np, ^{241}Am, ^{243}Am, ^{242}Cm and ^{244}Cm are in support of the summation calculations for β decay heat, but suggest notable uncertainties in γ decay-heat summation calculations.

1. Introduction

There is a growing need for accurating evaluation of decay heat from the fission of minor actinides (MA) since increasing efforts are being made for realization of MA burner. However, at present only summation calculations are available for this purpose because no direct measurement has been performed for these nuclides. In this paper, decay heat powers from the fast fissions of ^{237}Np, ^{241}Am, ^{243}Am, ^{242}Cm and ^{244}Cm are calculated in an alternative approach, called hybrid method[1, 2], in which we utilize measured decay heat powers of Th, U and Pu isotopes, to examine the reliability of the summation calculations.

2. Hybrid method

The method used in this paper is based on the fact that the decay heat power is a linear function of the independent fission yield. In the matrix representation of the summation method, we can express the decay heat power , P, with a vector of independent fission yield, y, as

$$P=\boldsymbol{E}\boldsymbol{\Lambda}_0\exp(\Lambda t)y, \tag{1}$$

$$\exp(\Lambda t) = I + \Lambda t + \frac{1}{2!}(\Lambda t)^2 + \cdots, \quad (I: \text{ unit matrix}) \tag{2}$$

where $\boldsymbol{\Lambda}$ and $\boldsymbol{\Lambda}_0$ represent matrices with decay constants,

$$\Lambda=\begin{pmatrix} -\lambda_1 & b_{2\to1}\lambda_2 & \cdots & b_{N\to1}\lambda_N \\ b_{1\to2}\lambda_1 & -\lambda_2 & \cdots & b_{N\to2}\lambda_N \\ \vdots & \vdots & \ddots & \vdots \\ b_{1\to N}\lambda_1 & b_{2\to N}\lambda_2 & \cdots & -\lambda_N \end{pmatrix} \quad \text{and} \quad \Lambda_0=\begin{pmatrix} -\lambda_1 & 0 & \cdots & 0 \\ 0 & -\lambda_2 & \cdots & 0 \\ \vdots & \vdots & \ddots & \vdots \\ 0 & 0 & \cdots & -\lambda_N \end{pmatrix}, \tag{3}$$

respectively. In these matrices, λ_k and $b_{j\to k}$ are the decay constant of nuclei k, and branching ratio from nuclei j to nuclei k, respectively. The vector $\boldsymbol{E}$ is the average decay energy vector defined as

$$\boldsymbol{E} = (E_1 \quad E_2 \quad \cdots \quad E_N) \tag{4}$$

In the hybrid method, we start with writing y for a given fissioning system as a linear combination of yield vectors of other N fissioning systems, $y_1 \cdots y_N$,

$$y=a_1y_1+a_2y_2+\cdots+a_Ny_N+y_R, \tag{5}$$

where y_R is the residual vector. The values of the coefficients, a_i, are chosen to minimize $|y_R|$,

$$|y_R| = \min \quad \Leftrightarrow \quad \begin{cases} y \cdot y_1 = a_1 |y_1|^2 + a_2 y_2 \cdot y_1 + \cdots + a_N y_N \cdot y_1 \\ y \cdot y_2 = a_1 y_1 \cdot y_2 + a_2 |y_2|^2 + \cdots + a_N y_N \cdot y_2 \\ \vdots \\ y \cdot y_N = a_1 y_1 \cdot y_N + a_2 y_2 \cdot y_N + \cdots + a_N |y_N|^2 . \end{cases} \tag{6}$$

so that,

$$\begin{pmatrix} a_1 \\ a_2 \\ \vdots \\ a_N \end{pmatrix} = \begin{pmatrix} |y_1|^2 & y_2 \cdot y_1 & \cdots & y_N \cdot y_1 \\ y_1 \cdot y_2 & |y_2|^2 & \cdots & y_N \cdot y_2 \\ \vdots & \vdots & \ddots & \vdots \\ y_1 \cdot y_N & y_2 \cdot y_N & \cdots & |y_N|^2 \end{pmatrix}^{-1} \begin{pmatrix} y \cdot y_1 \\ y \cdot y_2 \\ \vdots \\ y \cdot y_N \end{pmatrix}. \tag{7}$$

The above-mentioned linearity leads to the following expression for the decay heat power, P, with the same coefficients, a_i, as obtained from (7),

$$P = a_1 P_1 + a_2 P_2 + \cdots + a_N P_N + P_R. \tag{8}$$

Here, P_i denotes the decay heat power of fissioning system i. The residual term P_R can be calculated in the summation method using the yield vector y_R. Note that P_R is expected to be small because $|y_R|$ has been minimized. We thus can evaluate P for such nuclides as MAs, for which no reliable measurement data exist, by using integral measurement data P_i for other fissioning systems.

We summarize the nuclear properties required for decay power evaluation with the hybrid method, the summation calculation and the integral measurement in Table 1. The accuracy of the summation calculation fully depends on the accuracy of the decay data whilst the hybrid method uses decay data only in the calculation of the small residual term P_R.

3. Results

The decay heat powers of ^{237}Np(F), ^{241}Am(F), ^{243}Am(F), ^{242}Cm(F) and ^{244}Cm(F) have been calculated in the hybrid method using the decay heat powers of ^{232}Th(F), ^{233}U(F), ^{235}U(F), ^{238}U(F), ^{239}Pu(F) measured at YAYOI. Here, the symbol "F" stands for the fast fission. We get the following five equations from Eq. (8),

$$P(^{237}\mathrm{Np}) = a_1 P(^{232}\mathrm{Th}) + a_2 P(^{233}\mathrm{U}) + a_3 P(^{235}\mathrm{U}) + a_4 P(^{238}\mathrm{U}) + a_5 P(^{239}\mathrm{Pu}) + P_R(^{237}\mathrm{Np}), \tag{9}$$

$$P(^{241}\mathrm{Am}) = b_1 P(^{232}\mathrm{Th}) + b_2 P(^{233}\mathrm{U}) + b_3 P(^{235}\mathrm{U}) + b_4 P(^{238}\mathrm{U}) + b_5 P(^{239}\mathrm{Pu}) + P_R(^{241}\mathrm{Am}), \tag{10}$$

$$P(^{243}\mathrm{Am}) = c_1 P(^{232}\mathrm{Th}) + c_2 P(^{233}\mathrm{U}) + c_3 P(^{235}\mathrm{U}) + c_4 P(^{238}\mathrm{U}) + c_5 P(^{239}\mathrm{Pu}) + P_R(^{243}\mathrm{Am}), \tag{11}$$

$$P(^{242}\mathrm{Cm}) = d_1 P(^{232}\mathrm{Th}) + d_2 P(^{233}\mathrm{U}) + d_3 P(^{235}\mathrm{U}) + d_4 P(^{238}\mathrm{U}) + d_5 P(^{239}\mathrm{Pu}) + P_R(^{242}\mathrm{Cm}), \tag{12}$$

$$P(^{244}\mathrm{Cm}) = e_1 P(^{232}\mathrm{Th}) + e_2 P(^{233}\mathrm{U}) + e_3 P(^{235}\mathrm{U}) + e_4 P(^{238}\mathrm{U}) + e_5 P(^{239}\mathrm{Pu}) + P_R(^{244}\mathrm{Cm}). \tag{13}$$

The fission yields and decay data of ENDF/B-VI have been used to calculate the values of coefficients a_i, b_i, c_i, d_i and e_i from Eq. (7) and then to obtain y_R and P_R. As shown in Table 2, the coefficients are all positive for ^{237}Np(F), but take also negative values for ^{241}Am(F), ^{243}Am(F), ^{242}Cm(F) and ^{244}Cm(F). We see from Table 2 that the offsets due to the negative terms are significant.

The decay heat power from ^{237}Np(F), ^{241}Am(F), ^{243}Am(F), ^{242}Cm(F) and ^{244}Cm(F) are shown in Figs. 1 through 5. The linear combination of measurement data, in the right hand side of Eqs. (9) through (13), amounts to about 90% of the total estimated decay power for each fissioning system as listed in Tables 3 through 7. Therefore the present results could be taken as almost independent of summation calculations. The present results are compared with the summation calculations in Fig. 6. For β decay heat, the hybrid and summation calculations agree reasonably within the uncertainties in summation calculations (3~5 % [4]). However, for γ decay heat the hybrid calculations differ appreciably from the summation calculations beyond their uncertainties (4~8 % [4]).

4. Conclusion

The decay heat powers from the fast fissions of ^{237}Np, ^{241}Am, ^{243}Am, ^{242}Cm and ^{244}Cm have been estimated from the measured decay heat powers from the fast fissions of Th, U and Pu isotopes. The fact that the decay heat power is a linear function of the independent fission yield was used to estimate the minor actinides decay heat powers, for which there exist no data, from data for other fissioning systems. The results have been used to examine the reliability of summation calculations for these minor actinide fissioning systems. Although the comparisons are favorable for the β decay heat summation calculations, they suggest that further confirmation should be done for the γ decay heat summation calculations.

References

[1] M. Akiyama et al., J. Atom. Enter. Soc. of Japan, 24, 709(1982)
[2] M. Akiyama et al., J. Atom. Enter. Soc. of Japan, 24, 803(1982)
[3] M. Akiyama, Proc. Int. Conf. on Nucl. Data for Sci. and Tech., Antwerp, 1982, p.273.
[4] H. Ohta et al., Proc. 1995 Symposium on Nuclear Data, JAERI-Conf 96-008, p.p.290-295.

Table 1. Nuclear properties required for calculation (●:required, △:partly required, ×:not required).

Nuclear properties	Summation method	New method	Integral measurement
Independent fission yields	●	●	×
Decay constants	●	△	×
Branching ratios	●	△	×
Average decay energies	●	△	×

Table 2. Values of coefficients a_i, b_i, c_i, d_i and e_i.

Coefficients	1	2	3	4	5
a_i	0.005	0.069	0.274	0.081	0.557
b_i	0.042	0.040	-0.180	-0.128	1.122
c_i	-0.002	-0.129	-0.006	0.061	0.995
d_i	0.107	0.314	-0.648	-0.162	1.140
e_i	0.079	-0.085	-0.170	-0.152	1.190

Table 3. Values of $[a_1P(^{232}\text{Th})+a_2P(^{233}\text{U})+a_3P(^{235}\text{U})+a_4P(^{238}\text{U})+a_5P(^{239}\text{Pu})]/P(^{237}\text{Np})$.

t(s)	β decay heat	γ decay heat
90	97.6 %	97.1 %
900	99.2 %	97.8 %
9000	98.6 %	99.4 %

Table 4. Values of $[b_1P(^{232}\text{Th})+b_2P(^{233}\text{U})+b_3P(^{235}\text{U})+b_4P(^{238}\text{U})+b_5P(^{239}\text{Pu})]/P(^{241}\text{Am})$.

t(s)	β decay heat	γ decay heat
90	89.9 %	89.9 %
900	89.4 %	93.3 %
9000	88.1 %	90.8 %

Table 5. Values of $[c_1P(^{232}Th)+c_2P(^{233}U)+c_3P(^{235}U)+c_4P(^{238}U)+c_5P(^{239}Pu)]/P(^{243}Am)$.

t(s)	β decay heat	γ decay heat
90	86.4 %	86.8 %
900	91.0 %	98.0 %
9000	93.9 %	99.9 %

Table 6. Values of $[d_1P(^{232}Th)+d_2P(^{233}U)+d_3P(^{235}U)+d_4P(^{238}U)+d_5P(^{239}Pu)]/P(^{242}Cm)$.

t(s)	β decay heat	γ decay heat
90	91.5 %	92.1 %
900	82.6 %	88.5 %
9000	87.0 %	92.9 %

Table 7. Values of $[e_1P(^{232}Th)+e_2P(^{233}U)+e_3P(^{235}U)+e_4P(^{238}U)+e_5P(^{239}Pu)]/P(^{244}Cm)$.

t(s)	β decay heat	γ decay heat
90	84.0 %	86.1 %
900	84.4 %	93.8 %
9000	89.1 %	104.7 %

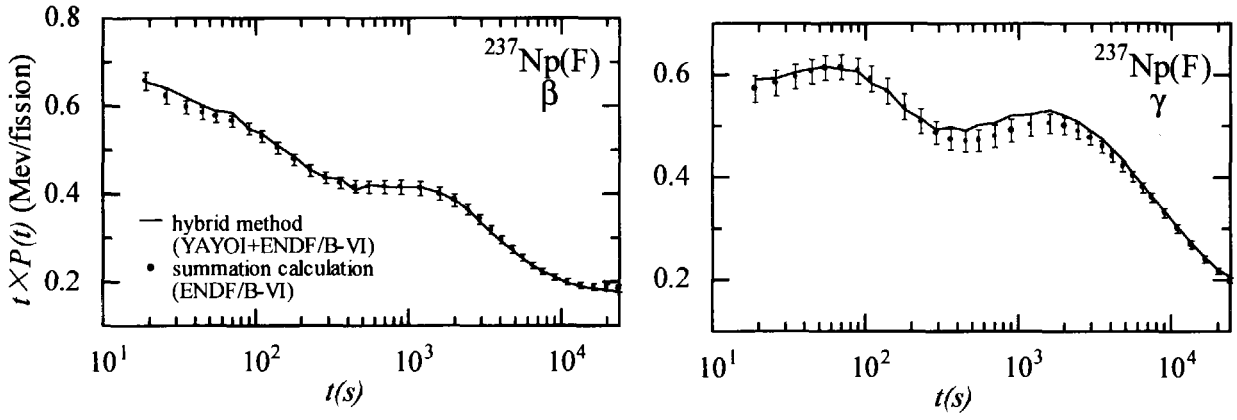

Fig. 1. The β and γ decay heat powers of ^{237}Np in the hybrid method (solid line) and in the summation method (filled circles with error bars).

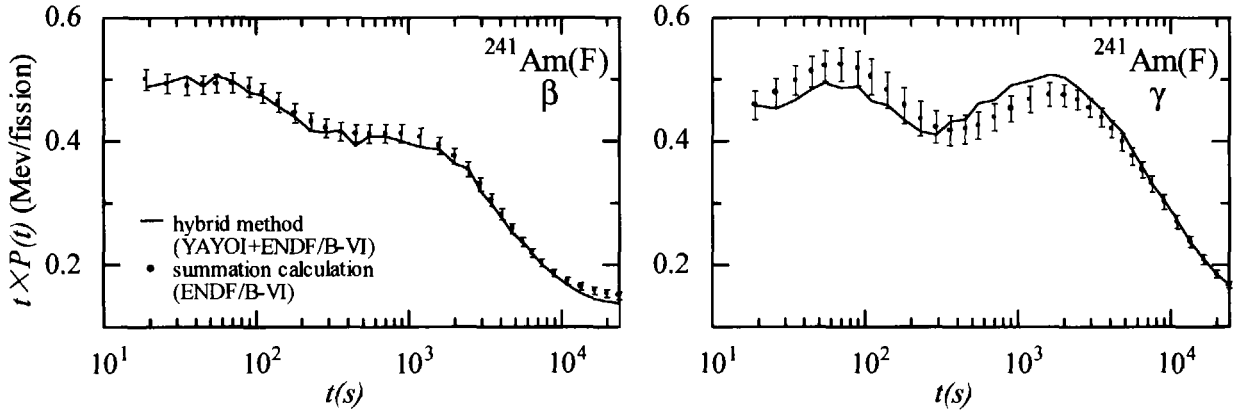

Fig. 2. The β and γ decay heat powers of ^{241}Am in the hybrid method (solid line) and in the summation method (filled circles with error bars).

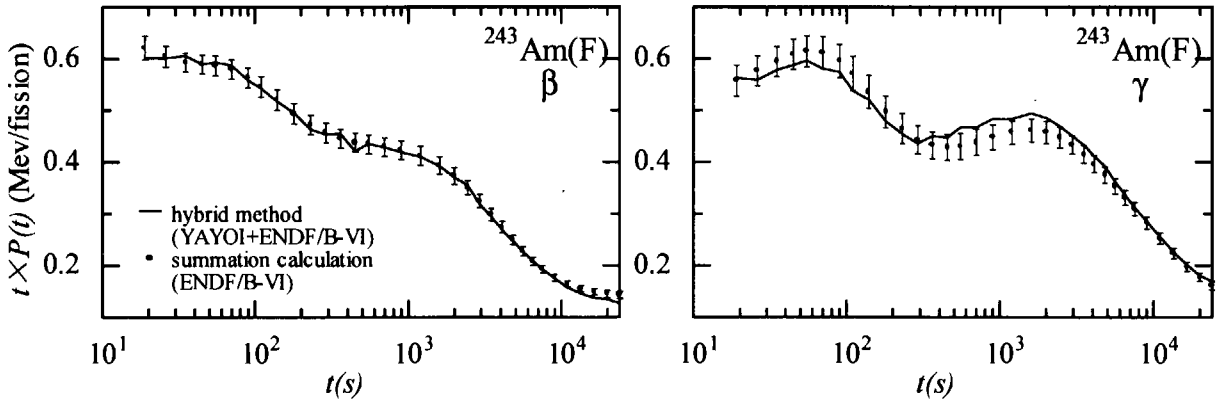

Fig. 3. The β and γ decay heat powers of ^{243}Am in the hybrid method (solid line) and in the summation method (filled circles with error bars).

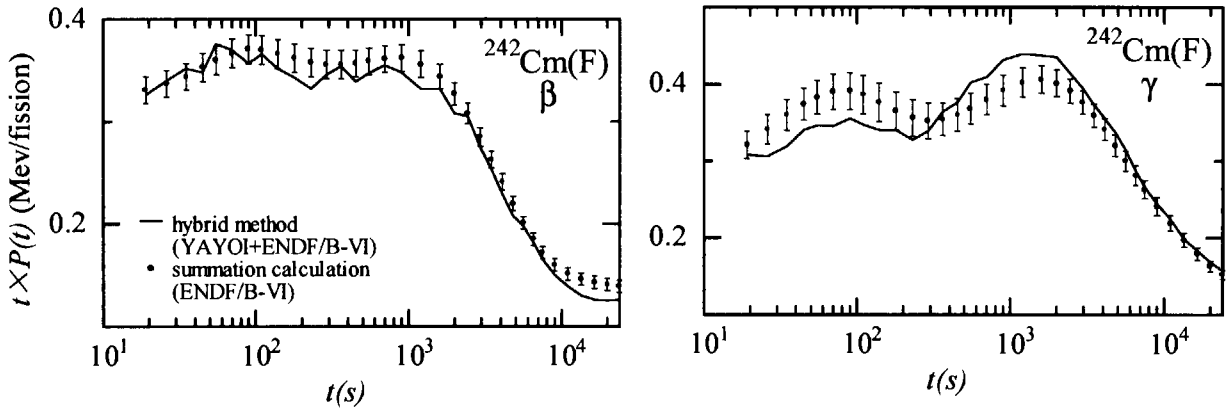

Fig. 4. The β and γ decay heat powers of ^{242}Cm in the hybrid method (solid line) and in the summation method (filled circles with error bars).

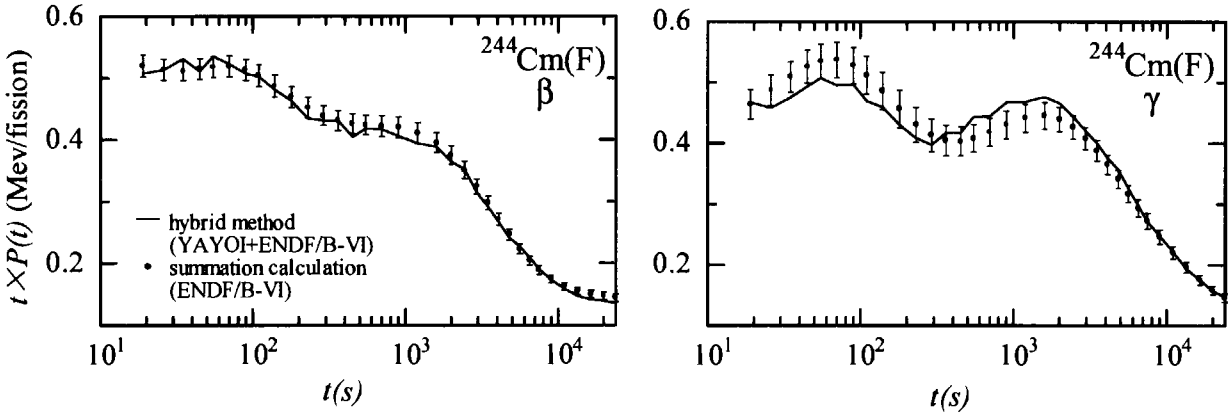

Fig. 5. The β and γ decay heat powers of ^{244}Cm in the hybrid method (solid line) and in the summation method (filled circles with error bars).

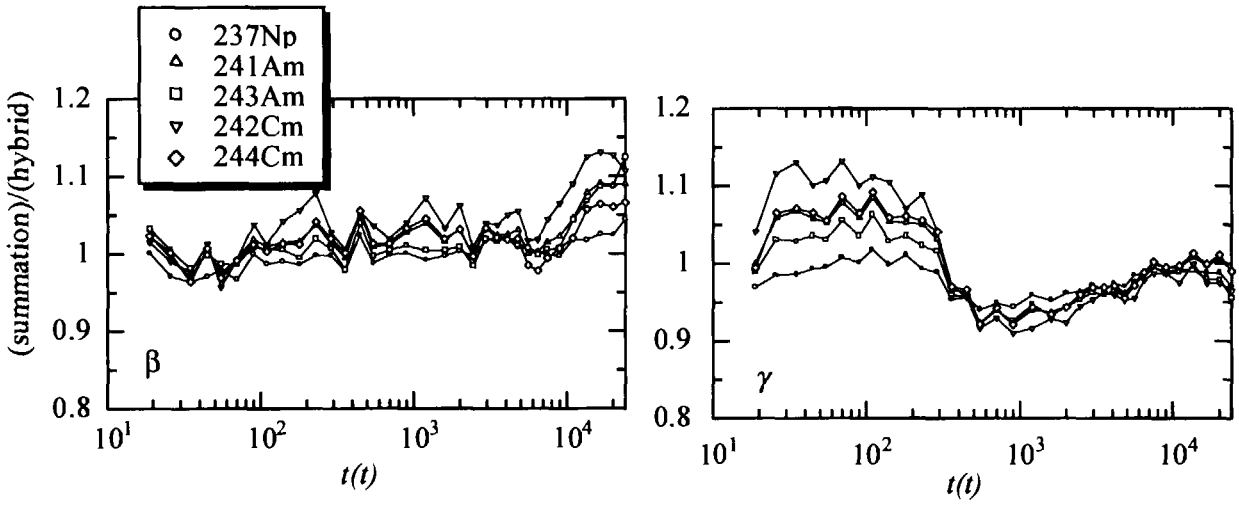

Fig. 6. Comparison between the summation and hybrid calculations for ^{237}Np, ^{241}Am, ^{243}Am, ^{242}Cm and ^{244}Cm.

JP9950323

3.6 Application of Multimodal Fission Model to Nuclear Data Evaluation

Takaaki OHSAWA, Tomoyo OYAMA and Miki MITSUHASHI
Depatment of Nuclear Engineering, Faculty of Science and Technology
Kinki University, 6-3-1 Kowakae, Higashi-osaka, Osaka 577-8502
e-mail: ohsawa@mvg.biglobe.ne.jp

Recent results of application of the multimodal fission model to analyses of prompt neutron spectra and delayed neutron yield in the resonance region are briefly described.

1. Introduction

Multimodal fission model, originally proposed by Brosa *et al.* [1] combining the multichannel and random-neck-rupture concepts, has been successfully applied to analyses of mass and total kinetic energy (*TKE*) distributions of fragments for many fissioning systems. From these studies it has been confirmed that the fission process proceeds through a few fission modes (prescission shapes), such as Standard-1 (S1), Standard-2 (S2), Standard-3 (S3), Superlong (SL), at the scission point.

From an evaluator's point of view, this model is interesting because it brings new possibilities of application for nuclear data evaluation. One of the applications is analysis of prompt neutron spectra, and another is analysis of delayed neutron yields in the resonance region (Fig.1). In this report we briefly described some results of our efforts toward this direction.

2. Analysis of Prompt Neutron Spectra

2.1 Multimodal Analysis of Prompt Neutron Spectra

The multimodal concept was introduced into the modified Madland-Nix model [2]. Considering that energy partition is substantially different for each mode, as can be seen from Fig. 2, we calculated the prompt neutron spectra (PNS) separately for each fission mode (called 'modal' spectra hereafter) using the results of multimodal analysis of experimental data by Geel group.

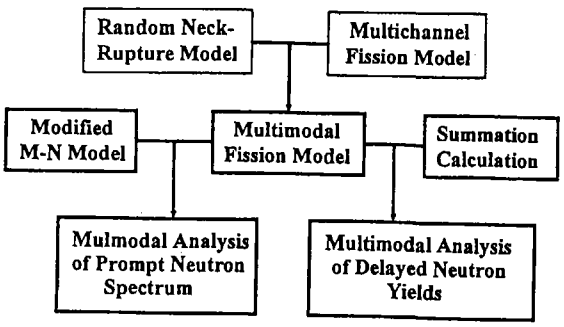

Fig.1 Application of multimodal model to prompt and delayed neutron nuclear data: a conceptual scheme.

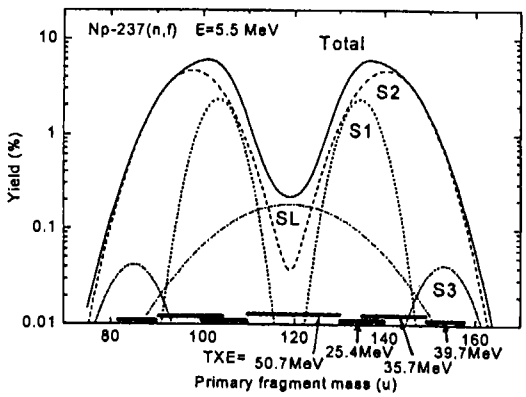

Fig.2 Total excitation energies according to different modes for ^{237}Np(n,f).

The total spectrum was calculated by synthesizing modal spectra $\chi_i(En)$ according to the following formula:

$$\chi_{tot}(En) = [\Sigma_i \nu_i \chi_i(En)] / (\Sigma_i w_i \nu_i) \quad (1)$$

where w_i is the branching ratio to mode i, and ν_i is the average neutron multiplicity for mode i (i = S1, S2, S3, SL, ...).

In the original MN model, an implicit assumption was made that an equal number of neutrons was emitted from the two fragments. However, it has been known from experiments that this is not always true, as can be seen from Fig.3. This is an important fact to notice because the laboratory-system (LS) spectra of neutrons emitted from light fragment (LF) are considerably harder than those from heavy fragment (HF) because of the larger velocity of LF (Fig.4). In calculating the modal spectra, account was taken of different number of neutrons emitted from LF and HF. We therefore used the following formula to calculate the modal spectra from LS-spectra $\chi_{iL}(En)$, $\chi_{iH}(En)$ of the two fragments

$$\chi_i(En) = [\nu_{iL} \chi_{iL}(En) + \nu_{iH} \chi_{iH}(En)] / (\nu_{iL} + \nu_{iH}) \quad (2)$$

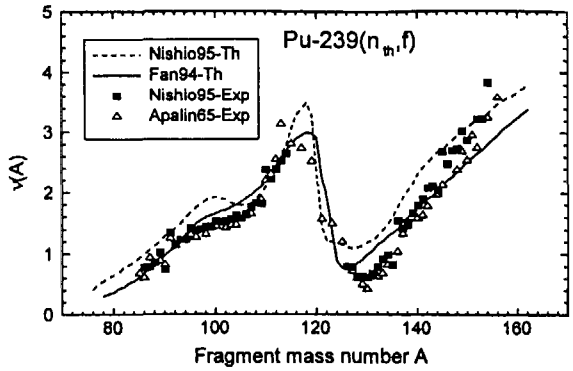

Fig.3 Average prompt neutron multiplicity as a function of fragment mass.

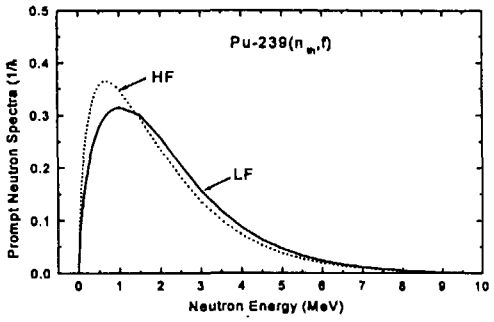

Fig.4 LS-spectra of neutrons from LF and HF.

2.2 PNS of Np-237 for Incident Energies from 0.3 to 5.5MeV

A multimodal analysis for ^{237}Np(n,f) for incident energies 0.3 to 5.5 MeV made by Siegler *et al.* [3] revealed that branching ratio (or weight) to S1-mode decreased, while branching to S2-mode increased with the incident energy. Systematic variation of PNS due to this change in branching with the incident energy was analyzed using these data [4]. The modal spectrum for S1-mode was found to be the softest, getting harder in ascending order for S2-, S3- and SL-modes (Fig.5). This tendency can easily be anticipated from Fig.2. This is interpreted as follows: although the total energy release E_R is largest for S1-mode, TKE is much larger due to small charge-center distance for S1-mode, so that the maximum nuclear temperature T_m is lowest for this mode. On the contrary, T_m is highest for the SL-mode due to the largest deformation energy. The total spectra obtained by synthesizing the modal spectra with eq.(1) well represented the experimental data.

In order to see the sensitivity of the multimodal and 'single-modal' (we refer to the conventional method of the MN-model as this) spectra to different incident energies E, the calculated spectra at E= 0.3 and 5.0 MeV are compared in Fig.6. It is observed that the multimodal calculation reflected the variation in E more sensitively than the conventional single-mode method. This is because not only the increase in the excitation energy E^* of the compound nucleus, but also the growth of S2-mode (with higher T_m) with increasing incident energy E were considered in this approach.

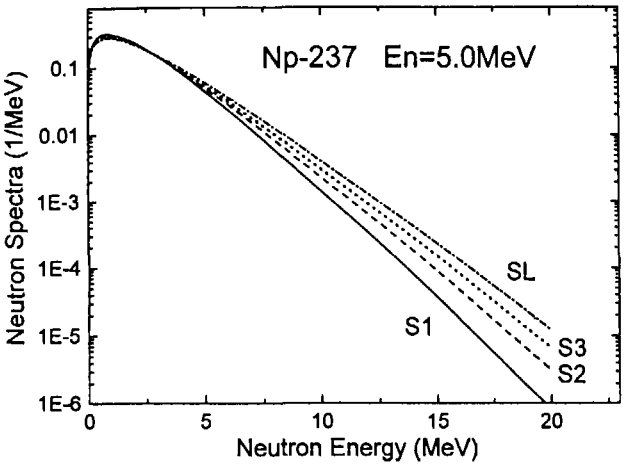

Fig.5 Modal spectra for ^{237}Np(n,f) at E= 5.0 MeV.

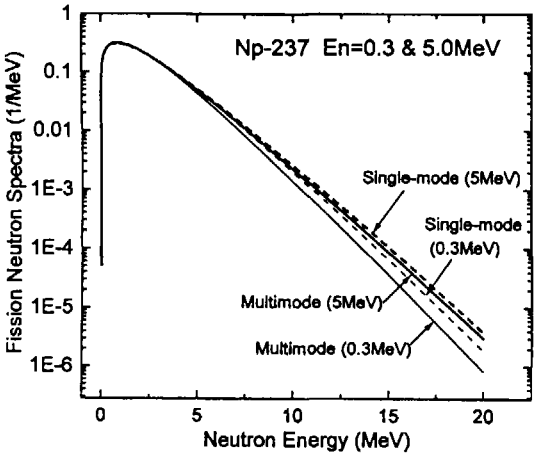

Fig.6 Calculated total spectra for ^{237}Np(n,f) at E= 0.3 and 5.0 MeV.

2.3 PNS of Pu-isotopes

Schillebeeckx *et al.* [5] performed analyses of mass and *TKE* distributions for ^{238}Pu(sf), ^{240}Pu(sf), ^{242}Pu(sf) and ^{239}Pu(n,f). These data were adopted as the basis of the present analysis (For more details, see [6]). The calculated modal and total spectra for ^{238}Pu(sf), ^{240}Pu(sf), ^{242}Pu(sf) are compared in Fig.7 and those for ^{239}Pu(n,f) is shown in Fig.8. The energy partition for the two cases are summarized in Table 1. The nuclear temperature distribution for ^{238}Pu(sf) is shown in Fig.9.

Table 1. Branching ratios and energy partition in ^{238}Pu(sf), ^{240}Pu(sf), ^{242}Pu(sf) and ^{239}Pu(n,f). The data of the mode branching ratio and TKE were taken from Schillebeeckx *et al.* [5].

	Modes	^{238}Pu(sf)	^{240}Pu(sf)	^{242}Pu(sf)	^{239}Pu(n,f)
Branching ratio	S1	9.7%	26.2%	30.7%	24.8%
w_i	S2	90.3%	73.8%	69.3%	74.2%
	S3	—	—	—	1.0%
Average fragments	S1	Mo-105, Te-133	Mo-106, Te-134	Mo-107, Te-135	Mo-105, Te-135
	S2	Y-98, Cs-140	Y-99, Cs-141	Zr-103, Xe-139	Y-99, Cs-141
	S3	—	—	—	As-83, Pm-157
E_R (MeV)	S1	206.11	205.56	205.44	205.40
	S2	198.61	199.81	198.37	196.28
	S3	—	—	—	182.12
TKE (MeV)	S1	192.7	192.2	191.9	190.4
	S2	175.1	174.8	175.8	174.2
	S3	—	—	—	164.2
E^* (MeV)	S1	13.41	13.36	13.54	21.53
	S2	23.51	23.01	22.57	28.61
	S3	—	—	—	24.46
T_m (MeV)	S1	0.798	0.811	0.803	1.017
	S2	1.001	0.990	0.986	1.095
	S3	—	—	—	1.032

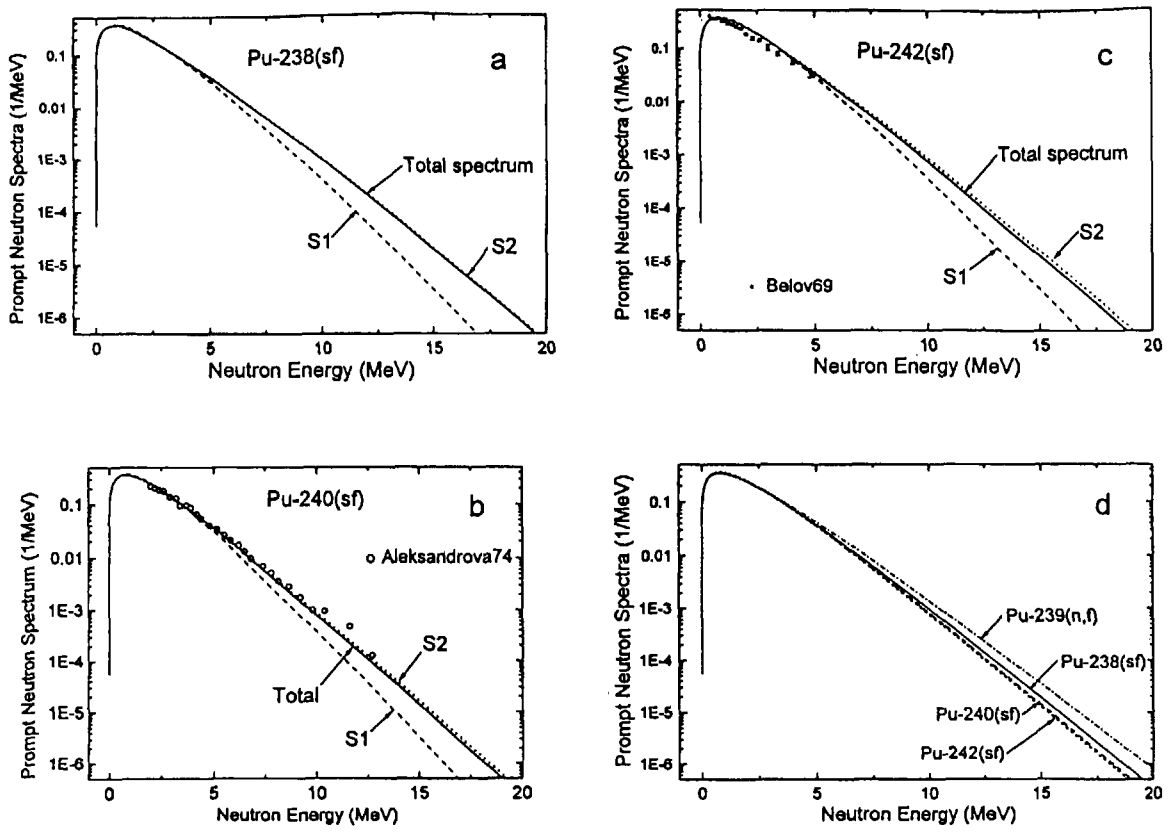

Fig.7. Modal and total spectra of prompt neutrons in ^{238}Pu(sf), ^{240}Pu(sf) and ^{242}Pu(sf) and their comparison..

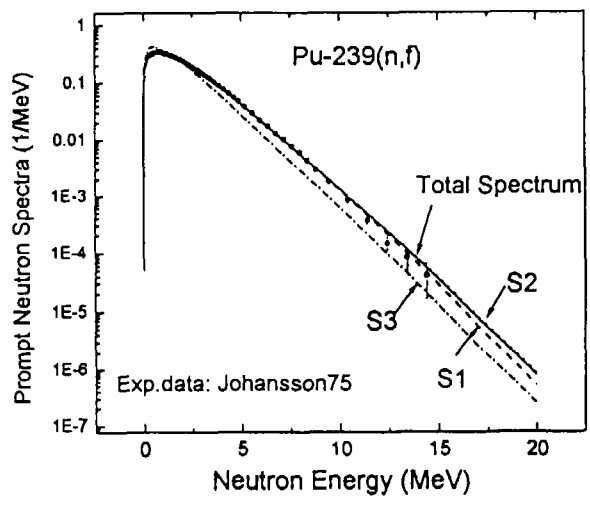

Fig.8 Modal and total spectra for prompt neutrons in ^{239}Pu(n,f).

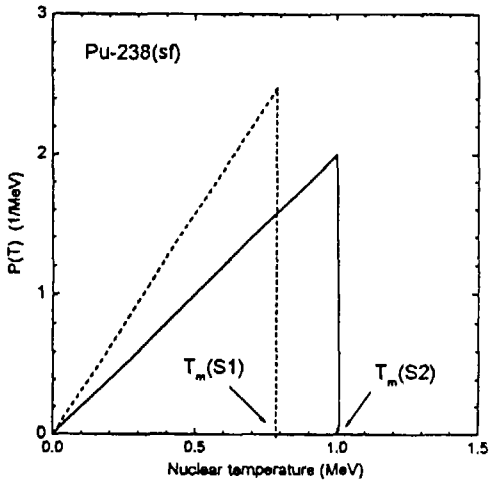

Fig.9. Nuclear temperature distribution of residual fission fragments for ^{238}Pu(sf).

Comparing the three spectra in Fig.7, we see that the total spectrum is determined by combination of the two components S1 and S2. For ^{238}Pu(sf), S2-mode (with harder spectrum) accounts for 90.3% of the total fission process, thus the resulting total spectrum is hardest among the three isotopes. In contrast, for ^{242}Pu(sf), the branching ratio to S2-mode decreases down to 69.3%, thus resulting in softest total spectrum

among the three isotopes. The average energies of prompt neutrons are: 2.005 MeV, 1.977 MeV, 1.973 MeV for ^{238}Pu(sf), ^{240}Pu(sf) and ^{242}Pu(sf), respectively. This can clearly be seen in Fig.7d, where the four spectra were compared. This should be compared with previous results of calculation by Madland [7] that the softest spectrum is that of ^{242}Pu(sf) whereas the hardest spectrum is that of ^{240}Pu(sf) among the even-mass plutonium isotopes.

3. Delayed Neutron Yields in the Resonance Region of U-235

3.1 Fission Mode Fluctuations at Resonances

Hambsch *et al.* [8] observed fluctuations in the fission fragment mass distributions as a function of resonance energy of U-235, which are correlated with fluctuations of the reaction Q-value and with the total kinetic energy averaged over all fragments. These data were analyzed in terms of multimodal fission model, and it was found that the mode branching ratios differ from resonance to resonance, the observed changes of the ratios $(w_{S1}/w_{S2})_{res}/(w_{S1}/w_{S2})_{th}$ ranging up to 20%. This amounts to a decrease of fission yields of the outside wings (A = 84–96, 140–152) and an increase of the inside wings (A = 96–108, 128–140) of the mass distribution (see Fig.10).

On the other hand, precursors of delayed neutrons (DN) lie the region where a nucleus has a few excessive neutrons just outside of the closed shell, because such a nucleus has higher neutron emission probability after beta-decay due to the lower neutron binding energy of the DN-emitter nucleus. These precursor regions are denoted in Fig.10 with bold horizontal lines. It can readily be seen that these regions overlap with the regions where substantial changes of mass yield is observed in the resonance-neutron fission. This implies that the yields of DN precursors fluctuate in the resonance region, resulting in local variation of DN yield. In order to verify this reasoning, estimation of possible changes in DN yield was made using the data of Hambsch *et al.* [8] as the basis.

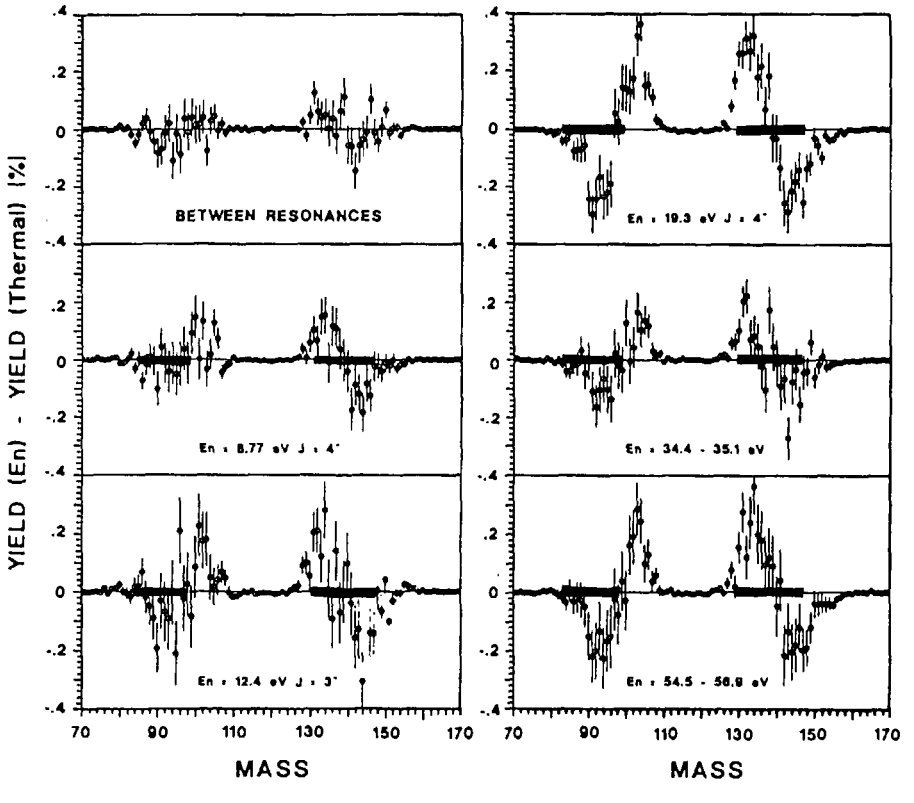

Fig. 10 Fragment yield differences at resonances with respect to the thermal values. (After F.-J.Hambsch *et al.* [8]. The bold horizontal lines, indicating the precursor regions, were added by the present author.)

3.2 Method

The total DN yield was calculated using the summation method:

$$\nu_d = \sum_i Y_i P_{ni}, \tag{3}$$

where Y_i is the fission yield of a precursor i, and P_{ni} is the neutron emission probability of precursor i. The fission yield Y_i was calculated by using the five-Gaussian representation and the data of Nishio *et al.* [9] on the prompt neutron multiplicity $\nu_p(A^*)$ as a function of preneutron-emission mass of the fragment. Fragment charge distribution of Gaussian shape with the standard deviation σ =0.56 and the most probable charge

$$Z_p = Z_{UCD} \pm 0.5 \tag{4}$$

was used to obtain the independent fission yields, where Z_{UCD} is the charge predicted with the UCD (unchanged charge distribution) hypothesis. The even-odd effect of the proton number on the fission yield, defined by

$$X = (Z_e - Z_o)/(Z_e + Z_o), \tag{5}$$

was considered, using the formula proposed by the present author [10]:

$$X = -0.1033 + 0.6907/(Z^2/A - 33.8486). \tag{6}$$

Two sets of data for the neutron emission probability were used: the set of Mann *et al.* [10], comprising 79 precursors, and the set of Wahl [12], comprising 271 precursors.

3.3 Results

The difference of DN yield at 10.18 eV-resonance with respect to thermal values as a function of precursor mass are shown in Fig.11, where Wahl's P_n-data were used. In the HF region, the structure similar to Fig.10 is observed, which means that positive and negative contribution almost cancel out. In the LF region, however, the positive contribution is much less than the negative contribution, thus resulting in negative total value in this region. Therefore the total DN yield at resonances is decreased compared with the thermal value, except for the resonance clusters at 81.9-86.2 eV, where the opposite tendency is observed in mode branching ratios.

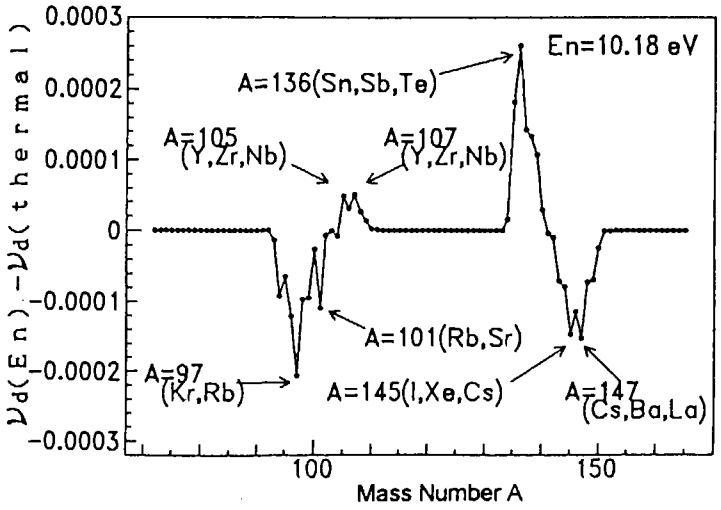

Fig.11 The difference of the DN yield at 10.18 eV-resonance with respect to thermal values as a function of precursor mass.

The relative variation of the DN yield $\nu_d(E)/\nu_d(\text{thermal})$ simulated using the resonance parameters in [13] is shown in Fig.13. The degree of decrease differs from one resonance to another, the maximum decrease being about 2.3% in the region less than 100 eV. The effect of these dips in $\nu_d(E)$ on reactor physics will be amplified many times more than this value due to locally enhanced fission cross section at resonances.

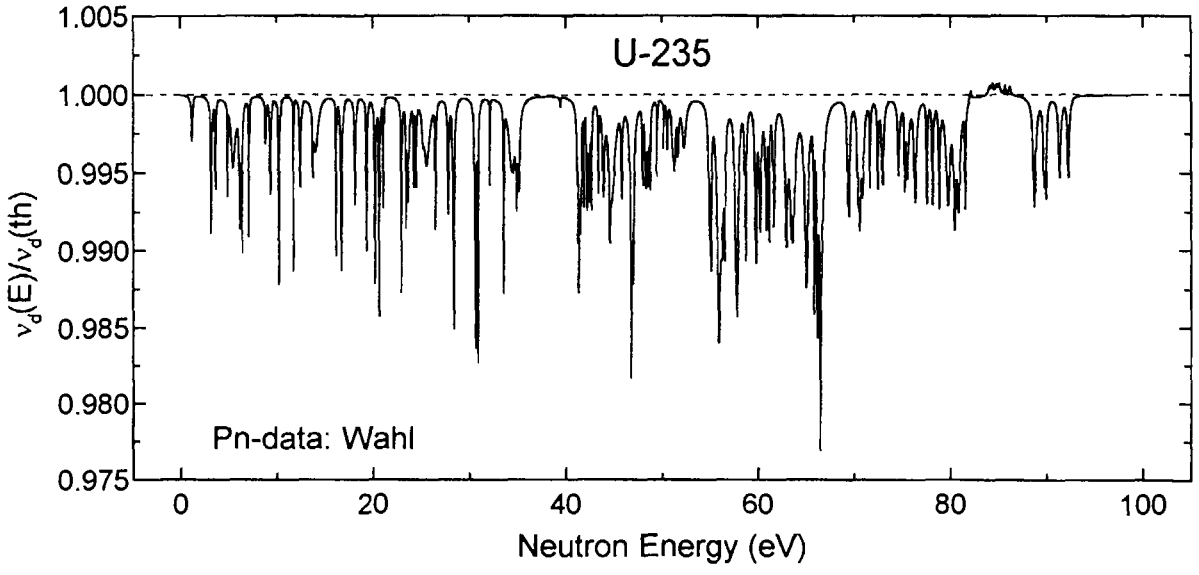

Fig.13 The relative variation of the DN yield $\nu_d(E)/\nu_d(\text{thermal})$ simulated using the resonance parameters in [13].

Two comments should be added here: *(1)* The present result is only preliminary one. The fragment charge distribution used in this work is just a rough approximation. Since the precursor nuclides lie in the tail region of the charge distribution curve, a slight change in the most probable charge Z_p will change the fission yield considerably. Refinement is required also for even-odd effect on fission yield; its dependence on the fragment mass and on the excitation energy should be further investigated. *(2)* Figure13 reminds us of the local dips at resonances observed in the average *prompt* neutron multiplicity $\nu_p(E)$ in ^{239}Pu. Fort *et al.* [14] analyzed the these dips in terms of spin effect and (n,γf)-effect and this evaluation was reflected in JEF-2 file. However, just because of these dips in ν_p, there appear prominent local 'spikes' in the DN fraction β ($=\nu_d / \nu_p$) at resonances in JEF-2 data. If actually there exist dips in the DN yield ν_d, there will be a possibility of eliminating or mitigating the local spikes in β. In addition, there is another possibility of interpreting the dips in ν_p as due to local changes of mode branching ratios. It is thus highly desirable that measurements of fluctuation in the mass distributions at resonances of ^{239}Pu should be made with high precision. This would bring us a possibility of solving a long-standing problem of probable decrease of β in the epithermal and resonance regions for which physical ground was not clear thus far.

4. Concluding Remarks

Recent precise measurements of fragment mass and kinetic energy distributions and their analyses in terms of multimodal fission model performed during the last decade revealed many interesting features of the fission process. These results are intriguing not only from nuclear physicist's point of view, but also from nuclear data evaluator's point of view, because the precise data of mass and kinetic energy partition in the fission process make it possible to analyze in detail the physical quantities related to fission in terms

of modal changes. However, multimodal analyses of experimental data have been made so far for only limited number of nuclides. Now that purely theoretical prediction of modal characteristics of arbitrary nucleus with Brosa's method [1] involves uncertainties at the present stage of knowledge, further systematic experimental studies over a wider range of nuclides and excitation energies would be necessary to obtain a deeper insight into the physics of modal changes in the fission process. This, in turn, will serve to improve the accuracy and predictive power of evaluation models.

References

[1] Brosa, U., S. Grossmasnn and A. Müller, Phys. Reports **197**, No.4, 167 (1990).
[2] Madland, D. G., and J. R. Nix, Nucl. Sci. Eng. **81**, 213 (1982).
[3] Siegler, P., F.-J. Hambsch, S. Oberstedt and J. P. Theobald, Nucl. Phys. **A594**, 45 (1995).
[4] Ohsawa, T., H.Hayashi and Y.Ohtani, Proc. Int. Conf. on Nuclear Data for Science and Technology, Trieste, Part.I, p.365 (1997).
[5] Schillebeeckx, P., C. Wagemans, A. J. Deruytter and R. Barthelemy, Nucl. Phys. **A545**, 623 (1992).
[6] Ohsawa, T., T.Horiguchi and M.Mitsuhashi, Proc. Int. Workshop on Nuclear Fission Physics, Obninsk, Oct. 1998. To be published.
[7] Madland, D.G., Proc. Int. Conf. on Nuclear Data for Science and Technology, Gatlinburg, 1994, Vol.**1**, p.532 (1994).
[8] Hambsch, F.-J., H.-H.Knitter and C.Budtz-Jorgensen, Nucl. Phys. **A491**,56 (1989).
[9] Nishio, K., Y. Nakagome, I. Kanno and I. Kimura, J. Nucl. Sci. Technol. **32**, 404 (1995).
[10] Ohsawa, T., Private communication (1996).
[11] Mann, F.M., M.Schreiber and R.E.Schenter, Nucl. Sci. Eng. **87**, 416 (1984).
[12] Wahl, A.C., Atomic and Nuclear Data Tables, **39**, 1 (1988).
[13] Mughabghab, S.F., Neutron Cross Sections, Vol.1, Part B, Academic Press (1984).
[14] Fort, E., J.Fréhaut, H.Tellier and P.Long, Nucl. Sci. Eng. **99**, 375 (1988).

JP9950324

3.7 Systematics of Average Radiative Width of Heavy Nuclides

Toru Murata
AITEL corporation
1-18-16 Shinbashi, Nihon-Seimei BLDG, Minatoku, Tokyo, Japan
e-mail:murata@aitel.toshiba.co.jp

Systematics of neutron capture radiative width were studied in the target element range from Th to Cm. Reduced radiative widths were analyzed with a simple radiative width formula based on E1 transition. Average radiative width is presented with the standard deviation of 15 %.

The revision works of heavy nuclide nuclear data of JENDL-3.2 are now in progress. As a part of the works, systematics of neutron capture radiative width were studied in the target element range from Th to Cm.

Experimental average radiative widths compiled by Mughabghab/1/ were investigated to have systematic trend or not with the mass number, neutron binding energy and primary capture gamma-ray average energy. Capture gamma-ray energy spectrum data were obtained from the NNDC,BNL web-site/2/ for the data available nuclides. Simple but not so good correlation was observed between the widths and neutron binding energy. No improvement was made in the correlation to average energy of primary capture gamma-rays .

Radiative capture width will be expressed by gamma-ray energy integration of transition probability multiplied by final state level density. At present, the following simple approximation based on E1 transition was made:

$$\langle \Gamma_\gamma \rangle = K_{E1} \sum_i \int_{Ex0}^{Ebn} E_\gamma{}^3 \rho(E_x, I_i) dE_x \quad ,$$

where K_{E1} is reduced radiative width, E_γ the photon energy of E1 transition and given by the difference of neutron binding energy E_{bn} and the excitation energy of the nucleus after the transition E_x, E_{x0} the minimum excited energy of spin I_i level which is fed by E1 transition. The values of E_{x0} are obtained from the ENSDF file and the Table of Isotopes /3/.

The level density ρ (Ex,I) is given by

$$\rho(E_X, I) = (2I+1)\exp\{-I(I+1)/c_t\}\rho_0 \exp\{(E_X)/T\},$$

where C_t is spin cut-off parameter and T nuclear temperature.

The reduced radiative width K_{E1} was calculated for 24 nuclides from Th to Cm using the data given in Table 1. The level density parameters were determined to minimize the χ^2 of K_{E1} distribution around the average value and given in Table 2. The average value of K_{E1} was obtained with the weight of inverse variance of experimental radiative width and

$$K_{E1} = (2.57 \pm 0.38) \times 10^{-3} \quad \text{meV/(MeV)}^3$$

Figure 1 shows the distribution of the reduced radiative width K_{E1}.

Other factors to describe radiative width are proposed in the reference/1/, such as level spacing and the giant-dipole resonance parameters. Further study should be made to reduce the standard deviation of the K_{E1} average value.

References

/1/ Mughabghab,S.F.: "Neutron Cross Sections,vol.1.part B", Academic Press(1984)

/2/ http://www.nndc.bnl.gov./

/3/ ENSDF: Evaluated Nuclear Structure Data File, NNDC, BNL.

Firestone,R.B.(Editor):"Table of Isotopes, 8th edition", Wiley International(1996)

Table 1. Radiative width related data summary Table

Target N.	G.S.Jπ	<Γγ>(meV)*	Comp.N.Jπ	n.Bind.E(MeV)	E-1Fed min.Ex(MeV),Jπ**
Th-228	0+	36±2	1/2+	5.254	0.165, 3/2-
Th-229	5/2+	43±4	3+,2+	6.794	0.508, 1-
Th-230	0+	26±2	1/2+	5.118	0.554, 1/2-
Th-232	0+	24±2	1/2+	4.786	0.540, 1/2-
Pa-231	3/2-	40±2	2-,1-	5.553	No E-1 feed level found
Pa-233	3/2-	47±2	2-,1-	5.219	0.074, 3+
U-233	5/2+	40±5	3+,2+	6.843	0.786, 1-
U-234	0+	26±4	1/2+	5.298	0.638, 3/2-
U-235	7/2-	35±2	4-,3-	6.544	0.744, 3-
U-236	0+	23±1	1/2+	5.126	0.541, 1/2-
U-238	0+	23. 2±0. 3	1/2+	4.806	0.739, 1/2-
Np-237	5/2+	40. 8±1	3+,2+	5.488	0.136, 3-
Pu-238	0+	34±3	1/2+	5.647	0.470, 1/2-
Pu-239	1/2+	43±4	1+,0+	6.533	0.597, 1-
Pu-240	0+	31±2	1/2+	5.241	0.833, 3/2-
Pu-241	5/2+	42±4	3+,2+	6.309	0.780, 1-
Pu-242	0+	22±1	1/2+	5.034	0.704, 3/2-
Pu-244	0+	20±2	1/2+	4.773	0.637, 3/2-
Am-241	5/2-	44±1	3-,2-	5.537	0.975, 3+
Am-243	5/2-	39±1	3-,2-	5.363	0.088, 1+(p)/0.420, 2+(n)
Cm-242	0+	34±6	1/2+	5.693	0.729, 1/2-
Cm-244	0+	37±2	1/2+	5.52	0.634, 3/2-
Cm-246	0+	28. 1±1. 8	1/2+	5.156	0.957, 1/2-
Cm-248	0+	25. 5±1. 4	1/2+	4.713	0.470, 3/2-

*Mughabghab,S.F.: "Neutron Cross Sections,vol.1,part B",Academic Press(1984)
**ENSDF and Table of Isotopes (8th edition)

Table 2. Level density parameters for reduced radiative width calculation

Type of Nucleus	ρo(1/MeV)	T(MeV)
even-even	2.2	1.4
even-odd	6.5	1.2
odd-odd	3.0	1.0

Ct = 8.0

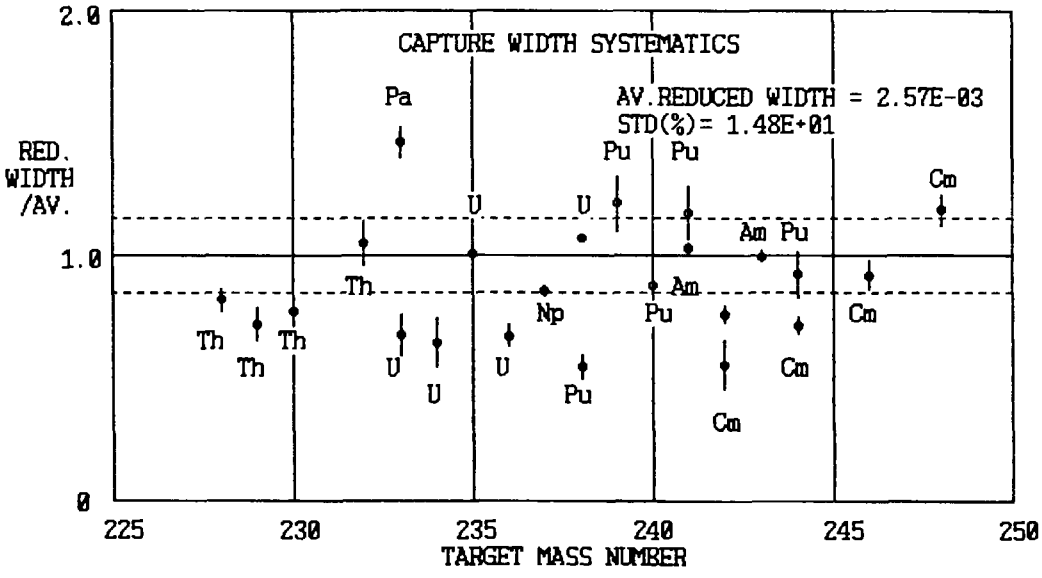

Fig.1 Analyzed reduced radiative width for various target nucleus .The ordinate shows the ratio to average value. Dashed lines show the range of the standard deviation.

3.8 Comparison of BFS-73-1 Benchmark Test using JENDL-3.2, JEF-2.2 and ENDF/B-VI.3

Jung-Do Kim, Choong-Sup Gil and Jonghwa Chang
Nuclear Data Evaluation Laboratory, Korea Atomic Energy Research Institute
150 Dukjin-dong, Yusong, Taejon, Korea
e-mail : jdkim@kaeri.re.kr

A comparative analysis for BFS-73-1 critical assembly, which is a benchmark of a fast reactor core with metal uranium fuel of 18.5% enrichment, was carried out with TWODANT code and three current evaluated data libraries of JENDL-3.2, JEF-2.2 and ENDF/B-VI.3. The results for criticality, spectral indices and reaction rate distributions are intercompared along with experimental data.

1. Introduction

As a part of critical benchmarks for developing the KALIMER(Korea Advanced LIquid MEtal Reactor), experimental studies on metal fueled liquid metal reactor core characteristics are carried out under contract between Korea Atomic Energy Research Institute and Institute of Physics and Power Engineering in Russia. The BFS-73-1 critical assembly is a benchmark core with metal uranium fuel of 18.5% enrichment. K_{eff}, spectral indices, axial and radial fission rate distributions of U-235 and U-238, $\mathbf{b}_{eff}$, Doppler effects of U-238 and sample reactivity worth etc. were measured in this experiment. An analysis of the experiment[1] has been performed using DIF-3D code and JEF-2.2-based KAFAX-F22[2] data set. In order to survey the impact of nuclear data on the BFS-73-1 benchmark test, a comparative analysis using JENDL-3.2, JEF-2.2 and ENDF/B-VI.3 was carried out and the results are presented in this symposium.

2. Benchamrk core of BFS-73-1

The BFS-73-1 was constructed at BFS-1 facility in 1997. The core is a homogeneous system, without control rods in the core. Axial blankets of ~50 cm thickness are located above and below the core, which are consisted of depleted uranium dioxide pellets. A radial blanket of ~35 cm thickness, surrounding the core, also contains only depleted dioxide uranium pellets in steel tubes. The core is composed of fuel elements with round stainless steel sticks between tubes, and the radial blanket is assembled with tubes of UO_2 pellets and triangular stainless steel sticks between these tubes. Table 1 shows some parameters of BFS-73-1 critical core. And layout of the core, and the fuel and blanket rods is shown in Fig. 1.

Table 1. Parameters of BFS-73-1 critical core

No. of rods in core	● 379 with 36.41% uranium enriched ● 46 with 36.45% uranium enriched ● 760 round steel sticks
No. of rods in blanket	● 708 UO_2 ● 1400 triangular steel sticks
Temperature(°C)	● +19 °C
Position of control rods	● All rods are in the upper position
K_{eff}	● 1.0008

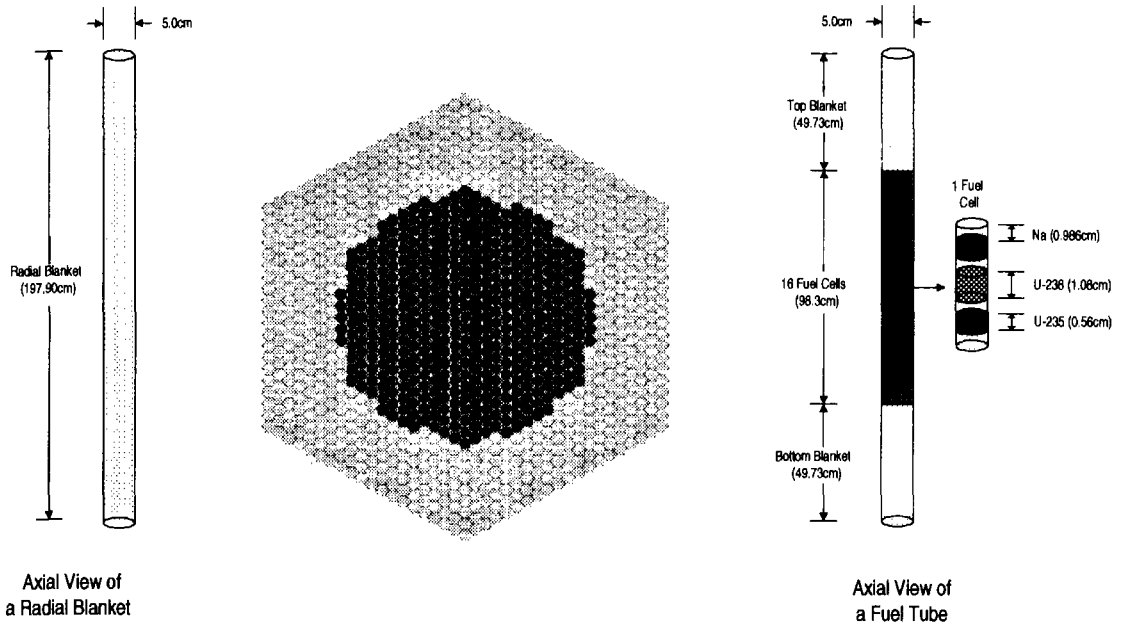

Figure 1. Layout of BFS-73-1

3. Data processing

Three multigroup cross section data sets were processed with the NJOY94.105[3] system from JENDL-3.2, JEF-2.2 and ENDF/B-VI.3, respectively. The data sets have MATXS-format and LANL 80-group structure . The MATXS-format data can be processed to ANISN-format data using TRANSX 2.15[4] pre-processing code for neutron transport calculations.

4. Calculation

Neutron transport calculations using each of these data sets were carried out with pre-processing code TRANSX 2.15 for MATXS-format data library and 2-dimensional discrete ordinates code TWODANT[5] using R-Z model of BFS-73-1 critical assembly. Figure 2 shows the R-Z model for the calculations. At first, the 80-group data were collapsed to 25-group with the flux calculated by R-Z model, coarse-mesh and P_3-S_8 approximations. And then, 2-dimensional 25-group fine-mesh(width of meshes: ~0.6cm for radial and ~0.5 cm for axial direction) calculations were performed with P_3-S_8 approximations. In this report, the results for criticality, spectral indices, and axial and radial reaction rate distributions of U-235 and U-238 are intercompared along with experimental data.

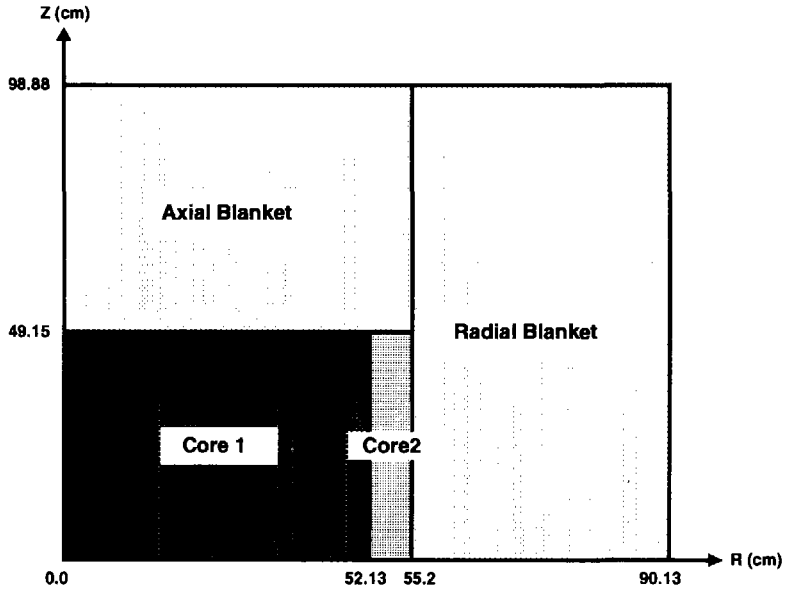

Figure 2. Calculational R-Z model of BFS-73-1

5. Results and Discussion

Calculated values of K_{eff} and central reaction rate ratios are compared with the measured data. The result is presented in Table 2, as the ratio of calculation to experiment(C/E). K_{eff} value using JEF-2.2 shows a little active result. Calculated central reaction rate ratios of U-238 capture to Pu-239 fission cross section using the three data sets underestimate the experimental values. And the value of s_f^{238}/s_f^{235} using ENDF/B-VI.3 overestimates the measured data. All of s_f^{239}/s_f^{235} are within measurement error range. C/E values of fission rate distribution of U-235 and U-238 in the core and blanket region are shown in Fig.3~6. Figure 3~4 and Figure 5~6 are for radial and axial distributions, respectively. Measurement uncertainties for U-235 fission rate distributions are ~2% in the core and they increase up to 4% in the blankets. For U-238, the uncertainties are ~3% in the core and ~7% in the blankets. For the most part, C/E-values of fission reaction rate distribution using the three data sets show reasonable tendency except U-235 fission rate in radial blanket, considering the

measurement errors. However, the results of fission rate distributions using ENDF/B-VI.3 are slightly better than those of JENDL-3.2 and JEF-2.2.

Table 2. C/E-values of Keff and spectral indices

	Exp. Error(%	JENDL-3	JEF-2.2	ENDF/B-VI.3
K_{eff}		0.9978	1.0064	1.0029
s_f^{238}/s_f^{235}	1.65	1.011	1.013	1.038
s_c^{238}/s_f^{239}	1.6	0.972	0.971	0.954
s_f^{239}/s_f^{235}	1.6	0.983	0.989	0.992

Acknowledgements

The authors would like to thank Mr. Hoon Song, Development Project of Core Design Technology For KALIMER, for his assistance in preparing input data for analysis of the experiment.

References

[1] Hoon Song et al., "Analysis of BFS-73-1 Experiment," KAERI/TR-1138/98 (1998).

[2] J.D. Kim and C.S. Gil, "Development and Benchmark of Multi-group Library for Fast Reactor using JEF-2.2," KAERI/TR-842/97 (1997).

[3] R.E. MacFarlane and D.W. Muir, "The NJOY Nuclear Data Processing System, Version 91," Los Alamos National Laboratory, LA-12740-M (Oct. 1994).

[4] R.E. MacFarlane, "TRANSX 2: A Code for Interfacing MATXS Cross-Section Libraries to Nuclear Transport Codes," Los Alamos National Laboratory, LA-12312-MS (Dec. 1993).

[5] R.E. Alcouffe, et al, "User's Guide for TWODANT: A Code Package for Two-Dimensional, Diffusion-Accelerated, Neutron Transport," Los Alamos National Laboratory, LA-10049-M (Feb. 1990).

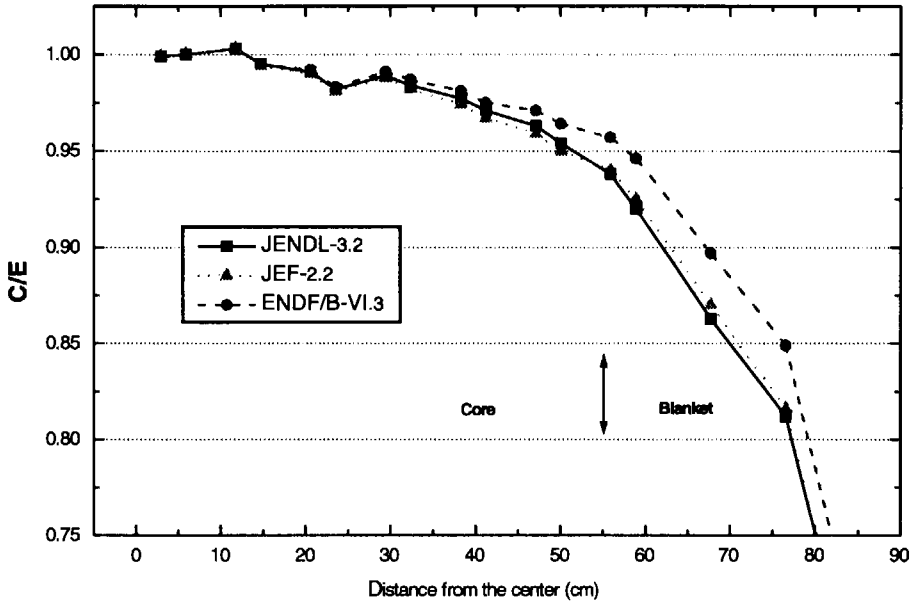

Fig. 3. Radial distribution of U-235 fission rate

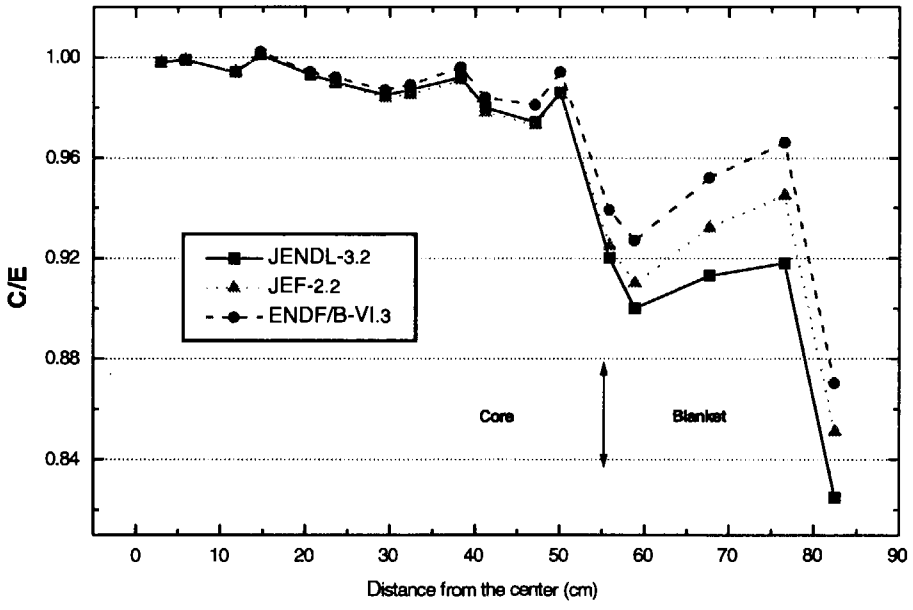

Fig. 4. Radial distribution of U-238 fission rate

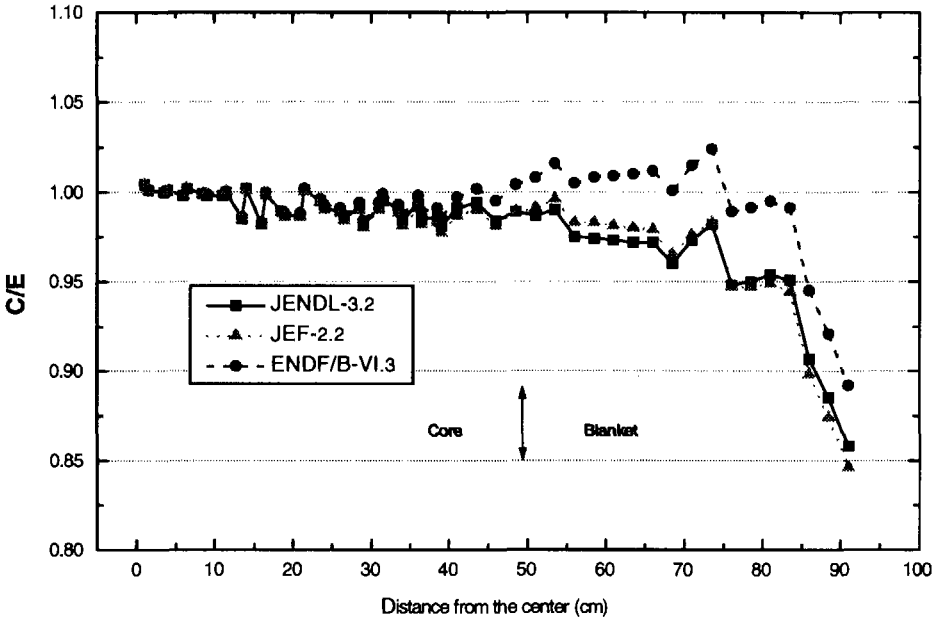

Fig. 5. Axial distribution of U-235 fission rate

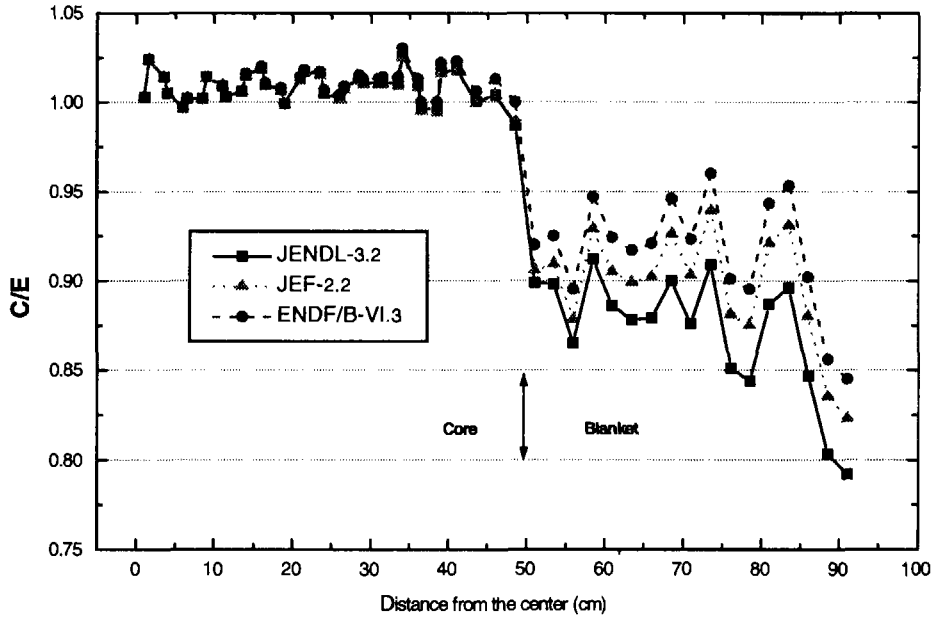

Fig. 6. Axial distribution of U-238 fission rate

3.9 Measurements of secondary particles produced from thick targets bombarded by heavy ions

Tadahiro KUROSAWA[1], Takashi NAKAMURA[1], Noriaki NAKAO[2]
Tokushi SHIBATA[3], Yoshitomo UWAMINO[4] , Akifumi FUKUMURA[5]

[1]Cyclotron and Radioisotope Center, Tohoku University
Aoba, Aramaki, Aoba-ku, Sendai, 980-8578, Japan
kurosawa@cyric.tohoku.ac.jp
[2]High Energy Accelerator Research Organization, Tanashi Branch
Midori-cho 3-2-1,Tanashi,Tokyo,188-8501, Japan
[3] High Energy Accelerator Research Organization
Oho-cho 1, Tsukuba, Ibaraki, 305-0801, Japan
[4]Institute of Physical and Chemical Research
Hirosawa 2-1,Wako, Saitama 351-0198, Japan
[5]National Institute of Radiological Sciences
Anagawa 4-9-1, Inageku, Chiba-shi, 263-8555, Japan

We measured angular and energy distributions of neutrons, protons, deuterons and tritons produced by 100 MeV/nucleon He ions stopping in thick carbon, aluminum, copper and lead targets using the HIMAC (Heavy Ion Medical Accelerator in Chiba) of NIRS (National Institute of Radiological Sciences), Japan by using the time-of-flight method coupled with the ΔE-E counter system. The experimental spectra were compared with the calculation using the LCS code and the calculated spectra are generally in rather good agreement with the measured spectra of these four secondary particles.

1. INTRODUCTION

With the increasing use of high energy (higher than 100MeV/nucleon) heavy ions (heavier than He ion) in various fields, the energy-angle distribution of neutrons produced from a thick target which fully stops heavy ions becomes very important as the source-term data of shielding design of the accelerator facility. Although only one paper has ever been published on thick target neutron yield (TTY) for 177MeV/nucleon He ions [1], Heilbronn et al. [2] and our group [3, 4] have recently performed the experiments on TTY for 155MeV/nucleon He ions [2] and for 100, 180 MeV/nucleon He and 100, 180, 400MeV/nucleon C ions [3] , and for 100, 180, 400MeV/nucleon Ne ions [4]. In this work we present the angular - energy distributions of neutrons, protons, deuterons and tritons produced from thick carbon, aluminum, copper and lead targets bombarded by 100 MeV/nucleon helium ion. The charged particle spectra from thick targets are not so important in physical meaning due to the energy loss in the target depending on the target thickness, but these results will be useful as benchmark experimental data to investigate the accuracy of the particle-transport calculation code. Here, the measured spectra are compared with those calculated with the LAHET Code System, LCS [5] as a benchmark test.

2. EXPERIMENTAL PROCEDURE

The energy of neutrons, protons, deuterons and tritons produced in the target was measured by the time-of-flight (TOF) method. A thin NE102A plastic scintillator (3cm diam. by 0.05cm thick) was placed just behind the end window of the beam line as a beam pick-up scintillator. The output pulses of this scintillator were used as start signals of the TOF measurement, and also to count the absolute number of projectiles incident on the target. A target was set on the beam line 10 cm behind the beam pick-up scintillator. The beam spot size incident on the target was about 1.5 cm diameter and the beam height was 1.25m above the concrete floor of the experimental area. The NE213 liquid scintillator (12.7cm diam. by 12.7cm thick), which was designed to expand the dynamic range of output pulses for high energy neutron measurements[6], was used for neutron detector (E counter), and the NE102A plastic scintillator (15 cm by 15cm square and 0.5cm thick) for the ΔE counter was placed in front of the E counter to discriminate charged particles from noncharged particles, neutrons and photons. Three sets of E and ΔE counters were used for simultaneous angular distribution measurements at three different angles. The detectors were located 2 m at large angles to 5 m at small angles away from the target to provide better energy resolutions in the forward directions where there are larger yields of high energy neutrons. In order to minimize

neutrons in scattering, no local shielding was used near the detectors. By interposing an iron shadow bar of 15cm by 15cm square and 60cm thickness between the target and detector, the background neutron components from room scattering were measured particularly at large angle. Target thicknesses were selected to stop the incident particles completely. Target materials are C (1.77g/cm^3), Al (2.7g/cm^3), Cu (8.93g/cm^3) and Pb (11.34g/cm^3) and each target has a shape of 10cm by 10cm square. The C, Al, Cu and Pb targets are 5.0, 4.0, 1.5 and 1.5 cm thick, respectively.

3. DATA ANALYSIS

3.1 Neutrons

As the ΔE counter does not scintillate by neutrons and gamma rays, the neutron and gamma ray events could be selected from the charged particle events, by using two-dimensional ΔE-E graphical plots shown in Fig. 1 (a). After this discrimination, the neutron and the gamma ray events were clearly separated by using two-dimensional graphical plots of total-slow pulse height components of the E counter as shown in Fig. 1 (b). In this discrimination, the pulse shapes from high energy neutron events in which recoil protons escape from the E counter are close to those from gamma-ray events, and these events were eliminated from the neutron events. After each experimental run, each E counter was calibrated with a ^{60}Co gamma-ray source, and the Compton edge in the gamma-ray spectrum was used as the bias point of 1.25MeVee (electron equivalent) which corresponded to 3 MeV neutron energy. After obtaining the TOF spectrum of neutrons, the data were converted into the energy spectrum of neutrons. For this conversion, the detection efficiency of the NE213 E counter is essential. The experimental data of the detection efficiency for this scintillator has been published by Nakao et al.[6], but there is no data for neutrons of energy higher than 135MeV. Therefore, the neutron detection efficiency was calculated with the Monte Carlo code by Cecil et al.[7] for all energy range. Corresponding to the elimination of high energy neutron events as described above, the recoil proton events escaped from the E counter were also excluded from these calculated efficiencies.

3.2 Charged particles

To separate proton, deuteron and triton events, three kinds of two dimensional graphical plots were used. Two dimensional ΔE-E graphical plots in Fig. 1(a) were first used to identify different Z number particles, but this plots could not identify different mass number particles. From Fig. 1(a) only Z=1 particles were selected, and only a small fraction of Z=2 particles can be seen in Fig. 1(a) because the incident alpha particles fully stopped in a thick target. The two dimensional plots of TOF-E pulse height distributions for Z=1 particles are shown in Fig. 2(a). In Fig. 2(a), different mass particles of protons (m=1) deuterons (m=2) and tritons (m=3) are clearly separated, but the pulse heights of high energy particles escaped from the E counter intersect between those of different mass particles. This intersection was resolved in the following way. It is well known that slow components from the NE213 scintillator increase with increasing the specific energy loss (dE/dx) for a given type of charged particle. The charged particles escaped from the detector, which have the longer stopping range than the detector size, give small dE/dx values compared with the charged particles stopped in the detector and then slow components of the light outputs from escaped particles approach to the pulse heights of gamma rays. These results are shown in the two dimensional total-slow pulse height plots. The proton, deuteron and alpha particles have three separate lines in the order of dE/dx values of these three particles and the charged particles escaped from the detector are in the uppermost line independent to the particle mass. We first selected proton events by setting the region of interest (ROI) in Fig. 2(a) which included the events of escaped deuterons and tritons, and then eliminated the latter events by identifying the escaped particle events, as shown in Fig. 2(b). This procedure was repeated for deuterons and tritons in this order. We finally obtained the TOF spectra for protons, deuterons and tritons separately. The TOF spectra were then converted to the energy spectra by approximating 100% detection efficiency of the NE213 detector.

4. MONTE CALRO SIMULATIONS

These experimental results were compared with the calculations as a benchmark test. The secondary particle spectra were calculated by using the LAHET Monte Carlo Code System, LCS[5]. The LCS calculations were performed for 100MeV/nucleon He incidence on stopping-length C, Al, Cu and Pb targets to investigate the calculational accuracy. The majority of the LAHET parameters was set to their default settings. The target dimension was fixed to be the same size as used in the experiment. The target was set at the center of the vacuum sphere and a total number of 200,000 He particles were injected normally to the target in the central circular surface of 0.5 cm diameter which simulated the actual beam geometry. The angular flux of particles of neutrons, protons, deuterons and tritons emerged from the target were stored at each angle corresponding to the

experimental results.

5. RESULTS AND DISCUSSIONS

5.1 Neutron spectra

Fig. 3 shows the experimental and calculated neutron spectra. Neutron spectra measured in the forward direction have a plateau peak at high energy end which corresponds to about 60 to 70 % of the projectile energy per nucleon. This peak is mainly due to high energy neutron components produced in the forward direction by a break-up process and becomes more prominent for lighter target, since the momentum transfer from projectile to target nuclei are higher for lighter nucleus than for heavier nucleus. The high energy neutrons in the forward direction spread up to the energy which is about the twice as much as the incident particle energy per nucleon. The calculated spectra shown in Fig. 3 generally give rather good agreement with the experimental results in absolute values. Precisely speaking, the following three tendencies can be seen between experiments and calculations. In the calculation, a broad high energy peak in the forward direction appears more distinctly around incident particle energy per nucleon, compared with more flattened high energy peak in the experiment. This discrepancy also reveals that the LCS calculation gives the underestimation of the neutron spectra in the intermediate energy region of 5 to 50 MeV. The calculated spectra at angles larger than 30 degree are harder than the measured spectra, which means that the LCS calculation gives the underestimation of evaporation neutrons and the overestimation of pre-equilibrium neutrons extended to higher energy region.

5.2 Proton spectra

The experimental proton spectra are shown in Fig 4. The lower energy limit in the measured spectra was estimated to be 27MeV considering the proton energy absorption through the air between the target and the detector (500cm), the ΔE counter (0.5cm thick plastic of $CH_{1.104}$ and the density of 1.032g/cm^3) and the aluminum cover (0.5mm thick) of the E counter. These energy absorption was calculated for proton, deuteron and triton using the SPAR code [8], and the lower energy limits of proton, deuteron and triton which are reachable to the E counter are then estimated to be 27.0, 36.6 and 43.7MeV. Although proton spectra are similar to neutron spectra in shapes and absolute values at forward angles, proton yields rapidly decrease with increasing angles. At large angles, low energy proton components are dominant which can easily be absorbed by the thick target itself. Compared with measured and calculated proton spectra, the LCS calculation for proton spectra gives rather good agreement with the experiment in the forward direction.

5.3 Deuteron spectra

The experimental deuteron spectra are shown in Fig. 5. At 90 degree, the deuterons emitted from the target could not be detected because of its strong forwardness. Measured spectra in the forward direction have a broad peak around 140MeV and yields decrease drastically with increasing angles. For C target, the calculated and experimental results agree well at 0, 7.5, 15 and 60 degrees. At 30 degree, the calculated spectrum is larger than the measured one. As a general tendency, the agreement between calculated and measured deuteron spectra is surprisingly good.

5.4 Triton spectra

The experimental triton spectra are shown in Fig. 6. Triton could not be detected at 60 and 90 degrees because of much stronger forwardness than deuteron. Measured spectra in the forward direction have a broad peak around 200MeV and yields decrease drastically with increasing angles. In the triton spectra, the LCS calculation gives good agreement with the experiment in the forward direction, especially for heavier target.

6. CONCLUSION

We measured angular and energy distributions of neutrons, protons, deuterons and tritons produced by 100 MeV/nucleon helium ions stopping in carbon, aluminum, copper and lead targets. The experimental spectra were compared with the calculation using the LCS code and the calculated spectra are generally in rather good agreement with the measured spectra for these four secondary particles. These experimental results were found to be useful as the benchmark data for investigating the accuracy of high energy particle transport calculation code.

Acknowledgments

We gratefully acknowledge the support and assistance of the accelerator operation staff of HIMAC. This work was supported in part by the Research Project with Heavy Ions at NIRS-HIMAC.

References

[1] Cecil, R. A. et al., Phys. Rev., **C21**, 2471(1980)
[2] Heilbronn, L. et al., to be published in Nucl. Sci. Eng. May issue, 1999
[3] Kurosawa, T. et al., to be published in Nucl. Sci. Eng. May issue, 1999
[4] Kurosawa, T. et al., to be published in J. Nucl. Sci. Technol., January issue, 1999.
[5] Prael, R.E. and Lichtenstein, H., LA-UR-89-3014, Los Alamos National Laboratory (1989)
[6] Nakao, N. et al., Nucl. Instr. Meth. Phys. Res. **A362** 454(1995)
[7] Cecil, R. A. et al., Nucl. Instr. and Meth. **161** 439(1979)
[8] Armstrong T.W. and Chandler K.C., Oak Ridge National Laboratory Report ORNL-4869 (1973)

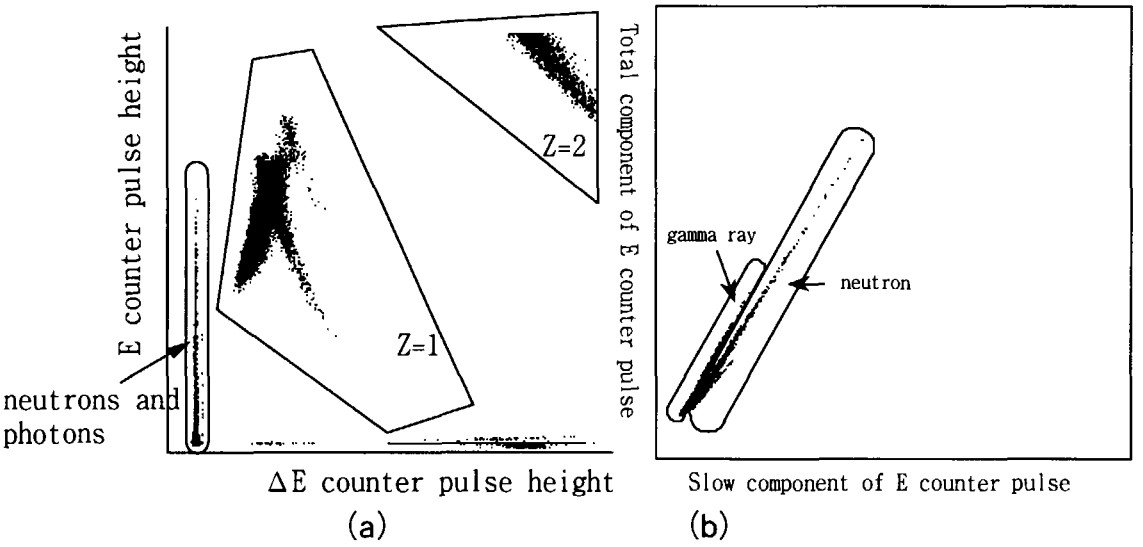

Fig. 1 (a) Two dimensional plot of E and ΔE counter pulse heights and (b) total and slow pulse heights.

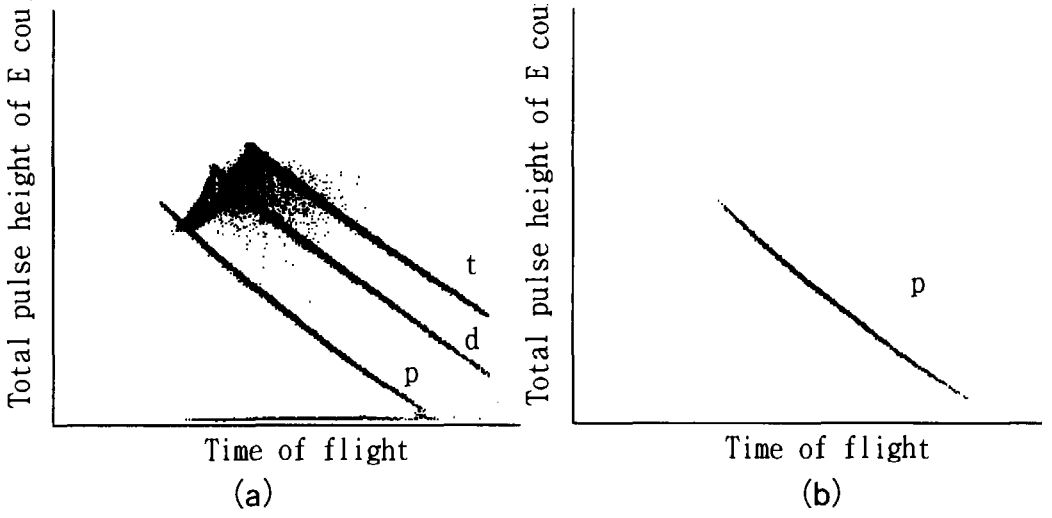

Fig. 2 (a) Two dimensional plot of TOF- E counter pulse height for Z=1 events selected from two dimensional plot of E and ΔE counter pulse heights and (b) that of only proton events.

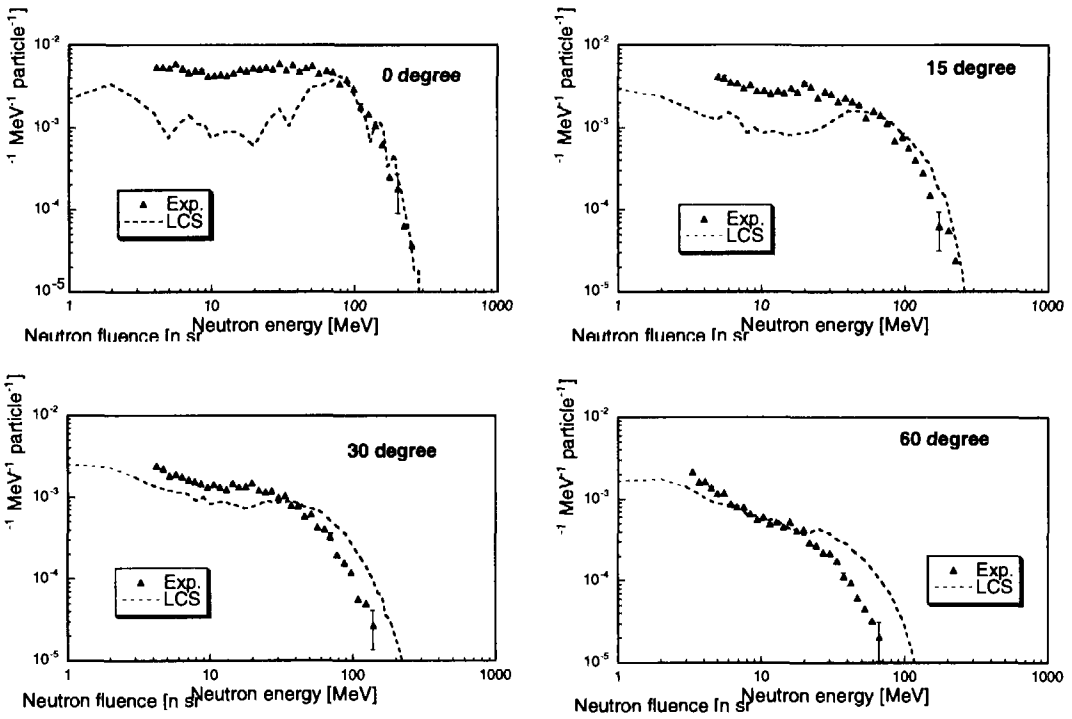

Fig. 3 Comparison of measured and calculated neutron spectra from carbon target.

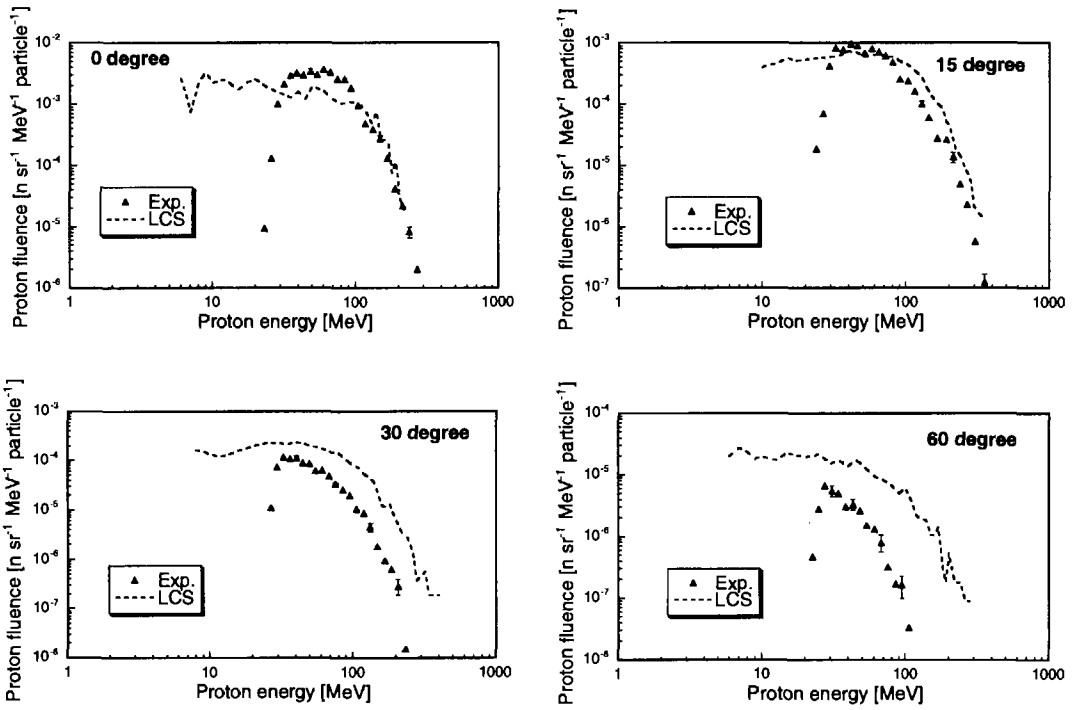

Fig. 4 Comparison of measured and calculated proton spectra from carbon target.

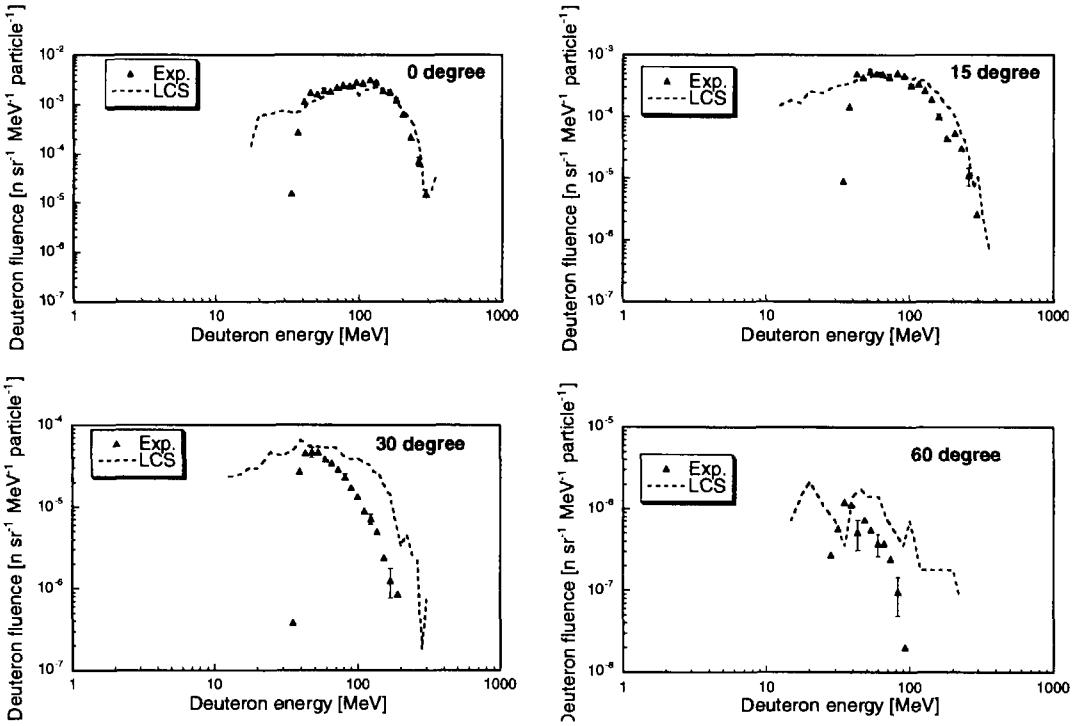

Fig. 5 Comparison of measured and calculated deuteron spectra from carbon target.

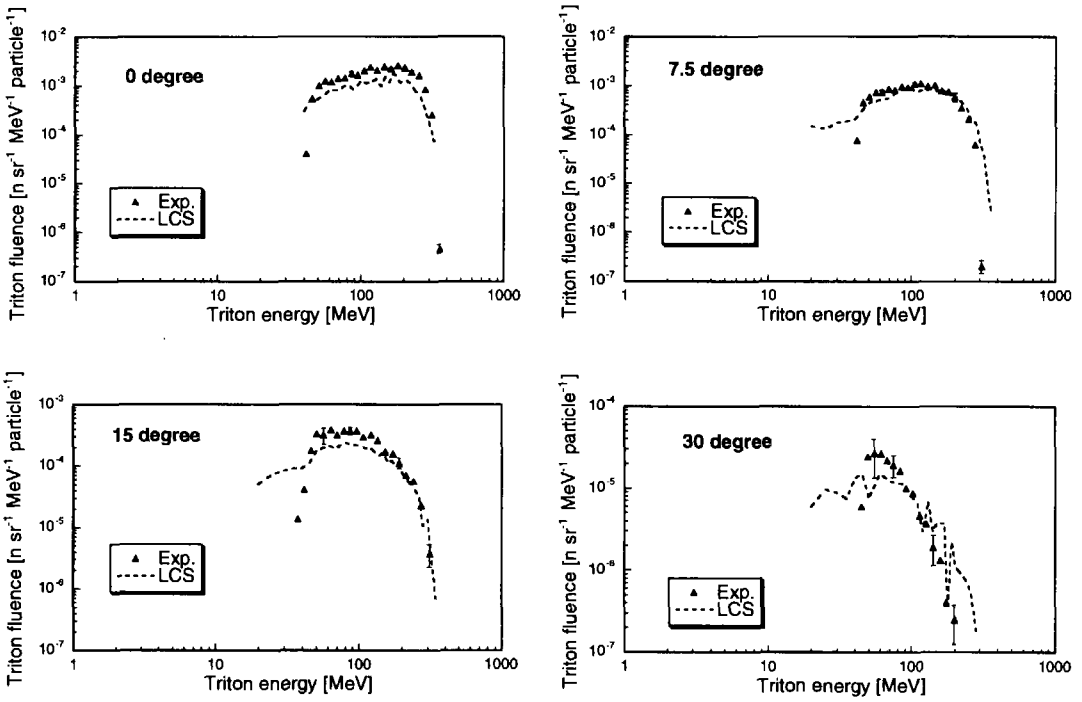

Fig. 6 Comparison of measured and calculated triton spectra from carbon target.

3.10 Measurements of Elastic Scattering Cross Sections of Carbon, Iron and Lead for 75 MeV Neutrons

Masanobu IBARAKI, Hiroshi NAKASHIMA[1], Shin-ichiro MEIGO[1], Mamoru BABA, Yasushi NAUCHI, Takako MIURA, Yoshitaka HIRASAWA, Susumu TANAKA[2], Naohiro HIRAKAWA

Department of Quantum Science and Energy Engineering, Tohoku University, Sendai, 980-8579, Japan
[1] Tokai Establishment, Japan Atomic Energy Research Institute, Tokai-mura, Naka-gun, Ibaraki-ken, 319-1195, Japan
[2] Takasaki Establishment, Japan Atomic Energy Research Institute, Takasaki, 370-1292, Japan

Abstract

We have performed the measurements of elastic scattering cross sections of carbon, iron and lead for 75 MeV neutrons using a $^{7}Li(p,n)$ quasi-monoenergetic neutron source. Elastically scattered neutrons were measured with a time of flight method (TOF) using five liquid scintillation detectors. The data were obtained at 25 laboratory angles between 2.6° and 53.0°. The experimental data were compared with the neutron cross section libraries, systematics used in cascade/transport codes and optical model calculations.

1.Introduction

The neutron emission cross sections for neutron incident reactions are very important for the shielding design of the high-energy accelerator facilities. In particular, the importance of the elastic scattering cross sections was pointed out by the analysis of shielding experiments using the 40 and 65 MeV quasi-monoenergetic neutrons at TIARA facility [1]. Experimental data is very scanty and poor above 40 MeV. Experimental data reported in the past were restricted to only forward angles. Recently, two measurements were reported from U.C.Davis group [2][3]. These data were measured by using the neutron spectrometer consisting of a multi wire chamber and a recoil proton telescope, with source neutrons produced by the $^{7}Li(p,n)$ reaction (E_n=65MeV) and by the spallation reaction (E_n=50~250MeV). The data by spallation source were available only for forward angle (~23°) and has relatively large systematic errors.

In this study, we have performed measurements of elastic scattering cross sections of carbon, iron and lead for 75 MeV neutrons. The data were obtained by using the $^{7}Li(p,n)$ quasi-monoenergetic neutron source and the time-of-flight (TOF) method for scattering angle between 2.6° and 56°. Experimental results were compared with the cross section libraries, systematics used in cascade/transport code and optical model calculations.

2.Experiment

Experiment was carries out at TIARA AVF cyclotron facility [4]. Source neutron were produced via the $^{7}Li(p,n)$ reaction. Figure.1 shows the source neutron spectrum. The peak around 75 MeV is due to the $^{7}Li(p,n_{0,1})$ process and continuum component is attributed to multi-body breakup

process. Figure 2 shows a setup of the elastic scattering measurement. The scattering samples, carbon (5cmϕ×8cm), iron (4cmϕ×6cm) and lead (3cmϕ×6cm), were placed at 10 m from the Li neutron production target. Elastically scattered neutrons were measured by a time of flight method (TOF) using five liquid scintillation detectors (12.7cmϕ×12.7cm, four NE-213 and a BC501A detectors) concurrently. We employ a CAMAC system for data acquisition. The detector anode signals were fed into QDC (charge-to-digital converter) and integrated by two types of the integration gate for n-γ discrimination, one is for total component and the other for slow component. The TOF is obtained by measuring the time difference between the anode signals and the RF signal of the cyclotron by using TDC (time-to-digital converter). A set of three data for pulse-height (total and slow components) and TOF is acquired event by event for each detector.

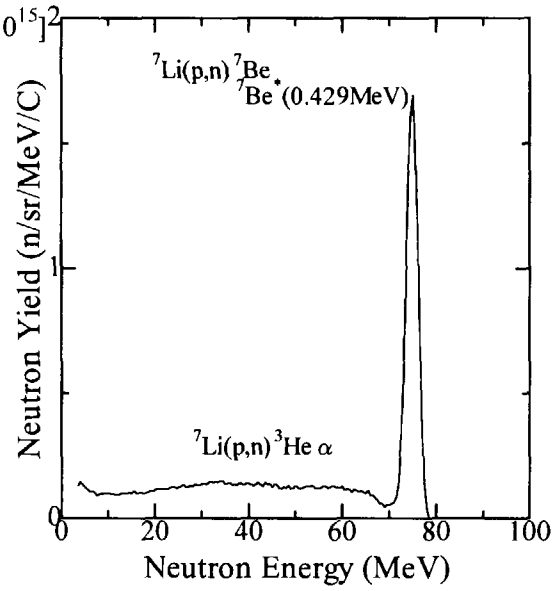

Fig.1 Source neutron spectrum

The TOF spectra were obtained at 25 points between 2.6° and 56° in laboratory scattering angle. In addition to sample measurements, background runs with no sample were done for removing the sample independent background. Scattering angle were changed by rotating the detector array. The flight paths were around 5m for forward angles and 2m for backward angles. Fission chambers (^{238}U and ^{232}Th) located near by the Li target were used as neutron monitor for normalization between foreground and background run. Thin plastic scintillator, which was set at collimator exit, monitored source neutron TOF spectrum. The absolute elastic scattering cross sections were determined relative to the incident neutron flux measured by the scintillation detectors, which were identical with ones for scattering measurements.

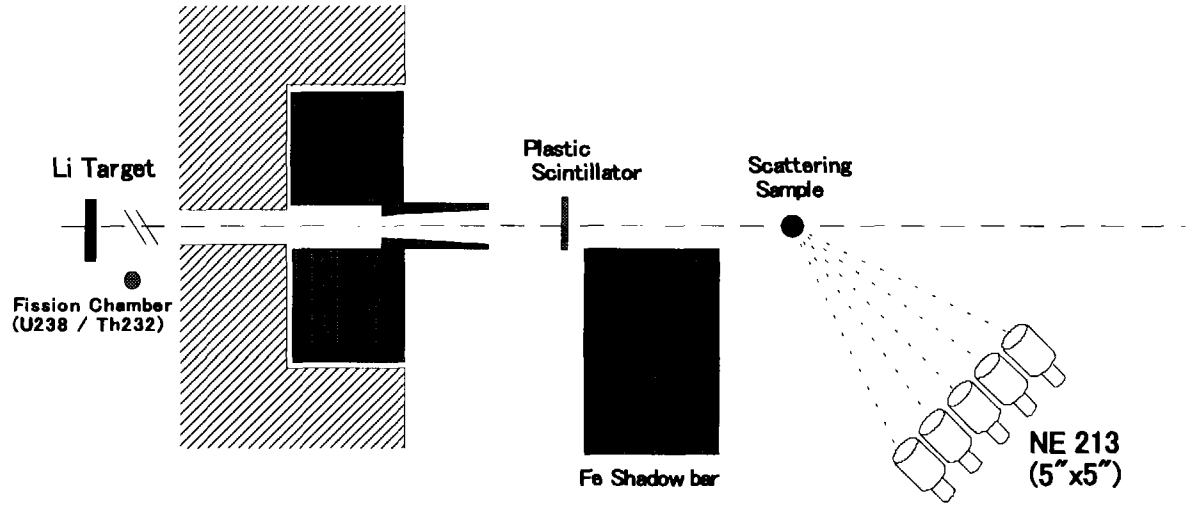

Fig.2 Experimental setup

3.Data reduction and correction

Figure 3 shows the TOF spectra for foreground and background in the Fe run. The peak area subtracted with a background was converted to cross sections. The elastic scattering cross sections deduced were further corrected for the effects of the inelastic scattering and the finite sample-size, i.e. the effect of flux attenuation and multiple scattering, by Monte Carlo calculation [5]. Corrections for the effects of inelastic scattering were to remove inelastically scattered neutrons included in the "elastic" peak because of limited energy resolution, and done by calculating the ratio of the inelastically scattered neutrons to the total (elastic and inelastic) ones considering experimental energy resolution. In this calculation, we used the LANL 150 MeV library [6] as input data for the neutron-sample nuclide interaction. In fig.4, the cross, triangle and circle indicate the raw data, sample size corrected data and inelastic neutron corrected data of Fe, respectively. Because of strong forward peaking of the elastic scattering angular distribution, inelastically scattered neutrons do not affect the results at forward angles, but the correction factors vary from 20% around 30° to 40% around 50°.

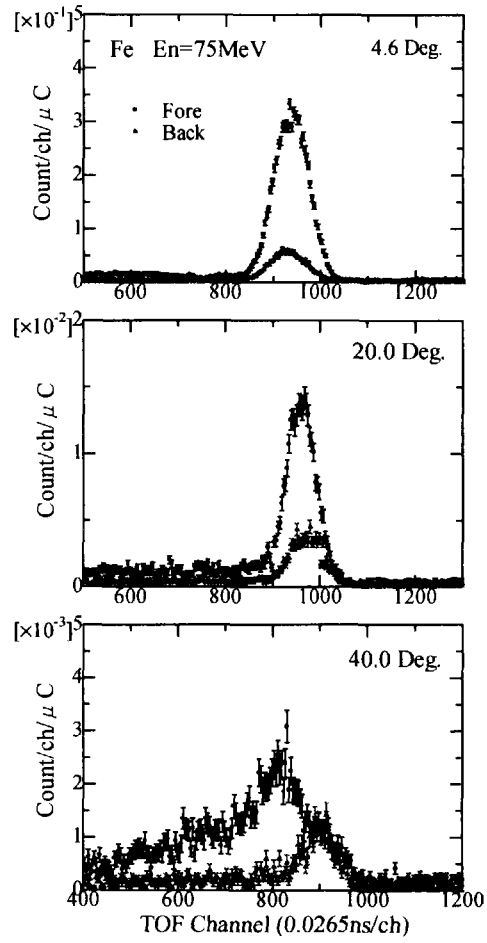

Fig.3 TOF spectra of Fe

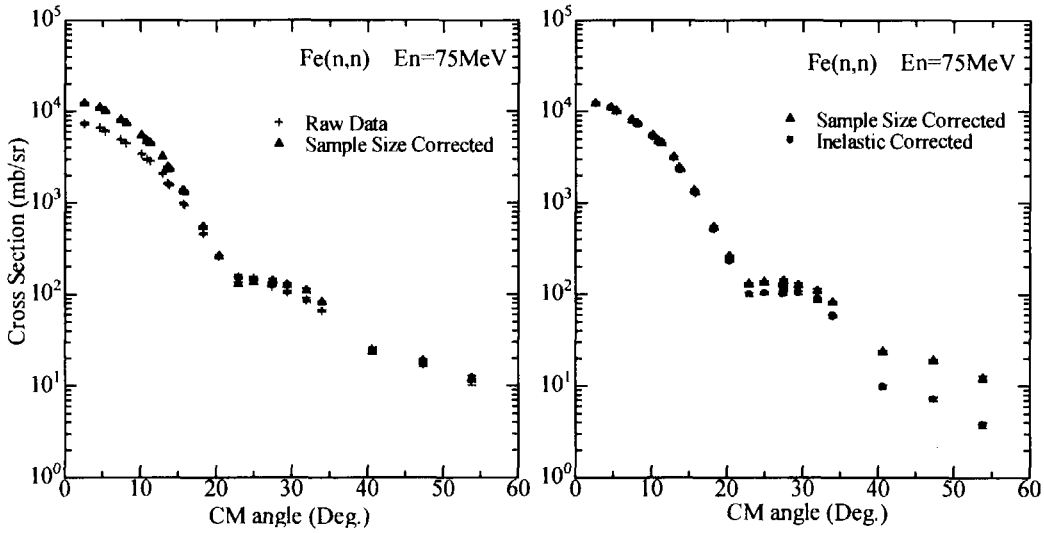

Fig.4 Correction for the effects of the sample size and the inelastic scattering neutrons

4.Results

Figure 5 shows the present results together with LANL 150 MeV library [6] and the experimental data at WNR/LAMPF [3]. Agreement between our experimental data and evaluation is good except for forward angle of carbon, but WNR/LAMPF data are milder forward peaking than our data and evaluation.

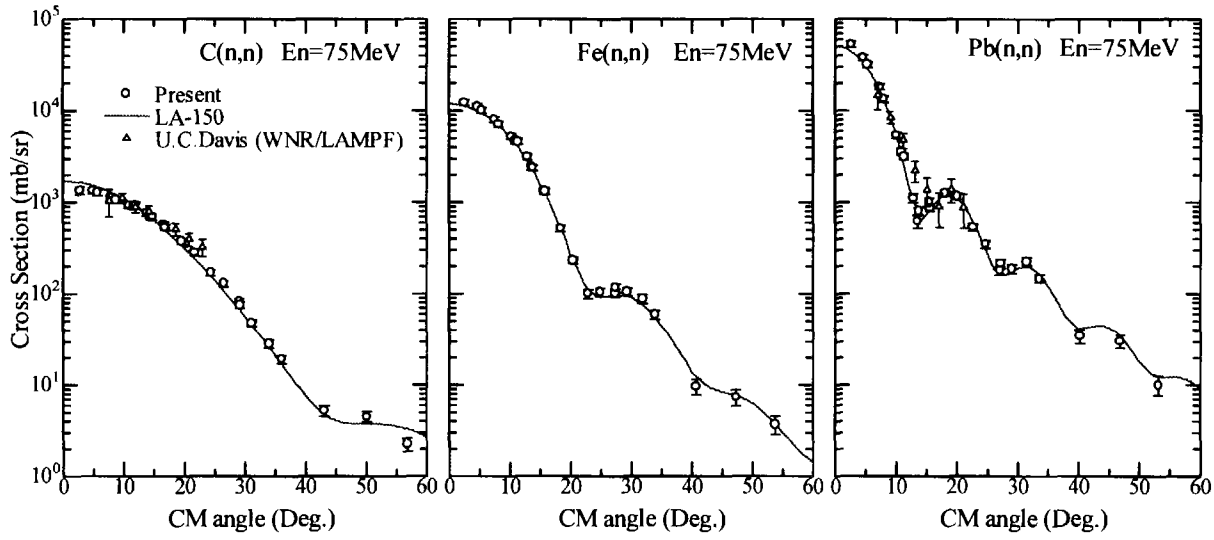

Fig.5 Comparison of the present data with the U.C.Davis data [3] and the LANL 150 MeV library [6]

Figure 6 shows comparison with the DLC119/HILO86 multi-group library [7] and the systematics used in the cascade/transport code [8]. These data were normalized to the experimental data at 0°. Both of the data show large discrepancy because DLC119 library applies P5 Legendre expansion and the systematics ignores scattering to backward angles.

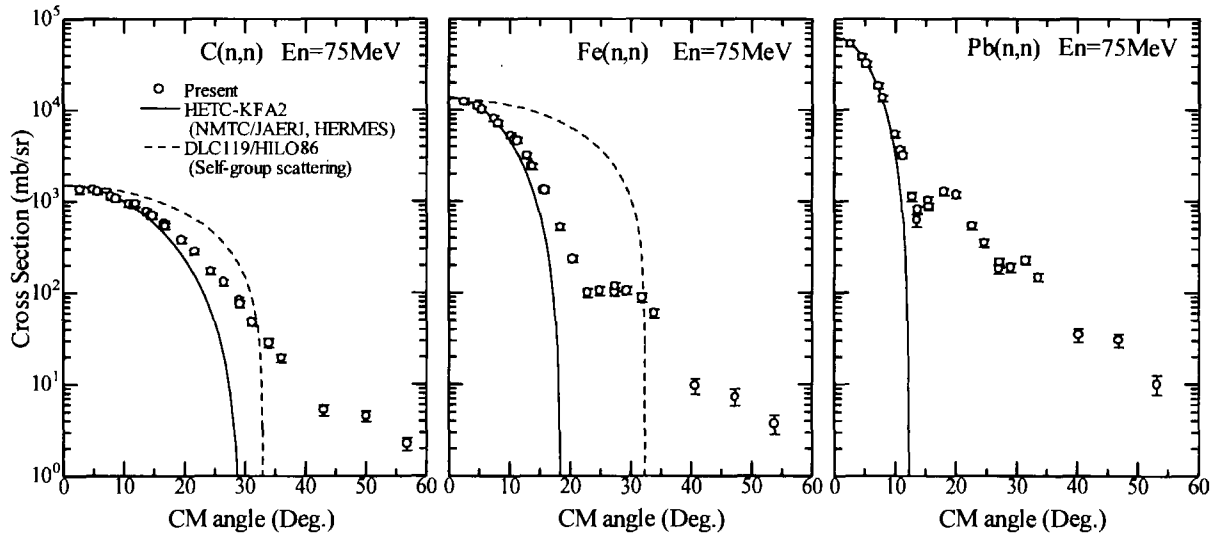

Fig.6 Comparison of the present data with the DLC119 Library [7] and the systematics [8]

Figure 7 shows comparison with the optical model calculations with the global potentials proposed by Madland [9] and JLM (Jeukene, Lejeune and Mahaux) [10]. The calculation results by JLM potential underestimates the experimental data with 10~20% at forward angles for carbon, iron and lead. The results by Madland potential agree with the experimental data for iron very well but differ largely for lead at backward angles.

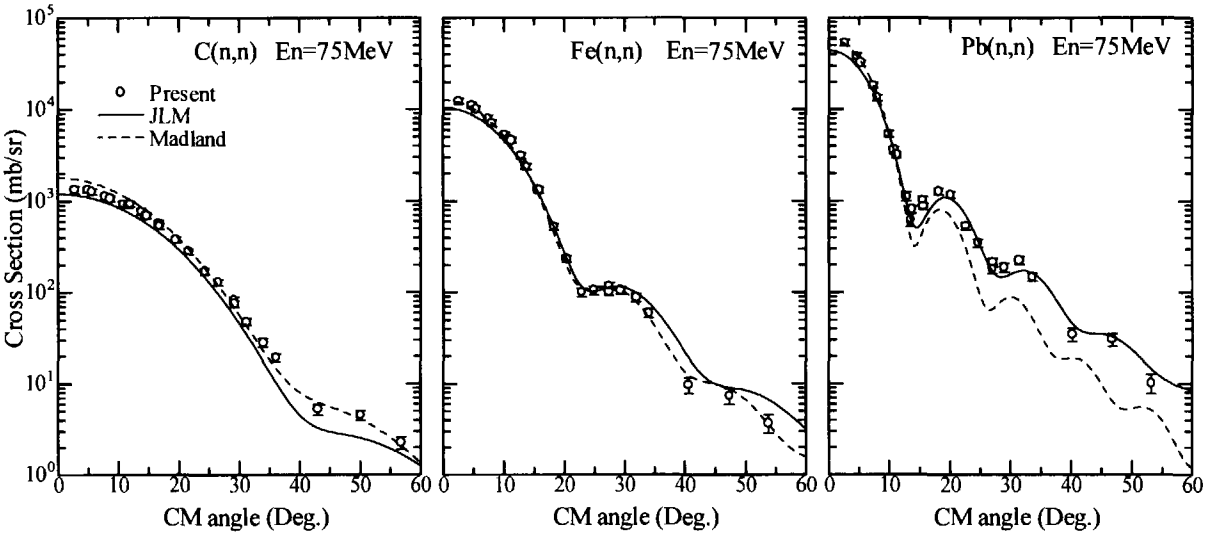

Fig.7 Comparison of the present data with the optical model calculations [9][10]

References

[1] H.Nakashima et. al., Nucl. Sci. Eng., 124, (1996) 243
[2] E.L.Hjort et.al., Phys. Rev. C 50, (1994) 275
[3] J.H.Osborne, Ph.D. Dissertation, University of California, Davis, 1995.
[4] M.Baba et. al., Nucl. Instrum., to be published
[5] M.Baba et. al., Nucl. Instrum. Methods A 366, (1995) 354
[6] M.B.Chadwick et. al., LANL report, LA-UR-98-1825, (1998)
[7] R.G.Alsmiller and J.M.Barish, ORNL/TM-7818, (1981)
[8] P.Cloth et. al., Jul-2203, Kernforschungsanlage Julich, (1988)
[9] D.G.Madland, Proc. OECD/NEANDC Specialist's Mtg. on Preequilibrium Nuclear Reactions, Semmering, Austria, 10-12 Feb. 1988, NEANDC-245 (1988)
[10] J.-P.Jeukenne et.al., Phys. Rev. C 16, (1977) 80

3.11 Benchmark Test of JENDL High Energy File with MCNP

Masayuki WADA, Fujio MAEKAWA, Chikara KONNO
Intense Neutron Source Laboratory, Department of Materials Science
Japan Atomic Energy Research Institute, Tokai-mura, Naka-gun, Ibaraki-ken 319-1195 JAPAN
e-mail: wada@fnshp.tokai.jaeri.go.jp

Hiroshi NAKASHIMA
Planning Division for Neutron Science, Center for Neutron Science
Japan Atomic Energy Research Institute, Tokai-mura, Naka-gun, Ibaraki-ken 319-1195 JAPAN

Kazuaki KOSAKO
Sumitomo Atomic Energy Industries, Ltd.
2-10-4, Ryogoku, Sumida-ku, Tokyo 130-0026 JAPAN

Benchmark tests of the preliminary version of JENDL High Energy File with the MCNP code have been continued. A problem in JENDL High Energy File is pointed out that the angular distribution of elastically scattered neutrons by iron-56 is too emphasized toward 0 degree. Good results are obtained in the analyses of concrete shield experiments and iron secondary gamma-ray experiments.

1. Introduction

Evaluation of JENDL High Energy (JENDL-HE) File is now in progress, and expected to be completed by the end of 1998 for the phase-I data up to 50 MeV. We have started benchmark tests of the preliminary version of JENDL-HE File for neutron transport cross section data up to 50 MeV by analyzing available shielding benchmark experiments [1-5] summarized in Table 1. The first results of the tests

Table 1 Benchmark experiments employed for the tests.

Facility / Institute	INS / Univ. Tokyo	RCNP / Osaka Univ.	TIARA / JAERI
Neutron Source	52-MeV Proton on Graphite	65-MeV Proton on Copper, Collimated	43- & 68-MeV Proton on Lithium, Collimated
Source Spectrum	White	White	Quasi-Mono-Energetic
Material	C, Fe, Concrete, Water	C, Fe, Pb, Concrete	Fe, Concrete, Polyethylene
Measured Quantity	Neutron & Photon Spectrum	Neutron & Photon Spectrum	Neutron Spectrum, Fission Rate
References	[1]	[2]	[3-5]

have been reported elsewhere [6]. After that, we have obtained some new findings about cross section data in JENDL-HE through the benchmark tests. In this report, results of the benchmark tests are described featuring the new findings.

2. Benchmark Calculation

The Monte Carlo transport calculation code MCNP-4B [7] was used for the benchmark calculations. Cross section data of the preliminary version of JENDL-HE were processed into an ACE format cross section data library for MCNP by the NJOY-94.66 code. The LA-150 cross section library up to 150 MeV [8], which is now being developed at Los Alamos National Laboratory, U. S., was also processed. Since JENDL-HE was under evaluation, some cross section data needed for the calculations were not available. Benchmark calculations were performed for the iron and concrete experiments in Table 1. Calculations for iron could be performed by using the JENDL-HE data while those for concrete were performed with cross section data of Al, Si,Ca and Fe in JENDL-HE File by supplying cross section data of H and O from ENDF/B-VI and 100XS [9], respectively.

Source neutron conditions provided by each benchmark experiment [1-5] were used as source terms for the neutron transport calculations. Neutron events were scored by track length estimators of which sizes were the same as the neutron detectors used in the experiments.

In the INS and RCNP experiments, gamma-ray spectra measured behind the shields were given. To test secondary gamma-ray production cross sections in the libraries, neutron-gamma-ray coupled transport calculations were also performed. Since the high energy proton bombardment on the targets generates source gamma-rays as well as source neutrons, gamma-ray transport calculations were performed with using source gamma-ray conditions obtained in the experiment [1, 2]. Gamma-ray spectra obtained in the source neutron and gamma-ray calculations were summed to compare with the experimental data.

Calculated results with JENDL-HE and LA-150 were compared with the experimental data and some previous calculations with the 100XS library.

3. Summary of the Previous Benchmark Test

Brief summary of the previous benchmark results [6] is as follows.

(1) In the analysis of the TIARA iron shield experiment, JENDL-HE underestimates neutron fluxes above 10 MeV with increase of shield thickness. This underestimation can be explained by the too small elastic and too large non-elastic scattering cross sections in the energy range from 20 to 50 MeV.

(2) Calculations with JENDL-HE give good results for concrete shields. In the analysis of the TIARA concrete shield experiment, calculated to experimental ratios (C/Es) for the peak neutron flux (35 ~ 45 MeV) and tail neutron flux (10 ~ 35 MeV) range from 0.9 to 1.5 for the shield thicknesses up to 150 cm.

(3) In the analysis of the FNS iron benchmark experiment [10, 11] for fusion, the calculation with JENDL-HE does not reproduce the experimental neutron spectrum in a low energy range from 1 eV to 1 MeV although calculated spectra with both JENDL Fusion File and JENDL-3.2 agree fairly well with the experimental data. The reason is that JENDL-HE does not adopt the validated elemental iron data in JENDL Fusion File nor JENDL-3.2 as the cross section data below 20 MeV but merges the isotopic iron data in JENDL Fusion File that have not been validated.

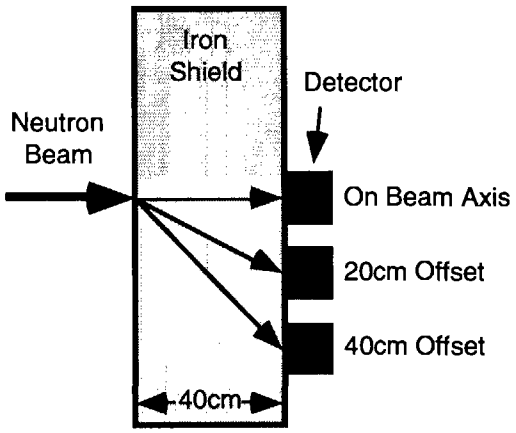

Fig. 1 Detectors located on the neutron beam axis and the two offset positions in the TIARA iron shield experiment. Detectors located with large offset distances are likely to observe neutrons scattered with large angles.

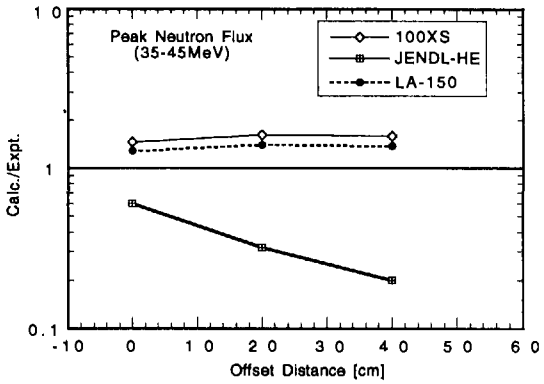

Fig. 3 The C/E values of peak neutron fluxes from 35 to 45 MeV for JENDL-HE, LA-150 and 100XS calculations as a function of the offset distance for the TIARA iron shield experiment.

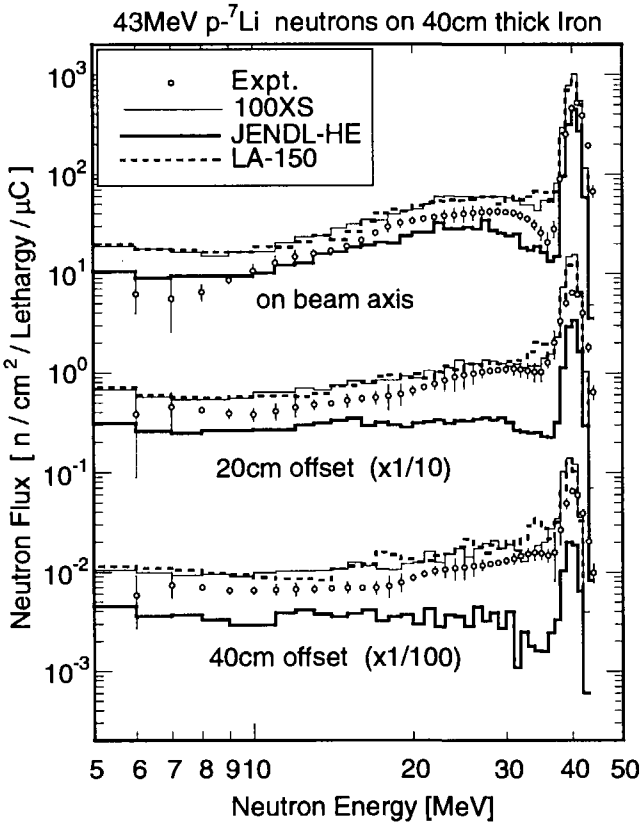

Fig. 2 Neutron spectra measured in the TIARA iron shield experiment in comparison with calculations with JENDL-HE, LA-150 and 100XS. Spectra are measured on the beam axis and with offset distances of 20 cm and 40 cm behind the iron shield of 40 cm thickness.

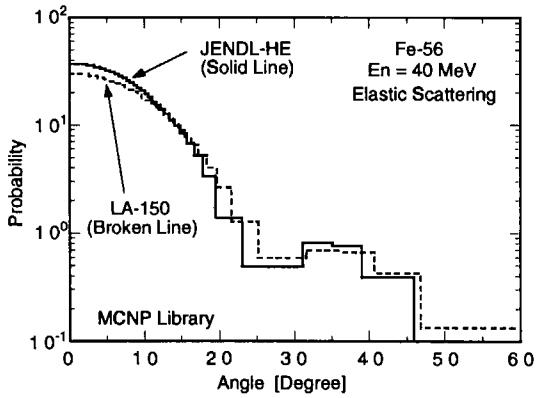

Fig. 4 Angular distribution of elastically scattered neutrons by iron-56 for incident neutron energy at 40 MeV contained in the MCNP libraries for JENDL-HE and LA-150.

4. New Findings through the Benchmark Test

In addition to the previous results, the following new findings were obtained.

(1) The TIARA shielding experiment has a unique feature that neutron spectra are measured at several detector positions not only on an extension of the incident neutron beam axis but also with offset distances of 20 cm and 40 cm as illustrated in Fig. 1. This feature is very useful to test angular distribution of scattered neutrons because neutron spectra measured with large offset distances likely to observe neutrons scattered with large angles. Figure 2 compares measured and calculated neutron spectra for the TIARA iron shield experiment. A trend is found in Fig. 2 that the calculation with JENDL-HE underestimates neutron fluxes with increase of the offset distance. The trend is exhibited clearly in Fig. 3 which shows C/E values for peak neutron fluxes for the neutron spectra in Fig. 2 as a function of the offset distance. The C/E curves by LA-150 and 100XS are almost flat while C/E values by JENDL-HE decrease with increase of the offset distance. A possible reason of the trend is found in the angular distribution of elastically scattered neutrons by iron-56 shown in Fig. 4. Anisotropy of the angular distribution toward 0 degree for JENDL-HE is too emphasized, and less neutrons are scattered with large scattering angles. When the angular distribution is emphasized toward 0 degree, the peak neutron flux measured on the beam axis (0 cm offset) will increase. However, the C/E value without the offset distance (0 cm) by JENDL-HE is still less than 1.0. This contradiction can be explained by the too small elastic scattering cross sections in JENDL-HE, as mentioned earlier.

The flat C/E curves by LA-150 and 100XS suggests that the angular distribution of secondary neutrons for the iron data in these libraries are adequate. Those C/E curves are, however, systematically larger than 1.0. A possible reason of this is that the elastic scattering cross section is somewhat larger contrary to JENDL-HE.

(2) Neutron spectra measured in the TIARA concrete shield experiment are compared with calculated results by JENDL-HE, LA-150 and 100XS in Fig. 5. The LA-150 result is newly obtained. All the three calculations predict the measured neutron spectra transmitted through the thick concrete shields up to 150 cm fairly good. Especially, the JENDL-HE calculation shows the best results among the three.

(3) Figures 6 and 7 show gamma-ray spectra behind the iron shields measured in the INS and RCNP experiments in comparison with calculated results by JENDL-HE and LA-150. In general, calculations with both libraries show good agreements with the experimental

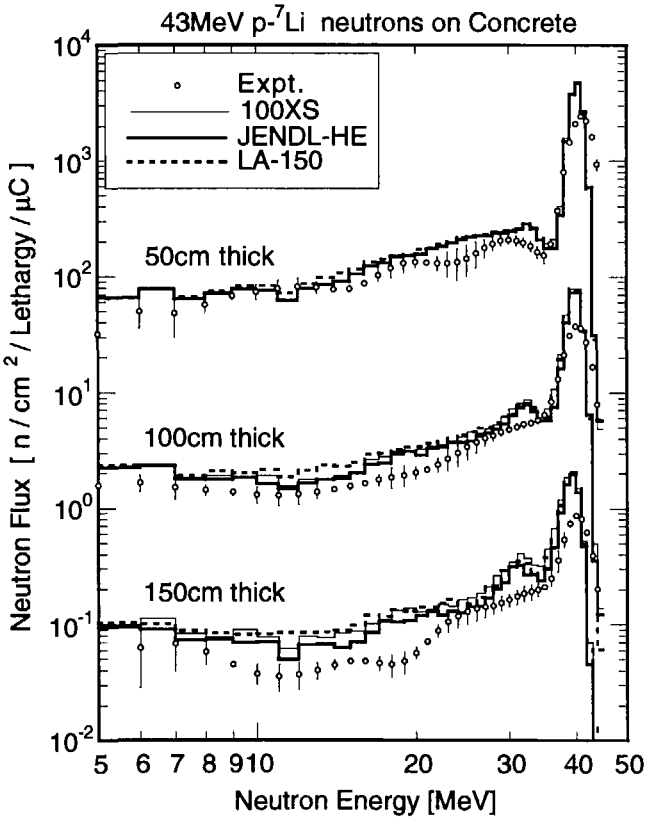

Fig. 5 Neutron spectra measured in the TIARA concrete shield experiment compared with calculations by JENDL-HE, LA-150 and 100XS.

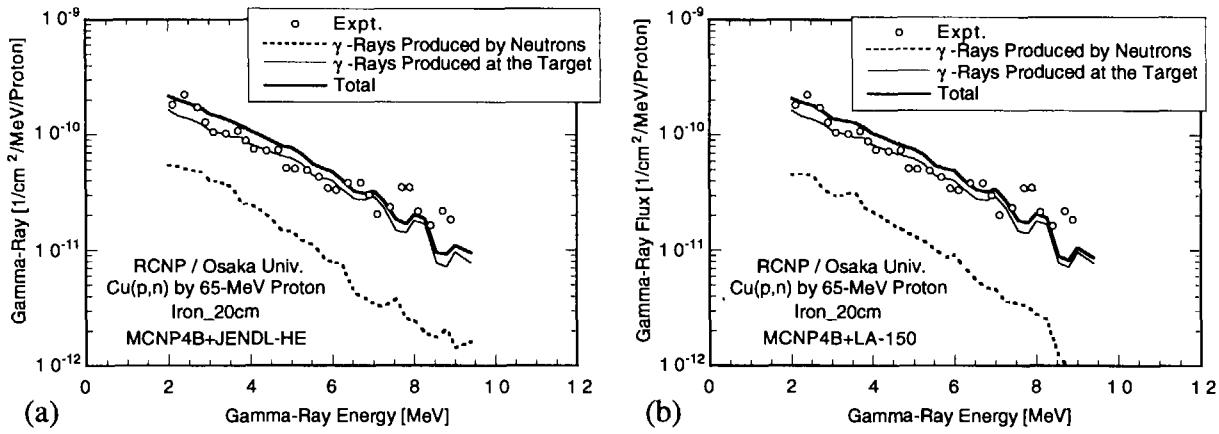

Fig. 6 Gamma-ray spectrum measured behind the iron shield of 20 cm in the RCNP experiment compared with the calculations by (a) JENDL-HE and (b) LA-150.

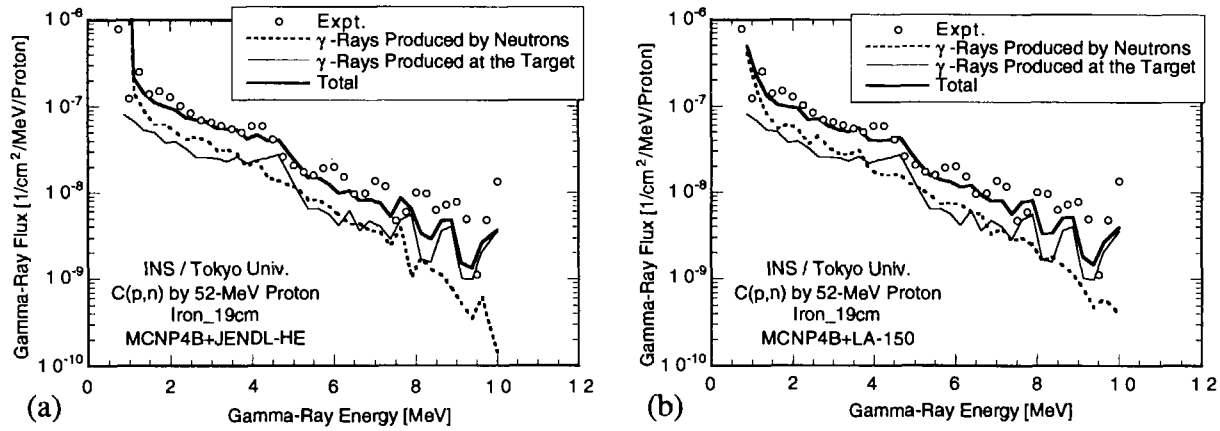

Fig. 7 Gamma-ray spectrum measured behind the iron shield of 19 cm in the INS experiment compared with the calculations by (a) JENDL-HE and (b) LA-150.

data. Gamma-rays observed have two origins: gamma-rays produced by neutron interactions in the iron shield, and gamma-rays produced at the target by high energy proton bombardment on the targets. The former component is obtained by the neutron-gamma-ray coupled calculations with source neutrons while the latter component is obtained by just gamma-ray transport calculations with source gamma-rays. Since what we should test here is secondary gamma-ray production cross section data, we are interested in only the former component. Those experiments, the RCNP experiment especially, are not very suitable for our purpose because the latter component is strong. Nevertheless, the general agreements between the measured and calculated gamma-ray spectra suggests that there is no serious problem in the gamma-ray production cross section data of iron in JENDL-HE and LA-150.

5. Concluding Remarks

Benchmark tests of the preliminary version of JENDL-HE with the MCNP code have been continued. A problem in JENDL-HE is pointed out that the angular distribution of elastically scattered neutrons by iron-56 is too emphasized toward 0 degree. Good results are obtained in the analyses of concrete shield experiments and iron secondary gamma-ray experiments. Problems found through the

tests are expected to be considered in revision of JENDL-HE.

Acknowledgments

The authors are grateful to Dr. T. Fukahori of JAERI Nuclear Data Center and Dr. S. Chiba of Research Group for Hadron Science for their help to conduct the benchmark tests.

References

[1] Uwamino Y., et al: Nucl. Sci. Eng., 80, 360 (1982).
[2] Shin K., et al.: Nucl. Sci. Eng., 109, 380 (1991).
[3] Nakao N., et al: Nucl. Sci. Eng., 124, 228 (1996).
[4] Nakashima H., et al.: Nucl. Sci. Eng., 124, 243 (1996).
[5] Nakao N., et al: Nucl. Sci. Eng., 134, 348 (1997).
[6] Maekawa F. and Wada M.: "Results of Benchmark Test with MCNP Code", Proc. 3rd Specialists' Meeting on High Energy Nuclear Data, March 30-31, 1998, JAERI/Tokai, JAERI-Conf 98-016, pp. 76-85 (1998).
[7] Briesmeister J. F. (Ed.): "MCNP™ - A General Monte Carlo N-Particle Transport Code, Version 4B", LA-12625-M, Los Alamos National Laboratory (1997).
[8] Young P. G. and Chadwick M. B.: "Neutron- and Proton-Induced Nuclear Data Libraries to 150 MeV for Accelerator-Driven Applications", Proc. International Conference on Nucl. Data for Sci. and Technol., 19-24 May, 1997, Trieste, Italy, pp. 1440-1442 (1998).
[9] Little R. C.: "Summary Documentation for the 100XS Neutron Cross Section Library (Release 1.0)", LA-UR-96-24, Los Alamos National Laboratory (1995).
[10] Konno C., et al.: Fusion Eng. Des., 18, 297 (1991).
[11] Maekawa F. and Oyama Y.: Nucl. Sci. Eng., 125, 205 (1997).

3.12 DORT Analysis of Iron and Concrete Shielding Experiments at JAERI/TIARA

Chikara KONNO, Fujio MAEKAWA, Masayuki WADA
Intense Neutron Source Laboratory, Japan Atomic Energy Research Institute
Tokai-mura, Naka-gun, Ibaraki-ken 319-1195 JAPAN
e-mail: konno@fnshp.tokai.jaeri.go.jp

Hiroshi NAKASHIMA
Planning Division for Neutron Science, Japan Atomic Energy Research Institute
Tokai-mura, Naka-gun, Ibaraki-ken 319-1195 JAPAN

Kazuaki KOSAKO
Sumitomo Atomic Energy Industries, Ltd.
2-10-4, Ryogoku, Sumida-ku, Tokyo 130-0026 JAPAN

The accuracy of DORT calculations with HILO86R and multigroup libraries processed from LA-150 (P_5 Legendre expansion) was investigated through the analysis of the shielding experiments on iron and concrete for 40 and 65 MeV neutrons at JAERI/TIARA.

1. Introduction

Legendre expansion order for scattering matrix in Legendre-expanded multigroup libraries is usually at most 5 because of calculation constraint. The accuracy of Sn calculations with multigroup libraries of P_5 Legendre expansion may become poor with increase of neutron energy since P_5 Legendre expansion can not present forward-peaked angular distribution of secondary neutrons precisely. Reference 1 showed that the two-dimensional Sn code DORT3.1 [2] calculations with multigroup libraries of P_5 Legendre expansion represent the shielding experiments for D-T neutrons as accurately as the continuous energy Monte Carlo code MCNP [3] calculations with libraries (no Legendre expansion) . P_5 Legendre expansion is considered to be adequate up to 14 MeV neutrons. Recently Sn calculations with HILO86 [4] or HILO86R [5], which is a multigroup library of P_5 Legendre expansion up to 400 MeV, are carried out for shielding calculation of ion accelerators of more than a few hundreds MeV. Therefore we analyzed the shielding experiments [6,7] on iron and concrete for p-^{7}Li quasi-monoenergetic source neutrons (40 MeV and 65 MeV) performed at JAERI/TIARA with DORT3.1 in order to examine accuracy of Sn calculations with multigroup libraries of P_5 Legendre expansion for neutrons above a few tens MeV.

2. Overview of Shielding Experiments on Iron and Concrete at JAERI/TIARA

The shielding experiments were performed with collimated p-^{7}Li neutron source of 40

and 65 MeV at Takasaki Ion Accelerator for Advanced Radiation Application (TIARA), at JAERI. Figure 1 shows the experimental arrangement. The test shield of iron and concrete from 10 cm up to 200 cm in thickness was located at the end of the collimator with or without an additional iron shield. Neutron spectra were measured with a BC501A scintillator and Bonner Ball detectors on the beam axis and at 20 and 40 cm off the beam axis behind the test shield.

3. Calculation Procedure

The Sn code DORT3.1 was used in the analysis. Only the collimated source neutrons and experimental assembly, which was modeled as a cylinder instead of a rectangular parallelepiped, were adopted in the analysis according to Ref. 5. The first collision source was calculated from collimated source neutrons with the GRTUNCL code. The following multigroup libraries (P_5 Legendre expansion) were used.

1) HILO86R, 2) LA-150 52g without ETA, 3) LA-150 100g without ETA,
4) LA-150 52g with ETA, 5) LA-150 100g with ETA

The multigroup libraries of 2) - 5) below 100 MeV were generated with NJOY94.105 [8] patched for LA-150 and TRANSX2.15 [9] codes from the nuclear data library LA-150 [10] up to 150 MeV which LANL released recently. The 52g and 100g mean the group structure; 52g is the same structure (52 groups) as that of HILO86R and 100g is the structure (100 groups) of 1 MeV interval from 0.5 MeV to 100.5 MeV. The ETA is an abbreviation of extended transport approximation [9], which was devised mainly for fast breeding reactors in order to mitigate the effects of truncating the Legendre expansion at finite order. The multigroup libraries of 4) and 5) were used to examine the effect of ETA on high energy neutrons. Moreover MCNP-4A calculations [11] were also carried out with the continuous energy library processed from LA-150 with NJOY94.105 for accuracy check of LA-150 itself.

4. Results and Discussion

The comparison between the calculations and measurements for neutron spectra above 10 MeV on the beam axis is carried out in this paper. Figure 2 shows the measured and calculated neutron spectra of the iron experiment for 43 MeV neutrons. The calculations overestimate neutron flux more with the thickness of the assembly. In order to compare the calculations with the measurements precisely, the ratios of the calculated values to the experimental ones (C/E) of integrated neutron flux at the peak and continuum regions are plotted in Figs. 3 - 10. The C/Es of all the calculations tend to increase with the thickness of assembly, though the increase rates of C/Es are different each other. The main reason of the overestimation of the calculations with LA-150 is attributed to LA-150 itself, since the increase tendency of C/Es also appears in the MCNP calculation. Although the DORT calculations with 100g are larger than those with 52g, the effect of the group structure is not so large since the largest difference is 20 %.

The DORT calculations without ETA are smaller than the MCNP calculation. This reason is that neutrons elastically scattered to forward direction are smaller since the multigroup libraries of P_5 Legendre expansion produce less forward-peaked angular distribution for elastic scattering than the original LA-150, which is strongly forward-peaked. It is noted that the DORT calculations without ETA underestimate the measurements even for thinner assemblies. This

reason is not clear yet, but this is also one of influences due to P_5 Legendre expansion. The C/Es of the DORT calculations without ETA are 0.5 - 2.1 for the assembly of more than 1 m in thickness. The DORT calculation with HILO86R shows the similar tendency with those without ETA. Probably the ETA is not considered in HILO86R.

The correction of the influences due to P_5 Legendre expansion by ETA seems to be well in the iron experiment for 43 MeV neutrons; the DORT calculations with ETA are similar with the reference MCNP calculations. However, the ETA overcorrects much in the other experiments; DORT calculations with ETA are larger by 2.5 times at maximum than the reference MCNP calculations. It is found that the ETA is not always appropriate for neutrons above a few tens MeV. The C/Es of the DORT calculations with ETA are 1.5 - 3.5 for the assembly of more than 1 m in thickness.

5. Concluding Remarks

The accuracy of DORT calculations with HILO86R and multigroup libraries processed from LA-150 (P_5 Legendre expansion) was investigated through the analysis of the shielding experiments on iron and concrete for 40 and 65 MeV neutrons at JAERI/TIARA. The following remarks were found through the comparison of measurements and calculations of neutron flux above 10 MeV.

1) All the calculations tend to overestimate the measurements with the thickness of assembly.
2) DORT (LA-150 without ETA) and DORT (HILO86R) is smaller by 50 % at maximum than MCNP (LA-150). Their C/Es are 0.5 - 2.1 for the assembly of more than 1 m in thickness. They also underestimate the measurements for thinner assemblies.
3) The ETA overcorrects the influences due to P_5 Legendre expansion too much. DORT (LA-150 with ETA) is larger by 2.5 times at maximum than MCNP (LA-150). Their C/Es are 1.5 - 3.5 for the assembly of more than 1 m in thickness.

References

[1] Konno C., et al. : Proc. 20th Symposium on Fusion Technology, Sep. 7-11, 1998, Marseille, France, pp. 1263 - 1266 (1998).
[2] Rhodes W.A. and Mynatt F.R. : Nucl. Sci. Eng., 99, 88 (1988).
[3] Briesmeister J.F. (edited): LA-12625-M, Los Alamos National Laboratory, (1993).
[4] Alsmiller R.G., et al. : ORNL/TM-9801 (1986).
[5] Kotegawa H., et al. : JAERI-M 93-020 (1993).
[6] Nakao N., et al. : Nucl. Sci. Eng., 124,228 (1996).
[7] Nakashima H., et al. : Nucl. Sci. Eng., 124,243 (1996).
[8] MacFarlane R.E. and Muir D.W.: LA-12740-M (1994).
[9] MacFarlane R.E. : LA-12312-MS (1992).
[10] Young P.G., et al. : Proc. International Conference on Nuclear Data for Science and Technology, May 19-24, 1997, Trieste, Italy, pp.1440 - 1442 (1998).
[11] Wada M. et al. : "Benchmark Test of JENDL High Energy File with MCNP," in this proceeding.

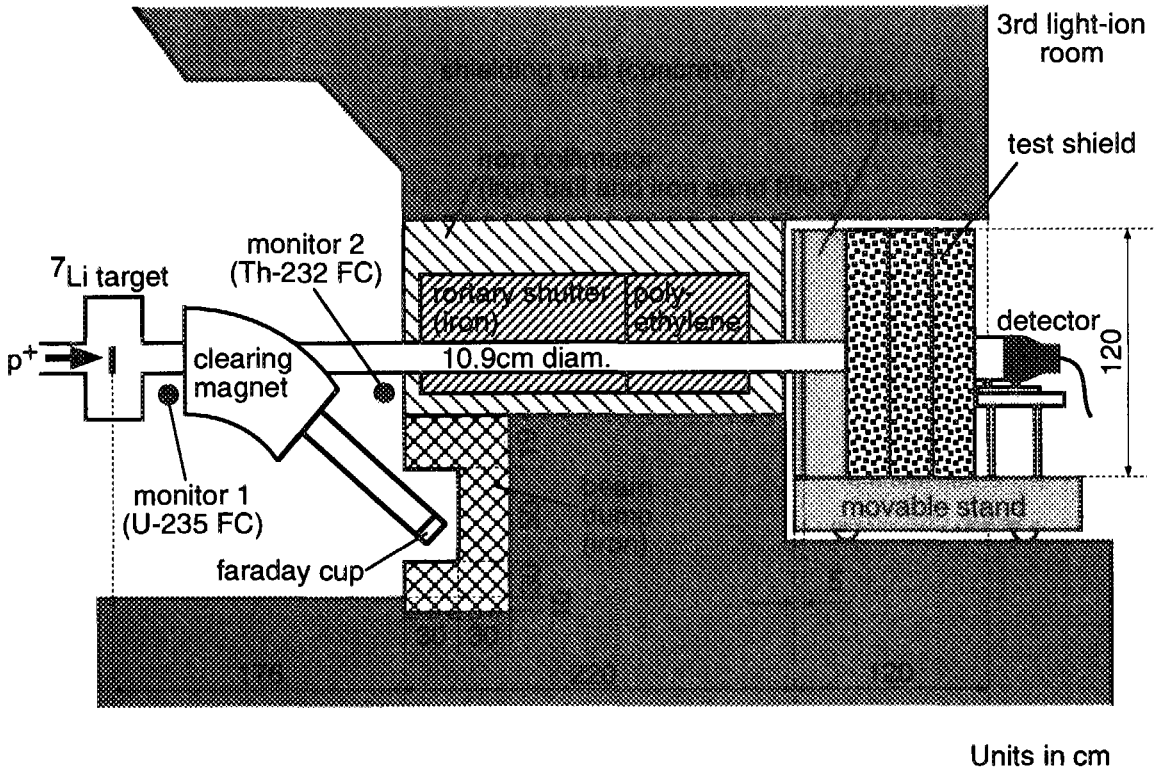

Fig. 1 Experimental arrangement of shielding experiments at JAERI/TIARA.

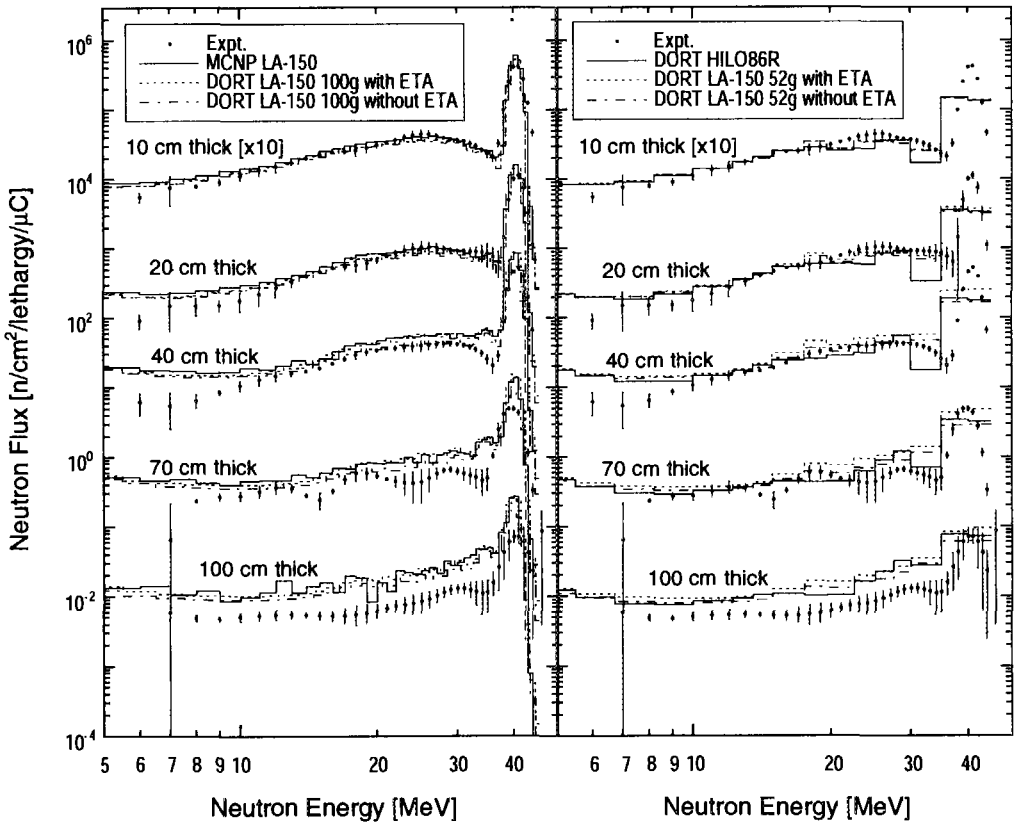

Fig. 2 Measured and calculated neutron spectra of the iron experiment for 40 MeV neutrons.

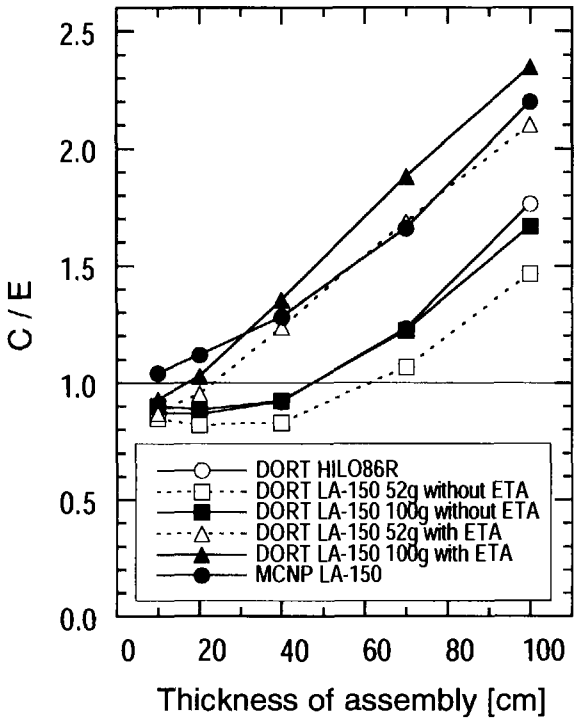

Fig. 3 C/E of peak neutron flux (35 - 45 MeV) of the iron experiment for 40 MeV neutrons.

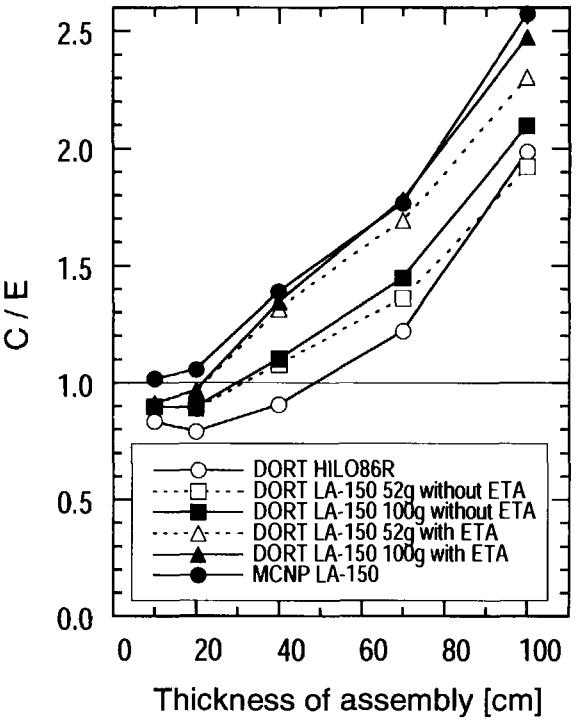

Fig. 4 C/E of continuum neutron flux (10 - 35 MeV) of the iron experiment for 40 MeV neutrons.

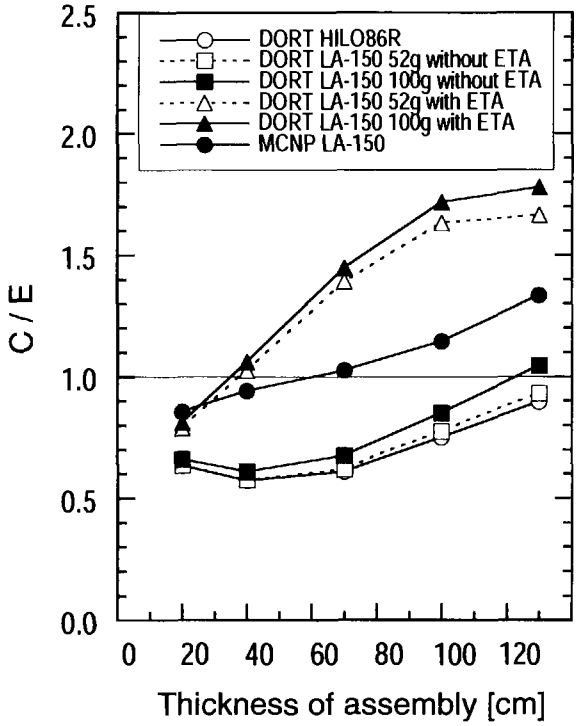

Fig. 5 C/E of peak neutron flux (60 - 70MeV) of the iron experiment for 65 MeV neutrons.

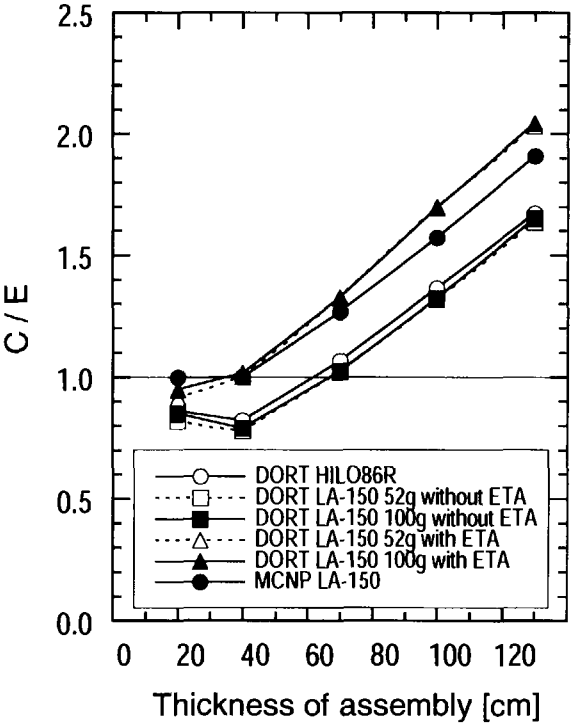

Fig. 6 C/E of continuum neutron flux (10 - 60 MeV) of the iron experiment for 65 MeV neutrons.

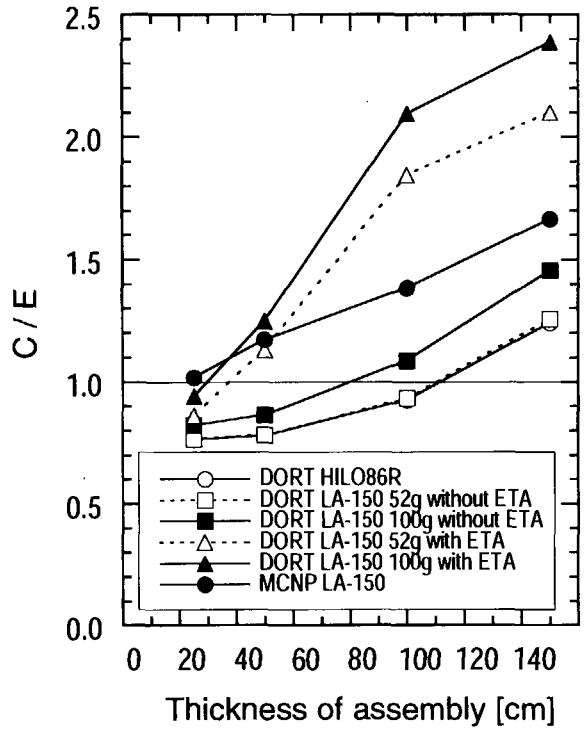

Fig. 7 C/E of peak neutron flux (35 - 45 MeV) of the concrete experiment for 40 MeV neutrons.

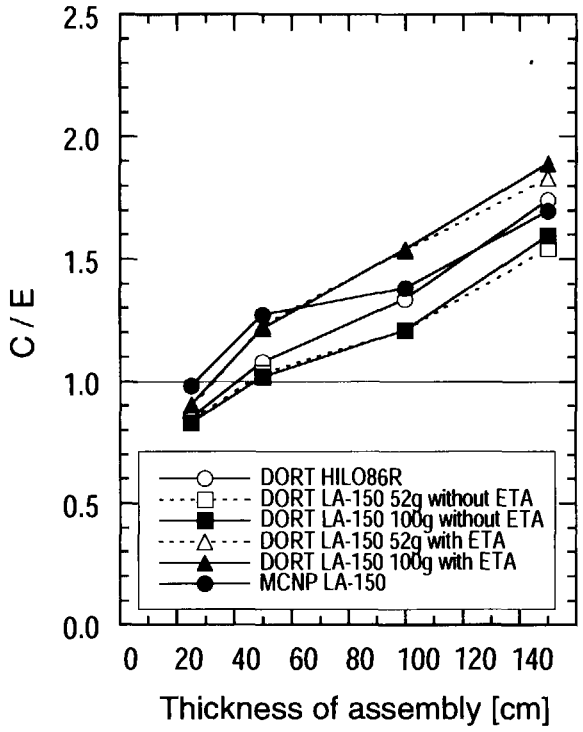

Fig. 8 C/E of continuum neutron flux (10 - 35 MeV) of the concrete experiment for 40 MeV neutrons.

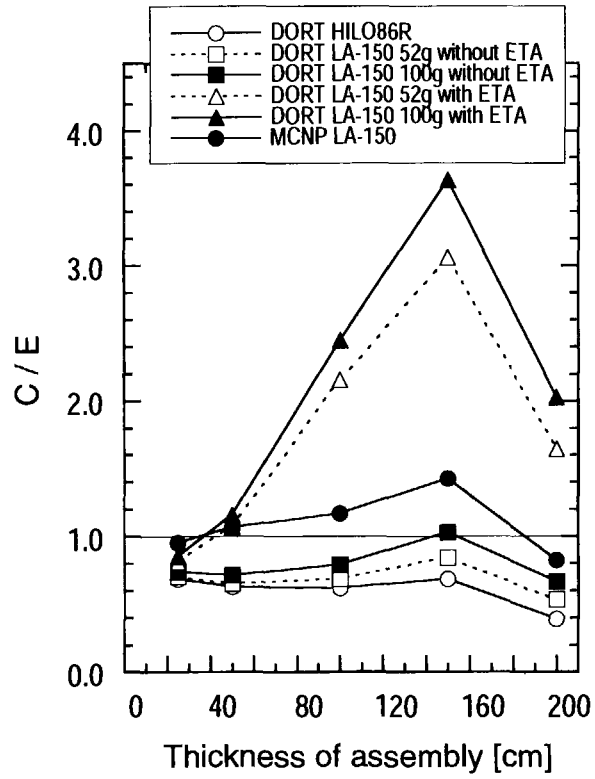

Fig. 9 C/E of peak neutron flux (60 - 70 MeV) of the concrete experiment for 65 MeV neutrons.

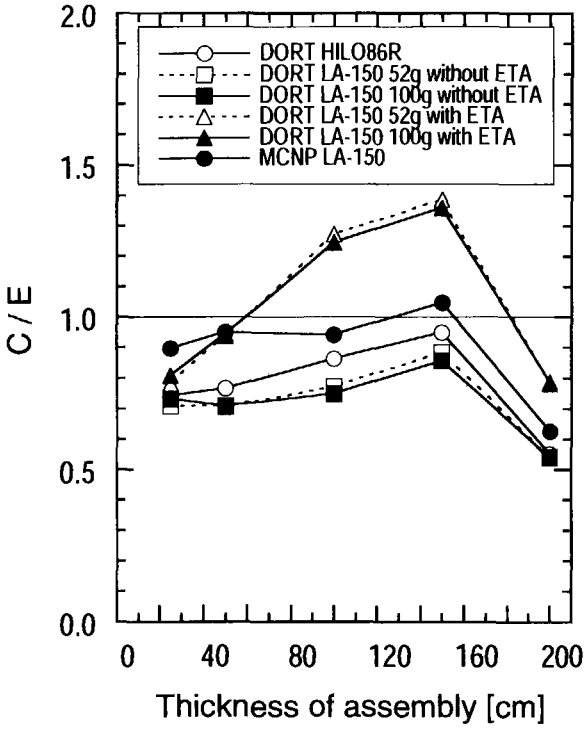

Fig. 10 C/E of continuum neutron flux (10 - 60 MeV) of the concrete experiment for 65 MeV neutrons.

3.13 Measurement of residual radioactivity in copper exposed to high energy heavy ion beam

Eunjoo Kim, Takashi Nakamura
Cyclotron and Radioisotope Center, Tohoku University
Aoba, Aramaki, Aoba-ku, Sendai 980, Japan
eunju@risun1.cyric.tohoku.ac.jp, nakamura@ cyric.tohoku.ac.jp

Yoshitomo Uwamino, Sachiko Ito
Institute of Physical and Chemical Research
Hirosawa, Wakooui, Saitama, 351-01, Japan
uwamino@postman.riken.go.jp, ito@postman.riken.go.jp

Akifumi Fukumura
National Institute of Radiological Sciences
9-1, Anagawa-4-chome, Inage-ku, Chiba 263, Japan
fukumura@nirs.go.jp

The residual radioactivities produced by high energy heavy ions have been measured using the heavy ion beams of the Heavy Ion Medical Accelerator (HIMAC) at National Institute of Radiological Sciences. The spatial distribution of residual radioactivities in 3.5cm, 5.5cm and 10cm thick copper targets of 10cm×10cm size bombarded by 290MeV/u, 400MeV/u-^{12}C ion beams and 400MeV/u-^{20}Ne ion beam, respectively, were obtained by measuring the gamma-ray activities of 0.5mm thick copper foil inserted in the target with a high purity Ge detector after about 1hour to 6 hours irradiation.

1. Introduction

In radiation safety design of high energy and high intensity accelerator, the evaluation of residual radioactivities of accelerator and shielding materials is very important for protection of radiation workers, especially during maintenance work. The radioactivities of air, coolant water and soil are also important for protection of natural environment and nearly inhabitants. The residual radioactivities are produced by accelerating charged particles and secondary neutrons. Those by charged particles are a main source in accelerator materials exposed to a beam. Nevertheless, there exist very few experimental data of residual radioactivities produced by high energy heavy ions and the accurate estimation method has not been established yet. Several experimental studies on the reaction between carbon ion beam and copper target have been reported at projectile energies of 15 to 90MeV/u [1-3]. In this study, we performed irradiation experiments of copper target using the 290MeV/u and 400MeV/u ^{12}C ions and 400MeV/u ^{20}Ne ion beams of the Heavy Ion Medical Accelerator in Chiba (HIMAC) at National Institute of Radiological Sciences.

2. Materials and Methods

Irradiation was performed with 290 and 400MeV/u-^{12}C ion beams , and 400MeV/u-^{20}Ne ion beam delivered from HIMAC. Figure 1 shows an assembly of the natural copper target of 10cm×10cm size and 0.5cm thickness which has total thickness of copper target of 3.5cm, 5.5cm and 10cm to stop the projectile heavy ion beams, 290 and 400MeV/u-^{12}C ion beam and 400MeV/u-^{20}Ne ion beam, respectively. Additional copper activation foils of 10cm×10cm and 0.5mm thickness were inserted at every 5mm to 20mm interval in the copper target to measure the spatial distribution of residual radioactivities in the copper target.

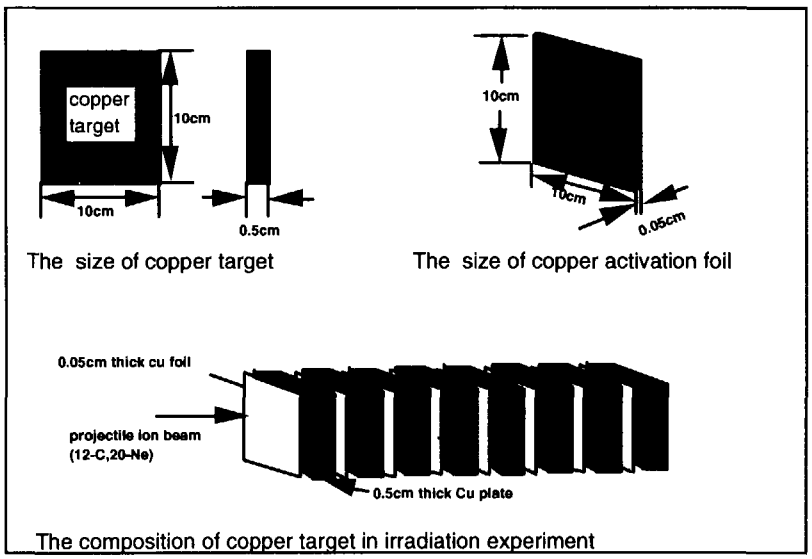

Fig.1 : Schematic view of copper target assembly used for irradiation experiment

The size of projectile beam is about 1cm in diameter and the beam perpendicularly bombarded the target. The irradiation condition and the activation foils used in the experiment are listed in Table1. During irradiation experiment, the beam intensities were measured with an transmission-type ionization chamber .

Table1 Projectile beam and activation foil used for irradiation experiment

Projectile heavy ion beam	Integrated beam intensity	Irradiation time	Activation foil
290MeV/u ^{12}C	1.949×10^{-7} C	1 hour	^{nat}Cu
400MeV/u ^{12}C	2.006×10^{-7} C	1 hour	^{nat}Cu
400MeV/u ^{20}Ne	2.666×10^{-7} C	1 hour	^{nat}Cu
400MeV/u ^{12}C	8.186×10^{-6} C	6 hour	^{27}Al, ^{nat}Fe, ^{nat}Cu, SUS

The gamma rays from residual radioactivities in copper foil inserted in the copper target were

measured by the high purity Ge detector by coupling with the 4096 multi-channel analyzer. The measuring time of copper foils was between 60min and 5hours, and the cooling time was between 6min and 5days from beam off, considering the half lives of residual radioactive nuclides.
From the measured gamma-ray spectra , we identified a number of radionuclides and the reaction rate of residual nuclei were obtained from the peak counts after corrected with the peak efficiency of Ge detector

3. Results and Discussion

From the irradiation experiments, we identified the residual nuclei of these activation foils and obtained the spatial distribution of their reaction rates in the copper target. Table2 gives the measured residual nuclides in copper activation foil. The number of identified radionuclides is 14, 17 , 20 and 38, the mass number of residual nuclides is between 27(^{27}Mg) and 61(^{61}Cu) for 290MeV/u ^{12}C ion bombardment during 1hour irradiation time, 24(^{24}Na) and 61(^{61}Cu) for 400MeV/u ^{12}C ion bombardment during 1hour irradiation time, 27(^{27}Al) and 63(^{63}Zn) for 400MeV/u ^{20}Ne ion bombardment during 1hour irradiation time, 7(^{7}Be) and 63(^{63}Zn) and for 400MeV/u ^{12}C ion bombardment during 6 hours irradiation time, respectively.

Table 2 Residual nuclides measured in the copper activation foil

Projectile heavy ion beam	Residual nuclides in copper activation foil
290MeV/u ^{12}C ion-^{nat}Cu	^{27}Mg, ^{29}Al, ^{34m}Cl, ^{38}Cl, ^{39}Cl, ^{41}Ar, ^{44}Sc, ^{49}Cr, ^{56}Mn, ^{53}Fe, ^{61}Co, ^{62m}Co, ^{60}Cu, ^{61}Cu (14)
400MeV/u ^{12}C ion-^{nat}Cu	^{24}Na, ^{29}Al, ^{34m}Cl, ^{38}Cl, ^{39}Cl, ^{40}Cl, ^{41}Ar, ^{43}Sc, ^{44}Sc, ^{49}Cr, ^{52m}Mn, ^{56}Mn, ^{53}Fe, ^{61}Co, ^{62m}Co, ^{60}Cu, ^{61}Cu (17)
400MeV/u ^{20}Ne ion-^{nat}Cu	^{24}Na, ^{29}Al, ^{38}Cl, ^{40}Cl, ^{41}Ar, ^{43}Sc, ^{44}Sc, ^{44m}Sc, ^{49}Cr, ^{52}Mn, ^{52m}Mn, ^{56}Mn, ^{53}Fe, ^{61}Co, ^{62m}Co, ^{60}Cu, ^{61}Cu, ^{56}Ni, ^{65}Ni, ^{63}Zn (20)
400MeV/u ^{12}C ion-^{nat}Cu	^{7}Be, ^{24}Na, ^{28}Mg, ^{29}Al, ^{34m}Cl, ^{38}Cl, ^{39}Cl, ^{41}Ar, ^{42}K, ^{43}K, ^{44}K, ^{43}Sc, ^{44m}Sc, ^{44}Sc, ^{46}Sc, ^{47}Sc, ^{48}Sc, ^{48}V, ^{49}Cr, ^{51}Cr, ^{52}Mn, ^{54}Mn, ^{56}Mn, ^{52}Fe, ^{59}Fe, ^{55}Co, ^{56}Co, ^{57}Co, ^{58}Co, ^{61}Co, ^{62m}Co, ^{60}Cu, ^{61}Cu, ^{56}Ni, ^{57}Ni, ^{65}Ni, ^{62}Zn, ^{63}Zn (38)

Figures 2 to 5 show the spatial distributions of ^{61}Cu, ^{56}Mn, ^{44}Sc and ^{38}Cl in the copper target for 290 and 400MeV/u ^{12}C ion and 400MeV/u ^{20}Ne ion bombardments.
Figures 2 and 3 show the spatial distributions of ^{61}Cu and ^{56}Mn in the copper target for 290 and 400MeV/u ^{12}C ion and 400MeV/u ^{20}Ne ion bombardments. These figures indicate that the

spatial distributions of activation rates of ^{61}Cu and ^{56}Mn which are close to the target nucleus of natural Cu (^{63}Cu and ^{65}Cu) increase with penetrating the copper target, while on the other hand, the spatial distributions of ^{44}Sc and ^{38}Cl which have much smaller atomic number and mass number than natural Cu have a constant distribution in the copper target and steeply decrease at the point of energy range of the incident beam (2.5cm for 290MeV/nucleon ^{12}C , 4.0cm for 400MeV/u- ^{12}C and 2.5cm for 400MeV/u-^{20}Ne). It is also clear from Figs.2 to 5 that the spatial distributions of ^{61}Cu, ^{56}Mn, ^{44}Sc and ^{38}Cl which were produced by the 290 and 400MeV/u-^{12}C ions give similar activation rate curves with depth each other and steeply decrease at the stopping range of an incident beam, especially for ^{44}Sc and ^{38}Cl activation rates. We can find that the ^{61}Cu and ^{56}Mn spatial distributions extend in the copper target beyond the energy range of an incident beam, especially for 400MeV/u-^{12}C and ^{20}Ne ion incidences. This may be explained from the phenomenological fact that the ^{61}Cu and ^{56}Mn isotopes were mainly produced through ^{nat}Cu (n,xn) and (p,px) reactions by the secondary fragment particles, such as protons and neutrons, produced by ^{12}C interaction with copper, in addition to that by the direct reactions of an incident beam. On the other hand, ^{44}Sc and ^{38}Cl isotope productions have rather high threshold energy and were mainly produced by the direct reactions of ^{12}C and ^{20}Ne ion beams with copper target.

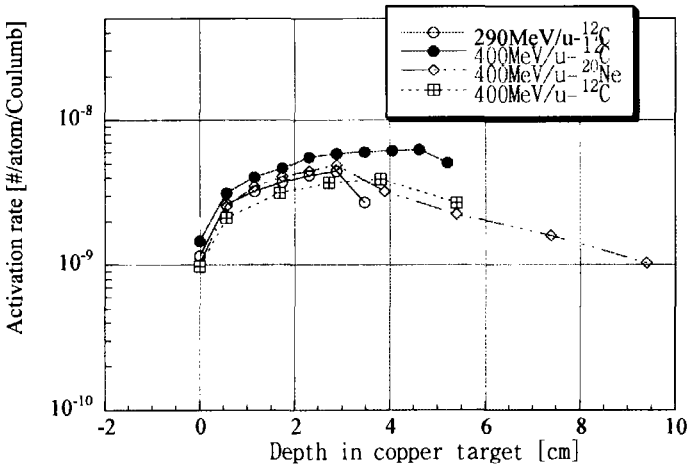

Fig.2 Spatial distribution of ^{61}Cu activation rate in the copper target

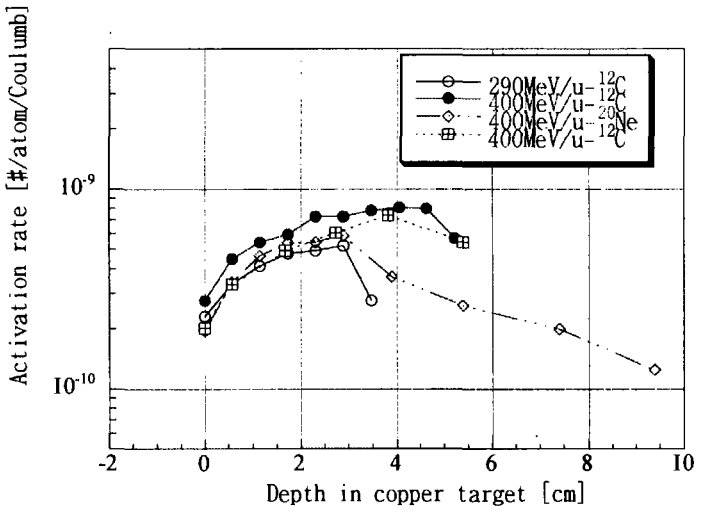

Fig.3 Spatial distribution of ^{56}Mn activation rate in the copper target

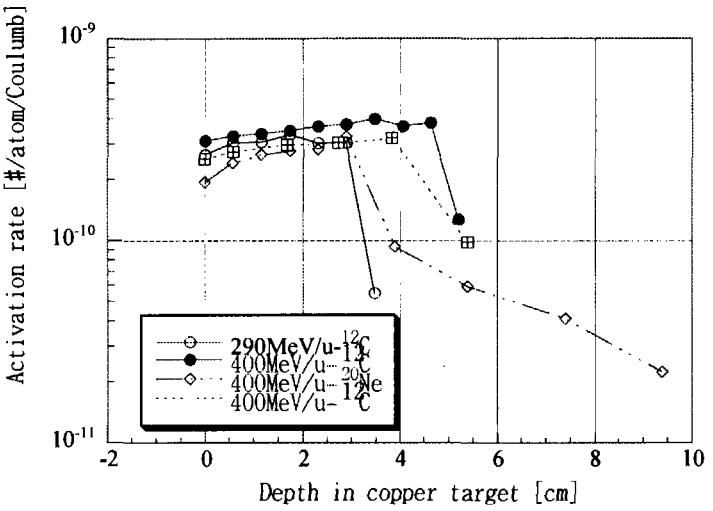

Fig.4 Spatial distribution of ^{44}Sc activation rate in the copper target

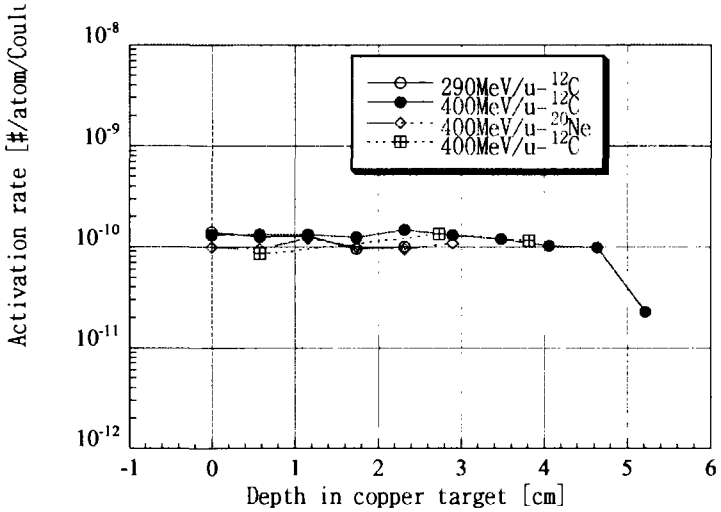

Fig.5 Spatial distribution of ^{38}Cl activation rate in the copper target

Acknowledgments

This work has been done as a Research Projectile with Heavy Ions at NIRS-HIMAC (National Institute of Radiological Sciences).

References

[1]Whitfield. J.P., Porile.N.T. : Phys. Rev. C47, 1636 (1993)
[2]Land T., Kolzahan D., Bergersen B., Hagebo E., Haldorsen I.R., Richared-Serre C.,: Z.Phys,A306,43(1982).
[3]Li Wenxin , Sun Tongyu, Wu Dingqing, Sun Rulin.: Radiochimaca Acta 72, 109 (1996)
[4]Annals of the ICRP, ICRP publication 51. (1987)

JP9950331

3.14 Measurements of Thermal Neutron Capture Cross Sections for some FP Nuclides

Shoji NAKAMURA[1], Kazuyoshi FURUTAKA[1], Hideo HARADA[1] and Toshio KATOH[1,2]

1 Japan Nuclear Cycle Development Institute, Tokai Works, Tokai-mura, Naka-gun, 319-1194
2 Visiting staff at Gifu College of Medical Technology, Ichihiraga, Seki, 501-3892
E-mail : rgm@tokai.pnc.go.jp

The thermal neutron capture cross sections (σ_0) and the resonance integrals (I_0) of some FP elements, such as ^{80}Se, ^{94}Zr, ^{124}Sn, ^{127}I and ^{133}Cs, were measured by the activation and γ-ray spectroscopic method.

1. Introduction

The thermal neutron capture cross sections (σ_0) and the resonance integrals (I_0) of long-lived fission products (FP) is required for the transmutation study by reactor neutrons in the nuclear waste management. The nuclear waste, sometimes, contains a large amount of stable nuclei having the same atomic number as that of long-lived FP. These stable nuclei absorb thermal neutrons during the neutron irradiation of the nuclear waste and disturb the neutron filed near the objective target nuclei; the reaction rate of the target nuclei will be reduced. Also, more radioactive nuclei may be produced by the neutron capture process of the stable nuclei. Therefore, the cross section data are needed for the stable nuclei, such as ^{80}Se, ^{94}Zr, ^{124}Sn, ^{127}I and ^{133}Cs.

2. Experiment

The cross section measurements for those nuclei were performed by the activation and γ-ray spectroscopic method. The high purity(99.99%) natural SeO_2, ZrO_2, SnO_2 and CsCl powders were used as targets. The ^{127}I elements were also used for the target, which were involved in the ^{129}I standardized solution as the contamination, since the measurements were performed together with those for ^{129}I. The adequate amount of each sample was poured into each quartz case. The wires of 0.112wt% Au/Al alloy (0.510mm in diameter) and 0.46wt% Co/Al alloy (0.381mm in diameter) were used as activation detectors to monitor the neutron flux. The method of measuring the neutron flux was the same for the cross section measurements, and will be explained later in **Sec. 3**.

The irradiations were performed in the rotary specimen rack (RSR) of the Research Reactor TRIGA MK-II at Rikkyo University, whose thermal neutron flux was 5.0×10^{11} n/cm^{2}sec and the epithermal index of Westcott's convention[(1)] 0.039. Each target was irradiated without and within a Cd capsule (1mm in thickness, 22mm in outer diameter and 63mm in outer length). The Cd capsule was used to reduce the flux of thermal neutrons at the target.

The yields of γ-rays emitted from the irradiated targets were measured by a high purity Ge detector with a 90% relative efficiency and an energy resolution of 2.1keV FWHM at 1.33MeV of ^{60}Co. The details of the data taking system were described elsewhere[(2)].

3. Analysis

The following equations obtained by modifying Westcott's convention[1] were used for analysis to deduce neutron fluxes at the irradiation position and cross sections. Equations based on Westcott's convention are rewritten[2] by using simplified flux notation as follows;

$$R/\sigma_0 = \phi_1 + \phi_2 s_0 \tag{1}$$

for irradiation without the Cd shield capsule,

$$R'/\sigma_0 = \phi_1' + \phi_2' s_0 \tag{2}$$

for irradiation with the Cd shield capsule. Here, the R (or R') is the reaction rate, σ_0 the thermal neutron (2,200m/s neutron) capture cross section, and s_0 is defined by

$$s_0 = \frac{2}{\sqrt{\pi}} \frac{I_0'}{\sigma_0} \tag{3}$$

where I_0' is the reduced resonance integral after subtracting the 1/v components. The resonance integral I_0 is calculated as follows;

$$I_0 = I_0' + 0.45\sigma_0 \tag{4}$$

where $0.45\sigma_0$ is the 1/v contribution given by assuming the Cd cut-off energy to be 0.5eV.

Using the known data of the cross sections σ_0 and the parameter s_0 for cobalt and gold, the values of the flux terms $\phi_{1,2}$ and $\phi'_{1,2}$, were determined by solving the simultaneous equations for cobalt and gold from Eqs. (1) and (2). **Table 1** summarized the experimental results of the R and R' values of the flux monitors, and also the neutron flux.

After the deletion of σ_0, Eqs.(1) and (2) give the relation,

$$s_0 = -\frac{\phi_1 - \phi_1'(R/R')}{\phi_2 - \phi_2'(R/R')}, \tag{5}$$

so that the s_0 value for each target nuclide is obtained from R/R' value of each irradiated target. The value of σ_0 is obtained by substituting the s_0 into Eq.(1), and then the values of I_0' and I_0 are calculated from Eqs.(3) and (4).

4. Results and Discussion

The results of the cross sections were shown in **Tables 2-6** together with the previously reported data.

Selenium-80

The cross sections for the formations of the isomeric state ^{81m}Se and the ground state ^{81g}Se were measured respectively by following the γ-ray counting rate after the irradiation. The present results are listed in Table 2 together with the values reported previously[3]-[6]. The present data of

$\sigma_{0,m+g}$ and $I_{0,m+g}$ in the reaction $^{80}Se(n,\gamma)^{81m,g}Se$ support the evaluated ones. The $\sigma_{0,m}$ for the formation of the ^{81m}Se was 43% smaller than the value (0.08 b) reported by Holden et al[4]. This reason is owed to the revision of the γ-ray emission probability data from 9.7%[7] to 12.7%[8].

Zirconium-94

The present results are listed in Table 3 together with the data reported previously[9],[10],[11]. The σ_0 value for ^{94}Zr supports the evaluated one. The present result of I_0 was 14% smaller than the evaluated one, but close to the value given by Santry et al[10]. The ratio of I_0/σ_0 was found to be 5.78 which agreed with the measured value by Moens et al[9]. The present values for ^{94}Zr have the consistency in point of the results of the σ_0 value and the I_0/σ_0 ratio. This fact supports the reliability of the present values.

Tin-124

The present results for ^{124}Sn are listed in Table 4. There have been no previously reported values for the reaction $^{124}Sn(n,\gamma)^{125g}Sn$. The measurements of the $\sigma_{0,g}$ and $I_{0,g}$ for the formation of ^{125g}Sn were performed in the present work. However, the γ-ray emission probability data for ^{125g}Sn had 30% error. After now, the accurate measurement of the γ-ray emission probability should be performed by means of β-γ coincidence counting technique[12].

Iodine-127

The present results for ^{127}I are listed in Table 5 with the data reported[13],[14]. The value of the thermal neutron capture cross section was 6.40 ± 0.29 b and in agreement with the evaluated and previously reported data within the limit of the error, but not in agreement with the data, 4.7 ± 0.2 b by Friedmann et al[14]. The difference between the present result and the result by Friedmann et al. may be caused by the difference of the γ-ray emission probability used for the deduction of reaction rate from the γ-ray peak counts. Friedmann et al. used a value of 0.16 for the emission probability of the 443keV γ-ray from the reaction product ^{128}I. The emission probability of this γ-ray was measured recently by Miyahara et al.[15] by using a two dimensional $4\pi\beta$–γ coincidence method, and was determined as 0.1261 ± 0.0008. If the new value of 0.1261 for the emission probability of the 443keV γ-ray is used in the analysis of the data by Friedmann et al., their result of the σ_0 will change to 5.96 b and becomes close to the value obtained in the present analysis.

Cesium-133

The cross sections for the formations of the isomeric state ^{134m}Cs and the ground state ^{134g}Cs were measured respectively by following the γ-ray counting rate after the irradiation. The present results for ^{133}Cs are listed in Table 6 together with the reported data[16]-[20]. As shown in Table 6, many authors have ever measured the thermal neutron capture cross sections and the resonance integrals for the formations of the ^{134m}Cs and $^{134m+g}Cs$. With respect to the thermal cross section, the present result agrees with data in references within the limits of the error. The thermal cross section leading to the $^{134m+g}Cs$ agreed with the evaluated value in JENDL-3.2 (29.00 b[3]), and one leading to ^{134m}Cs was in good agreement with the data reported previously, e.g. 2.82 ± 0.07 b by Baerg et al[19].

On the other hand, the resonance integral for $^{134m+g}Cs$ was 25% smaller than the evaluated value in JENDL-3.2 (396.2 b[3]).

5. Conclusion

①For the $^{80}Se(n,\gamma)$, $^{94}Zr(n,\gamma)$, $^{124}Sn(n,\gamma)$, $^{127}I(n,\gamma)$ and $^{133}Cs(n,\gamma)$ reactions, the thermal neutron capture cross sections and the resonance integrals were measured to obtain fundamental data for research on the transmutation of nuclear wastes.

②The σ_0 of ^{80}Se, ^{127}I and ^{133}Cs agreed with JENDL-3.2 and previous data. However, the I_0 of ^{94}Zr, ^{127}I and ^{133}Cs were different from JENDL-3.2 and any other data.

③The cross sections for the formations of the isomeric and ground states, such as $^{81m,g}Se$ and $^{134m,g}Cs$, were measured separately.

④The σ_0 and I_0 for the formation of ^{125g}Sn was obtained for the first time.

Acknowledgment

The authors wish to acknowledge their indebtedness to Prof. K. Tomura of Rikkyo University for his help and valuable discussion on the neutron irradiation and the activity measurements and to the crew of the Rikkyo Research Reactor for their cooperation. The authors also wish to thank Mr. Y. Ogata of Nagoya University for the preparation of Iodine target and its impurity analysis.

This work was supported by JNC and Inter-University Program for the Joint Use of Rikkyo University Reactor.

References

(1) C. H. Westcott et al.: "*Proc. 2nd Int. Conf. Peaceful Uses of Atomic Energy, Geneva*", United Nations, New York, **Vol.16,** 70(1958).
(2) H. Harada et al.: J. Nucl. Sci. Technol., **Vol.32**, No.5, 395(1995).
(3) K. Shibata et al.: *JAERI-Data/Code* 97-003, (1997).
(4) N. E. Holden et al.: Chart of the Nuclides, General Electric Co., Schenectady, New York, (1968).
(5) M. D. Goldberg et al.: Brookhaven Natl. Lab. Rept. BNL-325, 2nd ed., Suppl.2 (1966).
(6) S. F. Mughabghab et al.: "*Neutron Cross Section*", **Vol.1**, Academic Press Inc., New York(1981).
(7) C. M. Lederer et al.: "*Table of Isotopes*", (7th ed.), John Wiley & Sons, New York(1978).
(8) R. B. Firestone et al: "*Table of Isotopes*", (8th ed.), John Wiley & Sons, New York(1996).
(9) L. Moens et al.: J. Radioanal. Chem., **54**, 377(1979).
(10) D. C. Santry et al.: Can. J. Phys., **51**, 2441(1973).
(11) R. H. Fulmer et al.: Nucl. Sci. Engin., **46**, 314(1971).
(12) K. Furutaka et al.: Proc. of 1998 Symposium on Nucl. Data, JAERI Tokai, Nov.19-20, 1998 (to be published).
(13) T. B. Ryves: J. Nucl. Energy, **24**, 35(1970).
(14) L. Friedmann et al.: Radiochim. Acta, **33**, 183(1983).
(15) H. Miyahara et al.: Nucl. Instr. Method in Phys., **A595**, 409(1995).
(16) M. Takiue et al.: Nucl. Instr. and Meth., **148**, 157(1978).
(17) E. Steinnes: J. Inorg. Nucl. Chem., **34,** 2699(1972).
(18) G. H. E. Sims et al.: J. Inorg. Nucl. Chem., **30**, 349(1968).
(19) B. Keish: J. Inorg. Nucl. Chem., **17**, 180(1961).
(20) A. P. Baerg et al.: Can. J. Chem., **38**, 2528(1960).

Table 1 Summary of the neutron flux measurements in RSR of Rikkyo Reactor

Irradiation Type	Irradiation period	Reaction rates of the flux monitors ^{60}Co	^{198}Au (10^{-11}/s)	ϕ_1 or ϕ_1' (10^{11} n/cm^{2}sec)	ϕ_2 or ϕ_2'
bare	10min	1.76 ±0.04	7.31±0.15	4.42 ±0.09	0.173±0.004
with Cd	25min	0.155±0.003	3.20±0.06	0.099±0.004	0.183±0.004
Cadmium ratio		11.3 ±0.3	2.28±0.07		

Table 2 Results of Cross Sections for the $^{80}Se(n,\gamma)^{81m,81g}Se$ Reactions

Author (Year)	$\sigma_{0,m}$	$\sigma_{0,g}$	$\sigma_{0,m+g}$	$I_{0,m}$	$I_{0,g}$	$I_{0,m+g}$
Present results	0.046±0.002	0.542±0.042	0.588±0.042	0.147±0.005	0.847±0.071	0.994±0.071
JENDL-3.2[3]			0.610			0.9739
Holden[6]('68)	0.08 ±0.01[4]	0.53 ±0.04	0.61 ±0.05[5]			2.0 ±0.6

Table 3 Results of Cross Section for the $^{94}Zr(n,\gamma)^{96}Zr$ reaction

	σ_0 (b)	I_0 (b)	$Q=I_0/\sigma_0$
Present Result	0.0479±0.0010	0.277±0.007	5.78±0.19
JENDL-3.2[3]	0.04981	0.3207	
Moens[9] ('79)	———	———	5.78±0.12
Santry[10] ('73)	0.0475±0.0024	0.218±0.010	4.6
Fulmer[11] ('71)	0.052 ±0.003	0.30 ±0.03	5.77±0.67

Table 4 Results of Cross Section for the $^{124}Sn(n,\gamma)^{125g}Sn$ Reaction

	σ_0 (b)	I_0 (b)
Present Results	0.0042±0.0013	0.083±0.025
Reference	(no data)	

Table 5 Results of Cross Section for the $^{127}I(n,\gamma)^{128}I$ Reaction

	σ_0 (b)	I_0 (b)	$Q=I_0/\sigma_0$
Present Results	6.40±0.29	162±8	25.3±1.7
JENDL-3.2[3]	6.200	148.2	
Friedman[14]('83)	4.7 ±0.2	109±5	
Moens[9]('79)			24.6
Ryves [13]('70)	6.12±0.12	145±9	

Table 6 Results of Cross Sections for the $^{133}Cs(n,\gamma)^{134m,134g}Cs$ Reactions

Author (Year)	$\sigma_{0,m}$	$\sigma_{0,g}$	$\sigma_{0,m+g}$	$I_{0,m}$	$I_{0,g}$	$I_{0,m+g}$
Present results	2.70±0.14	26.3±1.1	29.0±1.1	23.2±1.8	275±16	298±16
JENDL-3.2[3]('97)			29.00			396.2
Takiue et al.[16]('78)			28.7±0.7			
Steines [17]('72)						437±26
Sims et al.[18]('68)			29.2±2.3			495±17
Keish et al.[19]('61)	2.44±0.15					
Baerg et al.[20]('60)	2.82±0.07		30.4±0.8	34.4±1.9		461±25

JP9950332

3.15 Construction of a γ–γ and β–γ Coincidence Measurement System for Precise Determination of Nuclear Data

Kazuyoshi FURUTAKA, Shoji NAKAMURA, Hideo HARADA and Toshio KATOH

Japan Nuclear Cycle Development Institute, Tokai works,
Tokai-mura, Naka-gun, Ibaraki-ken 319-1194
email : furutaka@tokai.pnc.go.jp

A γ–γ and β–γ coincidence measurement system was constructed for the precise determination of nuclear data, such as thermal neutron capture cross sections and γ-ray emission probabilities. The validity of the system was tested by a γ–γ coincidence measurement with a ^{60}Co standard source.

1 Introduction

It is of fundamental importance for the nuclear transmutation study of radioactive waste to obtain precise value of nuclear data, such as thermal neutron capture cross sections, $\sigma_{n\gamma}$. From this point of view, we have performed a series of experiments to determine precisely thermal neutron capture cross sections of the FP nuclides by the activation method.

To determine $\sigma_{n\gamma}$ precisely in the conventional activation method, in which γ rays emitted from an activated sample are measured using only one detector, accurate data for γ-ray emission probabilities I_γ are required. For some nuclides, $\sigma_{n\gamma}$ can be determined more precisely if the I_γ of their capture products are obtained with better accuracy.

For the precise determination of $\sigma_{n\gamma}$ and I_γ, a γ–γ and β-γ coincidence measurement system was constructed. In this system, the data is accumulated in list format with singles trigger condition, i.e. singles as well as coincidence data are taken simultaneously. This feature makes dead times of singles and coincidence measurements being canceled out in deducing the activity, so cross sections can be obtained precisely.

In the next section, the feature of the system is described. Section 3 describes an experiment in which γ–γ coincidence measurement was done using standard source, to test the validity of the system. Details of the analysis are also presented in this section, including corrections for sum coincidence and angular correlation. Finally, section 4 summarizes the present work.

2 Feature of the system

A schematic diagram of the system is shown in Figure 1. It consists of two detectors and a fast data acquisition system. Gamma rays are measured by a large Ge detector (relative efficiency 90% of 3"×3" NaI). In β–γ measurements, a thin (0.5–2mm^t) plastic scintillator is used for β detection.

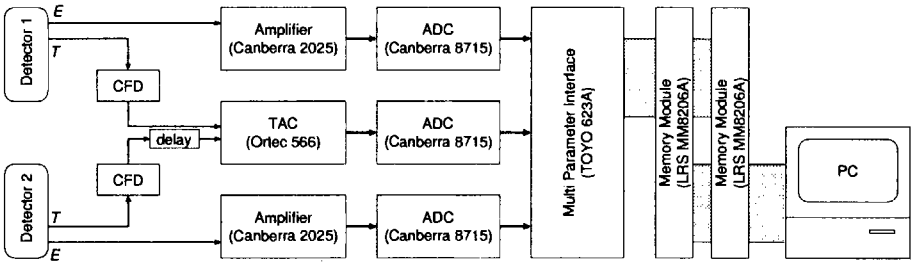

Figure 1: Schematic diagram of the system

The data acquisition system consists of two series of amplifier(Canberra2025)–Fast ADC(Canberra 8715) and a timing circuitry (TAC(ORTEC 566)–ADC(Canberra 8715)) connected to a multi–parameter interface(TOYO 623A). The list data gathered by the interface are temporarily accumulated in one of the two cascade–connected large capacity (64k words) CAMAC memory modules. The data in a memory module are transferred to a PC (NEC PC-9821 Xa16) when the module is not in use, and stored in hard disk of the PC, so the data is accumulated fast and efficiently. The data are accumulated when there's at least one ADC with valid datum. Coincidence events are extracted from the list data in off–line analysis. In γ–ray measurement in singles mode, photo–peak counts N_{i,γ_j} of a γ ray γ_j in a detector i can be expressed as the following:

$$N_{i,\gamma_j} = A \times I_{\gamma_j}\, \epsilon_{i,\gamma_j}\, R_i \times T, \tag{1}$$

where A is activity, I_{γ_j} emission probability of γ_j, ϵ_{i,γ_j} peak efficiency of γ_j in the detector i, T the measurement time, and R_i the ratio of live–time to elapsed time for the measurement. In γ–γ coincidence measurement, the yield is described by the following equation:

$$N_{1,\gamma_1\,2,\gamma_2} = A \times I_{\gamma_1}\, \epsilon_{1,\gamma_1} \times I_{\gamma_2}\, \epsilon_{2,\gamma_2} \times R_C \times T, \tag{2}$$

where R_C is live–time ratio for coincidence measurement. According to the above relations, the activity A reads

$$A = \frac{1}{T}\, \frac{N_{1,\gamma_1}\, N_{2,\gamma_2}}{N_{1,\gamma_1\,2,\gamma_2}}\, \frac{R_1\, R_2}{R_C}. \tag{3}$$

In this system, $R_C = R_1\, R_2$, and

$$A = \frac{1}{T}\, \frac{N_{1,\gamma_1}\, N_{2,\gamma_2}}{N_{1,\gamma_1\,2,\gamma_2}}, \tag{4}$$

i.e. the dead times in singles and coincidence measurements are canceled out.

3 Validity test of the system

To test the validity of the system, a γ–γ coincidence measurement was performed using a ^{60}Co standard source with known activity. Gamma rays emitted from the

source were measured with the two Ge detectors. The detectors were placed face–to–face, and the distance between the source and the front surfaces of the detectors were 20cm. Counting rate for a detector was $\sim$ 2k cps. A total of 1.6×10^7 events were accumulated within about an hour.

Shown in Figure 2 are projection spectra of the energy of the two detectors and TAC data. The two γ rays (1173 and 1333 keV) from the source are clearly seen. Also seen in the figures is 1461 keV peak, which is originated from ^{40}K in the room background. From these projection spectra, yields of the 1173(1333)keV γ ray in Ge–1(Ge–0) was

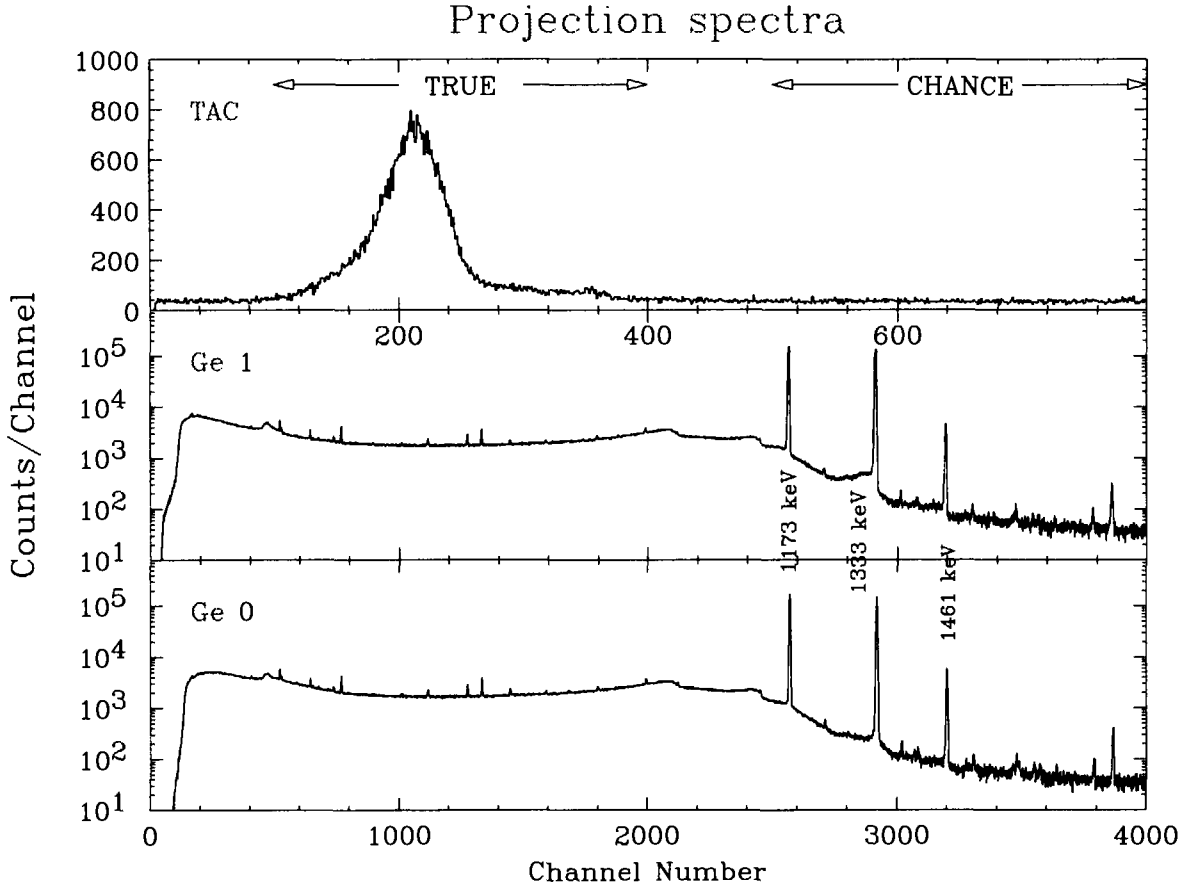

Figure 2: Projection spectra.

obtained.

To extract γ–γ coincidence events, gates were applied to TAC peak ('TRUE' in Figure 2) and Ge–1 1173 keV peak ('G_P' in Figure 3). Spectrum thus obtained is shown in Figure 4.

One of the advantages of list–form data acquisition is that it enables various corrections such as chance coincidence and background contributions, without relying on empirical formula. To estimate contributions from chance coincidence and background component in the coincidence events, separate gates were applied, and the resultant yields were subtracted from the number of coincidence events. Chance coincidence

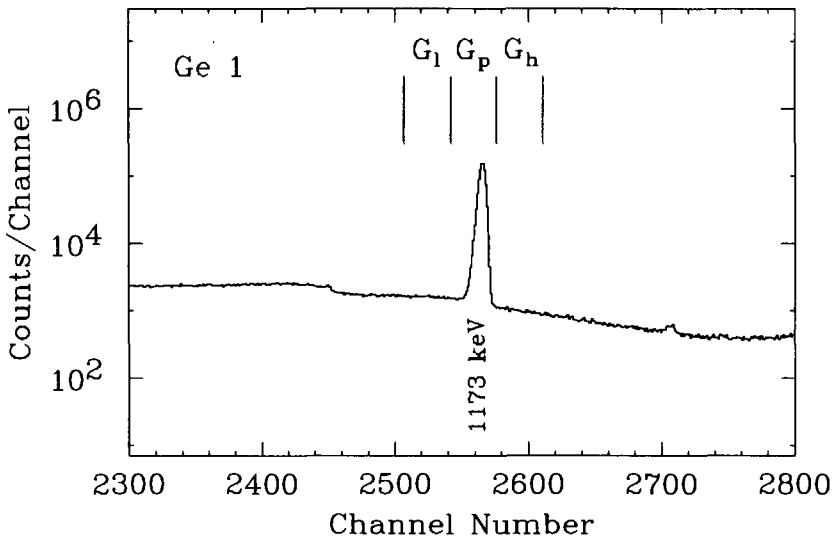

Figure 3: The gates applied to the Ge–1 data.

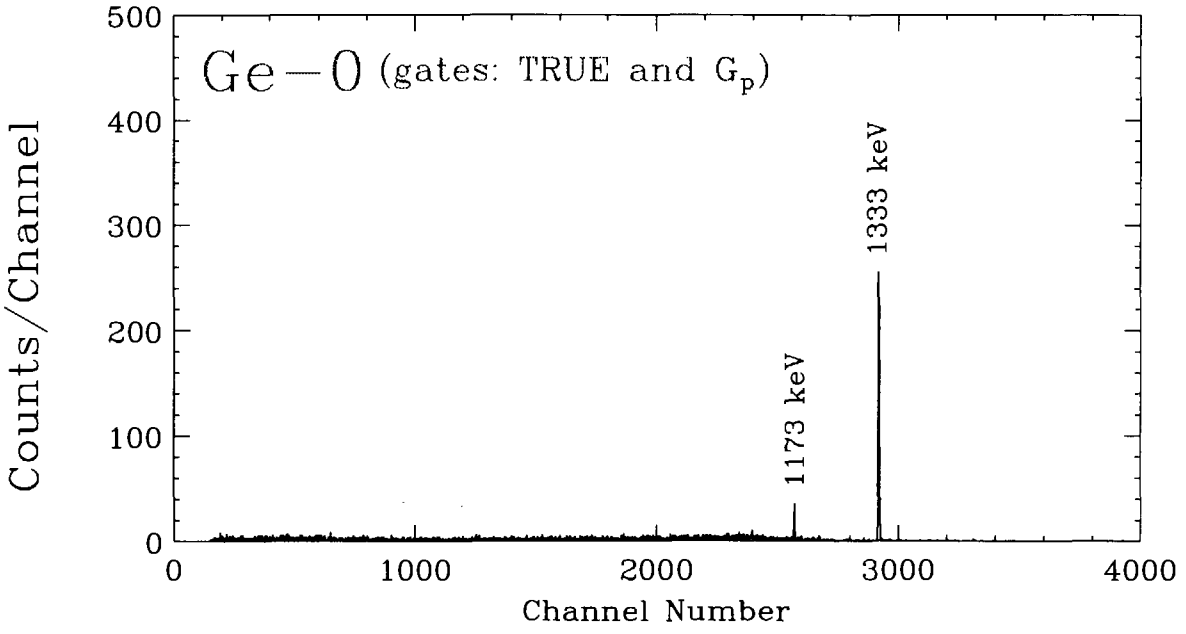

Figure 4: Spectrum obtained by gating Ge–1 1173 keV peak and TAC peak.

contribution was estimated by gating 'G_p' and off-peak portion of TAC data. For background estimation, two gates with the same width were applied on both sides of the peak ('G_l' and 'G_h' in Figure 3), and an average of the resultant counts was regarded as the background.

In addition to the corrections described above, corrections for angular correlation and sum coincidences were made. The correction of coincidence counts, $N_{1,\gamma_1\,2,\gamma_2}$, for the angular correlation was done using the following well-known angular correlation function of the two γ rays,

$$W(\theta) = 1 + 0.102 \times P_2(\cos\theta) + 0.0091 \times P_4(\cos\theta), \tag{5}$$

where θ is the opening angle between the two γ rays. The correction factor amounted to 1.112. In sum coincidence events, the two cascade γ rays are detected in the same detector, and therefore singles photo-peak counts are reduced. The correction factors, F_{SC}, of the sum coincidence were calculated for the two cascading γ rays to be

$$F_{SC,1173} = (1.0 - \epsilon_{T,1333} \times f_W)^{-1} \tag{6}$$

and

$$F_{SC,1333} = \left(1.0 - \frac{I_{\gamma,1173}}{I_{\gamma,1333}} \times \epsilon_{T,1173} \times f_W\right)^{-1}, \tag{7}$$

where $\epsilon_{T,1173}(\epsilon_{T,1333})$ is the total detection efficiency of 1173(1333) keV γ ray, $I_{\gamma,1173}(I_{\gamma,1333})$ emission probability of the 1173(1333) keV γ ray, and f_W is the average value of angular correlation function over the detector solid angle weighted by the γ-ray attenuation probability in the Ge crystal. f_W was calculated using the relation (5) above. The factors for the present setup are $F_{SC,1173} = 1.00517$ and $F_{SC,1333} = 1.00531$.

Taking into account all of the above corrections, the activity of the source was obtained as 135.4 ± 5.8 kBq, which agreed to the catalog value with decay correction, 132.5 ± 2.5 kBq. Thus, validity of the system was confirmed in the γ–γ coincidence experiment. The error of the obtained value was mainly (99.6%) originated from the statistical error of the number of coincidence events, and can be reduced with long-time measurements.

4 Conclusion

For precise determination of source activities and γ-ray emission probabilities, a γ–γ and β–γ coincidence measurement system was constructed. Using this system, in which the data are accumulated in essentially singles mode, the dead times for singles and coincidence measurements are canceled out, and the activity can be determined accurately.

To check the validity of the system, the activity of the ^{60}Co standard source was measured with the system using γ–γ coincidence method. The obtained value was agreed to the catalog value within the error, and the validity of the system was confirmed.

JP9950333

3.16 Preparation of 3-7 MeV Neutron Source and Preliminary Results of Activation Cross Section Measurement

T. Furuta, H. Sakane*, T. Masuda, Y. Tsurita, A. Hashimoto, N. Miyajima, M. Shibata*, H. Yamamoto* and K. Kawade*

Department of Nuclear Engineering, Nagoya University

**Department of Energy Engineering and Science, Nagoya University*

e-mail:h982422m@sunspot.eds.ecip.nagoya-u.ac.jp

A d-D gas target producing monoenergetic neutrons has been constructed for measurement of activation cross sections in the energy region of 3 to 7 MeV at Van de Graaff accelerator of Nagoya university. Neutron spectra and neutron fluxes were measured as a function of the incident deuteron energy. Preliminary results of activation cross sections were obtained for reactions ^{27}Al(n,p)^{27}Mg, ^{27}Al(n,α)^{24}Na, ^{47}Ti(n,p)^{47}Sc, ^{56}Fe(n,p)^{56}Mn, ^{58}Ni(n,p)^{58}Co and ^{64}Zn(n,p)^{64}Cu. The results are compared with the evaluated values of JENDL-3.2. A well-type HPGe detector was used for highly efficient detection.

1 Introduction

A knowledge of activation cross section data for neutron energies up to 15 MeV are indispensable for fusion technology, especially for calculations on activation of materials, radiation damage, nuclear heating and so on. Considerable amounts of data exist around 14 MeV. However, in an energy range between 3 and 13MeV, the experimental data are rather scarce owning to the lack of available monoenergetic neutron sources. In the energy range of 5 to 10 MeV, Qaim *et al.*[1] also reported on the characteristics of a deuteron gas target and cross sections of nickel isotopes using it. In this work, we measured the (n,p) and (n,α) reaction cross sections. A d-D gas target was constructed for production of the monoenergetic neutrons of 3 to 7 MeV energy region, and investigated the characteristics of the neutron sources: neutron spectra and flux.

2 Experimental

2.1 Gas target

An exploded view of a gas target assembly is shown in Fig.1. The target consists of a small Al cell (30-mm-innerlong. 8-mm-innerdiam. 1-mm-thick) which is filled with

D_2 gas at 1.6 kg/cm^2. The cell is separated the vacuum and the gas area with a 2.2-μm-thick Havar foil. The deuteron beam from the Van de graaff accelerator produces neutrons in the cell via the D(d,n)^{3}He reaction. Incident d^+ beam energy and intensity were 1.5 $\sim$ 3.5 MeV and about 1.5 μA, respectively. The cell is cooled by a jet of air. The degradation of the deuteron energy in the Havar foil and the D_2 gas was calculated using the range-energy data[2] as shown in Fig.2.

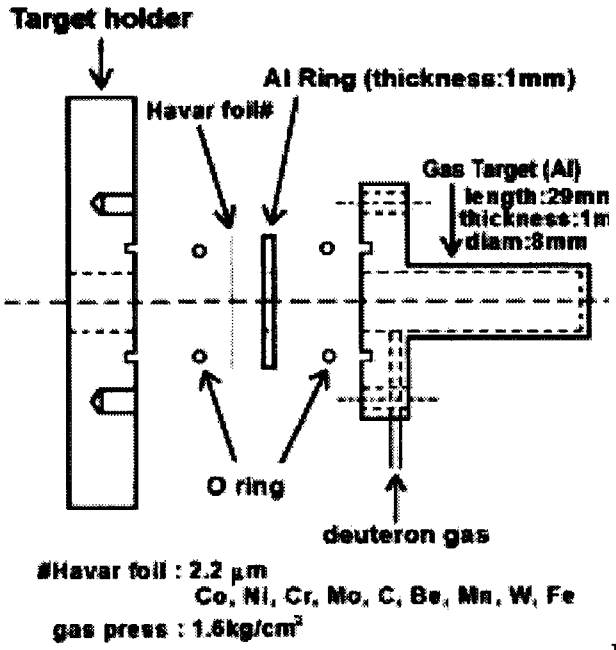

Fig. 1: Exploded view of gas target assembly

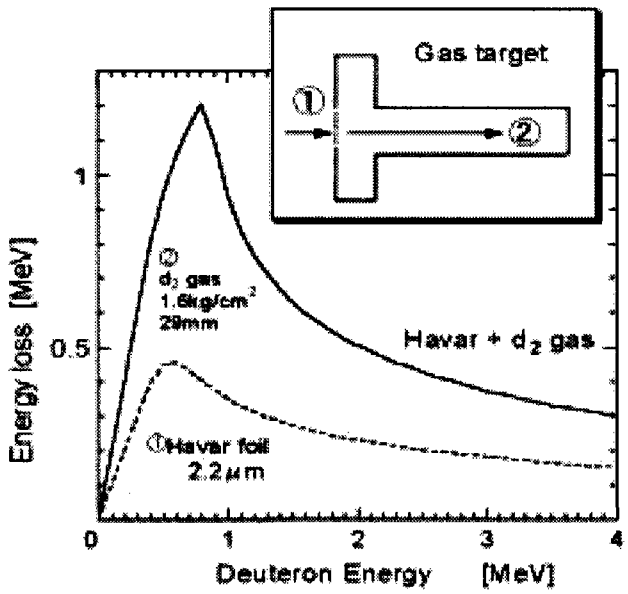

Fig. 2: Energy loss of d^+ beam in Havar foil and D_2 gas

2.2 Neutron Spectra and Flux

Neutron spectra at 1m and zero degree with respect to the d^+ beam and at deuteron energy of 1.5 up to 3.5MeV were measured using the organic liquid scintillator NE213 encapsulated by an aluminum cell (50-mm-high. 50-mm-diam.), by mean of the pulse shape discrimination technique.

The neutron flux was measured with use of the standard reaction ^{115}In(n,n')^{115m}In ($T_{1/2}$ = 4.486h), whose cross section is the evaluated in JENDL-3.2. For a deuteron energy of 2.5 MeV, a typical value of 2.3 $\times$ 10^6 [n/cm^2 s/μA] was obtained at 1.2 cm from the surface of the cell.

The obtained neutron spectra are shown in Fig.3. Quasi-monoenergetic neutrons are clearly seen. However some contributions of low-energy neutrons are also seen. As the produced neutron energy increased, the component of low-energy neutrons increased.

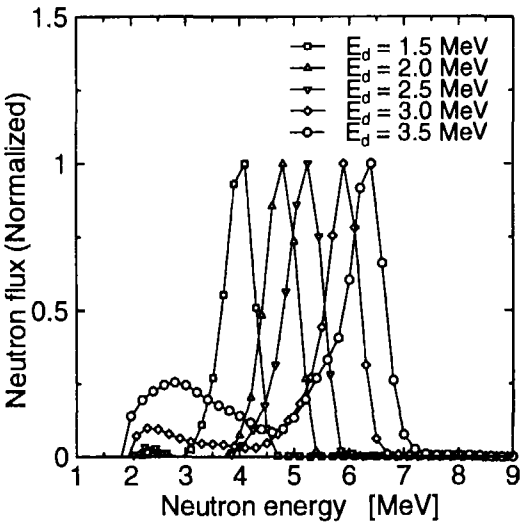

Fig. 3: Measured Neutron spectra

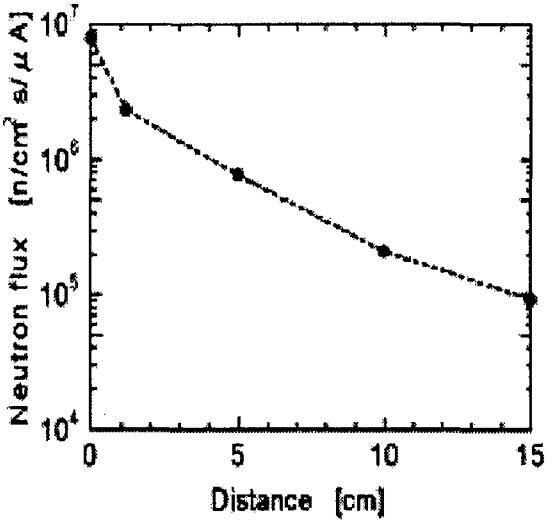

Fig. 4: Measured neutron flux as a function of the distance between the surface of the gas target and a sample.

The ratio of scattered neutrons to total is about 35%. It is necessary for the reliable measurement of cross sections to correct the contribution of low-energy neutrons.

As shown in Fig.4, neutron flux is dependent on the distance between the surface of the cell and sample. Since the neutron flux was obtained about 10^7 unit, sub-mb cross sections can be measured.

3 Cross Section Measurement

We measured activation cross sections of six reactions, ^{27}Al(n,p)^{27}Mg, ^{27}Al(n, α)^{24}Na, ^{47}Ti(n,p)^{47}Sc, ^{56}Fe(n,p)^{56}Mn, ^{58}Ni(n,p)^{58}Co and ^{64}Zn(n,p)^{64}Cu by the activation method. Samples were irradiated at 0 degree to d^+ beam and 1.2cm from the end of the D_2 cell by using a pneumatic sample transport system (Fig. 5). The samples of 10mm×10mm and 1mm^t were sandwiched between two In foils of 10mm×10mm and 0.5mm in thickness. To monitor the fluctuation of neutron flux, a multi-channel scaling measurement was carriedd out at an interval of every 10s with a plastic scintillation detector. The induced activities were measured with a well-type an 22% HPGe detectors. The efficiency of both detectors is determined by the calicration method[3]. Decay parameters of the radioactivity are listed on Table 1.

The following principle corrections were made: (1) contribution of low energy neu-

trons, (2) time fluctuation of neutron flux, (3) deviation of γ-ray detection efficiency due to sample thickness, (4) self-absorption of γ-rays, (5) counting loss due to coincidence sum effect. Details of the corrections are described elsewhere[3].

The total errors (δ_t) were described by combining the experimental errors (δ_e) and the errors of nuclear data (δ_r) in quadratic : $\delta_t^2 = \delta_e^2 + \delta_r^2$.

The results for six reactions are shown in Fig.6. They are compared with the evaluated value of JENDL-3.2 and previous works[4]. The experimental cross sections of ^{27}Al(n,p)^{27}Mg, ^{47}Ti(n,p)^{47}Sc, ^{58}Ni(n,p)^{58}Co, and ^{64}Zn(n,p)^{64}Cu are well agreement with the evaluated value of JENDL-3.2. On the other hand the results of ^{27}Al(n,α)^{24}Na and ^{56}Fe(n,p)^{56}Mn in the low energy region (points indicated by arrows), are 10 $\sim$ 100 times larger than the JENDL-3.2.

Table 1. Measured reactions and decay parameters

Reaction	Half life	E_γ	I_γ	Q-value
^{27}Al(n,p)^{27}Mg	9.458 m	843.7 keV	73 %	-1827.9 keV
^{27}Al(n,α)^{24}Na	14.959 h	1368.6 keV	99.994 %	-3132.9 keV
^{47}Ti(n,p)^{47}Sc	3.3492 d	159.3 keV	68.3 %	182.2 keV
^{56}Fe(n,p)^{56}Mn	2.5785 h	846.7 keV	98.87 %	-2913.0 keV
^{58}Ni(n,p)^{58}Co	70.82 d	810.7 keV	99.45 %	400.7 keV
^{64}Zn(n,p)^{64}Cu	12.700 h	511 keV	17.4 %†	203.4 keV

† annihilation of β^+-ray

4 Discussion

The results of ^{27}Al(n,α)^{24}Na and ^{56}Fe(n,p)^{56}Mn in the low energy region are 10 $\sim$ 100 times larger than the JENDL-3.2. The probable reason for the deviation of the above mentioned two reactions is to be due to the contribution of higher side neutron tail of each peak in Fig.3 which is caused by the energy straggling of a d^+ particle through the Havar foil and D_2 gas.

5 Conclusion

The deuteron gas target was constructed for production of the monoenergetic neutrons. The neutron flux was obtained to be 2.3 $\times$ 10^6[n/cm^2 s/μA] at 1.2cm in 0 degree with respect to the incident 2.5 MeV deuteron beam. Activation cross sections can be measured down to 1 mb using a well-type HPGe detector. By correcting above mentined five factor in chapter 3 properly, experimental cross section data of ^{27}Al(n,p)^{27}Mg,

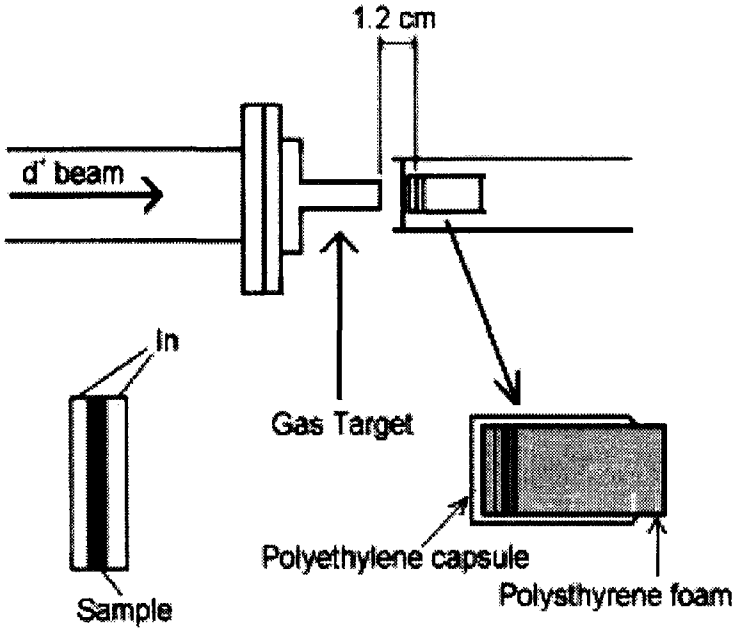

Fig. 5: Pneumatic sample transport system

^{47}Ti(n,p)^{47}Sc, ^{58}Ni(n,p)^{58}Co, and ^{64}Zn(n,p)^{64}Cu are well agreement with the JENDL-3.2. However the energy straggling of the incident deuteron are needed to correct for ^{27}Al(n,α)^{24}Na and ^{56}Fe(n,p)^{56}Mn because these excitation functions have a sharp slope. We are now planning to prepare the self-loading target with Ti coated for the neutron production of the energy range 3 to 5MeV.

The following reactions are planned to measure: ^{29}Si(n,p)^{29}Al, ^{31}P(n,α)^{28}Al, ^{41}K(n,p)^{41}Ar, ^{45}Sc(n,α)^{42}K, ^{59}Co(n,p)^{59}Fe, ^{59}Co(n,α)^{56}Mn, ^{75}As(n,α)^{72}Ga, ^{93}Nb(n,α)^{90m}Y and ^{113}In(n,n')^{113m}In.

References

[1] Qaim, S.M., et al.: *Nucl. Sci. Eng.*, **88**, 143, (1984)

[2] Andersen, H.H., Ziegler, J.F.: "*Hydrogen Stopping Powers and Ranges in All Elements*", Pergamon Press, New York(1977)

[3] Kasugai, Y., et al.: *Ann. Nucl. Energy*, **25**, 23, (1998)

[4] Mclane, V., et al.: "*Neutron Cross Sections*", Vol.2, Academic Press, New York, (1988)

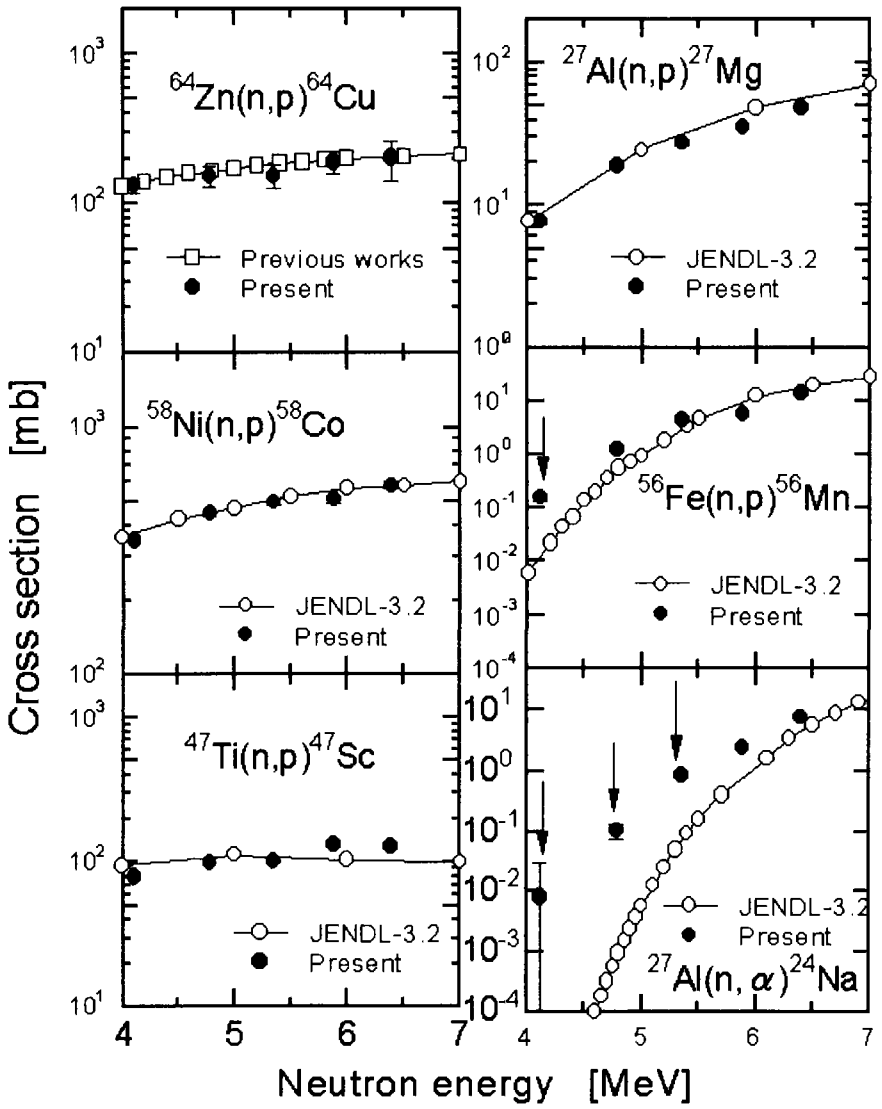

Fig. 6: Experimental cross section data of (n,p), (n,α) reaction.

JP9950334

3.17 Measurement of ^{9}Be-*d* Nuclear Reaction Cross Sections at Low Energy

Kentaro Ochiai, Kimiya Ishii, Isao Murata, Hiroyuki Miyamaru, Akito Takahashi
Department of Nuclear Engineering, Osaka University, 2-1Yamadaoka, Suita, Osaka, 565-0871, Japan
e-mail: kochiai@nucl.eng.osaka-u.ac.jp

We obtained angular differential cross sections of ^{9}Be-d nuclear reaction at low energy and the energy dependence of astrophysical S-factors. Angular distributions were asymmetric around 90 degree (back- or forward-peaking) and the values of S-factors for ^{9}Be(d,p) and ^{9}Be(d,α_0) were about 3 MeV barn and 9 MeV barn at E_{lab} = 290 keV, respectively.

1. Introduction

Differential cross section data of charged-particle emission from light elements with incident low energy protons and deuterons are useful for estimating basic dose-rate data (PKA and KERMA) and material damage. Beryllium (^{9}Be) metal and ^{9}Be compound material are prospective candidates for the first wall materials of future fusion reactors. The use of neutral beam injector with several hundred keV and several amperes has been reported recently for inducing high density plasma heating[1,2]. To study plasma-particle/first-wall interaction problems on low energy nuclear reactions, we have measured charged-particle emission cross sections of ^{9}Be (d,x) and ^{9}Be (p,x) at low energies, where x = p, d , t or α, since, the cross section data at low energies have not been obtained sufficiently up to now. Especially, there are only few data of differential particle emission cross sections available for charged-particles produced by ^{9}Be (d,x) at low deuteron energy.

2. Experimental Procedure and Analysis

In this work, we have used a Cockcroft-Walton type accelerator, OKTAVIAN at Osaka University, to measure the cross sections below 300 keV. Figure 1 shows the schematic view of experimental system with components in the vacuum chamber and signal acquisition and analysis system for charged-particles. This chamber (30 cm diameter, 40 cm height) was made of stainless steel. It is equipped with flanges, metal-gaskets for vacuum seal, feedthroughs for electric measurements. The sample, Si-SBD detectors and Faraday cup were inserted from the flanges-ducts and set up inside the chamber. The sample was set up at the beam irradiation position by a manipulator with a stepping motor to obtain the flesh point on the sample for the beam implantation. Charged-particles emitted by ^{9}Be (d,x) reactions have been measured with two Si-Surface Barrier Detectors (SSBD: depletion layer; about 200 μm). One detector (Er-detector) is movable between the angle from 30 degree to 160 degree for the measurement of angular-

distributions of cross sections (differential cross sections). The other detector (Ef-detector) was fixed at 60 degree to make relative normalization for counts of particles detected at each angle. A Faraday-cup for beam-current monitor was set up at the backside of the beryllium sample.

Observable charged-particles emitted by ^{9}Be-d nuclear reactions at low energy are as follows:

^{9}Be(d,p)^{10}Be g.s	:	Q = 4.59MeV	(1)
^{9}Be(d,t)^{8}Be g.s.	:	Q = 4.59MeV	(2)
^{9}Be(d,t)2α	:	Q = 4.68MeV	(3)
^{9}Be(d,α)^{7}Li g.s	:	Q = 7.51MeV	(4)

For screening the scattered deuterons by D-beam injection, aluminum foils of 3-13mm thickness were mounted in front of the SSBDs.

Figure 2 shows the energy spectra of the charged-particles emitted from the beryllium target with implanted deuteron beam of E_{lab} = 300 keV. The clear energy spectra with resolved peaks were observed at Er-detector-angle θ r = 90degree (lab) and with a 3 μm aluminum screening foil as shown in Fig.2. We obtained some other peaks than the charged-particle spectra of lighter nuclei emitted from the above reactions (1)-(4). The peak near 3.7MeV is the α-particle spectrum emitted from the ^{9}Be(d,α_1)^{7}Li* reaction. The differential energy between the α_0-peak and the α_1-peak is about 470 keV and this energy corresponds to the energy of the first excited state level of ^{7}Li. Also the peak spectrum near 1.1 MeV is the triton peak emitted from the ^{9}Be(d,t_1)^{8}Be*reaction and the difference energy between t_0-peak and t_1-peak corresponds to the first excited level (3.03 MeV) of ^{8}Be. Moreover, we observed another particle-peak near 0.5 MeV. It is seemed that the spectrum near 0.5 MeV is the α-particle-spectrum produced by ^{9}Be(d,α_2)^{7}Li*. However at present we are investigating if the reaction process is due to the second excited level (4.63 MeV) of ^{7}Li[3]. It is thought that a bumpy spectrum below 2MeV was due to α-particles by the three body brake-up reaction by ^{9}Be(d,t)2α.

To estimate the cross sections ($\sigma_{(E,\theta)}$) from the yield of the spectrum, we have used the following formula

$$<\sigma_{(E,\theta)}> = \Delta Y \sin\theta_{in} (dE/dx)^{-1} \Delta E / N\phi \qquad (5)$$

where ΔE is the difference of two neighboring incident energies E_1 and E_2 and we have defined the E as the mean energy between E_1 and E_2 (e.g. if E_1 = 300 keV and E_2 = 280 keV, we obtain ΔE = 20 keV and E = 290 keV). Also ΔY is the difference of two yields at the two neighboring energies. dE/dx, N, and ϕ were the stopping power calculated by SRIM code, beryllium density at room temperature and incident beam flux, respectively.

3. Results and Discussion

We carried out the investigation for angular differential cross sections of the ^{9}Be-d reactions with p, t and α-particle emission for 9 angles with at 10 degree interval. Figure 3-(a) and (b) show the angular

distributions of the differential cross sections of ^{9}Be(d,p) and ^{9}Be(d,t) at E_{lab} = 280 keV and 180 keV. The angular distributions of both cross sections tend to be backward-peaking. The differential cross sections of ^{9}Be(d,p) at θr = 160 degree for 280 keV is ten times larger than the value of the differential cross section at θr = 20 degree as shown in Fig.3-(a). and also the curve of the differential cross sections of ^{9}Be(d,t_0) for 280 keV tend to have a broad maximum value at about θr = 110 degree and the differential cross section of ^{9}Be(d,t_0) at θr =110 degree is larger by two and a half times than the differential cross section at θr = 20 degree as shown in Fig.3-(b). As compared with the data by De. Jong et al., [4] the tendency of angular distributions correspond to the their data relatively. However, the absolute values of our differential cross sections tend to be larger than their data. For the reason, we assumed that it was due to the difference of the used detectors. Jong's group used a track detector which might not resolve ^{12}C(d,p)^{13}C and D(d,p)T reactions. Figure 4 shows the angular distributions of differential cross sections of ^{9}Be(d,α_0) and ^{9}Be(d,α_1) at E_{lab} =280 keV. Though the differential cross sections of ^{9}Be(d,α_0) tend to increase at backward angle, the cross sections of ^{9}Be(d,α_1) tend to increase at forward angles rather than at backward angles.

It was shown that the angular distributions of all differential cross sections tend to be asymmetric around 90degree (forward- or backward- peaking). Up to now, we can not theoretically describe the mechanism of the asymmetry of angular distributions at low energy. Also it is recently reported that the similar asymmetries of angular distributions for ^{15}N(p,α), ^{12}C(d,p), and ^{13}C(d,p) differential cross sections at low energy were seen around 90degree[5,6]. To clarify the phenomena theoretically, we need studies based on the theory of Distorted Wave Born Approximation (DWBA) processes, Channel Coupling (CC) considering α-cluster model[7], or R-Matrix theory for the stripping, α-emission, and/or pick-up, processes.

Nuclear reaction cross sections ($\sigma_{(E)}$) which drops exponentially according to energies E at low energy is given as

$$\sigma_{(E)} = S_{(E)} E^{-1} \exp(-2\pi\eta) \qquad (6)$$

where $2\pi\eta = 31.29 Z_1 Z_2 (m/E)^{1/2}$ is the Sommerfeld parameter (Z_1 and Z_2 = charge numbers of interacting nuclei, m = reduced mass in amu, E = c.m. energy in keV)[8]. For a cross section which dorps steeply at low energy, it is useful to transform the cross sections into the astrophysical $S_{(E)}$-factor defined by the above equation. Figure 5 shows the astrophysical $S_{(E)}$-factors obtained from the cross sections of ^{9}Be(d,p), ^{9}Be(d,t_0), ^{9}Be(d,α_0) and 9Be(d,α_1) at E = 100 – 280 keV. The $S_{(E)}$-factors slightly increase with Increase of E. We made linear-fitting of the $S_{(E)}$-factors for (d,p) and (d,α_0) by the method of least squares and shown in the figure with solid lines. From the calculation, we obtained

^{9}Be(d,p)^{10}Be: $S_{(E)} = 0.82 \times 10^{-3} E + 0.94$ MeV barn (7)

^{9}Be(d,α_0) 7Li: $S_{(E)} = 2.66 \times 10^{-2} E + 1.88$ MeV barn (8)

and it is suggested that the astrophysical $S_{(0)}$ factor of (d,α) reactions is about twice larger than the $S_{(0)}$ factors of the stripping (d,p) and pick-up (d,t) reactions.

4. Summary and Future works

As a result of our experiments, spectral data with several discrete peaks of (d,p), (d,t_0), (d,t_1), (d,α_0), (d,α_1) and (d,α_2) reactions with ^{9}Be target could be measured clearly and the differential cross sections of individual particle-emission channel could be obtained in the 100-300 keV region. Energy dependencies of cross-sections for all reactions fit very closely to the Coulomb barrier transmission coefficients for the free charged particle reaction. From the cross sections, we estimated energy dependencies of S-values as follows.

^{9}Be(d,p)^{10}Be : $S(E) = 8.2\times10^{-3}E + 0.94$ MeV barn

^{9}Be(d,α_0)^{7}Li : $S(E) = 2.66\times10^{-2}E + 1.88$ MeV barn

It was shown that angular distributions of cross sections for some reactions tended to be asymmetric around 90 degree (forward- or backward-peaking). We need the studies based on the theory of DWBA, CC, and R-matrix theory considering α-cluster model for the stripping, α-emission and /or pick-up reactions. Moreover, we have started the measurement of ^{9}Be-p nuclear reaction cross sections for the comparative and comprehensive understanding of the process of nuclear reactions at low energy.

References

[1] ITER Design Report: The Journal of Japan Society of Plasma Science and Nuclear Fusion Research Vol.73, Supplement, June 1997 published by JSPSNFR.

[2] Large Helical Device(LHD) Project: The Journal of Japan Society of Plasma Science and Nuclear Fusion Research Vol.74, Supplement, May 1998 published by JSPSNFR.

[3] Data available via; http://www.tunl.duke.edu/NuclData/

[4] D. De Jong, P. M. Endt and L. J. G. Simos.: "Angular Dependence and Yield of The ^{9}Be(d,p)^{10}Be and ^{9}Be(d,t)^{8}Be Reactions", Physica 18 (1952) 10.

[5] A. Redder, H. W. Becker, H. Lorenz-Wizba, C. Rolfs, P. Schmalbrock, and H. P. Trautvetter.: "The ^{15}N(p,α_0)^{12}C Reaction at Stellar Energies" Z. Phys. A – Atoms and Nuclei 305, 325 – 333 (1982).

[6] Donald R. Maxson and Andrew T. Sornborger.: "Reactions induced by 150-350 keV deuteron on ^{12}C and ^{13}C", Nuclear Instruments and Methods in Physics Research B79 (1993) 293-296.

[7] H.HORIUCHI, KIYOMI IKEDA: in International Review of Nuclear Physics, Vol. 4 (World Scientific, 1986)p.2

[8] C. Rolf and E.Somorjai.: "Status report on electron screening", Nuclear Instruments and Methods in Physics Research B99 (1995) 297-300.

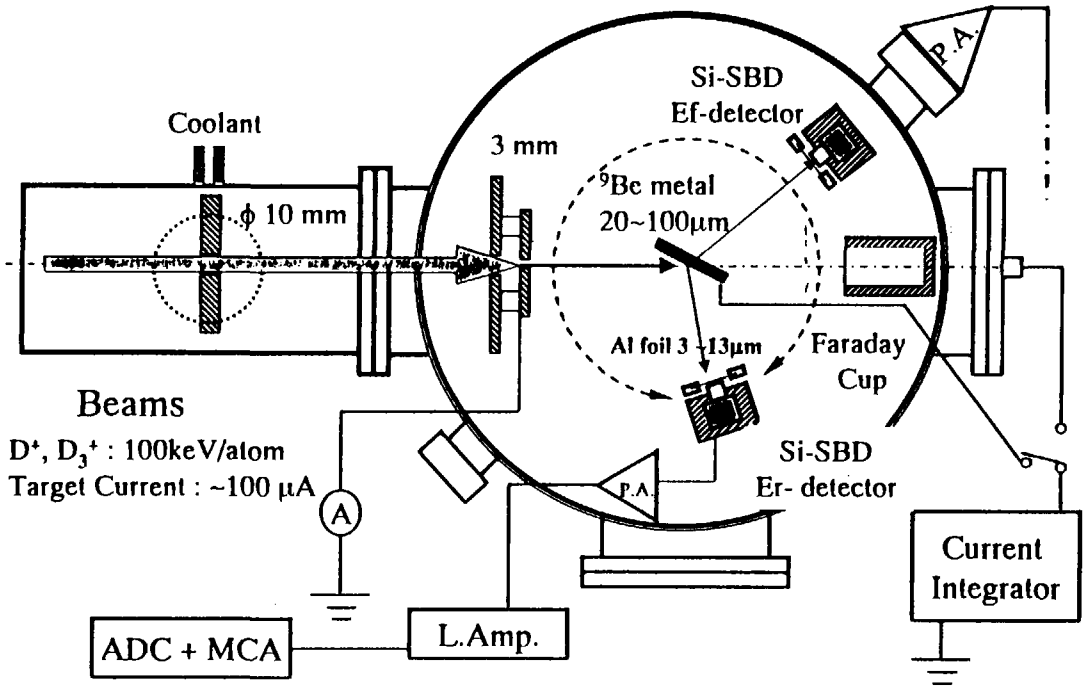

Figure 1 Schematic view of experiment system

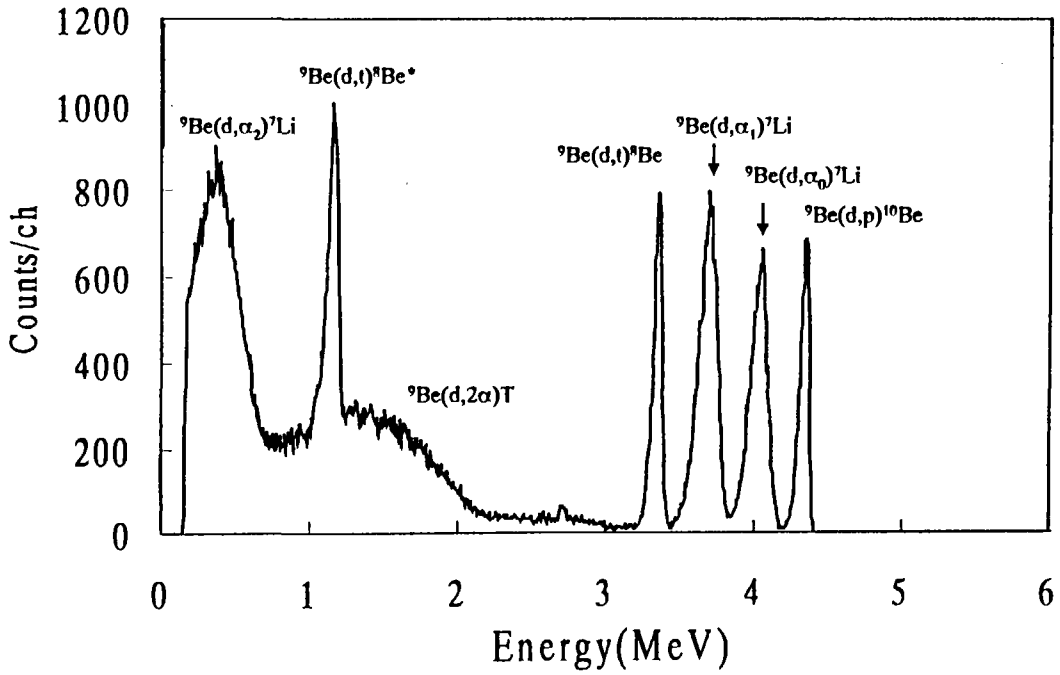

Figure 2 The energy spectra of the charged-particles emitted from the beryllium target with implanted deuteron beam of E_{lab} = 300 keV

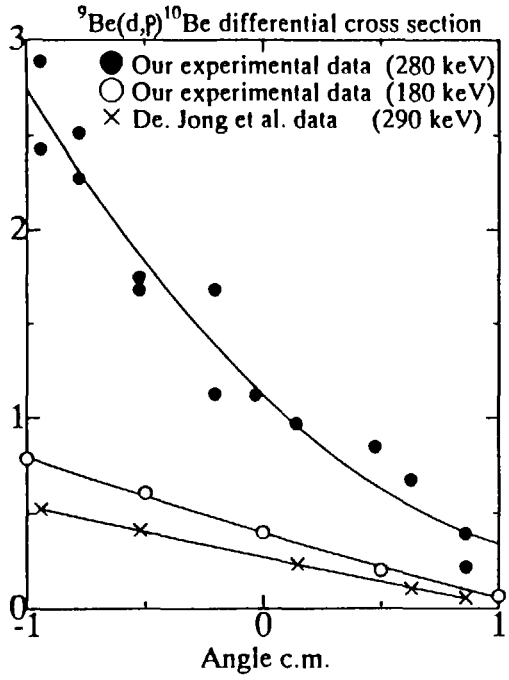

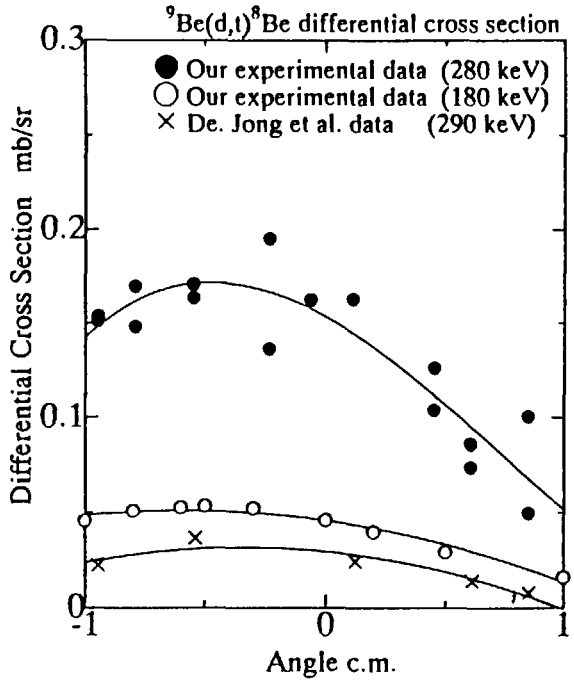

Figure 3-(a) (left) Anguler differential cross section of ^{9}Be(d,p)^{10}Be
Figure 3-(b) (right) Anguler differential cross section of ^{9}Be(d,t)^{8}Be

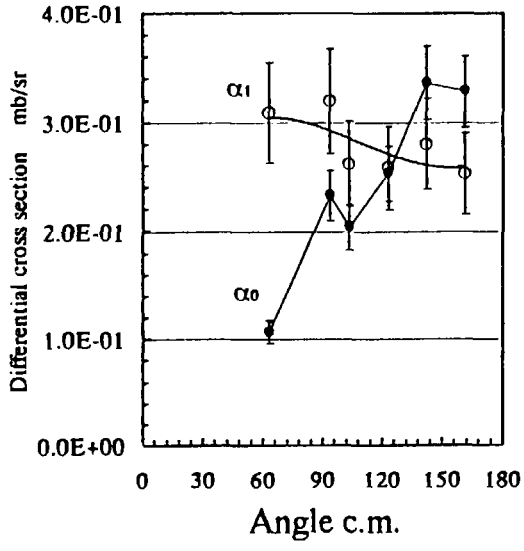

Figure 4 Differential cross sections of ^{9}Be(d,α)^{7}Li (E = 280 keV)

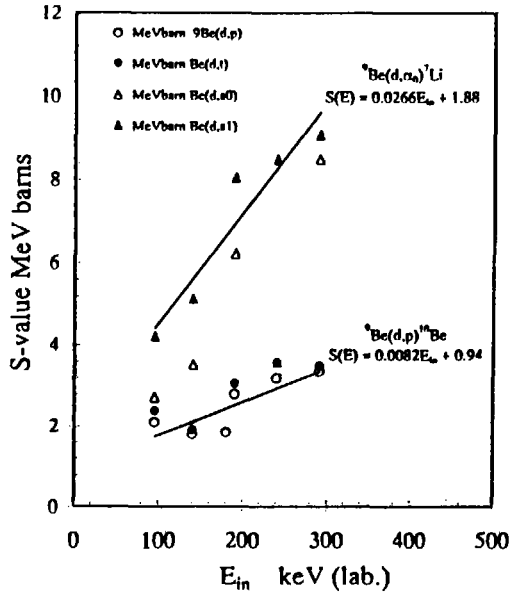

Figure 5 Dependances of incident energy for astrophysical S-factors of ^{9}Be(d,x)

3.18 Measurement of secondary gamma-ray production cross sections of vanadium induced by D-T neutrons

Tetsuo Kondo, Isao Murata, and Akito Takahashi
Department of Nuclear Engineering, Osaka University
Yamada-oka, 2-1, Suita, 565-0871, Japan
e-mail:tkondo@newjapan.nucl.eng.osaka-u.ac.jp

The secondary gamma-ray production cross sections of vanadium induced by D-T neutrons have been measured. The experimental values were compared with the theoretical calculation results by SINCROS-II and the evaluation result based on experimental data compiled by Simakov. The calculation results supported our data, while Simakov's evaluation did not agree with the present result very well.

1. Introduction

Vanadium is a candidate element for the structural material of the fusion power reactor, because of its low activation property. Concerning this, at JAERI[1] and Osaka University[2],neutronics experiments such as neutron integral experiment and measurement of charged particle emission reaction cross section were done for vanadium. In the present study, the secondary gamma-ray production cross sections of vanadium induced by D-T neutrons have been measured because there exist very few measurements of secondary gamma-ray data of vanadium. The measured raw data were corrected carefully considering the sample size and air attenuation. The theoretical calculations for the cross sections were done to compare with the measured data.

2. Experimental Techniques

The measurement was carried out using OKTAVIAN pulse line at Osaka University as D-T neutron source. The pulse frequency and beam current were 2MHz and about 10μA, respectively. An HP-Ge semiconductor detector was used to measure gamma-rays with a high energy resolution. The absolute value of neutron flux was determined by the activation method with Al foils, and the relative value was monitored by using NE213 scintillator. Fig.1 shows the experimental geometry. The sample shape was a hollow cylinder(30mm-OD,26mm-ID,70mm in length) in order to suppress neutron multiple scattering and attenuation of produced gamma-rays in the sample. The flight path for the TOF measurement was 184cm. Fig.2 shows the block diagram of electronic circuits. Gamma-ray scattering angle was fixed at 125deg. so that we didn't have to consider the angular distribution for secondary gamma-rays to estimate the total gamma-rays production cross sections. The HP-Ge detector was shielded heavily by lead, polyethylene, heavy concrete, cadmium, and so on.

3. Measured Pulse Height Spectra

Figs.3, 4a and 4b show the TOF spectrum, foreground spectrum and background spectrum, respectively. As shown in Fig.3, the time interval between n-signal and γ-signal was about 30ns. Extracting the signals in the regions of FG and BG described in Fig.3, foreground and background spectra were obtained as in Figs.4a and 4b. We can find discrete gamma-rays from vanadium in Fig.4a by comparing with 4b.

4. Data Analysis

The data analysis was done as follows:

(1) Data corrections by MCNP-4A and absorption coefficient for air
(2) Derivation of experimental values
(3) Theoretical calculation with SINCROS-Ⅱ
(4) Comparison with other experimental data

(1) Data corrections

For deriving the gamma-ray production cross sections from vanadium, some corrections were considered. We calculated the effect of neutron multiple scattering and gamma-ray attenuation in the sample as a function of the sample thickness by using MCNP-4A. The result is shown in Fig.5. The correction factor is 12.7% for the present sample, the thickness of which is 2mm. Gamma-ray attenuation by air was also corrected with the absorption coefficient. The correction factor is 1.8% at 500keV and 1.3% at 1MeV for example. The correction factor for air is shown in Fig.6.

(2)Derivation of experimental values

①Gamma-ray Production Cross Sections

The cross sections were obtained using the following expression:

$$\sigma = \frac{C \cdot 4\pi R^2}{T \cdot N \cdot \phi \cdot S \cdot f}$$

where

C: net counts of the peak in the pulse height spectrum
T: measurement time (sec)
f: intrinsic efficiency for HP-Ge detector
R: distance between sample and detector (cm)
Φ: neutron flux at the sample($cm^{-2} \cdot s^{-1}$)
S: active area of the detector facing toward the sample(cm^2)
N: number of V-51 nuclei

The neutron flux at the sample was measured by using the activation method with Al foils. The average neutron flux was estimated to be 4.0×10^4 n/sec/cm^2.

②Uncertainties

The experimental results had uncertainties based on several factors. These factors were assumed to introduce independent random errors. Therefore the overall uncertainty could be written as the square root of the linear summation of the individual factors squared.

(3)Theoretical Calculation

We executed a theoretical calculation for vanadium by SINCROS-Ⅱ and the results were compared with the experimental data. Input parameter F2 which means the normalization factor for the Kalbach pre-equilibrium model was set to be 0.45. This value was determined by fitting experimental data of DDX for charged particle and secondary neutron emission reaction cross sections to the calculation results as shown in Fig.7.

(4)Comparison with other experimental data

Our experimental values were also compared with the evaluation result based on other experimental data compiled by Simakov et al.[3]. He collected and examined the experimental data on discrete gamma-ray production cross sections under the support of IAEA. He averaged several other experimental data obtained at various laboratories to give the evaluated experimental data. The data were normalized with respect to incident neutron

energy, angular distribution and so on. The neutron energy was selected as 14.5MeV. On the other hand, in our measurement, the energy was 14.1MeV. We used the compiled data of vanadium for this comparison.

5. Results

Table 1 shows the obtained gamma-ray production cross sections. The table excludes the data in evaluated nuclear data files, because insufficient data of discrete gamma-rays exist for vanadium. It is found from Fig.7 that SINCROS-Ⅱ can well reproduce the experimentally obtained neutron and charged particle DDXs. Thus the present calculation results are reliable.

Fig.8 shows the ratios of SINCROS-Ⅱ results and Simakov's data to our experimental data. The results by SINCROS-Ⅱ support our data, giving the conclusion that the consistency among neutron, charged particle and gamma-ray was confirmed in the theoretical calculation. On the other hand, Simakov's data fairly deviated mainly because the number of experimental data of vanadium is few, i.e., 2 to 4. Simakov's evaluation should be re-examined considering the reliability of the experiments included.

6. Conclusion

The secondary gamma-ray production cross sections of vanadium have been measured. The experimental data were compared with the theoretical calculation results and the evaluation results based on other experimental data. From the results of comparisons, we can conclude as follows:

①The calculation results by SINCROS-Ⅱ supported our data.

②The consistency among neutron, charged particle and gamma-ray was confirmed in the calculations by SINCROS-Ⅱ.

③The data evaluated by Simakov should be re-examined.

References:

[1] Maekawa,F. et al. Fall Meeting of the Atomic Energy Society of Japan,A-11(1997)

[2] Kokooo et al. Annual Meeting of the Atomic Energy Society of Japan,E-6(1998)

[3]Simakov,S.P., Pavlik,A., Vnach,H., Hlavac,S. 「Status of Experimental and Evaluated Discrete γ-ray Production Cross Section at E_n=14.5MeV」 INDC(CCP)-413

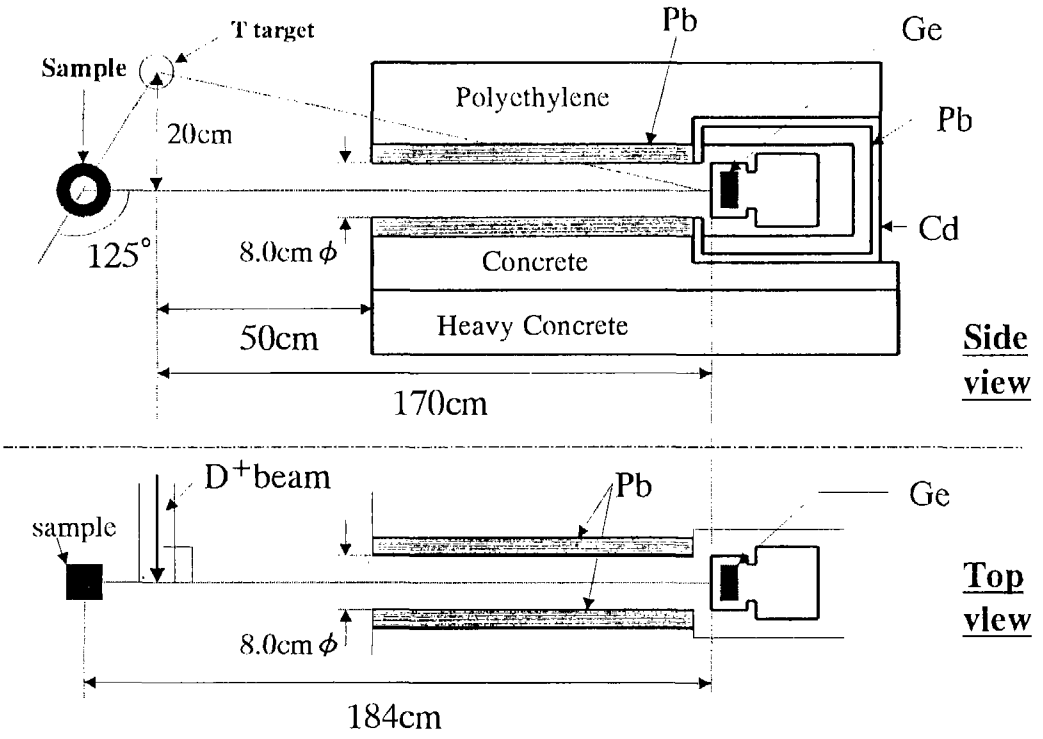

Fig.1 Experimental Geometry in OKTAVIAN

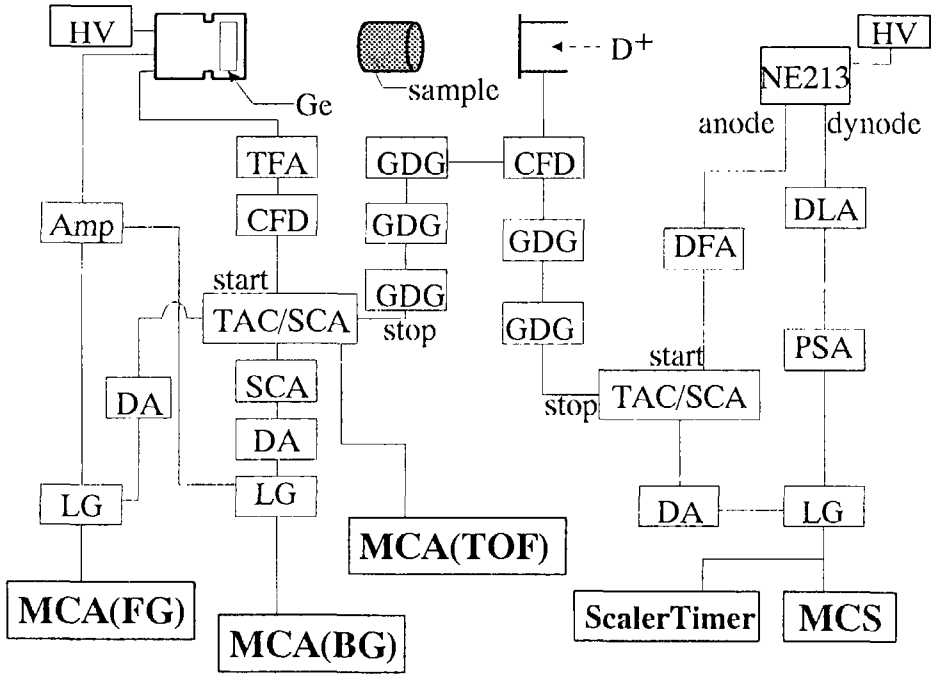

Fig.2 Block diagram of electronic circuits for TOF system

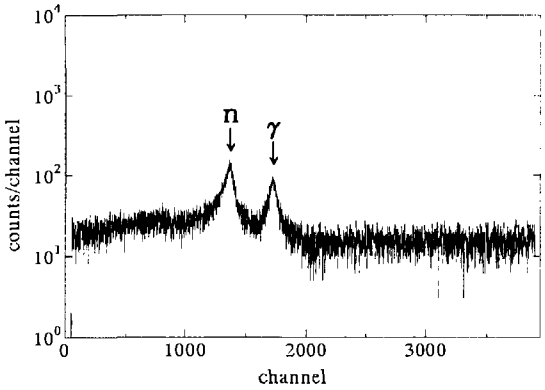

Fig.3 TOF Spectrum for V-51

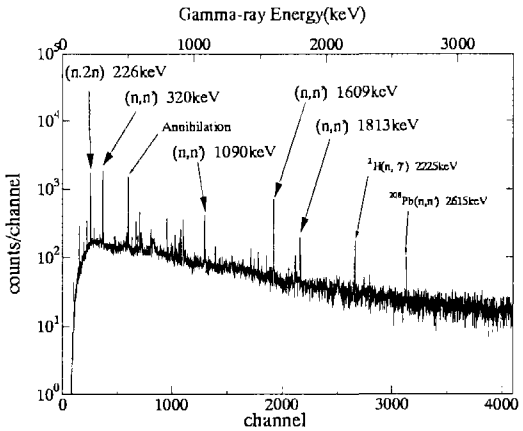

Fig.4a Secondary Gamma-ray(Foreground) Spectrum from V-51(At 125 deg.)

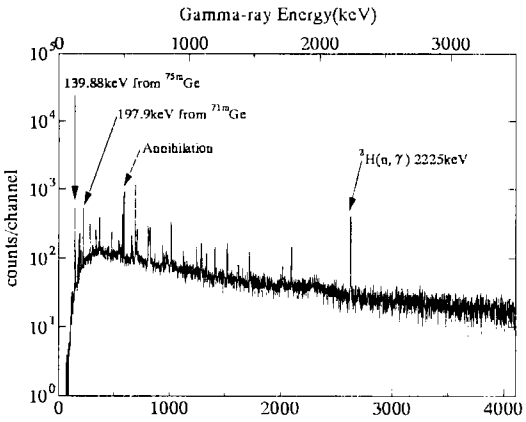

Fig.4b Background Spectrum

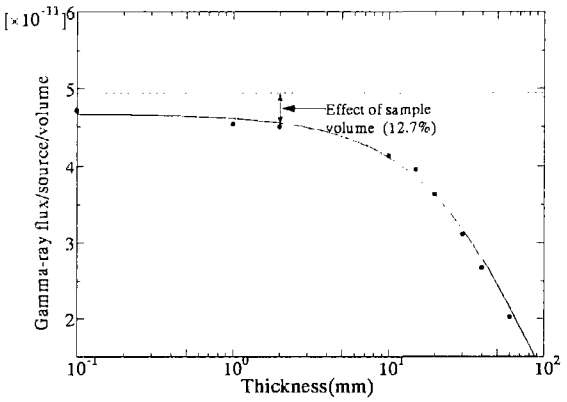

Fig.5 Caluclation results of neutron multiple scattering and gamma-ray attenuation inV-51 sample by MCNP-4a

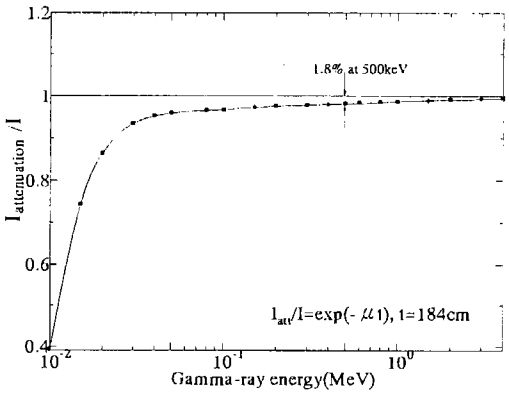

Fig.6 Correction curve about attenuation by air obtained from absorption coefficient

Table 1 Discrete γ-ray Production Cross Sections of vanadium

energy	cross section(mb)		
(keV)	125 deg.	SINCROS-II	S.P.Simakov
226	313±29	354	368±48
320	135±12	126	313±14
684	21.9±2.7	25.9	
815	3.1±1.0		19±1.6
836	10.7±1.5	17.3	31±3
910	42.8±5.0	58.9	88±6.9
929	38.0±4.3	55.8	49±2.4
946	10.0±1.4	1.62	19±1.5
1090	65.7±6.6	60.4	60±2.4
1121	3.6±1.0	3.07	13.4±1.5
1174	18.8±3.5	1.53	20±1.9
1437	17.2±2.0	18.8	18±2.9
1494	13.8±1.7	13.1	17.1±2.8
1554	15.8±1.7	17.6	30.3±1.8
1609	184±17	159	214±8
1777	10.0±1.3		32.5±8.5
1813	46.9±4.7	46.3	68.1±4.4
2004	6.52±1.0		11.6±3.8
2334	6.97±1.0	1.69	17.3±1.7

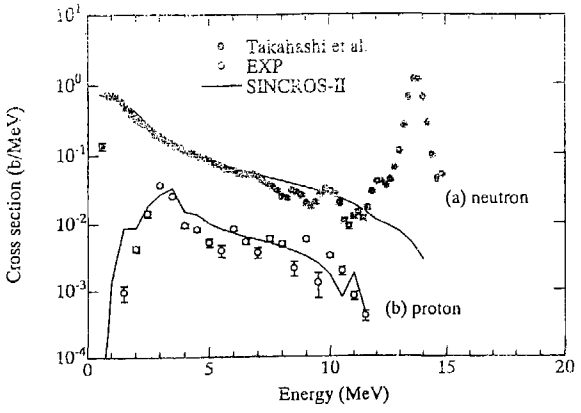

Figiure 7 Comparison of neutron(a) and proton(b) emission cross sections of vanadium

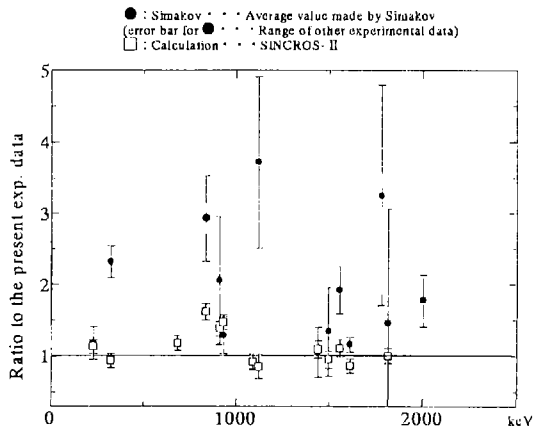

Fig.8 The ratios of SINCROS-Ⅱ and Simakov's data to our experimantal data (present exp. = 1)

JP9950336

3.19 Measurement of Double Differential Cross Sections of Charged Particle Emission Reactions for ^{nat}Zr, ^{27}Al and ^{nat}Ti by Incident DT Neutrons

Hiroyuki Takagi, Kokooo, Isao Murata, Akito Takahashi
Department of Nuclear Engineering, Osaka University
Yamadaoka 2-1, Suita, Osaka, 565-0871, Japan
E-mail: takagi@newjapan.nucl.eng.osaka-u.ac.jp

The double differential cross sections of $^{nat}Zr(n,xp)$, $^{27}Al(n,xp)$, $^{27}Al(n,x\alpha)$, $^{nat}Ti(n,xp)$ and $^{nat}Ti(n,x\alpha)$ reactions have been measured by E-TOF two-dimensional analysis method. The measured data were compared with other experimental data, evaluated nuclear data of JENDL fusion-file and theoretical calculation results by SINCROS-Ⅱ.

1.Introduction

Double differential cross sections (DDXs) of charged particle emission reactions induced by incident DT neutrons are important for the evaluation of nuclear heating and material damages in fusion reactor design. However, until now only a few data have been measured because of experimental difficulties, such as very large background and low counting rates. Li_2ZrO_3, $LiAlO_2$ and Li_2TiO_3 can be considered to use as solid breeder material in fusion power reactors because of their inherent advantages, e.g., chemical stability at high temperature, compatibility with structural materials, good tritium recovery characteristics and so on [1]. Thus, the fusion neutronics benchmark experiments have been done for various materials including these breeder materials, low-activation elements and so on at FNS in JAERI [2]. In connecting with these experiments, DDXs of $^{nat}Zr(n,xp)$, $^{27}Al(n,xp)$, $^{27}Al(n,x\alpha)$, $^{nat}Ti(n,xp)$ and $^{nat}Ti(n,x\alpha)$ reactions induced by incident DT neutrons have been measured at OKTAVIAN in Osaka University.

2. Experimental procedure

Experiments were carried out by using the charged particle spectrometer based on the two dimensional analysis of energy and time-of-flight of emitted charged particle [3]. The schematic arrangement of the spectrometer is shown in Fig. 1. The spectrometer was located in a vacuum chamber of 1m ϕ × 1m long. The chamber was evacuated to keep a pressure of about 1.3 Pa. The shield assembly made of iron, polyethylene and lead reduced the backgrounds. The CsI(Tl) scintillator, 2mm in thickness and 50mm in diameter, was used as a charged particle detector. The tritium target of pulsed neutron source was positioned in a through tube of the chamber and out of vacuum. The spectrometer can be used to measure the DDX data for emission angles between 30° and 135° . The flight path of emitted particle varies from 30.8 cm to 56.7 cm according to change of the emission angle. The sample

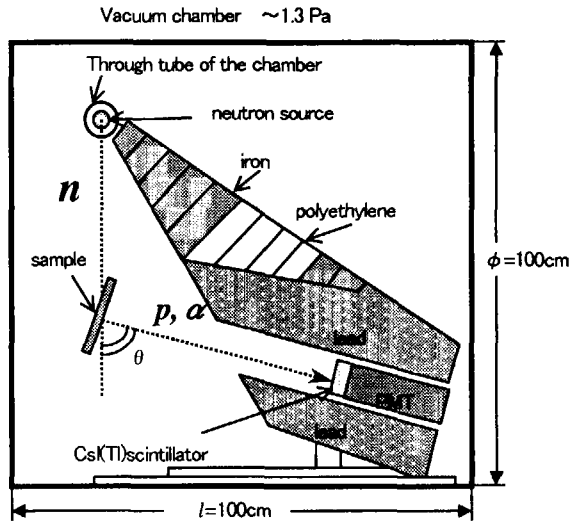

Fig.1 Schematic arrangement of the charged particle spectrometer.

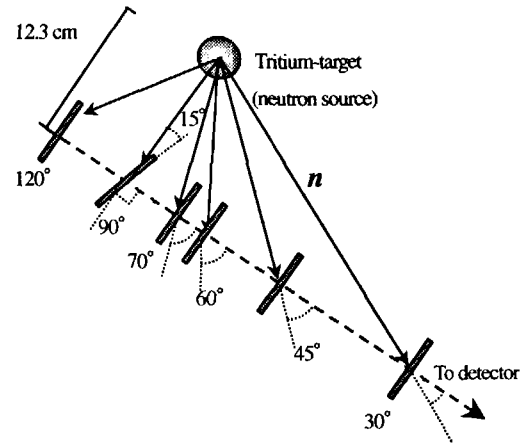

Fig. 2 Sample position for various emission angles.

position for various scattering angles can be seen in Fig. 2.

The block diagram of the measuring system is shown in Fig. 3. The two dimensional data acquisition has been done by using the pulse-height of dynode signal corresponding to energy and the time-of-flight signal made from the anode signal as start and the beam pick-up ring signal (with delay) as stop. The logic signal created by pulse-shape discrimination (PSD) circuit has been used as the gate signal for E-TOF two-dimensional acquisition. The details about the E-TOF measurement are described in Ref. [3]. An NE213 scintillator is used as a relative neutron flux monitor. In this experiment, thin foil samples of zirconium, aluminum and titanium were employed. The details of the samples are shown in Table 1.

The reason why the CsI(Tl) detector was chosen is its typical property of pulse-shape discrimination. Fig. 4 shows an example of two-dimensional distribution of energy and rise-time for α -particle, proton and γ -ray, by

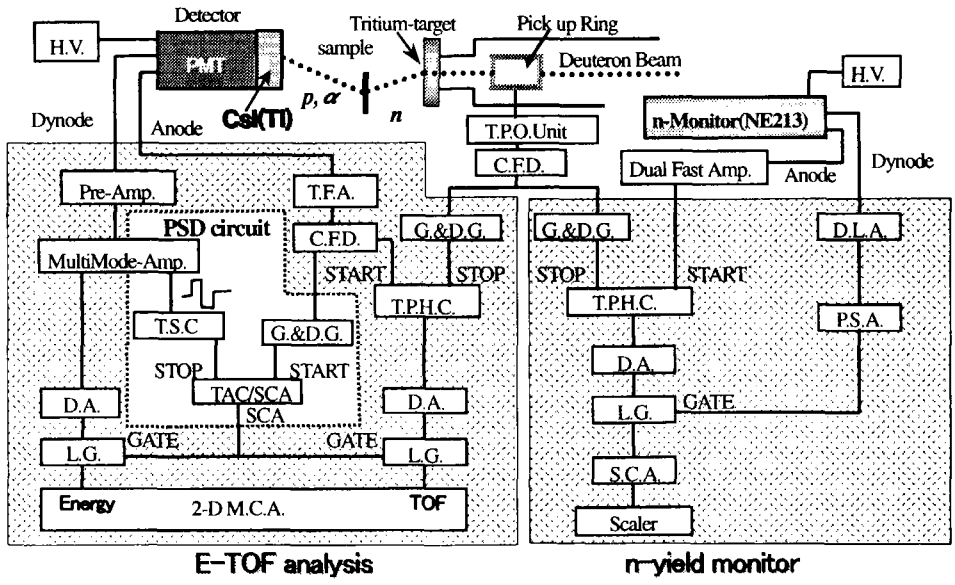

Fig. 3 Block diagram of the measuring system.

using CsI(Tl) detector. The proton reference source was obtained by bombarding the polyethylene sample by DT neutrons. The ^{241}Am standard source was used as α reference. As shown in the figure, the contours of each particle signals were separated each other. Thus, we can choose either α -particle or proton signal by this technique. However, there still exist background counts by the charged particles produced in the surrounding structural materials, such as through tube, vacuum chamber, shield assembly and so on. So, an additional technique, namely the two-dimensional E-TOF analysis for charged particles, was applied. It is based on the following equation,

Table 1 The dimension of the samples.

Sample	Measured particle	ϕ [cm]	Thickness [μ m]	Isotopes (abundance)[%]
^{nat}Zr	*proton*	6.0	25.0	^{90}Zr 51.453 ^{91}Zr 11.224 ^{92}Zr 17.152 ^{94}Zr 17.384
^{27}Al	*proton*	6.0	25.0	^{27}Al 100.00
	α-particle		10.0	
^{nat}Ti	*proton*	6.0	20.0	^{46}Ti 8.25 ^{47}Ti 7.44 ^{48}Ti 73.22 ^{49}Ti 5.41 ^{50}Ti 5.18
	α-particle		10.0	

$$T = F_p \sqrt{\frac{M}{2E}}, \quad (1)$$

where, T is the time-of-flight, F_p the flight path length, and E and M the energy and mass of the particle, respectively. According to this equation, measurement of charged particles produced in samples was achieved successfully.

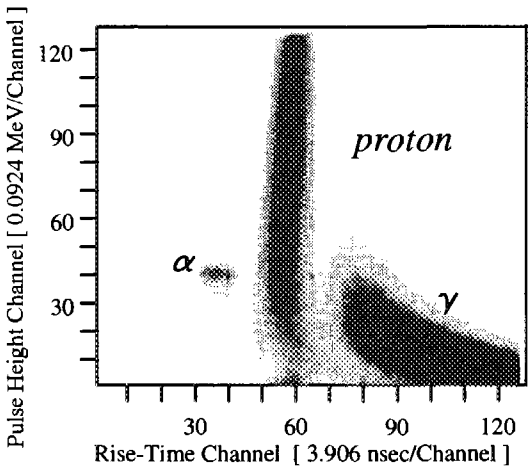

Fig. 4 Two-dimensional distribution of rise time and pulse height spectrum.

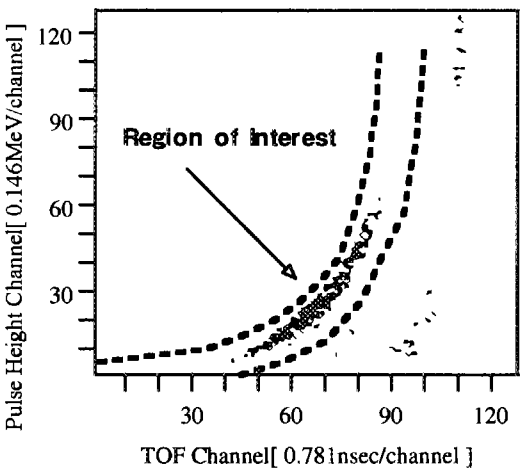

Fig.5 Measured E-TOF spectrum from 27-Al(n,x α) reaction at the emission angle of 60 degree.

3. Data analysis

The net raw data were obtained by subtracting the data in background run from that of foreground run. The background run was undertaken without sample. In Fig. 5, the net raw data spectrum of α -particle from ^{27}Al(n,x α) reaction at the emission angle of 60° is shown as an example. The integral counts of respective charged particle, i.e., proton and α -particle, for each pulse-height channel, namely the net energy spectrum, have been obtained by properly choosing the region of interest within the corresponding contour of E-TOF spectrum.

In this experiments, the lower-energy thresholds of proton and α-particle measurements were 2.5 MeV and 3 MeV, respectively.

To obtain absolute DDX, $\sigma(E, \theta)$ barn/sr/MeV, the net energy spectrum was normalized by comparing the value of angular differential cross section (ADX) of evaluated nuclear data files for recoil proton from H(n,p) reaction with the yield of recoil proton obtained by measurement of thin polyethylene sample [3].

The raw data must be corrected because the broadening functions of angular resolution and the energy loss of the charged particle in the sample are not negligible. The Monte-Carlo simulation calculations with the JENDL-FF cross section data and Bethe-Bloch formula were used to obtain the correction factors for every angle point.

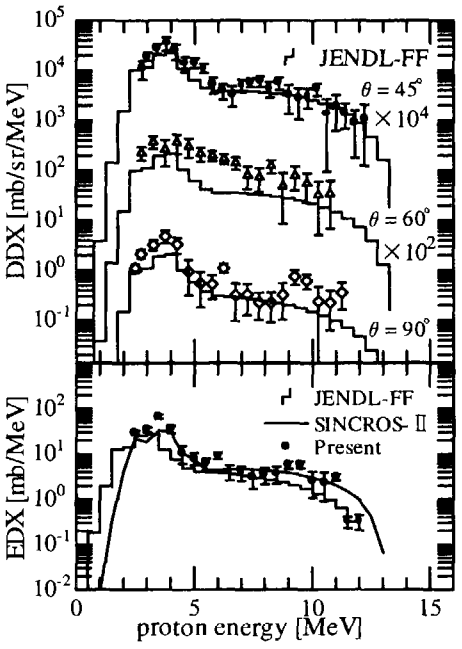

Fig.6 The DDX and EDX data of Zr(n,xp) reaction.

4. Results and discussions

The EDXs and total cross sections were deduced by using the measured DDXs. The measured data were compared with other experimental results, JENDL-FF and SINCROS- II calculation. In SINCROS- II calculations, the normalization factors were determined by comparing the calculated EDX data for neutron emission reaction with the measured data of Takahashi [4,5] for the same nuclides. The experimental results and discussion are described in the following in detail. The comparisons of the total cross sections among the measured data, JENDL-FF and other experimental results are summarized in Table. 2.

4.1. Zirconium

The measurements of proton emission DDXs have been done for three emission angles, i.e., 45, 60, and 90 degrees. The measured DDX and EDX data are shown in Fig. 6. The measured EDX data are larger than the JENDL-FF and SINCROS- II calculations mainly in the energy region between 2 to 4 MeV and 9 to 11 MeV. In the total cross section, the JENDL-FF is largely underestimated.

4.2. Aluminum

The DDX data for proton emission reactions were

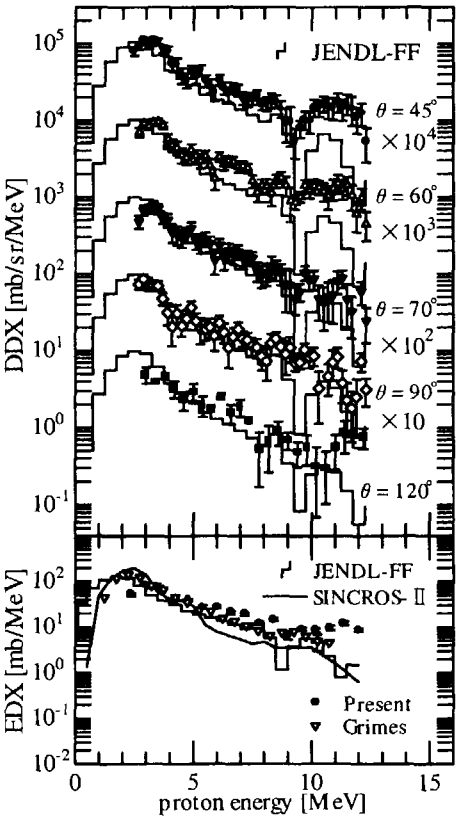

Fig. 7 The DDX and EDX data of Al(n,xp) reaction.

obtained at the emission angles of 45, 60, 70, 90 and 120° . Fig. 7 shows the measured DDX and EDX data. The present EDX data agree well with other reference data in the energy region between 3 to 5 MeV, while it gives larger data for the energies greater than 5 MeV. In the total cross section, the measured value is smaller than Grimes' data [8] and JENDL-FF, due to low-energy cutoff of this experimental method.

The measured DDX data for α emission reactions at the emission angles of 45, 60, 70, 90 and 120° were provided. In Fig. 8, the measured DDX and EDX data are shown. A fairly good agreement between the present EDX result and JENDL-FF was obtained in the energy region from 4.5 to 9 MeV. However, overestimate of the JENDL-FF is shown in energies lower than 4.5 MeV. For the total cross section, the measured value is slightly smaller than other data.

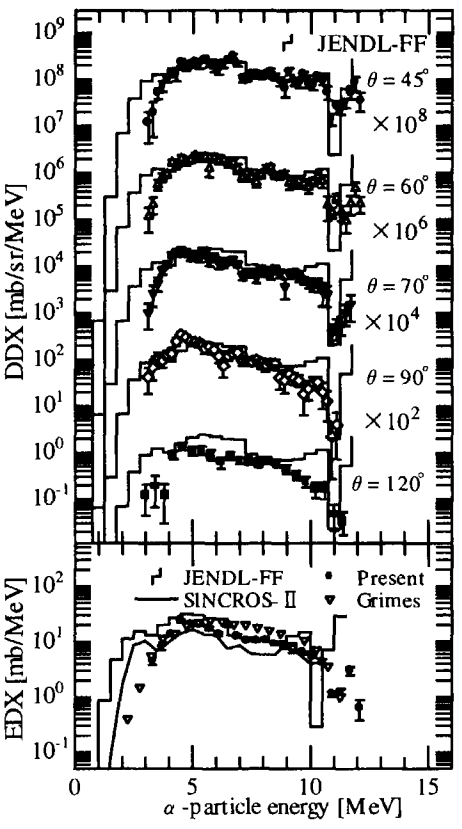

Fig. 8 The DDX and EDX data of Al(n,x α) reaction.

4.3. Titanium

The DDX data of proton emission reactions at emission angles of 60, 70, 90 and 120° were measured. The measured DDX and EDX data are shown in Fig. 9. The JENDL-FF and SINCROS-II calculations were smaller than the measured EDX data for energies greater than 7.5 MeV. The total cross section of JENDL-FF is something smaller than the measured data.

The obtained DDX data of α emission reactions at emission angles of 45, 60, 70 and 90° and EDX data are shown in Fig. 10. The measured EDX data were not in agreement with JENDL-FF and SINCROS-II calculation. The total cross section of the measured data agrees well with the JENDL-FF.

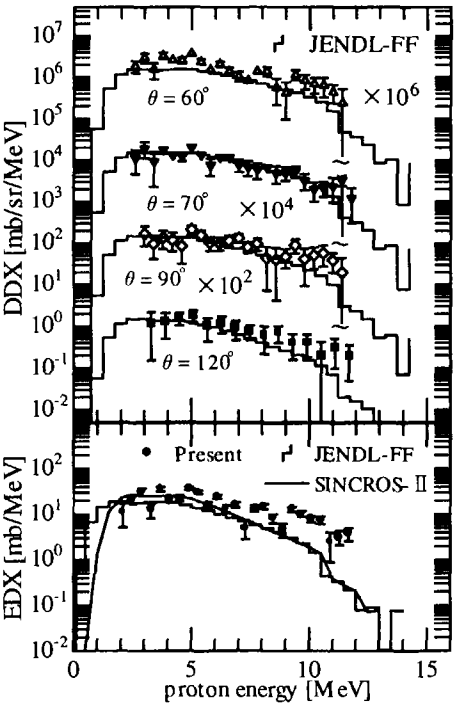

Fig. 9 The DDX and EDX data of Ti(n,xp) reaction.

5. Conclusions

The DDXs of ^{nat}Zr(n,xp), ^{27}Al(n,xp), ^{27}Al(n,x α), ^{nat}Ti(n,xp) and ^{nat}Ti(n,x α) reactions have been measured at the emission angles between 45 to 120° . The measured data were compared with other experimental data, evaluated nuclear data of JENDL-FF and theoretical calculation results by SINCROS-II. The JENDL-FF data for ^{nat}Zr(n,xp) reaction is largely underestimated. In DDX and EDX data of ^{27}Al(n,x α) reaction, the disagreement of the

measured data and JENDL-FF is shown in low energy region (<5 MeV). The measured DDX and EDX spectrum for ^{nat}Ti(n,x α) reaction were not in agreement with JENDL-FF and SINCROS-II calculation overall.

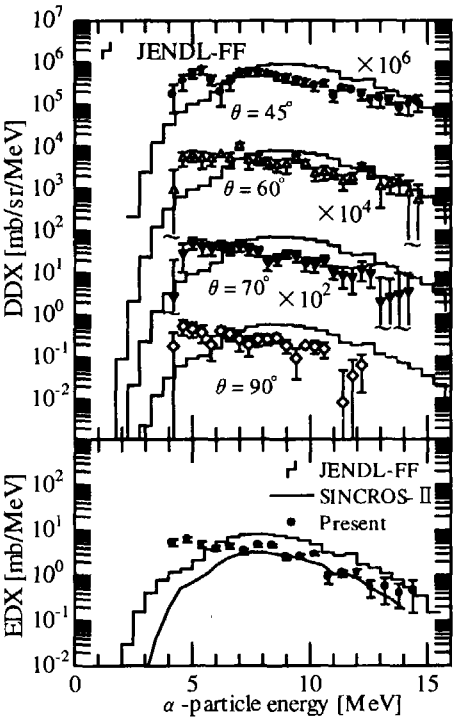

Fig. 10 The DDX and EDX data of Ti(n,x α) reaction

References

[1] Johnson, C. E., *et al.*: "Solid Breeder Materials", *J. Nucl. Mat.*, 103&104, 547 (1981).

[2] Kokooo *et al.*: "Benchmark Experiment on Vanadium Assembly with D-T Neutrons -Leakage Neutron spectrum Measurement-", *Fusion Technol.*, 34, 980 (1998).

[3] Takahashi, A., *et al.*: "A Time-of-Flight Spectrometer with Pulse-Shape Discrimination for the Measurement of Double-Differential Charged-Particle Emission Cross Sections", *Nucl. Instr. Meth.*, A 401, 93 (1997).

[4] Takahashi, A., *et al.*: "Double and Single Differential Neutron Emission Cross Section at 14.1 MeV: Vol.1", *OKTAVIAN Report*, A-87-03, Osaka University, (1987).

[5] Takahashi, A., *et al.*: "Double and Single Differential Neutron Emission Cross Section at 14.1 MeV: Vol.2", *OKTAVIAN Report*, A-92-01, Osaka University, (1992).

[6] Ahn, S. H., *et al.*: "Charged Particles from the 14-MeV Neutron Interaction with Zirconium", *Phys. Rev.*, 119, 1667 (1960).

[7] Armstrong, A. H., *et al.*: "14-MeV (n, α) and (n,p) Cross Sections in Zirconium. II", *Phys. Rev.*, 99, 330 (1955).

[8] Grimes, S. M., *et al.*: "Measurement of Sub-Coulomb-Barrier Charged Particles Emitted from Aluminum and Titanium Bombarded by 15-MeV Neutrons", *Nucl. Sci. Eng.*, 62, 187 (1977).

[9] Kneff, D. W., *et al.*: "Helium Production in Pure Elements, Isotopes, and Alloy Steels by 14.8-MeV Neutrons", *Nucl. Sci. Eng.*, 92, 491 (1986).

Table 2 The measured total cross-sections of charged particle emission reactions compared with JENDL-FF and other experimental results.

Reaction	Present Work σ (mb) (E_n = 14.1 MeV)	JENDL-FF σ (mb)	Other experiment σ (mb)
^{nat}Zr(n,xp)	124.7±6.6	68.5	87±22 (E_n=14 MeV) Ahn [6] 180±70 (E_n=14 MeV) Armstrong [7]
^{27}Al(n,xp)	286.2±5.8	361.4	399±60 (E_n=15 MeV) Grimes [8]
^{27}Al(n,x α)	91.3±1.5	125.2	121±25 (E_n=15 MeV) Grimes [8] 143±7 (E_n=14.8 MeV) Kneff [9]
^{nat}Ti(n,xp)	153.1±6.4	105.4	117.4 (E_n=15 MeV) Grimes [8]
^{nat}Ti(n,x α)	34.8±1.2	39.5	36.1 (E_n=15 MeV) Grimes [8]

JP9950337

3.20 Measurement of cross sections in the region of sub-mbarn by 14 MeV neutron with well-type HPGe detector

H. Sakane*, M. Shibata*, H. Yamamoto*, K. Kawade*, Y. Kasugai** and Y. Ikeda**
*Energy Engineering and Science, Nagoya University,
Furo-cho, Chikusa-ku, Nagoya 464-8603
e-mail: sakane@fnshp.tokai.jaeri.go.jp
**Japan Atomic Energy Research Institute,
Tokai-mura, Naka-gun, Ibaraki-ken 319-11

Seven neutron activation cross sections were newly measured at energy range between 13.4 and 14.9 MeV by a high efficiency well-type HPGe detector. The cross sections of the ^{95}Mo(n,n'p)^{94m}Nb, ^{100}Mo(n,n'p)^{99m}Nb, ^{116}Cd(n,np)^{115g}Ag, ^{123}Te(n,n'p)^{122m}Sb and ^{176}Yb(n,np)^{175}Tm reactions were obtained for the first time. The cross section of ^{176}Yb(n,α)^{173}Er and ^{190}Os(n,p)^{190g}Re reactions were obtained at the six energy points between 13.4 and 14.9 MeV, although the previous results had been obtained at one energy point.

1 Introduction

Neutron activation cross section data around 14 MeV are important from the view point of the fusion reactor technology in terms of estimations of radiation damage, nuclear transmutations, induced activity and so on. In the view point of gas production, we need to know the (n,p), (n,α) and (n,np) reaction cross sections, although producing short-lived nuclei are not important for the problem of induced activity. Our systematics proposed on the basis of 58 cross section data of (n,p) and 33 data of (n,α) reaction. The systematics predicts well the excitation functions around 14 MeV within $\pm$30%. To construct the systematics for (n,np) reaction, we needs to obtain the cross section data for (n,np) reaction. By the use of a high efficiency well-type HPGe detector, generally weak (n,np) cross section were mainly measured. Measured reactions and decay parameters are listed in Table 1.

2 Experiment

Experiments were carried out at the FNS (Fusion Neutronics Source) facility. A pneumatic sample transport system was used for the irradiation of samples. The angles of the irradiation position to the d^+ beam were 0, 45, 70, 95, 120 and 155 degree, which covered the neutron energies from 14.9 to 13.4 MeV. The distance between the D-T neutron target and the irradiation position was 10 cm. The average neutron flux at the irradiation position was about 1×10^8 n/cm^2/s. The effective incident neutron energy at the irradiation position was determined by the ratio of the ^{90}Zr(n,2n)^{89}Zr and ^{93}Nb(n,2n)^{92m}Nb reaction rates. The induced activities were measured by a well-type HPGe detector. The efficiency in the bottom of the detector is 6-7 times larger than those at the surface position of the detector as shown Fig. 1. Corrections were made for time fluctuation of neutron flux, contribution of low energy neutron below 10 MeV, thickness of samples, self-absorption of the gamma ray and sum-peak effect of the gamma ray. The details of each correction are described elsewhere [1]. The total errors (δ_t) were described by combining the experimental errors (δ_e) and the errors of nuclear data (δ_r) in quadratic: $\delta_t^2 = \delta_e^2 + \delta_r^2$.

3 Experimental Results

Experimental results for the cross sections are shown in Table 2 and Figs. 2 − 8. The The σ_{14} and the relative slope calculated by the systematics for^{176}Yb(n,α)^{173}Er reaction is good agreement with experimental value.

4 Conclusion

By the use of a high efficiency well-type detector, the cross sections of the ^{95}Mo(n,n'p)^{94m}Nb, ^{100}Mo(n,n'p)^{99m}Nb,^{116}Cd(n,np)^{115g}Ag, ^{123}Te(n,n'p)^{123m}Sb and ^{176}Yb(n,np)^{175}Tm reactions were obtained for the first time. The cross section of ^{176}Yb(n,α)^{173}Er and ^{190}Os(n,p)^{190g}Re reactions were obtained at the six energy points between 13.4 and 14.9 MeV, although the previous results had been obtained at one energy point. The study of the systematics for (n,np) reaction are now in progress.

References

[1] K.Kawade et al.: JAERI-M 92-020 (1992)

[2] E. Browne et al.: "Table of Radioactive Isotope", John Wiley & Sons, New York (1986).

[3] R.B. Firestone et al.: "Table of isotopes 8th Edition", John Wiley & Sons, New York (1996).
[4] Y. Kasugai et al.: Ann. Nucl. Energy Vol. 23, 1429 (1996)

Table 1 Measured reactions and decay parameters

Reaction	Half-life	Gamma-ray Energy (keV)	Intensity per decay (%)	Q-value(MeV)
^{95}Mo(n,n'p)^{94m}Mo	6.26m	871.097	0.50±0.06	-8.63
^{100}Mo(n,n'p)^{99m}Mo	2.6m	365.1	2.53±0.17	-11.1
^{116}Cd(n,np)^{115g}Ag	20.0m	229.1	18±8	-11.1
^{123}Te(n,n'p)^{122m}Sb	4.21m	61.413	53.7±6.1	-8.14
^{176}Yb(n,np)^{175}Tm	15.2m	514.867	65±7	-8.49
^{176}Yb(n,α)^{173}Er	1.4m	895.2	53.8±2.7	5.92
^{190}Os(n,p)^{190g}Re	3.1m	186.68	48.4±2.2	-2.39

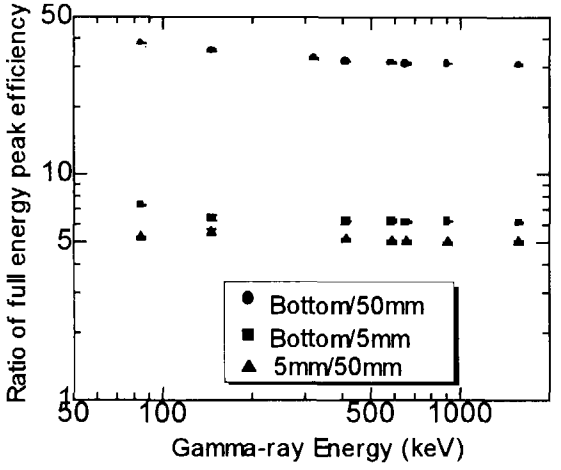

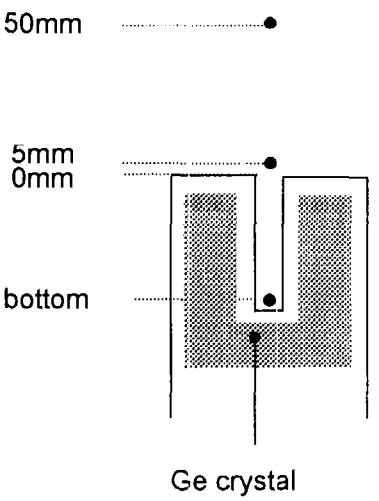

Fig. 1 Ratios of full-energy efficiencies of the well-type HPGe at 50mm, 5mm and bottom potision. Lines are given for eye guide.

Table 2 Activation cross sections of short-lived nuclei

Neutron Energy(MeV)	^{95}Mo(n,np)^{94m}Nd				^{100}Mo(n,np)^{99m}Nd			
	Sigma(mb)	δ_t(%)	δ_e(%)	δ_r(%)	Sigma(mb)	δ_t(%)	δ_e(%)	δ_r(%)
14.87	28	30	16	12	3.2	23	21	11
14.64	21	36	25	12	2.9	23	20	11
14.35	17	36	25	12	2.6	24	22	11
14.02	11	43	35	12	2.3	25	23	11
13.70					1.3	34	33	11
13.40					1.2	43	41	11

Neutron Energy(MeV)	^{116}Cd(n,np)^{115g}Ag				^{123}Te(n,np)^{122m}Sb			
	Sigma(mb)	δ_t(%)	δ_e(%)	δ_r(%)	Sigma(mb)	δ_t(%)	δ_e(%)	δ_r(%)
14.87	0.57	59	32	45	0.56	31	20	5.0
14.64	0.45	61	35	45	0.47	30	20	5.0
14.02					0.19	39	32	5.0
13.70	0.40	84	68	45	0.13	71	68	5.0
13.40	0.27	87	71	45				

Neutron Energy(MeV)	^{176}Yb(n,np)^{175}Tm				^{176}Yb(n,α)^{173}Er			
	Sigma(mb)	δ_t(%)	δ_e(%)	δ_r(%)	Sigma(mb)	δ_t(%)	δ_e(%)	δ_r(%)
14.87	0.87	26	8	12	0.76	43	35	10
14.64	0.73	27	9	12	0.52	46	38	10
14.35	0.55	27	10	12	0.41	47	40	10
14.02	0.30	30	16	12	0.48	47	40	10

Neutron Energy(MeV)	^{190}Os(n,p)^{190g}Re			
	Sigma(mb)	δ_t(%)	δ_e(%)	δ_r(%)
14.87	2.9	37	26	14
14.64	2.6	36	25	14
14.35	2.5	43	34	14
14.02	1.6	37	26	14
13.70	1.2	45	37	14
13.40	0.8	63	57	14

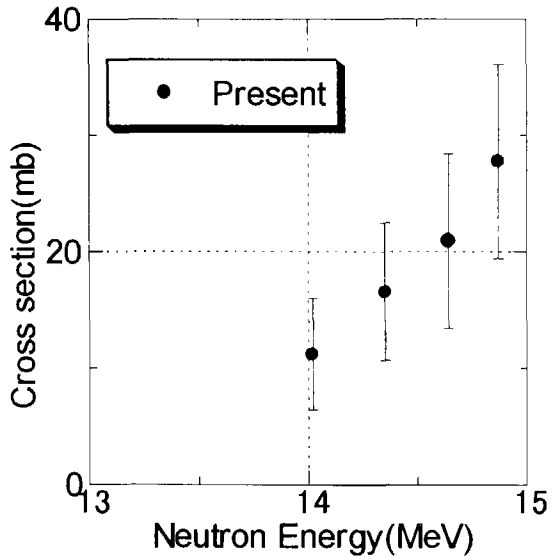

Fig. 2 Measured cross section data of $^{95}Mo(n,n'p)^{94m}Nb$ reaction.

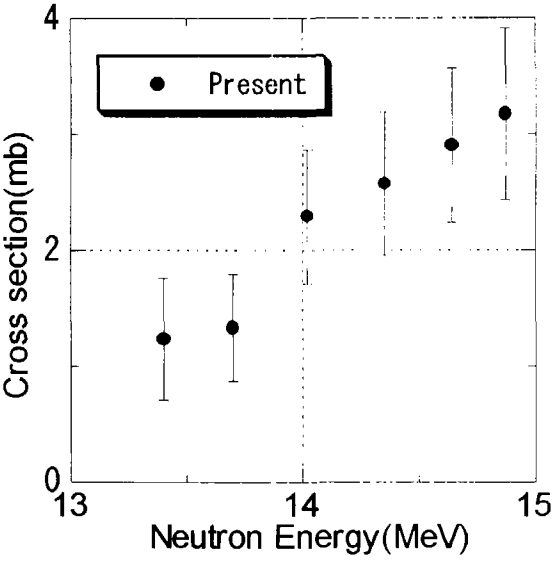

Fig. 3 Measured cross section data of $^{100}Mo(n,n'p)^{99m}Nb$ reaction.

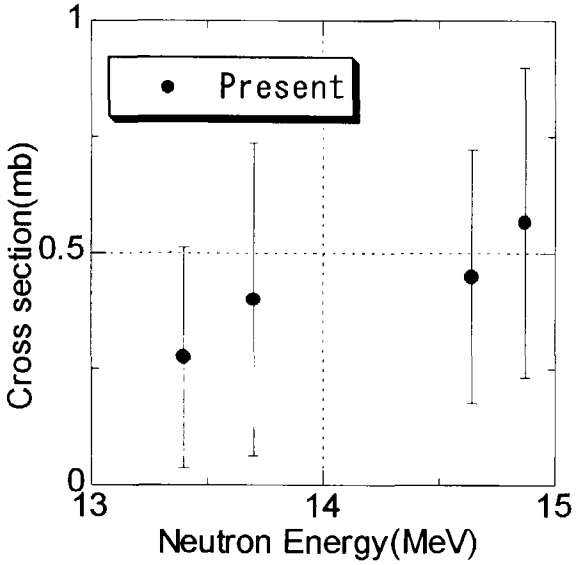

Fig. 4 Measureed cross section data of $^{116}Cd(n,np)^{115g}Ag$ reaction.

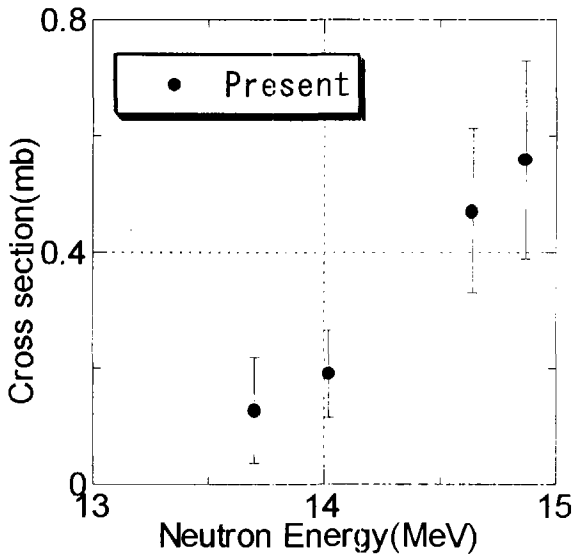

Fig. 5 Measured cross section data of $^{123}Te(n,n'p)^{122m}Sb$ reactions.

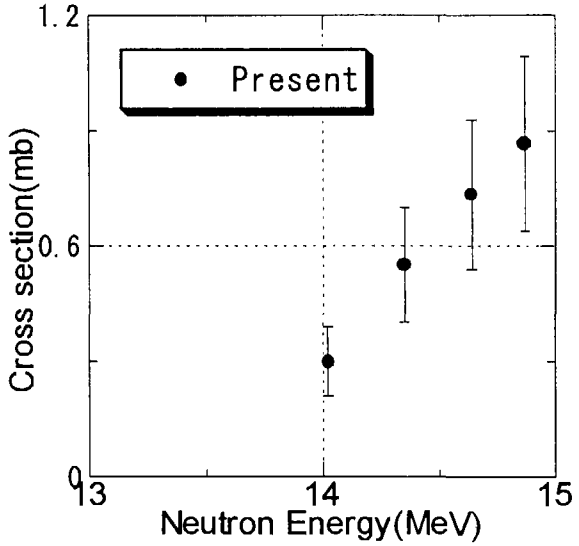

Fig. 6 Measured cross section data of ^{176}Yb(n,np)^{175}Tm reaction.

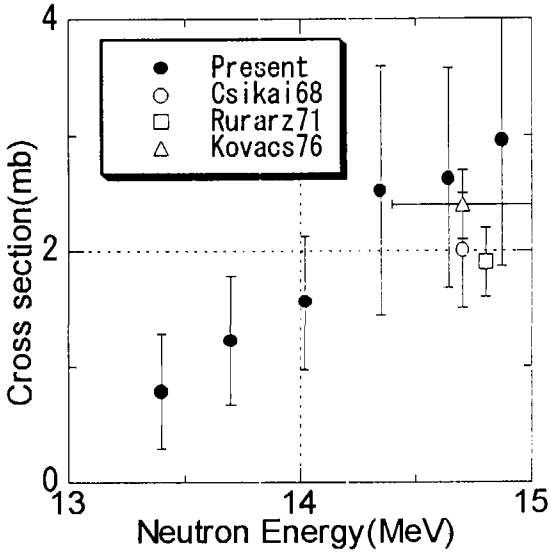

Fig. 7 Measured cross section data of ^{190}Os(n,p)^{190g}Re reaction.

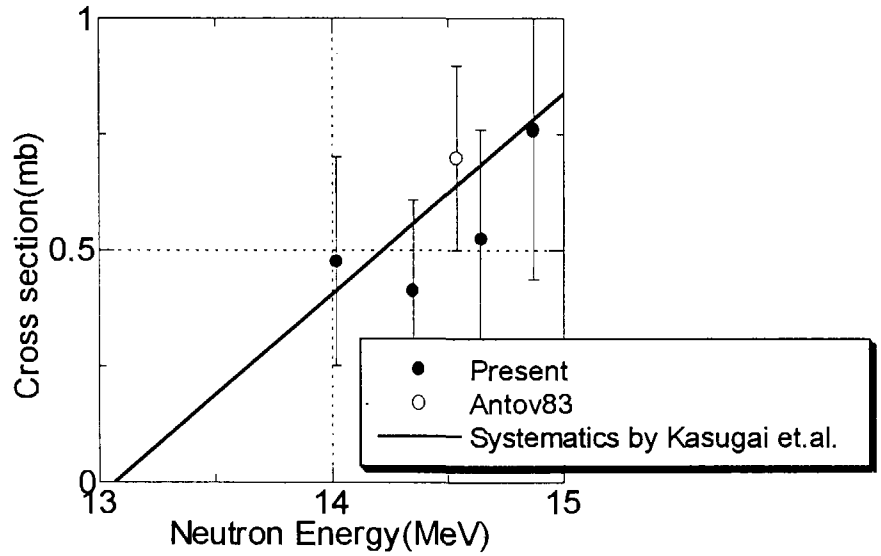

Fig. 8 Measured cross section data of ^{176}Yb(n,α)^{173}Er reaction.

3.21 Measurement of Discrete Gamma-ray Production Cross Sections for Interactions of 14 MeV Neutron with Mg, Al, Si, Ti, Fe, Ni, Cu, Nb, Mo and Ta

Hitoshi Sakane*, Yoshimi Kasugai**, Fujio Maekawa**,
Yujiro Ikeda** and Kiyoshi Kawade*
*Energy Engineering and Science, Nagoya University,
Furo-cho, Chikusa-ku, Nagoya 464-8603
e-mail: sakane@fnshp.tokai.jaeri.go.jp
**Japan Atomic Energy Research Institute,
Tokai-mura, Naka-gun, Ibaraki-ken 319-1195

We started to measure systematically discrete gamma-ray production cross sections by 14 MeV DC neutron beam. Measured targets were Mg, Al, Si, Ti, Fe, Ni, Cu, Nb, Mo and Ta. Some discrete gamma-ray production cross section data for these targets were newly obtained. The data for Ta were obtained for the first time. The experimental efficiency attained by the use of the method was about 50 times larger than the general experiments using pulsed neutrons. In result, good statistic data could be obtained in a short span of time.

1 Introduction

Gamma-ray production cross sections for 14 MeV neutrons are of importance not only for radiation shielding designs of nuclear facilities but also for evaluation of gamma-ray heating of fusion reactors. Besides the practical importance, discrete gamma-ray spectra and production cross sections are required to understand the nuclear structure and the neutron reaction mechanism. However accurate experimental data have not been measured sufficiently or there are no available data for some specific materials, because a suitable experimental environment has been limited. Thus, we started to measure systematically discrete gamma-ray production cross sections for 14 MeV neutrons. For the measurement, a high performance collimator system was installed at FNS to extract 14 MeV neutron beam.

2 Experiment

The experimental arrangement is shown in Fig. 1. The main collimator was composed of a Fe block 120 cm thick, a polyethylene block 40 cm thick, a Cd sheet 1mm thick and a Pb block 20 cm thick, and the pre-collimator was composed of a Fe block 50 cm thick.

The diameter of collimator was 2 cm. The angle between the deuteron beam and the axis of the collimated neutron beam was 80 degree, which resulted in a 14.2 MeV neutron energy. The absolute neutron flux was determined by the $^{27}Al(n,\alpha)^{24}Na$ and $^{93}Nb(n,2n)^{92m}Nb$ reaction rate, and a fission chamber was used as a relative flux monitor. The average neutron flux at the irradiation position was about 5×10^5 n/cm^2/s. Samples were metals of natural abundance with 1.5 cm in diameter and 1 cm in thickness. Purity of the samples was more than 99.9%. Gamma-rays produced by interactions of neutrons with the samples were detected by an anti-compton spectrometer consisting of a HPGe detector and a BGO scintillation counter, which reduced compton continuum by high energy gamma-rays. The HPGe detector was placed at 29.6 cm from the sample with an angle of 90 degree with respect to the axis of the neutron beam. Detected gamma-ray peaks often contained prompt gamma-rays and decay gamma-rays. Decay gamma-rays were measured immediately after stop of the irradiation. They were subtracted from the total gamma-rays measured during the irradiation. Target materials, measurement times and principal gamma-rays are shown in Table 1.

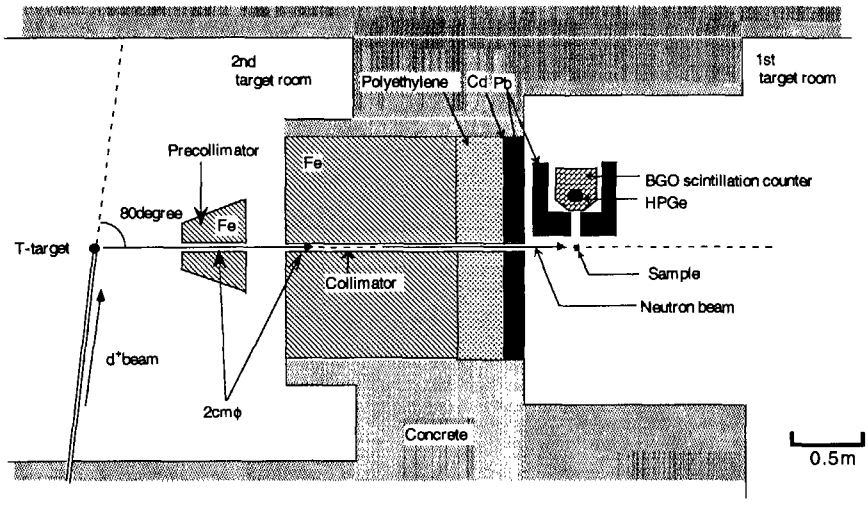

Fig. 1 The experimental arrengement (horizontal cross section).

Table 1 Target materials, measurement times and principal gamma-rays detected.

Material	Measurement time(sec)	Major gamma-ray
Mg	36000	90.993(Mg(n,xpγ)),1368.633(Mg(n,xγ)
Al	33910	472.202(^{27}Al(n,nαγ)), 843.7(^{27}Al(n,n'γ))
Si	36679	1778.7(^{28}Si(n,n'γ)), 2838.67(^{28}Si(n,n'γ))
Ti	35410	983.517(Ti(n,xγ))
Fe	35278	846.8(Fe(n,xγ)), 1238.282(Fe(n,xγ))
Ni	36781	1332.5(Ni(n,xγ)), 1454.45(^{58}Ni(n,n'γ))
Cu	35493	962.06(^{63}Cu(n,n'γ))
Nb	23216	357.49(^{93}Nb(n,2nγ))
Mo	31313	787.374(Mo(n,xγ))
Ta	36000	482.182(^{181}Ta(n,n'γ))

3 Experimental Results and Discussion

Figure 2 and Table 2 show a gamma-ray spectrum for the Fe(n,xγ) reaction and the cross section data, respectively. The structure of Table 2 is following. Figure 3 shows ratios of cross section data for Fe target previously reported to the present data. In the case of intense gamma-rays, good agreements were showed among those data, but in the case of weak gamma-rays, large discrepancies were found among those data. Discrepancies between the present and previous data could be mainly due to the poor energy resolution of NaI(Tl) detectors or the poor counting statistics with use of the pulsed neutron sources. The data of Hlavac, which were systematically measured by using of the pulsed neutron, were in good agreement with the present data.

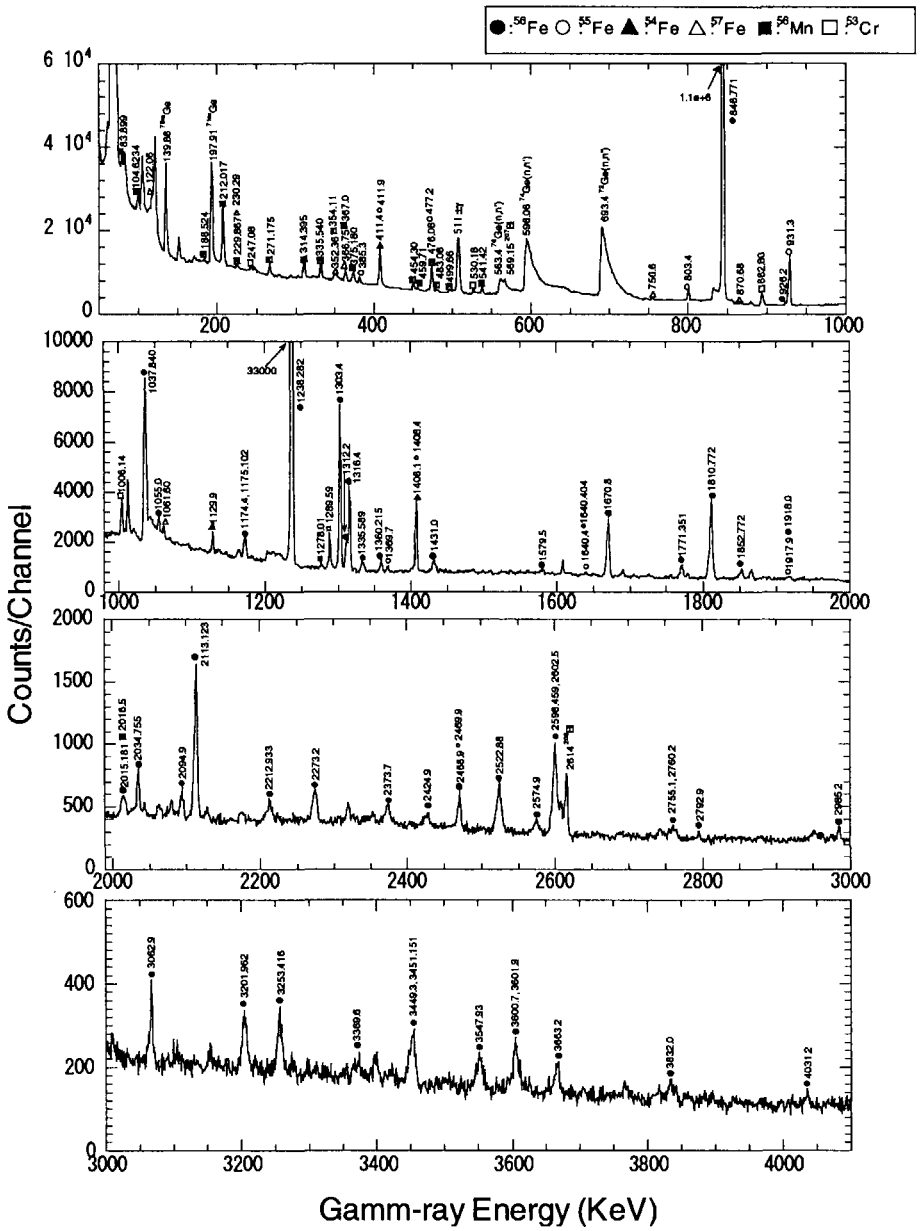

Fig. 2 Gamma-ray spectrum for Fe target at En=14.2 MeV.

Table 2(1/2) Measured discrete gamma-ray production cross section(preliminary)
Column 1- producing reaction; 2 - decay scheme (initial and final levels, their spins and parities); 3 - energy of gamma-ray in keV; 4 – experimental cross section in mb/sr; 5- error of data.

Reaction	Transition	Eγ(keV)	dσ/dΩ(mb/sr)	error(%)
Fe(n,p+np)^{56}Mn	111(1+) → 27(2+)	83.899	1.1	7
Fe(n,p+np)^{56}Mn	215(1+,2+) → 111(1+)	104.6243	0.8	9
Fe(n,n'+2n)^{57}Fe	136(5/2−) → 14(3/2−)	122.06	1.5	7
Fe(n,p+np)^{56}Mn	215(1+,2+) → 27(2+)	188.524	0.2	20
Fe(n,p+np)^{56}Mn	212(4+) → 0(3+)	212.017	3.2	5
Fe(n,p+np)^{56}Mn	716 → 486(3+)	229.867	0.3	19
Fe(n,n'+2n)^{57}Fe	367(3/2−) → 136(5/2−)	230.29		
^{56}Fe(n,α)^{53}Cr	1537(7/2−) → 0(3/2−)	247.08	0.2	19
Fe(n,p+np)^{56}Mn	486(3+) → 215(1+,2+)	271.175	0.7	8
Fe(n,p+np)^{56}Mn	341(3+) → 27(2+)	314.395	0.8	9
Fe(n,p+np)^{56}Mn	336(5+) → 0(3+)	335.54	0.8	8
Fe(n,n'+2n)^{57}Fe	367(3/2−) → 14(3/2−)	352.36	0.5	15
Fe(n,p+np)^{56}Mn	840 → 486(3+)	354.11	0.2	32
Fe(n,n'+2n)^{57}Fe	367(3/2−) → 0(1/2−)	366.75	0.6	8
	3756(6+) → 3388(6+)	367		
Fe(n,p+np)^{56}Mn	716 → 341(3+)	375.18	1.0	7
^{58}Fe(n,2n)^{55}Fe	1317(7/2−) → 931(5/2−)	385.3	0.4	11
^{54}Fe(n,n')^{54}Fe	2949(6+) → 2538(4+)	411.4	2.9	6
^{56}Fe(n,2n)^{55}Fe	411(1/2−) → 0(3/2−)	411.9		
Fe(n,p+np)^{56}Mn	454(3+9 → 0(2+)	454.3	0.4	11
Fe(n,p+np)^{56}Mn	486(3+) → 27(2+)	459.71	0.1	28
Fe(n,p+np)^{56}Mn	1192(4+) → 716	476.08	2.1	6
^{56}Fe(n,2n)^{55}Fe	1408(7/2−) → 931(5/2−)	477.2		
Fe(n,p+np)^{56}Mn	1237 → 753(3+)	483.08	0.1	33
Fe(n,p+np)^{56}Mn	840 → 341(3+)	499.66	0.1	35
^{56}Fe(n,α)^{53}Cr	1537(7/2−) → 1006(5/2−)	530.18	0.4	12
Fe(n,p+np)^{56}Mn	753(3+) → 212(4+)	541.42	0.7	9
^{56}Fe(n,α)^{53}Cr	564(1/2−) → 0(3/2−)	564.3	0.8	10
^{54}Fe(n,n')^{54}Fe	3295(4+) → 2538(4+)	756.6	5.3	17
^{58}Fe(n,2n)^{55}Fe	2212(9/2−) → 1408(7/2−)	803.4	1.0	14
Fe(n,n'+2n)^{56}Fe	847(2+) → 0(0+)	846.771	49.4	7
Fe(n,n'+2n)^{57}Fe	1007(7/2−) → 136(5/2−)	870.68	0.3	24
^{56}Fe(n,α)^{53}Cr	2172(11/2−) → 1290(7/2−)	882.8	0.6	12
^{56}Fe(n,2n)^{55}Fe	931(5/2−) → 0(3/2−)	931.3	7.9	5
^{56}Fe(n,α)^{53}Cr	1006(5/2−) → 0(3/2−)	1006.14	1.2	8
Fe(n,n'+2n)^{56}Fe	3123(4+) → 2085(4+)	1037.84	5.5	9
Fe(n,n'+2n)^{56}Fe	4887 → 3832(2+)	1055	0.8	23
Fe(n,n'+2n)^{57}Fe	1198(9/2−) → 136(5/2−)	1061.6	0.0	27
^{54}Fe(n,n')^{54}Fe	2538(4+) → 1408(2+)	1129.9	8.2	13
Fe(n,n'+2n)^{56}Fe	3832(2+) → 2658(2+)	1174.4	0.9	28
	4298(4+) → 3123(4+)	1175.102		
Fe(n,n'+2n)^{56}Fe	2085(4+) → 847(2+)	1238.282	27.3	5
Fe(n,p+np)^{56}Mn	1613 → 336(5+)	1278.01	0.2	22
^{56}Fe(n,α)^{53}Cr	1290(7/2−) → 0(3/2−)	1289.59	1.4	7
Fe(n,n'+2n)^{56}Fe	3388(6+) → 2085(4+)	1303.4	5.7	5
Fe(n,n'+2n)^{56}Fe	4701(7+) → 3388(6+)	1312.2	1.0	8
^{56}Fe(n,2n)^{55}Fe	1317(7/2−) → 0(3/2−)	1316.4	3.1	6
Fe(n,n'+2n)^{56}Fe	4459(4+) → 3123(4+)	1335.589	0.5	26

Table 2(2/2) Measured discrete gamma-ray production cross section(preliminary)

Reaction	Transition	E γ (keV)	dσ/dΩ (mb/sr)	error(%)
Fe(n,n'+2n)^{56}Fe	3445(3+) → 2085(4+)	1360.215	0.6	11
^{56}Fe(n,2n)^{55}Fe	2301(9/2) → 931(5/2−)	1369.7	0.3	20
^{54}Fe(n,n')^{54}Fe	1408(2+) → 0(0+)	1408.1	2.8	6
^{56}Fe(n,2n)^{55}Fe	1408(7/2−) → 0(3/2−)	1408.4		
Fe(n,n'+2n)^{56}Fe	4554(2+,3+,4+) → 3123(4+)	1431	0.7	11
Fe(n,n'+2n)^{56}Fe	4540(1+,2+) → 2960(2+)	1579.5	0.2	25
^{56}Fe(n,2n)^{55}Fe	2052(3/2−) → 411(1/2−)	1640.4	0.2	30
Fe(n,n'+2n)^{56}Fe	4298(4+) → 2658(2+)	1640.404		
Fe(n,n'+2n)^{56}Fe	3756(6+) → 2085(4+)	1670.8	3.4	6
Fe(n,n'+2n)^{56}Fe	3856(3+) → 2085(4+)	1771.351	0.9	9
Fe(n,n'+2n)^{56}Fe	2658(2+) → 847(2+)	1810.772	3.4	7
Fe(n,n'+2n)^{56}Fe	4510(3−) → 2658(2+)	1852.4	0.6	13
^{56}Fe(n,2n)^{55}Fe	1918(1/2−) → 0(3/2−)	1917.9	0.2	21
Fe(n,n'+2n)^{56}Fe	4878(2+) → 2960(2+)	1918		
Fe(n,n'+2n)^{56}Fe	4100(4+) → 2085(4+)	2015.2	0.4	12
Fe(n,p+np)^{56}Mn	2016(2+) → 0(3+)	2016.5		
Fe(n,n'+2n)^{56}Fe	4120(3+) → 2085(4+)	2034.755	0.5	14
Fe(n,n'+2n)^{56}Fe	2942(0+) → 847(2+)	2094.9	0.5	15
Fe(n,n'+2n)^{56}Fe	2960(2+) → 847(2+)	2113.123	1.4	10
Fe(n,n'+2n)^{56}Fe	4298(4+) → 2085(4+)	2212.933	0.5	18
Fe(n,n'+2n)^{56}Fe	3120(1,2) → 847(2+)	2273.2	0.8	11
Fe(n,n'+2n)^{56}Fe	4459(4+) → 2085(4+)	2373.7	0.6	22
Fe(n,n'+2n)^{56}Fe	4510(3−) → 2085(4+)	2424.9	0.4	26
Fe(n,n'+2n)^{56}Fe	4554(2+,3+,4+) → 2085(4+)	2468.9	0.6	14
^{56}Fe(n,2n)^{55}Fe	2470(3/2−) → 0(3/2−)	2469.9		
Fe(n,n'+2n)^{56}Fe	3370(2+) → 847(2+)	2522.88	1.5	29
Fe(n,n'+2n)^{56}Fe	4660(2+,3+,4+) → 2085(4+)	2574.9	0.5	22
Fe(n,n'+2n)^{56}Fe	3445(3+) → 847(2+)	2598.459	2.5	7
	3449(1,2) → 847(2+)	2602.5		
Fe(n,n'+2n)^{56}Fe	3602(2+) → 847(2+)	2755.1	0.5	12
	3607(0) → 847(2+)	2760.2		
Fe(n,n'+2n)^{56}Fe	4878(2+) → 2085(4+)	2792.9	0.2	26
Fe(n,n'+2n)^{56}Fe	3832(2+) → 847(2+)	2985.2	0.3	24
Fe(n,n'+2n)^{56}Fe	5148 → 2085(4+)	3062.9	0.7	15
Fe(n,n'+2n)^{56}Fe	4049(3+) → 847(2+)	3201.962	3.7	10
Fe(n,n'+2n)^{56}Fe	4100(4+) → 847(2+)	3253.416	0.6	17
Fe(n,n'+2n)^{56}Fe	3370(2+) → 0(0+)	3369.6	0.4	20
Fe(n,n'+2n)^{56}Fe	3449(1,2) → 0(0+)	3449.3	0.8	17
	4298(4+) → 847(2+)	3451.151		
Fe(n,n'+2n)^{56}Fe	4395(3+) → 847(2+)	3547.93	0.9	11
Fe(n,n'+2n)^{56}Fe	4447.6 → 847(2+)	3600.7	0.4	28
	3602(2+) → 0(0+)	3601.9		
Fe(n,n'+2n)^{56}Fe	4510(3−) → 847(2+)	3663.2	0.7	11
Fe(n,n'+2n)^{56}Fe	3832(2+) → 0(0+)	3832	0.5	16
Fe(n,n'+2n)^{56}Fe	4878(2+) → 847(2+)	4031.2	0.2	36

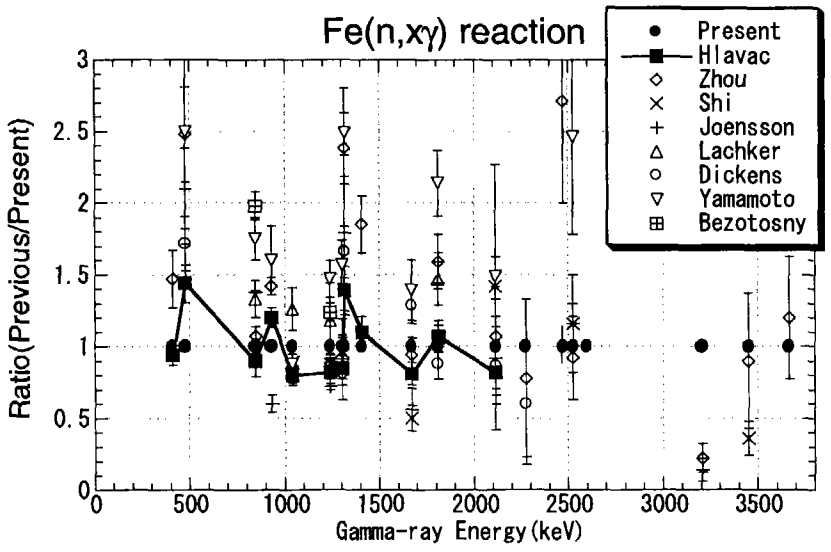

Fig. 3 The ratio of the previous cross sections to the present cross sections for the Fe(n,xγ) reaction with respect to gamma-ray energy.

4 Conclusion

Discrete gamma-ray production cross section data for Mg, Al, Si, Ti, Fe, Ni, Cu, Nb, Mo and Ta were obtained. Some cross section data for these targets are newly obtained. The data for Ta were obtained for the first time. The experimental efficiency obtained by the use of this system were about 50 times larger than the previous experiments using pulsed neutrons. Decay gamma-ray In result, good statistic data could bea obtained in a short span of time.

References

[1] S.P.Simakov et al.: "STATUS OF EXPERIMENTAL AND EVALUATED DATA FOR DISCRETE GAMMA-RAY PRODUCTION AT 14.5 MeV NEUTRON INCIDENT ENERGY", Report INDC(CCP)-413, IAEA (1998)

3.22 Development of Utility System of Charged Particle Nuclear Reaction Data on Unified Interface

Shigeyoshi AOYAMA
Yosihide OHBAYASI, Hiroshi MASUI [a)]
Kiyoshi KATO, Akira OHNISHI [b)]
Masaki CHIBA [c)]

Information Processing Center, Kitami Institute of Technology, Kitami 090, JAPAN
a) Meme Media Laboratory, Hokkaido University, Sapporo 060, JAPAN
b) Graduate School of Science, Hokkaido University, Sapporo 060, JAPAN
c) Faculty of Social Information, Sapporo Gakuin University, Ebetsu 069, JAPAN
e-mail: dbadmin@nrdf.meme.hokudai.ac.jp

Abstract

We have developed a utility system, WinNRDF, for a nuclear charged particle reaction data of NRDF (Nuclear Reaction Data File) on a unified interface of Windows95, 98/NT. By using the system, we can easily search the experimental data of a charged particle reaction in NRDF and also see the graphic data on GUI (Graphical User Interface). Furthermore, we develop a mechanism of making a new index of keywords in order to include the time developing character of the NRDF database.

1. Introduction

For about twenty years, NRDF (Nuclear Reaction Data File) has been accumulated by JCPRG (Japan Charged Particle Reaction Group). NRDF contains the experimental data of the nuclear charged particle reaction in Japan. The number of accumulated data files is several ten thousands, which may be almost all data in Japan. However, the utility system for searching data is very poor, which was made more than ten years ago on the main frame of the computer center in Hokkaido University [1]. For example, we must know the grammar and the codes of NRDF and input thier commands on CUI (Character User Interface) in order to search even a simple data (Fig. 1). The obtained date itself can not be understood by a person who is not a specialist of JCPRG (Fig. 2). Furthermore, it is almost impossible to modify the old system to accept new applications because of the old architecture. On the other hand, recently, PC (Personal Computer) has been widely spread all over the world. The EXFOR (EXchange FORmat) database which is an international standard is determined to support it on the PC (Windows) interface and WWW (World Wide Web). Then, it is meaningful to develop the utility system of NRDF on the Windows interface and WWW.

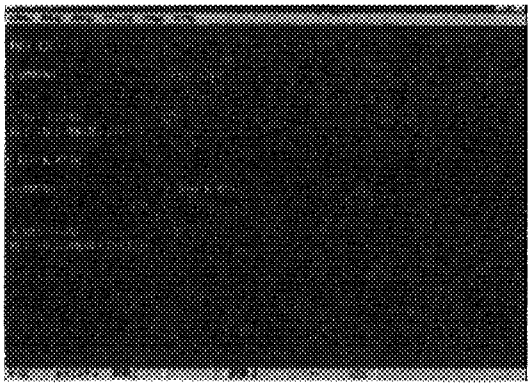

Fig. 1 Searching window of NRDF on CUI

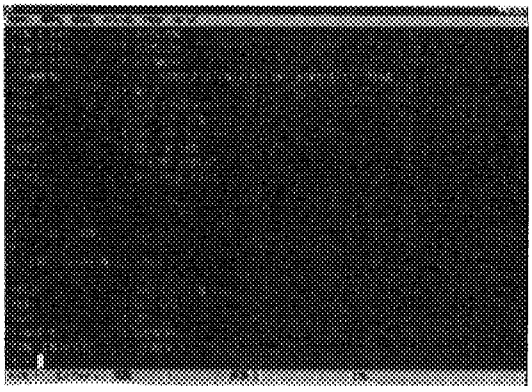

Fig. 2 Data of NRDF

On such a situation, we have three projects of the development of new data searching and utility systems for NRDF; i) A data search and utility system with Windows interface on the local PC (present paper). ii) A data search system on the network circumstance such as WWW (http://nucl.sci.hokudai.ac.jp/cgi-bin/nrdffind). iii) A data search and utility system by Intelligent Pad (IP) architecture [2] (see a paper by Ohbayasi *et al.* in this proceeding). In this paper, first, we describe an overview of the present system, WinNRDF, for the local PC with Windows interface in brief. Next, we explain the practical uses of WinNRDF. Third, we discuss the time developing architecture of NRDF on this system. Finally, summary and future problems are given.

2. Overview of WinNRDF

We describe an overview of WinNRDF for a local PC with the Windows interface in brief. The details of each window will be explained in the next section. The programming language of the present system is C++ one of the Borland C++ Builder. Because we also want to apply the system to the EXFOR database whose format on PC was already given in a Borland DBASE format, we select the Borland's one in order to do an easy connection to it. In Fig. 3, we show the overview of the system. The main window to input or select keywords is the upper middle part of the desktop. The left bottom is a data file select window. The right bottom is a graphic window in order to show the graphic data such as nuclear reaction cross-sections. These windows are programmed by the C++ language and the searching data file of NRDF is obtained by using an index file that is essentially the same one of the WWW system (http://nucl.sci.hokudai.ac.jp/cgi-bin/nrdffind). It should be mentioned that the replacement of the SQL language in the searching system or using a DBMS is easy. However, we can not include all the architecture of NRDF by such systems, though it is sufficient for the EXFOR database of a simple data structure.

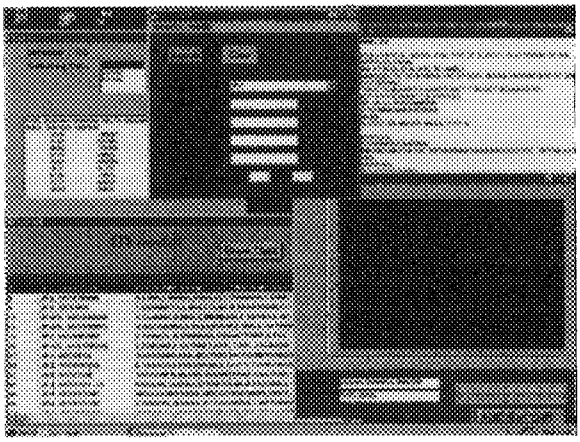

Fig. 3 Overview of WinNRDF

3. How to use WinNRDF?

In this section, we explain how to use WinNRDF. We input some codes (keywords) to the input boxes in the searching window (Fig. 4). If we do not know code (keywords) in NRDF, we can use a dictionary from the popup menu of the input boxes. In Fig. 4, we show the popup menu for references. In the case of pushing the "Search" button, we can see the list of the so called D-number in NRDF (Fig. 5) which is an identification number of the data file basically corresponding to an article. If we select one of the D-numbers and push the "Open File" button in the list window (Fig. 5), then we get the data file (Fig. 6) with the D-numbers, which is corresponding to that of the old system in Fig. 2.

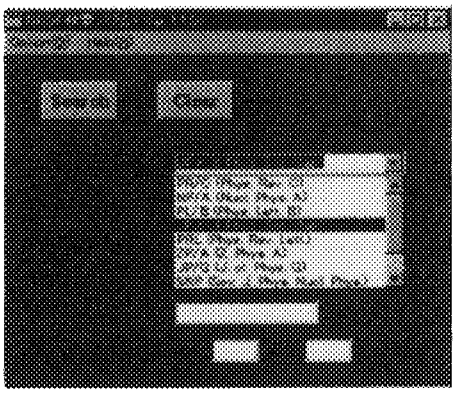

Fig. 4 Searching window

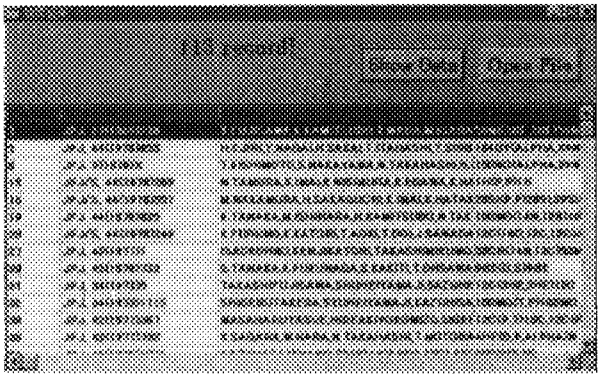

Fig.5 List window

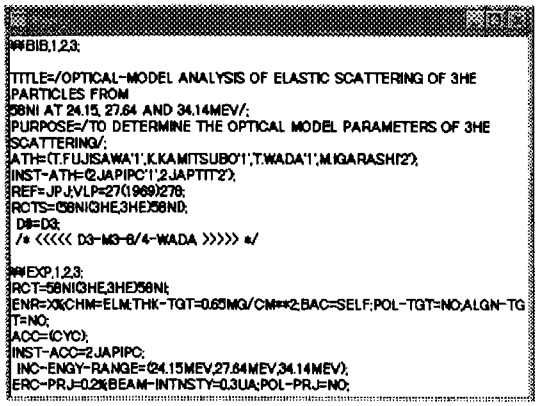

Fig. 6 Data file editor

In the old system, we can see a graph in a character pattern. However, it is not graphical at all now. Then, we should have a graphic window in the present system. The NRDF architecture has a kind of a tree structure. The data section in the data file of a D-number corresponds to a figure or a table in an article. In the old system, we must know the grammar of NRDF to treat such a data structure. In the present system, we do not need a knowledge of such a grammar. If we push the "Show Data" button in the list window (Fig. 5), a data select window openes as Fig. 7. When we select a data section corresponding to a figure, we can see the data itself in the lower part of the data select window. Furthermore, if you want to see the graph and push the graph button, a graphic window is also opened as Fig. 8. This graphic window has a scaling mechanism and a parallel moving mechanism. If users want to other excellent graphic software, he can use the graphic data itself which is saved as a new file.

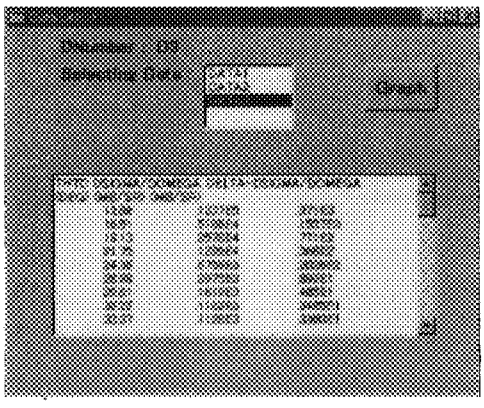

Fig. 7 Data select window

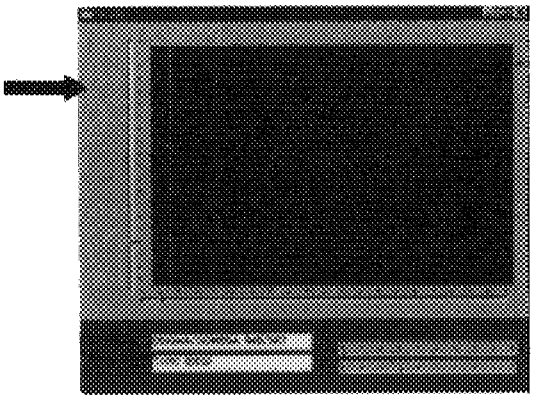

Fig. 8 Graphic window

4. Mechanism of searching new keyword

In this section, we show how to make a new window including a new keyword which is not contained in the original searching window. The original NRDF database has more than a hundred of keywords (items). The number of those will increase because keywords which are meaningful for researchers will change in the future and new concepts will be also given in some articles. The data structure of NRDF is made in considering the time dependence and the user's dependence of the meaningful keywords in articles. Then, if we make a database with the original data structure of NRDF, we have to do that we can also search new keywords of NRDF. In order to have such a mechanism, we make a window of making a new index file (Fig. 9). This window appears when we select "Make New Index" in the menu bar (Fig. 10). In the new window (Fig. 9), we input the keyword and select a code of NRDF, and push the left "Make Index" button. Then, the original window will change that of including the new keyword as seen in Fig. 11. The present example of Fig. 9-11 is that of the accelerator.

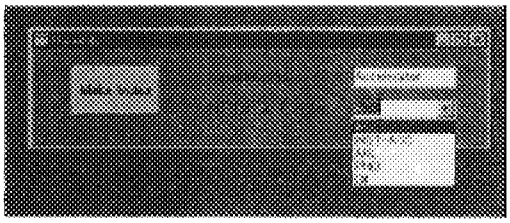

Fig. 9 Making a new file window

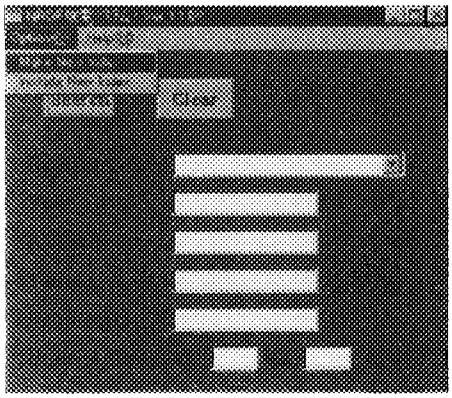

Fig. 10 Original searching window

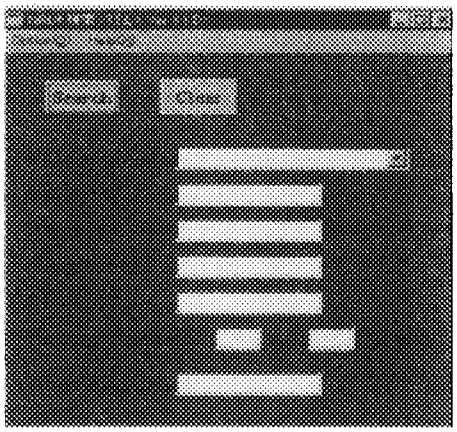

Fig. 11 New searching window

5. Summary and future problem

In this paper, we have described a new utility system, WinNRDF, for a nuclear charged particle reaction data of NRDF (Nuclear Reaction Data File) on a unified interface of Windows95, 98/NT. By using the system, we can easily search the experimental data of charged particle reactions in NRDF and see the graphic data on GUI. Furthermore, we developed a mechanism of making a new index of keywords by which we include the time developing character of the NRDF database. In the near future, we will want to apply the same interface to the EXFOR database. We show a preliminary version of WinEXFOR in Fig. 12.

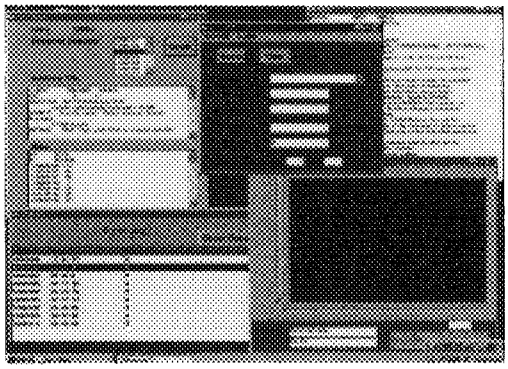

Fig. 12 Overview of WinEXFOR (preliminary)

Acknowledgment

This work is supported by the meme media laboratory in Hokkaido University. The authors thank to Professor Y. Tanaka for variable supports and encouragement.

References

[1] M. Togashi and H. Tanaka, Jour. Inf. Sci. **Vol.4**, No.5(1982), 213.

[2] Y. Tanaka, Inf. and Sof. Tec. **38** (1996), 201.

JP9950340

3.23 Development of Charged Particle Nuclear Reaction Data Retrieval System on IntelligentPad

Yosihide OHBAYASI [a], Shigeyoshi AOYAMA [b], Hiroshi MASUI [a],
Kiyoshi KATÔ [c] and Masaki CHIBA [d]

a) Meme Media Laboratory, Hokkaido University, Sapporo, Hokkaido 060-8628

b) Information Processing Center, Kitami Institute of Technology, Kitami, Hokkaido 090-8507

c) Division of Physics, Graduate School of Science, Hokkaido University, Sapporo, Hokkaido 060-0810

d) Division of Social Information, Sapporo Gakuin University, Ebetsu, Hokkaido 069-8555

Email: **dbadmin@nrdf.meme.hokudai.ac.jp**

An newly designed database retrieval system of charged particle nuclear reaction database system is developed with IntelligentPad architecture. We designed the network-based(server-client) data retrieval system, and a client system constructs on Windows95, 98/NT with IntelligentPad. We set the future aim of our database system toward the "effective" use of nuclear reaction data : I. **"Re-produce, Re-edit, Re-use"**, II. **"Circulation, Evolution"**, III. **"Knowledge discovery"**. Thus, further developments are under way.

1. Introduction

The systematic information of the nuclear reaction data can't be missed in the development of atomic energy problems. Especially, the needs toward the charged particle nuclear reaction data will rise all the more from now on. Therefore, the main theme of this report is the development of database system of nuclear reaction data. In this report, we develop the retrieval system of Nuclear Reaction Data File (NRDF) compilation[1,5] using IntelligentPad architecture.

NRDF has been constructed as a database mainly connected with nuclear physics. Typical property of the charged particle reaction is varieties of both reaction type and observable that are evolved with the development of the reactor and the accelerator physics. The designation of NRDF is developed with this point of view. Since JCPRG (Japan Charged Particle Reaction data Group) maintained NRDF over 20 years, NRDF have over 20,000 of charged particle nuclear reaction data that originate from Japan[1].In order to distribute NRDF, the data compilation, storage and retrieval system of NRDF was constructed at a main-flame computer of Hokkaido University[2] . Furthermore, a system which transforms the NRDF data to the EXFOR was implemented, thus NRDF contributed as an important part of the charged particle data of EXFOR data compilation[3]. However, as we shown in the Ref.[4], The current system of NRDF on the main-flame computer is out of date. With the following background, Ref.[5] is one of the our recent extension of data retrieval system. In addition, to get benefit of recent computer and network technologies, such as multimedia, object-oriented system construction, graphical user interface, and so on, we select to use the IntelligentPad architecture.

IntelligentPad is a kind of object-oriented "graphical user interface(GUI) based" system construction environment. This architecture is proposed in 1989 by Yuzuru Tanaka at Hokkaido University[6]. In order to develop and enlighten this architecture, over 60 domestic and foreign companies makes the IntelligentPad Consortium(IPC)[7]. Recently, we can get the IntelligentPad as some commercial softwares[8]. A "pad" can be treated as an object of the graphical user interface on the screen of computer, like a view of "real paper pad", and each "pad" have functions as data control programs, input/output devices between other pads, and so on. On the "pad" environment, programming of any tools on GUI is can be done by 'intuitively' cut and paste action of pad.

2. System design of the trial system

Fig.1 shows an image of the basic design of this system. The recent trend of the computer environment is expressed as words "Network", "Graphical", "Interactive", "Reuse of resources". The fundamental concepts of our data retrieval system are based on them. Using an database management system(DBMS) based on SQL, we construct the NRDF data management server on the UNIX WS. (SUN Ultra1). UniSQL[9] is adopted at the present. Provided that common gateway interface(CGI) on this server, The network communications between the NRDF server and clients are achieved.

Once the NRDF server is constructed, data retrieval "client" is constructed with the IntelligentPad architecture. A connection between a server and a client based on CGI through the network connection . Such clients was previously constructed on IntelligentPad by SmallTalk[10-12]. Now, we construct the Windows95, 98/NT-based IntelligentPad[8]. Fig.2 shows the overall appearance of the trial product of the NRDF data retrieval system. Let us show in detail with the next section.

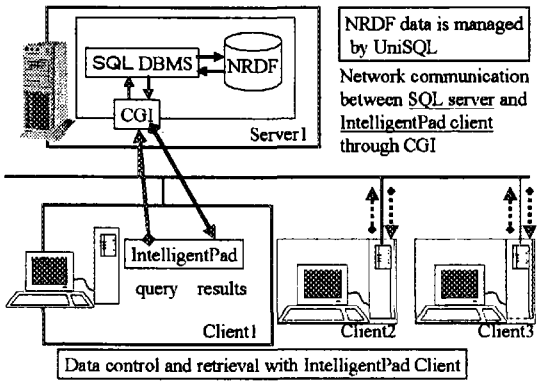

Fig.1 Network-based system.

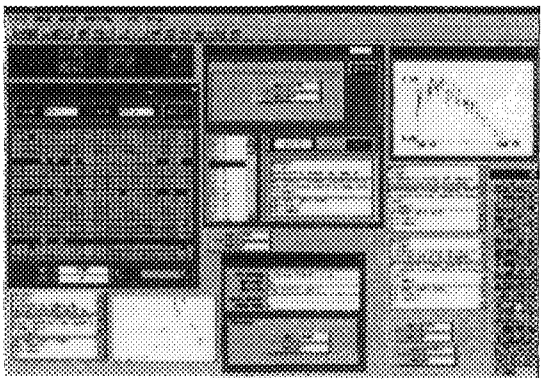

Fig.2 Overview of the system.

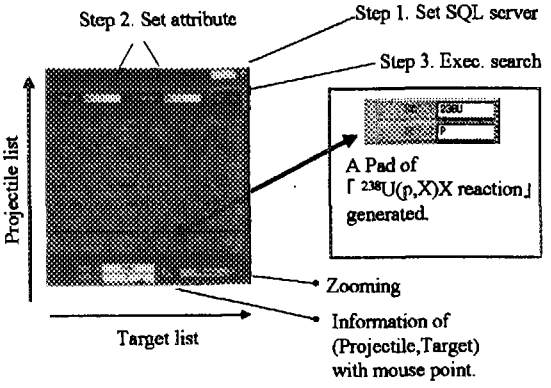

Fig.3. Data navigation.

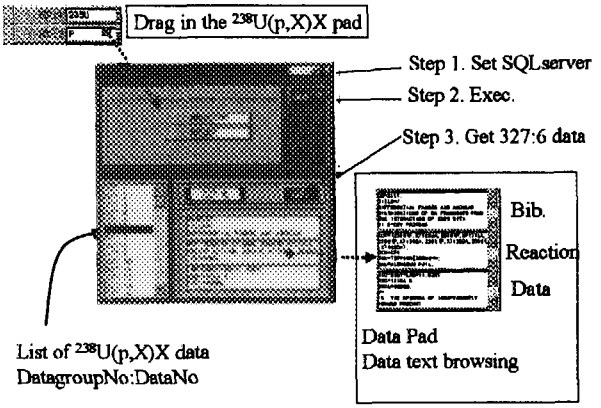

Fig.4. Data retrieval.

3. Reference example and functions of the trial system

Showing some reference example, let us discuss about features of this trial product. Suppose you want to get the data of the $^{238}U(p,X)X$ reaction, Fig.3-Fig.5 shows the process of data retrieval step by step.

1). Examine the existence of the $^{238}U(p,X)$ reaction data.

Fig.3. shows the Pad to search whether the $^{238}U(p,X)$ data is exist or not : i) Set the network address of SQL server. ii) Specify the two attributes of the NRDF database, e.g., Target and Projectile. iii) Execution of a search. As a result, the grid which placed in the middle region of the Pad displays the 2-dimensional information that displays the current status of the NRDF database from a point of view of target and projectile. colored crossing point (X,Y) shows NRDF have some reaction data about target = X, projectile = Y. In this way, we find NRDF have some data about X = ^{238}U, Y = p , thus we get the "$^{238}U(p,X)X$ reaction" Pad using click and drag operation of the Pad.

2). Data retrieval.

Once you get the Pad connected with "$^{238}U(p,X)X$ reaction", you retrieve the data using the Pad shows in Fig.4. We can get the list of "$^{238}U(p,X)X$ reaction" data, and

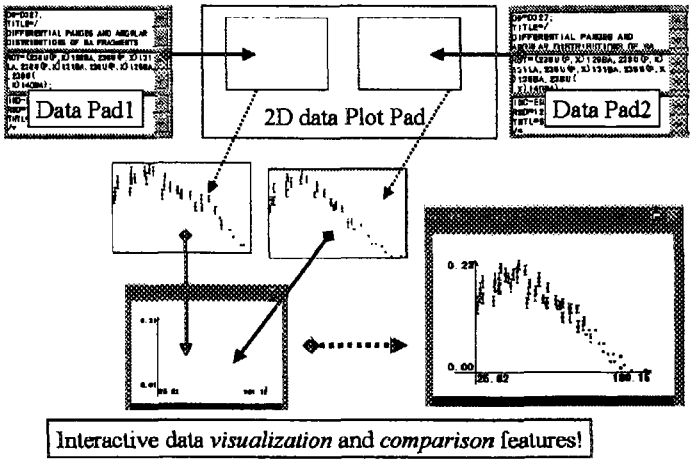

Fig.5. Interactive data visualization and comparison.

generate the specific data as a text browsing Pad. Consequently, we get the "^{238}U(p,X)X reaction" data.

3). Interactive data visualization and comparison.

The data pad shown in Fig.4 have features not only data browsing but visualization(Fig.5). Once you drug in the Data pad to 2D data plot pad, you can see the graph representation of the data. Data comparison is also achieved by just a drug and drop!

4. The aim of nuclear reaction database towards the effective use

In the previous section, we show the features of current trial system. In particular, major features of this system are : i) interactive data visualization and comparison, ii) 2-dimensional display function of the status of database. Furthermore, we determined the aim of the system towards support of the effective use of nuclear reaction data with computer facilities.

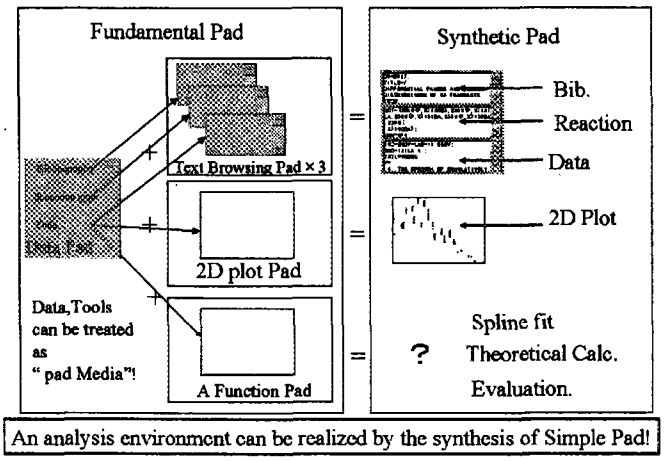

Fig.6. Synthetic feature of IntelligentPad.

I) Re-produce, Re-edit, Re-use.

Once any data and tool can be made by resolved by fundamental pad, we can reuse the existent pad to make new tools. As you see the Fig.6. Synthetic feature of IntelligentPad supports "Re-,produce, edit, use" of nuclear data and tools.

II) Circulation and evolution.

IntelligentPad supports co-operation with web browser software. Once we make an web page to distribute and circulate not only tools but also data. It is already the basis of the circulation field of nuclear data and tools. Fig.7. shows a schematic figure for the circulation system of data and tools as pad media. Constructing such a sharing space on the network, many user can retrieve many tools and data through the pad media

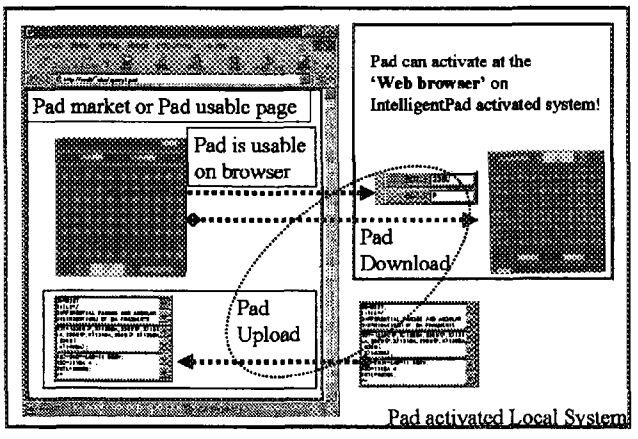

Fig.7. Support of Circulation and Evolution.

III) Knowledge discovery.

The amount of nuclear reaction data is huge, and increasing day by day. In addition, variety of the data will also be complex. We will have many data, but it will be difficult to get essentially important information from huge databases. Fig.8. shows the pad same as we shown in Fig.2. Development of such pad will proceed us to easier navigation to the needed data, and will support something new discovery of knowledge connected with nuclear reaction data.

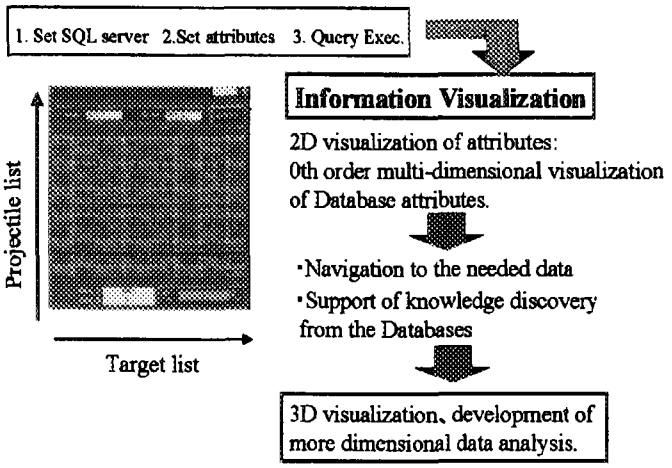

Fig.8. Support of knowledge discovery.

You will find the fundamental concepts of IntelligentPad is quite matched with above three aims. Consequently, we decide that our development will proceed to embody them through IntelligentPad. If it will be done, such as Fig.9. , we believe that quite "effective" use of nuclear reaction data is promising.

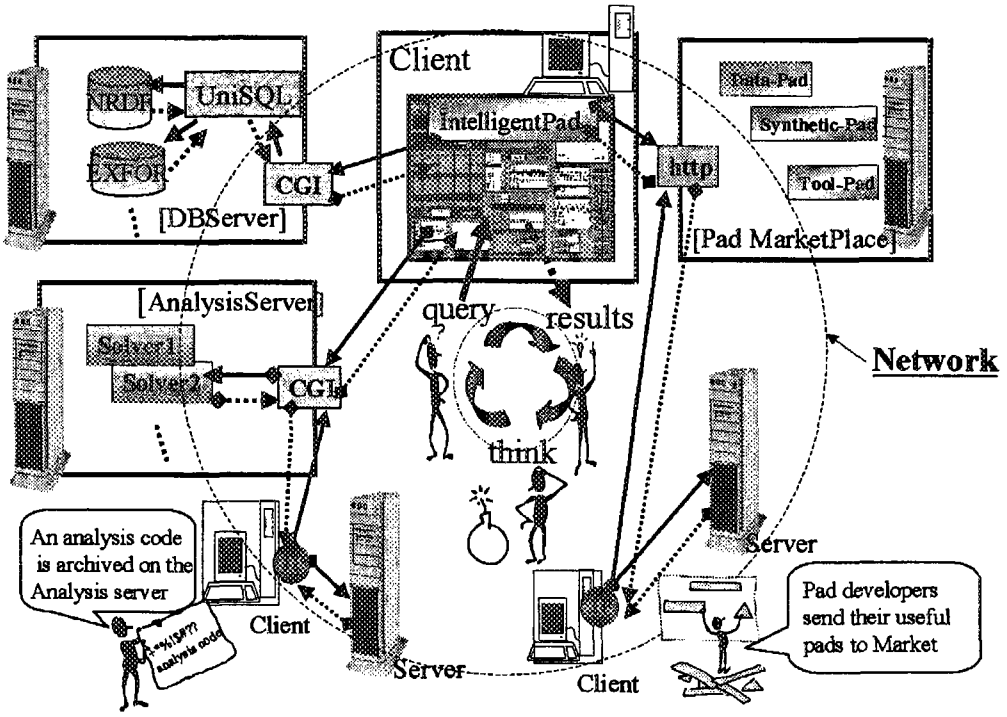

Fig.9. An ideal system of nuclear reaction database. Exp. data, evaluated data, theoretical solver, ...etc. ,are treated with this system as "pad media".

5. Summary and future extension

We developed the "NRDF" charged particle database system on IntelligentPad. In this report, the current trial system products are shown. Major features of this system are i) interactive data visualization and comparison, ii) 2D database survey. From now on, we will include the EXFOR data in this system , distribute the system to researchers, repeat test use and blush-up of the trial system. Furthermore, we will proceed to develop the system to embody the aim of "effective" use of nuclear reaction data, such as Fig.9.

Acknowledgment

This work is supported by Meme Media Laboratory, Hokkaido University. To develop the retrieval system on Windows95,98/NT, essential pad modules are constructed by C'sLab. LTD that is based on the SmallTalk-based trial production by one of the authors(C. M.) [10-12]. The authors would like to express their thanks to Prof. Y. Tanaka for helpful discussions and suggestions.

References

[1] Katô, K.: "Charged particle nuclear reaction database NRDF - Present status and its usage -", Genshikaku Kenkyu, **39**, 63 (1995, in Japanese).

[2] Togashi, M. and Tanaka, H.: "An information system for charged particle nuclear reaction data", Journal of Information Science , **4,** 213 (1982) .

[3] Chiba, M., Katayama, T. and Tanaka, H. : "A database translator of nuclear reaction data for international data exchange", Journal of Information Science, **12**, 153 (1986).

[4] Aoyama, S., et al.: "Development of utility system of charged particle nuclear reaction data on unified interface", JAERI-Conf(this volume).

[5] NRDF web page : **http://nucl.sci.hokudai.ac.jp/~nrdf/**.

[6] Tanaka, Y.:"A Meme Media architecture IntelligentPad and its applications", Journal of IPSJ, **38**, 222 (1997, in Japanese) ; International Conference on Multimedia Modeling '98, Lausanne, p.1 (1998)

[7] IntelligentPad Consortium : **http://www.pads.or.jp/**.

[8] For example, **http://www.fujitsu.co.jp/hypertext/softinfo/product/use/ipad/.;**
http://www.hitachi-sk.co.jp/Products/IntelligentPad/HomePage.html.

[9] UniSQL. web page. : **http://unisql.www.nttdata.co.jp/.**

[10] Chiba, M.: "IntelligentPad for exchanging and reusing nuclear reaction data information as shared resources", web publication, **http://nrdf.meme.hokudai.ac.jp/ip/chiba/main.html**.

[11] Chiba, M: "IntelligentPad for exchanging and reusing nuclear reaction data information as shared resources", JAERI-Conf, **96-008**, 320 (1996).

[12] Chiba, M.: "An IntelligentPad system for the reuse of nuclear reaction data", Conference proceedings Vol.59 "Nuclear data for science and Technology" G.Reffo, A.Ventura and C.Grandi, SIF, Bologna , p.1057 (1997).

JP9950341

JAERI-Conf 99-002

3.24 Easy-to-use Application Programs to Calculate Aggregate Fission-Product Properties on Personal Computers

K. Oyamatsu

Department of Energy Engineering and Science, Nagoya University
Furo-cho, Chikusa-ku, Nagoya, 464-8603, Japan
e-mail : oyak@luna.nucl.nagoya-u.ac.jp

Fission Products (FP) are dominant sources of activities in spent nuclear fuels over tens of years. Small Fortran programs for personal computers have been developed primarily to study the aggregate FP decay heat and delayed-neutron activities with the latest fission yield and decay data in Japanese, US and European Nuclear Data libraries. This paper describes how to use these programs together with two new features of our codes; i) unified front-end ii) capability of calculating the aggregate β and γ decay energy spectra.

1. Introduction

Fission products (FP) are inevitable by-products which are primary sources of activities in spent nuclear fuels for about 30 years (=10^9 s). Hence, the fission-product properties are not only key nuclear data required in designing the nuclear fuel cycle, but also of interest of the general public who are not working in the nuclear industry

In our fission-product studies, we have developed and utilized programs on personal computers for calculating the aggregate decay heat and the aggreagete delayed neutron emission as functions of cooling times. The calculations in the codes are based on the summation method and use fission yields and decay data in three major nuclear data libraries, JNDC nuclear data library of fission products version 2 (Japan), ENDF/B-VI (USA) and JEF2.2 (Europe).

These computer codes can calculate decays of about 1000 fission product nuclides after a fission burst or finite irradiation for a single fissile nuclide. One may calculate the following FP properties as functions of cooling time; concentrations of radioactive FP's, aggreagate FP decay heat, aggregate delayed neutron emission, and aggregate (β and γ) decay energy spectra. The calculations can be performed for 51 fissioning systems when one uses ENDF/B-VI fission yield data.

In the present release of the codes, previously developed small separate programs are unified in a compact form in order to improve operational easiness, and the β and γ decay energy spectra can now be calculated.

2. Features

Capable to calculate the aggregate β and γ decay energy spectra

In the present release, the aggregate β and γ decay energy spectra can be calculated, too. The FP properties that can be calculated with the code is summerized in Table 1.

New unified front-end

A unified user-friendly control panel is provided for the six programs.

Easy data transfer

The output files are text files. Therefore, the output data can be easily transferred to Excel (Microsoft Corporation), Transform (Fortner Research LLC) or any other application programs for detailed analyses.

3. Quick start

In the following, we describe how to calculate the aggregate decay energy spectrum after a finite irradiation. One can perform other calculations easily in the same way.

Note : A cooling time file should be prepared beforehand when one calculate the aggregate decay heat powers ("1. Aggregate Decay Heat Power" in the Main Control Panel). See also Sect. 6 b).

1) Open a HyperCard stack named "panel98", and choose "2. Aggregate Decay Energy Spectra" by pushing the button in the panel.

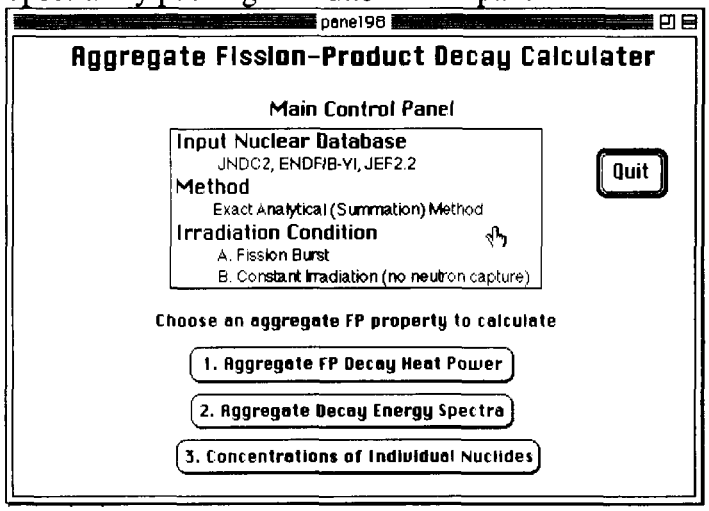

2) Choose an irradiation condition by pushing a button in the panel.

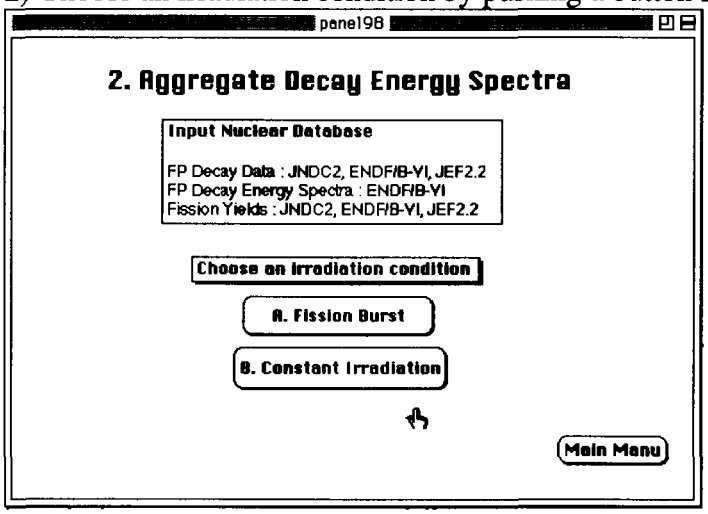

3. Enter irradiation time and cooling time in the boxes, and choose fission-yield, decay-data, and spectrum files. Then, push "run spectrafinite98" button.

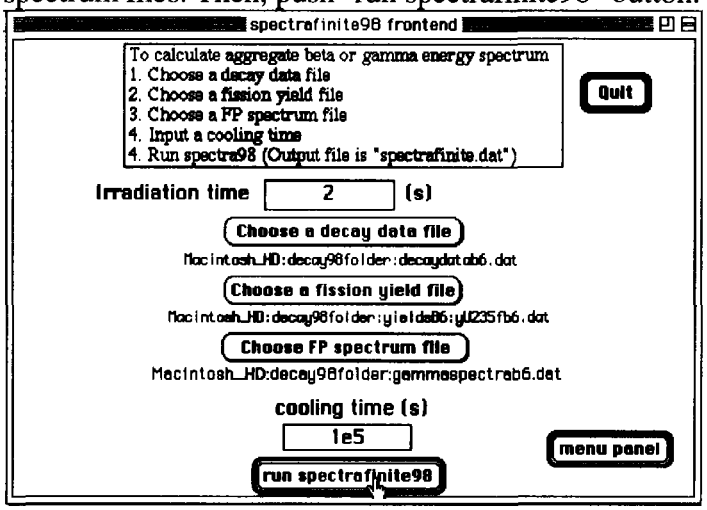

4. Input FP nuclear data

The FP nuclear data required in the codes are categorized into three;

a) fission yield data

y_i independent fission yield of FP nuclide i

b) decay data

$b_{i\to j}$ branching ratio of FP nuclide i decaying to nuclide j

λ_i decay constant of FP nuclide i

E_i average decay energy per decay of nuclide i

$P_{n\,i}$ delayed neutron emission probability of nuclide i

c) spectrum data

$\chi(E)$ decay energy spectrum of nuclide i (ENDF/B-VI only)

The present codes can perform calculations with the above data in ENDF/B-VI, JNDC 2 and JEF2.2. It is noted that the input FP data for a calculation can be taken from different libraries. For example, one may use the fission yields in JEF2.2 and the decay data in JNDC2 to calculate the aggregate decay heat powers.

5. Numerical method

The codes solve analytically decays and buildups of FP nuclides. The definitions of the irradiation conditions, a fission burst and constant (finite) irradiation, are shown in Fig. 1. Specifically, the equations for the concentration of nuclide i, $N_i(t)$, is given as follows;

a) fission burst

$$\frac{d}{dt}N_i(t) = -\lambda_i N_i(t) + \sum_{j \neq i} b_{j \to i} \lambda_j N_j(t),$$
$$N_i(0) = y_i .$$

b) constant (finite) irradiations

For simplicity, the codes utilize the solution for infinite irradiation. Therefore, concentrations of the stable nuclides can not be calculated with the present codes. The concentration of nuclide i, $N_{\infty i}(t)$, after infinite irradiation is obtained from

$$\frac{d}{dt}N_{\infty i}(t) = -\lambda_i N_{\infty i}(t) + \sum_{j \neq i} b_{j \to i} \lambda_j N_{\infty j}(t) ,$$
$$N_{\infty i}(0) = Y_i / \lambda_i .$$

Here, Y_i is the cumulative fission yield of nuclide i, defined as

$$Y_i = y_i + \sum_{j \neq i} b_{j \to i} Y_j .$$

Finally, the concentration of radioactive nuclide i, $N_i(t)$, after irradiation time T (see Fig. 1) is given by

$$N(t) = N_\infty(t) - N_\infty(t+T) .$$

6. Program and data files

a) program files

panel98 Main control panel (HyperCard stack). The following six programs are called from this panel.

decay98, decayfinite98, distel98, distelfinite98, spectra98, spectrafinite98

These six calculation programs are called from "panel98". Therefore, users do not have to open directly these programs.

b) cooling time file for aggregate decay heat calculations

To use "decay98" and "decayfinite98", one should prepare a text file which contains the arbitrary number of cooling times with an arbitrary file name. The file named "egct.dat" is a sample cooling time file.

c) fission yield files and folders

Fission yield files are stored in the following three folders;

yieldsB6	ENDFB/VI fission yield folder
yieldsJNDC2	JNDC fission yield folder
yieldsJEF2.2	JEF2.2 fission yield folder

The nomenclature of the files is as follows;

(file name)="y"+(isotope)+(isomeric state)+(neutron energy)+(library name)+".dat".

(isomeric state) = "M" used only for a fissile in an excited state.

(neutron energy) = "t" (thermal), "f" (fast), "h" (14 MeV), s (spontaneous).

(library name) = "b6" (ENDF/B-VI), "jndc2" (JNDC2), jef22 (JEF2.2).

d) decay data files ($b_{i\to j}$, λ_i , E_i , P_{ni})

decaydatab6.dat	decay data from ENDF/B-VI
decaydatajndc2.dat	decay data from JNDC2
decaydatajef22.dat	decay data from JEF2.2

e) spectrum files

betaspectrab6.dat	FP β spectra from ENDF/B-VI
gammaspectrab6.dat	FP γ spectra from ENDF/B-VI

f) miscellaneous files

egct.dat	sample cooling time file for decay98 and decayfinite98
nameofelements.dat	element names
rtyp.dat	reaction types
InputFiles	work file created by "panel98"

7. Output files

a) decayheat.dat (decay98) and decayfinite.dat (decayfinite98)

time (s), t*Pb (MeV), t*Pg (MeV), t*Pa (MeV), t*d.n.act.

The symbols Pb, Pg and Pa stand for the aggreagte β, γ and α decay heat powers, respectively, while "d.n.act." indicates the aggreagte delayed neutron activity. These powers and activity are multiplied by cooling time "t" in the output file.

b) distel.dat (distel98) and distelfinite.dat (distelfinite98)

N Z A M isotope yield Pb (MeV/s) Pg (MeV/s) Pa (MeV/s) d.n.(1/s)

For each isotope identified by N, Z, A and M (ismeric state), its β, γ and α decay heat powers are tabulated together with its delayed neutron activity.

c) spectra.dat (spectra98) and spectrafinite.dat (spectrafinite98)

Energy range (MeV) Eav (MeV) Spectra

"Energy range" defines the energy bin with "Eav" being its median. "Spectra" indicates the aggregate β or γ spectrum. The aggregate spectrum is normalized to the aggregate decay heat power.

8. Remarks

The present programs described in this paper is available upon request to the author. They can be used and freely distributed if no part of the programs or data is modified.

The author keeps the copyright of the above programs described in this paper. However, he is not responsible to any damages due to the use of these programs.

Lastly, we welcome any suggestions and helps for the future development of the programs. The codes have been used for the researches on the aggregate FP properties. We are now planing to run the codes on other PC systems than Macintosh and utilize them for educational purposes.

Table 1. List of the codes and their outputs.

code	irradiation	cooling time	output
decay98	fission burst	multiple	aggregate decay heat power and delayed-neutron activity
decayfinite98	constant (finite)	multiple	
distel98	fission burst	single	individual FP yields, decay-energy releases and delayed-neutron emission
distelfinite98	constant (finite)	single	
spectra98	fission burst	single	aggregate β or γ decay-energy spectra
spectrafinite98	constant (finite)	single	

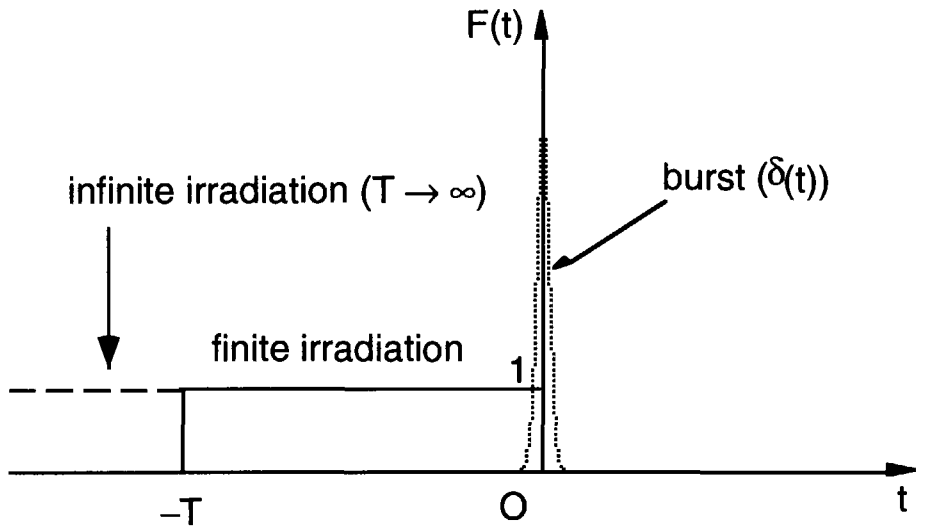

Fig. 1. Definitions of irradiation time and cooling time. The fission rates for the three irradiation conditions are shown as functions of time. Infinite irradiation is defined as the limitting case of the finite irradiation with $T \rightarrow \infty$.

JP9950342

3.25

Fission Cross Section Measurement for Am-242m with TOF Methods in Low Energy Region

Tetsuya Kai*[1], Katsuhei Kobayashi[1], Shuji Yamamoto[1], Cho Hyun-Je[1],
Yoshiaki Fujita[1], Itsuro Kimura[2],Yasushi Ohkawachi[3] and Toshio Wakabayashi[3]

1 Research Reactor Institute, Kyoto University
Kumatori-cho, Sennangun, Osaka 590-0494, Japan
2 Department of Nuclear Engineering, Kyoto University
Yoshidahonmachi, Sakyo-ku, Kyoto 606-8501, Japan
3 Japan Nuclear Cycle Development Institute
4002 Narita, O-arai machi, Ibaraki, 311-1313, Japan
* Present Address: Japan Atomic Energy Research Institute
Tokai-mura, Naka-gun, Ibaraki 319-1195, Japan

e-mail: kai@shield4.tokai.jaeri.go.jp

The neutron-induced fission cross section for Am-242m was measured with time-of-flight(TOF) method from 0.003 eV to 30 eV. We already measured the cross section using Kyoto University lead slowing-down spectrometer(KULS) from 0.1 eV to 10 keV and using the standard thermal neutron field (D_2O facility) at 0.025 eV. The present result was compared with both of them. Although the JENDL-3.2 and ENDF/B-VI were slightly higher in the energy region lower than ~1 eV, the present result agreed with the KULS result and the D_2O result within their experimental error.

1 Introduction

Americium(Am) isotopes are burdensome minor actinides which are abundantly produced in power reactors. The nuclear data for them are of grate importance for system design of spent fuel reprocessing and its transmutation from the standpoint of the disposal of radioactive waste [1]-[5]. The cross section for Am-242m is also notable as well as Am-241 and Am-243 because of its large fission cross section in lower energy region (thermal neutron-induced fission cross section for Am-242m is about ten times larger than uranium-235). But there exist large discrepancies among the evaluated fission cross sections for Am-242m in the JENDL-3.2 and the ENDF/B-VI data file especially at resonance energies. Recently, the authors measured the fission cross section for Am-242m using Kyoto University lead slowing-down spectrometer (KULS[6]) from 0.1 eV to 10 keV[7] and using the standard thermal neutron field (D_2O facility) at 0.025eV[8]. In fig.1, the results of them and the evaluated data (the ENDF/B-VI and the JENDL-3.2) were compared each other. The evaluated data were broadened with the energy resolution of the KULS. In this figure, it was difficult to discuss whether the result using the D_2O facility was consistent with that obtained using the KULS since the KULS result was broadened. We took place the

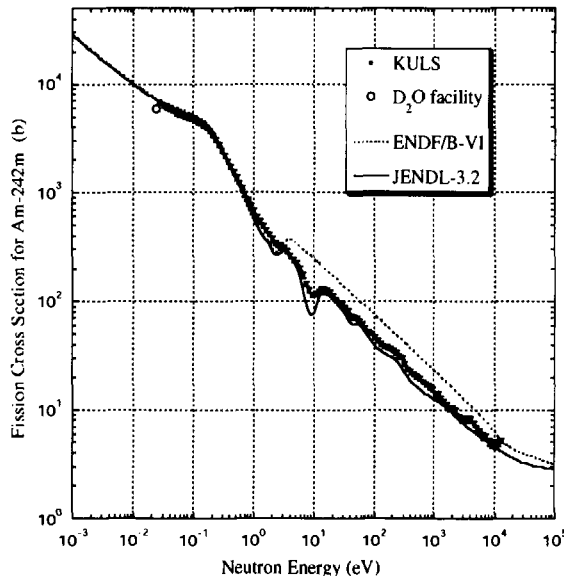

Fig. 1: The result measured with the KULS and the D_2O facility was compared with the evaluated data broadened with the energy resolution of the KULS.

cross section measurement for Am-242m with TOF method for the two purposes. One was discussion about the consistency between the KULS result and the D_2O facility one. Another was to measure the cross section in further lower energy region.

2 Experimental Methods

2.1 The Am-242m and U-235 samples

The Am-242m deposit was purchased from Chemotrade GMBH, and the Am-242m was electrodeposited (radioactive area of 20 mm in diameter) on the stainless steel disk (28 mm in diameter and 0.2 mm in thickness). The purity of the Am-242m was 85.25 %, and the major impurities were 14.42 % for Am-241 and 0.53 % for Am-243. The number of Am-242m atoms was determined by alpha and gamma-ray spectroscopies. As a result of both analyses, the number of Am-242m atoms was determined to be $(2.04 \pm 0.04) \times 10^{16}$.

The highly enriched uranium oxide (99.91 % of U-235) was gotten from ORNL. The uranium was also electrodeposited on the stainless steel disk. The U-235 sample was used to monitor the neutron flux in this study as the well-known reference cross section of the ^{235}U(n,f) reaction. As well as the Am-242m sample, the number of U-235 atoms was determined to be $(3.28 \pm 0.04) \times 10^{17}$.

2.2 Back-to-back Type Double Fission Chamber

The fission chamber was composed of two identical parallel plate-type ionization chambers, as shown in fig.2. The back sides of the sample deposit (Am-242m) and the reference one (U-235) were face each other. This chamber was originally designed for in-core fission ratio measurement [9]. This chamber was made of aluminum and filled with a mixed gas of 97 % Ar and 3 % of N_2 at pressure of 1 atm. Fission pulses were clearly discriminated from background ones caused by the alpha-rays since the electrodeposited layers of Am and U are enough thin not to reduce the energy of fission fragments.

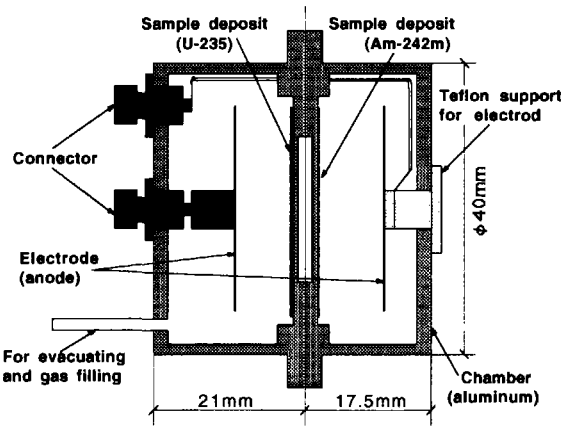

Fig. 2: Cross Sectional view of the back-to-back type doubele fission chamber.

2.3 The BF_3 Counter

The $^{10}B(n,\alpha)$ reaction is well known to be one of the standard cross section and is often applied to cross section measurement as a reference. Instead of $^{235}U(n,f)$ reaction, the $^{10}B(n,\alpha)$ reaction was applied as a reference using a BF_3 counter in resonance region in order to avoid resonance interference between Am-242m and U-235 fission cross sections. The BF_3 counter was of a cylindrical type, 50 mm in effective length, 12 mm in diameter, 1 atm in gas pressure and high-voltage bias was 1100 V.

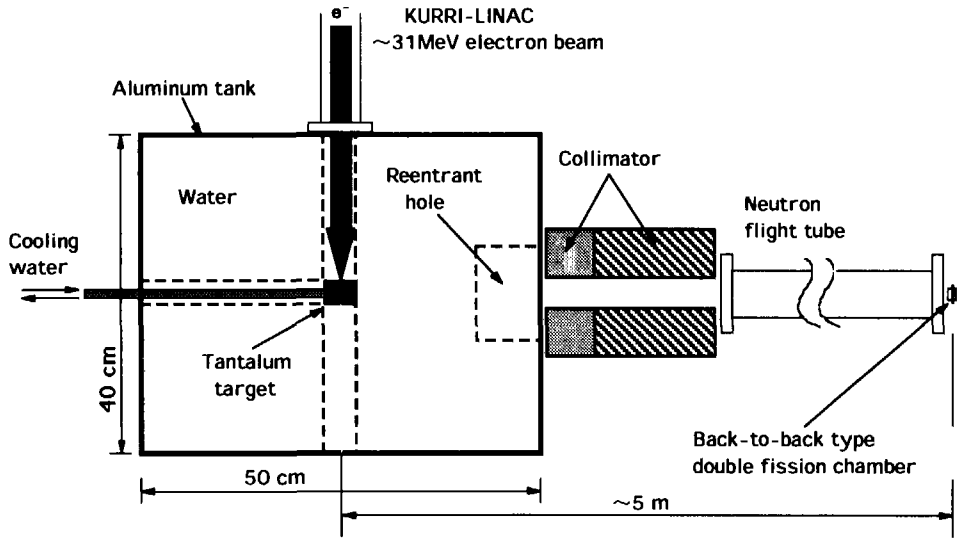

Fig. 3: The schematic view of the experimental arrangement for the present measurement.

2.4 Experimental Arrangement

The measurement with TOF method was made using the 46 MeV electron linac at Kyoto University Research Reactor Institute. The schematic view of experimental arrangement is shown in fig.3. The pulsed neutron produced at the water-cooled tantalum(Ta) target as a result of electron beam irradiation were taken out from the reentrant hole (19 cm in diameter) in the center of the water tank (aluminum, $50\times40\times50$ cm^3). The sample deposit(Am-242m) and the reference one (U-235) was set in the back-to-back type double fission chamber, and the chamber was placed at approximately 5 m from the Ta target. The typical operating conditions of the linac during this measurement were as follows: pulse repetition of 80 Hz, pulse width of 22 ns, electron average current of $\sim 75\mu$s, and the energy of ~ 31 MeV.

2.5 Energy Calibration

In general, the energy of neutron could be determined from flight time and path of the neutron. The reason why we took place energy calibration with the resonance filters was that the neutron source region was unnegligibly wide comparing with the flight path. The characteristics of the resonance filters are shown in tab.1. During the energy calibration, neutrons reached the BF_3 counter trough the resonance filters. The depressions corresponding to resonance energy of the filter materials were found in the time spectrum. The effective flight path was determined to be 5.01 ± 0.02m as a result of fitting with least squares method for the dependency between resonance energy and the flight time (fig.4).

Table 1: The characteristics of the resonance filters used for energy calibration.

Material	Energy (eV)	Thickness (mm)	Form
Samarium	0.87 8.05	0.5	Matel Plate
Silver	5.19 16.3	0.5	Matel Plate
Indium	1.46	0.2	Metal plate

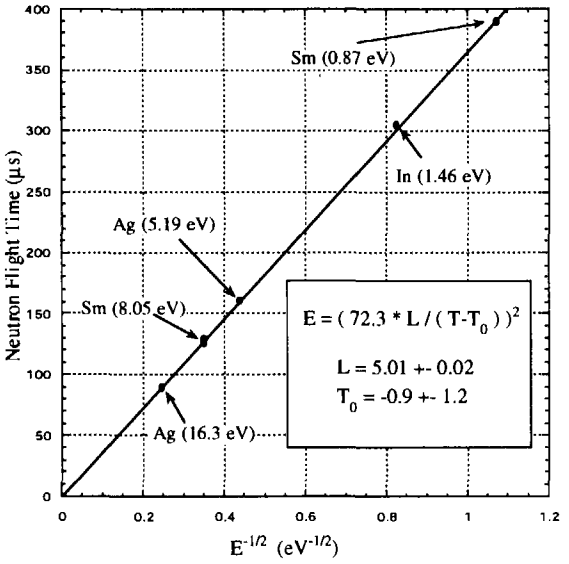

Fig. 4: Dependency between neutron flight time and its energy.

2.6 Data taking and Fission Ratio Measurement

Two identical electronic circuits were employed for the Am-242m and U-235 chambers. Through the amplifiers and discriminators, signals from the chambers were fed into the 4096-channel time-analyzer with 2 μs/channel, which was initiated by the linac electron burst, and the time-of-flight data of fission counts were stored for each measurement of ~5-hour duration in a data acquisition system.

The fission cross section for Am-242m ($\sigma_{Am}(E)$) was obtaind by eq.1.

$$\sigma_{Am}(E) = \begin{cases} \dfrac{C_{Am}(E)}{C_U}\dfrac{N_U}{N_{Am}}\sigma_U(E) & (0.003 \sim 0.2\,eV) \\ \dfrac{C_{Am}(E)}{C_B}N_r\sigma_B(E) & (0.2 \sim 35\,eV) \end{cases} \quad (1)$$

where

$C_{Am}(E), C_U(E)$	: fission counts of Am-242m and U-235 for neutron energy E,
$C_B(E)$	: number of $^{10}B(n,\alpha)$ reactions for neutron energy E,
N_{Am}, N_U	: number of Am-242m and U-235 atoms in the deposits,
$\sigma_U(E), \sigma_B(E)$	: the $^{235}U(n,f)$ and $^{10}B(n,\alpha)$ cross section cited from the ENDF/B-VI,
N_r	: normalizing factor.

The absolute value of the fission cross section for Am-242m was measured relative to that for U-235 from 0.003 eV to 1 eV making use of the back-to-back type double fission chamber. In order to avoid the resonance interference between Am-242m and U-235, the relative fission cross section measurement was made using a BF_3 counter as a good $1/v$ detector instead of the U-235 fission chamber from 0.2 eV to 10 eV. This relative cross section was normalized to the absolute value measured relative to U-235 between 0.2 eV and 1 eV.

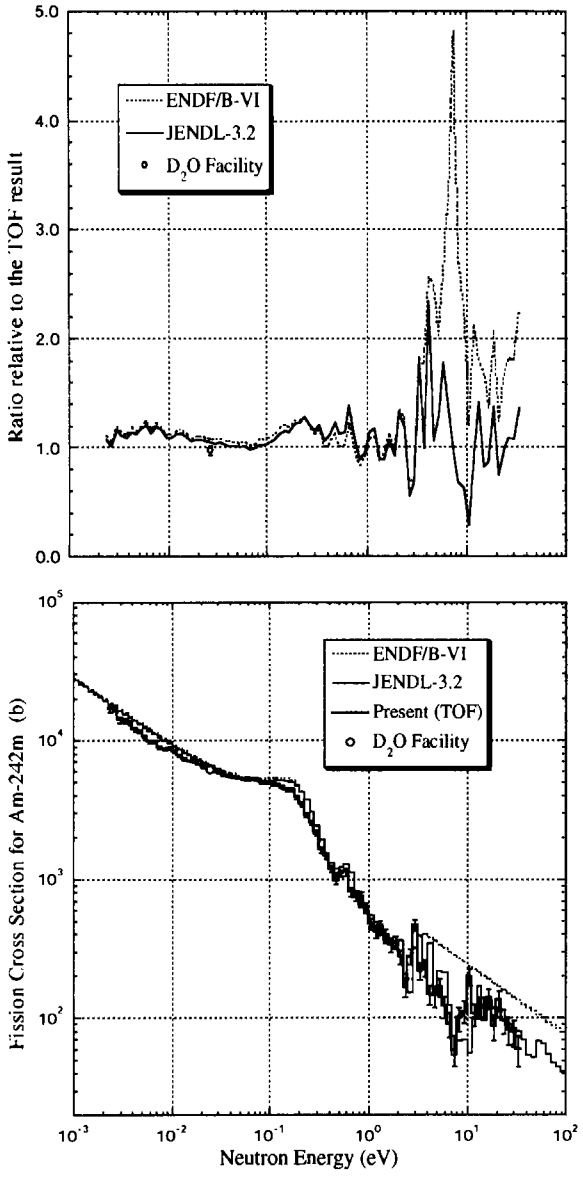

Fig. 5: Comparison between the present result and the value obtained with the D_2O facility and the evaluated data.

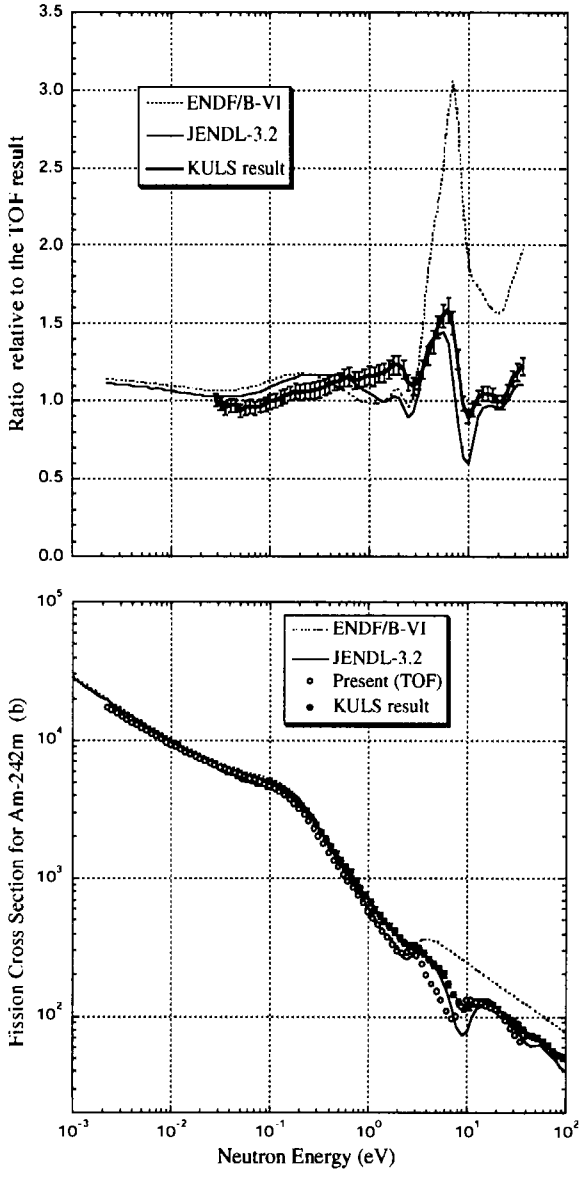

Fig. 6: Comparison between the present result and evaluated data and the KULS result. The present one and evaluated data were broadened for comparison.

3 Results and Discussion

The present result, the D_2O result and the evaluated data of the JENDL-3.2 and the ENDF/B-VI were compared in fig.5. Although the present result and the D_2O result agree in their experimental error at 0.025 eV, the JENDL-3.2 and the ENDF/B-VI were slightly larger than our results. In higher energy region (>~3 eV), the ENDF/B-VI data was much higher than the present result and the JENDL-3.2. As shown in fig.6, the result with the TOF method and that with the KULS were compared with the evaluated data. For the comparison, the TOF result and the evaluated data were broadened with the energy resolution of the KULS. Although the present result was systematically differ from the KULS result and evaluated data from 5 to 7 eV, good agreement could be seen between the TOF result and the KULS result in the energy region lower than ~0.2 eV. The reason for the systematical difference might be that the statistical accuracy during the present measurement was not enough.

4 Conclusion

(1) 0.003~3 eV

The thermal neutron-induced fission cross section obtained with the D_2O facility is consistent with the result measured using the KULS since both results show good agreement with the result with the TOF method. But the JENDL-3.2 and the ENDF/B-VI data are slightly higher than our results in this energy region.

(2) 3~ 35 eV

The KULS data and the evaluated data are systematically higher than the present result in the energy region from 5 to 7 eV. But the ENDF/B-VI data is apparently larger than not only the present result but also the KULS result and the JENDL-3.2 data.

References

[1] D. Lancaster, *Proc. of the Int. Conf. and Technol. Exposition on Future Nucl. Systems: Global '93"*, ANS, La Grange Park, Illinois, p.609 (1993).

[2] J. Tommashi, et al., ibid., p.1252 (1993).

[3] T. Wakabayashi, et al., *Proc. of the Int. Conf. of Evaluation of Emergency Nuclear Fuel Cycle Systems: Global '95"*, CEA, p.800 (1995).

[4] J. L. Kloosterman, J. M. Li, ibid., p1106 (1995).

[5] T. Mukaiyama, et al., J. At. Energy Soc. Japan, **37**,3, p.159 (1995).

[6] K. Kobayashi, et al., Nucl. Instr. and Meth. in Physics Research A **385**, p.145 (1997).

[7] T. Kai, K. Kobayashi, et al., JAERI-Conf 98-003, pp225-230 (1998).

[8] T. Kai, K. Kobayashi, et al., 1997 Fall Meeting of the Atomic Energy Society of Japan **A1** (in Japanese).

[9] M. Obu, JAERI-M 9757 (1981).

JP9950343

JAERI-Conf 99-002

3.26 Evaluation of Neutron- and Proton-induced Cross Sections of ^{27}Al up to 2 GeV

Young-Ouk LEE and Jonghwa CHANG
Korea Atomic Energy Research Institute
Tokio FUKAHORI and Satoshi CHIBA
Japan Atomic Energy Research Institute

We have evaluated neutron and proton nuclear data of ^{27}Al for energies up to 2 GeV. The best set of optical model parameters were obtained above 20 MeV for neutron and above reaction threshold for proton up to 250 MeV with the phenomenological potential forms proposed by Chiba. The transmission coefficients for neutron and proton derived from the optical models are fed into the GNASH code system to calculate angle-energy correlated emission spectra for light ejectiles and gamma rays. For energies above 250 MeV and below 2 GeV, the total, reaction and elastic scattering cross sections were evaluated by an empirical fit and recent systematics. Emitted nucleon and pion were estimated by use of QMD+SDM (Quantum Molecular Dynamics + Statistical Decay Model).

1. Introduction

Nuclear data for conventional fission reactors and fusion devices mainly consist of neutron-induced cross sections in energy below 20 MeV. However, recent new applications such as radiation transport simulations of cancer radiotherapy and the accelerator-driven transmutation of nuclear wastes require evaluated nuclear data on neutron- and proton-induced reaction above 20 MeV up to a few GeV.

Currently some evaluation works are underway to make high energy libraries for neutron and proton data above 20 MeV. Among the higher-priority materials being evaluated for such applications, aluminum is important in structure for the accelerator-driven system, and its cross sections are often used as a reference to determine other cross sections.

The optical model provides the basis for theoretical evaluations of nuclear cross sections. It is a convenient means for calculations of reaction, shape elastic and (neutron) total cross sections, and also supplies particle transmission coefficients for Hauser-Feshbach statistical theory analyses. In order to perform nuclear data evaluation without unphysical discontinuities, optical models should cover the whole energy range of interest continuously. For energies above 150 MeV where pion production reaction channel opens, the microscopic nuclear reaction calculations are often performed by using intra-nuclear cascade (INC) model together with macroscopic transport calculations by computer codes such as LCS, LAHET and HERMES. Therefore, separate evaluated nuclear data in ENDF-6 format above pion threshold energy are not as abundant as those for energies below 150 MeV when consistency and integrity of evaluated data are to be checked.

Under these circumstances, we evaluated neutron-induced nuclear data of ^{27}Al for energies above 20 MeV up to 2 GeV, and proton-induced nuclear data above threshold up to 2 GeV.

2. Evaluations up to 250 MeV

(1) Optical Model Analyses

Evaluation starts with determination of global optical model parameters of neutron and proton for aluminum to describe measured total, reaction and elastic scattering cross sections. As a reference data set, we collected measured total (or reaction for proton) cross sections and elastic angular distributions from the EXFOR at NEA Data Bank. The potential form factor was chosen to be of Woods-Saxon form for V_r and W_v, derivative Wood-Saxon for W_d and Thomas-Fermi form for spin-orbit parts as

$$U(r) = -V_r f_v(r) - iW_v f_w(r) + 4i\, a_{wd} W_d \frac{df_{wd}(r)}{dr} - \frac{1}{r}\left(\frac{\hbar}{m_\pi c}\right)^2 \left(V_{so}\frac{d}{dr} f_{vso}(r) + iW_{so}\frac{d}{dr} f_{wso}(r)\right) \boldsymbol{l}\cdot\boldsymbol{s}\,, \quad (1)$$

where m_π is the mass of pion and the form factors f are of the standard Woods-Saxon shape :

$$f_i(r) \equiv \frac{1}{1+\exp((r-r_i A^{1/3})/a_i)} \quad (2)$$

Here, the a_x is the diffuseness parameter, and A the target mass number.

We adopted following potential energy dependencies which are similar to that proposed by Delaroche et al.[1]:

$$V_r(E) = V_0 e^{-\lambda_{Vr}(E-E_f)} + V_1 + V_2 E \qquad r_v(E) = r_{v0} + r_{v1}E \qquad a_v(E) = a_{v0} + a_{v1}E$$

$$W_v(E) = W_{v0}\frac{(E-E_F)^4}{(E-E_f)^4 + W_{v1}^4} \qquad r_{wv}(E) = r_v(E) \qquad a_{wv}(E) = a_v(E)$$

$$W_d(E) = W_{d0} e^{\lambda_{Wd}(E-E_f)}\frac{(E-E_f)^4}{(E-E_f)^4 + W_{d1}^4} \qquad r_{wd}(E) = r_{wd0} + r_{wd1}E \qquad a_{wd}(E) = a_{wd0} + a_{wd1}E \quad (3)$$

where the Fermi energy E_f for neutron is given by

$$E_f(Z,A) = -\frac{1}{2}[S_n(Z,A) + S_n(Z,A+1)] \quad (4)$$

with S_n the neutron separation energy, and for protons by

$$E_f(Z,A) = -\frac{1}{2}[S_p(Z,A) + S_p(Z+1,A+1)] \quad (5)$$

with S_p the proton separation energy.

The potential parameters of spin-orbit form parts were taken from Delaroche et al.[1] as

$$V_{so}(E) = 6.0e^{-0.005E} \qquad W_{so}(E) = 0.2 - 0.011E$$

$$r_{vso},\ w_{vso} = 1.017 \qquad a_{vso},\ a_{wso} = 0.60 \quad (6)$$

The energy dependent parameters are determined through adjusting the coefficients defined in eq. (3) by use of ECISPLOT[2], an interactive optical parameter searcher with simulated annealing algorithm, developed by one of authors.

(2) Emission Cross Sections

Compound reaction calculations with preequilibrium corrections were performed by using the GNASH[3] code based on the exciton model of Kalbach, discrete level data from nuclear data sheets, continuum level densities using the formulation of Ignatyuk and pairing and shell parameters from the Cook analysis. Besides neutron and proton potentials, the following global potentials were employed in the evaluations for composite particles:

Deuterons : Perey and Perey[4]
Tritons : Becchetti and Greenlees[5]
Alphas : Arthur and Young[6]

The transmission coefficients for neutron and protons calculated from the optical model analyses as well as for deuteron, triton and alpha particles are fed into the GNASH to evaluate angle-energy correlated emission spectra for light ejectiles and gamma rays. Gamma-ray transmission coefficients were calculated using the Kopecky-Uhl model. Direct reaction contributions to inelastic scattering from discrete states were provided by a DWBA calculation. So the orignal reaction cross section were reduced by the amount of direct reaction cross sections in GNASH calculation.

3. Evaluations up to 2 GeV

(1) Total and Reaction Cross Sections

Since there are not enough measurements and reliable physics descriptions for optical model

approach above few hundred energies where pion production becomes important, we made an empirical fit with available measurements and applied a systematics for total and reaction cross sections.

For neutron and proton reaction cross sections, we adopted the recent systematics developed by NASA[7]. The NASA systematics has following form for the reaction cross section:

$$\sigma_R = \pi r_0^2 \, (A_P^{1/3} + A_T^{1/3} + \delta_E)^2 (1 - \frac{B}{E_{cm}}) \, , \qquad (7)$$

where r_0 = 1.1 fm, A_P and A_T the projectile and target mass numbers and E_{cm} the colliding system center of mass energy in MeV. Details of parameters δ_E (Pauli blocking factor) and B (energy-dependent Coulomb interaction barrier) are explained in the reference[7]. We applied this systematics first for reaction cross sections for energies from 250 MeV to 2 GeV, and the results are merged with those obtained from optical model approach below 250 MeV.

For neutron total cross sections, we made a data fitting combined with the NASA systematics for the reaction cross section to describe measured data as:

$$\sigma_T(E) = \sigma_R(E) \cdot (a + b*E), \quad 250 \; MeV < E < 2000 \; MeV. \qquad (8)$$

and again the results were merged with those obtained from optical model approach below 250 MeV.

(2) Emission of nucleons above Pion Threshold

To evaluate emission of nucleons for energies above pion production threshold, we tried QMD+SDM[8,9] instead of well-known INC (Intra Nuclear Cascade) model to calculate nucleon emission spectra for incident neutron and proton of energies above 150 MeV up 2 GeV.

This model is based on quantum molecular dynamics (QMD) incorporated with a statistical decay model (SDM) to describe various nuclear reaction in a unified way. INC and pre-equilibrium processes are described by QMD model, and equilibrium process by SDM. The details of the QMD+SDM calculations are given in Ref. [8,9].

4. Results and Comparisons

(1) Optical Model and Total, Reaction and Elastic Cross Sections up to 250 MeV

Figure 1 show the resulting potential depths of real and imaginary volume as a function of both neutron and proton energies obtained by use of ECISPLOT. The proton depths for real and imaginary potentials are shown to be higher than that of neutron. Table 1 lists finally optimized coefficients giving two sets of potential depths and form functions for neutron and proton that describe the reference experimental data with minimum variance. The total (for neutron), reaction (for proton) cross sections and elastic angular distributions resulted from optical model analyses are shown in Figs. 2-5, with various measurements, and compared with JENDL and LANL evaluations up to 250 MeV. Our optical model parameters give excellent agreements with most of experimental data over entire energy range for both incident neutron and proton.

(2) Emission Cross Sections up to 250 MeV

Figure 6 compares the evaluated Na-23 isotope production cross sections of incident neutron against Los Alamos data together with evaluations from LANL and JENDL. The production cross sections consists of emission reactions of (n,na), (n,dt), (n,npt), (n,n2d), (n,2npd) and (n,3n2p) to give the residual Na-23 isotope. Our evaluated cross sections sections and other two evaluated ones give good agreements with the measured data in energies from the threshold up to 45 MeV. Around the neutron energy of 22 MeV having peak cross sections, our evaluations are slightly closer to the measurements than the other two. Above the neutron energy of 45 MeV, all evaluated cross sections have similar values to have lower cross sections than the measurements.

(3) Total and Reaction Cross Sections up to 2 GeV

The dotted line in Fig. 7 shows the evaluated reaction cross sections of neutron up to 2 GeV consisting of the optical model calculations and NASA systematics (eq. (7)), together with various measurements. The good agreement is shown between the evaluation and the data except mismatches in the energies around 400 MeV where the measured data are considered to have larger errors than reported. Our evaluations around these energies could be validated by the consistency with the evaluated neutron total cross sections which are described next.

The solid line in Fig. 7 shows the evaluated total cross section of neutron up to 2 GeV consisting of the optical model calculations and data fitting using eq. (8), together with available measurements. The evaluated neutron total cross sections reproduced most of measured data well except one point at 1731 MeV, which has largest errors among all data points. Our evaluation for neutron total cross sections validates the evaluated neutron reaction cross sections which show consistent behaviour with both measured and evaluated total cross sections despite of the mismatches for some measured data around 400 MeV mentioned earlier.

Solid line in Fig. 8 shows the evaluated reaction cross sections of proton up to 2 GeV merged from the optical model calculations and NASA systematics (eq. (7)), together with various measurements and LANL evaluations with dotted line. The evaluated reaction cross sections agree well with all of measured data.

(4) Emission of nucleons above Pion Threshold

Figure 9 shows our evaluation by use of QMD+SDM for neutron emission spectra for the reaction of 597 MeV proton with ^{27}Al at different laboratory angles, compared with the measurements from Juelich. As shown in the figure, the evaluated neutron spectra at all directions reproduce well the measured data except the higher energy emissions in 30 degree angle. In Fig. 10, QMD+SDM evaluations are presented for the negative pion emission spectra for the reaction of 585 MeV proton with ^{27}Al at 5 different laboratory angles together with the measured data from Juelich. The evaluated pion spectra give an overall agreement with the measured data for all directions.

The results presented above give us an applicability of QMD+SDM for producing separate evaluated data, especially for nucleon emission spectra in energies above pion production threshold as an alternative to the INC model codes combined with macroscopic transport calculations.

5. Conclusion

We evaluated the neutron and proton cross sections of ^{27}Al which is important in shielding and structural material for accelerator-driven system for energies up to 2 GeV. Optimized potential parameters describes well the experimental data of total, reaction cross section and elastic angular distributions. The resulting transmission coefficients of neutron and proton are fed into the GNASH code to evaluate production cross sections of residual nuclei and angle-energy correlated emission spectra for light ejectiles with $A \leq 4$ and gamma rays. Some of cross sections from GNASH calculations were compared with experimental data, giving good agreements. For energies above 250 MeV up to 2 GeV, the total and reaction cross sections were evaluated by an empirical fit and recent systematics. The neutron, proton and pion emission spectra for energies above pion production threshold energy were estimated by use of QMD+SDM.

References

[1] Delaroche, J.P., Wang, Y., J. Rapaport: Phys. Rev. C39, 391 (1989)

[2] Lee, Y.O., et al.: "ECISPLOT: Interactive Optical Model Searcher with Simulated Annealing Algorithm", to be published.

[3] Young, P.G., Arthur, E.D., Chadwick, M. B.: "Comprehensive Nuclear Model Calculations: Introduction to the Theory and Use of the GNASH Code," LA-12343-MS (1992).

[4] Perey, C.M., Perey, F.G.: Phys. Rev. 132, 755 (1963)
[5] Becchetti, F.D. Jr., Greenlees, G.W.: "Polarization Phenomena in Nuclear Reactions", (Ed: H.H. Barschall and W. Haeberli, The University of Wisconsin Press,1971) p.682.
[6] Young, P.G.: IAEA INDC(NDS)-335 p.109 (1995)
[7] Tripathi, R.K., et al.: "Universal Parameterization of Absorption Cross Sections" , NASA Technical Paper 3621, Jan. 1997.
[8] Niita, K., et al.: Phys. Rev., C52, 2620 (1995)
[9] Chiba, S., et al.: Phys. Rev., C54, 285 (1996)

Table 1. Optical potential parameters for n,p + ^{27}Al interaction up to 250 MeV.

	V_0 (MeV)	λ_{vr} (MeV^{-1})	V_1 (MeV)	V_2 (MeV^{-1})	r_{v0} (fm)	r_{v1} (fm/MeV)	a_{v0} (fm)	a_{v1} (fm/MeV)
Neutron	109.8	0.006	-48.27	0.168	1.190	0.00013	0.627	0.0004
Proton	111.0	0.007	-44.87	0.176	1.153	0.00016	0.552	0.0016

	W_{v0} (MeV)	W_{v1} (MeV)	λ_{wd} (MeV^{-1})	W_{d0} (MeV)	W_{d1} (MeV)	r_{wd0} (fm)	r_{wd1} (fm/MeV)	a_{wd0} (fm)	a_{wd1} (fm/MeV)
neutron	10.58	41.50	0.065	46.50	18.32	1.06	0.0	0.62	0.0008
proton	10.89	35.86	0.057	38.91	28.09	1.30	0.0	0.60	0.0

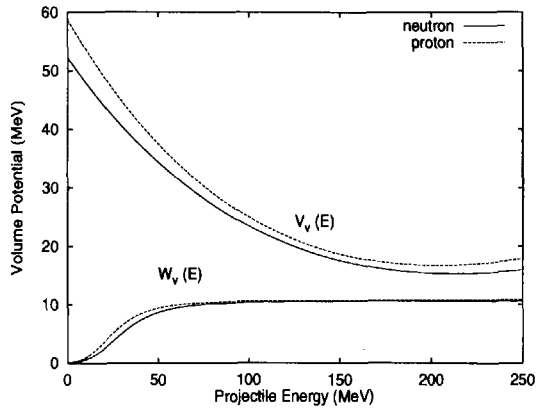

Fig. 1. The real volume potential depths as a function of neutron and proton energy for aluminim

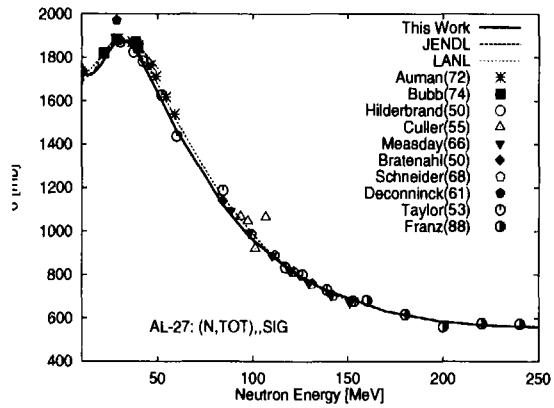

Fig. 2. Total cross sections of neutron for ^{27}Al from optimized optical potential parameters for energies up to 250 MeV

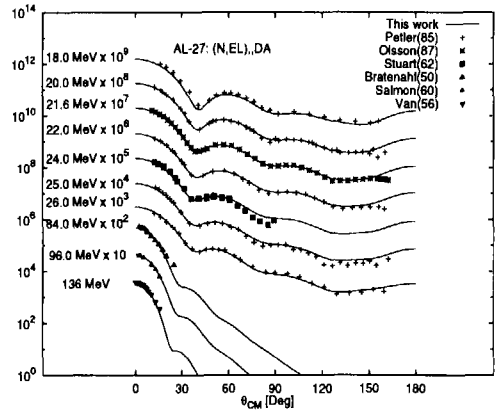

Fig. 3 Elastic angular distributions of neutron for ^{27}Al from optimized optical potential parameters for energies up to 250 MeV

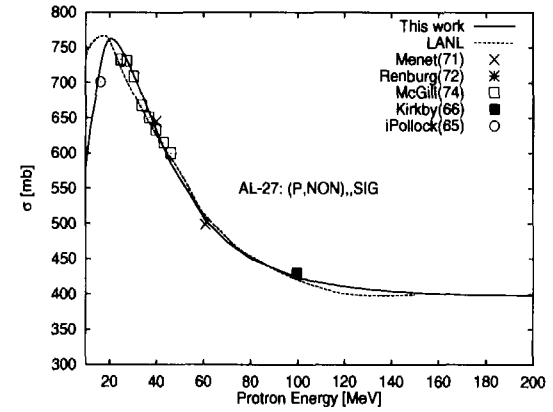

Fig. 4 Reaction cross sections of proton for ^{27}Al from optimized optical potential parameters for energies up to 250 MeV

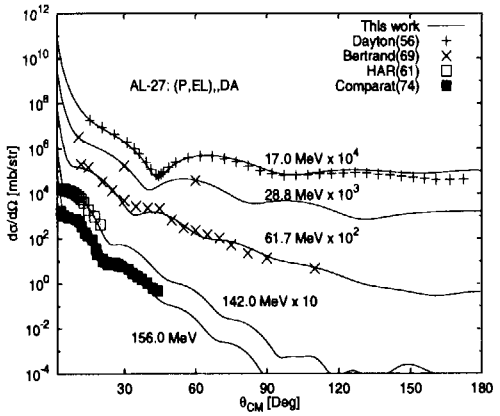

Fig. 5 Elastic angular distributions of proton for ^{27}Al from optimized optical potential parameters compared with measurements for energies up to 250 MeV

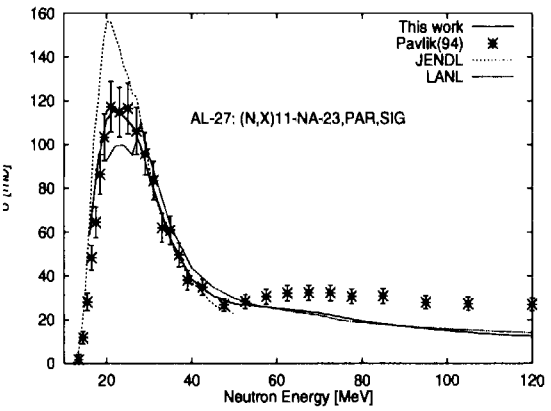

Fig. 6 Evaluated Na-23 production cross sections of neutron for ^{27}Al. Reactions included: (n,na), (n,dt), (n,npt), (n,n2d), (n,2npd), (n,3n2p), (n,n2d) (n,2npd) (n,3n2p)

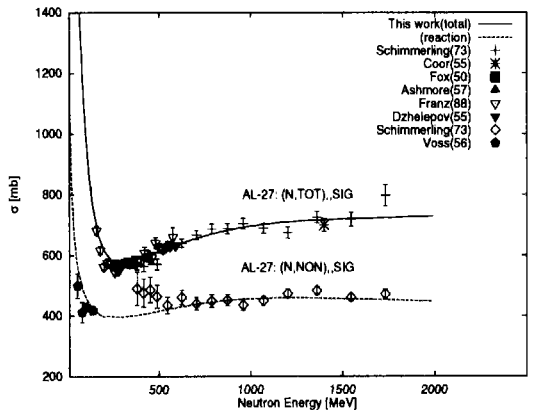

Fig. 7 Neutron total and reaction cross sections up to 2 GeV for ^{27}Al

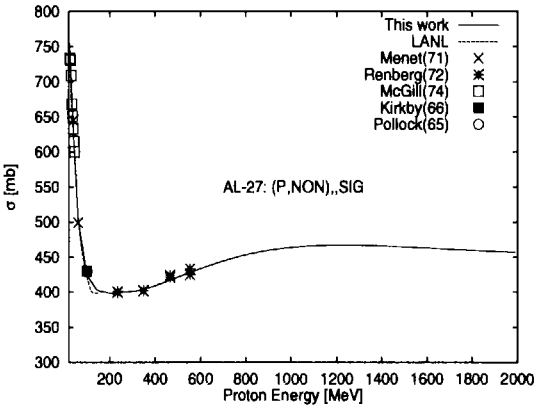

Fig. 8 Proton reaction cross sections up to 2 GeV for ^{27}Al

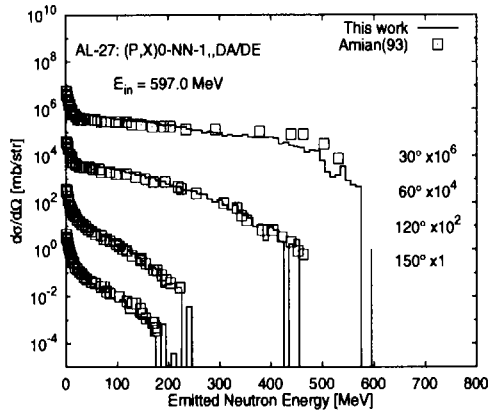

Fig. 9 Neutron emission spectra from the reaction of proton (597 MeV) + ^{27}Al at different laboratory angles

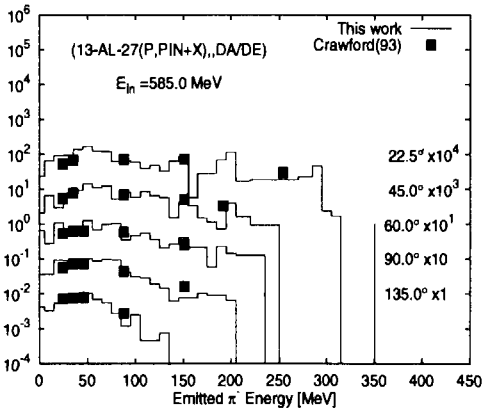

Fig. 10 Negative pion emission spectra from the reaction of proton (585 MeV) + ^{27}Al at different laboratory angles

JAERI-Conf 99-002

3.27 Optical Potential Parameterization in High Energy Region

Nobuhiro SHIGYO, Hirohiko KITSUKI and Kenji ISHIBASHI
Department of Applied Quantum Physics and Nuclear Engineering, Kyushu University
Hakozaki, Higashi-ku, Fukuoka-shi 812-8581.
mailto:shigyo@kune2a.nucl.kyushu-u.ac.jp

The optical potentials by Maruyama are reparameterized by new parameters. These potentials are appropriate to reproduce the total cross sections for neutron incidence with the energies in the GeV region.

1. Introduction

Some amounts of proton incident data have been published on elastic-scattering and total reaction cross sections up to 1 GeV of incident proton energies. Such results as well as experimental data obtained by polarized proton beams are useful for parameterizing global optical model potentials. However, the experimental data are poor above 1 GeV. For the neutron incidence with energies up to 1 GeV, Maruyama et al. derived the optical potentials by converting the proton incidence potentials by the use of the symmetry term that is dependent on (N-Z)/A [2]. However It is complicated to obtain the values of potentials requiring since the number of parameters is as many as about 170.

Recently the nuclear data for the energies in the GeV region are required for the engineering purposes. The High Energy Transport Code (HETC) based on the intranuclear cascade evaporation (INCE) model is used to the engineering design. The INCE model appropriately represents the neutron production double differential cross sections. However, the INCE models poorly reproduces total cross sections and the elastic scattering cross sections for the nucleon-incidence in the forward direction.

The total cross sections and the elastic scattering cross section are calculated by the optical model. To simplify the calculation of the optical potentials, the potentials by Maruyama are reparameterized by new parameter set. These potentials are appropriate to reproduce the total cross sections for neutron incidence with the energies in the GeV region.

2. Calculation model

In this work, 4-vector potential U_V and Lorentz scalar potential U_S are adopted as the phenomenological optical potentials.

$$\begin{aligned} U_V(r) &= V_V(E_{inc},A)f_{VV}(r) + iW_V(E_{inc},A)f_{WV}(r) \\ U_S(r) &= V_S(E_{inc},A)f_{VS}(r) + iW_S(E_{inc},A)f_{WS}(r) \\ f_i(r) &= \frac{1}{1+\exp(-\frac{r-r_{0i}}{a_i})} \\ & \quad i = VV, WV, VS, WS \quad . \end{aligned}$$

To simplify the calculation, Dirac equation is converted to Shrödinger form as follows,

$$[p^2 + 2E(U_{cent} + U_{so}\vec{\sigma}\cdot\vec{L})]\Phi(r) = [(E-V_c)^2 - m]\Phi(r)$$

where p is momentum, m mass, E total energy, $\vec{\sigma}$ spin, $\vec{L}$ orbital momentum, V_c coulomb potential. Central and spin orbit potentials U_{cent}, and U_{so} are represented as,

$$\begin{aligned} U_{cent} &= \frac{1}{2E}(2EU_V + 2mU_S - U_V^2 + U_S^2 - 2V_cU_V + 2EU_{Darwin}) \\ U_{so} &= -\frac{1}{2EBr}\frac{\partial B}{\partial r} \quad . \end{aligned}$$

Darwin and B terms are

$$
\begin{aligned}
U_{Darwin} &= -\frac{1}{2}\frac{1}{Br^2}\left(\frac{\partial}{\partial r}r^2 - \frac{\partial}{\partial r}B\right) + \frac{3}{4}\frac{1}{B}\left(\frac{\partial}{\partial r}B\right) \\
B &= \frac{E + m + U_S - U_V - V_c}{E + m} \quad .
\end{aligned}
$$

Maruyama et al [2]. obtained the values of V_V, W_V, V_S and W_S by modifying the potentials parametrized by Cooper [1]. The potentials by Cooper is made of about 170 parameters. to simplify the parametrization, V_V, W_V, V_S and W_S are reparameterized as follows.

$$
\begin{aligned}
V_S &= (7.256 \times 10^{-10}A - 2.124 \times 10^{-7})[E_{inc}^{3/2} - (-44.06A + 2.919 \times 10^4)]^2 - 0.2327A - 256.9 \\
r_{0VS} &= (1.065 - 2.924 \times 10^{-5}E_{inc})A^{1/3} \\
a_{VS} &= 0.5930 + 1.72625 \times 10^{-4}E_{inc}
\end{aligned}
$$

$$
\begin{aligned}
W_S &= -32.7A^{1/6}(\log E_{inc} - 5.496)^2 + 62.28A^{1/7} \\
r_{0WS} &= (1.144 - 1.279 \times 10^{-4}E_{inc})A^{1/3} \\
a_{WS} &= 0.5823 + 2.081 \times 10^{-4}E_{inc}
\end{aligned}
$$

$$
\begin{aligned}
V_V &= (-8.12 \times 10^{-9}A + 3.3684 \times 10^{-6})E_{inc}^{1.3} - (5.963A - 7737)^2 + 0.1447A + 155.5 \\
r_{0VV} &= (1.075 - 4.4 \times 10^{-5}E_{inc})A^{1/3} \\
a_{VV} &= 0.5748 + 1.321 \times 10^{-4}E_{inc}
\end{aligned}
$$

$$
\begin{aligned}
W_V &= 13.62A^{1/6.5}(\log E_{inc} - 5.685)^2 - 57.9A^{1/8} \\
r_{0WV} &= (1.154 - 1.237 \times 10^{-4}E_{inc})A^{1/3} \\
a_{WV} &= 0.6554 - 2.396 \times 10^{-5}E_{inc}
\end{aligned}
$$

3. Results

Figures 1 to 4 stand for the optical potentials V_V, W_V, V_S and W_S, respectively. In these figures crosses is the values from Reference [2] and solid lines the results by this parameter set. One can see that the potentials by this parameter sets are represent the values from Ref.[2] for the incident neutron energies up to 1000 MeV.

Fig. 5 shows the 4-vector and Lorentz scalar potentials in the case of 500 MeV neutron incident on ^{208}Pb target. In this figure, dashed lines with cross are the values from Ref. [2] and the solid lines the results by this parameter set.

Figs. 6 and 7 indicates the total cross sections for the neutron incidence on ^{27}Al, ^{40}Ca, ^{56}Fe, ^{63}Cu, ^{90}Zr, ^{93}Nb, ^{181}Ta, ^{208}Pb, ^{209}Bi and ^{238}U targets. In these figures, closed circles, cross marks and solid lines stand for the experimental values [3], the values from Ref. [2] and the results by this parameter set, respectively. The optical potentials by this parameter set reproduce the experimental values in the incident neutron energy up to 1000 MeV.

4. Summary

To simplify the calculation of the total cross section by he optical potentials, the parameter set by Maruyama is reparameterized by new parameters. the reparameterized potentials are appropriate to reproduce the total cross sections for neutron incidence with the energies in the GeV region.

References

[1] Cooper, E.D., *et al.*: *Phys. Rev.*, **C47**, 297 (1993).

[2] Maruyama, S., *et al.*: *Proc. Int. Conf. Nuclear Data for Science and Technology*, 336, Trieste (1998), and their in.

[3] OECD/NEA Data Bank <http://www.nea.fr/html/databank >

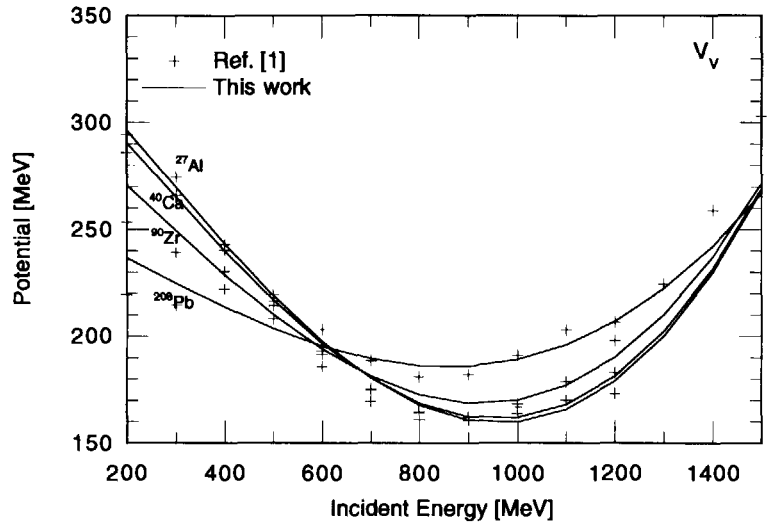

Fig. 1: V_V for neutron incidence on ^{27}Al, ^{40}Ca, ^{90}Zr and ^{208}Pb targets.

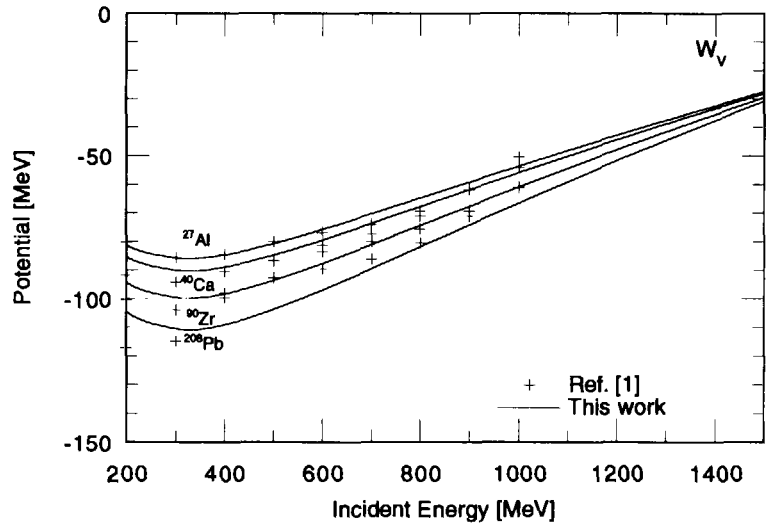

Fig. 2: W_V for neutron incidence on ^{27}Al, ^{40}Ca, ^{90}Zr and ^{208}Pb targets.

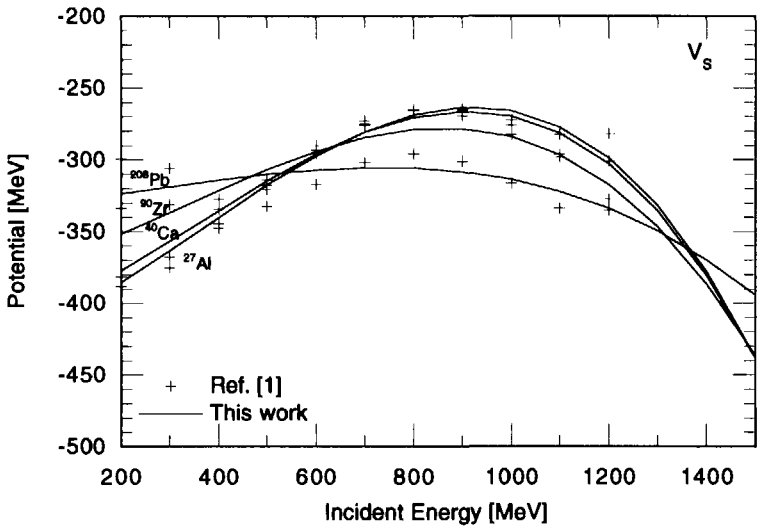

Fig. 3: V_S for neutron incidence on ^{27}Al, ^{40}Ca, ^{90}Zr and ^{208}Pb targets.

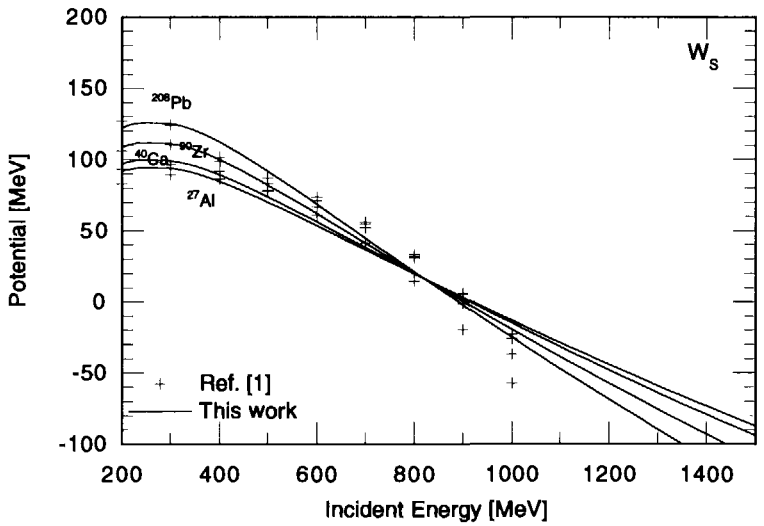

Fig. 4: W_V for neutron incidence on ^{27}Al, ^{40}Ca, ^{90}Zr and ^{208}Pb targets.

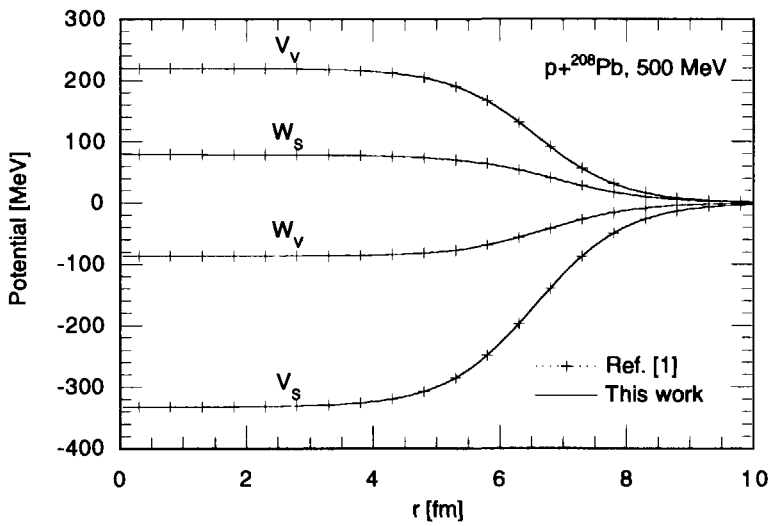

Fig. 5: The scalar and vector potentials for 500 MeV neutron incidence on ^{208}Pb target.

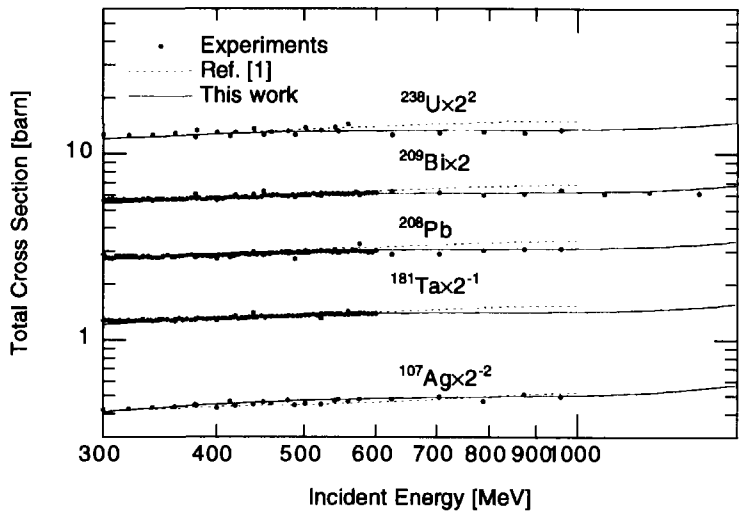

Fig. 6: Neutron incident total cross sections.

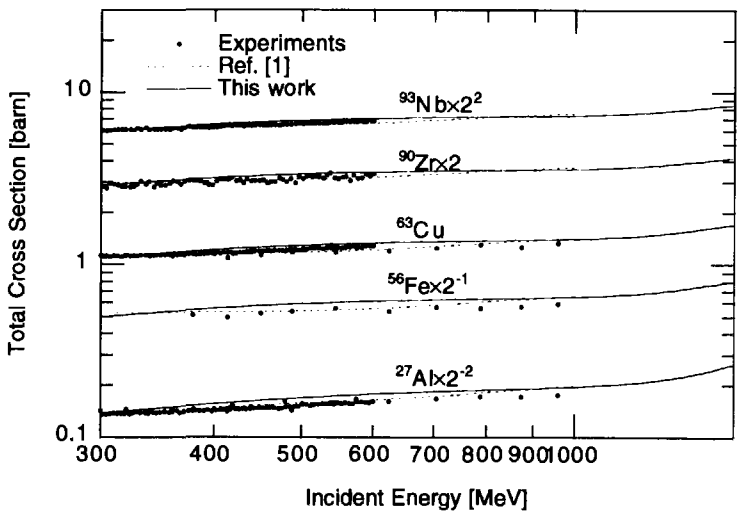

Fig. 7: Neutron incident total cross sections.

JP9950345

3.28

Parameterization of neutron production double differential cross section up to 3 GeV in terms of moving source model

Hirohiko KITSUKI, Nobuhiro SHIGYO, Kenji ISHIBASHI
Department of Energy Science and Engineering, Kyushu University
Hakozaki, Higashi-ku, Fukuoka 812-8185
mailto:kituki@meteor.nucl.kyushu-u.ac.jp

The parameterization of the double differential cross section is made for the neutron emission from proton-induced spallation reaction. The emitted neutron data for incident proton energies above 800 MeV are well analyzed by the moving source model based on the Maxwell-like energy distribution with Gaussian shape terms.

1 Introduction

Evaluated nuclear data covering incident energies up to several GeV are required in application of the spallation reaction. Neutron emission double differential cross sections, however, have been measured for several targets and incident energies. The moving source (MS) model[1] which is based on Maxwell-like distribution has been employed for analyzing the experimental neutron emission data for the proton-induced spallation reaction. The parameters obtained from this type of analysis represented well the experimental neutron spectra in the incident energy region from 113 MeV to 800 MeV[2].

In this study, the parameterization of the (p,xn) double differential cross sections is made for the neutron emission from the spallation reaction induced by protons above 800 MeV. The neutron data in incident proton energy region up to 3 GeV are analyzed by the moving source model. The experimental data[3] of the double differential cross section on neutron emission are available on C, Al, Fe, In and Pb for the incident energies of 0.8, 1.5 and 3 GeV. In addition, the quantum molecular dynamics (QMD) plus statistical decay model (SDM) code[4] is employed to calculate the cross sections which were not measured.

2 MS model

The MS model have originally been proposed to represent the high-energy collision phenomena where a locally heated spot is moving with evaporating particles in a nucleus. Since the particle emission behavior in this reaction is also explained to a considerable extent by such models as the intranuclear-cascade model, the reaction may not always produce the physical moving source. In this model, the collision phenomena are seen from an observation point moving with an appropriate velocity β (moving frame). Neutrons are assumed to be emitted isotropically with an exponential-type energy distribution of a temperature T (MeV) in the moving frame. The neutron emission double cross section is expressed by

$$\frac{d^2\sigma}{d\Omega dE_{kin}} = \frac{1}{p}\frac{A}{T}\exp\left\{-\left(\frac{E_{kin}+m-p\beta\cos\theta}{(1-\beta^2)^{\frac{1}{2}}}-m\right)/T\right\},$$

E_{kin} (MeV) and P (MeV/c) is kinetic energy and momentum of an emitted neutron. The parameters A, β and T are called amplitude, velocity and temperature, respectively. They are adjustable in fitting the equation with double differential cross section data. For the spallation reaction, the MS model is applied in a form of summation of three components as

$$\frac{d^2\sigma}{d\Omega dE_{kin}} = \sum_{i=1}^{3}\frac{1}{p}\frac{A_i}{T_i}\exp\left\{-\left(\frac{E_{kin}+m-p\beta_i\cos\theta}{(1-\beta_i^2)^{\frac{1}{2}}}-m\right)/T_i\right\}.$$

Three components correspond to the intranuclear-cascade, the preequilibrium and the nuclear-evaporation processes, respectively. Figure. 1 shows the results of fitting for the 0.8 GeV proton incidence on the Fe

target. The marks stand for the experimental cross sections. The dotted lines show the calculated data by QMD+SDM. In this figure,the results by this MS model are indicated by dash-dotted-line. The MS model reproduces the experimental and calculated cross sections at whole emission angles in the energy region below 100 MeV. In the forward direction below 30°, however, the MS model underestimates the neutron data at neutron energy above 200 MeV. It is supposed that the quasi-elastic and quasi-inelastic scattering processes are dominant in the reaction, where neutron emission spectrum is known to be forward-peaked.

3 Evaluation for quasi-elastic scattering

A Gaussian shaped term is introduced into the usual MS model for analysis of the neutron spectra derived from the quasi-elastic and quasi-inelastic scattering processes, and is written as

$$\frac{d^2\sigma}{d\Omega dE_{kin}} = A_q \exp\left\{-\frac{(E_{kin}-E_0)^2}{\kappa^2}\right\} + \sum_{i=1}^{3}\frac{1}{p}\frac{A_i}{T_i}\exp\left\{-\left(\frac{E_{kin}+m-p\beta_i\cos\theta}{(1-\beta_i^2)^{\frac{1}{2}}}-m\right)/T_i\right\},$$

where A_q, E_0 and κ are adjustable parameters dependent on the emission neutron angle and kinetic energy. The second term in right side indicates the usual MS model. In Figs. 1 and 2, solid lines show neutron spectra by the use of MS model which includes the Gaussian shaped term for 0.8 and 1.5-proton incidence, respectively. The MS model with the Gaussian shaped term represents the experimental and calculated neutron data over the whole angle well. Parameters A_q, E_0 and κ were fitted by smooth functions as

$$A_q = c_1 e^{c_2 q}, \qquad E_0 = c_3 + c_4 E_{el}, \qquad \kappa = c_5 E_{el}.$$

where q is momentum transfer of incident proton at an neutron emission angle, E_{el} that neutron kinetic energy after elastic collision with incident proton, and c_i that adjustment parameter. Figure. 3 shows the parameters obtained from fitting for 0.8, 1.5 and 3.0 GeV proton incidence on Fe. Momentum transfer of 700 MeV/c for 0.8GeV-proton incidence is equivalent to scattering angle of 28°. The values of E_0 and κ are almost constant, while A_q arises with increasing momentum transfer.

The neutron production differential cross sections from C, Al, Fe, In and Pb were obtained by the use of the MS model with the Gaussian term for incident proton energy region up to 3.0 GeV. Figures. 4 and 5 show the results of the MS model for 1.5 GeV-proton incidence on Al and Pb, respectively. The MS model with the Gaussian shaped term reproduces the neutron production spectra from Al to Pb in the wide range of incident energy and emission angles.

The mass number dependance of parameters A, β and T for 0.8 GeV-proton incidence was shown in Fig. 6, where subscripts 1, 2 and 3 indicate the intranuclear-cascade, preequilibrium and nuclear-evaporation processes, respectively. The black marks show the present work, whereas the open ones indicate the values estimated in reference[2]. The values of β and T are nearly constant for all targets, while A depends on mass number strongly. The incident energy dependance of parameters A, β and T for the Fe target was plotted in Fig. 7. While A_2 and A_3 are monotonously increasing functions of mass number, A_1 arises with decreasing mass number. The velocity and temperature parameters are raised smoothly with the incident proton energy.

4 Conclusion

The moving source model based on Maxwell-like distribution was employed to analyze the neutron production double cross section in the incident proton energy region up to 3.0 GeV. The use of the MS model with the three components of cascade, preequilibrium and evaporation reaction reproduced the experimental neutron data and the calculated results by QMD plus SDM model on C, Al, Fe, In and Pb. In the forward direction of neutron emission, the introduction of the Gaussian term into the moving source model leads to good agreement with the experimental and calculated quasi-elastic spectra. The moving source model with the Gaussian term were found to be applicable to the nuclear data evaluation for a wide range of target masses and incident.

References

[1] Bogatoskaya, I.G., *et al.* : *Phys. Rev.* **C22**, 209 (1980).

[2] Ishibashi, K., *et al.* : *J. Nucl. Sci. Tech.*, **29**, 499 (1992).

[3] Ishibashi, K., *et al.* : *J. Nucl. Sci. Tech.*, **34**, 529 (1992).

[4] Niita, K., *et al.* : *Phys. Rev.*, **C52**, 2620 (1995).

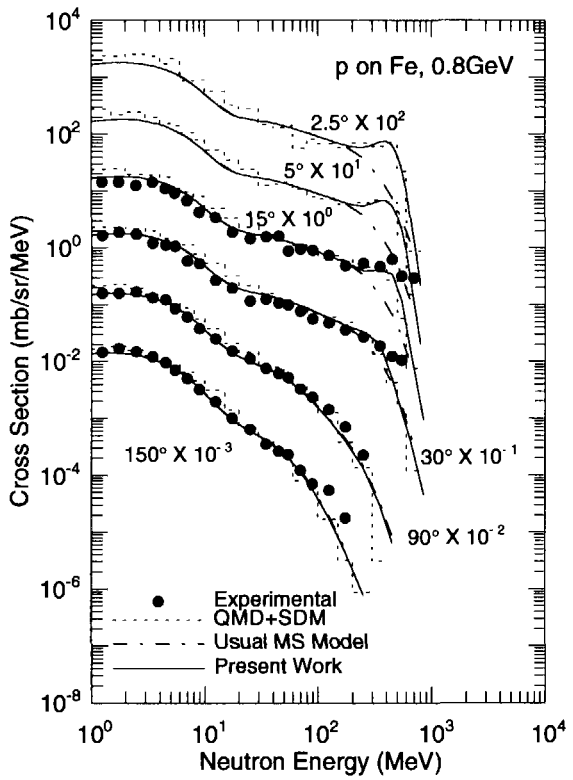

Fig. 1 Neutron production double differential cross section for 0.8GeV-proton incidence on Fe

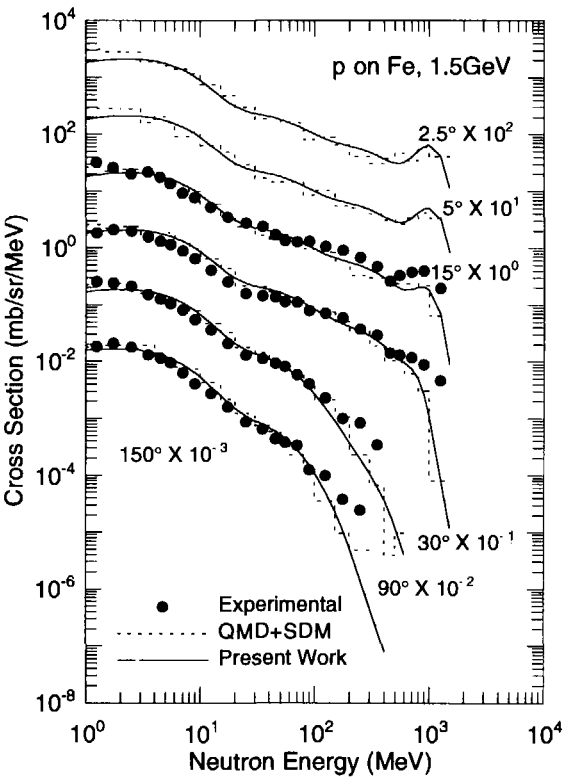

Fig. 2 Neutron production double differential cross section for 1.5GeV-proton incidence on Fe

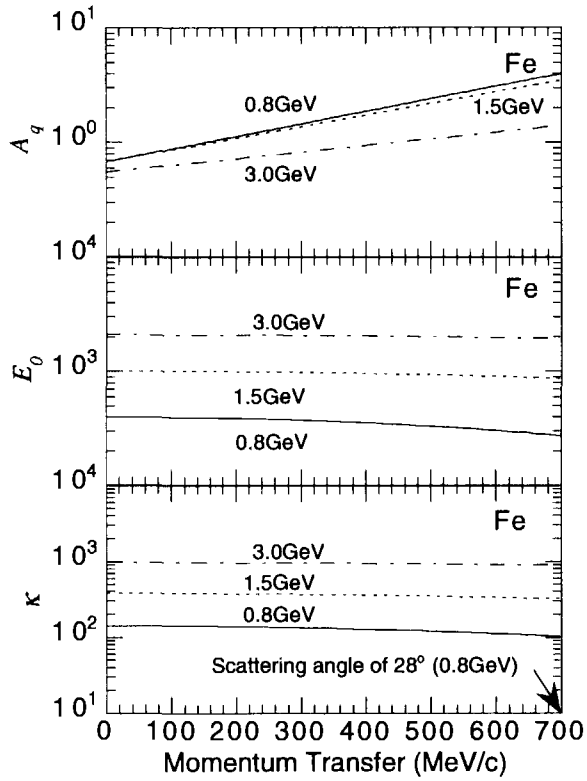

Fig. 3 Adjustable parameters A, E_0 and κ of Gaussian term obtained by fitting for the experimental and calculated neutron data. Solid, dotted and dashed-dotted lines indecate the values for the proton incident energies of 0.8, 1.5 and 3.0 GeV, respectivly

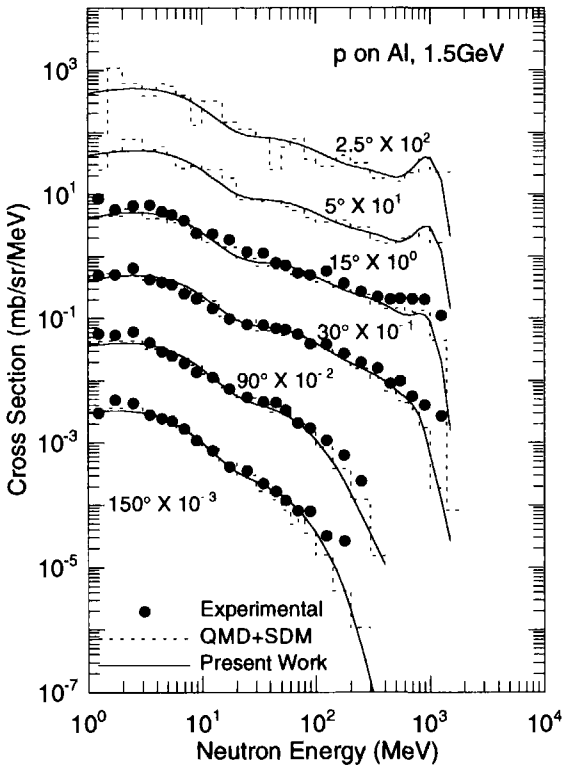

Fig. 4 Neutron production double differential cross section for 1.5GeV-proton incidence on Al

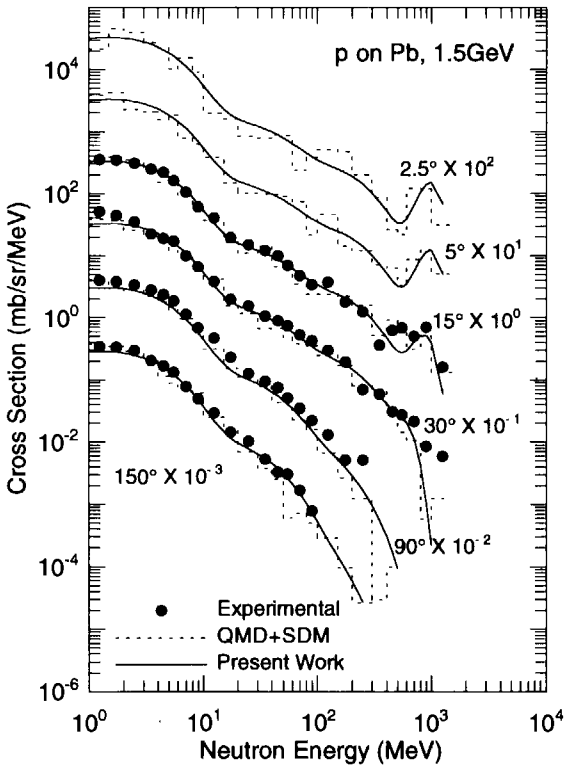

Fig. 5 Neutron production double differential cross section for 1.5GeV-proton incidence on Pb

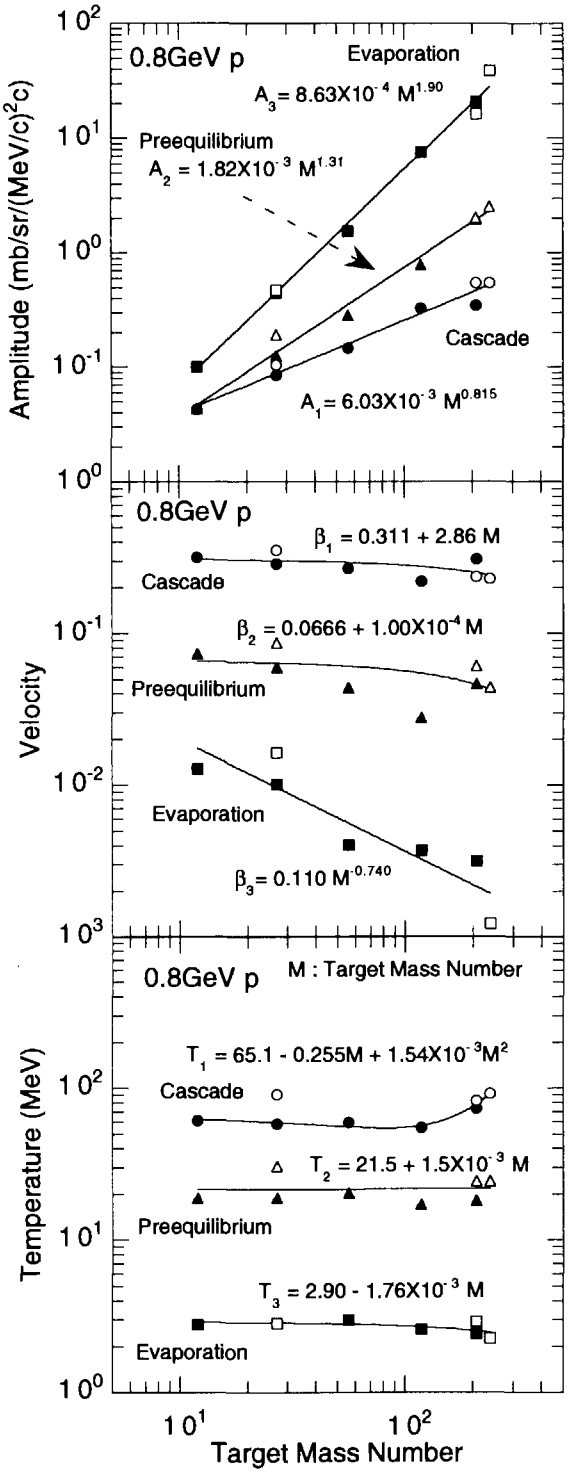

Fig. 6 Mass number dependance of parameters A, β and T for incident protns of 0.8GeV

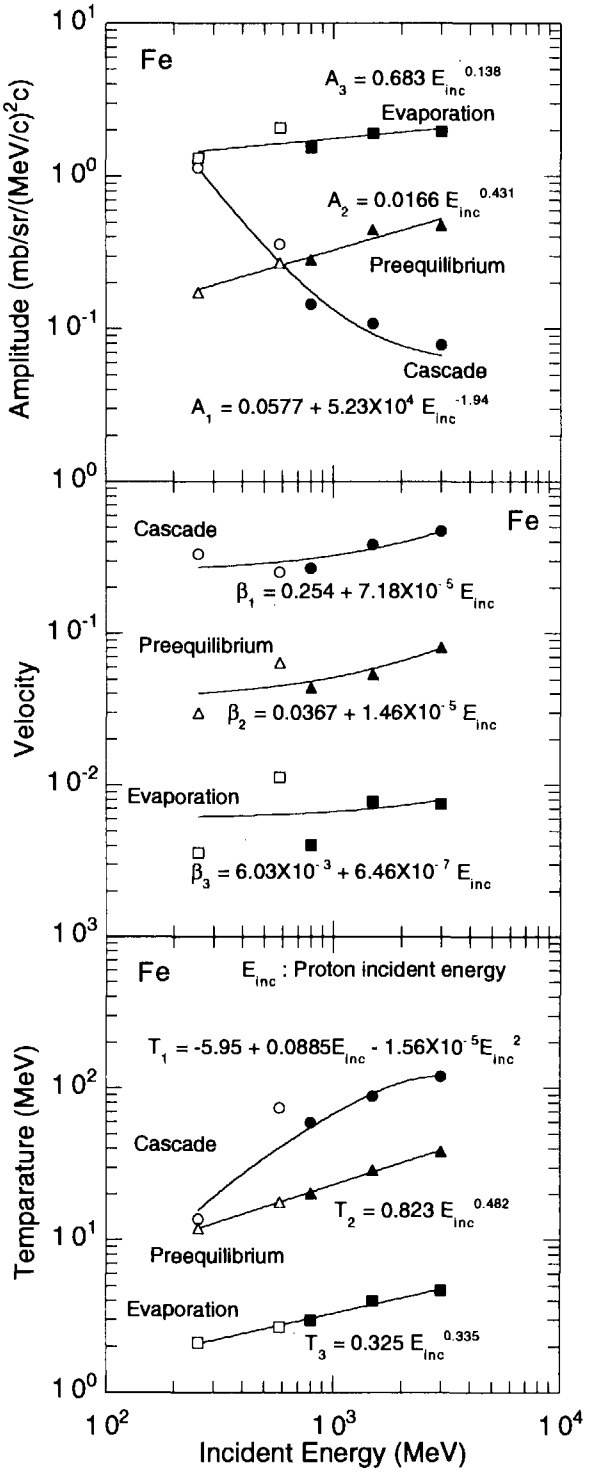

Fig. 7 Incident energy dependance of parameters A, β and T for Fe target

3.29 Analysis of (p,p'x) reactions by semi-classical distorted-wave (SCDW) model with single particle wave functions for Woods-Saxon potential

Sun Weili [a)*], Y. Watanabe[a)], K. Ogata[c)], M. Kohno[b)], and M. Kawai[c)]

[a)]*Department of Energy Conversion Engineering, Kyushu University, Kasuga, Fukuoka 816-8580, Japan*

[b)]*Physics Division, Kyushu Dental College, Kitakyushu 803-8580, Japan*

[c)]*Department of Physics, Kyushu University, Fukuoka 812-8581, Japan*

[*]*email: sun@aees.kyushu-u.ac.jp*

Multi-step direct (p,p'x) processes are analyzed in terms of SCDW model that is extended so as to use single particle wave functions for finite range potentials, i.e., harmonic oscillator and Woods-Saxson potentials, by means of the Wigner transform of one-body mixed density. The effects of momentum distributions of target nucleons on the multi-step direct processes are discussed. The calculated angular distributions including multi-step processes up to 3-step are compared with experimental data of ^{90}Zr(p,p'x) reactions at incident energies of 80 and 160 MeV.

I. Introduction

In recent years, proton nuclear data in the intermediate energy region are required for various engineering and medical applications. In this energy region, the multistep direct (MSD) processes in preequilibrium nuclear reactions become important. We applied SCDW model to analyze the experimental data of MSD processes in (p,p'x) reactions [1-4]. The results showed underestimation of the angular distributions at forward and backward angles. It was found that one of the reasons was the use of a local density Fermi-gas (LFG) model to describe the nuclear states. Hence, SCDW model was reformulated in terms of the Wigner transform of one-body mixed density, so that more realistic single-particle wave functions of target nucleons can be used. The first calculations with the single-particle wave functions for harmonic oscillator (HO) potential [5] showed that the cross sections at forward and backward angles were enhanced as expected, because of the higher momentum components of target nucleons. However, they were somewhat small compared with the experimental data.

In the present work, we use the single-particle wave functions for Woods-Saxon (WS) potential and carry out the calculations for ^{90}Zr(p,p'x) reactions at two incident energies of 80 and 160 MeV. The analysis is extended to include the MSD processes up to 3-step. We discuss the effects of the momentum distributions of target nucleons on MSD angular distributions for three cases, LFG, HO, and WS.

II. SCDW model with Wigner transform of one-body mixed density

The detailed description and formulation of SCDW model have been given in elsewhere[1-4]. Here, we explain the extension of SCDW model with the Wigner transform of one-body mixed denisty.

In each step of MSD, a target nucleon collides with a leading particle and is excited from

a single particle state $\phi_\alpha(\mathbf{r})$ at energy ε_α below the Fermi level, F, to a state $\phi_\beta(\mathbf{r})$ at ε_β above F. Then, the 1-step cross section is written by

$$\frac{\partial^2\sigma^{(1)}}{\partial E_f \partial\Omega_f} = \frac{4\mu^2}{(2\pi\hbar^2)^2}\frac{k_f}{k_i}\int d\mathbf{r}d\mathbf{r}'d\mathbf{r}_0 d\mathbf{r}_0' \chi_f^{(-)*}(\mathbf{r}_0)v(\mathbf{r}_0,\mathbf{r})\chi_i^{(+)}(\mathbf{r}_0) \times\chi_f^{(-)}(\mathbf{r}_0')v(\mathbf{r}_0',\mathbf{r}')\chi_i^{(+)*}(\mathbf{r}_0')K(\mathbf{r},\mathbf{r}') \ , \tag{1}$$

where the non-local kernel $K(\mathbf{r},\mathbf{r}')$ is given by

$$K(\mathbf{r},\mathbf{r}') = \sum_{\beta>F}\sum_{\alpha<F}\phi_\beta^*(\mathbf{r})\phi_\alpha(\mathbf{r})\phi_\beta(\mathbf{r}')\phi_\alpha^*(\mathbf{r}')\delta(\varepsilon_\beta-\varepsilon_\alpha-\omega) \ , \tag{2}$$

where ω is the energy transfer and the definition of other quantities is same as used in Refs. [3,4]. Due to the closure property of the ϕ, $K(\mathbf{r},\mathbf{r}')$ is appreciable only when $\mathbf{r}\approx\mathbf{r}'$. If the LFG model is used to describe the nuclear states, the ϕ are approximated by plane waves within a small cell centered at $\mathbf{r}\approx\mathbf{r}'$. In terms of the Wigner transform of one body density matrix [6], we can treat more realistic single particle wave functions in the finite range potentials, such as HO or WS potential, in SCDW model. In Ref. [5], we gave the expressions of Wigner transform for numerical calculations with a variation method. Here, we describe how to incorporate them into SCDW model on the basis of Ref. [7].

Let us start from general single particle model. The wave functions of struck nucleon, $\phi_\alpha(\mathbf{r})$ and $\phi_\beta(\mathbf{r})$, satisfy the following Schrödinger equation:

$$h_\gamma\phi_\gamma = (T_\gamma+U_\gamma)\phi_\gamma = \varepsilon_\gamma\phi_\gamma \qquad \text{for} \quad \gamma=\alpha \text{ or } \beta \ . \tag{3}$$

Then, $K(\mathbf{r},\mathbf{r}')$ can be re-written by

$$K(\mathbf{r},\mathbf{r}') = \delta(h_\beta(\mathbf{r})-h_\alpha(\mathbf{r})-\omega)\sum_{\alpha<F}\phi_\alpha(\mathbf{r})\phi_\alpha^*(\mathbf{r}')\sum_{\beta>F}\phi_\beta^*(\mathbf{r})\phi_\beta(\mathbf{r}') \ , \tag{4}$$

where $h_\alpha(\mathbf{r})$ operates on $\phi_\alpha(\mathbf{r})$, $h_\beta(\mathbf{r})$ on $\phi_\beta^*(\mathbf{r})$.

The Wigner transforms corresponding to hole and particle states, respectively, are given as follows:

$$f_h(\mathbf{k}_\alpha,\mathbf{r}) = \int e^{-i\mathbf{k}_\alpha\mathbf{s}}\sum_{\alpha<F}\phi_\alpha(\mathbf{r}+\mathbf{s}/2)\phi_\alpha^*(\mathbf{r}-\mathbf{s}/2)d\mathbf{s}, \tag{5}$$

$$f_p(\mathbf{k}_\beta,\mathbf{r}) = \int e^{-i\mathbf{k}_\beta\mathbf{s}}\sum_{\beta>F}\phi_\beta(\mathbf{r}+\mathbf{s}/2)\phi_\beta^*(\mathbf{r}-\mathbf{s}/2)d\mathbf{s}, \tag{6}$$

where $\mathbf{k}_\alpha$ is the momentum of struck nucleon before collision and $\mathbf{k}_\beta$ the one after collision. By making inverse Fourier transform, $\sum_{\alpha<F}\phi_\alpha(\mathbf{r})\phi_\alpha^*(\mathbf{r}')$ and $\sum_{\beta>F}\phi_\beta^*(\mathbf{r})\phi_\beta(\mathbf{r}')$ are obtained by

$$\sum_{\alpha<F}\phi_\alpha(\mathbf{r})\phi_\alpha^*(\mathbf{r}') = \frac{1}{(2\pi)^3}\int e^{i\mathbf{k}_\alpha(\mathbf{r}-\mathbf{r}')}f_h(\mathbf{k}_\alpha,(\mathbf{r}+\mathbf{r}')/2)d\mathbf{k}_\alpha \ , \tag{7}$$

$$\sum_{\beta>F}\phi_\beta^*(\mathbf{r})\phi_\beta(\mathbf{r}') = \frac{1}{(2\pi)^3}\int e^{-i\mathbf{k}_\beta(\mathbf{r}-\mathbf{r}')} f_p(\mathbf{k}_\beta,(\mathbf{r}+\mathbf{r}')/2)d\mathbf{k}_\beta . \tag{8}$$

If we assume the potential U_α acting on struck nucleon before collision is approximately equal to U_β acting on struck nucleon after collision, then

$$h_\beta(\mathbf{r}) - h_\alpha(\mathbf{r}) \approx T_\beta(\mathbf{r}) - T_\alpha(\mathbf{r}) \ . \tag{9}$$

Furthermore, if $f\ (\mathbf{k},\mathbf{r})$ is a slowly varying function of $\mathbf{r}$, we can make an approximation

$$T_\alpha(\mathbf{r})e^{i\mathbf{k}_\alpha(\mathbf{r}-\mathbf{r}')} f_h(\mathbf{k}_\alpha,(\mathbf{r}+\mathbf{r}')/2) \approx (\hbar^2k_\alpha^2/2\mu)e^{i\mathbf{k}_\alpha(\mathbf{r}-\mathbf{r}')} f_h(\mathbf{k}_\alpha,(\mathbf{r}+\mathbf{r}')/2) \tag{10}$$

$$T_\beta(\mathbf{r})e^{-i\mathbf{k}_\beta(\mathbf{r}-\mathbf{r}')} f_p(\mathbf{k}_\beta,(\mathbf{r}+\mathbf{r}')/2) \approx (\hbar^2k_\beta^2/2\mu)e^{-i\mathbf{k}_\beta(\mathbf{r}-\mathbf{r}')} f_p(\mathbf{k}_\beta,(\mathbf{r}+\mathbf{r}')/2) \tag{11}$$

Under these approximations, $K^{(c)}(\mathbf{r},\mathbf{r}')$ is finally given by

$$K^{(c)}(\mathbf{r},\mathbf{r}') \approx \frac{1}{(2\pi)^6}\int d\mathbf{k}_\alpha d\mathbf{k}_\beta e^{i\mathbf{q}(\mathbf{r}-\mathbf{r}')} f_h^{(c)}(\mathbf{k}_\alpha,\mathbf{R})[1-f_h^{(c)}(\mathbf{k}_\beta,\mathbf{R})]\delta(\hbar^2k_\beta^2/2\mu - \hbar^2k_\alpha^2/2\mu - \omega), \tag{12}$$

where c denotes neutron or proton shell, $\mathbf{q}=\mathbf{k}_\alpha-\mathbf{k}_\beta$, and $\mathbf{R}=(\mathbf{r}+\mathbf{r}')/2$. In deriving Eq.(12), the normalization condition for all states is used, which leads to $f_p(\mathbf{k}_\beta,\mathbf{R}) = 1 - f_h(\mathbf{k}_\beta,\mathbf{R})$. For convenience, we write $f^{(c)}(\mathbf{k},\mathbf{R}) = f_h^{(c)}(\mathbf{k},\mathbf{R})$ hereafter.

As did in Refs. [1-4], we use a local semi-classical approximation to distorted wave $\chi_c^{(\pm)}(\mathbf{r}_0')$ in Eq. (1) we also make the approximation $f^{(c)}(\mathbf{k},\mathbf{R}) \approx f^{(c)}(\mathbf{k},\mathbf{r})$. Thus, the final 1-step cross section is given as follows:

$$\frac{\partial^2\sigma^{(1)}}{\partial E_f \partial\Omega_f} = \left(\frac{A}{A+1}\right)^2 \int d\mathbf{r}\left|\chi_i^{(+)}(\mathbf{r})\right|^2\left|\chi_f^{(-)}(\mathbf{r})\right|^2 \frac{k_f/k_f(\mathbf{r})}{k_i/k_i(\mathbf{r})}\left[\frac{\partial^2\sigma}{\partial E_f\partial\Omega_f}\right]_{\mathbf{r}} \rho^{(c)}(\mathbf{r}), \tag{13}$$

where the product of local average N-N scattering cross section and density is given by

$$\left[\frac{\partial^2\sigma}{\partial E_f\partial\Omega_f}\right]_{\mathbf{r}} \rho^{(c)}(\mathbf{r}) = \frac{8}{(2\pi)^3}\frac{k_f(\mathbf{r})}{k_i(\mathbf{r})}\int d\mathbf{k}_\alpha \int d\mathbf{k}_\beta \left[\frac{\partial\sigma}{\partial\Omega}\right]_{NN} f^{(c)}(\mathbf{k}_\alpha,\mathbf{r})[1-f^{(c)}(\mathbf{k}_\beta,\mathbf{r})]$$
$$\times\delta(\mathbf{k}_f(\mathbf{r})+\mathbf{k}_\beta-\mathbf{k}_i(\mathbf{r})-\mathbf{k}_\alpha)\delta(\hbar^2k_\beta^2/2\mu-\hbar^2k_\alpha^2/2\mu-\omega), \tag{14}$$

where $\left[\frac{\partial\sigma}{\partial\Omega}\right]_{NN}$ is the two-body N-N scattering cross section.

The extension to the 2- and 3-step processes is straightforward with Eq. (14) for each collision point.

III. Results and Discussion

Figs.1 and 2 show the momentum distributions, $n(k)$, of target nucleons for HO and WS potentials compared with that given by the LFG model in linear and logarithmic scales, respectively. It should be noted that the one for WS potential is different from the previous calculation[5], because the number of Gaussian basis as the variational function is different between both the calculations, i.e., 20 in the present calculation and 10 in the previous one. Enough large number of Gaussian basis is necessary for precise calculations of the Wigner transform when the momentum k is larger than 2 fm^{-1}. The other parameters used in the calculation are the same as those in Ref. [5]. One can see that the momentum distribution by the LFG model contains too much low momentum components and no higher momentum components above the Fermi momentum. On the other hand, the momentum distributions calculated by both finite range potentials show remarkable reduction of low momentum components below 0.3 fm^{-1} and existence of higher momentum components compared with LFG. Also, one can see some differences between momentum distributions for HO and WS potentials in the high momentum region.

The SCDW model with the Wigner transform was applied to the ^{90}Zr(p,p'x) reaction at two incident energies of 80 and 160 MeV in order to investigate the effects of the nucleon momentum distribution on MSD processes. The basic input parameters, i.e., distorting potentials, N-N scattering cross sections and nuclear density, were the same as in the previous calculations [3,4]. Fig.3 shows comparisons of individual multi-step cross sections calculated for three cases, LFG, HO, and WS, for the incident energy of 160 MeV. The 1-step cross sections calculated with HO and WS potentials are enhanced remarkably at backward angles compared with the LFG result that drops steeply at backward angles. The 1-step cross sections for HO and WS are also larger than those for LFG at very forward angles near 0 degree. In addition, some differences are seen between both HO and WS results; 1-step cross section for WS is larger than that for HO at backward angles, but the 2-and 3-step cross sections show the opposite behavior at backward angles.

For three cases, (a) LFG, (b) HO and (c) WS, the SCDW calculations including 3-step process are compared with experimental data in Fig. 4. The results with HO and WS potentials are in better agreement with the experimental data[8] than that with LFG at backward angles. Also, both results lead to some reduction of cross sections around 30 degree corresponding to the quasi-elastic scattering angle and improve the shape of angular distributions in the entire angular region. It is worthwhile to note that the sum of individual cross sections for HO is almost same as that for WS, even if the individual cross sections are different, particularly for the 1-step process, as shown in Fig. 3. For both cases of HO and WS, the cross sections summed up to 3-step are somewhat smaller than the experimental data. This might suggest the contribution from higher MSD steps.

Fig. 5 shows comparisons of SCDW calculations for three cases with experimental data[9] at the incident energy of 80 MeV. Similar behavior in individual cross sections can be seen as in Figs.3 and 4. The summed cross sections for both HO and WS show much better agreement with the experimental data at backward angles than those for LFG.

IV. Summary

The SCDW model with the Wigner transform of one-body mixed density was applied to the analysis of the ^{90}Zr(p,p'x) reaction at 80 and 160 MeV. In the analysis, HO and WS potentials was employed as the finite range potential to use more realistic single-partile wave functions than the LFG model in SCDW. The SCDW calculations with HO and WS potentials

obviously improve the underestimation to the experimental data at backward angles, which is seen in the calculation with LFG. The 1-step cross sections calculated with WS potential increase at very forward and backward angles, more than those of HO potential. However, the sum of individual cross sections is almost same for both potentials, because 2- and 3-step cross sections calculated with W-S potential are smaller than those with HO potential at backward angles. This result shows that the momentum distribution of target nucleons affects strongly the 1-step cross sections at the forward and backward angles and the effect becomes weak as the step number increases. Our calculation still somewhat underestimates the experimental data at backward angles even if the higher momentum components of target nucleons are considered, which should be further investigated. In addition, it will be necessary to investigate the validation of the approximations used in Eqs. (10) and (11) in Sec. II.

Acknowledgment

This work is partly supported by Grand-in-Aid Scientific Research of the Ministry of Education, Science and Culture (No. 09558059).

References

[1] Y.L. Luo and M. Kawai, Phys. Rev.C **43**, 2367 (1991).
[2] M. Kawai and H.A. Weidenmüller, Phys. Rev.C **45**, 1856 (1992).
[3] Y. Watanabe and M. Kawai, Nucl. Phys. **A560**, 43 (1993).
[4] Y. Watanabe et al., to be submitted to Phys. Rev. C, (1998).
[5] Sun Weili et al., JEARI-Conf. 98-003, p.282 (1998).
[6] See, for example, H. Feshbach, *Theoretical Nuclear Physics, Nuclear Reactions* (John Wiley and sons, 1992).
[7] M. Kawai et al., *Proceedings of the Fifteenth International Workshop on Nuclear Theory*, Rila mountains, Sofia, Bulgaria, 10-16 June,1996.
[8] W.A. Richter et al., Phys. Rev. C **49**, 1001 (1994).
[9] A.A. Cowley et al., Phys. Rev. C **43**, 678 (1991).

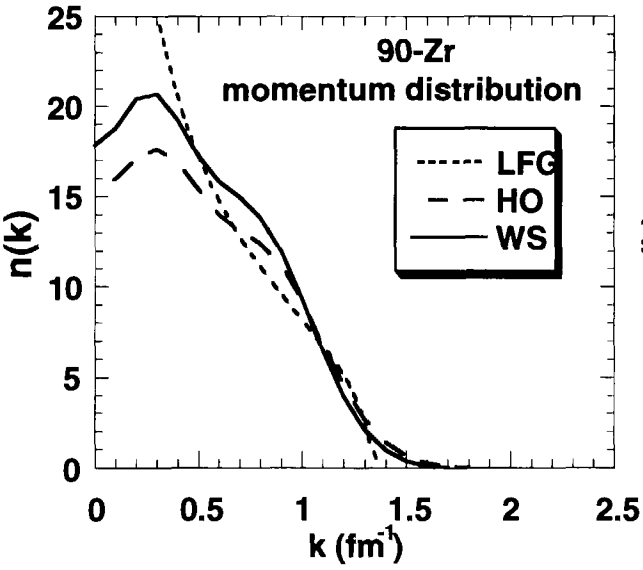

Fig.1 Momentum Distribution of target nucleon for ^{90}Zr in a linear scale

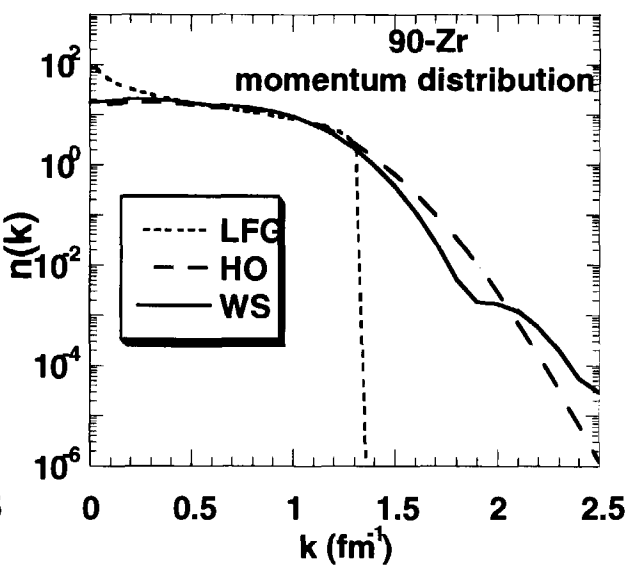

Fig.2 Same as Fig.1 but in a logarithmic scale

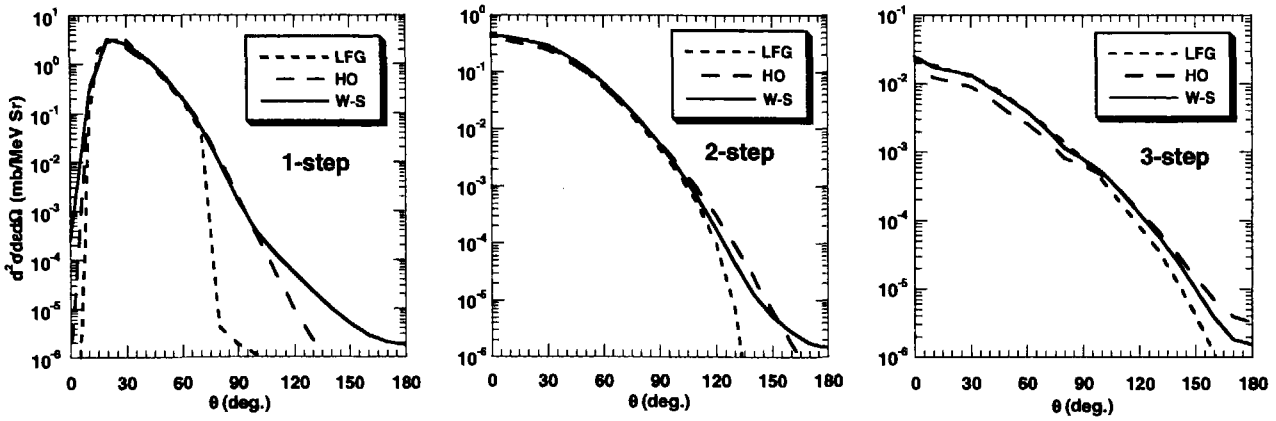

Fig.3 Comparison of individual multistep cross sections for three cases, (a) LFG model, (b) HO and (c)WS for the ^{90}Zr(p,p'x) reaction at an incident energy of 160 MeV and an outgoing energy of 120 MeV.

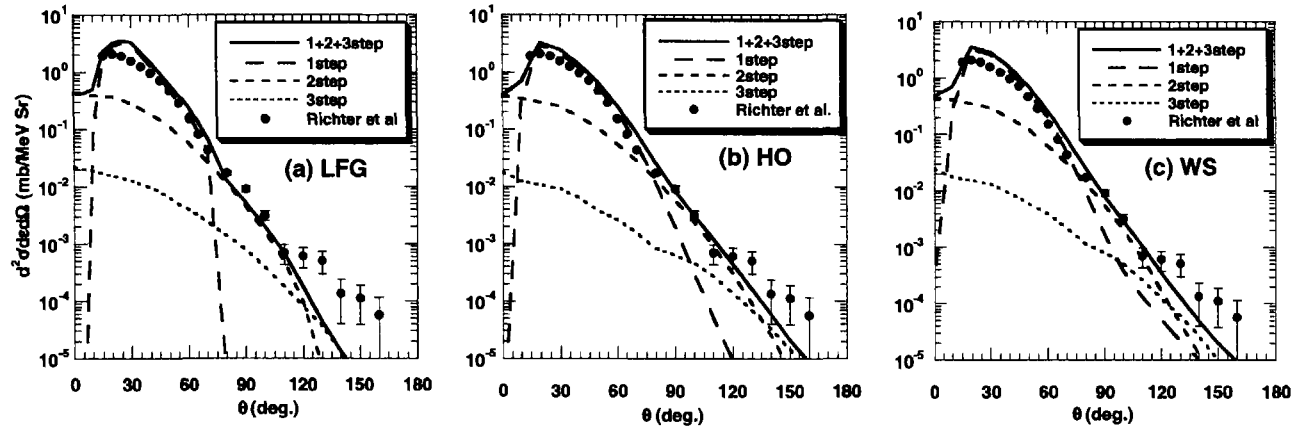

Fig.4 Comparison of calculation with experimental data for three cases, (a) LFG model, (b) HO and (c) WS for the ^{90}Zr(p,p'x) reaction at an incident energy of 160 MeV and an outgoing energy of 120 MeV. The experimental data are taken from Ref.[8].

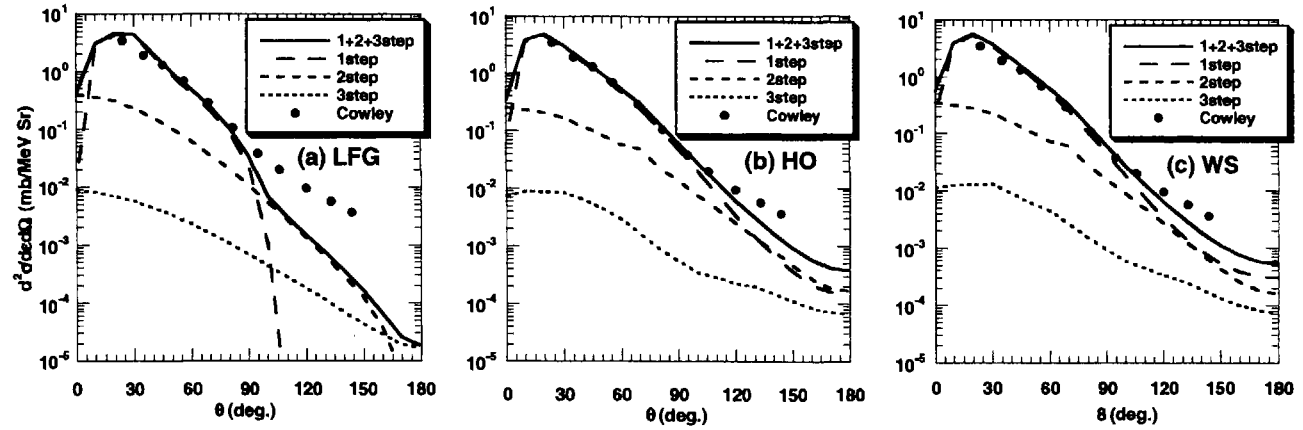

Fig.5 Same as Fig. 4, but at an incident energy of 80 MeV and an outgoing energy of 60 MeV. The experimental data are taken from Ref.[9].

JP9950347

3.30 Study of secondary charged-particle production by proton-induced reactions at several tens of MeV

M. Harada[a)], A. Yamamoto, Y. Tanaka, Y. Watanabe, K. Shin[*],
S. Meigo[**], O. Iwamoto[**], H. Nakashima[**], H. Takada[**],
S. Chiba[**], T. Fukahori[**], T. Sasa[**] and Su. Tanaka[***]
Department of Energy Conversion Engineering, Kyushu University, Kasuga,Fukuoka 816-8580, Japan
[*]*Department of Nuclear Engineering, Kyoto University, Kyoto, 606-8501, Japan*
[**]*Tokai Establishment, JAERI, Tokai-mura, Ibaraki 319-1195, Japan*
[***] *Takasaki Establishment, JAERI, Takasaki, Gunma 370-1292, Japan*
[a)]e-mail : harada@aees.kyushu-u.ac.jp

Double differential cross sections (DDXs) of charged particles emitted from proton-induced reactions on ^{12}C and ^{27}Al were measured at E_p=42 and 68 MeV. Experimental DDXs of protons were in fairly good agreement with LA150 evaluation, except for very forward angles. Coupled-channels calculation with the soft-rotator model reproduced well experimental angular distributions of elastic and inelastic proton scattering. Experimental angular distributions of continuum proton spectra showed overall good agreement with the Kalbach systematics.

1. Introduction

Proton and neutron nuclear data in the intermediate-energy region are requested in various applications, e.g. evaluation of radiation dose in proton radiotherapy and LSI damage estimation in cosmic space. Some of the authors[1)] have recently evaluated the neutron nuclear data and kerma factor of ^{12}C for energies up to 80 MeV. As the second step, we have started the evaluation of proton nuclear data of ^{12}C in the energy region up to 200 MeV.

Double-differential cross sections (DDXs) are needed for calculations of particle transport in matter. There are currently some available experimental DDXs data of proton-induced reactions, but few systematic measurements in the energy region ranging from a few tens of MeV to 200 MeV. Thus, we have started the experiments to measure DDXs of secondary charged-particles emitted from proton-induced reactions on several targets.

In the present work, we have measured DDXs of all emitted light-charged particles from ^{12}C and ^{27}Al with 42 and 68 MeV proton beams at the AVF cyclotron facility, TIARA. In this paper, preliminary results of the measurements and analyses are reported.

2.Measurement

The experiments were carried out with 42 and 68 MeV proton beams delivered to the HB-1 beam line at the AVF cyclotron facility. Detailed information on each experiment is summarized in Table 1. A 60 cmϕ scattering chamber was installed in the beam line as illustrated in Fig. 1. To reduce γ-ray backgrounds, a beam dump made of graphite was placed at a distance of 3 m from the chamber. Targets, which were self-supporting natural carbon foil (0.5 mg/cm^2 in thickness) and aluminum foil (0.9 mg/cm^2 in thickness), were located at the center of the chamber.

In order to measure the energy spectra of emitted charged particles, we have used a counter telescope consisting of three detectors: two thin silicon-semiconductor ΔE-detectors (30 μm and 500 μm in thickness, respectively), and a CsI(Tl) E-detector (18 mmϕ x 30 mm) with photo-diode readout. Fig. 2 shows a schematic side-view of the counter telescope. Those thickness and size were optimized using a Monte Carlo simulation of energy deposit in the detectors in which the effect of energy straggling

was taken into account. The counter telescope was placed at a distance of 14.5 cm from the target in the scattering chamber and detected light-charged particles over the outgoing energy range from 1.5 MeV to 90 MeV for protons.

Energy signals from each detector were converted to digital data by using conventional NIM and CAMAC modules, and those data were stored event by event on an MO disk with SDAQ system[2]. Off-line data processing was made with the PAW system in CERNLIB[3].

3. Experimental results and analyses

In Fig. 3, experimental differential cross sections of proton elastic and inelastic scattering from ^{12}C at 42 and 68 MeV are compared with the coupled-channels calculations based on the soft-rotator model (SRM)[4]. The optical potential parameters used in the calculation were the same as in Ref.[4]. The SRM prediction is in good agreement with the experimental data.

Figure 4 shows measured DDXs of proton, deuteron, triton, ^{3}He and α-particle from 42 MeV proton-induced reactions on ^{12}C and 68 MeV proton-induced reactions on ^{27}Al at 30° in the laboratory system. Similar results were obtained for other angles. There is the energy region where no data were taken in Fig. 4 (a), because of higher discrimination level that was set to eliminate the electric noise in the signals from CsI detector. Since we failed to take low pulse signals from the $\Delta E1$ detector in the 42 MeV proton-induced experiment, the threshold energies of proton, deuteron and triton in the experiment were rather high as shown in Fig. 4 (b). Also, continuum proton spectra measured at angles smaller than 45° may include a background component due to edge-penetration of elastic protons in the defining collimator. The background components are now under detailed investigation.

To check the reliability of the present data, the DDXs are compared with other experimental data[5,6] and LA150 evaluation[7] in Fig. 5. Our data show overall agreement with other experimental data, although they are slightly smaller than the data of Bertrand and Peelle[5] at lower outgoing energies. The LA150 evaluation underestimates the measured DDXs in the continuous region between 15 and 50 MeV at 30°, while it shows fairly good agreement with the experimental data for the other angles.

Angular distributions of continuum proton spectra are compared with the Kalbach systematics[8] in Fig. 6. A parameter "f_{msd}" which stands for the ratio of MSD component, were the same as used in LA150 evaluation[7]. The calculations of the Kalbach systematics are in good agreement with the experimental angular distribution, except for underestimation seen at backward angles and overestimation at intermediate angles.

4. Summary

We have carried out the proton-induced experiments for ^{12}C and ^{27}Al at E_p=42 and 68 MeV at TIARA facility and measured the DDXs of secondary charged-particles (p, d, t, ^{3}He and α) emitted from these reactions. The experimental angular distributions of elastic and inelastic proton scattering from ^{12}C were in quite good agreement with the coupled-channels calculation based on SRM. Comparisons with other experiments and LA150 evaluation showed good agreement for ^{12}C(p,xp) and ^{27}Al(p,xp) reactions. The shape of continuum (p,p') angular distributions were reproduced well by the Kalbach systematics. The detector system developed in the present work was found to be reliable and useful in DDXs measurements, although there was a difficulty on the elimination of electric noise in the signal from the CsI-detector. The obtained data will be useful for intermediate-energy proton nuclear data evaluation.

In the future, we plan further measurements of DDXs for some different incident energies and supplementary experiments to measure deficient region of the energy spectra.

Acknowledgments

This work was undertaken as the Universities-JAERI Collaboration Research Project. We wish to thank the staff of AVF cyclotron team for their cyclotron operation during our experiment. This work is partly supported by Grand-in-Aid Scientific Research of the Ministry of Education, Science and Culture (No. 09558059).

Reference

[1] M. Harada *et al.*: *J. of Nucl. & Technol.* **34**, 116 (1997).
[2] K. Sato: Master thesis, Kyushu Univ., (1993) (unpublished).
[3] PAW-Physics Analysis Workstation CERN Program Library entry Q121 (1993).
[4] E.S. Sukhovitskii, *et al.*: *Nucl. Phys.*, **A640**, 147 (1998).
[5] F.E. Bertrand and R.W. Peelle: *Phys. Rev. C*, **8**, 1045(1973); ORNL report *ORNL*-4799, (1973).
[6] H. Sakai *et al.*: *Nucl. Phys.* **A344**, 41 (1980).
[7] M.B. Chadwick *et al.*: *LA-UR*-98-1825 (1998); to be published in *Nucl. Sci. Eng.* (1998).
[8] C. Kalbach: *Phys. Rev. C*, **37**, 2350 (1988).

Table 1: Details of the proton-induced experiments at TIARA.

Incident energy	42 MeV		68 MeV
Accelerator	JAERI TIARA AVF cyclotron Accelerator		
Target	Self-supporting natural Carbon foil 0.5 mg/cm^2 Self-supporting Aluminum foil 0.9 mg/cm^2		
Configuration of counter telescope (applied bias voltage)	ΔE1 : Si-SSD 30 μm, 13 V ΔE2 : Si-SSD 500 μm, 135 V E3 : CsI(Tl) 3 cm, 80 V, Photo-diode readout		
Measured particles	p, d, t, ^{3}He, α-particle		
Measured angles (lab.)	^{12}C 25, 30, 35, 40, 45, 60, 75, 90, 105, 120, 130, 140, 150°	^{27}Al 25, 30, 35, 40, 45, 60, 75, 90, 105, 150°	^{12}C & ^{27}Al 25, 30, 35, 45, 60, 75, 90, 120, 150°
Beam current	2 ~ 23 nA*		2 ~ 16 nA*

*Beam currents depend on target and angle.

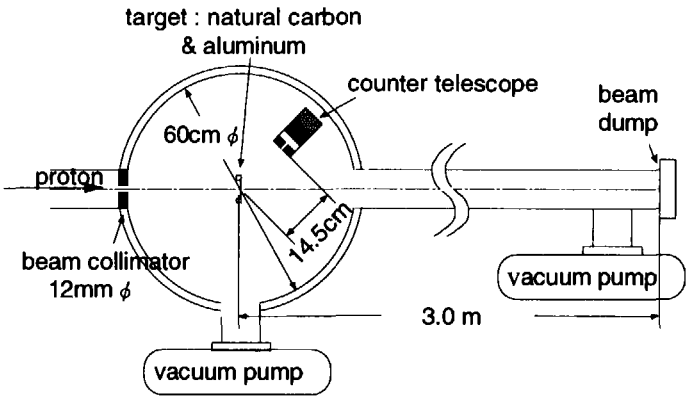

Fig. 1: Experimental setup of the HB-1 beam line at TIARA.

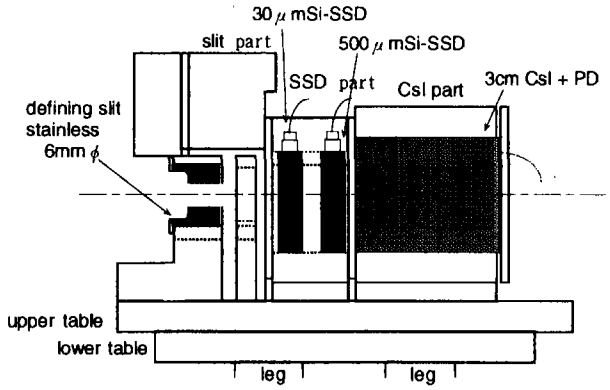

Fig. 2: Schematic side-view of ΔE-E counter telescope.

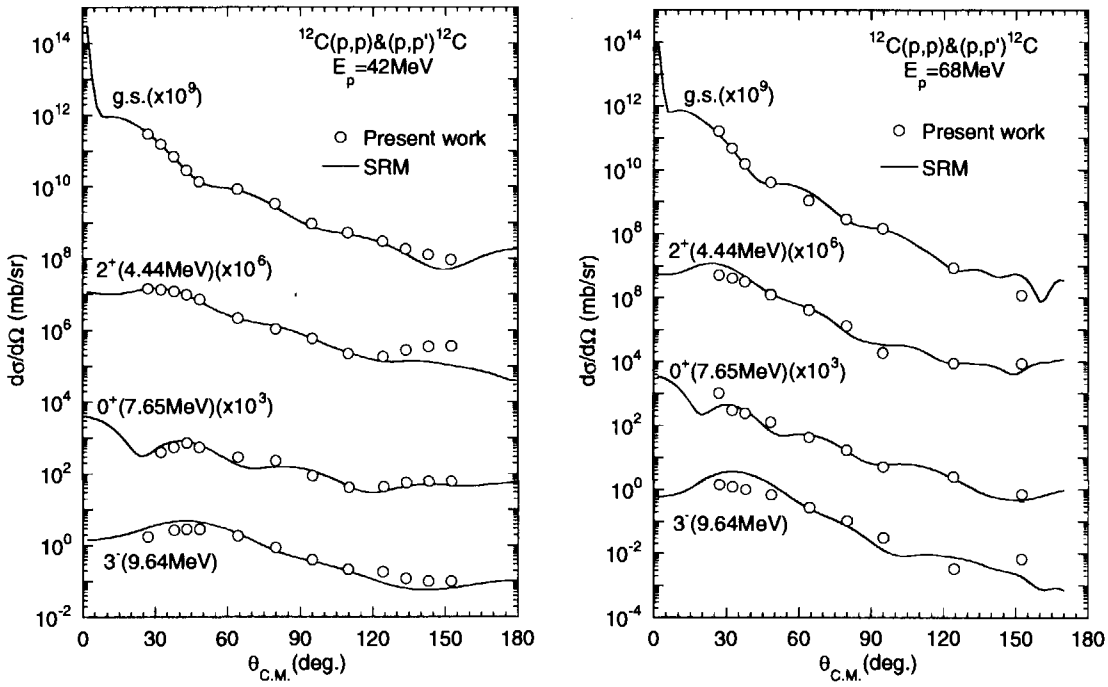

Fig. 3: Comparison of experimental angular differential cross sections of ^{12}C(p,p) and ^{12}C(p,p') scattering with coupled-channels calculation based on the soft-rotator model at 42 MeV (left-panel) and 68 MeV (right-panel).

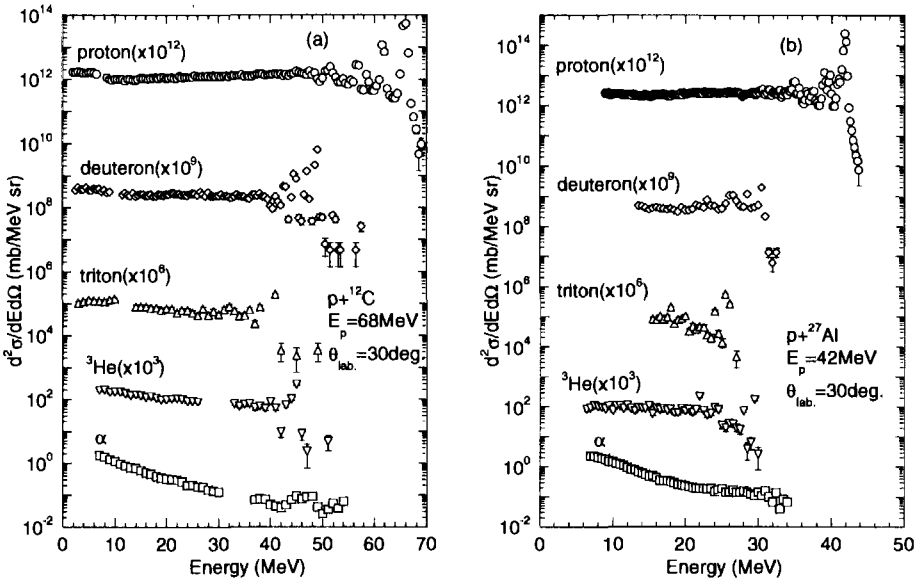

Fig. 4: Measured DDXs of proton, deuteron, triton, ^{3}He and α-particles: (a) 68 MeV p+^{12}C reaction and (b) 42 MeV p+^{27}Al reaction at 30° in the laboratory system.

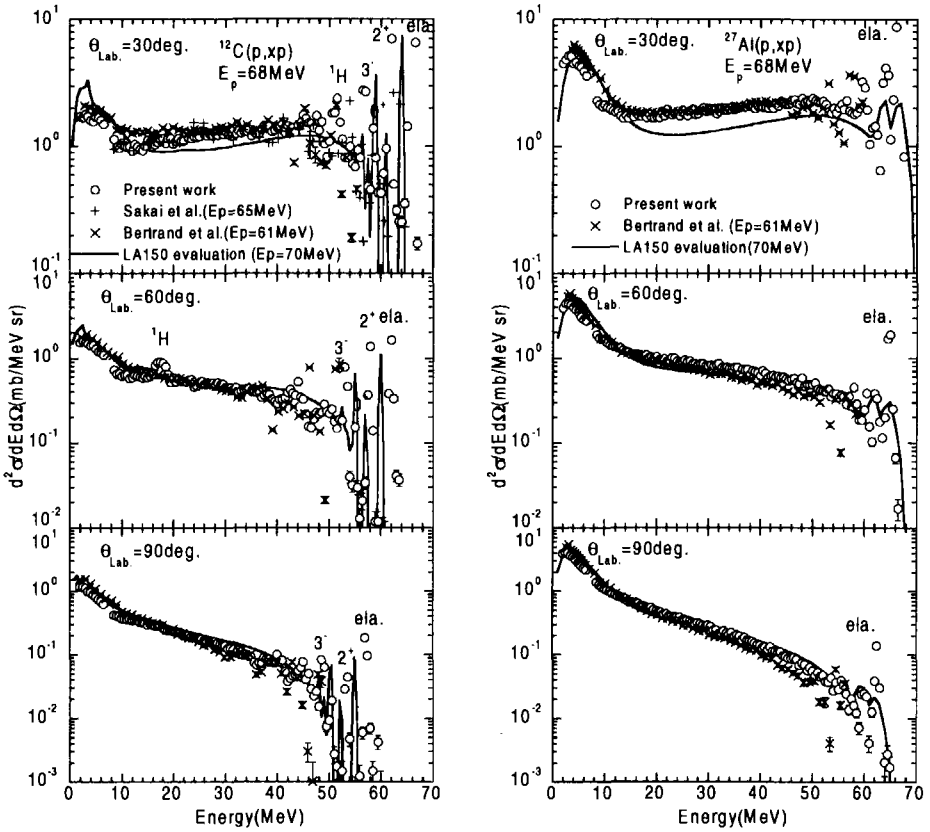

Fig. 5 : Comparison of experimental double differential cross sections of ^{12}C(p,xp) (left panel) and ^{27}Al(p,xp) (right panel) with other experimental data and evaluation of LA150 library for three angles and an incident energy of 68 MeV.

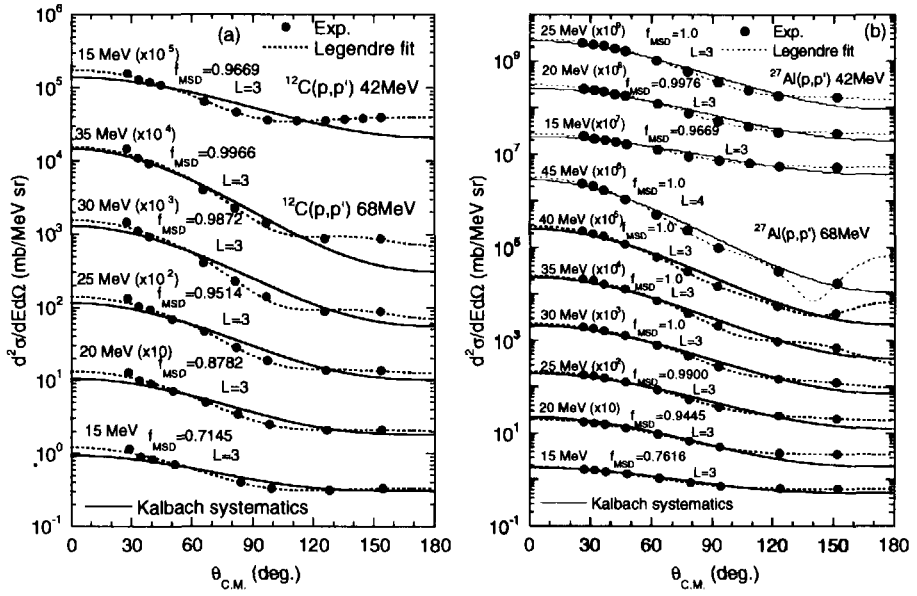

Fig. 6: Comparisons of experimental double differential cross sections with calculations using the Kalbach systematics at 42 and 68 MeV: (a) ^{12}C(p,p') and (b) ^{27}Al (p,p').

JP9950348

3.31

Measurements of Hydrogen and Helium Isotopes Emission Spectra from Neutrons Induced Reaction at Ten's of MeV

*Yasushi NAUCHI, Mamoru BABA, Yoshitaka HIRASAWA, Tomoya NUNOMIYA, Masanobu IBARAKI,Takanori SUZUKI, Naohiro HIRAKAWA, Hiroshi NAKASHIMA[1)], Shin-ichiro MEIGO[1)] Susumu TANAKA[2)], Shin IWASAKI

Department of quantum Science and Energy Engineering, Tohoku University, Sendai, 980-8579, JAPAN
[1)]Tokai Establishment, Japan Atomic Energy Research Institute , Tokai-Mura, Naka-Gun, Ibaraki-Ken, 319-1195, Japan
[2)]Takasaki Establishment, Japan Atomic Energy Research Institute, Takasaki, 370-1292, Japan
*e-mail: nauchi@rpl.qse.tohoku.ac.jp

Abstract

We have developed a wide dynamic range spectrometer for the measurements of (n,xZ) double differential cross sections (DDXs) for ten's of MeV neutrons at TIARA. The spectrometer consists of a 40-cm diameter vacuum reaction chamber and three counter telescopes. Each telescope consists of a gas proportional counter, an SSD and a BaF_2 scintillator. By using the spectrometer, we achieved simultaneous measurements from ~MeV α particles to 75MeV protons with an acceptable counting rate.

1. Introduction

Charged particle emission double differential cross sections (DDXs) for Ten's MeV neutrons are of prime importance for accelerator applications, such as the high intensity neutron sources for material research, accelerator cancer therapy and accelerator-based transmutation systems.

For the reason, we have continued the measurements of DDXs for (n,xZ) reactions at 40-80 MeV mono-energetic neutron source facility in TIARA (Takasaki Establishment, JAERI) [1]. Last year, we reported the (n,xp) and (n,xd) DDXs of Al and C at 5 angles, and compared the data with theoretical calculation codes of ISOBAR and GNASH[2] for the (n,xp) DDXs. The two codes agrees each other and trace our data above the detection threshold (Ep~10MeV), but show differences in magnitude below 10MeV. Thus, marked low threshold measurements for (n,xp) reactions are desirable to validate the calculations. In addition, α particle spectra are also needed because the (n,xα) reactions are major components of neutron KERMA (Kinetic Energy Released in MAterials)[3] and a He accumulation effect plays an important role in material damage.

In order to expand the measurement to lower energy protons and α particles, we have developed a new spectrometer. In the present paper, we report the design of the spectrometer and the results of test experiments for a low detection threshold, wide range particle identification of hydrogen and helium Isotopes and a better signal-to-noise ratio (S/N). Thick sample correction methods now under research are also mentioned.

2. Design of the New Spectrometer

2-1. wide Range Measurements

In the energy region above 20MeV, many kind of hydrogen and helium isotopes are emitted from neutron induced reactions. Therefore, particle identification (PI) is expected to be needed over a wide

energy range from ~5MeV up to 80MeV at TIARA. For PI, the ΔE-E method is widely applied utilizing a counter telescope which consists of a transmission detector and a stop detector. It is difficult to achieve the PI over the wide energy range because the ΔE value of 5MeV α particles are more than 100 times as large as that of 80MeV protons. To achieve such a wide range particle identification, we choose a ΔE1-ΔE2-E method, which utilizes two transmission detector ΔE1 and ΔE2, and treats the ΔE2 as the stop detector for particles which stop in ΔE2. The schematic view of the telescope with a vacuum reaction chamber is shown in fig. 1.

To measure ~MeV α particles, the ΔE1 detector must be thin to reduce energy loss. In the ordinary (p,xZ) DDX measurements, silicon surface barrier detectors (SSD) of 20~25 μm thick are used as the ΔE1 detector[4]. For (n,xα) measurements, even thinner SSDs (< 10 μm) with a large effective area is desirable. The latter is required because the neutron flluence ($1\sim2\times10^4$ /cm^{2}s) at sample (20cm^2) was lower than ordinary proton experiment (1nA) by four order of magnitude. In order to reduce the energy loss and obtain large acceptable area, we chose a low pressure gas proportional counter as the ΔE1 counter. The counter is of ordinary cylindrical shape (5.4cm long, 4.3cm in diameter) and the area of the entrance window is 1200mm^2. As the operation gas, 0.1~0.2atm Ar+5%CO_2 is used in gas-flow mode. With 0.1atm a gas pressure, the detection threshold of α particles can be low as ~2.4MeV. The gas pressure is automatically regulated by a mass-flow controller (STEC PCU2000 and PIEZO valve). The entrance window of the gas counter was a 5.4 μm thick mylar film which was supported by a stainless wire grid (0.1mm in diam., 4mm spacing) to withstand a gas pressure up to ~0.4atm. As for the ΔE2 detector, we employ a SSD (CANBERRA PIPS) 150 μm thick and 900mm^2 wide, that was proved to be useful for PI of proton and deuteron up to 75MeV[1]. As for the E detector, a BaF_2 scintillator (2.2cm thick, 4cm in diameter) are selected owing to its chemical stability requiring no entrance window and its fast timing feature is needed to measure time of flight of particles.

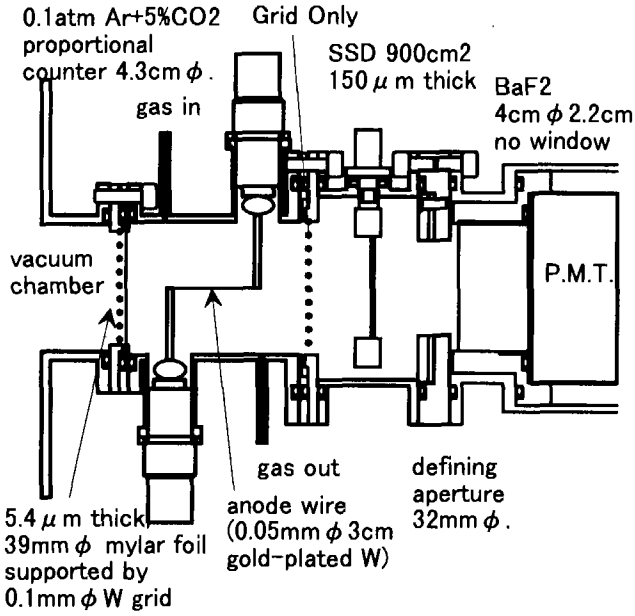

Fig. 1: Schematic View of Wide Range Telescope

2-2. Counting Efficiency and S/N

In addition to the extension in an energy range, the improvement of counting efficiency and S/N is also considered. In order to improve the counting efficiency without deteriorating angular resolution, we adopted multi telescope system shown in fig. 2. The three counter telescopes are set on the vacuum reaction chamber (37cm in diameter) every 20° . The detection angles can be set 25-150° with 10° steps by turning the chamber around sample without breaking the vacuum. In the previous work[2], the (n,xp) and (n,xd) measurements suffered from backgrounds from nitrogen and oxygen in the air environment. Thus we

expect the reduction of background by adopting the new vacuum chamber (< 5Pa). To avoid neutrons bombardment of the chamber, an taper shaped iron collimator (80cm long, inner diameter at the exit is 5.5cm) is used to neutron collimation and neutron entrance port is 72mm in diameter. A thin aluminum plate (2mm) was used as the entrance window. The disk-shaped sample (5cm in diam.) was located at the center of the chamber and to be exposed to direct neutrons from the Li target.

2-3. Data Acquisition circuit

For the data acquisition, we employ the CAMAC systems to gather three sets of six parameter data described below. The schematic view of the circuit is shown in fig. 3. Good events are chosen either by gas-SSD coincidence or SSD-BaF2 coincidence. To simplify the circuit, two-out-of-three condition is adopted using a majority coincidence module (Philips 755). The energy signals of BaF_2 were obtained by charge integration methods with $2\mu s$ gate. The ΔE (or E) signals from SSD and gas counter was integrated with pre-amplifiers, and amplified, then converted into digital values by peak ADCs. The time of flight of the charged particles are also measured at BaF_2 and SSD.

To enhance PI, the SSD pulse heights were acquired with two gain: high gain is for the hydrogen Isotope separation and low gain is for the Isotope separation.

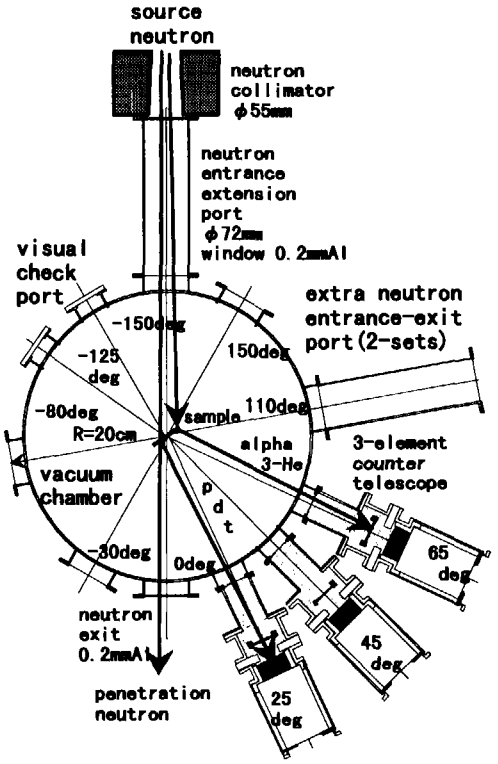

Fig2: Multi telescope system

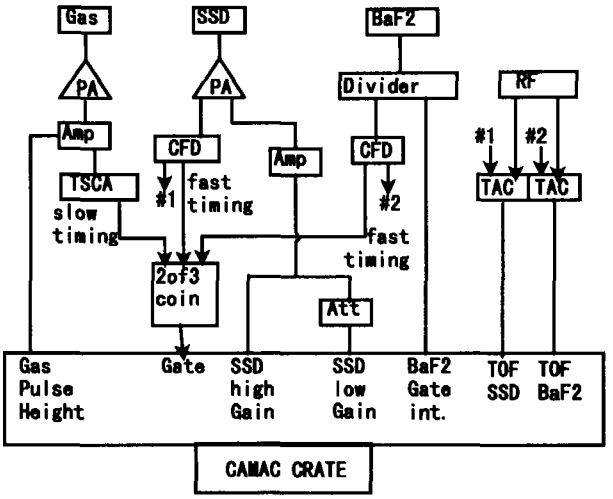

Fig. 3: Data Acquisition System

3. Test Experiments and Results

3.1. Experiment

PI over a wide range and S/N were tested. A sheet of polyethylene, carbon and iron samples were set at the center of the vacuum chamber and irradiated by 75MeV neutrons. Emitted charged particles (proton, deuteron, triton ^{3}He and α) were detected by the counter telescopes. In addition, an ^{241}Am calibration α source was also incorporated in the chamber to obtain to determine the energy scale of the detector pulse heights. The pressure of the gas counter was set 0.1 atm.

3.2. Particle Identification

In fig. 4, two dimensional spectra are shown for BaF_2-SSD (high gain), BaF2-SSD (low gain) and SSD (high gain)-Gas. In the BaF_2-SSD (high gain) plot, proton , deuteron and triton spectra are clearly separated, while He spectra are out of range of SSD axis. For the He isotope separation, BaF_2-SSD(low gain) spectra are used. Although the separation of hydrogen isotopes from electrical noise is poor, ^{3}He and α particle are clearly identified. Few data has been reported for such good separation of He isotopes for the ten's MeV neutron experiments[5][6] except for a specialized spectrometer for α particles measurements.[7] In the SSD(high gain)-Gas spectra, helium are separated clearly from hydrogen and detector noise, but an isotope separations of helium are not be visible because of limited resolution of gas counter due to low energy loss and a low yield. The peaks in the spectra is α particles from the ^{241}Am source (5.6MeV). It assures the detection threshold for α particle measurements is lowered well below 5MeV.

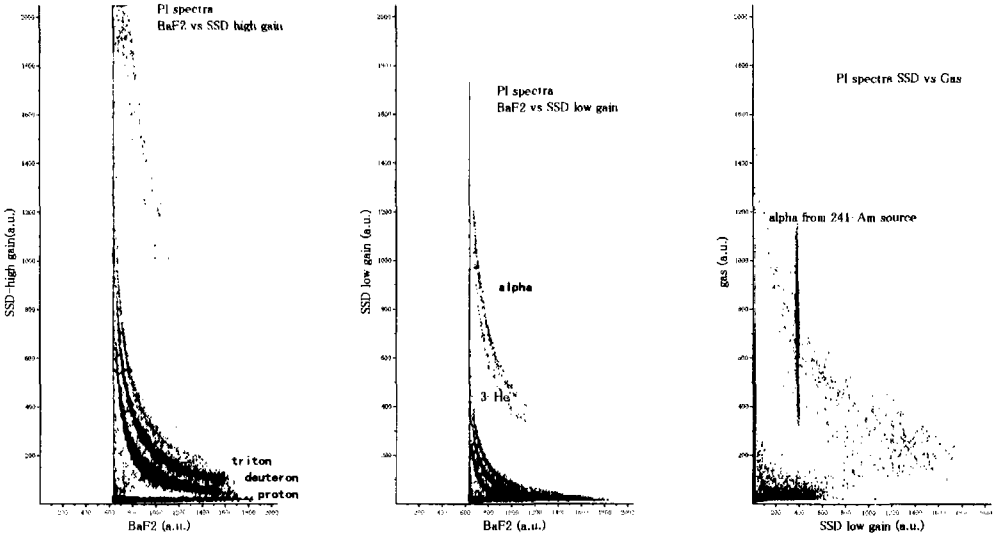

Fig. 4: 3-mode Particle Identification Spectra

The energy scales of the spectra are determined by the α particles from the ^{241}Am, and peak spectra of secondary proton and deuteron from H(n,xp) and C(n,xd) reaction, respectively.

P.I. mode	SSD(high gain)-BaF_2	SSD(low gain)-BaF_2	Gas-SSD(high gain)
Particles and Energy Range	Proton > 5MeV Deuteron > 6MeV Triton > 7.5MeV	^{3}He > 16MeV α > 18.5MeV	He 2.5-19.5MeV

3.3. Improvement of S/N

In order to examine the effect of the vacuum chamber, neutron collimator and neutron entrance window, we compared the S/N in the present C(n,xp) measurements with that in the air environment[2]. The S/N values are compared about the total yields of secondary protons normalized to the sample weight. The results are shown in fig. 5. By the present aparatus, the S/N values are enhanced more than decades than conventional telescopes in the air environment.

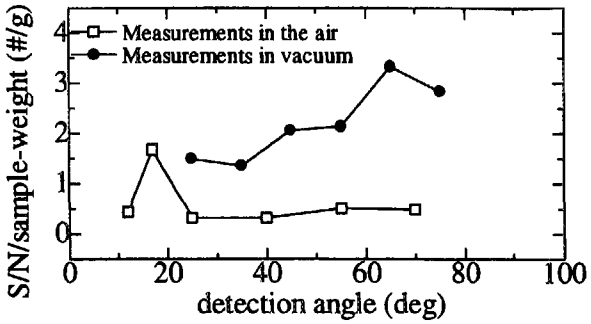

Fig. 5: S/N improvements

4. Thick Sample Condition

The sample for the spectra measurements should be much thinner than the shortest charged particle range in the sample, because the energy loss distorts the spectra. However, we often must use samples which is too thick for α particle (large dE/dX) measurements to obtain acceptable counting because of limited neutron flux. Therefore, a data correction method to correct the charged particle spectra for the effect of energy loss is desirable. We are considering to apply Baysian theorem for the corrections (unfolding).

4-1. Response Function

In order to apply unfolding methods, the response function should be examined. We calculate it for a sample(fig. 6). For protons, the energy of detected particles is very close to the primary energy, but it differs largely in the α particle measurements because of large energy loss.

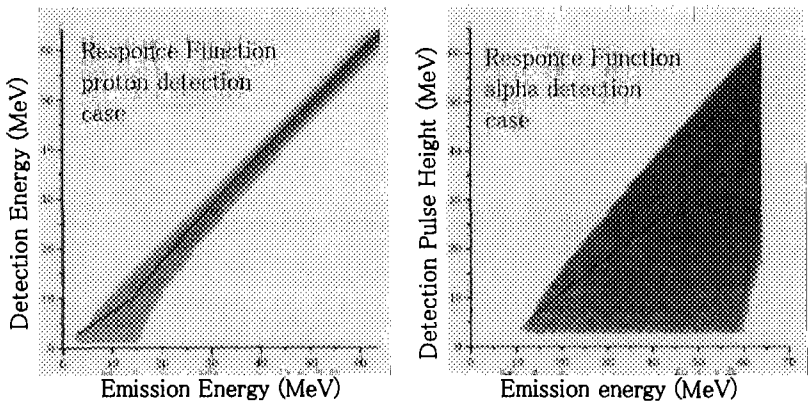

Fig. 6: Response Function of thick sample measurements

The measured spectrum dY/dH is the folded spectra of Reaction spectrum dY/dE by the response function.

$$\frac{dY}{dH}(h) = \int r(e \rightarrow h)\frac{dY}{dE}(e)de$$

To solve this Fredhorm integral equation, a simple approximation such as "average detected energy" (solid lines in fig. 6) are currently used[8]. However it usually results in the overestimation of the maximum energy of the spectra. Therefore, another unfolding methods are needed.

4-2. New Unfolding Methods based on Bayes's Theory

Let the d_i(i=1,m) be the measured spectra corresponding to pulse height bin h_i , and p_j(j=1,n) be the primary spectra corresponding to energy bin e_j . Then r_{ij} is defined as the probability that a particle of e_j is measured as pulse height h_i. When we know the prior $est^{(l)}_j$ to the p_j, if we have measured one particle of pulse height h_i, then the estimated spectrum $est^{(l)}_j$ is improved by Bayes' theory. After successive iteration, the primary spectrum can be estimated.

$$est_j^{l+1} = \frac{est_j^l \times r_{i,j}}{\sum_j^n est_j^l \times r_{i,j}}$$

Then we expand the theory to the present case: the measured spectrum d_i(i=1,m) is given.
In this methods, we assume the flat spectra as the initial prior spectrum $est^{(0)}_j$, then repeat the improvement calculations until convergence.

$$est_j^{l+1} = \sum_i^m d_i \frac{est_j^l \times r_{i,j}}{\sum_j^n est_j^l \times r_{i,j}}$$

4-3. Tests of Unfolding Capability using simulated spectra

We test the unfolding capability using simulated spectra (fig. 7). The ideal primary spectra is the solid line and the triangles are folded spectra by the response of α particle measurements in fig. 6. The dots are the unfolded spectra obtained by 30times correction calculations. As the results, while the peak separation is poor, the total yield and overall spectral shape are reproduced. This result indicates the potential of the Bayses' unfolding methods to solve the thick sample condition in the charged particle spectra measurements.

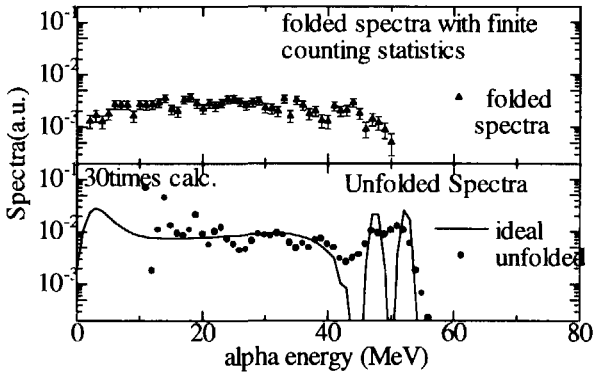

Fig. 7: unfolding tests using simulation calculation

References

[1]Nauchi, Y. et. al., *Proc. Int. Conf. Nucle. Data for Sci. Technol.,* May 1997, Trieste, Italy, p. 613
[2]Nauchi, Y. et. al., *JAERI-Conf* **98-003** *proc 1997 Sympo. Nucl. Data,* 1997 p. 270
[3]Harada, M. et. al., J. Nucl. Sci. Technol., **34** 116 1997
[4]Harada, M. et al, *JAERI-Conf* **98-003** *proc 1997 Sympo. Nucl. Data,* 1997 p. 276
[5]Subramanian, T. S. et al., *Nucl Instr. Meth.* **174** 489 (1980)
[6]Slypen, I. et al., *Phys. Rev.* **C51** 1303 (1995)
[7]Height, R. C. et al., *Fus. Eng. Design* **37** 73 (1997)
[8]Slypen, I. et al., *Nucl. Instr. Meth.* **B88** 275 (1994)
[9]S. Iwasaki, *KEK Proc* **95-1** *"Radiation detectors and their uses"*, KEK, Jan (1995) p. 319

JP9950349

3.32 Calculation of Photonuclear Process in the Region of Several Tens MeV

- Formulation of Exact Transition Rate for High Energy γ -Ray -

Hiroaki Wada and Hideo Harada

Japan Nuclear Cycle Development Institute (JNC),

Tokai-mura, Naka-gun, Ibaraki-ken 319-1194

e-mail: hwada@tokai.pnc.go.jp

The electromagnetic field approximated by using long wave-length limit is not valid for heavy nuclear mass or high energy γ-ray transition. To examine the contribution of the electric multipole field that is neglected in long wave-length limit, we formulize the El transition rate for the strict electric multipole field and compare quantitatively this result with Weisskopf estimate.

Ⅰ. Introduction

The long wave-length approximation is often used to estimate nuclear electric and magnetic transition for wide range of nuclear mass or γ-ray energy. However, the long wave-length approximation is not accurate in case of estimation of the transition rate for the heavy nuclei or high energy γ-ray. Therefore, in this work, we treat the electric multipole field strictly to formalize the El transition rate that is valid for heavy nuclei or high energy γ-ray. For simplification, we take the nuclear wave functions that are the same as Weisskopf estimation. We compare the transition rate with the Weisskopf unit in preliminary case.

Firstly, we briefly follow a derivation process of the El transition rate without the long-wavelength approximation in section Ⅱ. Next, we compare the obtained transition rate with the Weisskopf unit in section Ⅲ. Lastly, we summarize the result in section Ⅳ.

Ⅱ. Method

In this section, we survey formalization of the transition rate with the electric multipole field that is not approximated by using the long-wavelength.

We rewrite the El electric multipole field

$$\vec{A}_{l\mu}(\vec{x};E) \equiv \sqrt{\frac{l+1}{2l+1}}\, j_{l-1}\left(|\vec{k}|r\right)\vec{Y}_{l\mu,l-1}(\Omega) - \sqrt{\frac{l}{2l+1}}\, j_{l+1}\left(|\vec{k}|r\right)\vec{Y}_{l\mu,l+1}(\Omega) \qquad (2.1)$$

into the two parts of the longitudinal multipole field

$$\vec{A}_{l\mu}(\vec{x};L) \equiv \sqrt{\frac{l}{2l+1}}\, j_{l-1}\left(|\vec{k}|r\right)\vec{Y}_{l\mu,l-1}(\Omega) + \sqrt{\frac{l+1}{2l+1}}\, j_{l+1}\left(|\vec{k}|r\right)\vec{Y}_{l\mu,l+1}(\Omega)$$

$$= \frac{1}{|\vec{k}|}\nabla\left[j_l\left(|\vec{k}|r\right)Y_{l\mu}(\Omega)\right] \qquad (2.2)$$

and another term. Thus, the rewritten El electric multipole field is

$$\vec{A}_{l\mu}(\vec{x};E) = \sqrt{\frac{l+1}{l}}\,\frac{1}{|\vec{k}|}\nabla\left[j_l\left(|\vec{k}|r\right)Y_{l\mu}(\Omega)\right] - \sqrt{\frac{2l+1}{l}}\, j_{l+1}\left(|\vec{k}|r\right)\vec{Y}_{l\mu,l+1}(\Omega) \quad . \qquad (2.3)$$

Where, $\vec{k}$ and $\mu = \pm 1$ are wave vector and polarization index of photon fields, respectively. $\vec{Y}_{l\mu,l\pm1}(\Omega)$ are vector spherical harmonic functions defined as

$$\vec{Y}_{l\mu,l\pm1}(\Omega) \equiv \sum_{\alpha=-(l+1)}^{l+1}\sum_{\beta=-1}^{1}\left((l\pm1)\,1\,l\,|\alpha\ \beta\ \mu\ \right)Y_{(l+1)\alpha}(\Omega)\vec{e}_\beta \quad , \qquad (2.4)$$

and $\left((l\pm1)\,1\,l\,|\alpha\ \beta\ \mu\ \right)$ indicate the Clebsch-Gordan coefficients. In long-wavelength limit ($|\vec{k}|r << 1$), the electric multipole field is approximated as

$$\vec{A}_{l\mu}(\vec{x};E) = \sqrt{\frac{l+1}{l}}\,\frac{1}{|\vec{k}|}\nabla\left[\frac{\left(|\vec{k}|r\right)^l}{(2l+1)!!}Y_{l\mu}(\Omega)\right] \quad . \qquad (2.3)'$$

The matrix element of the El transition that photon is emitted from excited nuclear state is

$$M_{fi}\left(|\vec{k}|,\mu;El\right) = -\sqrt{2\pi}(-i)^{l+1}\sqrt{2l+1}\int d^3x\,\langle f|\vec{j}(\vec{x})|i\rangle\cdot\vec{A}^*{}_{l\mu}(\vec{x};E) \qquad (2.5)$$

$$= \sqrt{2\pi}(-i)^{l+1}\sqrt{2l+1}\left\{\sqrt{\frac{l+1}{l}}ic\int d^3x\,\langle f|\hat{\rho}(\vec{x})|i\rangle\, j_l\left(|\vec{k}|r\right)Y^*_{l\mu}(\Omega)\right.$$

$$\left. + \sqrt{\frac{2l+1}{l}}\int d^3x\,\langle f|\hat{\vec{j}}(\vec{x})|i\rangle\cdot j_{l+1}\left(|\vec{k}|r\right)\vec{Y}^*_{l\mu,l+1}(\Omega)\right\} \quad . \qquad (2.6)$$

In viewpoint of one-particle model, the wave function of the nuclear state is given by the wave function of the nucleon. We take the same wave functions of the nuclear states as ones of Weisskopf estimation. The initial (ψ_i) and final state wave functions (ψ_f) of the one

proton state are given as

$$\psi_i(r,\theta,\phi) = u(r)\, Y_{lm}(\theta,\phi) \tag{2.7}$$

and

$$\psi_f(r,\theta,\phi) = u(r)\, Y_{00}(\theta,\phi) = u(r)\frac{1}{\sqrt{4\pi}} \quad . \tag{2.8}$$

A radial wave function $u(r)$ is defined as

$$u(r) = \begin{cases} \sqrt{3/R^2} & , \ (0 \le r \le R) \\ 0 & , \ (r > R) \end{cases} \quad . \tag{2.9}$$

Where, R indicate a nuclear radius. The expression of $u(r)$, Eq.(2.9), means that the probability of proton is uniform in the spherical nucleus and zero outside the nucleus. The excited nuclear state is characterized by spherical harmonic functions. The excited initial state has non-zero orbital angular momentum l and magnetic quantum number m. The quantum number l and m of the ground final state are equal to zero. For these wave functions, Eq.(2.7) and Eq.(2.8), we get the matrix element

$$M_{fi}\left(|\vec{k}|,\mu;El\right) = \frac{(-i)^l}{\sqrt{2}}\sqrt{\frac{(2l+1)(l+1)}{l}}\, ce_p \frac{3}{R^3}\left\{\delta_{\mu m}\int_0^R dr\, r^2\, j_l\left(|\vec{k}|r\right)\right.$$

$$\left. -\frac{\hbar}{2M_p c}\delta_{\mu m}\, l\int_0^R dr\, r\, j_{l+1}\left(|\vec{k}|r\right)\right\} \quad . \tag{2.10}$$

Where, the symbol M_p (e_p) indicate the mass (charge) of proton.

Averaging over m of initial state and summing over the two polarization of the photon, we get the El transition rate

$$T(l;E) = \frac{4\pi}{2l+1}\sum_{\mu=\pm1}\frac{1}{2l+1}\sum_{m=-l}^{l}\left[\frac{1}{4\pi}\frac{|\vec{k}|}{2\pi\hbar c^2}\left|M_{fi}\left(|\vec{k}|,\mu;El\right)\right|^2\right] \tag{2.11}$$

$$= \frac{e_p^{\,2}}{4\pi\hbar c}c|\vec{k}|3^2\frac{2(l+1)}{l(2l+1)}2^{2l}\left(|\vec{k}|R\right)^{2l}\left[\right.$$

$$\left.\sum_{n=0}^{\infty}\frac{1}{2n+l+3}\frac{(n+l)!}{(2n+2l+1)!}\frac{(-1)^n}{n!}\left(|\vec{k}|R\right)^{2n}\left(1-\frac{E_\gamma}{M_p c^2}\frac{l}{2(2n+2l+3)}\right)\right]^2 \tag{2.12}$$

for the emission of unpolarized photon. The El transition rate is invariant with space rotation, and $4\pi/(2l+1)$ of Eq.(2.11) is a normalization factor for space rotation. If we substitute the electric multipole field Eq.(2.3)' for the matrix element Eq.(2.5), the transition rate Eq.(2.11) is equal to Weisskopf unit

$$T_{WU}(l;E) = \frac{e_p^{\,2}}{4\pi\hbar c} c|\vec{k}| \left(\frac{3}{l+3}\right)^2 \frac{2(l+1)}{l(2l+1)[(2l+1)!!]^2} \left(|\vec{k}|R\right)^{2l} \quad . \qquad (2.12)'$$

Ⅲ. Result

In this section, we estimate quantitatively the ratio of the El transition rate $T(l;E)$, Eq.(2.12), formularized in last section to Weisskopf unit $T_{WU}(l;E)$ Eq.(2.12)'. We consider only the $E1$, $E2$ and $E3$ transition rate in here.

From the ratio $T(l;E)/T_{WU}(l;E)$ with the nuclear mass number A (the γ ray energy E_γ) at fixed $E_\gamma = 60\text{MeV}$ ($A = 50$) [Fig.1,2], it is shown that the transition rate $T(l;E)$ is less than the Weisskopf unit $T_{WU}(l;E)$ and the ratio $T(l;E)/T_{WU}(l;E)$ decrease with increasing the mass number A or the γ ray energy E_γ. Moreover, the ratio $T(l;E)/T_{WU}(l;E)$ of the $E1$, $E2$ and $E3$ transition rate are nearly equal to 1 at $A \approx 0$ or $E_\gamma \approx 0\text{MeV}$, and split for the larger A or E_γ. These ratios satisfy the relation

$$\begin{matrix} [\text{E1}] & & [\text{E2}] & & [\text{E3}] \\ \dfrac{T(l=1;E)}{T_{WU}(l=1;E)} & \le & \dfrac{T(l=2;E)}{T_{WU}(l=2;E)} & \le & \dfrac{T(l=3;E)}{T_{WU}(l=3;E)} \end{matrix} \qquad (3.1)$$

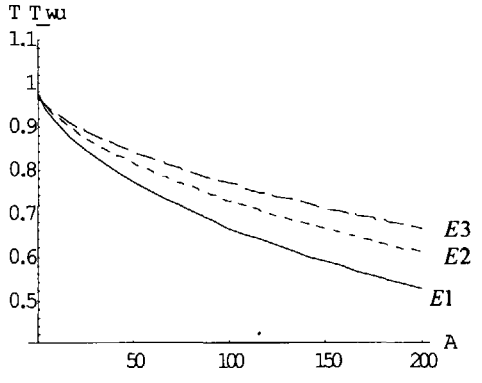

Fig.1 T/T_{WU} vs. mass number A at $E_\gamma = 60MeV$

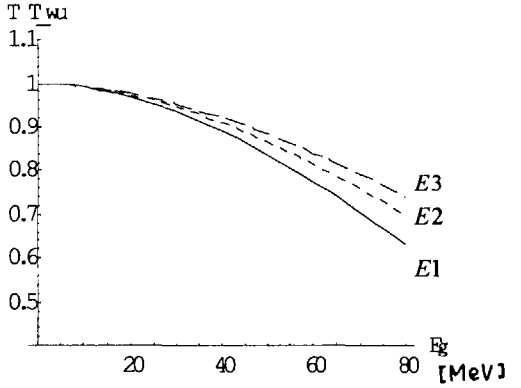

Fig.2 T/T_{WU} vs. γ energy E_γ at $A = 50$

We make table of the ratio $T(l;E)/T_{WU}(l;E)$ with the various combination of the nuclear

mass number A and the γ ray energy E_γ [Table 1, 2, 3]. The above properties are valid for all A and E_γ also. As extreme example, the $T(l=1;E)/T_{WU}(l=1;E)$ of the $E1$ transition is 0.061 at $E_\gamma = 110\text{MeV}$ and $A = 250$ ($|\vec{k}|R = 4.22$).

		A					
		10	50	100	150	200	250
Eγ [MeV]	10	0.996	0.991	0.987	0.984	0.981	0.978
	30	0.973	0.935	0.902	0.875	0.852	0.831
	50	0.934	0.835	0.755	0.693	0.642	0.598
	70	0.880	0.705	0.575	0.484	0.413	0.357
	90	0.813	0.560	0.396	0.293	0.222	0.171
	110	0.736	0.417	0.243	0.150	0.095	0.061

Table 1. $T(l=1;E)/T_{WU}(l=1;E)$ of $E1$ transition rate

		A					
		10	50	100	150	200	250
Eγ [MeV]	10	0.995	0.992	0.989	0.986	0.984	0.982
	30	0.975	0.946	0.921	0.900	0.881	0.865
	50	0.942	0.865	0.802	0.751	0.709	0.672
	70	0.898	0.759	0.652	0.573	0.510	0.458
	90	0.843	0.636	0.493	0.396	0.324	0.269
	110	0.780	0.510	0.344	0.245	0.180	0.134

Table 2. $T(l=2;E)/T_{WU}(l=2;E)$ of $E2$ transition rate

		A					
		10	50	100	150	200	250
Eγ [MeV]	10	0.995	0.992	0.990	0.988	0.986	0.984
	30	0.977	0.953	0.932	0.914	0.899	0.885
	50	0.948	0.884	0.831	0.788	0.752	0.720
	70	0.909	0.793	0.701	0.631	0.575	0.527
	90	0.861	0.686	0.558	0.468	0.400	0.345
	110	0.807	0.573	0.419	0.320	0.251	0.200

Table 3. $T(l=3;E)/T_{WU}(l=3;E)$ of $E3$ transition rate

Finally, we investigate the variation of the $T(l;E)/T_{WU}(l;E)$ with $|\vec{k}|R$ at $E_\gamma = 10\text{MeV}$ and $E_\gamma = 110\text{MeV}$ [Fig. 3, 4, 5]. The shape of the $T(l;E)/T_{WU}(l;E)$ are almost independent

with γ ray energy.

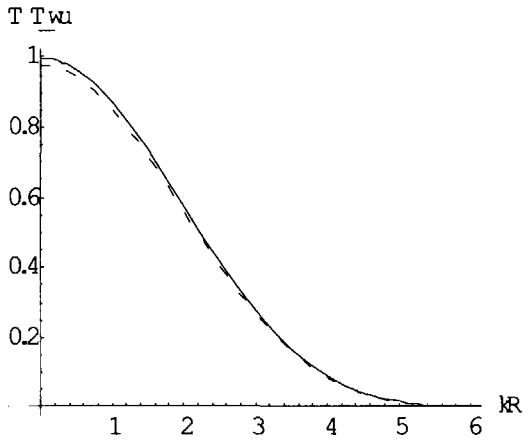

Fig.3 T/T_{WU} vs. $|\vec{k}|R$ in $E1$ transition

at $E_\gamma = 10\text{MeV}$ (a solid line)

and $E_\gamma = 110\text{MeV}$ (a broken line)

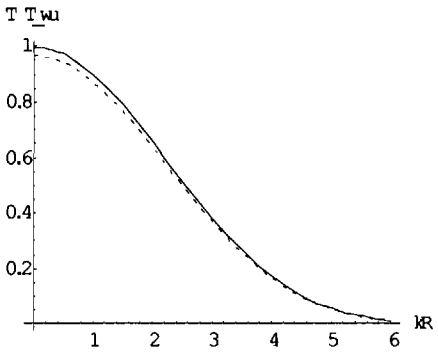

Fig.4 T/T_{WU} vs. $|\vec{k}|R$

in $E2$ transition

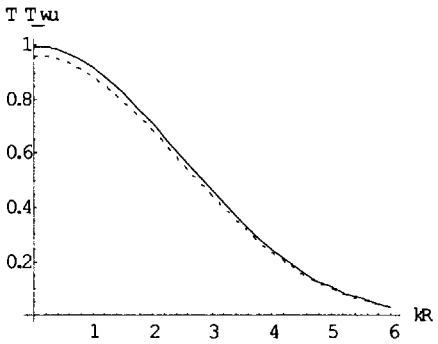

Fig.5 T/T_{WU} vs. $|\vec{k}|R$

in $E3$ transition

Ⅳ. Conclusion

We treated the electric multipole field strictly and formalized the El transition rate using the simple wave function that is used in the Weisskopf estimation. We estimated quantitatively the ratio of the transition rate $T(l;E)$ formulated by the strict electric multipole field to the Weisskopf unit $T_{WU}(l;E)$. In consequence, The ratio $T(l;E)/T_{WU}(l;E)$ is less than 1 and decrease with increasing the nuclear mass or γ-ray energy.

We did not consider the magnetic transition rate yet. But, it is possible to extend the electric transition to the magnetic transition with introducing the spin of the nucleon.

References

[1] V. F. Weisskopf, Phys. Rev. **83**, 1073 (1951)

JP9950350

JAERI-Conf 99-002

3.33 Photoneutron Production with the Laser-Compton Backscattered Photons

Hiroyuki TOYOKAWA, Hideaki OHGAKI, Suguru SUGIYAMA, Tomohisa MIKADO, Kawakatsu YAMADA, Ryoichi SUZUKI, Toshiyuki OHDAIRA, Norihiro SEI, and Mitsukuni CHIWAKI

Electrotechnical Laboratory, IBARAKI 305-8568, Japan

A method to produce quasi-monoenergetic photoneutrons for detector calibration was examined. The photoneutrons were produced with a photo-induced neutron emission of a ^{9}Be using the Laser-Compton backscattered photons. Because the photon energy is continuously tunable, neutrons with various energies are obtained. Yield of the neutrons was measured with a liquid scintillation detector at the photon energies from 1651 keV to 3019 keV. Neutron yield at around the threshold energy for the ^{9}Be(γ,n) reaction was measured by changing the photon energy in a 10 keV step.

1. Introduction

Influences on human body of the exposure of the intermediate-energy neutrons with the energies from epithermal to about a few tens of keV play an important role on the evaluation of total dose. While monoenergetic neutron sources of intermediate energy are useful to calibrate neutron detectors, there are few neutron sources with these energies. A thin metal foil, such as scandium and beryllium, bombarded by an accelerated proton beam produces neutrons of a few tens of keV. However, the proton energy must be strictly controlled and a fluctuation of the energy deposition on a target should be small enough so that the neutron energy do not fluctuates.

Photoneutron sources using gamma-rays from radioisotopes produce monoenergetic neutrons with almost no energy fluctuation. Some photoneutron sources, such as ^{124}Sb-^{9}Be, ^{24}Na-^{9}Be, and ^{24}Na-D, are practically used as intermediate-energy neutron sources. Photoneutrons usually accompany with a large background of gamma-rays. Because the cross section for (γ,n) reaction is small, typically on the order of microbarns to millibarns, the ratio of the photoneutrons to gamma-rays from a typical photoneutron source is on the order of 10^{-5} to 10^{-6}. Moreover, the gamma-ray background is enhanced by the geometry of the photoneutron sources, because most of the photoneutron sources consists of a gamma-ray emitter surrounded by a photon-neutron converter and, hence, the neutrons and the gamma-rays are emitted into the same direction. Then, the neutrons will appear in a shower of background gamma-rays. Neutron separation energies for most nuclei are almost 8 MeV, except for ^{9}Be and ^{2}H (1666 keV and 2226 keV, respectively). So only these two materials are used as a photon-neutron converter. The gamma-ray energies from radioisotopes practically used as a photon-emitter are usually below about 3 MeV, because the life-time of the radioisotopes becomes too short as the gamma-ray energy became higher.

Although the photoneutron sources have a stability for the energy fluctuation, low neutron yield, high gamma-ray background, and the short life-time limit the use of the photoneutron sources. So, we have been trying to develop an energy-variable photoneutron source using the laser-Compton backscattered (LCS) photons [1].

2. LCS Photon Facility

The LCS photon facility of Electrotechnical Laboratory (ETL-LCS) [2] started its operation in 1984. It generates photon beams with the energies continuously tunable from 1 MeV to 40 MeV with an intensity of about 10^7 cm^{-2} s^{-1}. Figure 1 shows the layout of the ETL-LCS facility. LCS photons are produced with the Compton scattering of an intense beam of monochromatic photons, typically a laser beam, from relativistic electrons. In the ETL-LCS facility, an 800 MeV electron storage ring TERAS [3] is used as an electron source. Because most of the photons are backscattered (180°), the LCS photons are usually confined in a small solid angle at around a direction of the electron beam. Quasi-monochromatic photon beams are obtained by a collimation of the backscattered photons with an appropriate collimator. The solid angle subtended by the collimator at the laser-electron scattering point is usually on the order of 10^{-9} steradians.

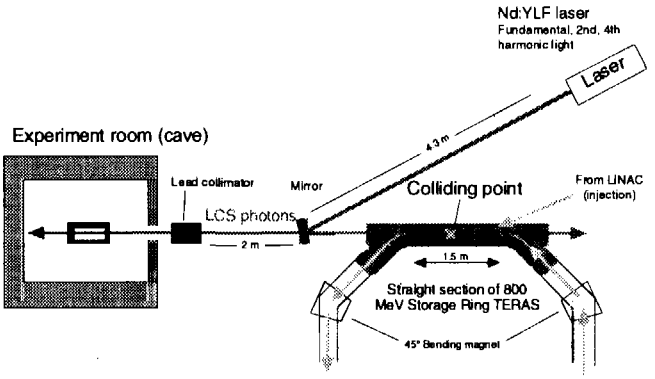

Fig. 1 Layout of the ETL-LCS facility.

3. Experiment

Figure 2 shows an experimental setup for the photoneutron measurement. We used a Q-switched Nd:YLF laser (1053 nm) whose repetition frequency and a pulse width were 5 kHz and 150 ns, respectively. The LCS photons that are collimated with a lead collimator of ϕ2 mm are incident on the front face of a ^{9}Be rod target (ϕ5 x 100 mm). Because the LCS photons are narrowly collimated, the target should be long, and as slender as possible to suppress an energy-degradation due to a scattering and absorption within the target. Then, it is placed along the axis of a cylindrical 4 π neutron detector [4], which is filled with a gadolinium-loaded liquid scintillator (NE323).

The capture cross section of thermal neutrons of ^{155}Gd and ^{157}Gd is extremely large (6 x 10^4 and 2.5 x 10^5 barns, respectively). Some of the photoneutrons emitted from the target rod are captured by the gadolinium nuclei in the liquid scintillator. The gadolinium nuclei, then, emitt intense flashes of cascade gamma-rays which amounts to about 8 MeV per a captured neutron. The gamma-ray bursts tell the neutron detection as an intense flash of scintillation lights. Although the method is commonly used as a neutron counting [5], it is effective only for a large-tank detector when the cascade gamma-rays are fully absorbed. The size of our detector is, however, too small for the gamma-rays deposit all their energy into the detector. So, the flash was not distinguished simply with a pulse-height discrimination. We tried a pulse-shape discrimination, as well. Although the method itself was successful using an Am-Be neutron source, the neutron

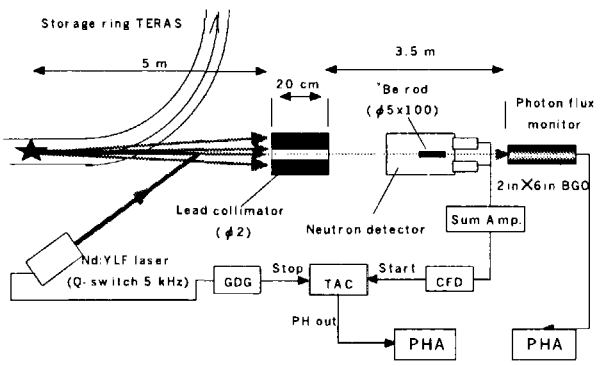

Fig. 2 Experimental setup for the photoneutron measurement.

signals were not distinguished from those of gamma-rays for the present experiment using the LCS photons, because of the signal pile-up of the neutrons and the gamma-rays. The LCS photons are generated in every 200 μs with the pulse width of 150 ns, so the photoneutrons are generated and enter the detector almost the same time as the annihilation and Compton-scattered photons from the target. Then, most of the signals will pile up.

Then, we tried to count neutrons with a time profile of a scintillation output. Neutrons are moderated in the detector, and some of them are captured. If the scintillation lights by recoil protons were discriminated by a pulse-height discrimination, only the gamma-ray signals are obtained. So, the neutron events are distinguished from the other signals with the time profile of the gamma-ray flashes, because they occur according to the neutron moderation, while the other events occur almost simultaneously as the photon incidence.

The block diagram of the signal processing system is shown in fig. 2. Signals from the photomultipliers summed by the sum-amplifier (Sum Amp.) were fed to the constant fraction discriminator (CFD), whose output is fed to the time-to-amplitude converter (TAC) as a start signal. A trigger signal from the laser, properly delayed with the gate-and-delay generator (GDG), stop the time-to-amplitude conversion. The pulse height from the TAC is analyzed with a multichannel analyzer.

Photon flux is monitored with a BGO detector placed at the back of the target rod. Attenuation of the flux was evaluated by experiments using a blank target. The flux is reduced to about half of the incident photons at 1700 keV. The energy of the LCS photons was tuned by changing the electron energy of the storage ring according to the following formula:

$$E_{\gamma\,\max} = \frac{4E_e^2\varepsilon_L}{m_0c^2 + 4E_e\varepsilon_L}$$

Where $E_{\gamma max}$, E_e, ε_L are the maximum photon energy, electron energy, and the energy of the laser photon quanta, respectively, and m_0c^2 is the electron rest mass. Figure 3 shows a pulse height spectrum for the 2975 keV LCS photons measured with a HPGe of 120 % relative efficiency. The energies of the LCS photons were measured with the HPGe detector during the experiments. Maximum and mean energies of the LCS photons used in the present experiments are summarized in table 1.

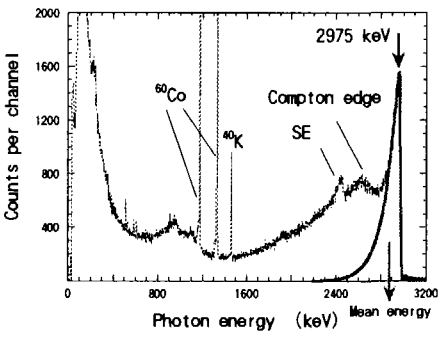

Fig. 3 Pulse height spectrum from a HPGe of 120 % relative efficiency for the 2975 keV photons (broken line). A sharp spike (thick solid line) corresponds to the LCS photons. A mean energy is 2879 keV.

4. Discussion

Figure 4 shows the time profiles of the gamma-ray flashes, which were measured below (1651 keV) and above (1707 keV) the threshold energy for the ^{9}Be(γ,n) reaction. A sharp spike in the figure is due to the annihilation or the Compton-scattered photons from the target caused by the LCS photons, and, hence, it indicates the incident time of the LCS photons. The prompt photon emission extended about 3 μs after the photon incidence. The bump, peaked at about 8 μs after the incidence of the LCS photons are due to the neutrons from the target, and only seen in the

time profile measured above the threshold energy. It was necessary to keep the count rate of the prompt flashes low enough to prevent the neutron-induced flashes merge into the prompt flashes, because the neutron gamma-ray event ratio in the present experiments was 10^{-4} to 10^{-5}, which is summarized in table 1. So, the count rates for the prompt flashes were kept less than 50 cps during the experiment by a proper attenuation of the LCS photons with lead plates.

While the absolute yield of the photoneutrons can not be deduced, because the detection efficiency of the neutron detector is currently unknown, relative yield and the (γ,n) cross section times the detection efficiency were measured and summarized in table 1. Figure 5 shows the (γ,n) cross section assuming the constant detection efficiency of 15 %, which was deduced by fitting the present data to that of Berman et al. [5], at 1670 keV. The present data showed a sharp rise at 1666 keV, and the maximum value was seen at about 10 keV above.

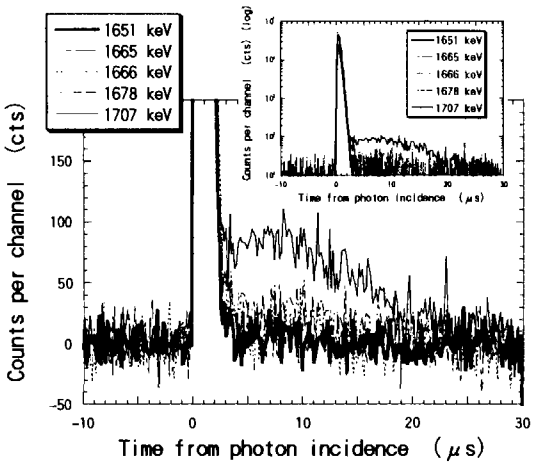

Fig. 4 Time profiles of the gamma-ray flashes. The maximum photon energies are indicated in the figure. The small figure at right-hand is the whole view of the spectra (log).

Table 1 Experimental results of the photoneutron experiment. E_{max} and E_{ave} are the maximum and mean energy of the LCS photons. Neutron yield per gamma-ray and the uncertainty are summarized in column 3, the measured value of the(γ,n) cross sections are listed together with the uncertainty in column 4. Cross section assuming the detection efficiency of 15 % is listed in column 5.

E_{max} (keV)	E_{ave} (keV)	n-γ ratio ($\times 10^{5}$)	$\varepsilon*\sigma$ (10^{29} barn)	σ (mb)
1650.6	1650.6	NA	NA	NA
1664.9	1664.9	NA	NA	NA
1666.4	1666.0	14.2 ± 4.2	11.2 ± 3.3	0.747 ± 0.220
1678.3	1670.6	30.0 ± 3.6	23.7 ± 2.8	1.580 ± 0.187
1707.0	1685.3	20.1 ± 2.5	15.9 ± 2.0	1.060 ± 0.133
2080.0	1888.5	5.61 ± 0.58	4.43 ± 0.46	0.295 ± 0.031
2145.8	1948.2	4.35 ± 0.45	3.43 ± 0.36	0.229 ± 0.024
2200.0	1997.4	3.70 ± 0.39	2.92 ± 0.31	0.195 ± 0.021
2934.7	2840.2	8.02 ± 0.84	6.33 ± 0.65	0.422 ± 0.043
2954.3	2859.2	8.09 ± 0.84	6.39 ± 0.66	0.426 ± 0.044
2964.6	2869.1	8.80 ± 0.91	6.95 ± 0.72	0.439 ± 0.048
2974.8	2878.9	9.44 ± 0.97	7.45 ± 0.77	0.497 ± 0.051
2990.2	2893.9	9.93 ± 1.0	7.84 ± 0.81	0.523 ± 0.054
2999.5	2902.9	10.7 ± 1.1	8.45 ± 0.87	0.563 ± 0.058
3010.8	2913.9	11.1 ± 1.1	8.76 ± 0.91	0.584 ± 0.061
3019.0	2921.8	15.8 ± 1.6	1.25 ± 0.13	0.833 ± 0.087

6. Conclusion

Photoneutron yield of a ^{9}Be rod was measured by using the Laser-Compton backscattered photons. The neutrons were counted with the Gd-loaded liquid scintillator. The prompt flash was seen within 3 μs of the photon incidence, and the delayed one followed, which was peaked at about 8 μs. The former flashes are due to the annihilation and the Compton-scattered photons from the target, while the latter corresponds to the gamma-ray cascade from gadolinium nuclei due to the neutron capture. Relative yield of the photoneutrons and the ^{9}Be(γ,n) cross section folded by the detection efficiency of the neutron detector were measured in the energy range from 1650 keV to 3019 keV, while the absolute cross section was not obtained, yet. If the detection efficiency of the neutron detector was calibrated, the absolute value will be obtained. A Monte Carlo simulation will be helpful for a measurement of the response function of the neutron detector.

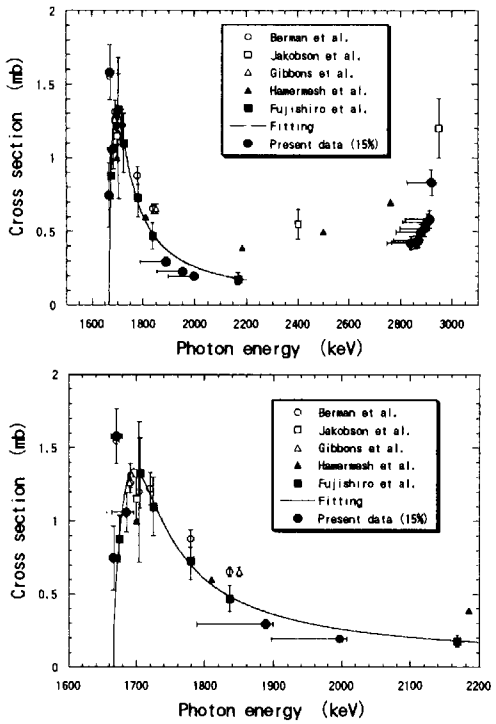

Fig. 5 (γ,n) cross sections measured in the present experiment (black circles) in the energy range from 1500 keV to 3000 keV (above), and from 1600 keV to 2200 keV (below). Reference data are those of Berman et al. [6] (open circles), Jakobson [7] (squares), Gibbons et al. [8] (triangles), Hamermesh et al. [9] (black triangles), Fujishiro et al. [10] (black squares). The fitting curve (solid line) was taken from ref. 9.

Acknowledgements

We would like to thank Professor Hiroaki Utsunomiya of Konan University for valuable discussions. This work was supported by Science and Technology Agency of Japan.

References

[1] R.H. Milburn: Phys.Rev. Lett. 10(1963)75.
[2] T. Yamazaki et al.: IEEE Trans. Nucl. Sci. 32[5](1985)3406..
[3] T. Tomimasu et al.: IEEE Trans. Nucl. Sci., 30[4](1983)3133
[4] H. Toyokawa et al.: Nucl Instr. and Meth. A422(1999)95.
[5] H. Beil, R. Bergere and A. Veyssiere: Nucl. Instr. And Meth. 67(1969)293.
[6] B. L. Berman, R. L. Van Hemert, and C. D. Bowman: Phys. Rev. 163[4](1967)163.
[7] Mark J. Jakobson: Phys. Rev. 123[1](1961)229.
[8] J. H. Gibbons, R. L. Macklin, J. B. Marion, and H. W. Schmitt,: Phys. Rev. 114[5](1959)1319
[9] B. Hamermesh and C. Kimball: Phys. Rev. 90[6](1953)1063.
[10] M. Fujishiro, T. Tabata, K. Okamoto, and T. Tsujimoto: Can. J. Phys. 60(1982)1672.

JP9950351

JAERI-Conf 99-002

3.34 Direct reaction model analysis of continuum region in one particle transfer reaction

Shozo AOKI[1], Katsuhiro YAMAGUCHI[1], Syafarudin[1], Genichiro WAKABAYASHI[1], Fujio ARAMAKI[2], Yusuke UOZUMI[1], Akihiro NOHTOMI[3], Takeji SAKAE[3], Masaru MATOBA[1], Norihiko KOORI[4], Takashi MAKI[5], Yosuke TANAKA[6]

[1] *Graduate school of Engineering, Kyushu University, Fukuoka, 812-8581*
[2] *Kyushu Information University, Dazaihu, 818-01*
[3] *Proton Medical Research Center, Tsukuba University, Ibaraki,305-8575*
[4] *College of General Education, University of Tokushima, Tokushima 770*
[5] *University of Occupational and Environmental Health, Kitakyushu 807*
[6] *Kyushu Kyoritsu University, Kitakyushu 807*
email : aoki@nucl.kyushu-u.ac.jp

Abstract

Single particle strength in (p, d) reaction has been studied with 65 MeV polarized protons. From the study of level assignment at low excitation energy region, realistic function of spreading width has been extracted. A calculation method of cross section in direct reaction continuum is proposed using the strength function and DWBA calculation and the results of comparisons between the calculation and experimental data are described.

1. Introduction

In one particle transfer reaction at low projectile energy, the continuum spectra which appear succeeding the discrete region (direct reaction continuum) have been studied with several methods. Due to its structureless there has not been a decisive one. A few methods were proposed to make approach toward this problem. In these methods, cross section in this energy region was considered as incoherent sum of the direct reaction components which would preserve the sum rule limit of each shell orbit.

An approach proposed by Lewis was to treat the direct reaction continuum spectra as a damping of deep hole states on that assumption and it reproduced the direct continuum spectra measured in ^{209}Bi(p, d)^{208}Bi at 62 MeV by using the spreading width and single-hole energies[1].

Recently, from the studies of level assignment in Ni isotopes at low excitation energy region, more realistic function of spreading width has been extracted. In this study, a calculation method of direct reaction continuum by using the extracted strength function and DWBA calculation is proposed as following of the Lewis's approach.

2. Experiment

The experiment was carried out at Research Center for Nuclear Physics (RCNP), Osaka University using the AVF cyclotron which provided the 65 MeV polarized protons. The accelerated protons were bombarded onto the ^{48}Ca,^{58,64}Ni targets. The emitted deuterons were momentum-analyzed in the focal plane of the spectrograph RAIDEN viewed with the focal plane detector system Kyushu. Measured excitation energy regions were 0–10 and/or 20 MeV and measured angles were at 5–45 laboratory angles. Fig.1 shows double differential cross sections $d^2\sigma/d\Omega dE$ and analyzing powers A_y obtained after summing up over the energy bin of 500 keV in ^{58}Ni target.

3. Direct Reaction Model Analysis

The theoretical calculation is based on the assumption that the direct continuum is considered as incoherent sum of the direct reaction components which would preserve the sum rule limit of each shell orbit. In calculation, direct process is only considered in order to investigate the direct continuum since the process is expected to be dominant at excitation energy region (

Ex<5 MeV). The double differential cross sections is expressed by

$$\frac{d\sigma}{d\Omega}(E) = \sum_{\ell,j} C^2 S_{\ell,j}(E) \times \left.\frac{d\sigma}{d\Omega}\right|_{\ell,j}^{DWBA}(E) \tag{1}$$

with

$$C^2 S_{\ell,j}(E) = \sum C^2 S_{\ell,j} \times f_{\ell,j}(E) \tag{2}$$

and σ is the DWBA cross section calculated with the code DWUCK[2], a non-symmetry Lorentz function[3,4] that gives a strength distribution of the single-hole states;

$$f_{\ell,j}(E) = \frac{n_0}{2\pi} \frac{\Gamma(E)}{\left(|E - E_F| - E_R^{\ell,j}\right)^2 + \frac{\Gamma^2(E)}{4}} \tag{3}$$

where E_F is the Fermi energy calculated by an empirical formula[5] and n_0 is a normalization factor adjusted to fill the sum rule on the ℓ, j orbit. $\Gamma(E)$ is a spreading width expressed by

$$\Gamma(E) = \frac{\varepsilon_0 (E - E_F)^2}{(E - E_F)^2 + E_0^2} + \frac{\varepsilon_1 (E - E_F)^2}{(E - E_F)^2 + E_1^2} \tag{4}$$

where ε_0, ε_1, E_0 and E_1 are constants that express effects of the nuclear damping in the nucleus[6]. The parameters used are ε_0 = 19.4 MeV, ε_1 = 1.40 MeV, E_0 = 18.4 MeV and E_1 = 1.60 MeV. The sum rule of the spectroscopic factor and the resonance energy E_R are estimated for each ℓ, j orbit by the BCS theory. Single particle energies used in the BCS calculation are calculated by a prescription[7]. Isobaric analog states (IAS) were observed in the excitation energy regions larger than 12.535, 5.162 and 11.729 MeV for ^{48}Ca, ^{58}Ni and ^{64}Ni, respectively. The sum rule of the spectroscopic factor of neutron orbits for $T \pm 1/2$ isospin states are estimated with simple shell model prediction[8]

$$\sum C^2 S = \begin{cases} n_n - \dfrac{n_p}{2T+1} & \text{for } T_< = T - \frac{1}{2} \text{ states} \\ \dfrac{n_p}{2T+1} & \text{for } T_> = T + \frac{1}{2} \text{ states} \end{cases} \tag{5}$$

where n_n and n_p are the number of neutrons and protons for each ℓ, j orbit , respectively and T is the target isosipn. The calculated results are plotted in Fig.1.

4. Results and Discussion

From a comparison of the calculated spectra and experimental ones in Fig.1, it is found that the spectral shape is considerably well reproduced at forward angles for all the targets while the direct continuum spectra (E_x > 5 MeV) are appreciably underestimated at backward angles. As for the analyzing power A_y, all the targets show the same results in which positive A_y are observed at around the ground state and negative A_y in the higher excitation energy regions at forward angles (5, 8 deg.). The direction and magnitude of A_y in the higher excitation energy regions become positive and large with angles. It should be noted that A_y is perfectly positive at overall excitation energies in backward angle spectra more than 29 deg.. The calculation reproduce the polarization and the magnitude well. This tendency is indicating the validity of this calculation method.

Fig.2–5 shows angular distributions of the cross sections obtained after summing up over the excitation energy bin of 5 MeV. In the discrete region (E_x<5 MeV) the theoretical cross sections are smaller than that of experiment at all the measured angles for all targets but their distributions are in good agreement with the experimental ones. The normalization factors extracted after scaling the theoretical cross sections to the experimental ones are 1.17, 1.40 and

1.15 for ^{48}Ca, ^{58}Ni, and ^{64}Ni, respectively. The factors are very close values in all the target nuclei.

At continuum regions (E_x=5–10 MeV), the same factors are applied for ^{58,64}Ni nuclei since the distributions are similar to that of descrete regions while ^{48}Ca data doesn't show such a systematic results. In the normalized distributions for ^{58,64}Ni, theoretical cross sections are appreciably small at backward angles. It is expected that the contributions from the other reaction processes such as multi-step process become important at this excitation energy regions.

5. Conclusion

In this study, double differential cross sections and analyzing powers of direct reaction continuum were calculated with the spreading widths and single-particle energies which were determined through the experimental studies. Spectral shape is well reproduced and the abusolute values ofcross sections are in good agreement with experimental ones. It is found that in direct reaction contiuum contributions from the processes such as multi-step process become large at backward angles.

References

[1] M.B. Lewis, Phys. Rev. C 11,145 (1975).
[2] Kunz P.D., Code DWUCK, University of Colorado (unpublished).
[3] C. Mahaux and H. Ngô, Phys. Lett. B 100, 285 (1981):Nucl. Phys. A 378, 205 (1982).
[4] G.E. Brown and M. Rho, Nucl. Phys. A 372, 397 (1981).
[5] K. Hisamochi et al., Nucl. Phys. A 564, 227 (1993).
[6] M. Matoba et al., Nucl. Phys. A 581, 21 (1995).
[7] A. Bohr and B.R. Motelson, "Nuclear Structure"(W.A. Benjamin, INC., 1969, New York, Amsterdam) Vol.1, Appendix 2D.
[8] M. Matoba et al., Phys Rev. C 53, 1792 (1996).

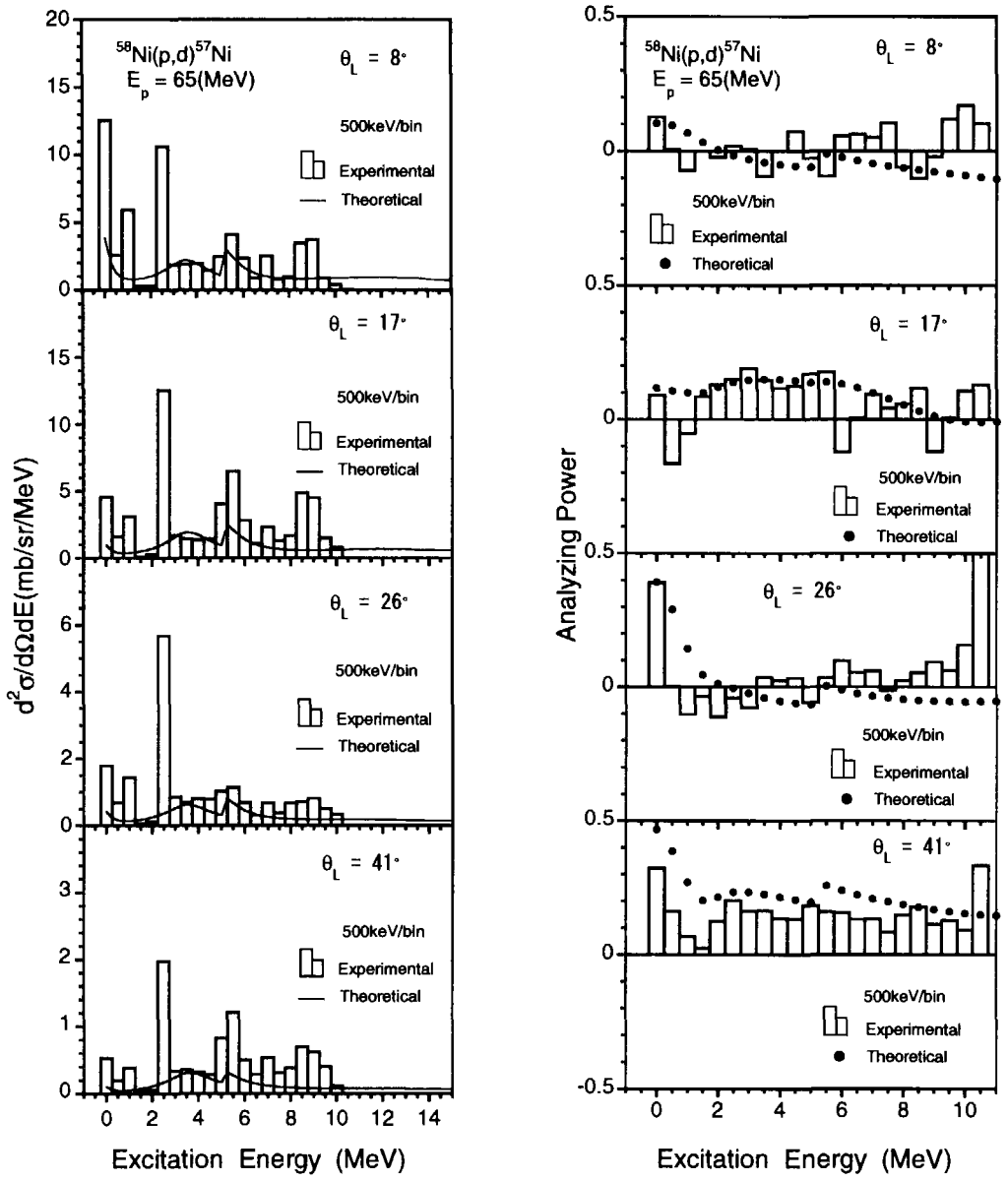

Figure 1: Double differential cross section (left) and Analyzing Power (A_y) from a ^{58}Ni target.

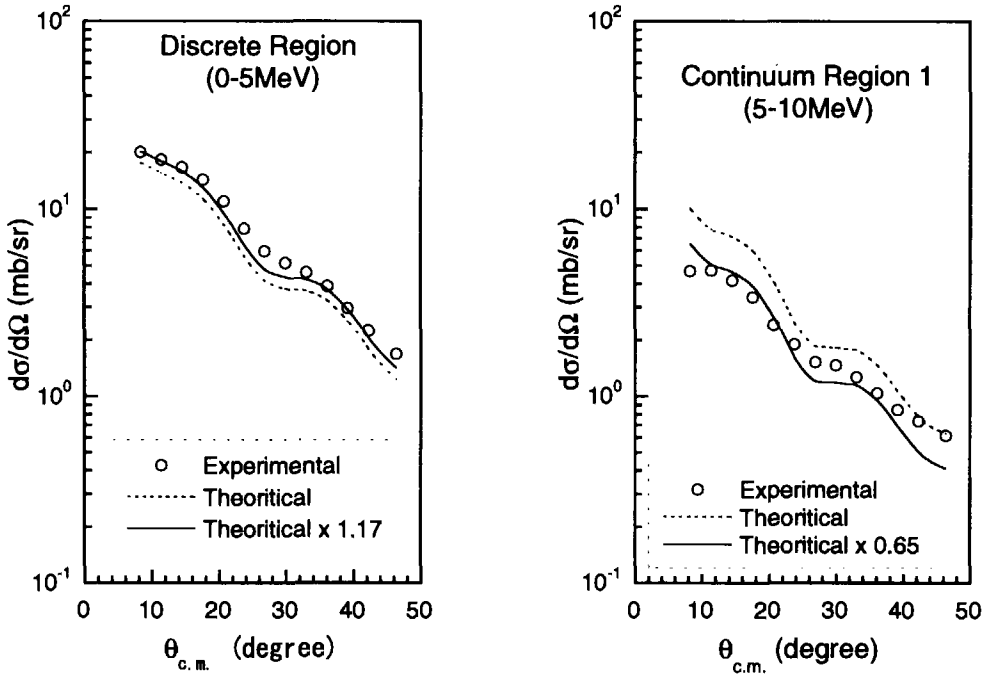

Figure 2: Angular distributions of summed cross sections from a ^{48}Ca target. Ex=0–5 MeV (left) and 5–10 MeV(right).

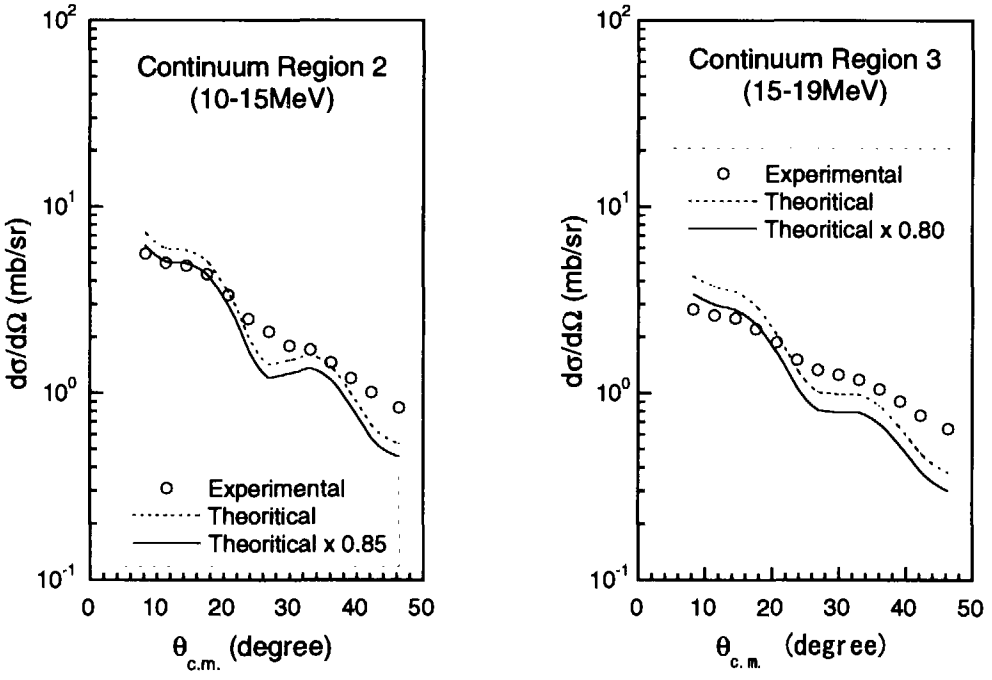

Figure 3: Angular distributions of summed cross sections from a ^{48}Ca target. Ex=10–15 MeV (left) and 15–19 MeV(right).

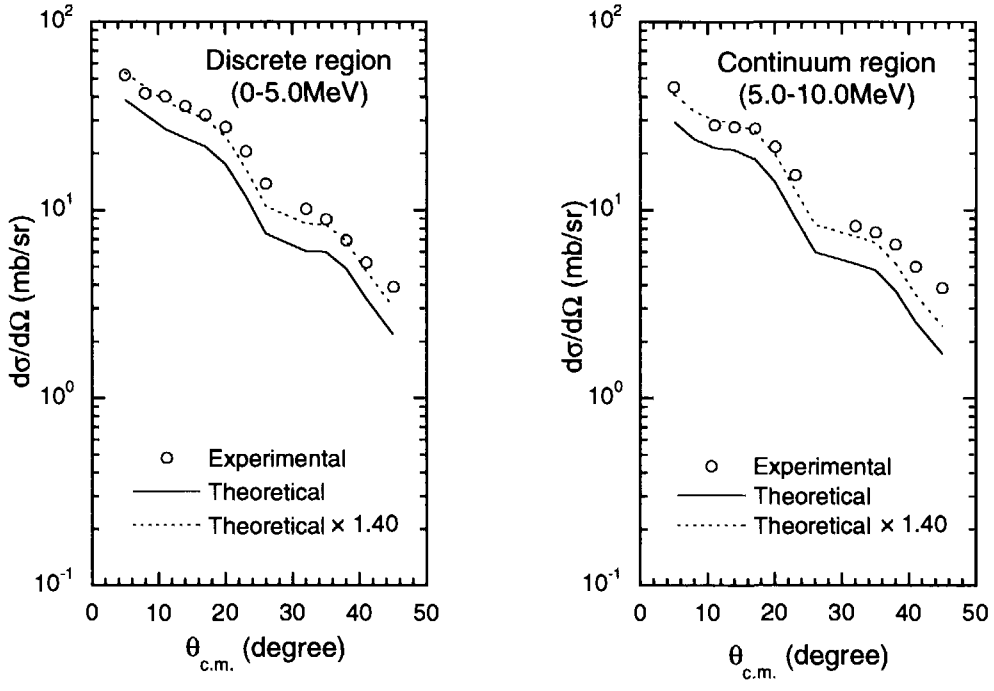

Figure 4: Angular distributions of summed cross sections from a ^{58}Ni target. Ex=0–5 MeV (left) and 5–10 MeV(right).

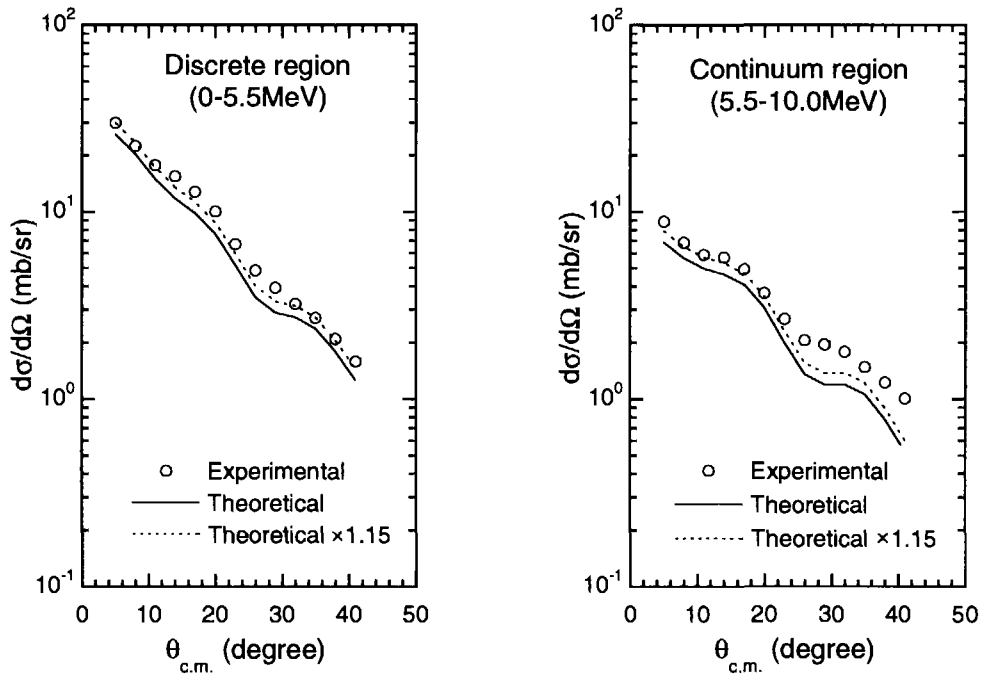

Figure 5: Angular distributions of summed cross sections from a ^{64}Ni target. Ex=0–5.5 MeV (left) and 5.5–10 MeV(right).

3.35 Ceramic Breeder Material with Catalytic Function

Kenzo Munakata, Toshihiko Kawano, Atsushi Baba,
Hideki Nakashima and Masabumi Nishikawa
Kyushu University, Department of Advanced Energy Engineering Science,
Interdisciplinary Graduate School of Engineering Science,
Kasuga-shi, 816-8580, Japan
Phone: +81-92-642-3784, Fax: +81-92-642-3784
E-mail: kenzo@nucl.kyushu-u.ac.jp

1. Introduction

In most current designs of D-T fusion reactor blankets employing ceramic breeder materials such as Li_2O, $LiAlO_2$, Li_2ZrO_3 and Li_4SiO_4, the use of a helium sweep gas containing 0.1 % of hydrogen is contemplated to extract tritium efficiently via isotopic exchange reactions. However, at lower temperatures, the release process of tritium from the breeders is dominated by the desorption of tritiated water and are therefore rather slow. For this reason, there is still a need to develop techniques that contribute to the acceleration of the recovery of bred tritium.

In our previous studies, the isotope exchange reactions and water adsorption on the surface of several solid blanket materials were investigated [1-3]. The results revealed that these isotope exchange reactions proceed fast only at more elevated temperatures. Because of the strong temperature dependence of the exchange reactions, a considerable decrease in the reaction rate takes place as temperature is lowered. Taking into consideration that there is a broad temperature distribution within a blanket module [2], it is anticipated that the tritium bred in the regions of lower temperature will presumably be poorly recovered. The result could be an increased overall steady state tritium inventory in the blanket module.

In order to obtain an improved recovery of tritium from a blanket over a broad range of temperatures, the effect of catalytic active metal additives, such as platinum and palladium, on the heterogeneous isotope exchange reactions at the breeder–sweep gas interface was examined.

These catalytic additives are irradiated in the 14 MeV neutron field during the operation of fusion reactors, which could lead to the nuclear transmutation of Pd and Pt and thus change in the chemical properties of these noble metals. Moreover, there is a possibility that nuclear reactions cause induced radioactivity related to additive metals. The authors also investigate these aspects using cross sections of the nuclear reactions.

2. Experimental

Platinum and palladium were deposited on solid breeder material pebbles (Li_4SiO_4, 0.51-0.94 mm (av. 0.68 mm) in diameter, >98 %TD) by the incipient wet impregnation method generally used for the fabrication of catalysts. The exact content of the deposited Pt or Pd has not yet been determined, but according to the mass balance in the fabrication process the concentrations can be estimated being within a range of 0.7 to 2 weight %; the contents never exceed 2 weight %.

A schematic diagram of the experimental apparatus is shown in Fig. 1. For a run between 2.5 and 20.0 g of Pt/Li_4SiO_4, Pd/Li_4SiO_4 or Li_4SiO_4 pebbles were placed in reactors made of quartz. The gaseous compositions of inlet and outlet streams of the reactor were analyzed with respect to H_2, HD and D_2 by gas chromatography. A hygrometer was used to determine the water vapor content in these streams. The gas flow rate was controlled with conventional mass flow controllers. The gases employed were purified with a cold trap containing 5A molecular sieve that was cooled with an ice/water mixture to remove residual water vapor. To achieve controlled concentrations of deuterated water in the carrier gas molecular deuterium was quantitatively oxidized with a CuO bed held at 350 °C.

During runs, which were carried out under steady state conditions, the reactor temperature was stepwise decreased from the maximum experimental temperature. The experimental conditions employed are summarized in Table 1. The space velocity (SV) in Table 1 is defined as

$$SV = \frac{Q}{V}, \qquad (1)$$

where Q and V are the volumetric velocity of the gas introduced to the reactor and the bed volume of the breeder materials, respectively. As seen in the above equation, SV is the reciprocal of the residence time of the process gas. Thus, the higher SV corresponds to the lower residence time. As shown in Table 2, the experiments on Pt/Li_4SiO_4 and Pd/Li_4SiO_4 were performed under higher SV conditions than that for the virgin material Li_4SiO_4. A blank test was also performed with an empty reactor, and it was confirmed that no exchange reactions take place within the experimental condition of this work.

3. Experimental Results and Discussion

In each experiment a gaseous mixture of helium containing H_2 (3500–4300 ppm) and D_2O (260–300 ppm) was passed through the reactor packed with the breeder pebbles. The extent of the exchange reactions taking place on the surface of the breeder materials was obtained from the composition of the exhaust stream of the reactor measured by gas chromatography.

The ratio of conversion R is defined as

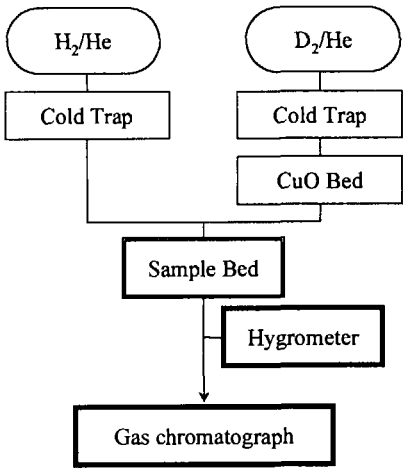

Fig.1 Experimental flow diagram

Table 1 Experimental conditions

	Li_4SiO_4	Pt/Li_4SiO_4	Pd/Li_4SiO_4
Amount [g]	30	2.4	2.5
Gas velocity [ml/min]	955	326	320
Bed diameter [mm]	22	16.2	16.2
Space velocity [h^{-1}]	2700	5500	5200
Temperature [°C]	200 – 600	25 – 400	25 – 400
Inlet gas composition			
H_2 [ppm]	3500	3900	4300
D_2O [ppm]	300	260	260

$$R = \frac{C_{D,out}}{C_{D,in}}, \tag{2}$$

where $C_{D,in}$ and $C_{D,out}$ are the molar concentration of D-atoms in D_2O in the inlet stream and the molar concentration of D-atoms in HD and D_2 in the outlet stream, respectively.

Figure 2 shows conversion ratios as function of temperature for the investigated breeder materials. In the case of Li_4SiO_4 (without noble metals), a conversion ratio of only 33 % was attained even at 400 °C. On the contrary, on the surface of the lithium silicate containing dispersed platinum (Pt/Li_4SiO_4), conversion ratios of nearly 90 % (almost corresponding to the equilibrium condition of the isotope exchange reaction) were obtained at temperatures of only little over 200 °C. This higher degree of conversion was attained in spite of employing a much higher space velocity than in the experiment with Li_4SiO_4 (virgin material). Even at 25 °C a conversion ratio of 28 % was obtained over the Li_4SiO_4 pebbles impregnated with platinum. Similar results were obtained in experiment with Pd/Li_4SiO_4 pebbles, which indicates that palladium is also an effective catalyst for the enhancement of the exchange reaction. For comparison, experimental results for other ceramic breeders ($LiAlO_2$ and Li_2ZrO_3) are also shown in Fig. 2, which indicates poor conversions even at higher temperatures. By these results it can be concluded that isotope exchange reactions proceed at very fast rates even at temperatures below 400 °C when lithium silicate pebbles contain dispersed catalytic active noble metals. The improved solid breeder materials are here designated as catalytic breeder material. Thus, a considerable enhancement effect for the release of tritium from catalytic breeder materials is expected. One could consider the use of the insoluble residues from nuclear reprocessing of spent nuclear fuel that is known to contain large amounts of metals like Pt, Pd or Rh. While these materials cannot be utilized by conventional industries, a use for the fabrication of catalytic breeder materials is thought to become their practical application.

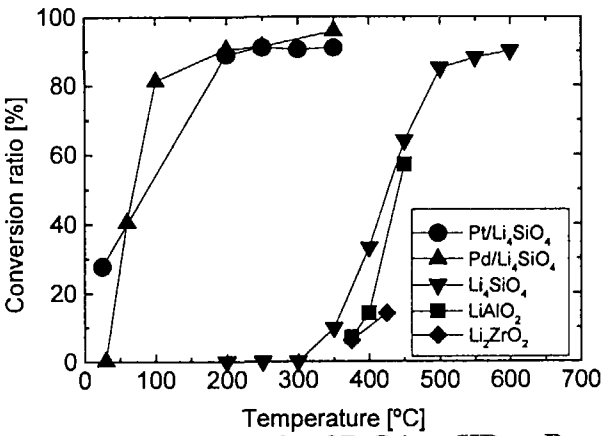

Fig. 2 Conversion ratio of D_2O into HD or D_2 over various breeders

Table 2 Experimental Conditions

	H_2 at inlet (ppm)	D_2O at inlet (ppm)	SV (h^{-1})
Li_4SiO_4	3500	300	2700
Pt/Li_4SiO_4	3900	260	5500
Pd/Li_4SiO_4	4300	260	5200
$LiAlO_2$	3000	500	4500
Li_2ZrO_2	3000	300	1500

4. Need for Nuclear Data of Catalytic Breeder Materials

Nuclear data of the catalytic metals are required for two aspects, the evaluation of induced radioactivity and nuclear transmutation. To estimate the induced radioactivity of Pd and Pt, we surveyed long-lived nuclei in the decay chain of the nuclear reactions. A particle

emission process is dominant in the 14 MeV neutron–induced reactions, and thus residual nuclei produced via $(n,2n)$, (n,p), and (n,α) reactions are the parents of the decay chains. For Pd the important nuclear decay processes, which produce long-lived nuclei, are ($T_{1/2}$ data taken from Ref. [4]),

$$^{102}\mathrm{Pd}\,(n,2n)\,^{101}\mathrm{Pd} \xrightarrow[\mathrm{EC}]{8.47\mathrm{h}} {}^{101}\mathrm{Rh} \xrightarrow[\mathrm{EC}]{3.3\mathrm{y}} {}^{101}\mathrm{Ru},$$

and

$$^{108}\mathrm{Pd}\,(n,2n)\,^{107}\mathrm{Pd} \xrightarrow[\beta^-]{6.5\times10^6\mathrm{y}} {}^{107}\mathrm{Ag}.$$

The first process produce only a small amount of radioactive nuclei (^{101}Pd) because the natural abundance of ^{102}Pd is only 1.02 %, and the half life of ^{101}Rh is not so long in comparison with the duration of operation of the fusion blanket modules. The second process yields a long-lived product ^{107}Pd. The natural abundance of ^{108}Pd is 26.5 % and therefore an accurate cross section of the ^{108}Pd $(n,2n)$ reaction is required to estimate the inducded radioactivity of the catalytic breeder materials. This nucleus is also produced by the chain

$$^{110}\mathrm{Pd}\,(n,\alpha)\,^{107}\mathrm{Ru} \xrightarrow[\beta^-]{3.75\mathrm{m}} {}^{107}\mathrm{Rh} \xrightarrow[\beta^-]{21.7\mathrm{m}} {}^{107}\mathrm{Pd} \xrightarrow[\beta^-]{6.5\times10^6\mathrm{y}} {}^{107}\mathrm{Ag},$$

but its yield is expected to be small since the (n,α) reaction cross section at 14 MeV is <1 mb in JENDL-3.2.

In the case of 14 MeV neutron–induced reactions on Pt, the charged particle emission processes is thought to be ignorable, and the $(n,2n)$ reaction could be an important process for the production of long-lived nuclei. The decay schemes of the residual nuclei are as follows:

$$^{192}\mathrm{Pt}(n,2n)^{191}\mathrm{Pt} \xrightarrow[\mathrm{EC}]{2.9\mathrm{d}} {}^{191}\mathrm{Ir}$$

$$^{194}\mathrm{Pt}(n,2n)^{193}\mathrm{Pt} \xrightarrow[\mathrm{EC}]{50\mathrm{y}} {}^{193}\mathrm{Ir}$$

$$^{198}\mathrm{Pt}(n,2n)^{197}\mathrm{Pt} \xrightarrow[\beta^-]{18.3\mathrm{h}} {}^{197}\mathrm{Au}$$

Residual nuclei of the ^{195,196}Pt $(n,2n)$ reaction are stable. Therefore, a $(n,2n)$ reaction on ^{194}Pt, of which natural abundance is 32.9 %, is a major process with regard to induced radioactivity.

The evaluated nuclear data of Pd are available in JENDL-3.2, whereas no data on Pt are given so far. Accordingly we calculated the cross sections of ^{nat}Pt $(n,2n)$ and $(n,3n)$ reactions with the GNASH code[5]. The model parameters used were the Walter and Guss' global optical potential[6], and the level density parameters proposed by Yamamuro[7]. The calculated cross sections of $(n,2n)$ and $(n,3n)$ reactions are compared with the experimental data[8] in Fig. 3. No attempt was made to improve the accuracy of fitting in this calculation, and thus the calculated cross section is about 15 % larger than the experimental values.

With these nuclear data, one can estimate transmutation rates of noble metals in the fusion blanket. A rough estimation of the transmutation rate R s^{-1} is given by $R = \Phi\sigma$,

where Φ is a flux of 14-MeV neutrons, and σ is a cross section of the reaction in which the residual nucleus changes into other atoms with different chemical property. The neutron flux for the ITER design is about $10^{13}cm^{-2}s^{-1}$ at just outer side of the first wall, then the estimated R is less than 1 % per 10 years for both Pt and Pd. Therefore, transmutation of noble metals is a minor problem for a design of the catalytic breeder materials.

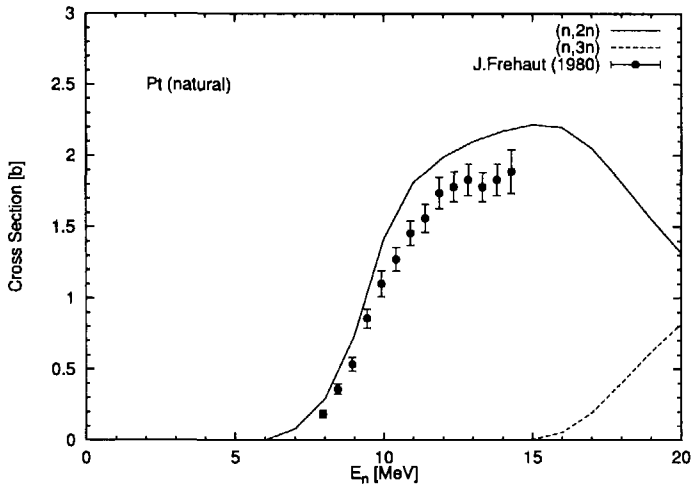

Fig.3 Comparison of the calculated $^{nat}Pt(n,2n)$ and $(n,3n)$ reaction cross section with the experimental data

5. Conclusions

Catalytic breeder materials were produced by impregnating lithium silicate with either platinum or palladium. The isotope exchange reactions between molecular protium and gaseous perdeuterated water over these new breeder materials were found to be very fast even at temperatures far below 400 °C. Nuclear data of noble metals were surveyed to estimate the induced radioactivity and the transmutation rate. It was found that the $(n,2n)$ reaction produces ^{107}Pd and ^{194}Pt which have long half-life, and that less than 1 % of noble metals will be transmuted during 10-year-operation of a fusion reactor of ITER-class design.

References

[1] K. Munakata and M. Nishikawa, J. Nucl. Mater. **170,** 187 (1990).
[2] K. Munakata, M. Nishikawa, and K. Yoneda, Fusion Technol. **15,** 1451(1989).
[3] A. Baba, M. Nishikawa and T. Eguchi, J. Nucl. Mater. to be published.
[4] Table of Isotopes Eighth Edition," Ed. R. B. Firestone and V. S. Shirley, John Wiley & Sons, Inc., (1996).
[5] P. G. Young and E. D. Arthur : "GNASH, A Pre-equilibrium, Statistical Nuclear-Model Code for Calculation of Cross Section and Emission Spectra," LA-6947, (1977).
[6] R. L. Walter and P. P. Guss, Rad. Effect **95,** 73(1986).
[7] N. Yamamuro, JAERI-M 90-006 (1990).
[8] J. Frehaut, A. Bertin, R. Bois, and J. Jary, *Proc. Symp. on Neutron Cross Sections from 10–50 MeV*, Brookhaven, New York, USA, May 12–14, 1980, BNL-NCS-51245, p.399 (1980).

3.36 Retrieval Transmutation and Decay Process of Nuclides Using Nuclear Reaction Database on Internet

Mitsutane FUJITA, Misako UTSUMI and Tetsuji NODA
National Research Institute for Metals
1-2-1, Sengen, Tsukuba, Ibaraki 305 Japan
fujita@tamamo.nrim.go.jp

Abstract

In the data system for alloy design and selection of materials used in various nuclear reactors, huge material databases and several kinds of tools for data analysis or simulation code of the phenomena under neutron irradiation are required. A nuclear reaction database system based on the data of FENDL-II on the Internet has been developed in NRIM site of "Data-Free-Way". The user interface in this database was made for the retrieval of the necessary data and for the expression of the graph of the relation between the nuclear energy spectrum of neutron and neutron capture cross section. It is indicated that using the database, the possibility of chemical compositional change and radioactivity in a material caused by nuclear reactions can be easily retrieved, though the evaluation is qualitatively.

1. Introduction

The computer aided data systems are required in order to the alloy design and selection of materials used in various nuclear reactors. The system should consist of huge material databases and several kinds of tools for data analysis or simulation code of the phenomena under irradiation. The huge martial database has several small databases stored the special data such as nuclear data and decay data. Thus, a database on transmutation for nuclear materials had constructed on PC [1,2]. The database converted to a system used on Internet. As a database for nuclear material design and selection used in various reactors are developed in NRIM site in "Data-Free-Way"[3-5].

The database storing the data on nuclear reaction needs to calculate of the simulation for chemical compositional change and radio-activation in transmutation. Using the database, we can retrieve the data of nuclear reaction for material design on the Internet and understand qualitatively the behavior of nuclear reaction such as the transmutation or decay. The database is required for the friend user-interface for the retrieval of necessary data.

In the paper, features and functions of the developed system are described and especially, examples of the easy accessible search of nuclear reactions are introduced.

2. Outline of the database on transmutation for nuclear materials

2.1 Database system

In the database of transmutation for nuclear materials, the data of nuclear reaction for material design is stored and we can understand qualitatively the behavior of nuclear reaction such as the transmutation or decay. The database is managed by ORACLE where RDBMS (relational database management system) is supported on work station with unix OS.
As the RDBMS and WWW were connected, user are able to retrieve necessary data using Netscape or Explorer as a user-interface through the Internet.

Fig. 1 shows the home page in the WWW of NRIM site on "Data-Free-Way". Users be able to access the database by selecting the term of "transmutation of material" in the home page. Then. the opening screen of the database as shown Fig. 2 is appeared. Users are able to select various interfaces for retrieval and obtain the necessary data. The interfaces are used in the periodic table or the chart of nuclides.

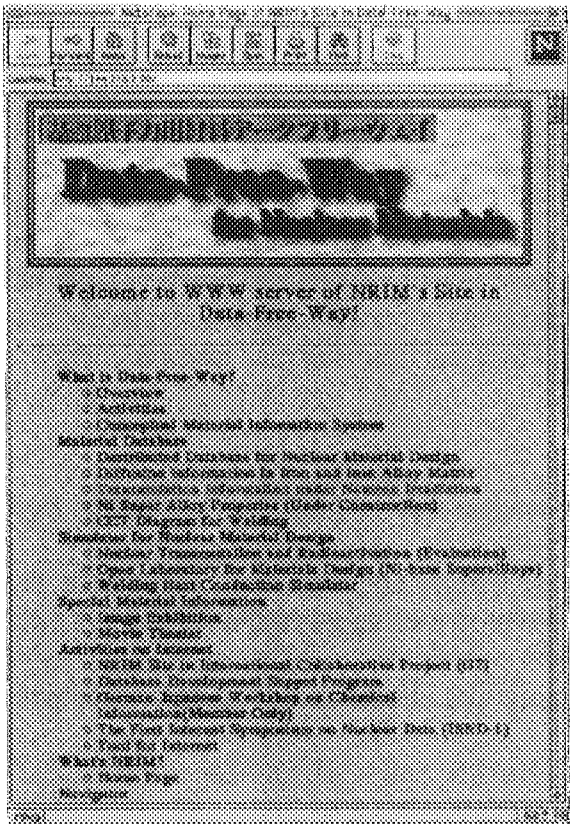

Fig. 1 Home page in the WWW of NRIM site on "Data-Free-Way"

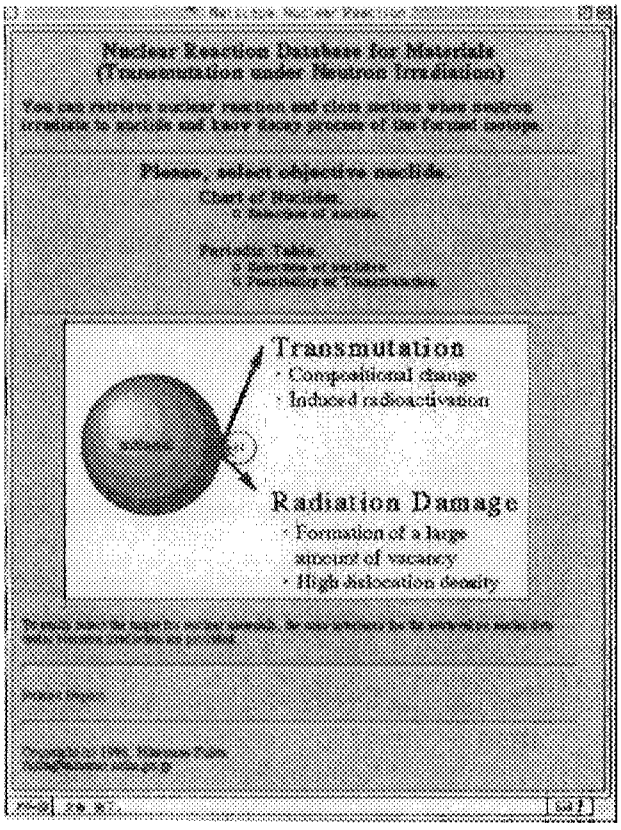

Fig. 2 Opening screen of the for transmutation under neutron irradiation..

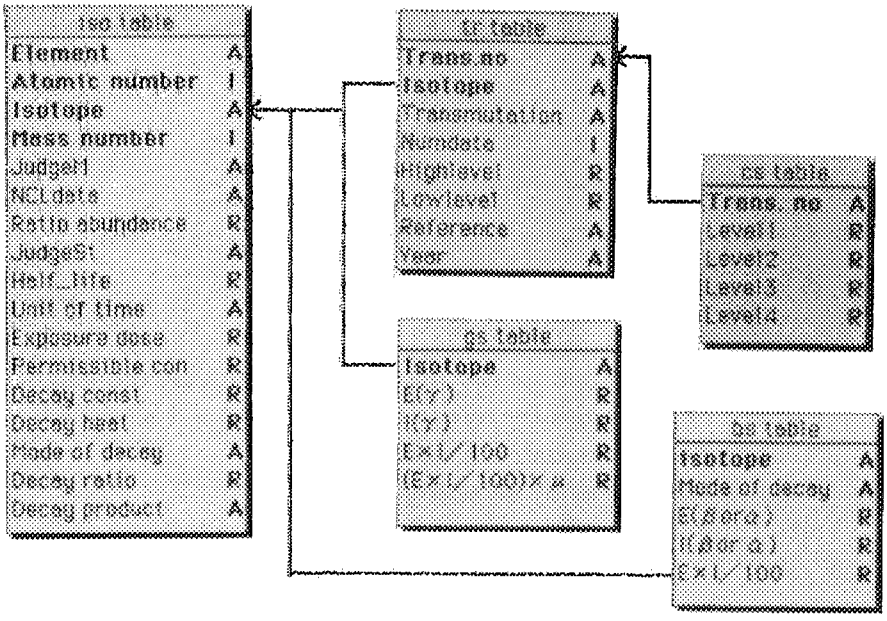

Fig. 3 The data structures of the database on transmutation for nuclear materials.

2.2 Data structure

The database consists of five main tables, as shown Fig. 3. The main tables are isotope (iso table), decay (gs table and bs table), transmutation (tr table) and cross section (cs table). The isotope table consists of the data such as element name, atomic number, isotope name, mass number, the natural abundance ratio, half-life data, gamma-ray or beta-ray energy and maximum permissible concentration in air (MPC), which are taken from isotope table. The energies of gamma- ray and bata-ray on decay are stored in two tables of gs and bs. The decay heat are calculated from the data of these tables. The transmutation table has the data of transmutation process, produced nuclide and etc.. The neutron capture cross-section table has the data with 42-energy group covering from thermal neutron energy to 15MeV.

2.3 Stored data

Various data, which are required for simulation on nuclear reaction, have been collected from reports as follows;

I. Nuclear data such as neutron cross-section are mainly collected from FENDL II. The number of cross section for nuclear reactions which was stored in the database is 3213 in stable nuclides and 5484 in unstable ones.

II. The data on Decay process, gamma ray, isotope and element are collected respectively from

a. "Table of Radioactive Isotopes" E. Browne and R. B. Firestone, 1986, LBLU of C, John Wiley & Sons,
b. "Radiation Data Book", edited by Y. Murakami, H. Danno and A. Kobayashi, 1982, Chijin-Shokan.
c. "Chart of the Nuclides" compiled by Y. Yoshizaw and T. Horiguchi and M. Yamada, 1996, JNDC and NDC in JAERI.
d. "Elsevier's Periodic Table of the Elements", compiled by P. Lof, 1987, Elsevier.

3. Functions and user-interface

3.1 Functions

Fig. 2 shows opening main menu screen of the database. This database has four retrieval functions of nuclear reaction process, properties of radioactive isotope, spontaneous decay
of each isotope and decay of produced nuclides after nuclear reaction. We can understand qualitatively the behavior of nuclear reaction such as the transmutation or decay. Fig. 4 shows screen of the selection of the isotope or the nuclide from the cart of nuclides. Fig. 5 shows a example of the screen of properties for retrieved ^{93}Zr nuclide. User is able to know mass number, the natural abundance ratio, half-life data, gamma-ray or beta-ray energy on retrieved nuclide. Fig. 6 shows screen that by selecting the desired nuclear reaction in right folder, user is able to know records on a given transmutation and spontaneous decay in the reaction process. If user clicks the graph button in the screen shown Fig. 5 or Fig. 6, the graph as shown in Fig 7 appears. The graphs are shown the relation between transmutation cross section and neutron energy spectrum on various reactions. The high value of the cross section means qualitatively that the nneutron reaction easily occurs.

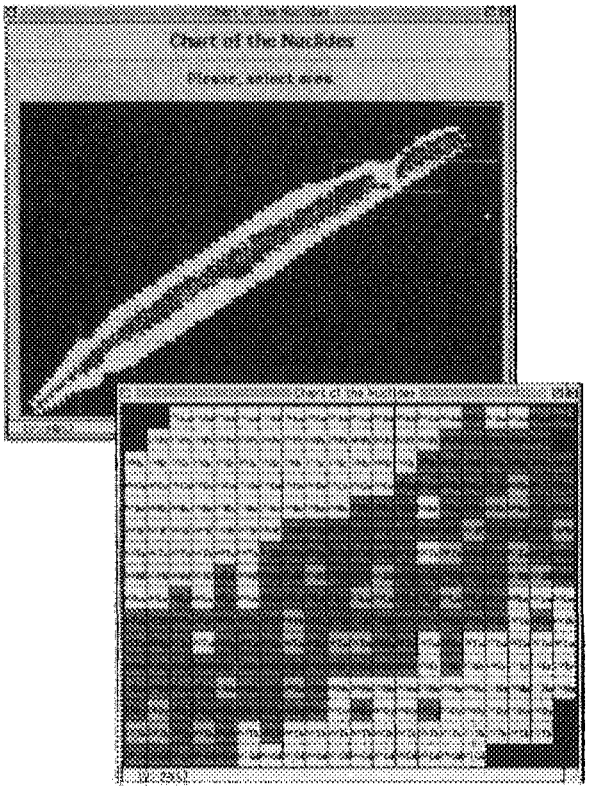

Fig. 4 Selection of isotope or nuclide by the chart of the nuclides

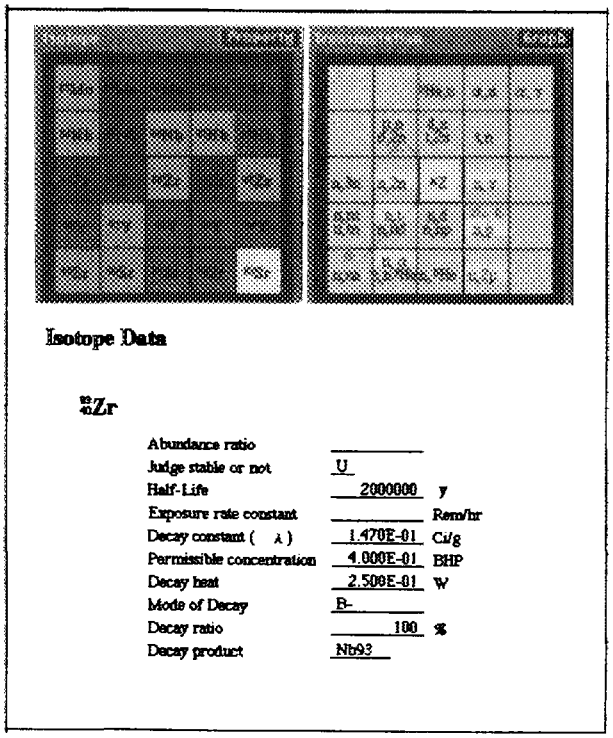

Fig. 5 Screen of properties for retrieved ^{93}Zr nuclide

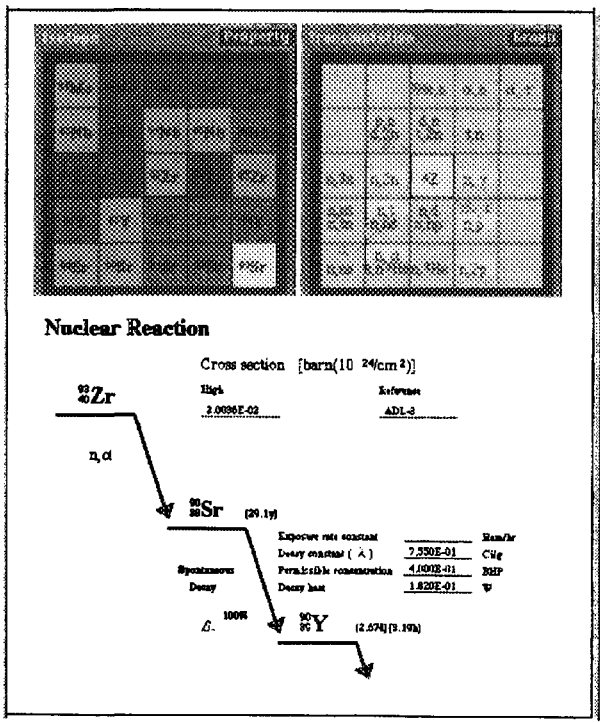

Fig. 6 Screen to retrieve data on nuclear transmutation and decay process of ^{93}Zr nuclide and the results.

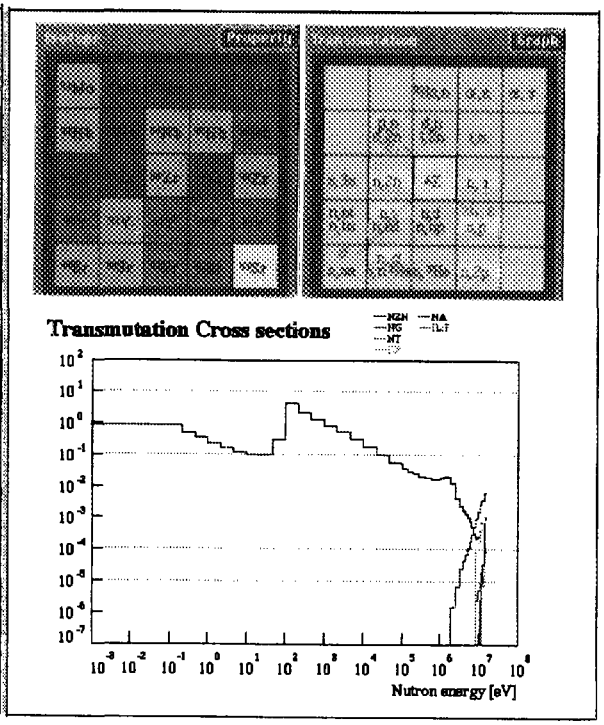

Fig. 7 A example of graph of relation between neutron capture cross section for various reactions and neutron energy spectrum.

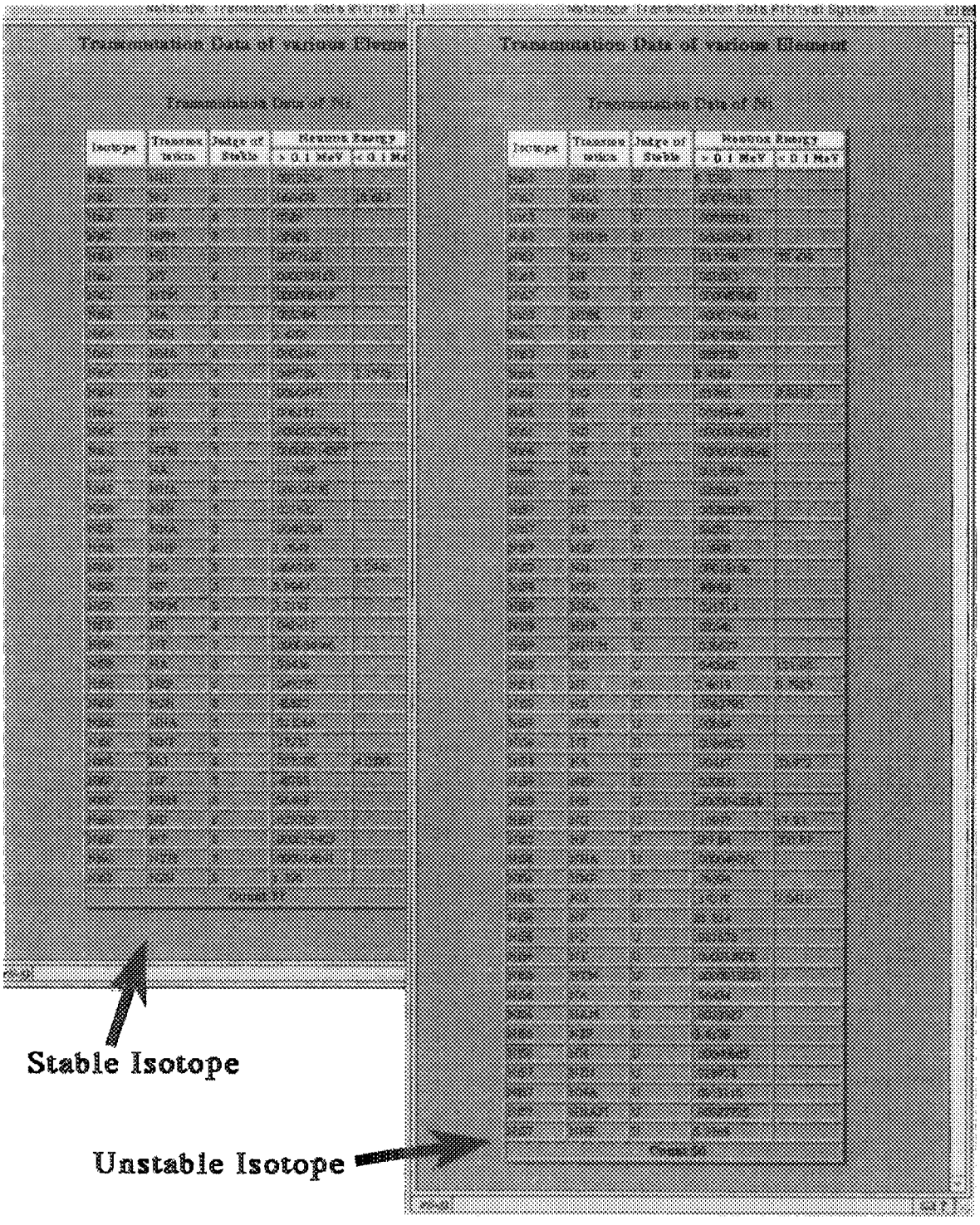

Fig. 8 Screen to retrieve data on formed nuclides and cross section under high neutron energy (>0.1eV) or low that (<0.1eV)on various transmutations in Ni.

4. Example of system operation

Fig. 8 shows the screen to retrieve data on formed nuclides and cross section under high neutron energy or low that on various transmutations in Ni. It is able to know that the reaction in nutron transmutation in Ni easily occurs qualitatively.

Type 316 stainless steel is used as the structural material of the fuel sub-assemblies in the sodium cooled fast breeder reactors. This steel is regarded as a candidate material for blanket structures of the fusion reactors. However it is required that materials should have a high resistance against swelling and low radioactivation under the high-energy neutron irradiation environment such as in fusion reactors. Ferritic 9Cr1WVTa steel is also being considered as an alternate candidate structural material to type 316 stainless steel [3]. An amount of He formation and radioactivity under neutron irradiation of both steels will be evaluated as an example of application of the present simulation system.

Using the database, the possibility of large amount of He formation and radioactivity in the candidate materials can be easily evaluated qualitatively. The possibility of He formation is known by retrieving cross section size of (n, alpha;) reaction on compositional atoms of materials. The radioactivity is known by retrieving half-life of transmuted products of compositional atoms of material. Transmuted products with half-life of more than one year in type 316 and ferritic steel can be easily know qualitatively. These result suggest that type 316 stainless steel has more radioactive nuclides and is radioactivated more easily than ferritic 9Cr-1WVTa steel under neutron irradiation. It is found that this system will be frequently used by nuclear material scientists as a material information tool, if this system is jointed to networking system such as "Data-Free-Way"[3-5].

5. Summary

1) A database on transmutation for nuclear materials with user friendly interface was constructed in WWW server on the Internet. (http://inaba.nrim.go.jp//Irra/).
2) The database consists of mainly five tables stored the information of isotope, two decay tables of gamma-ray and beta-ray, transmutation and cross section for 42 neutron energy group converted from FENDL-II.
3) The compositional change and radioactivity in materials can be easily evaluated qualitatively.
4) The radioactivity is known by retrieving half-life of transmuted products of compositional atoms of material. Transmuted products with half-life of longer than one year in type 316 and ferritic steel. These result suggest that type 316 stainless steel has more radioactive nuclides and radioactivated more easily than ferritic 9Cr-1WVTa steel for reduced activation under neutron irradiation .

References

[1] M. Utsumi, Noda T and Fujita M.; JAERI-Conf 96-008 p.332-336
[2] Fujita M., Utsumi M., Noda T.; JAERI-Conf 97-004 p.208-217
[3] Nakajima H., Yokoyama N., Ueno F., Kano S., Fujita M., Kurihara Y. and Iwata S., J. Nucl. Mater. vol.212-215 (1994) p.1171-1714.
[4] Ueno F., Kano S., Fujita M., Kurihara Y., Nakajima H., Yokoyama N. and Iwata S., J. Nucl. Sci. Technol, vol.31 (1994) p.1314-1334.
[5] Fujita M., Kurihara Y., Shindo H., Yokoyama N., Ueno F., Kano S., and Iwata S., ASTM STP 1311, ASTM (1997) p.249-260.

Appendix: Participant List

Akino, F.	JAERI
Ando, Y.	Toshiba Co.
Annou, A.	Taisei Co.
Aoki, S.	Kyushu Univ.
Aoki, T.	Fuji Electric Co., Ltd.
Aoyama, S.	Kitami Inst. of Tech.
Aoyama, T.	JNC
Aruga, T.	JAERI
Asami, T.	DEI
Baba, M.	Tohoku Univ.
Chiba, S.	JAERI
Chongkum, S.	OAEP
Fujishiro, Y.	DEGDO
Fujita, M.	NRIM
Fukahori, T.	JAERI
Fuketa, T.	IES
Furuta, T.	Nagoya Univ.
Furutaka, K.	JNC
Fushimi, A.	Hitachi Ltd.
G. Ah Auu	MINT
Goto, Y.	Nissei Sangyo Co., Ltd.
Gotou, M.	Hitachi Ltd.
Guinyun Kim	PAL
Harada, H.	JNC
Harima, Y.	CRC
Hasegawa, A.	JAERI
Huang Xiaolong	JAERI
Hyun-Je Cho	Kyoto Univ.
Ibaraki, M.	Tohoku Univ.
Iga, K.	Kyushu Univ.
Igarasi, S.	
Igashira, M.	Tokyo Inst. of Tech.
Ikeda, Y.	JAERI
Ishii, K.	Osaka Univ.
Ito, C.	JNC
Iwai, T.	Univ. of Tokyo
Iwamoto, O.	JAERI
Jung-Do Kim	KAERI
Kai, T.	JAERI
Kano, S.	Shimizu Co.
Katakura, J.	JAERI
Kawade, K.	Nagoya Univ.
Kawai, M.	KEK
Kawanishi, T.	MHI
Kawano, T.	Kyushu Univ.
Kikuchi, K.	JAERI
Kim, Eunjoo	Tohoku Univ.
Kishida, N.	JAERI
Kitano, T.	MES
Kitao, K.	DEI
Kitsuki, H.	Kyushu Univ.
Kiyosumi, T.	JRI
Kobayashi, K.	Kyoto Univ.
Kobayashi, T.	Teikyo Univ.
Komuro, Y.	JAERI
Kondo, T.	Osaka Univ.
Konno, C.	JAERI
Kosako, K.	SAEI
Kubono, S.	Univ. of Tokyo
Kugo, T.	JAERI
Kurata, Y.	JAERI
Kurosawa, M.	JAERI
Kurosawa, T.	Tohoku Univ.
Lee Young-Ouk	KAERI
Maekawa, A.	Hitachi Ltd.
Maekawa, F.	JAERI
Maki, K.	Hitachi Ltd.
Maruyama, H.	Hitachi Ltd.
Matsunobu, H.	DEI
Matsuoka, H.	JAERI
Meigo, S.	JAERI
Miura, T.	Tohoku Univ.
Miyahara, A.	NIFS
Mizumoto, M.	JAERI
Mori, K.	Univ. of Tokyo
Mori, S.	KHI
Mori, T.	JAERI
Munakata, K.	Kyushu Univ.
Murata, I.	Osaka Univ.
Murata, T.	AITEL
Murazaki, J.	JAERI
Nagame, Y.	JAERI
Nagao, T.	JAERI
Nagaya, Y.	JAERI
Naito, Y.	NAIS
Nakagawa, M.	JAERI
Nakagawa, T.	JAERI
Nakajima, H.	JAERI
Nakajima, K.	JAERI
Nakajima, Y.	RIST
Nakamura, S.	JNC
Nakane, Y.	JAERI
Nauchi, Y.	Tohoku Univ.
Nishihara, K.	JAERI
Nishinaka. I	JAERI
Nose, S.	JNC
Ochiai, K.	Osaka Univ.
Odano, N.	JAERI
Ohbayasi, Y.	Hokkaido Univ.
Ohkawachi, Y.	JNC
Ohno, S.	Tokai Univ.
Ohsaki, T.	Tokyo Inst. of Tech.
Ohsawa, T.	Kinki Univ.
Ohshima, T	DEGDO
Oigawa, H.	JAERI
Okajima, S.	JAERI

Okuno, H.	JAERI
Onchi, T.	CRIEPI
Osugi, T.	JAERI
Oyama, Y.	JAERI
Oyamatsu, K.	Nagoya Univ.
Raman, S.	ORNL
Saitou, M.	HEC
Sakae, T.	Tsukuba Univ.
Sakane, H.	Nagoya Univ.
Sanami, T.	Nagoya Univ.
Sasa, T.	JAERI
Sasahara, A.	CRIEPI
Sasaki, K.	JNC
Sasaki, M.	MHI
Sasamoto, N.	JAERI
Satou, O.	MRI
Seung-Gy Ro	KAERI
Shibata, K.	Hitachi Ltd.
Shibata, K.	JAERI
Shibata, N.	Nissei Sangyo Co., Ltd.
Shibata, T.	KEK
Shibata, T.	JAERI
Shigyo, N.	Kyushu Univ.
Shimada, S.	JAERI
Shimakawa, S.	JAERI
Shono, A.	JNC
Sugi, T.	JAERI
Sugimoto, M.	JAERI
Sukegawa, T.	JAERI
Sun Weili	Kyushu Univ.
Suyama, K.	JAERI
Suzuki, S.	JNC
Suzuki, T.	
Suzuki, T.	
Tahara, Y.	MHI
Takagi, H.	Osaka Univ.
Takahashi, A.	Osaka Univ.
Takano, H.	JAERI
Takeuchi, H.	Nagoya Univ.
Tamiya, T.	Hitachi Ltd.
Tamura, T	RIST
Teshigawara, M.	JAERI
Than Win	Tohoku Univ.
Toyokawa, H.	ETL
Tsubosaka, A.	JAERI
Tsukiyama, T.	HEC
Umano, T.	Toshiba Co.
Utsumi, M.	NRIM
Veerapaspong, T.	Tokyo Inst. of Tech.
Wada, H	JNC
Wada, M.	JAERI
Watanabe, T.	KHI
Watanabe, Y	Kyushu Univ.
Watanabe. N.	JAERI
Yamaguchi, M.	HEC
Yamamoto, A.	Kyushu Univ.
Yamamoto, T.	NUPEC
Yamamoto, T.	JAERI
Yamane, T.	JAERI
Yamano, N.	SAEI
Yokoyama, K.	JNC
Yoshida, T.	Musashi Inst. of Tech.
Yoshioka, K.	Toshiba Co.
Yoshizawa, N.	MRI
Zhang Baocheng	EDC
Zukeran, A.	Hitachi Ltd.

This is a blank page.

国際単位系（SI）と換算表

表1　SI基本単位および補助単位

量	名称	記号
長さ	メートル	m
質量	キログラム	kg
時間	秒	s
電流	アンペア	A
熱力学温度	ケルビン	K
物質量	モル	mol
光度	カンデラ	cd
平面角	ラジアン	rad
立体角	ステラジアン	sr

表2　SIと併用される単位

名称	記号
分，時，日	min, h, d
度，分，秒	°, ′, ″
リットル	l, L
トン	t
電子ボルト	eV
原子質量単位	u

1 eV=1.60218×10^{-19}J

1 u=1.66054×10^{-27}kg

表3　固有の名称をもつSI組立単位

量	名称	記号	他のSI単位による表現
周波数	ヘルツ	Hz	s^{-1}
力	ニュートン	N	m·kg/s^2
圧力，応力	パスカル	Pa	N/m^2
エネルギー,仕事,熱量	ジュール	J	N·m
工率，放射束	ワット	W	J/s
電気量，電荷	クーロン	C	A·s
電位，電圧，起電力	ボルト	V	W/A
静電容量	ファラド	F	C/V
電気抵抗	オーム	Ω	V/A
コンダクタンス	ジーメンス	S	A/V
磁束	ウェーバ	Wb	V·s
磁束密度	テスラ	T	Wb/m^2
インダクタンス	ヘンリー	H	Wb/A
セルシウス温度	セルシウス度	℃	
光束	ルーメン	lm	cd·sr
照度	ルクス	lx	lm/m^2
放射能	ベクレル	Bq	s^{-1}
吸収線量	グレイ	Gy	J/kg
線量等量	シーベルト	Sv	J/kg

表4　SIと共に暫定的に維持される単位

名称	記号
オングストローム	Å
バーン	b
バール	bar
ガル	Gal
キュリー	Ci
レントゲン	R
ラド	rad
レム	rem

1 Å=0.1nm=10^{-10}m

1 b=100fm^2=10^{-28}m^2

1 bar=0.1MPa=10^{5}Pa

1 Gal=1cm/s^2=10^{-2}m/s^2

1 Ci=3.7×10^{10}Bq

1 R=2.58×10^{-4}C/kg

1 rad=1cGy=10^{-2}Gy

1 rem=1cSv=10^{-2}Sv

表5　SI接頭語

倍数	接頭語	記号
10^{18}	エクサ	E
10^{15}	ペタ	P
10^{12}	テラ	T
10^9	ギガ	G
10^6	メガ	M
10^3	キロ	k
10^2	ヘクト	h
10^1	デカ	da
10^{-1}	デシ	d
10^{-2}	センチ	c
10^{-3}	ミリ	m
10^{-6}	マイクロ	μ
10^{-9}	ナノ	n
10^{-12}	ピコ	p
10^{-15}	フェムト	f
10^{-18}	アト	a

（注）

1．表1－5は「国際単位系」第5版，国際度量衡局1985年刊行による。ただし，1 eVおよび1 uの値はCODATAの1986年推奨値によった。

2．表4には海里，ノット，アール，ヘクタールも含まれているが日常の単位なのでここでは省略した。

3．barは，JISでは流体の圧力を表わす場合に限り表2のカテゴリーに分類されている。

4．EC閣僚理事会指令ではbar，barnおよび「血圧の単位」mmHgを表2のカテゴリーに入れている。

換算表

力	N(=10^{5}dyn)	kgf	lbf
	1	0.101972	0.224809
	9.80665	1	2.20462
	4.44822	0.453592	1

粘度　1 Pa·s(N·s/m^2)=10 P(ポアズ)(g/(cm·s))

動粘度　1m^2/s=10^{4}St(ストークス)(cm^2/s)

圧力	MPa(=10bar)	kgf/cm^2	atm	mmHg(Torr)	lbf/in^2(psi)
	1	10.1972	9.86923	7.50062×10^3	145.038
	0.0980665	1	0.967841	735.559	14.2233
	0.101325	1.03323	1	760	14.6959
	1.33322×10^{-4}	1.35951×10^{-3}	1.31579×10^{-3}	1	1.93368×10^{-2}
	6.89476×10^{-3}	7.03070×10^{-2}	6.80460×10^{-2}	51.7149	1

エネルギー・仕事・熱量	J(=10^7 erg)	kgf·m	kW·h	cal(計量法)	Btu	ft·lbf	eV
	1	0.101972	2.77778×10^{-7}	0.238889	9.47813×10^{-4}	0.737562	6.24150×10^{18}
	9.80665	1	2.72407×10^{-6}	2.34270	9.29487×10^{-3}	7.23301	6.12082×10^{19}
	3.6×10^6	3.67098×10^5	1	8.59999×10^5	3412.13	2.65522×10^6	2.24694×10^{25}
	4.18605	0.426858	1.16279×10^{-6}	1	3.96759×10^{-3}	3.08747	2.61272×10^{19}
	1055.06	107.586	2.93072×10^{-4}	252.042	1	778.172	6.58515×10^{21}
	1.35582	0.138255	3.76616×10^{-7}	0.323890	1.28506×10^{-3}	1	8.46233×10^{18}
	1.60218×10^{-19}	1.63377×10^{-20}	4.45050×10^{-26}	3.82743×10^{-20}	1.51857×10^{-22}	1.18171×10^{-19}	1

1 cal= 4.18605J（計量法）

= 4.184J（熱化学）

= 4.1855J（15℃）

= 4.1868J（国際蒸気表）

仕事率　1 PS(仏馬力)

= 75 kgf·m/s

= 735.499W

放射能	Bq	Ci
	1	2.70270×10^{-11}
	3.7×10^{10}	1

吸収線量	Gy	rad
	1	100
	0.01	1

照射線量	C/kg	R
	1	3876
	2.58×10^{-4}	1

線量当量	Sv	rem
	1	100
	0.01	1

（86年12月26日現在）

PROCEEDINGS OF THE 1998 SYMPOSIUM ON NUCLEAR DATA NOVEMBER 19–20, 1998, JAERI, TOKAI, JAPAN